

Habilitation à diriger les Recherches
en
SCIENCES DE LA TERRE ET DES PLANÈTES

présenté et soutenu publiquement le XXX XXX 2021 par
JOHN ARMITAGE

Rivers of Melt

**Exploring how physical processes are stored in
the geological record**

Institut de Physique du Globe de Paris
École Doctorale STEP

COMPOSITION DU JURY

Mme.	GOES Saskia	Rapporteur	Professeur, Université de Qeulquechose
M.	MORGAN Jason	Rapporteur	Professeur, Université de Qeulquechose
Mme.	PERSON Geomorph	Rapporteur	Professeur, Université de Qeulquechose
M.	JAUPART Claude	Examinateur	Professeur, Somewhere
Mme.	PERSON Geomorph	Examinateur	Professeur, Nowhere

Remerciements

Je tiens à remercier les membres de mon jury qui m'ont fait l'honneur et le plaisir de participer à cette habilitation.

Table des matières

1	Introduction	3
2	Synthesis of Past Research	5
2.1	Overview	5
2.2	Mantle Processes	5
2.3	Surface Processes	16
2.4	Predicting geological observations	23
2.5	Summary	24
3	Perspectives	25
3.1	Short-Term Research Perspectives	25
3.2	Long-Term Research Perspectives	27
4	Résumé	29
	Education	29
	Employment History	29
	Funding	30
	Awards	30
	PhD Supervision	31
	Masters and Undergraduate Supervision	31
	Teaching	31
	Selected Invited Presentations	31
	Selected Oral Conference Presentations	32
	Invited Seminars	32
	List of publications	33
A	Example Publications Part 1 : Mantle	37
B	Example Publications Part 2 : Surface	137

TABLE DES MATIÈRES

Chapitre 1

Introduction

This thesis for the ‘habilitation à diriger des recherches’ is split into four parts : a summary of my past research, a summary of my future research outlook, my résumé, and ten examples of my research publications. In this document I wish to explore how geological observations reflect processes that occur deep within the planet or deep with in time. In Earth science we are faced with a great difficulty, there are rarely experiments that can recreate the processes that we which to understand. This means we cannot test hypothesis with experiments, but instead we must attempt to infer how the Earth operates. Inference is not a science, rather it is reasoned argument, and this can lead to some interesting debates but also to a lack in scientific rigour.

[Need to expand on this statement here. I cannot leave the last phrase hanging.](#)

My working life has been spent, for the majority of the time, in trying to develop methods that allow hypothesis to be tested against observations. Throughout my career I have tried to replace the impossible experiment with numerical models hat approximate the fundamental processes and predict geological observations. These tools allow inferences, interpretations, to be tested. I have worked with observationas from seismology to sedimentology and the central core of my work has been to test how the Earth works against the information left behind in the rocks.

Why are silicic sediments preserved within Antarctic deep sea sediments ? This is the question that started my research career. Deep sea sediments around Antarctica are anomalously high in silica content, but is this due to enhanced preservation or enhanced productivity ? For a few months I explored the dissolution rates of diatamoceous sediments collected from the Antarctic shelf sea environment, and explored the structure of the diatoms using a scanning electric microscope and Fourier transform infra-red microscopy. No scientific publications came of this study. However, I learnt two things : (1) I am not good in the lab, and (2) I wanted to stay in research. Both remain true today.

My past research is broadly split into two areas. I have focused some time on trying to understand how mantle melting is expressed in surface observations. I have also spent an equal amount of time trying to work out how past climatic change is recorded within sedimentary deposits. It is for this reason that I gave the title ‘Rivers of Melt’. I will roughly divide this thesis into two parts, mantle and surface. I will subsequently pull these two parts together and present the direction I hope my work will take in the coming years.

Chapitre 2

Synthesis of Past Research

2.1 Overview

In the last decade and more I have worked on a diverse range of projects and problems. These problems are woven together by a desire to understand how the Earth works from observations. Generally, my research sits in two categories : mantle processes and surface processes. In some cases, notably work I did in collaboration with Rob Duller and Stefan Schmalholz in 2014 ([Armitage et al., 2014](#)), and a collaboration with Miguel Andrés-Martínez, Marta Pérez-Gussinyé, and Jason Morgan ([Andrés-Martínez et al., 2019](#)), these two areas have combined and we have looked at the connectivity between surface processes and the upper mantle. In this Chapter I will however focus on the two areas as separate cases, and bring forward my overall aim, which is to use observations to build an understanding of the processes at play. At the end of the thesis there are two annexes. In Annex A I include five example publications that focus on mantle processes, and in Annex B I include five example publications that focus on surface processes. These publications should expand and compliment the summary of my past research.

There is one notable omission in this synthesis of my research, that I want to mention up front : intracratonic basins. These long-lived and exceptionally dull sedimentary basins exist across every continent, including the well known Paris Basin. With Philip Allen, I developed a theory for how they form : by exceptionally slow and long-lived extension ([Armitage and Allen, 2010; Allen and Armitage, 2012](#)). Subsequently with Claude Jaupart, Loïc Fourel, and Francis Lucaleau we explored how subsidence within these basins is further modified by convective instabilities at the margins of continental lithosphere ([Armitage et al., 2013; Lucaleau et al., 2015](#)). Intracratonic basins, while being a favourite of mine, do not form part of this thesis and shall not appear in the story developed below.

2.2 Mantle Processes

Observations from seismic arrivals and rock geochemistry have, for decades, been used to infer mantle conditions both at large depths and throughout the Earth's history. Below regions of active volcanism, such as La Réunion or Afar, Africa, there are regions of slow seismic velocity (e.g. [Mazzullo et al., 2017; Bastow et al., 2005](#)). Such regions of low seismic velocity can be interpreted to be due to increased mantle temperature relative to the background and the retention of melt within the rock matrix (e.g. [Goes et al., 2012; Armitage et al., 2015b](#)). The lava erupted from the volcanic massifs at locations such as these have a major element oxide composition that is high in magnesium, and indicative of melting at high temperatures (e.g. [Rooney et al., 2012; Herzberg et al., 2007](#)). Isotope ratios within the

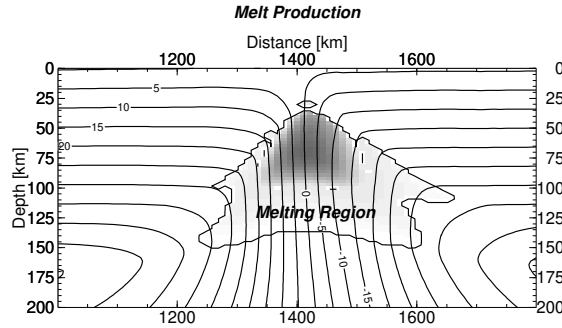


FIGURE 2.1 – Diagram of the zone of partial melting with stream lines of mantle flow.

erupted lavas can be used to infer the rate of melt migration (e.g. [Elliot and Spiegelman, 2014](#)). These are examples of surface observations that can be used to infer the structure of the mantle.

For the geological past images of the mantle generated from the inversion of seismic arrivals are less useful. Here we have to look at the structure of the crust and the composition of exposed basaltic rocks. A classic example is the North Atlantic Igneous province. Here for example drill cores recovered from the East Greenland margin contained basaltic glasses with very high magnesium oxide concentrations ([Fitton et al., 1998](#)), which can be interpreted to be due to very high mantle temperatures at the time of decompression melting.

[Perhaps should expand a bit on the observations, this is quite brief.](#)

I have worked on six key geological regions : the North Atlantic volcanic margins, the South Atlantic volcanic margins, the India-Seychelles margins, the East African Rift, Icelandic volcanism, and La Réunion. The first four regions were previously summarised in [Armitage and Collier \(2018\)](#). Here I will update the discussion on Afar based on more recent publications, and add recent work on Iceland and La Réunion. First I will describe the physical model used to model these regions.

2.2.1 A simplified model of decompression melting

Decompression melting occurs when the mantle loses pressure due to vertical movement and the rock matrix crosses the solidus (Figure 2.1). To numerically model this process we need a set of continuum equations, which in this case are a set of modified Stokes equations. The conservation of momentum can be expressed as (e.g. [Armitage et al., 2013](#)),

$$-\frac{\partial \tau_{ij}}{\partial x_j} + \frac{\partial p}{\partial x_i} = -\Delta \rho g \lambda_i, \quad (2.1)$$

where τ is stress, p is pressure, $\Delta \rho$ is the density change due to thermal and chemical change (melting), g is the acceleration due to gravity, and λ is a unit vector in the vertical direction.

The conservation of energy can be expressed as,

$$mL + \frac{\partial T}{\partial t} + \bar{v}_i \frac{\partial T}{\partial x_i} - \kappa \frac{\partial^2 T}{\partial x_i^2} = 0, \quad (2.2)$$

where m is the melt production rate, L is the latent heat of fusion, T is temperature, \bar{v} is the average velocity of the solid mantle and melt, and κ is the thermal diffusion coefficient.

The latent heat is given by $L = T\Delta S/C_p$, where ΔS is the entropy change due to melting and C_p is the heat capacity. The average velocity is given by (Scott, 1992),

$$\bar{v}_i = (1 - \phi)v_s + \phi v_l, \quad (2.3)$$

where ϕ is porosity, v_s is the solid mantle velocity, and v_l is the melt velocity. The conservation of mass for the system can be written as [I am assuming incompressible flow here, that is $\rho = \text{constant}$, but this is not the case. Need to explain.],

$$\frac{\partial}{\partial x_i} \bar{v}_i = 0 \quad (2.4)$$

In the case where there the melt phase is not explicitly modelled, the three equations that make a modified Stokes flow problem can be solved, as I have done throughout my career, using finite differences (e.g. Armitage et al., 2018b), finite elements (e.g. Armitage et al., 2008), or finite volumes (e.g. Civiero et al., 2019).

If melt is to be included then the conservation of the liquid phase is written as,

$$\partial \frac{\partial \phi}{\partial t} + \frac{\partial}{\partial x_i} (\phi v_l) = m. \quad (2.5)$$

In this case to create a closed set of equations we need to relate the solid mantle velocity to the liquid melt velocity. If we assume that the melt percolates through a porous medium we can assume that the flows can be related by Darcy's law,

$$\phi(v_l - v_s) = \frac{k_0 \phi^n}{\eta_l} \left(\Delta \rho_m g + \frac{\partial P}{\partial x_i} \right), \quad (2.6)$$

where k_0 is the permeability coefficient (not well constrained), n is the exponent on the assumed power relation between permeability and porosity, $\Delta \rho_m$ is the density difference between melt and the solid mantle, and P is the pore pressure. I will simplify equation 2.6 by assuming that the compaction length scale is small, the 'zero-compaction length approximation' (Ribe, 1985). This means that Darcy's law becomes,

$$\phi(v_l - v_s) = \frac{k_0 \phi^n}{\eta_l} \Delta \rho_m g, \quad (2.7)$$

and by substituting for the average velocity (equation 2.3) we get,

$$v_l - \bar{v} = \frac{k_0 \phi^{n-1}}{\eta_l} \Delta \rho_m g \lambda. \quad (2.8)$$

This allows the substitution for v_l within equation 2.5. However there remains one fundamental unknown, and that is the relationship between permeability and porosity. The value of n in equation 2.6 is estimated to between 2 and 3. The most recent laboratory experiments would suggest that for mantle rock $n = 2.6 \pm 0.2$ (Miller et al., 2014). Mathematically it is more expedient to assume that n is an integer, therefore it has been assumed to be either 2 (e.g. Scott and Stevenson, 1989; Goes et al., 2012) or 3 (e.g. Hewitt, 2010; Armitage et al., 2019). Assuming $n = 3$ the conservation of melt can be written as,

$$\frac{\partial \phi}{\partial t} + \bar{v} \frac{\partial \phi}{\partial z} + \frac{3k_0 \Delta \rho_m g}{\eta_l} \phi^2 \left(1 - \frac{4}{3}\phi \right) \frac{\partial \phi}{\partial z} = m. \quad (2.9)$$

This non-linear partial differential can be solved numerically using various iterative techniques (e.g. Armitage et al., 2019; Franken et al., 2020).

The conservation of energy and mass are coupled by the melt production rate, which is calculated from the temperature difference above the solidus. This solidus is a function of

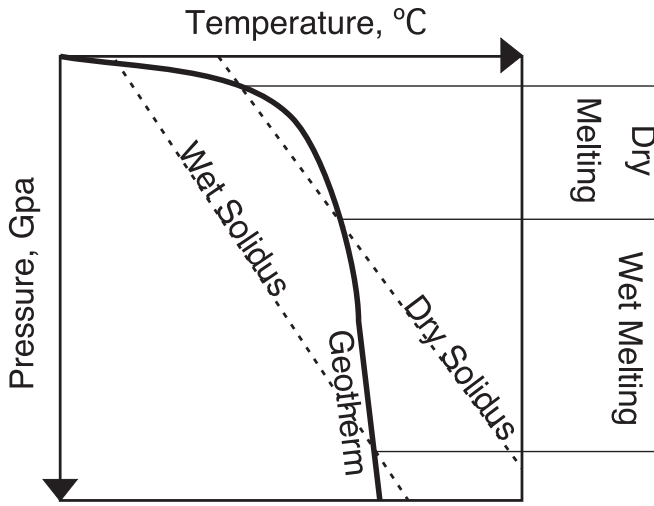


FIGURE 2.2 – Diagram of the mantle geotherm crossing the wet and dry solidus.

volatile content, depletion, temperature, and pressure (Figure 2.2). In the energy balance I ignore the loss of heat due to decompression, but the adiabatic gradient needs to be accounted for within the thermodynamic balance for the melting equations. Assuming the mantle is dehydrated, no volatiles, it is calculated as,

$$T_{Sdry} = T_{S0} + \frac{\partial T_S}{\partial F}|_p F + \left(\frac{\partial T_S}{\partial p}|_F + \frac{\alpha T_0}{\rho C_p} \right) p, \quad (2.10)$$

where $\partial T_S / \partial F|_p$ is the solidus depletion gradient, F is depletion, $\partial T_S / \partial P|_F$ is the solidus pressure gradient, α is the coefficient of thermal expansion, T_0 is the mantle potential temperature, C_p is the heat capacity, and p is pressure. The solidus is assumed to deepen in the presence of water,

$$T_{Swet} = T_{Sdry} + K (D_{H_2O} C_{H_2O})^\gamma, \quad (2.11)$$

where the coefficients K and γ are from the parametrisation of Katz et al. (2003), D_{H_2O} is the partition coefficient for water, and C_{H_2O} is the concentration of water within the solid mantle. Therefore the melt productivity is given by,

$$m = \frac{\Delta T}{L + \frac{\partial T_S}{\partial F}|_P + \frac{\partial T_S}{\partial F}|_{H_2O}}, \quad (2.12)$$

where $\Delta T = T - T_S$ is the temperature difference between the mantle and the solidus, and $\partial T_S / \partial F|_{H_2O}$ is the solidus depletion gradient during the melting of a hydrated mantle. This is calculated using the chain rule,

$$\frac{\partial T_S}{\partial F}|_{H_2O} = \frac{\partial T_S}{\partial C_{H_2O}} \frac{\partial C_{H_2O}}{\partial F}. \quad (2.13)$$

The change in water composition as a function of depletion is calculated assuming a mass balance between the partitioning of water between the solid and melt phase,

$$\frac{\partial C_{H_2O}}{\partial F} = -C_{H_2O} \frac{1}{D_{H_2O}} (1 - F)^{\frac{1}{D_{H_2O}} - 2} \quad (2.14)$$

and the gradient in solidus with water composition is from equation 2.11,

$$\frac{\partial T_S}{\partial C_{H_2O}} = \gamma K (D_{H_2O} C_{H_2O})^{\gamma-1} \quad (2.15)$$

To track the composition of the melt I assume disequilibrium melting, where the conservation of the solid composition, C_s , is given as (Spiegelman, 1996),

$$\frac{\partial C_s}{\partial t} + v_s \frac{\partial C_s}{\partial z} = \left(\frac{1}{D} - 1 \right) \frac{C_s m}{1 - \phi}, \quad (2.16)$$

and the melt composition, C_l , can be written as follows (Spiegelman, 1996),

$$\frac{\partial C_l}{\partial t} + v_l \frac{\partial C_f}{\partial z} = \left(\frac{C_s}{D} - C_l \right) \frac{m}{\phi}. \quad (2.17)$$

The melt composition is calculated from the solid composition and knowledge of the partition coefficient D . The partition coefficient is a function of the mineral phase stability (McKenzie and O’Nions, 1991),

$$D = f_{ol} D_{ol \rightarrow melt} + f_{opx} D_{opx \rightarrow melt} + f_{cpx} D_{cpx \rightarrow melt} + f_X D_{X \rightarrow melt} \quad (2.18)$$

where f is the proportion of each mineral within plagioclase, spinel, and garnet peridotite, D_{ol} , etc, are the partition coefficients for each phase into melt, and X represents plagioclase, spinel and garnet, respectively (e.g. Armitage et al., 2011a, 2018b).

The above set of equations, which are arguably an over simplification, allow for the tracking of key parameters that control the surface seismic and chemical observations. Melt depletion, porosity, temperature and depth can be converted into major, trace and rare Earth element compositions for comparison with observations from erupted lava and the P-wave velocity of the crust (Figure 2.3; Armitage et al., 2008, 2009, 2010, 2011a, 2015b, 2018b, 2019). Temperature, pressure, composition and porosity can be converted to density, bulk, and shear modulus to then be converted into synthetic tomographic images (Figure 2.4; Goes et al., 2012; Armitage et al., 2015b, 2018b, 2019). In the following sections I describe how these methods have been used to understand the mantle structure from the observations.

2.2.2 East African Rift

Active continental break-up in Afar is volcanic in nature, as the volcanism is due to anomalously hot mantle below this region of slow extension (Figure 2.3d; Armitage et al., 2015b). Along the region of extension within the East African Rift, there is a transition from regions of wide extension, where faulting is distributed over a large area, such as in the Danakil depression, to narrower extension towards the south and into the Main Ethiopian Rift (Figure 2.5). The causes of this narrowing have been attributed to pre-existing weak zones within the lithosphere fabric (Keranen et al., 2009). However, the width of the region of extension has been shown, numerically, to depend on the rheological laws chosen for the crust and lithosphere (e.g. Buck, 1991; Brun, 1999; Brune et al., 2017). Furthermore, the timing of the onset of volcanism is affected by the crustal strength within numerical models (Ros et al., 2017). Therefore, it is possible that the structure of early rifting in the northern East African Rift is due to crustal rheology rather than an unknown inheritance.

In collaboration with Kenni Petersen, we developed a 2D model of visco-elasto-plastic deformation of the upper mantle (MESS, see <https://bitbucket.org/johnjarmitage/mess>) that includes melting and in particular the prediction of melt composition (Petersen et al., 2015; Armitage et al., 2018b). By varying the strength of the crust we showed that evolution of the depletion of lavas in light trace elements is a function of the strength of the crust. When the crust is strong, it thins rapidly and extension localises creating a narrow rift. This is analogous to there being only a thin lithospheric lid on top of the zone of partial melting. This thin lid does not suppress the development of a ‘triangular’ zone of partial melting (as shown in Figures 2.1 and 2.3). The result is that light trace elements,

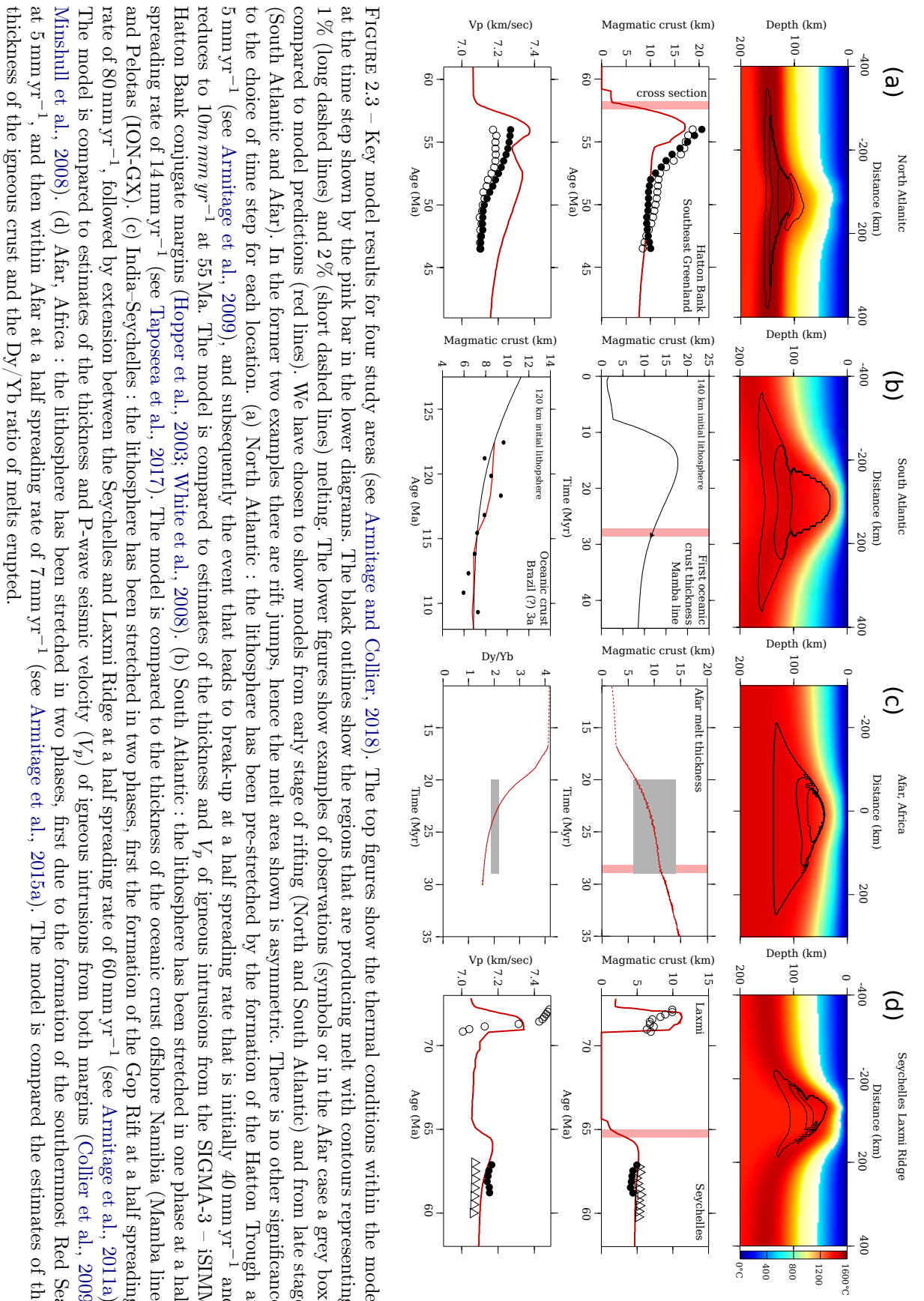


FIGURE 2.3 – Key model results for four study areas (see Armitage and Collier, 2018). The top figures show the thermal conditions within the model at the time step shown by the pink bar in the lower diagrams. The black outlines show the regions that are producing melt with contours representing 1% (long dashed lines) and 2% (short dashed lines) melting. The lower figures show examples of observations (symbols or in the Afar case a grey box) compared to model predictions (red lines). We have chosen to show models from early stage of rifting (North and South Atlantic) and from late stage (South Atlantic and Afar). In the former two examples there are rift jumps, hence the melt area shown is asymmetric. There is no other significance to the choice of time step for each location. (a) North Atlantic : the lithosphere has been pre-stretched by the formation of the Hatton Trough at 5 mm yr^{-1} (see Armitage et al., 2009), and subsequently the event that leads to break-up at a half spreading rate that is initially 40 mm yr^{-1} and reduces to 10 mm yr^{-1} at 55 Ma. The model is compared to estimates of the thickness and V_p of igneous intrusions from the SIGMA-3 – iSIMM Hatton Bank conjugate margins (Hopper et al., 2003; White et al., 2008). (b) South Atlantic : the lithosphere has been stretched in one phase at a half spreading rate of 14 mm yr^{-1} (see Taposee et al., 2017). The model is compared to the thickness of the oceanic crust offshore Namibia (Mamba line) and Pelotas (ION-GX). (c) India–Seychelles : the lithosphere has been stretched in two phases, first the formation of the Gop Rift at a half spreading rate of 80 mm yr^{-1} , followed by extension between the Seychelles and Laxmi Ridge at a half spreading rate of 60 mm yr^{-1} (see Armitage et al., 2011a). The model is compared to estimates of the thickness and P-wave seismic velocity (V_p) of igneous intrusions from both margins (Collier et al., 2009; Minshull et al., 2008). (d) Afar, Africa : the lithosphere has been stretched in two phases, first due to the formation of the southernmost Red Sea at 5 mm yr^{-1} , and then within Afar at a half spreading rate of 7 mm yr^{-1} (see Armitage et al., 2015a). The model is compared the estimates of the thickness of the igneous crust and the Dy/Yb ratio of melts erupted.

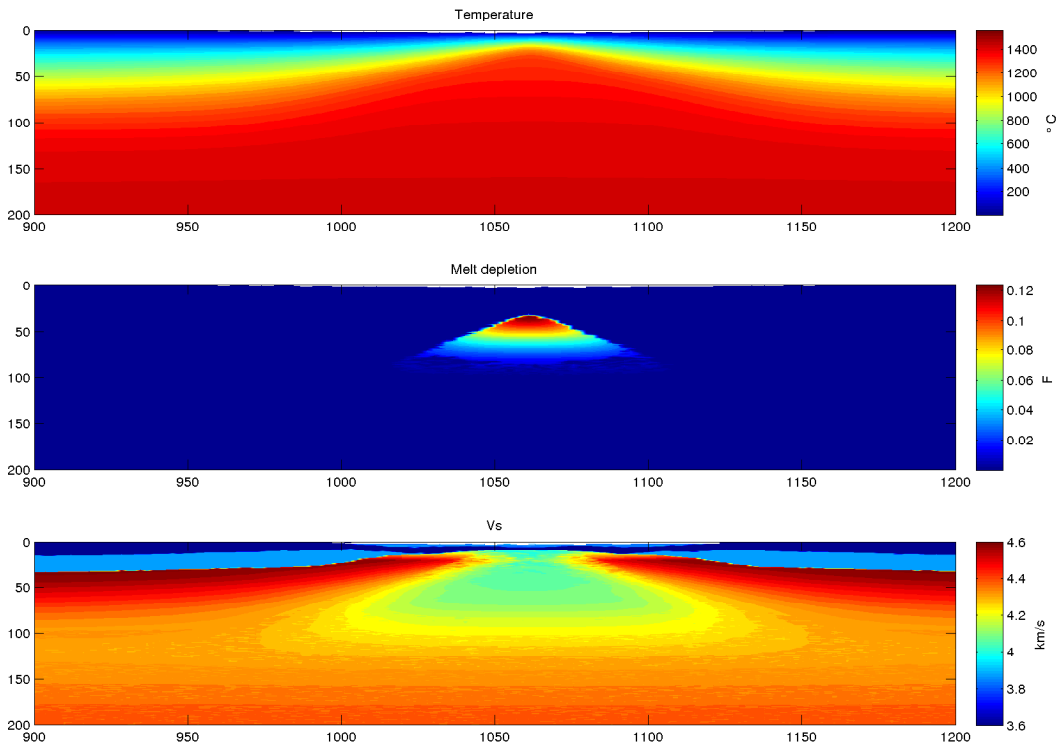


FIGURE 2.4 – Predicted thermal structure, melt depletion, and S-wave seismic velocity after 25 Myr of extension for with an extension rate of 5 mm yr^{-1} and mantle potential temperature of 1350°C . (a) Temperature, (b) melt fraction, and (c) S-wave seismic velocity. Figure taken from Armitage et al. (2018b).

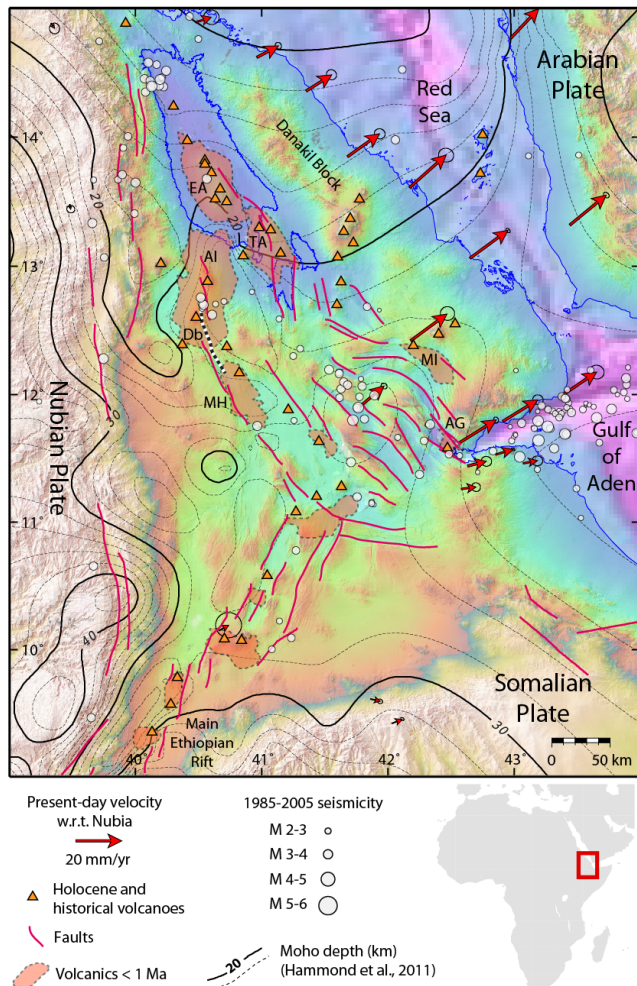


FIGURE 2.5 – Map of the Afar Rift zone and the northern Main Ethiopian Rift showing elevation in the colour scale and contours of the depth to the Moho in kilometres from Hammond et al. (2011). The three key volcanic locations, Erta Ale, Dabbahu and Asal, are labelled in bold text. The other labelled volcanics in red that are less than 1 Ma are : TA – Tat Ali, Al – Alaita, MH – Manda-Harraro and MI – Manda-Inakir. Velocities are from Nooner et al. (2009) and Reilinger and McClusky (2011).

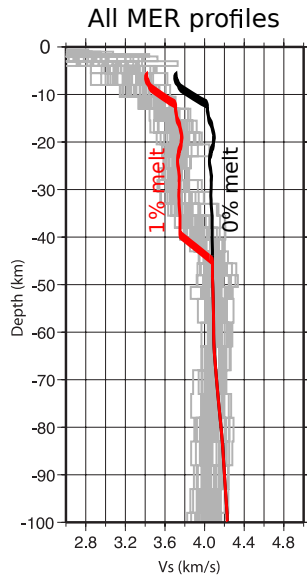


FIGURE 2.6 – Comparison of the predicted S-wave seismic velocity from the forward model with a strong lower crust (Figure 2.4c), and the ensemble vertical profiles from the joint inversion of Rayleigh waves and receiver functions below the Main Ethiopian Rift (Keranen et al., 2009). The black line is the model V_S assuming no melt storage, the red line assumes that 1% melt is stored above 40 km depth.

such as lanthanum (La), are depleted rapidly with respect to heavier trace elements, such as ytterbium (Yb). If however the crust is weak, extension is not localised and a thicker lithospheric lid rests upon the zone of partial melting. This results in a slower reduction in light relative to heavy trace elements within the erupted lava (Armitage et al., 2018b).

When this model was applied to the Main Ethiopian Rift it was found that in order to recreate the observed lava chemistry, only a model with a strong crust could achieve sufficient melt generation. Furthermore, when the predicted upper mantle structure was converted to S-wave velocity (Figure 2.4), it was found that the model velocities were within the range of the observed 1D inversions (Figure 2.6 black line). However, if it is assumed that 1% melt is stored within the lithosphere above a depth of 40 km, then the shallow structure can be even better explained. The 2D code MESS does not include melt transport (e.g. equation 2.5) and therefore the hypothesis that there is significant melt storage within the uppermost lithosphere below the Main Ethiopian Rift has not yet been tested. Yet, in the section below on Iceland, I will demonstrate how this hypothesis could be explored in a future study.

The volcanic nature of the East African Rift is due to the high mantle temperatures in this region. There has been significant debate as to the source of the anomalously hot mantle. Interpretations of inverse seismic models from the region would suggest that there are multiple (> 3) low S- and P-wave anomalies below the northern East African Rift (Chang and Van der Lee, 2011; Hammond et al., 2013; Emry et al., 2009, e.g.). In collaboration with Chiara Civiero and Saskia Goes, we tested this interpretation. From running forward models of the viscous flow of the upper mantle, converting the temperature and pressure to seismic velocity and then re-resolving the structures to the resolution of the tomographic images, we found that indeed the inversions are indicative of multiple small plumes, or ‘plumelets’ (Civiero et al., 2019). To create these plumelets the models required that they were seeded with an initial condition of buoyant hot material inserted at the base of the model. This layer then destabilises in the form of a Rayleigh Taylor instability, giving rise to multiple regions of slow seismic velocity. The implication of this study is that the volcanism within the northern East African Rift is due to material leaking from the deep mantle into the

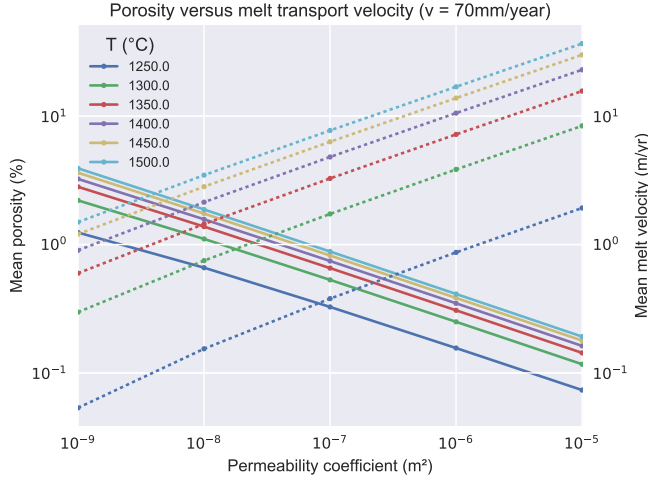


FIGURE 2.7 – Logarithmic plot of the variation in modelled porosity (solid) and melt flow velocity (dashed) with permeability coefficient and temperature, with up-welling velocity constant at 70 mm yr^{-1} . The relationship between porosity and mean melt flow velocity is inversely proportional as a function of the permeability coefficient, and proportional as a function of temperature. Figure is from Franken et al. (2020).

upper mantle.

2.2.3 Iceland

The retention of melt within the upper mantle has been cited as causing seismic discontinuities and regions of low velocity observed below volcanic islands, rift zones, and mid-ocean ridges (e.g. Forsyth et al., 1998; Harmon et al., 2009; Rychert et al., 2012, 2014). Typical estimates of the quantity of melt range from 0.1 % to 2 %. The low seismic velocities below Iceland can be explained by the presence of high temperatures but discontinuities required by receiver function inversions would require an extra $\sim 1\%$ melt (Rychert et al., 2018). High melt retention would naturally imply low melt velocities and low permeability (Figure 2.7; Weatherley and Katz, 2016; Franken et al., 2020). However, forward modelling of decompression melting below both the East Pacific Rise and Afar (Figure 2.3c; Goes et al., 2012; Armitage et al., 2015a), suggest that high melt retention, $> 0.5\%$ is unlikely.

The glaciers on Iceland have been reducing in size since the last glacial maximum. Iceland experienced a rapid deglaciation around ten thousand years ago (Figure 2.8). The rapid depressurisation of the upper mantle due to this loss in surface load could lead to a significant increase in decompression melting (Jull and McKenzie, 1996). This is in line with outcrop evidence of the volume and composition of lava erupted since the late-Pleistocene (MacLennan et al., 2002; Sinton et al., 2005; Eksinchol et al., 2019). However, if the observed change in lava composition and volume estimates were caused by deglaciation, the transport of melt from the zone of partial melting to the surface must be rapid, and rapid melt transport implies low melt retention (Figure 2.7). This is therefore again at odds with the interpretation of high melt retention derived from seismic inversions.

To understand if the observed change in lava composition is due to deglaciation I worked with Kenni Petersen, David Fergusson, and Tim Creyts, to create a 120 kyr history of ice sheet growth and decay on Iceland (Figure 2.8b) and develop a 1D model that can predict eruption rates, lava compositions, and melt retention as the surface load

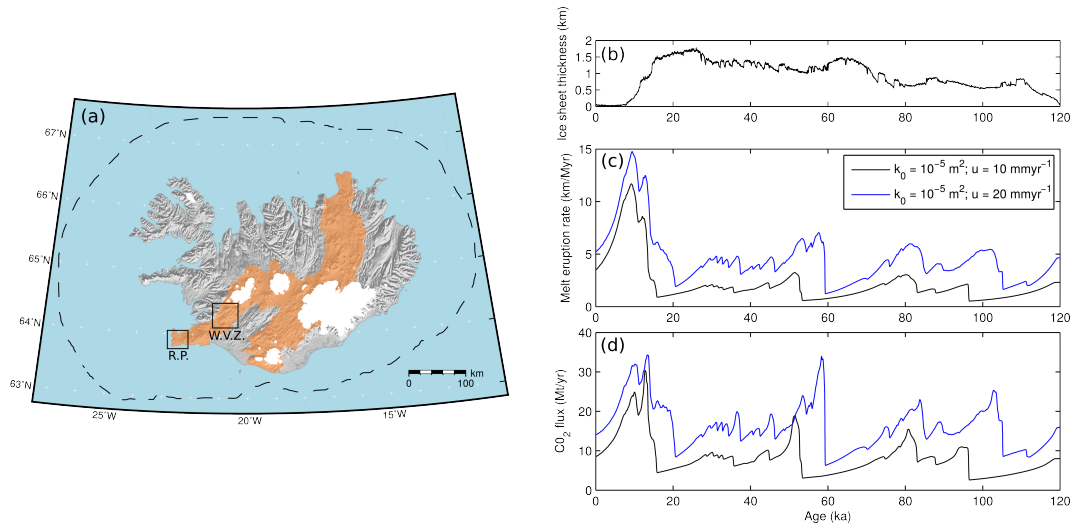


FIGURE 2.8 – Response of the model to periodic and observed ice sheet thickness changes of the last 120 ka. (a) Map of Iceland showing the locations of the volcanic rift zones in orange and the maximum extent of the ice sheet at the last glacial maximum (dashed line). The boxes show the location of the Reykjanes Peninsular (R. P.) and the Western Volcanic Zone (W. V. Z.). (b) The ice sheet thickness predicted from the ice sheet model M1 over the last 120 ka. (c) Melt eruption rate and (d) carbon flux response to the step change in ice sheet thickness : black line, an upper mantle permeability coefficient of $k_0 = 10^{-5} \text{ m}^2$ and up-welling velocity of 10 mm yr^{-1} , and blue line, an up-welling velocity of 20 mm yr^{-1} .

changes (<https://bitbucket.com/johnjarmitage/melt1d-icesheet/>; Armitage et al., 2019). From exploring the physically plausible parameter space, we found that deglaciation would indeed impact lava eruption rates if the mantle permeability is high (Figure 2.8c and d). In order to recover a system response that matched the estimated eruption rates from outcrops, and the observed neodymium (Nd) concentrations the permeability of the mantle $k_\phi = k_0\phi$ needs to be on the order of 10^{-14} m^{-2} , melt retention of $\sim 0.1\%$ (Armitage et al., 2019).

This model result has implications for volcanic CO₂ degassing post deglaciation, that I will not go into detail on here (see Armitage et al., 2019). The model result also has implications for assumptions of melt retention within the upper mantle. As stated above, low seismic wave speed anomalies within the mantle, inferred from inverse models, are often interpreted to be due to high melt retention within the mantle. This, I have demonstrated, is not possible if we also simultaneously have a mantle melting system that responds rapidly to deglaciation, and potentially sea level change (Huybers and Langmuir, 2009). Therefore, we need to change our interpretations and think harder as to why inverse models suggest sharp mantle seismic discontinuities and low velocities below regions of volcanism.

2.2.4 La Réunion

Building on the conclusions on the low retention of melt implied by the reactivity of the melting system to deglaciation, in collaboration with Thijs Franken, Nobu Fuji, and Alexandre Fournier, we attempted to understand better how melt retention impacts the seismic waveform. A strong low velocity region is imaged in tomographic models below La Réunion (Mazzullo et al., 2017), and we could be tempted to assume it is due to high melt retention. However, by creating a 1D forward model of melt production and retention we can propagate numerically a seismic wave through this 1D system. The arrival can then be

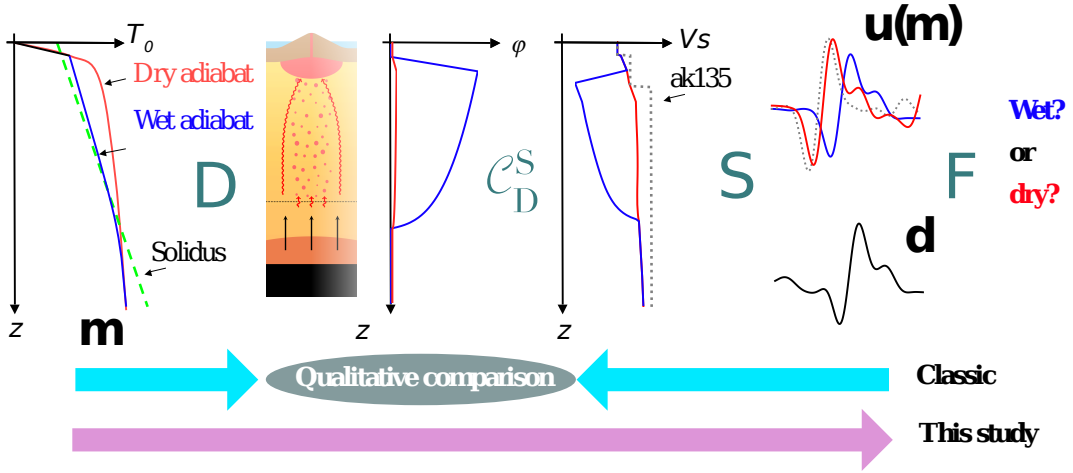


FIGURE 2.9 – Conceptual schema of the waveform seismic filtering strategy (see Franken et al., 2020). On the top from the left to right : we first generate (\mathcal{D}) geodynamical scenarios with different initial conditions \mathbf{m} (T_0 for example : wet and dry in blue and red, respectively) in order to obtain a steady-state snapshot (vertical variation of porosity ϕ for example). We then translate ($\mathcal{C}_{\mathcal{D}}^S$) the set of geodynamical parameters such as ϕ to a set of seismological parameters such as V_S . We then generate (\mathcal{S}) seismic waveforms \mathbf{u} to look for the sensitivity of \mathbf{u} with respect to \mathbf{m} . We define a filter \mathcal{F} that can distinguish the different scenarios \mathbf{m} : we then analyse the observed data \mathbf{d} to conclude the preferred geodynamical scenario. Classical approaches try to fit the intermediate parameter sets such as seismic velocity structure or porosity structure that has unknown error bars due to a series of inversion procedures.

compared to the observed waveforms, to try and find a best fit. This approach is more fully described in the PhD thesis of Thijs Franken, and is summarised in Figure 2.9.

We ran models through the full parameter space for 1D melting and melt transport, and found that only a select few models could match the travel time difference and the S-to-P travel time differential when synthetic waveforms were compared to the observations at the RER Geoscope permanent station. These few models implied either high melt retention (low porosity) and cold mantle temperature ($\sim 1250^\circ\text{C}$), or low melt retention (high porosity) and hot mantle temperature ($\sim 1450^\circ\text{C}$). The best fit model would suggest conditions below La Réunion of melt retention of $<0.28\%$ and high melt extraction rates of $8.37\text{--}18.35 \text{ m yr}^{-1}$ (Franken et al., 2020). Which would imply a melting system that can react rapidly, geologically speaking, to change.

2.3 Surface Processes

The surface of the Earth contains the most time-sensitive record of the past. Accumulations of sediment can give information about change in climate, tectonics and even the mantle throughout geological time. However, as with the fields of seismology and geochemistry, the observations require interpretation to extrapolate how physical processes have impacted the geological record. As with melt generation and transport, sediments are created and transported to create the final observation : a stratigraphic section. Over the last decade I have developed numerical models to try and predict observations of grain size change in stratigraphic units. In this section I will first introduce the mathematical construct for sediment transport and landscape evolution, and I will then describe two regions where I have used these models to try and understand what caused the observed sediment deposition : the Eocene Escanilla system in Spain and the Book Cliffs in central USA.

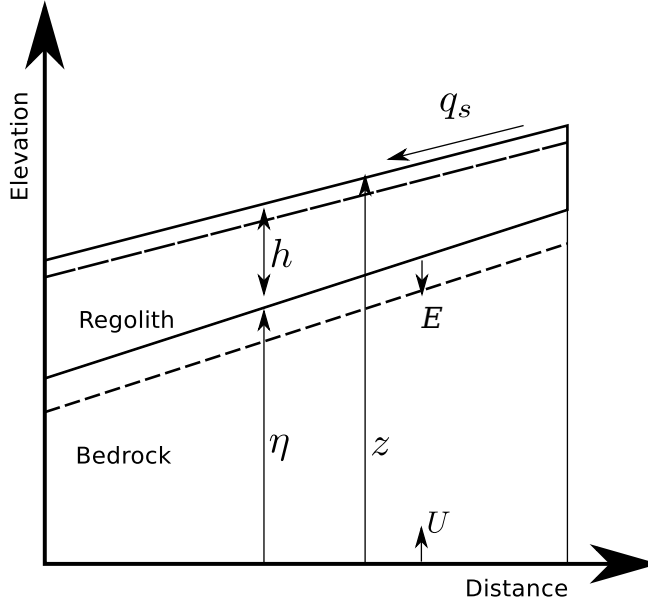


FIGURE 2.10 – Diagram showing the conservation of mass within a 2-D domain, where mass enters the system through uplift, U (units of m s^{-1}), and exists as sediment transported, q_s ($\text{m}^2 \text{s}^{-1}$) out of the domain. E (m s^{-1}) is the rate of production of regolith, h (m) is the thickness of regolith, η (m) is the bedrock elevation and z (m) is the total elevation.

2.3.1 A simplified model of surface processes

Following Dietrich et al. (2003) I define a landscape of elevation z composed of bedrock, thickness η (units of m), and a surface layer of sediment with thickness h (units of m; see Figure 2.10). This landscape is forced externally through uplift rate U (units of myr^{-1}). The bedrock is transferred into sediment through erosion at a rate E (units of myr^{-1}) and the sediment is transported across the system with a flux q_s (units of $\text{m}^2 \text{yr}^{-1}$). Assuming that the density of sediment and bedrock are equal, then the change in bedrock thickness is,

$$\partial_t \eta = U - E, \quad (2.19)$$

and the rate of change in sediment thickness is,

$$\partial_t h = E - \partial_x q_s. \quad (2.20)$$

It then follows that the rate of change in landscape elevation is,

$$\partial_t z = \partial_t \eta + \partial_t h. \quad (2.21)$$

To solve the mass balance I will make a strong assumption : there is always a supply of transportable sediment. Then I can follow through with the summation in equation 2.21 giving,

$$\partial_t z = U - \partial_x q_s. \quad (2.22)$$

This may be appropriate when modelling the transport of sediment along the river bed and when considering the formation of alluvial fans (e.g. Paola et al., 1992; Whipple and Tucker, 2002; Guerit et al., 2014). In the absence of surface water we can assume that sediment flux is simply a function of local slope $q_s = -\kappa \partial_x z$. In the presence of flowing water then the sediment flux is a function of the flowing water and local slope $q_s = -cq_w^\delta (\partial_x z)^\gamma$ where c is the transport coefficient (units $(\text{m}^2 \text{yr}^{-1})^{1-n}$), q_w is the water flux per unit width (units

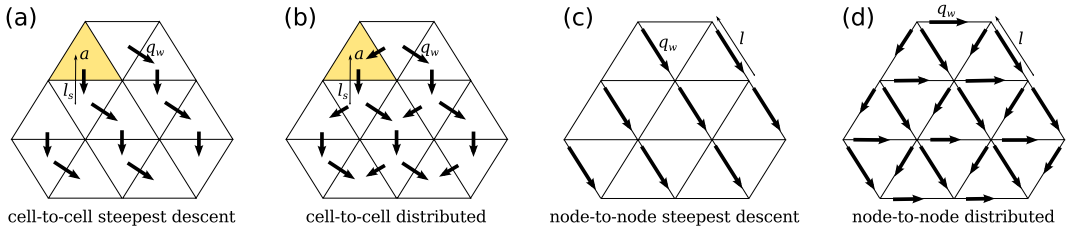


FIGURE 2.11 – Diagram of flow routing from cell-to-cell and node-to-node for either a single flow direction (SFD) and a multiple flow direction (MFD) algorithm weighted by the relative gradient.

$\text{m}^2 \text{yr}^{-1}$) and the exponents $\delta > 1$ and $\gamma \geq 1$ are dependent on how sediment grains are transported along the bed (Smith and Bretherton, 1972; Paola et al., 1992). Furthermore, $\delta > 1$ is required to create concentrated flow (Smith and Bretherton, 1972). The change in landscape elevation is then given by,

$$\partial_t z = U + \partial_x (\kappa \partial_x z + cq_w^\delta (\partial_x z)^\gamma). \quad (2.23)$$

which can be written as,

$$\partial_t z = U + \partial_x \left([\kappa + cq_w^\delta (\partial_x z)^{\gamma-1}] \partial_x z \right). \quad (2.24)$$

Equation 2.24 is non-linear in the case that $\gamma \neq 1$. In deriving this equation of elevation change due to sediment transport we have simply summed the two terms for sediment flux, the linear and potentially non-linear slope dependent terms. This summation has been done as it is the simplest way to generate landscape profiles that have the desired convex and concave elements observed in natural landscapes (Smith and Bretherton, 1972).

To solve this equation in one dimension I assume that the water flux is a function of the precipitation transported down the river network. The water collected is taken from the upstream drainage area, a , which is related to the main stream length, l , by $l \propto a^h$ where h is the exponent taken from the empirical Hack's law (Hack, 1957). The main stream length is related to the longitudinal length of the catchment by, $l \propto x^d$ where $1 \leq d \leq 1.1$ (Tarboton et al., 1990; Maritan et al., 1996). Therefore, we can write that $x \propto a^{h/d}$, and the water flux is the precipitation rate, α units (m yr^{-1}), multiplied by the length of the drainage system,

$$q_w = k_w \alpha x^p \quad (2.25)$$

where k_w is the width coefficient (units m^{1-p}), and $p = d/h$. Furthermore it is observed that river catchments are typically longer than they are wide, and so $p < 2$ (Dodds and Rothman, 2000). Therefore given that $0.5 < h < 0.7$ (e.g. Rigon et al., 1996) then $1.4 < p < 2$, and the transport model (equation 2.24) becomes,

$$\partial_t z = U + \partial_x \left([\kappa + ck_w \alpha^\delta x^{p\delta} (\partial_x z)^{\gamma-1}] \partial_x z \right). \quad (2.26)$$

To solve equation 2.24 over a 2-D domain requires an algorithm to route surface flow down the landscape. Water can be routed from cell-to-cell, where precipitation is collected over the area of each cell, sent downwards, and accumulates. In this cell-to-cell configuration the water flux has units of length squared per unit time and is given by :

$$q_w[\text{cell}] = \frac{\alpha a}{l_s}, \quad (2.27)$$

where α is precipitation rate, a is the cell area, and l_s is the length from cell centre to cell centre down the steepest slope (Figure 2.11a and b). This gives a water discharge per unit

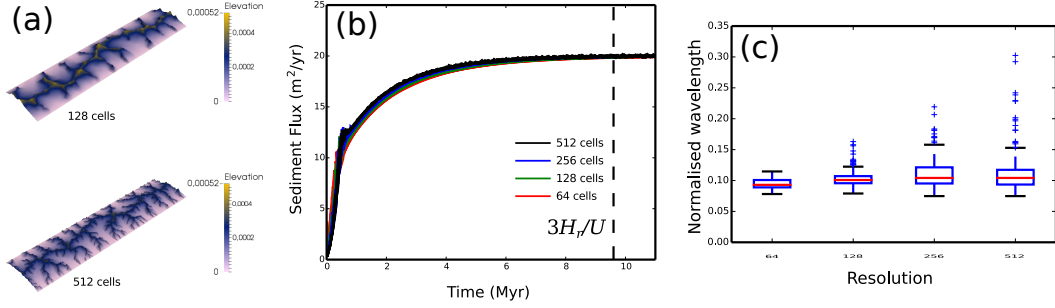


FIGURE 2.12 – A landscape evolution model (see Armitage, 2019). (a) Dimensionless elevation from the node-to-node flow routing landscape evolution model with different flow routing algorithms at different numerical resolutions after a dimensionless run time of 1.563×10^{-6} (5 Myr), with an aspect ratio of 4×1 . (b) Dimensional sediment flux that exits the model domain. (c) Box whisker plots of the dimensionless valley-to-valley wavelength for each model for different resolutions, where the number of cells along the y-axis is shown.

length, which has the advantage of not having to explicitly state the sub-grid width of the flow (Simpson and Schlunegger, 2003). However, implicitly this implies that the flow is over the width of a cell. An alternative is to route water from node to node along cell edges and for it to accumulate. I assume that along the length of each cell edge water can be added to the flow line, assuming that the input is linearly related to the length of the flow line,

$$q_w[\text{node}] = \alpha l, \quad (2.28)$$

where l is the length of the edge that joins the up-slope node to the down-slope node (Figure 2.11c and d). This means that the cell area is ignored and instead water enters the flow path uniformly along its length and accumulates down slope.

Equation 2.28 makes the assumption that water accumulates as a function of length. Water flux is observed to relate to catchment area, $Q_w \propto A^{0.8}$ (Syvitski and Milliman, 2007). The catchment length, l is then related to area by, $l \propto A^{1/p}$, where $1.4 < p < 2.0$ (Armitage et al., 2018c). At the lower end of the range this gives $Q_w \propto l^{1.12}$, suggesting that accumulating water as a linear function of flow length is a reasonable simplification. A knock on effect of this assumption is that the magnitude of the water flux predicted for the node-to-node routing is less than the cell-to-cell, as in the latter water is accumulated over cell areas, which is naturally larger than the cells edges.

Both equations 2.27 and 2.28 do not attempt to capture the interaction between water flux and river width, rather these are two methods to approximate run-off within a coarse numerical grid. For both the cell-to-cell and node-to-node methods the flow can then be routed down a single flow direction (SFD) or routed down multiple flow directions (MFD) weighted by the relative gradient, as in for example Schoorl et al. (2000). The choice of flow routing has a large effect on the numerical solution. I showed that SFD creates a numerical solution that is highly resolution dependent (Armitage, 2019). It is only by using the MFD routing that model solutions are not resolution dependent (Figure 2.12; <https://github.com/johnjarmitage/flem>; Armitage, 2019).

The sediment flux generated by erosion within the model and the accommodation space generated by subsidence can be used to generate grain size profiles of the stratigraphic layers. The 1D down-system grain-size distribution is modified down-system by selective deposition following the theoretical model and observations of Fedele and Paola (2007) and Duller et al. (2010). I assume perfect sorting, where only gravel is deposited until it is exhausted, followed by only sand and finally by fine-grained material (silt and clay grade; Paola et al., 1992). Gravel undergoes fining according to an exponential function of Sternberg type (Fedele and

Paola, 2007; Duller et al., 2010),

$$D(\tilde{x}) = D_{g0} + \phi_0 \frac{1}{C_v} (e^{-C_g \tilde{y}} - 1). \quad (2.29)$$

The fining of the sand and smaller grain sizes is given by Sternberg (1875),

$$D(\tilde{x}) = D_{si} e^{-C_s \tilde{y}}. \quad (2.30)$$

In equations 2.29 and 2.30 \tilde{x} is the dimensionless down-system length, $D_{g0} = \log_{10}(D_{50})$ is the median of the gravel input taken from the 50th percentile from Wolman pebble-count data, $\phi_0 = \log_{10}(D_{84}/D_{50})$ is the input variance of the gravel assuming that the distribution is log-normal, $D_{si} = \log_{10}(2 \text{ mm})$ is the initial grain-size for sand and finer material in the sediment input, and \tilde{y} is the spatial transformation of the down-system distance given by (Paola and Seal, 1995),

$$\frac{d\tilde{y}}{d\tilde{x}} = \frac{r}{q_s} \quad (2.31)$$

where r is the down-system distribution of deposition and q_s is the down-system distribution of sediment discharge.

I have used the above system of equations to explore sedimentary deposition in various terrestrial alluvial systems and have explored the consequences of pushing the system beyond the coastline in to submarine depositional environments (Armitage et al., 2011b, 2015a, 2018a; Duller et al., 2019). Most recently the 2D landscape evolution has been used to explore Quaternary sedimentary systems. In the following sections I will go through two example studies of using the numerical model to test hypothesis of past climate change (the articles for these two examples are included within Annex B).

2.3.2 Eocene Escanilla sedimentary system, Spain

The Escanilla sediment-routing system has its source regions in the south-central Pyrenean orogen (Figure 2.13). Sediment was transported throughout the Lutetian to Priabonian (41.6 to 33.9 Ma) from wedge top basins in the east to marine deposits in the west. It can be simplified into two major source regions that fed sediment into the Sis Paleovalley and Pobla Basin (Figure 2.13). The sediment fairway can then be simplified to a single depositional cross section that extends from the Gurb-Pobla and Sis depocenters through the Tremp-Graus, Ainsa, and Jaca basins (Figure 2.13; (Michael et al., 2013)). The position of the limit of gravel deposition, the gravel front, and sand deposition, the sand front, for three time periods were measured by Nicolas Michael and Philip Allen (Michael et al., 2013). It was found that the gravel front migrated westwards significantly in the final time period, from 36.5 to 33.9 Ma. A classic interpretation of this progradation would be that there was increased precipitation within this third time period, which lead to increased energy within the system and the migration of the gravel front towards the west.

By using the 1D model for sediment transport, combined with grain-size fining, a Monte-Carlo-like simulation was run to find the combination of change in surface run-off and catchment erosion that could match the position of the gravel and sand fronts within the system (Armitage et al., 2015a). The best fitting model suggests that precipitation increased significantly in the middle time period, and not the third time period (Figure 2.14). The reason the gravel front did not migrate with this change in precipitation is because input sediment flux rose to fill the extra accommodation space created. It was not until time period three where precipitation rates fell despite similar sediment flux input, that there was significant progradation of gravel towards the coastline. For a more detailed explanation see the full article in the Annex B.

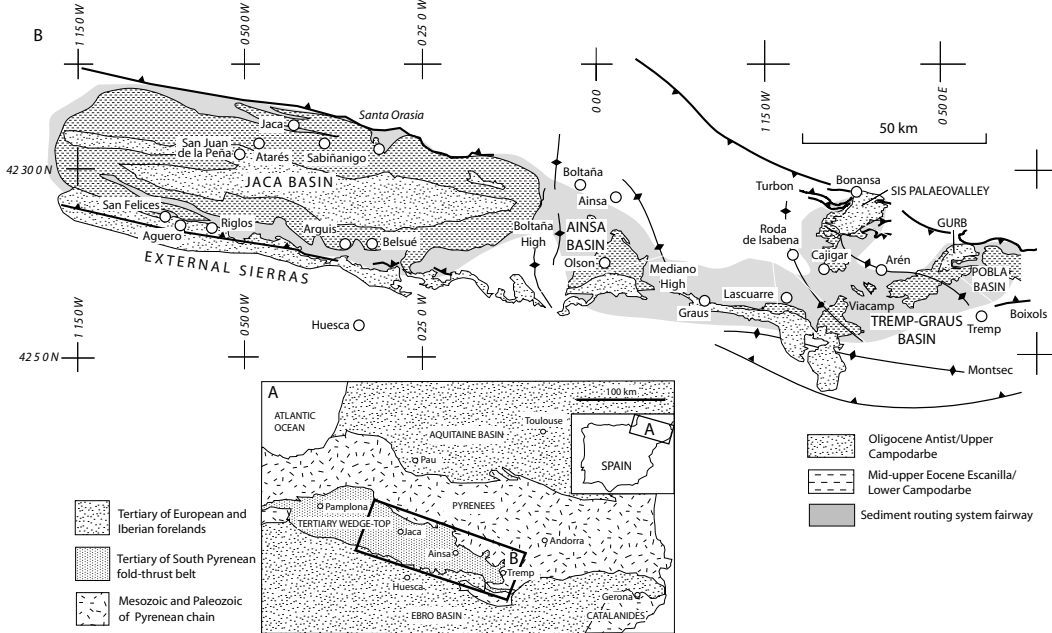


FIGURE 2.13 – A) Location of the Escanilla paleo–sediment-routing system in the Tertiary wedge top of the south-central Pyrenees, northern Spain. B) Detail of the Escanilla paleo–sediment-routing system fairway, after Michael et al. (2014).

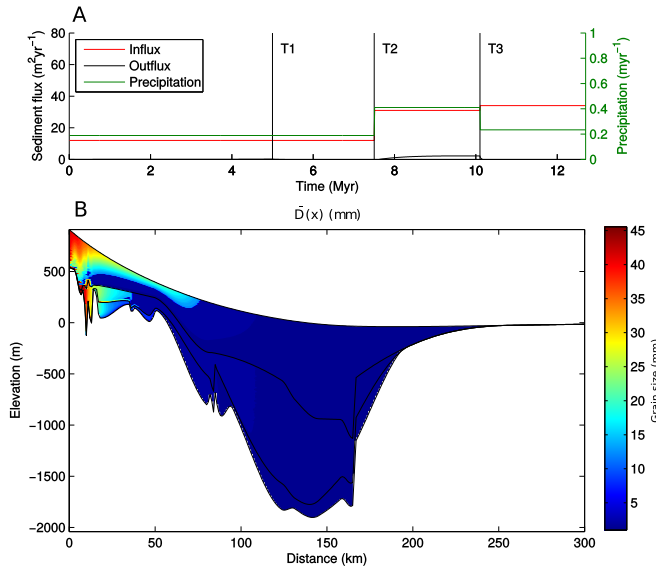


FIGURE 2.14 – Stratigraphic architecture predicted by the forward model run that most closely matches the observed location of the gravel front. A) Sediment flux in and out of the basin and precipitation rate against time. B) Distribution of grain-size deposited in the idealized Escanilla paleo–sediment-routing system.

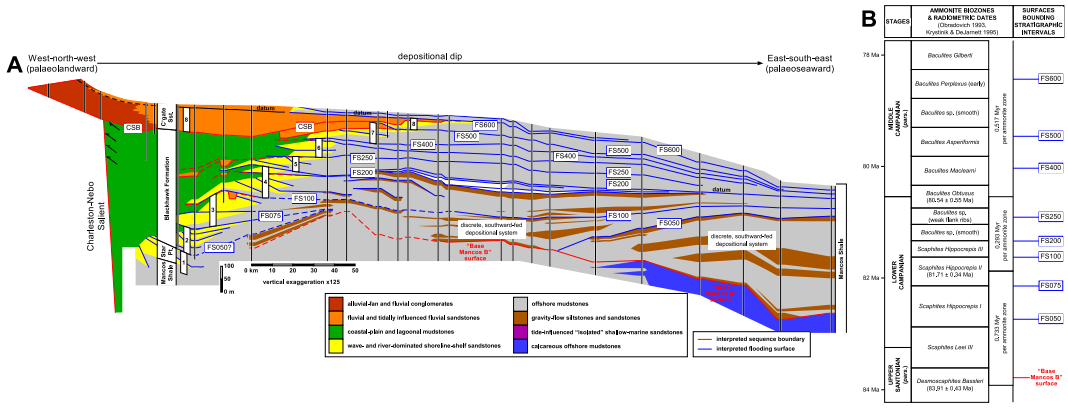


FIGURE 2.15 – (a) Correlation panel illustrating stratigraphic architecture through the Book Cliffs outcrops and adjacent areas (after Horton et al., 2004; Hampson, 2010; Hampson et al., 2014; and references therein). Interpreted major flooding surfaces and erosional unconformities (sequence boundaries) are labelled. Deposits corresponding to time intervals 1-8 are indicated. Up system correlation of the lower part of the Castlegate Sandstone (time interval 8) is after Robinson and Slingerland (1998) and McLaurin and Steel (2000). A variety of stratigraphic surfaces are used as datum surfaces for different parts of the panel, and each surface is assigned the depositional dip of an eastward-dipping coastal plain or shelf profile where used as a datum. (b) Ammonite biostratigraphy, radiometric dates (Obradovich, 1993), and estimated ammonite biozone durations (Krystnik and DeJarnett, 1995) for the studied strata, showing the interpreted ages of major flooding.

2.3.3 Book Cliffs, USA

The Book Cliffs of eastern Utah and western Colorado, USA, expose a record of a large palaeo-sediment-routing system. This is a classic site, where ancient clonglomeratic alluvial deposits transform into shoreline sandstones, marine deposits and shales (Figure 2.15). In collaboration with Philip Allen, Peter Burgess, and Gary Hampson, we decided to explore if the migration of the gravel front, sand front, and shoreline within this sedimentary system could likewise be ‘inverted’ for past forcing. The classic interpretation has been that cyclic progradation and retrogradation of the shoreline and sand front is due to cyclic sea level change (this is the birth place of sequence stratigraphy). The sediment transport equation (equation 2.24) was modified to include a transport law that was active when the surface was below sea level (Kaufman et al., 1991),

$$q_s = -\kappa_{sea} e^{-\kappa_{decay}(z_{sea}-z)} \frac{\partial z}{\partial x}, \quad (2.32)$$

where κ_{sea} is the linear diffusion coefficient for subaqueous sediment transport. κ_{decay} is the coefficient that parameterises the effect of water depth, z_{sea} , on subaqueous sediment transport. This heuristic model approximates the effect of tidal energy on moving sediment away from the shoreline. With this addition the effect of change in sea-level and surface run-off could be explored.

When the sediment transport model was applied to the Book Cliffs outcrop data the results showed that both high frequency (period of 100 kyr) sea level change and change in surface run-off can impact the sand front and shoreline (Figure 2.16). However, change in terrestrial forcing also impacted the gravel front. If we assume that the observed depositional thickness of sediment is representative of the sediment flux into the basin, then the migration history of the gravel front would be a quantifiable measure to distinguish whether cyclical patterns of progradation and retrogradation were the result of cyclical change in precipitation rates or sea level (Figure 2.16). Data describing the architecture of proximal

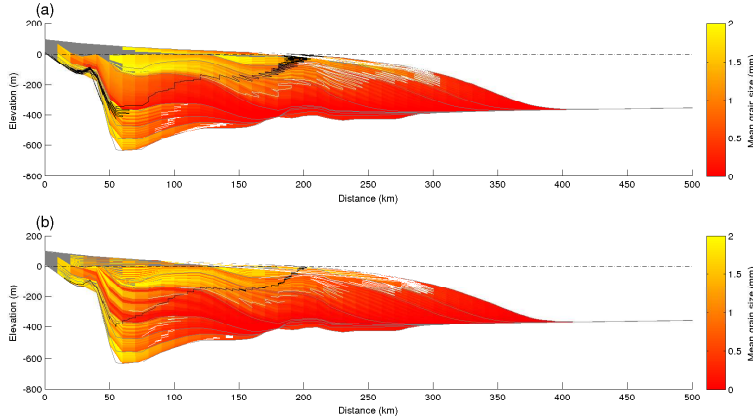


FIGURE 2.16 – Synthetic strata for two models of the stratigraphic architecture in the Star Point – Blackhawk – lower Castlegate wedge, based on the Book Cliffs outcrops. (a) Predicted stratigraphic architecture assuming a 100 kyr periodic oscillation in relative sea-level of amplitude ± 10 m. (b) Predicted stratigraphic architecture assuming a 100 kyr periodic oscillation in precipitation rate of amplitude $\pm 50\%$. Regions of gravel grains are blocked out in grey. The mean grain size of grains finer than 2 mm in diameter is plotted. The shoreline position through time is marked as a solid black line, and the dashed black line marks sea level.

deposits in the Star Point – Blackhawk – lower Castlegate – Mancos sediment-routing system are rare, however, on balance the evidence suggests limited movement of the gravel front. Therefore, a high-frequency cyclical change in relative sea level is the most probable of modelled mechanisms to account for the observed stratigraphic architecture. For a more detailed explanation see the full article in the Annex B.

This study, and the previous example from the Escanilla system, demonstrate the potential of applying physical models to test hypothesis (or interpretations) drawn from sedimentological observations. In both cases, the models gave insights into how the sedimentary system might respond to change, and how signals are transformed down system (Armitage et al., 2011b). This style of model is currently being used to investigate late-Pleistocene to Holocene deposition in alluvial fans within Death Valley (see Brooke et al., 2018). Sam Brooke has advanced upon the transport model by adding infiltration, methods to account for storm variation, and a more physically based grain-size sorting. Early results would suggest that an increase in the frequency of storms will have just as a significant effect on the gravel front as an increase in mean run-off.

2.4 Predicting geological observations

In Earth science the observations can become confused with interpretations. A tomographic image of the Earth's interior is not an observation, it is the result of an inversion and is therefore subject to various artefacts due to regularisation due to the quality of the input data. Stratigraphic sections are images created by interpolating sparse observations of rock type and age, from which an image is created that gives a sense of the distribution of sedimentary deposits. A stratigraphic section, like a tomographic image, is not an observation. Yet, it is tempting to treat these models as observations.

The core of my research has been to try and use numerical models to predict observations. This has evolved from predicting crustal velocities, major element oxides, and rare Earth compositions in basaltic glass during my post PhD research (Armitage et al., 2010, 2011a), to

predicting grain size within sedimentary deposits in sedimentary basins (e.g. Armitage et al., 2011b, 2015a, 2018a), fan topography on Mars (Armitage et al., 2011c), basin subsidence in various locations (e.g. Armitage and Allen, 2010; Armitage et al., 2013; Petersen et al., 2015), upper mantle seismic tomography at various locations (e.g. Goes et al., 2012; Armitage et al., 2015a), and more. One of the biggest challenges has been breaking down the seismic inverse models and getting to the actual observation, the seismic waveform.

In a large collaborative effort with David Ferguson, Saskia Goes, James Hammond, Eric Calais, Kate Rychert and Nick Harmon, we tried to use both observations from igneous geochemistry and inverse models from seismic stations, to understand the structure of the upper mantle below Afar (Armitage et al., 2015b). Here I found that the forward geodynamic model could consistently predict the lava chemistry and seismic tomography from surface waves. However, it could not predict the seismic velocity structure required from the inversion of S-to-P receiver functions. From this failure I decided to build a research project where the seismic observation, the displacement recorded at the seismometer, would be predicted. This involved a new collaboration with Nobu Fuji, Alexandre Fournier, and our PhD student Thijs Franken. The result is a new scientific work-flow where the forward geodynamic model is transformed in to a seismic structure. This structure is used as an input for forward wave propagation, and the subsequent seismic arrival is compared with the arrival at the earth's surface (Figure 2.9 ; Franken et al., 2020). This is the first time that anyone has, to my knowledge, tried to compare a geodynamic model with a seismic observation.

2.5 Summary

The reason Earth science exists is to understand how the Earth works. This is done through careful observations and the testing of hypothesis of how fundamental processes work. My research has always existed at the interface of these two aspects. I am interested in how basic physical processes get transformed into surface observations, from geomorphologic signals to deep mantle processes. At the end of this thesis I include ten publications that are examples of this focus, which can lead to some diversity of subject areas. Yet I strongly believe that without the connection between the fundamental physics and chemistry, and the geological observation, we won't get closer to understanding how the Earth works.

Chapitre 3

Perspectives

My research outlook over the coming decade is going to shift away from studying the Earth's deep interior and move towards the surface. In the next century run-off, which drives fluvial erosion, will likely change significantly due to the effects of global warming on the Earth system. To quote the IPCC's Fifth Assessment Report [IPCC \(2014\)](#) :

In many regions, changing precipitation or melting snow and ice are altering hydrological systems, affecting water resources in terms of quantity and quality (medium confidence). Glaciers continue to shrink almost worldwide due to climate change (high confidence), affecting run-off and water resources downstream (medium confidence). Climate change is causing permafrost warming and thawing in high-latitude regions and in high-elevation regions (high confidence).

The impact of such change on sediment storage and transport is uncertain. We can look to the past for evidence of how fluvial systems have responded, but at a time scale of hundreds of years it can become difficult to distinguish the importance of events such as individual storms. Furthermore, as I will expand upon below, there is a broad range of different numerical models developed to study landscape change on different time and spatial scales. One key process is being overlooked : groundwater. Beyond simple empirical laws for 1D infiltration, no numerical models to my knowledge include the impact of groundwater flow on the evolution of fluvial erosion and deposition. Yet rivers recharge by not only by surface run-off but from the ground (e.g. [Condon et al., 2020](#)), and river networks most likely grow as a network within the partially saturated ground (e.g. [Devauchelle et al., 2012](#)). The challenge is to translate this concept into a testable model that can be applied to fluvial systems.

3.1 Short-Term Research Perspectives

Landscape evolution modelling on geological time-scales ($> 10^4$ yr) has been dominated by one single equation : the stream power law (see [Howard and Kerby, 1983](#); [Howard, 1994](#)). If I return to the simple diagram of surface processes (Figure 2.10), the stream power law makes one very sweeping assumption : the rate of change in sediment thickness within the landscape is zero, which is to say all sediment created is transported out of the model domain. Furthermore, assuming surface flow is the primary driver of landscape erosion and that positive x is in the downstream direction then erosion, E , as a function of the power of the flow to detach particles of rock per unit width can be written as,

$$E = -k_b \rho_w g q_w^m (\partial_x z)^n, \quad (3.1)$$

where k_b is a dimensional constant that parametrises bedrock erodability ([Howard and Kerby, 1983](#); units $(\text{m}^2 \text{yr}^{-1})^{1-m} \text{yr kg}^{-1}$), ρ_w is water density, g is gravity, q_w is water flux

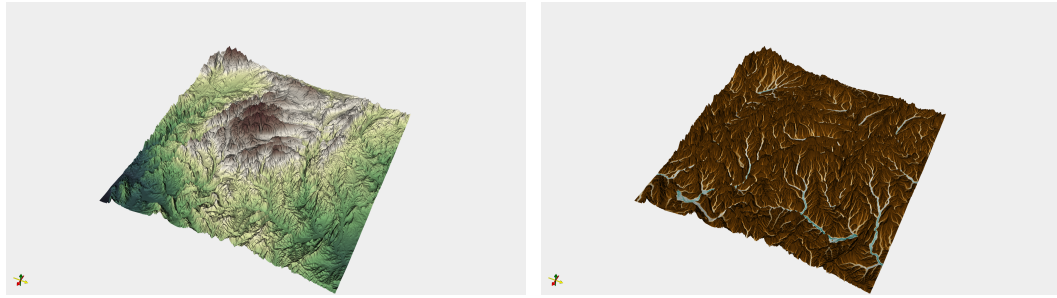


FIGURE 3.1 – Example model evolution of the Riu Bergantes and surrounding area in the Iberian Massif, Spain. The model fLEM (<https://github.com/johnjarmitage/flem>) is run on the SRTM DEM that includes the Riu Bergantes in the bottom corner. The model is run as described in Armitage (2019) for 20 kyr, for which the flow field is displayed on the right. No colour bars are shown, as this model is simply a demonstration of the idea rather than a full simulation.

per unit width (units $\text{m}^2 \text{yr}^{-1}$), m and n are constants. The exponent $m \sim 0.5$, as it is a function of how the stream flow width is proportional to the water flux (e.g. Lacey, 1930; Leopold and Maddock, 1953; Whittaker et al., 2007). The exponent $n > 0$ acts upon the slope. In two dimensions the change in elevation is then given by,

$$\partial_t z = U + k q_w^m (\partial_x z)^n, \quad (3.2)$$

where the constant k lumps together the other constants (units $\text{m}^{-1} (\text{m}^2 \text{yr}^{-1})^{1-m}$), and if $n \neq 1$ equation 3.2 becomes non-linear. But in any landscape, the assumption of instantaneous sediment transport does not hold. The above model does not work. This raises a question : **what are the key processes within landscape evolution ?**

The question of what processes dominate in landscape evolution becomes more important as the time scale of interest becomes shorter. This has led to the development of process based landscape evolution models (LEMs) for various applications (see for example Temme et al., 2017). I will briefly describe two that have been used to study landscape change over different time-scales :

- 1 **LAPSUS** This is a process based model, where sediment is eroded or deposited down slope based on the transport capacity of the fluvial system (Schoorl et al., 2000). It also includes processes such as soil formation and solid creep. It is a highly simplistic model with eight free parameters which can vary in space and time.
- 2 **CAESAR-Lisflood** This is a process based model but of increased complexity compared to LAPSUS. It is based on a cellular automaton approach, but the laws acting on each cell are many and complex. Overland flow is modelled using the Lisflood model of Bates et al. (2010), and a simple infiltration is included using TOPMODEL (Beven and Kirkby, 1979). Subsequently sediment is transported down slope given the shear velocity of the flow is sufficiently high (Coulthard et al., 2013; Van de Weil et al., 2007). Other processes are included such as soil creation, lateral erosion, vegetation cover, etc., giving a total of 49 free parameters (Skinner et al., 2018).

Given the number of processes typically modelled in LEMs it is difficult to assess which are significant and those to which there is no sensitivity. Recently sensitivity analysis has been carried out using a part of the full parameter space (Skinner et al., 2018). The result of this sensitivity analysis is that the greatest sensitivity was to the sediment transport law, which is a function of the flow of water. This is a first order variable within the model, and it suggests second order aspects such as the degree of vegetation, soil creation are of lower importance.

To better understand the key processes I am involved in a large project where we plan to compare multiple LEMs on one single catchment, the Riu Bergantes in Spain (Figure

3.1). The aim is to take a series of different LEMs : fLEM (Armitage, 2019), TISC (Garcia-Castellanos, 2002), LAPSUS (Schoorl et al., 2000), and CAESAR-Lisflood (Coulthard et al., 2013), and apply them to the same region and explore how they differ in terms of predicted topography and sediment flux.

Sensitivity analysis...

3.2 Long-Term Research Perspectives

The flow of water is what drives most erosional processes and the transport of sediment. The formation of rivers and the shape of river networks has been studied for decades if not centuries. The dendritic shape of river networks have proven difficult to pin down to any causal mechanism (e.g. Dodds and Rothman, 2000). Furthermore, the apparent relationship between drainage area and local slope has been shown to be acausal (Schorghofer and Rothman, 2002). Nonetheless, numerical models with power law relationships between water flux and drainage area are the staple of landscape evolution modelling (e.g. my own work Armitage, 2019).

In fluvial systems draining into saturated regions, such as the Florida Panhandle, channel growth has similarities with the growth of a network into a diffusional field (Devauchelle et al., 2012). This is perhaps an extreme case, as groundwater is pervasive, but it is clear stream and river networks are to an extent fed from seepage of groundwater (e.g. Fan et al., 2019). The infiltration of water into the critical zone¹ and into deeper storage has a critical impact on the flux of trace elements through the hydrological cycle (e.g. Condon et al., 2020). This impacts the weathering of the bedrock, and it means that the assumption of surface run-off implicit in all landscape evolution models is wrong.

3.2.1 Groundwater

To model the flow of groundwater it is first assumed that the flow is steady, *Bernoulli's theorem*. The equation of motion for a fluid can be expressed as,

$$\frac{\partial \mathbf{v}}{\partial t} + (\mathbf{v} \cdot \nabla) \mathbf{v} = -\frac{\nabla p}{\rho} - \nabla \phi \quad (3.3)$$

where p is pressure, ρ is density, and ϕ is the potential energy per unit mass (which for gravity is simply gz). This equation can be rearranged and through the addition of the vector field vorticity, Ω , be written as (see for example Feynman et al., 1964 p40-5),

$$\frac{\partial \mathbf{v}}{\partial t} + \Omega \times \mathbf{v} + \frac{1}{2} \nabla v^2 = -\frac{\nabla p}{\rho} - \nabla \phi \quad (3.4)$$

Steady flow is the assumption that the fluid flow along fixed streamlines. This means that $\frac{\partial \mathbf{v}}{\partial t} + \Omega \times \mathbf{v} = 0$, and therefore equation 3.4 simplifies to,

$$\mathbf{v} \cdot \nabla \left(\frac{p}{\rho} + \phi + \frac{1}{2} v^2 \right) = 0. \quad (3.5)$$

If the flow is assumed to be irrotational, then this further simplifies to,

$$\nabla \left(\frac{p}{\rho} + \phi + \frac{1}{2} v^2 \right) = 0. \quad (3.6)$$

1. Earth's critical zone is the "heterogeneous, near surface environment in which complex interactions involving rock, soil, water, air, and living organisms regulate the natural habitat and determine the availability of life-sustaining resources" (source https://en.wikipedia.org/wiki/Earth%27s_critical_zone).

Chapitre 3. Perspectives

and hence,

$$\frac{p}{\rho} + \phi + \frac{1}{2}v^2 = \text{constant.} \quad (3.7)$$

If we assume that the circulation of water is sufficiently slow then the v^2 term becomes small and the energy balance reduces to,

$$\frac{p}{\rho} + gz = \text{constant.} \quad (3.8)$$

where I have replaced the energy potential due to gravity. In hydrology the energy potential is often represented by the *hydraulic head*, h , and equation 3.8 is written as,

$$h = \frac{p}{g\rho} + z \quad (3.9)$$

The flow of water through the critical zone and deeper bedrock can be modelled as a Darcy flow through a porous medium. The velocity of the water is then given by,

$$\mathbf{v} = -K\nabla h, \quad (3.10)$$

where K is the hydraulic conductivity. At this point it is typical to make the *shallow water assumption*, where the vertical flow is assumed to be zero, and flow is only horizontal. In this case the hydraulic head is the water elevation, and the flux of the groundwater is given by the horizontal velocity, $q = vh$. From mass balance, the rate of change in the elevation of the groundwater is given by,

$$\frac{\partial h}{\partial t} = \frac{\partial}{\partial x} \left(Kh \frac{\partial h}{\partial x} \right) + S \quad (3.11)$$

where S is a source term. This non-linear equation can be solved numerically to predict groundwater flow (e.g. MODFLOW²). However, recent laboratory experiments and measurements of river flow post storm would suggest that the shallow water assumption is not advisable (Guérin et al., 2019).

It is clear, however, that water flows down topography and through a potential energy field. There are two fluxes, a surface water flux and a ground water flux. The interaction of these two fluxes drive landscape erosion. Over the next five to ten years I hope to develop the methods encapsulate these two fluxes to better understand how the Earth's surface erodes, and use this model to help understand how landscape will react to the coming climate crisis.

3.2.2 Seismic Noise

Groundwater content is estimated via seismic noise (Clements and Denolle, 2018). Test the interpretations for groundwater storage! Build on Mr. Franken's work.

2. MODFLOW : <https://www.usgs.gov/software/modflow-6-usgs-modular-hydrologic-model>

Chapitre 4

Résumé

Education

2004-2009 PhD in Geophysics - National Oceanography Centre, University of Southampton, UK

Title ‘How Does Melting Affect Continental Rift Development?’

Supervisors : Prof Tim Minshull, Dr Tim Henstock & Dr John Hopper

Awarded a fully funded NERC studentship

2003-2004 Masters in Oceanography - National Oceanography Centre, University of Southampton, UK

Masters Project Title ‘Dissolution of Silica from Antarctic Continental Shelf Sea Sediments’

Supervisor : Prof. Rachel Mills

Awarded a fully funded NERC scholarship

1999-2003 MSci in Physics - Imperial College London, UK

Employment History

Feb 2020 - [IFP Energies Nouvelles](#)

Present *Ingénieur de Recherche*

Oct 2019 - [Gekko SAS, Paris, France](#)

Feb 2020 *Cloud Computing and DevOps Consultant*

Sep 2015 - [Institut de Physique du Globe de Paris, France](#)

Aug 2019 *ANR Funded Research Scientist*

I was the principle investigator on a prestigious 4 year Agence National de la Recherche funded grant through the “Accueil de Chercheurs de Haut Niveau” call.

Chapitre 4. R  sum 

Sep 2013 - Department of Earth Sciences, Royal Holloway, University of London, UK
Aug 2015 Royal Astronomical Society Research Fellow

This fellowship, titled “Deciphering the sedimentary record : tectonic vs climate change”, was awarded by the Royal Astronomical Society. I explored how long-wavelength topography changes due to mantle flow, and whether long lived changes in climate have affected the sedimentary record of continental interiors. I am continuing collaborations with Prof. Jason Phipps Morgan, Prof. Peter Burgess and Prof. Marta P  rez-Gussiny  to couple numerical models of mantle flow to first order sedimentary processes.

Apr 2011 - Institut de Physique du Globe de Paris, France
Aug 2013 Marie Curie Research Fellow

This two year EU Marie Curie fellowship was titled “Cratonic basins : an archive of lithosphere-mantle interaction”. Collaborating with Prof. Claude Jaupart (IPGP) ; I studied how deep mantle dynamics is recorded in the rock record by exploring the relationship between lithosphere destabilisation and subsidence within the continental interior, with a focus on cratonic basins. The primary aim was to develop my numerical and laboratory experimental skills.

Mar 2008 - Department of Earth Science and Engineering, Imperial College London, UK
Mar 2011 Research Associate

I worked within the Sediment Routing Systems group, headed by Prof. Philip Allen, to (1) Develop models of basin formation and couple models of subsidence with the evolution of grain size. In particular I looked at the possibility of subsidence within the continental interior at cratonic basins being due to a low strain rate extension. (2) Develop models of catchment erosion and sediment deposition to explore the controls of basin stratigraphy due to changes in climate and uplift within the catchment.

Funding

Sep 2015 ANR Accueil de Chercheurs de Haut Niveau 4 year research project ‘InterRift : Interpreting Continental Break-up from Surface Observations’ – 450,000€
Aug 2013 Royal Astronomical Society Research Fellowship – £123,000
Apr 2011 E.U. Marie Curie Research Fellowship – 193,564€

Awards

2011 Young Author of the Year, Journal of the Geological Society, London, for the article “Cratonic basins and the long-term subsidence history of continental interiors”.
2009 Masanori Sakuyama Prize, for best publication of a PhD graduate of the National Oceanography Centre, Southampton : ‘Modelling the composition of melts formed during the continental break-up of the North Atlantic’, published in Earth and Planetary Science Letters.
2007 Best poster at the Faculty of Engineering, Science & Mathematics Research Showcase, University of Southampton.
2003 NERC scholarships including living costs for my Masters in Oceanography & my PhD.

4.0. PhD Supervision

PhD Supervision

2016 - Thijs Franken

2019 *Institut de Physique du Globe de Paris*

I was the primary supervisor of Thijs Franken. Thijs' PhD focused on developing models of seismic structure due to partial melt and wave propagation through regional domains. This project was funded through my ANR grant, and was in collaboration with Dr. Nobuaki Fuji and Prof. Alexandre Fournier (IPGP).

2014 - Sam Brooke

2018 *Imperial College London*

I co-supervised Sam Brooke with Dr. Alex Whittaker at Imperial College London. The aim of this project was to further develop models of sediment transport and the evolution of alluvial fans.

2012 - Chandra Taposeea

2017 *Imperial College London*

I co-supervised Chandra Taposeea with Dr. Jenny Collier at Imperial College London. The project further tests the hypothesis developed by myself, Jenny Collier and Tim Minshull (National Oceanography Centre, Southampton) that rift history controls the volume of melt generated during continental break-up.

Masters and Undergraduate Supervision

2017 Masters research project : Aimen Maghrebi, *Ecole Supérieure d'Ingénieurs Léonard de Vinci*.

2017 3rd year undergraduate project : Sabrina Ihaddadene, License, *Physique, Université Paris-Est Créteil*.

2016 3rd year undergraduate project : Leo Bourier, License, *Physique, Université Paris-Est Créteil*.

Teaching

2018 Université Paris Diderot, Surface Processes, Masters level, 50h

2017 Université Paris Diderot, UE Projet Tutoré, 3rd year undergraduate, 42h

2016 Institut de Physique du Globe de Paris, 'Frontiers in Earth surface dynamics : creating a research proposal', École doctorale (PhD level), 10h

2016 Université Pierre et Marie Curie, Séminaire Géodynamique, Masters level, 3h

2014 Royal Holloway, University of London, Sedimentary Basin Analysis, 3rd year undergraduate, 6h

2010 Imperial College London, Mathematics of Geology and Geophysics, 1st year undergraduate, 20h

2007-2008 University of Southampton, Biogeochemical cycles, Masters level, 20h

Selected Invited Presentations

EGU General Assembly 2018 : From induction to deduction : Using the Earth as a natural laboratory. EGU2018-10469, April, 2018.

Chapitre 4. R  sum  

Ordinary Meeting of the RAS : Can variations in the Earth's orbit create stratigraphic sequences ? 10th March 2017

Geological Society of London, Rifts III : Catching the wave, 2016 : Upper mantle temperature during extension and breakup, 22-24 March, 2016.

AGU Fall Meeting 2015 : Testing How Depletion, Dehydration and Melt Affect Seismic Expressions of the Asthenosphere, T34C-01, December 16th, 2015.

Volkswagen-Stiftung Funded Symposium : Bridging the Gap Between Field Evidence and Numerical Models : Modelling landscape and sediment flux responses to precipitation change, Herrenhausen Palace Conference Centre, Hanover, October 21-23rd, 2015.

Action Marges Workshop, Mouvements verticaux et Chantier Afar-Aden : Keynote : Controls of lithospheric extension on magma and sediment production, Total, La Defence, November 11-12th, 2014.

Volcanic & Magmatic Studies Group 2012 Conference : Keynote : Beyond Hotspots : the importance of rift history for volcanic margin formation, Durham University, UK, January 4-6th, 2012.

EarthScope - GeoPRISMS Science Workshop on Eastern North America (ENAM) : Analogue and numerical models that inform the rifting process, Lehigh University, Bethlehem, PA, USA, October 27-29th, 2011.

Selected Oral Conference Presentations

Armitage, J.J. (2017), The Effect of Climate Change on Volcanism During Continental Break-up, 79th EAGE Conference and Exhibition 2017.

Armitage, J.J. (2016), But What About Trees and Beavers? Simplicity, Complexity and Benchmarks for Landscape Evolution Models, AGU, Fall Meet., Abstract, EP12A-07

Armitage, J.J. (2015), Landscape response due to sediment transport and bedrock detachment, GeoBerlin, Dynamic earth – from Alfred Wegener to today and beyond, Berlin.

Armitage, J.J. (2014), The influence of large-scale tectonics, mantle flow and climatic change on sediment accumulation, William Smith Meeting 2014 : The Future of Sequence Stratigraphy : Evolution or Revolution ? The Geological Society, London.

Armitage J.J., Barrier, L. (2013), Is the Neogene series of the Northern Foreland Basin of the Tian Shan Range indicative of tectonic or climatic change ? AGU, Fall Meet., Abstract EP43E-04

Armitage J.J. (2012), The Instability of Continental Passive Margins and its Effect on Continental Topography and Heat Flow, Deep Water Margins, The Geological Society, London.

Goes, S.D., Armitage, J.J., Harmon, N., Huismans, R.S., (2011), Low seismic velocities below mid-ocean ridges : Attenuation vs. melt retention, AGU, Fall Meet., Abstract, T33H-05

Armitage J.J., Duller, R.A., Whittaker, A.C., Densmore, A., Allen, P.A., (2010) Response of sediment routing systems to tectonic and climatic perturbations, William Smith Meeting 2010 - Landscapes Into Rock, The Geological Society, London.

Armitage J.J., Collier, J.S., Minshull T.A., Hopper J.R., (2008), Geodynamic modelling of the opening of the northwest Indian Ocean, AGU, Fall Meet., Abstract, T53G-08

Armitage J.J., Henstock T.J., Minshull T.A., Hopper J.R., (2007), Lithospheric controls on the rifting of continents at slow rates of extension, AGU, Fall Meet. Suppl., Abstract, T32A-06

Invited Seminars

More than 20 invited seminars since 2012.

2018	University of Leeds
2017	ISTerre Grenoble ; GET Toulouse ; IRAP Toulouse
2016	Université de Lausanne ; GFZ Potsdam
2015	University of Edinburgh ; MINES ParisTech ; University of Southampton
2014	University of Southampton
2013	Université de Montpellier ; Université de Nantes ; Université Paris Sud, Orsay
2012	ENS, Paris ; FAST, Université Paris Sud, Orsay ; CPRG Nancy ; UPMC, Paris ; Université de Rennes ; EOST Strasbourg

List of publications

- 36 Franken, T, **Armitage, J.J.**, Fuji, N, Fournier, A., (2020) Seismic wave-based constraints on geodynamical processes : an application to partial melting beneath the Réunion island. *Geochemistry, Geophysics, Geosystems*, doi : TBA
- 35 Civiero, C., **Armitage, J.J.**, Goes, S., Hammond, J.O.S., (2019) The seismic signature of upper-mantle plumes : application to the northern East African Rift. *Geochemistry, Geophysics, Geosystems*, 20, 6106-6122, doi : 10.1029/2019GC008636
- 34 Andrés-Martínez, M., Pérez-Gussinyé, M., **Armitage, J.J.**, Morgan, J.P., (2019) Thermomechanical implications of sediment transport for the architecture and evolution of continental rifts and margins. *Tectonics*, 38, 641-665, doi : 10.1029/2018TC005346
- 33 Duller, R.A., **Armitage, J.J.**, Manners, H.R., Grimes, S., Jones, T.D., (2019) Delayed sedimentary response to abrupt climate change at the Paleocene-Eocene boundary, northern Spain. *Geology*, 47, 159-162, doi : /10.1130/G45631.1
- 32 **Armitage, J.J.** (2019) Short communication : flow as distributed lines within the landscape. *Earth Surface Dynamics*, 7, 67-75, doi : 10.5194/esurf-7-67-2019
- 31 **Armitage, J.J.**, Ferguson, D.J., Petersen, K.D., Creyts, T.T., (2019) The importance of Icelandic ice sheet growth and retreat on mantle CO₂ flux. *Geophysical Research Letters*, 46, 6451-658, doi : 10.1029/2019GL081955
- 30 **Armitage, J.J.**, Collier, J.S., (2017) The thermal structure of volcanic passive margins. *Petroleum Geoscience*, 24, 393-401, doi : 10.1144/petgeo2016-101
- 29 Brooke, S.A.S., Whittaker, A.C., **Armitage, J.J.**, D'Arcy, M., Watkins, S.E., (2018) Quantifying sediment transport dynamics on alluvial fans from spatial and temporal changes in grain size, Death Valley, California. *Journal of Geophysical Research – Earth Surface*, 123, 2039-2067, doi : 10.1029/2018JF004622

Chapitre 4. Rèsumé

- 28 Rychert, C.A., Harmon, N., **Armitage, J.J.**, (2018) Seismic imaging of thickened lithosphere resulting from plume pulsing beneath Iceland. 19, 1789-1799, doi : 10.1029/2018GC007501
- 27 **Armitage, J.J.**, Petersen, K.D., Perez-Gussinye, M., (2018) The role of crustal strength in controlling magmatism and melt chemistry during rifting and break-up. *Geochemistry Geophysics Geosystems*, doi : 10.1002/2017GC007326
- 26 **Armitage, J.J.**, Burgess, P.M., Hampson, G.J., Allen, P.A., (2018) Deciphering the origin of cyclical gravel front and shoreline progradation and retrogradation in the stratigraphic record. *Basin Research*, 30, 15-35, doi : 10.1111/bre.12203
- 25 **Armitage, J.J.**, Whittaker, A.C., Zakari, M., Campforts, B., (2018) Numerical modelling landscape and sediment flux response to precipitation rate change. *Earth Surface Dynamics*, 6, 77-99, doi : 10.5194/esurf-6-77-2018
- 24 Taposeea, C.A., **Armitage, J.J.**, Collier, J.S., (2017) Asthenosphere and lithosphere structure controls on early onset oceanic crust production in the southern South Atlantic. *Tectonophysics*, 716, 4-20, doi 10.1016/j.tecto.2016.06.026
- 23 Mareschal, J.-C., Jaupart, C., **Armitage, J.J.**, Phaneuf, C., Pickler, C., Bouquerel, H., (2017) The Sudbury Huronian Heat Flow Anomaly, Ontario, Canada. *Precambrian Research*, 295, 187-202, doi : 0.1016/j.precamres.2017.04.024
- 22 Allen, P.A., Michael, N.A., D'Arcy M., Roda-Boluda, D.C., Whittaker, A.C., Duller, R.A., **Armitage, J.J.**, (2017) Fractionation of grain size in terrestrial sediment routing systems. *Basin Research*, 29, 180-202, doi : 10.1111/bre.12172
- 21 Temme, A.J.A.M., **Armitage, J.J.**, Attal, M., van Gorp, W., Coulthard, T.J., Schoorl, J.M., (2017) Developing, choosing and using landscape evolution models to inform field-based landscape reconstruction studies. *Earth Surface Processes and Landforms*, 42, 2167–2183, doi : 10.1002/esp.416
- 20 Duller, R.A., Warner, N.H., De Angelis, S., **Armitage, J.J.**, Poyatos-More, M., (2015) Reconstructing the timescale of a catastrophic fan-forming event on Earth using a Mars model. *Geophysical Research Letters*, 42, 10324-10332, doi : 10.1002/2015GL066031
- 19 **Armitage, J.J.**., Allen, P. A., Burgess, P. M., Hampson, G. J., Whittaker, A. C., Duller, R. A., Michael, N. A., (2015) Physical stratigraphic model for the Eocene Escanilla sediment routing system : Implications for the uniqueness of sequence stratigraphic architectures. *Journal of Sedimentary Research*, 85, 1510-1524, doi :10.2110/jsr.2015.97

4.0. List of publications

- 18 Allen, P.A., **Armitage, J.J.**, Whittaker, A.C., Michael, N.A., Roda-Boluda, D., D'Arcy, M., (2015) Fragmentation model of the grain size mix of sediment supplied to basins. *Journal of Geology*, 123, 405-427, doi : 10.1086/683113
- 17 **Armitage, J.J.**, Ferguson D., Goes, S., Hammond, J.O.S., Calais, E., Harmon, N., Rychert, C.A., (2015) Upper mantle temperature and the onset of extension and break-up in Afar, Africa. *Earth and Planetary Science Letters*, 418, 78-90, doi : 10.1016/j.epsl.2015.02.039
- 16 Lucazeau, F., **Armitage, J.J.**, Kadima Kabongo, E., (2015) Thermal regime and evolution of the intracratonic Congo Basin, in *The Geology and Resource Potential of the Congo Basin* , de Wit, M.J., Guillocheau, F., Fernandez-Alonso, M., Kanda, N., and de Wit, M.C.J., Eds. Elsevier. doi : 10.1007/978-3-642-29482-2_12
- 15 Petersen, K.D., **Armitage, J.J.**, Nielsen, S.B., Thybo, H., (2015) Mantle temperature as primary control on the time scale of thermal evolution of extensional basins, *Earth and Planetary Science Letters*, 409, 61-70, doi : 10.1016/j.epsl.2014.10.043
- 14 **Armitage, J.J.**, Duller, R.A., Schmalholz, S.M., (2014) The influence of long-wavelength tilting and climatic change on sediment accumulation. *Lithosphere*, 6, 303-318, doi : 10.1130/L343.1
- 13 **Armitage, J.J.**, Dunkley Jones, T., Duller, R.A., Whittaker, A.C., Allen, P.A., (2013) Temporal buffering of climate-driven sediment flux cycles by transient catchment response. *Earth and Planetary Science Letters*, 369, 200-210, doi : 10.1016/j.epsl.2013.03.020
- 12 **Armitage, J.J.**, Jaupart, C., Fourel, L., Allen, P.A. (2013) The instability of continental passive margins and its effect on continental topography and heat flow. *Journal of Geophysical Research – Solid Earth*, 118, 1817–1836, doi : 10.1002/jgrb.50097
- 11 Allen, P.A., **Armitage, J.J.**, Carter, A., Duller, R.A., Michael, N., Sinclair, H.D., Whitchurch, A.L., Whittaker, A.C. (2013) The Qs problem : Sediment mass balance of proximal foreland basin systems. *Sedimentology*, 60, 102-130, doi : 10.1111/sed.12015
- 10 Goes, S., **Armitage, J.J.**, Harmon, N., Smith, H., Huismans, R., (2012) Low seismic velocities below mid-ocean ridges : Attenuation vs. melt retention. *Journal of Geophysical Research – Solid Earth*, 117(B12403), doi : 10.1029/2012JB009637

Chapitre 4. R  sum 

- 9 Duller, R.A., Whittaker, A.C., Swinehart, J.B., **Armitage, J.J.**, Sinclair, H.D., Bair, A.R., Allen, P.A., (2012) Abrupt landscape change post-6 Ma on the Central Great Plains, U.S.A. *Geology*, 40, 871-874
- 8 Allen, P.A. & **Armitage, J.J.**, (2012) Cratonic basins. In Busby, C. & Azor, A. (Eds.) *Syntectonic Basin Development, Active to Ancient : Recent Advances*. Ch. 30, p 602-620, Blackwell Publishing Ltd.
- 7 **Armitage, J.J.**, Warner, N.H., Goddard, K., Gupta, S., (2011) Timescales of alluvial fan development on Mars. *Geophysical Research Letters* , 38 (L17203), doi :10.1029/2011GL048907
- 6 **Armitage, J.J.**, Collier, J.S., Minshull, T.A. Henstock, T.J. (2011) Thin oceanic crust and flood basalts : Reconciling observations from the northwest Indian Ocean. *Geochemistry Geophysics Geosystems*, 12(Q0AB07), doi :10.1029/2010GC003316
- 5 **Armitage, J.J.**, Duller, R.A., Whittaker, A.C. Allen, P.A., (2011) Transformation of tectonic and climatic signals from source to sedimentary archive. *Nature Geoscience*, 4, 231-235, doi : 10.1038/ngeo1087
- 4 **Armitage, J.J.** & Allen, P.A. (2010) Cratonic basins and the long-term subsidence history of continental interiors. *Journal of the Geological Society, London*, 167, 61-70, doi : 10.1144/0016-76492009-108
- 3 **Armitage, J.J.**, Collier, J.S., Minshull, T.A., (2010) The importance of rift history for volcanic margin formation. *Nature*, 465, 913-917, doi : 10.1038/nature09063
- 2 **Armitage, J.J.**, Henstock, T.J., Minshull, T.A., Hopper, J.R., (2009) Lithospheric controls on melt production during continental breakup at slow rates of extension : Application to the North Atlantic. *Geochemistry Geophysics Geosystems*, 10(Q06018), doi : 10.1029/2009GC002404
- 1 **Armitage, J.J.**, Henstock, T.J., Minshull, T.A., Hopper, J.R., (2008) Modelling the composition of melts formed during continental break-up of the North Atlantic. *Earth Planetary Science Letters*, 269, 248-258, doi : 10.1016/j.epsl.2008.02.024

Annexe A

Example Publications Part 1 : Mantle

In this appendix I have selected five key publications from my research career that exemplify my approach and collaborations for understanding how upper mantle processes are reflected in surface observations, and how these processes interact to control how the Earth has evolved.

1 The importance of rift history for volcanic margin formation – Nature

The first paper was published in *Nature* in 2010 a year after completion of my thesis and represents the culmination of four years work with Tim Minshull and Jenny Collier. In this article we present the hypothesis that lithosphere structure controls volcanism during continental break-up. This is expressed by the different evolution of crustal thickness at two classic volcanic margins, the North Atlantic Igneous Province and the Seychelles, Laxmi Ridge and Deccan Traps.

2 Upper mantle temperature and the onset of extension and break-up in Afar, Africa – Earth and Planetary Science Letters

In this study I aimed to reconcile diverging interpretations on the structure of the mantle below Afar. Based on the igneous geochemistry, researchers had reasoned that the upper mantle below Afar must be hot, very hot. However, seismic observations pointed to the mantle being not cold, or at least not hotter than average. I developed the methods to predict simultaneously the igneous geochemistry and seismic structure to demonstrate, that within observational error, the mantle below Afar is hotter than average.

3 Thermomechanical implications of sediment transport for the architecture and evolution of continental rifts and margins – Tectonics

This study comes from a collaboration I was involved in while working at Royal Holloway, University of London. I worked closely with Miguel Andrés-Martínez to develop a coupled model of surface and shallow mantle processes. This model is the first to fully couple sedimentary processes with crustal deformation. In this study Miguel demonstrates that sediment deposition will alter the evolution of rifted basins. More importantly, geologic interpretation of sedimentary layers is oversimplified, with sediment sourced from one margin ending up on the other after break-up.

4 The importance of Icelandic ice sheet growth and retreat on mantle CO₂ flux – Geophysical Research Letters

Noting that surface processes has a key role in break-up, in collaboration with various colleagues, I became interested in how ice-sheet loading might have impacted melt migration and retention. In this study I developed a simple 1D model of melt migration and composition. This allowed the classic hypotheses that Holocene deglaciation caused increased volcanism in Iceland. In this interdisciplinary collaboration, we demonstrated with a range of geological observations, that this hypothesis is most

Chapitre A. Example Publications Part 1 : Mantle

likely true.
5 Thijis' paper!

LETTERS

The importance of rift history for volcanic margin formation

John J. Armitage¹, Jenny S. Collier¹ & Tim A. Minshull²

Rifting and magmatism are fundamental geological processes that shape the surface of our planet. A relationship between the two is widely acknowledged but its precise nature has eluded geoscientists and remained controversial. Largely on the basis of detailed observations from the North Atlantic Ocean, mantle temperature was identified as the primary factor controlling magmatic production¹, with most authors seeking to explain observed variations in volcanic activity at rifted margins in terms of the mantle temperature at the time of break-up^{2,3}. However, as more detailed observations have been made at other rifted margins worldwide, the validity of this interpretation and the importance of other factors in controlling break-up style have been much debated^{4–7}. One such observation is from the northwest Indian Ocean, where, despite an unequivocal link between an onshore flood basalt province, continental break-up and a hot-spot track leading to an active ocean island volcano, the associated continental margins show little magmatism^{5,8}. Here we reconcile these observations by applying a numerical model that accounts explicitly for the effects of earlier episodes of extension. Our approach allows us to directly compare break-up magmatism generated at different locations and so isolate the key controlling factors. We show that the volume of rift-related magmatism generated, both in the northwest Indian Ocean and at the better-known North Atlantic margins, depends not only on the mantle temperature but, to a similar degree, on the rift history. The inherited extensional history can either suppress or enhance melt generation, which can explain previously enigmatic observations.

Extensive surveys in the North Atlantic have shown that the breakup of Europe from North America was characterized by massive episodes of igneous activity. Such large magmatic events are potentially highly significant to the Earth's history, and have been linked to both mass extinctions and changes in global climate⁹. Magmatically enhanced (volcanic) margins extend laterally over distances of 2,000 km with spatial and temporal relationships suggesting a direct link to the Iceland hot spot¹⁰. These first-order observations were explained¹ using a model of melt generation due to uniform, instantaneous extension. The calculations¹ showed little dependence on the initial lithospheric thickness when full break-up occurred and it was concluded that the primary constraint on magmatism was mantle temperature. A later study showed that only for very slow extensional rates would the relationship between high mantle temperature and voluminous magmatism break down¹¹. It has therefore been widely assumed that all hot spots associated with continental break-up will generate a volcanic margin, with the volume of melt decreasing steadily along strike away from the hot-spot centre¹². Subsequent challenges to this idea have centred on examples of volcanic margins where the presence of a hot spot at the time of break-up is disputed^{4,7} or where rapid along-strike variations in magmatism are observed^{6,13,14}. Here we focus on new observations from the northwest Indian Ocean, where,

like in the North Atlantic, there is an unequivocal association between continental break-up, an onshore flood basalt province (the Deccan Traps) and a hot-spot track (the Chagos–Laccadive–Mascarene ridge) leading to an active volcanic island (Réunion). As the size of the Deccan Traps is similar to that of the North Atlantic igneous province, it has been widely inferred that the associated continental margins should also display volcanic characteristics^{12,15}.

Continental break-up is commonly preceded by a series of extensional episodes¹⁶, which have an effect on the subsequent volcanic nature of the rifted margin. However, such geological considerations are not generally incorporated into numerical models of melt generation during extension. Instead previous researchers implicitly assumed a geometry of the lithosphere^{1,11}, imposed the geometry of the rift location as an initial condition^{2,3} or assumed the lithosphere to have uniform vertical thickness with a predefined weakness¹⁷. We previously developed a self-consistent numerical modelling approach that incorporates multiple episodes of extension suggested by geological data¹⁸. Our early model outputs were tested against observations from southwest Greenland, where the extension rate was low (half-spreading rate, $<40 \text{ mm yr}^{-1}$), and suggested that at this particular margin extension before break-up thinned the lithosphere and that this thin region aided the decompression of hot upwelling mantle. Here we build upon this work by applying our model to the conjugate margin in the eastern Atlantic and to rifting between India and the Seychelles, where extension was fast (half-spreading rate, $>60 \text{ mm yr}^{-1}$). We show that mantle thermal structure alone is unable to explain the observations in either the northwest Indian Ocean or in the North Atlantic. Rather, it is the geological inheritance from previous episodes of extension that controls the volcanic nature of break-up. Therefore, our work provides a new framework in which to understand the structure of continental margins worldwide.

The key advance of our model is that as it evolves through time, it tracks melt generation and the associated depletion of the solid mantle, allowing for a better representation of the inherited melting conditions (see Methods Summary and Supplementary Information for more details). We solve the equations of thermal convection for a non-Newtonian viscous fluid using an extended version of Citcom^{3,18,19}, which tracks the melt and solid-mantle major-element composition throughout the lithosphere as melting progresses¹⁸. Melt generation results from decompression as the solid mantle crosses the solidus, which is a function of depth and depletion. The volume and seismic velocity of any melt generated through time is then calculated and compared with measurements from wide-angle seismic experiments. To assess the influence of hot mantle, a thermal anomaly beneath the lithosphere is included as a layer of predefined thickness and excess temperature. In the analysis presented here, this layer is not replenished, because we model distal volcanic margins where observations suggest that the excess magmatism takes the form of an initial pulse that decays

¹Department of Earth Science & Engineering, Imperial College London, London SW7 2AZ, UK. ²National Oceanography Centre, Southampton, University of Southampton, Southampton SO14 3ZH, UK.

once sea-floor spreading is under way³. Extension that leads to break-up is imposed in our dynamic model by applying divergent surface boundary conditions. We incorporate the multiple episodes of extension by shifting the centre of the divergent boundary condition on the basis of geological constraints, allowing the lithosphere to cool by conduction between periods of extension.

In 2003, we collected conjugate wide-angle seismic profiles across the Seychelles margin and the Indian margin in a region known as the Laxmi ridge, which were approximately 1,000 km from the Deccan Traps at the time of break-up (Fig. 1a). However, rather than a heavily intruded continent–ocean transition zone and thick oceanic crust, only a modest addition of magma within the transition zone and relatively thin oceanic crust was found^{5,8}. Rare-earth-element inversions suggest that mantle temperatures during the eruption of the Deccan Traps were up to 200 °C higher than the background temperatures¹⁵. If the Seychelles/Laxmi ridge margin inherited such a thermal structure, our model predicts that rifting of a previously unthinned lithosphere would generate igneous intrusions with a high P-wave seismic velocity, which would thicken the crust by up to 10 km (Fig. 1c, d, blue line). Such material is not observed; rather, the oceanic crust formed first has a normal seismic velocity and is only 5.2 km thick. However, a region of high-velocity, voluminous syn-rift magmatism was found nearby in an area known as the Gop rift (Fig. 1a). Geophysical observations have shown that the Gop rift is underlain by thick oceanic crust⁵ and opened before the main break-up between the Seychelles and India²⁰. We find that the

observed igneous thicknesses and seismic velocities can be explained if the opening of the Gop rift occurred 6 Myr before the main Deccan Traps eruption and tapped the anomalously hot asthenosphere. This initial extensional episode partly exhausted the thermal anomaly and depleted the underlying lithosphere (Fig. 1b–d, red line). Once extension had migrated southwards to the Seychelles/Laxmi ridge margin, what remained of the thermal anomaly had cooled by heat conduction. Melting was of a mildly depleted mantle that had no excess temperature, leading to thin oceanic crust seaward of the Seychelles and the Laxmi ridge with reduced seismic velocities in the lower crust.

A key question is how to reconcile these Indian Ocean results with our previous work on southeast Greenland, which suggested that previous extension focused upwelling and enhanced melt generation¹⁸. To answer this question, we present a more comprehensive numerical experiment that incorporates new observations from the conjugate Hatton Bank margin. This pair of margins is a similar distance from the Iceland hot spot as the Seychelles and the Laxmi ridge are from the Deccan Traps (Fig. 2a). Geological observations suggest that extension before break-up formed the Hatton Basin, thinning the continental crust by a factor of two²¹. We assign a late-Cretaceous age for this initial extensional episode on the basis of magnetic anomaly patterns²² and the Tertiary sedimentary sequence that overlies the Hatton Basin basement rock²³. Around 20 Myr after the formation of this basin, the earliest flood basalts were erupted on the southeast Greenland margin⁹. Interpretations

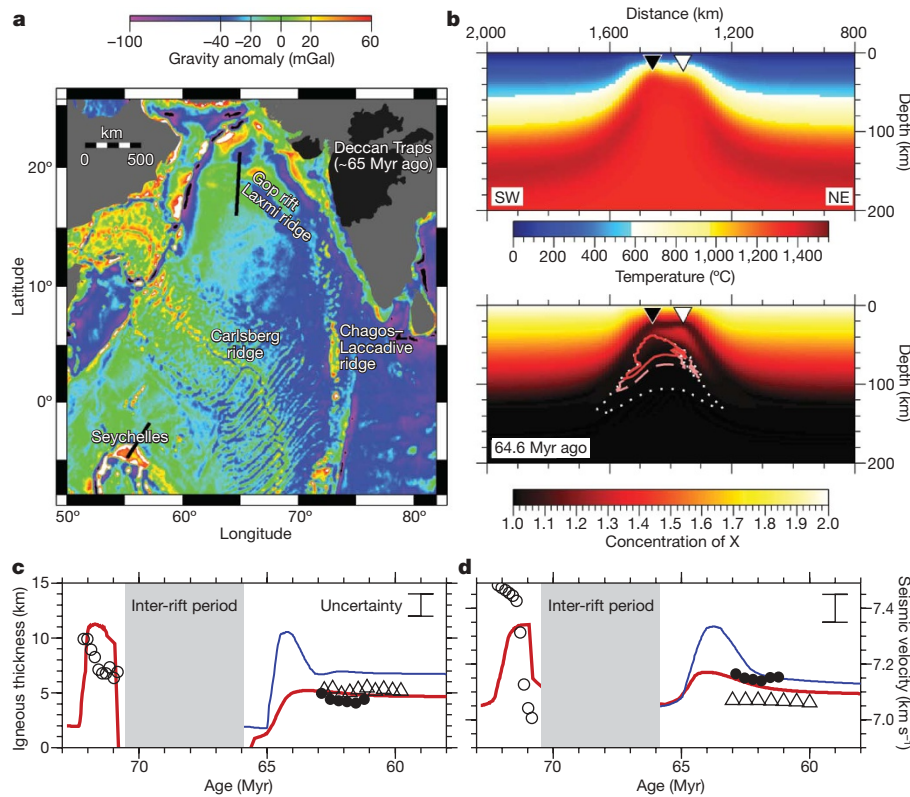


Figure 1 | Geological setting and model results for the northwest Indian Ocean. **a**, Gravity anomaly map showing the location of the conjugate Seychelles and Laxmi Ridge margin profiles. The black region marks the flood basalts of the Deccan Traps. $1 \text{ mGal} = 10^{-3} \text{ cm s}^{-2}$. **b**, Temperature and mantle depletion (trace element X, Methods) with melt fraction at the centre of extension before break-up of the Seychelles/Laxmi ridge margin (64.6 Myr ago), from our preferred two-rift model. The location of the Gop rift is marked by the white triangle and that of the Seychelles/Laxmi ridge break-up is marked by the black triangle. In the lower plot, we show the extent of the melt region (dotted line) and the 1% and 2% melt fraction contours (dashed and solid lines, respectively). **c**, **d**, Predicted igneous crustal thickness (**c**) and predicted average lower-crustal seismic velocity (**d**) from the Gop rift, the Laxmi ridge and the Seychelles margins^{5,8}. Uncertainties in the observations are representative values taken from ref. 8.

(d) over time, assuming that the lithosphere was initially underlain by a 50-km-thick thermal anomaly at 200 °C. The blue curve is for a model in which there is a single rift event 64.5 Myr ago (half-spreading rate, 60 mm yr^{-1}) and the red curve is for a model with two rift events, one 71 Myr ago (half-spreading rate, 80 mm yr^{-1}) and the other 64.5 Myr ago²⁰. In the double-rift model, the Gop rift taps the thermal anomaly and the subsequent melting in the Seychelles/Laxmi ridge margin is of a slightly depleted mantle⁸. Open circles, filled circles and open triangles respectively mark the observed igneous crustal thickness (c) or the average lower-crustal seismic velocity (d) from the Gop rift, the Laxmi ridge and the Seychelles margins^{5,8}. Uncertainties in the observations are representative values taken from ref. 8.

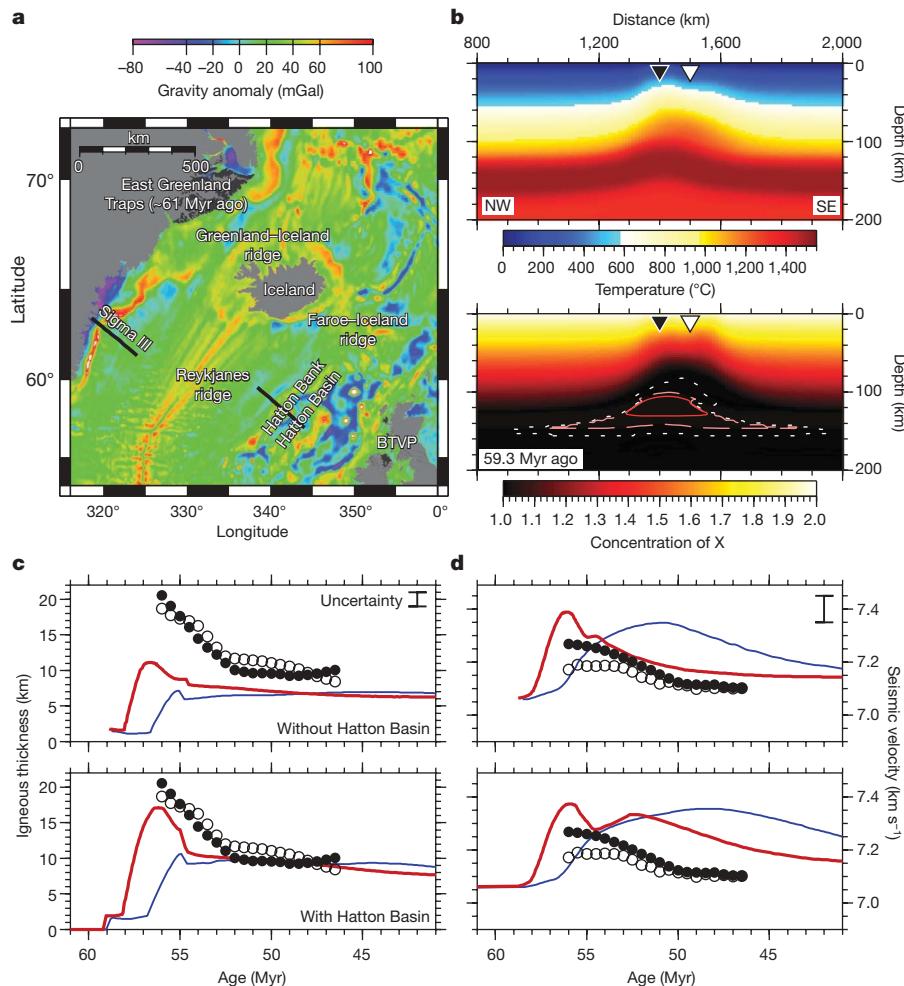


Figure 2 | Geological setting and model results for the North Atlantic Ocean. **a**, Gravity anomaly map showing the location of the conjugate southeast Greenland and Hatton Bank margin profiles^{24,25}. The black regions mark the North Atlantic igneous province: the flood basalts of the East Greenland Traps and the British Tertiary volcanic province (BTVP). **b**, Temperature and mantle depletion with melt fraction, contoured as in Fig. 1, at the centre of extension before break-up (59.3 Myr ago), from our preferred model that considers the Hatton Basin opening. The location of the Hatton Basin is marked by the white triangle and that of the southeast Greenland/Hatton Bank break-up is marked by the black triangle. In the model there is a 50-km-thick thermal anomaly at 200 °C beneath the lithosphere. **c, d**, Predicted igneous crustal thickness (**c**) and predicted

of initial sea-floor spreading anomalies in this part of the North Atlantic are disputed^{18,24,25}, and to account for these differing interpretations we show results from two models with different extension rates (Fig. 2c, d, blue and red lines). If the extension that led to the Hatton Basin is ignored, the thermal anomaly would be held beneath the 125-km-thick lithosphere. Extension in the range of the inferred half-spreading rates, although producing reasonable lower-crustal seismic velocities (Fig. 2d), would not thin the lithosphere enough to allow for significant upwelling of hot mantle to produce the 17-km-thick igneous crust observed (Fig. 2c, top). Instead, if the lithosphere is extended by a factor of two, 20 Myr before the break-up of the North Atlantic, the thermal anomaly spreads laterally beneath the slightly extended lithosphere before the eventual break-up (Fig. 2b). If the extension rate is sufficiently high, the upwelling of this hot material then generates enough melt to match the observed highly thickened igneous crust (Fig. 2c, bottom, red line) and is in reasonable agreement with the lower-crustal seismic velocity.

We conclude that the association of volcanic margins with flood basalts in the North Atlantic led to an overemphasis on the thermal

average lower-crustal seismic velocity (**d**) over time. Uncertainties in the observations are representative values taken from ref. 25. In each panel, the top plot assumes that the lithosphere is of uniform, 125-km thickness at the start of rifting between the Hatton Bank and southeast Greenland, and the bottom plot includes previous extension of the Hatton Basin that ceases 80 Myr ago. To account for competing models for the observed spreading rates, we show two alternative scenarios with half-spreading rates between Hatton Bank and Greenland that are 20 mm yr⁻¹ (blue) and 40 mm yr⁻¹ (red) for the first 4 Myr and then decrease to 10 mm yr⁻¹ (refs 18, 25). Open and filled circles respectively mark the observed igneous crustal thickness (**c**) and the average lower-crustal seismic velocity (**d**) from the Sigma III (southeast Greenland) and iSIMM (Hatton Bank) surveys^{24,25}.

structure to explain melt volumes during continental break-up. Our work shows how inherited lithosphere structure alters melting characteristics during margin formation. The interactions are individual to each margin and depend on the spatial pattern and timing of events. In the North Atlantic, extension before rifting focused upwelling and so enhanced melt generation (Fig. 3a). In the northwest Indian Ocean, previous extension exhausted the mantle thermal anomaly, leading to reduced melt generation (Fig. 3b).

Our study shows that continental rifted margins must be studied within a framework of the interaction between mantle conditions and the extension of the lithosphere. Rift history is individual to each margin, and is typically complex, but we suggest that two general considerations are required to understand melt volumes generated during break-up. First, according to our model, if thinning of the lithosphere is under way before the emplacement of a thermal anomaly, igneous crustal thickness increases by a factor of almost two across all extension rates (Fig. 4a). It is not simply the absolute lithosphere thickness that controls the melting, but the localization of thinning, or necking, of the lithosphere that focuses melt into the break-up region

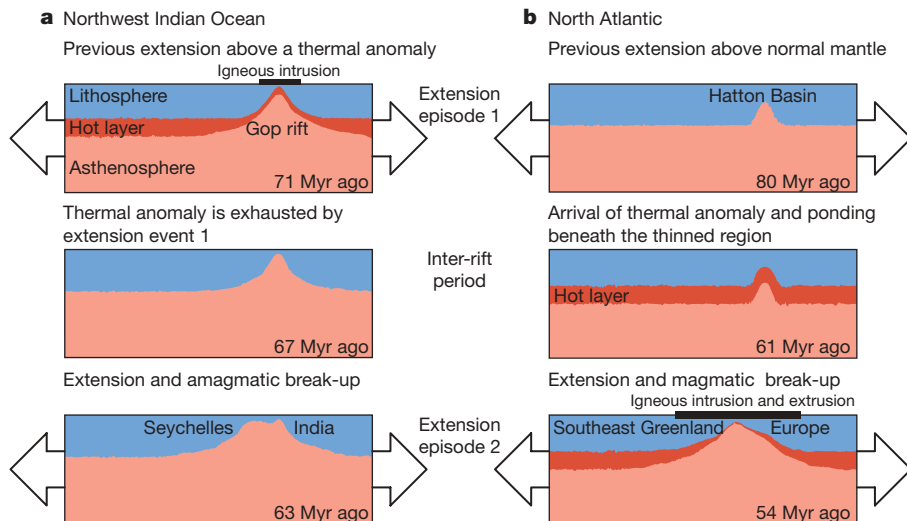


Figure 3 | Rift history controls magmatism at a rifted margin. **a**, Northwest Indian Ocean. The first episode of extension tapped the thermal anomaly, which is associated with the Deccan Traps. This formed the Gop rift and exhausted the thermal anomaly beneath the region of extension. The second episode of extension that led to break-up was above melt-depleted mantle and led to the amagmatic Seychelles/Laxmi ridge margin. **b**, North Atlantic.

The first episode of extension formed the Hatton Bank. During the inter-rift period, the thermal anomaly ponded beneath the lithosphere, such that during the second episode of extension this thermal anomaly was tapped, leading to the high volumes of melt generated during the break-up of southeast Greenland from the Hatton Bank.

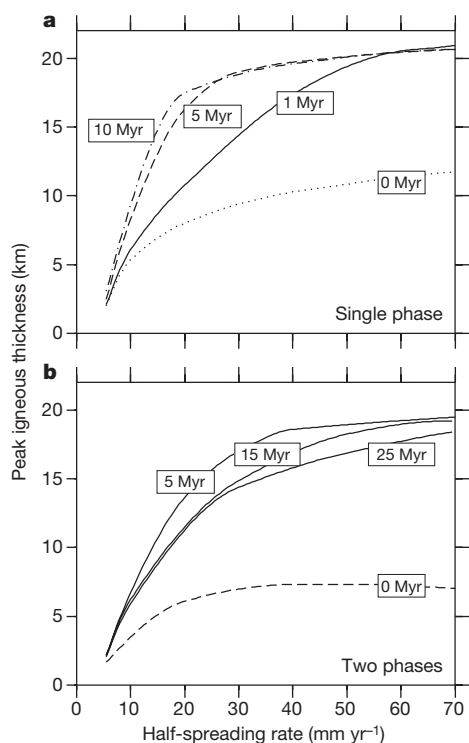


Figure 4 | The influence of rift history on melt generation during continental break-up. **a**, Peak igneous crustal thickness for extension at different half-spreading rates. In all model runs, break-up is achieved by a single, continuous extensional event. The four curves show cases for the arrival of a 50-km-thick thermal anomaly at 200 °C at different times after the initiation of extension. **b**, Peak break-up igneous thickness for a two-phase rift event. Extension is at the same half-spreading rate for both phases of rifting and the first extensional phase lasts for 5 Myr. There is a lateral migration of 100 km before the onset of the second extensional phase, which follows either immediately or after a time lag. The curves are labelled according to the arrival time of the hot layer (measured from the start of each model run), with the thermal anomaly arriving either at the start of phase one (dashed line) or the start of phase two (solid lines: 5 Myr, no time lag; 15 Myr, time lag = 10 Myr; 25 Myr, time lag = 20 Myr).

(Fig. 2b). This mechanism explains how, despite evidence that both the North Atlantic and northwest India mantle thermal anomalies were similar¹⁵, the Gop rift has a maximum melt thickness of 10 km and the North Atlantic margins have more than 17 km of melt (Figs 1 and 2). Second, break-up is normally preceded by periods of extension and these can exert a strong influence on the final magmatism. Such periods of precursor extension can tap the hot mantle material, leading to relatively insignificant break-up magmatism (Fig. 4b, dashed line; cf. northwest Indian Ocean (Fig. 1)). Alternatively, if such extension took place before the arrival of a mantle thermal anomaly, it will locally thin the lithosphere. Even allowing for the effects of thermal cooling, this localized thinning enhances melt generation during break-up (Fig. 4b, solid lines; cf. North Atlantic (Fig. 2)). The degree of magmatism is critically controlled by the relative timing of the extension and the mantle thermal history. Knowledge of previous rift history is therefore required to understand the volume of magmatism observed during continental break-up.

METHODS SUMMARY

Dynamic model of extension. The lithosphere is initially 125 km thick. Mantle potential temperatures are 1300 ± 25 °C to match the range of ‘normal’ oceanic crustal thickness found worldwide^{3,18,26}. We model anomalous mantle thermal history as a hot layer below the lithosphere. Rifting is driven by forces in the far field by imposing a divergent velocity along the top boundary. As mantle material is driven laterally by this divergence, material moves upwards to replace what has been removed. As solid mantle travels upwards it decompresses, melting when it crosses the solidus. We calculate the solidus as a function of depth and depletion. Melting depletes the solid mantle, altering the mantle composition and, hence, its subsequent melting characteristics. We track depletion by using a hypothetical completely compatible trace element, X, with an infinite partition coefficient²⁷. Multiple episodes of extension are simulated by terminating the extension and restarting it in a different location. We base the timing of these events and the location of the centre of extension on geological observations. Between periods of extension, the lithosphere cools and thickens by conduction.

Calculation of observables. We estimate the average seismic velocity of the igneous crust from the major-element composition of the melt, which is calculated from empirically derived partition coefficients^{28,29}. These values are then compared with the observed mean seismic velocity derived from wide-angle seismic data. To derive an estimate of the igneous crustal velocity that is unaffected by alteration or porosity, we base our mean velocities on material with a velocity greater than 6.85 km s^{-1} for all profiles^{10,25}. Finally, we calculate the predicted igneous crustal thickness assuming that all the modelled melt is erupted at the ridge axis, and compare this with observations from wide-angle seismic profiles. Further details are given in the Supplementary Information.

Received 20 November 2009; accepted 26 March 2010.

1. White, R. S. & McKenzie, D. Magmatism at rift zones: the generation of volcanic continental margins and flood basalts. *J. Geophys. Res.* **94**, 7685–7729 (1989).
2. Keen, C. E. & Boutilier, R. R. Interaction of rifting and hot horizontal plume sheets at volcanic margins. *J. Geophys. Res.* **105**, 13375–13387 (2000).
3. Nielsen, T. K. & Hopper, J. R. From rift to drift: mantle melting during continental breakup. *Geochim. Geophys. Geosyst.* **5**, Q07003 (2004).
4. Hopper, J. R., Mutter, J. C., Larson, R. L. & Mutter, C. Z. Magmatism and rift margin evolution: evidence from northwest Australia. *Geology* **20**, 853–857 (1992).
5. Minshull, T. A., Lane, C. I., Collier, J. S. & Whitmarsh, R. B. The relationship between rifting and magmatism in the northeastern Arabian Sea. *Nature Geosci.* **1**, 463–467 (2008).
6. Lizarralde, D. et al. Variation in styles of rifting in the Gulf of California. *Nature* **448**, 466–469 (2007).
7. Holbrook, W. S. et al. Seismic structure of the US Mid-Atlantic continental margin. *J. Geophys. Res.* **99**, 17871–17891 (1994).
8. Collier, J. S. et al. Factors influencing magmatism during continental break-up: new insights from a wide-angle seismic experiment across the conjugate Seychelles-Indian margins. *J. Geophys. Res.* **114**, B03101 (2009).
9. Storey, M., Duncan, R. A. & Swisher, C. C. III. Paleocene-Eocene thermal maximum and opening of the Northeast Atlantic. *Science* **316**, 587–589 (2007).
10. Holbrook, W. S. et al. Mantle thermal structure and active upwelling during continental breakup in the North Atlantic. *Earth Planet. Sci. Lett.* **190**, 251–262 (2001).
11. Bowin, J. W. & White, R. S. Effect of finite extension rate on melt generation at rifted continental margins. *J. Geophys. Res.* **100**, 18011–18029 (1995).
12. Campbell, I. H. Testing the plume theory. *Chem. Geol.* **241**, 153–176 (2007).
13. Shillington, D. J. et al. Abrupt transition from magma-starved to magma-rich rifting in the eastern Black Sea. *Geology* **37**, 7–10 (2009).
14. Voss, M., Schmidt-Aursch, M. C. & Jokat, W. Variations in magmatic processes along the East Greenland volcanic margin. *Geophys. J. Int.* **177**, 755–782 (2009).
15. White, R. S. & McKenzie, D. Mantle plumes and flood basalts. *J. Geophys. Res.* **100**, 17543–17585 (1995).
16. Reston, T. J. Polyphase faulting during the development of the west Galicia rifted margin. *Earth Planet. Sci. Lett.* **237**, 561–576 (2005).
17. Simon, K., Huismans, R. S. & Beaumont, C. Dynamical modelling of lithospheric extension and small-scale convection: implications for magmatism during the formation of volcanic rifted margins. *Geophys. J. Int.* **176**, 327–350 (2009).
18. Armitage, J. J., Henstock, T. J., Minshull, T. A. & Hopper, J. R. Lithospheric controls on melt production during continental breakup at slow rates of extension: application to the North Atlantic. *Geochim. Geophys. Geosyst.* **10**, Q06018 (2009).
19. Moresi, L. N. & Solomatov, V. S. Numerical investigation of 2D convection with extremely large viscosity variations. *Phys. Fluids* **7**, 2154–2162 (1995).
20. Collier, J. S. et al. Age of Seychelles-India break-up. *Earth Planet. Sci. Lett.* **272**, 264–277 (2008).
21. Smith, L. K., White, R. S. & Kusznir, N. J. in *Petroleum Geology: North-West Europe and Global Perspectives – Proceedings of the 6th Petroleum Geology Conference* (eds Doré, A. G. & Vining, B. A.) 947–956 (Geological Society of London, 2005).
22. Edwards, J. W. F. Development of the Hatton-Rockall Basin, North-East Atlantic Ocean. *Mar. Petrol. Geol.* **19**, 193–205 (2002).
23. Shannon, P. M., Moore, J. G., Jacob, A. W. B. & Makris, J. in *Petroleum Geology of Northwest Europe: Proceedings of the 4th Conference* (ed. Parker, J. R.) 1057–1066 (Geological Society of London, 1993).
24. Hopper, J. R. et al. Structure of the SE Greenland margin from seismic reflection and refraction data: implications for nascent spreading centre subsidence and asymmetric crustal accretion during North Atlantic opening. *J. Geophys. Res.* **108**, 2269 (2003).
25. White, R. S. & Smith, L. K. Crustal structure of the Hatton and the conjugate east Greenland rifted volcanic continental margins, NE Atlantic. *J. Geophys. Res.* **114**, B02305 (2009).
26. Bowin, J. W. & White, R. S. Variation with spreading rate of oceanic crust thickness and geochemistry. *Earth Planet. Sci. Lett.* **121**, 435–449 (1994).
27. Scott, D. R. in *Mantle Flow and Melt Generation at Mid-Ocean Ridges* (eds Phipps Morgan, J., Blackman, D. K. & Sinton, J. M.) 327–352 (Geophys. Monogr. 71, American Geophysical Union, 1992).
28. Niu, Y. Mantle melting and melt extraction processes beneath ocean ridges: evidence from abyssal peridotites. *J. Petrol.* **38**, 1047–1074 (1997).
29. Behn, M. D. & Kelemen, P. B. Relationship between seismic P-wave velocity and the composition of anhydrous igneous and meta-igneous rocks. *Geophys. Geosyst.* **4**, 1041 (2003).

Supplementary Information is linked to the online version of the paper at www.nature.com/nature.

Acknowledgements We are grateful to J. Hopper and R. White for giving us the southeast Greenland and Hatton Bank velocity grids. We are also grateful to T. Henstock for help developing the model. An earlier version of this manuscript was improved by comments from M. Coffin, K. Gallagher, S. Goes, S. Gupta and E. Rohling. This work was partly funded by the UK Natural Environment Research Council.

Author Contributions J.J.A. designed and performed the numerical experiments. J.J.A., J.S.C. and T.A.M. analysed the geophysical and numerical results, and contributed equally to the writing of the manuscript.

Author Information Reprints and permissions information is available at www.nature.com/reprints. The authors declare no competing financial interests. Readers are welcome to comment on the online version of this article at www.nature.com/nature. Correspondence and requests for materials should be addressed to J.J.A. (j.armitage@imperial.ac.uk).



Upper mantle temperature and the onset of extension and break-up in Afar, Africa



John J. Armitage ^{a,b,*}, David J. Ferguson ^c, Saskia Goes ^d, James O.S. Hammond ^d, Eric Calais ^e, Catherine A. Rychert ^f, Nicholas Harmon ^f

^a Dept. of Earth Science, Royal Holloway, University of London, Egham, TW20 0EX, UK

^b Dynamique des Fluides Géologiques, Université Paris Diderot, Sorbonne Paris Cité, Institut de Physique du Globe de Paris, UMR 7154 CNRS, F-75013 Paris, France

^c Dept. of Earth and Planetary Sciences, Harvard University, Cambridge, MA 02138, USA

^d Dept. of Earth Science and Engineering, Imperial College, London, SW7 2AZ, UK

^e Ecole Normale Supérieure, Department of Geosciences, UMR 8538 CNRS, Paris, France

^f National Oceanography Centre, University of Southampton, European Way, SO14 3ZH, UK

ARTICLE INFO

Article history:

Received 31 July 2014

Received in revised form 18 February 2015

Accepted 23 February 2015

Available online 13 March 2015

Editor: Y. Ricard

Keywords:

continental break-up
melt generation
melt chemistry
seismic structure
receiver functions
East African Rift

ABSTRACT

It is debated to what extent mantle plumes play a role in continental rifting and eventual break-up. Afar lies at the northern end of the largest and most active present-day continental rift, where the East African Rift forms a triple junction with the Red Sea and Gulf of Aden rifts. It has a history of plume activity yet recent studies have reached conflicting conclusions on whether a plume still contributes to current Afar tectonics. A geochemical study concluded that Afar is a mature hot rift with 80 km thick lithosphere, while seismic data have been interpreted to reflect the structure of a young, oceanic rift basin above mantle of normal temperature. We develop a self-consistent forward model of mantle flow that incorporates melt generation and retention to test whether predictions of melt chemistry, melt volume and lithosphere–asthenosphere seismic structure can be reconciled with observations. The rare-earth element composition of mafic samples at the Erta Ale, Dabbahu and Asal magmatic segments can be used as both a thermometer and chronometer of the rifting process. Low seismic velocities require a lithosphere thinned to 50 km or less. A strong positive impedance contrast at 50 to 70 km below the rift seems linked to the melt zone, but is not reproduced by isotropic seismic velocity alone. Combined, the simplest interpretation is that mantle temperature below Afar is still elevated at 1450 °C, rifting started around 22–23 Ma, and the lithosphere has thinned from 100 to 50 km to allow significant decompressional melting.

© 2015 Published by Elsevier B.V.

1. Introduction

The Afar region in northern Ethiopia forms the northern tip of the largest and most active present-day continental rift, where the Main Ethiopian Rift (MER) intersects the Red Sea Rift and the Gulf of Aden (Fig. 1). Beneath the Red Sea Rift, crust is thinned to about 15 km (Markis and Ginzburg, 1987; Hammond et al., 2011), volcanism is much more wide spread than in the MER, and much of the region has subsided below sea level in the past few million years, observations that point to the region being in transition from rifting to spreading (Markis and Ginzburg, 1987; Hayward and Ebinger, 1996; Bastow and Keir, 2011).

* Corresponding author at: Dept. of Earth Science, Royal Holloway, University of London, Egham, TW20 0EX, UK.

E-mail address: john.armitage@rhul.ac.uk (J.J. Armitage).

Afar is generally considered as a classic example of plume involvement in rifting, as it is flanked by ~30 million year old flood basalts that erupted as rifting started in the Gulf of Aden and Red Sea (Hofmann et al., 1997). Past and recent volcanism exhibits geochemical characteristics generally found in ocean island basalts, such as high $^3\text{He}/^4\text{He}$ ratios, and trace element and isotopic enrichments (Schilling et al., 1992; Pik et al., 2006; Ferguson et al., 2013). Furthermore, seismic velocities in the mantle below Afar are extremely low, as might be expected for high temperatures (e.g. Bastow and Keir, 2011). Yet, recent observations have questioned whether a plume is still involved in the present-day tectonics of the region.

Based on seismic S -to- P receiver functions and geodynamic modelling, Rychert et al. (2012) proposed that lithosphere–asthenosphere structure beneath the Afar is similar to a mid-ocean ridge system: with shallow melt generation (<80 km) due to adiabatic decompression of mantle with a potential temperature of roughly

1350 °C. Seismic travel-time tomography (Hammond et al., 2013) finds low seismic velocities under Afar consistent with such a shallow melt zone. At the other end of the debate, Ferguson et al. (2013) used the trace element composition of mafic lavas from Afar and petrogenetic modelling to argue that the erupted magmas are predominantly generated below a still thick lithosphere, at depths greater than 80 km, and at mantle potential temperatures close to 1450 °C. This temperature is more consistent with major element composition of lavas within the northern part of the East African Rift system, which suggest an elevated potential temperature of between 1370 and 1490 °C for rocks erupted in the last 10 Ma (Rooney et al., 2012b).

A central question is therefore whether there is still currently active rifting and the up-welling of deep and hot (>1400 °C) mantle material, which is possibly rooted in the African Superplume (e.g. Nyblade, 2011). The other possibility is that today Afar has evolved to the point of steady passive up-welling of the asthenosphere. Although estimates of the mantle potential temperature beneath Afar for these respective scenarios both lie between 1350 and 1490 °C, this range represents the difference between either minimal volcanism or the generation of a significant amount of melt (White and McKenzie, 1995; Armitage et al., 2010). Knowledge of how mantle temperature and lithospheric thinning have evolved in Afar is therefore essential to understanding which key tectonic and/or magmatic processes are driving the continued development of this rift system.

In this study we attempt to reconcile the seemingly contradictory geochemical and geophysical observations with a single tectonic scenario. We develop a set of models of lithospheric extension and mantle melting and compare the model predictions to observations of melt volume, melt chemistry, bulk seismic velocities and discontinuities of the lithosphere–asthenosphere. We focus on three regions of Afar where both seismic and geochemical constraints are available: (1) the Erta Ale rift zone, within the northern Danakil Depression, which is near the northwestern end of the main active rift, (2) the Dabbahu magmatic segment in central Afar, near the border of the rift zone, and (3) the Asal rift zone at the southeastern end of the Afar rift zone and the western edge of the Gulf of Aden (Fig. 1).

2. Methods

We use a relatively straightforward 2-D geodynamic model of extension of a viscous lithosphere–asthenosphere system and decompressional melting to explore the effect of mantle temperature on rift evolution. Modelling extension within the region of the Danakil Depression and Asal Rift as a 2-D process is reasonable given that extension is perpendicular to the rift axis (Fig. 1).

2.1. Geodynamic model

Evolution of upper mantle temperature and flow is modelled as Stokes flow driven by a divergent upper velocity boundary condition and a temperature difference between the surface and model base (Armitage et al., 2010). The most likely rheology for continental lithosphere and sublithospheric mantle is a temperature and pressure dependent dislocation creep (e.g. Lévy and Jaupart, 2011). We use a formulation that includes the effect of melt-weakening and dehydration strengthening (see Supplementary Material; Armitage et al., 2010). Thermal state and non-Newtonian viscous flow are solved in the finite-element code CitCom (Moresi et al., 1996). We use a 2800 km wide by 700 km deep 2-D Cartesian domain containing 512 by 512 equally spaced nodes, providing a resolution of 5.6 by 1.4 km.

Solid-mantle density in the models changes as a function of temperature, melt retention, and melt depletion, providing buoy-

ant flow due to melt generation. Melt production is calculated as a function of temperature, pressure and previous depletion (Scott, 1992; Phipps Morgan, 2001; Nielsen and Hopper, 2004; see Supplementary Material). Melt starts once the hydrous solidus is crossed, where up to 2% melt can be generated until temperature exceeds the dry solidus. We include a hydrous solidus as there is evidence of some water within the volcanics in Afar (e.g. Pik et al., 1999). Melt generated is assumed to be transported vertically by Darcy flow, using the methods described in Goes et al. (2012), for more explanation see the Supplementary Material.

Solid mantle-flow boundary conditions are a prescribed symmetric divergent-flow velocity condition on the top and free slip on the sides and base. Temperature boundary conditions are fixed temperature at the base (a mantle potential temperature of 1350, 1450 or 1550 °C) and the top (0 °C), and a zero normal temperature gradient at the sides. The initial condition is a 100, 150 or 200 km thick lithosphere defined by a linear increase in melt depletion (from 0% at the base to 50% at the surface) and reduction in temperature from the basal temperature condition at 100 km depth to 0 °C at the surface. The high buoyancy is to keep the high viscosity lithosphere at the top of the model domain. This material, due to its buoyancy, does not participate in the melting as it remains above the solidus and is moved to the sides due to the divergent boundary condition.

2.2. Melt chemistry

Partitioning of REEs between the solid mantle and partial melt is calculated from the melt depletion, temperature and pressure within the melt region assuming incremental batch melting (see Dean et al., 2008; Gibson and Geist, 2010; Armitage et al., 2011; and the Supplementary Material). Geochemical and isotopic evidence from erupted melts shows that mantle source beneath Afar is fertile compared to the depleted upper mantle source of MORBs (e.g. Schilling, 1973; Schilling et al., 1992; Barrat et al., 1998; Rooney et al., 2012a; Ferguson et al., 2013), and that this fertile source has been a long-lived feature of the mantle here (Pik et al., 1999). To examine how the extent and depths of melting evolve during rift development we calculate the REE concentration of melts generated by partial melting of mantle upwelling beneath the extending lithosphere. For the source we use a fertile mantle composition from McDonough and Sun (1995).

2.3. Conversion to seismic velocities

The models are converted to synthetic seismic structure (compressional velocity, V_P , shear velocity, V_S , density, and shear attenuation, Q_S) following the methods described in Goes et al. (2012). A thermodynamic formulation is used to determine elastic parameters and density as a function of temperature, pressure, composition, and phase, using the mineral parameter compilation of Xu et al. (2008), and the code PerPleX from Connolly (2005). For the fertile mantle we use a peridotite composition, and for the depleted mantle a harzburgite, both from Xu et al. (2008). Seismic velocities are not sensitive to more detailed variations in composition, so we linearly grade between these compositions as a function of degree of depletion (see Goes et al., 2012). Subsequently, we correct for shear attenuation using a semi-empirical temperature, pressure and dehydration dependent Q model, Q_g in Goes et al. (2012). We assume that the reference mantle is damp, as estimated for an MORB-source (1000 H/10⁶ Si; Hirth and Kohlstedt, 1996).

The presence of melt is in most models assumed to only affect the elastic response (Hammond and Humphreys, 2000a; Gribb and Cooper, 2000). We chose the melt derivatives for cuspatate melt geometries from Hammond and Humphreys (2000b): a 7.9%

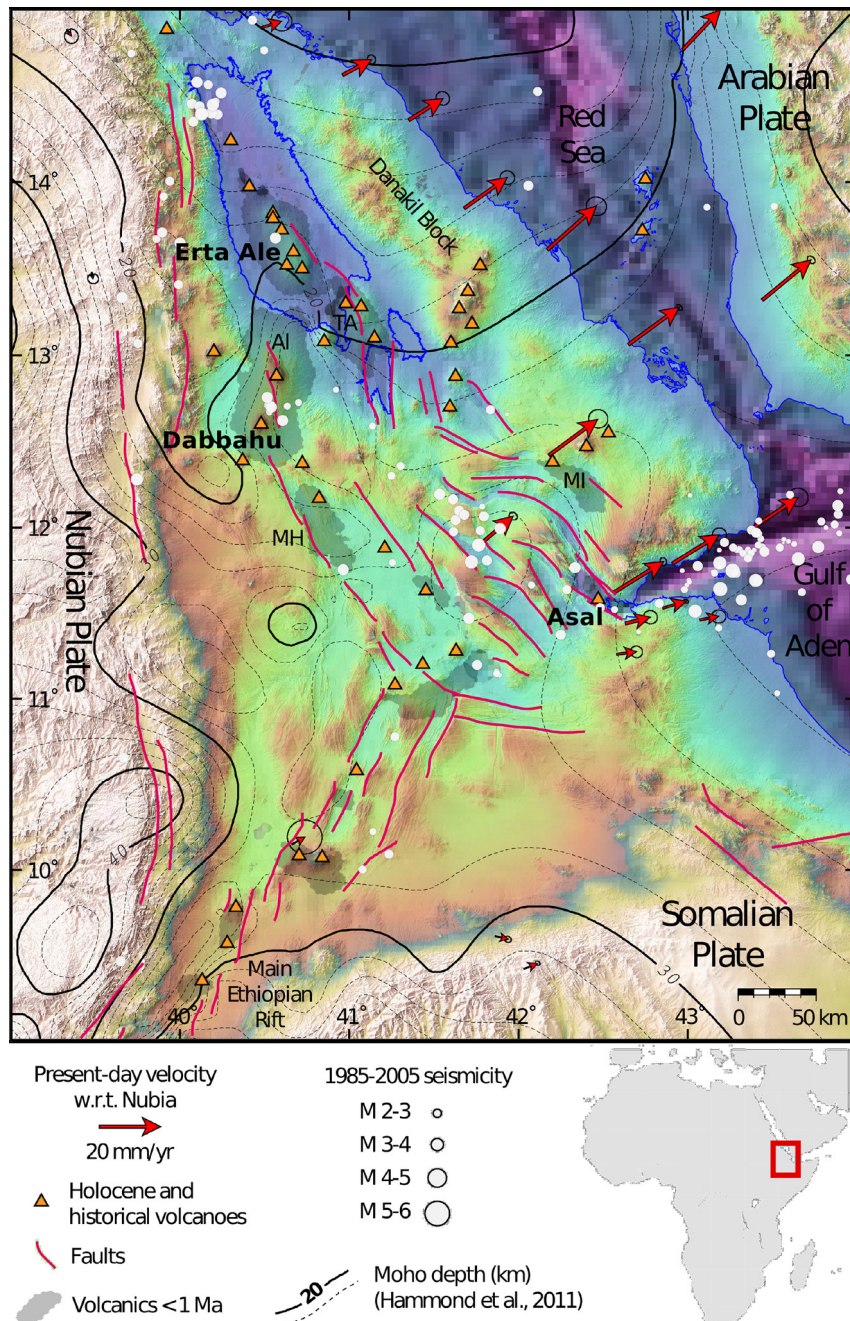


Fig. 1. Map of the Afar Rift zone and the northern Main Ethiopian Rift showing elevation in the colour scale and contours of the depth to the Moho in kilometers from Hammond et al. (2011). The three key volcanic locations, Ert A Ale, Dabbaahu and Asal, are labelled in bold text. The other labelled volcanics in red that are less than 1 Ma are: TA – Tat Ali, Al – Alaita, MH – Manda-Harraro and MI – Manda-Inikit. Velocities are from Nooner et al. (2009) and Reilinger and McClusky (2011). (For interpretation of the references to colour in this figure legend, the reader is referred to the web version of this article.)

reduction in V_S per percent melt and a 3.6% reduction in V_P per percent melt. These are the highest derivative estimates for melt fractions below 1%, commensurate with the low melt fractions predicted in most of the model. However, it should be noted that alternative melt geometries with a preferential orientation sufficient to cause significant seismic anisotropy may result in even larger velocity reductions (Blackman and Kendall, 1997). Some experimental studies indicate that the presence of melt might also effect attenuation within the seismic frequency range (Faul et al., 2004; McCarthy and Takei, 2011). To investigate the maximum effect that melt could have, we include in one of the models an additional effect on attenuation. We parameterised the effect simply by decreasing shear attenuation by half an order of magnitude (i.e.,

factor ~ 3) per percent melt. This is on the lower end of what Faul et al. (2004) measured for wave periods between 1 and 100 s but stronger decreases give unrealistically low S-wave velocities (as low as 3.2 km s^{-1}).

2.4. Synthetic S-to-P receiver functions

We calculated synthetic S-wave receiver functions for predicted 1-D velocity models beneath the rift, after adding a crustal velocity structure consistent with that determined from co-located P-wave receiver functions (thickness of between 20 and 30 km, $V_P = 6.2 \text{ km s}^{-1}$ and $V_S = 3.3 \text{ km s}^{-1}$; Hammond et al., 2011). Synthetic seismograms were calculated using a propagator matrix

Table 1

List of model variations.

Single phase of extension at 7 mm yr ⁻¹				
Name	T_p (°C)	Lithosphere thickness (km)		
L100	1450	100		
L150	1450	150		
L200	1450	200		

Two phases of extension at 3 mm yr ⁻¹ for 11 Myr and then 7 mm yr ⁻¹ Initial lithosphere thickness is 100 km				
Name	T_p (°C)	K (m ²)	Wet solidus	Melt threshold
1350N	1350	10^{-10}	yes	no
1350D ^a	1350	10^{-10}	no	no
1450N	1450	10^{-10}	yes	no
1450D ^a	1450	10^{-10}	no	no
1450L	1450	10^{-11}	yes	no
1450T	1450	10^{-10}	yes	yes
1550N	1550	10^{-10}	yes	no

^a Models 1350D and 1450D, which both assume there is no deep wet melting, were incapable of matching the observations. For completeness we discuss the results of these models in the [Supplementary Material](#).

method ([Keith and Crampin, 1977](#)). We assume a representative horizontal slowness of 0.106 s km⁻¹ and dominant period of 11 s. The three component synthetic seismograms were rotated into theoretical P and SV components using a free-surface transformation matrix ([Bostock, 1998; Cerveny, 2005](#)). The SV waveforms were then deconvolved from P waveforms using a simultaneous deconvolution ([Bostock, 1998; Rychert et al., 2007](#)). Filtering (0.05 to 0.14 Hz) and water level deconvolution (amplitude of 2×10^5) were applied to the waveform to match parameters used in the modelling of data from the Afar triple junction ([Rychert et al., 2012](#)).

2.5. Model cases

To reconcile the different observations we test a range of mantle temperatures, different durations of rifting, a range of initial lithospheric thicknesses, and several melt productivity and retention parameters. The range of models that will be discussed is given in [Table 1](#).

In most of the models we consider a two-phase extension history. Extension in the Afar region was initially slow until around 11 ± 2 Ma when extension shifted 100 km westwards and the southern Red Sea became a failed extensional basin. At this time, the rate of extension doubled to the current half spreading rates ([Reilinger and McClusky, 2011](#)). The onset of rifting in this region followed the major phase of volcanism that formed the Ethiopian flood basalts at ~ 30 Ma ([Hofmann et al., 1997](#)) and is estimated to have begun between 21 and 29 Ma ([Wolfenden et al., 2005; Reilinger and McClusky, 2011](#)). Extension is imposed on the models as a divergent upper velocity boundary condition on either side of the rift axis. The half-rate is initially set to 3.5 mm yr⁻¹, and increases to 7.0 mm yr⁻¹ after 11 Myr. The forward model is run for a duration of up to 35 Myr.

The thickness of the continental lithosphere prior to the formation of the East African Rift zone is not known. Phanerozoic continents are estimated to be between 80 and 120 km thick from surface heat flow ([Artemieva and Mooney, 2001](#)) and inferred from surface wave tomography for Africa away from the cratons and active rifts ([Fishwick and Bastow, 2011](#)). To explore the impact of the assumed initial lithosphere thickness, we first model simple extension at a half spreading rate of 7 mm yr⁻¹ of a lithosphere that has a thermal and compositional thickness of 100, 150 and 200 km above a mantle with a potential temperature of 1450 °C (models L100, L150 and L200). For other models we use an ini-

tial lithospheric thickness of 100 km which falls within the range expected for the region.

While melt volume and chemistry are sensitive to melt production history, seismic structure is sensitive to the amount of retained melt. As our reference value, we assume melt permeability 10^{-10} m². This gives a migration velocity of \sim cm yr⁻¹ ([Goes et al., 2012](#)), which is relatively slow compared to U-series constraints on melt-extraction rates (e.g. [Stracke et al., 2006](#)). However, as some seismic constraints ([Rychert et al., 2012; Stork et al., 2013](#)) have been interpreted with relatively large fractions of retained mantle melt, we also tested a model with higher melt productivity, a model with an order of magnitude lower permeability (model 1450L), and a model where melt only becomes mobile once it exceeds a threshold of 1% as suggested for mantle melts by [Faul \(2001\)](#) (model 1450T).

3. Results

The constraints that we have on Afar rifting are (1) an estimate of total melt volumes, (2) melt composition, (3) volumetric seismic velocities, (4) depths and contrasts of seismic discontinuities. Melt volumes and chemistry are sensitive to mantle temperature and the evolution of lithospheric thickness, i.e., initial lithospheric thickness and the history of rifting, and consequent evolution of mantle depletion. Volumetric seismic velocities give constraints on the thickness of the lithosphere and depth of the asthenosphere, while discontinuities may correspond to compositional or phase boundaries including the onset of dry melting, and the depth of dehydration.

3.1. Melt production

3.1.1. Constraints on igneous addition to the crust

The thickness of the crust that may be due to magma emplacement during rifting can be estimated from receiver functions and active seismic transects. Thickness of the original unstretched crust inferred from the rift's western margins and in Yemen/Arabia is between 19 and 21 km for the upper and 18 to 23 km for the lower crust ([Mechie et al., 1986; Markis and Ginzburg, 1987; Maguire et al., 2006](#)). At Erta Ale, we find an upper crustal thickness of 2 and 1 km and a lower crust of 11 and 9 km from a near-by seismic station and wide-angle seismic survey ([Markis and Ginzburg, 1987; Hammond et al., 2011](#)). If we assume that the upper crust contains no intrusions of magmatic material, the stretch factor is between 9.5 and 21, suggesting that the lower crust is intruded with between 6 and 10 km of material. Upper and lower crustal thicknesses measured near Dabbahu are 4 km and 16 km, respectively ([Hammond et al., 2011](#)), i.e., a stretch factor between 4.8 and 5.3, implying an addition of 11 to 15 km of volcanic material. At Asal, thicknesses of 2 to 6 km for the upper and 14 to 15 km for the lower crust ([Ruegg, 1975](#)) imply a stretch factor of 3.2 to 10.5 and the addition of 9 to 14 km of volcanic material. This yields total volumes of melt added during rifting that correspond to 6–14 km of crustal thickness.

3.1.2. Models: Effect of lithospheric thickness and mantle temperature

[Fig. 2](#) illustrates the influence of initial lithospheric thickness on melt production, for a spreading history at single constant spreading rate (models L100, L150, L200 in [Table 1](#)). The trend in mean melt fraction and igneous thickness shows an initial slow increase in melt production ([Fig. 2](#)), while melting only occurs deep and at temperatures below the dry solidus, where melt productivity is low. Once the lithosphere has sufficiently thinned to allow dry decompressional melting, productivity increases, causing the rapid rise in melt fraction, after 5, 15 and 23 Myr for 100, 150 and

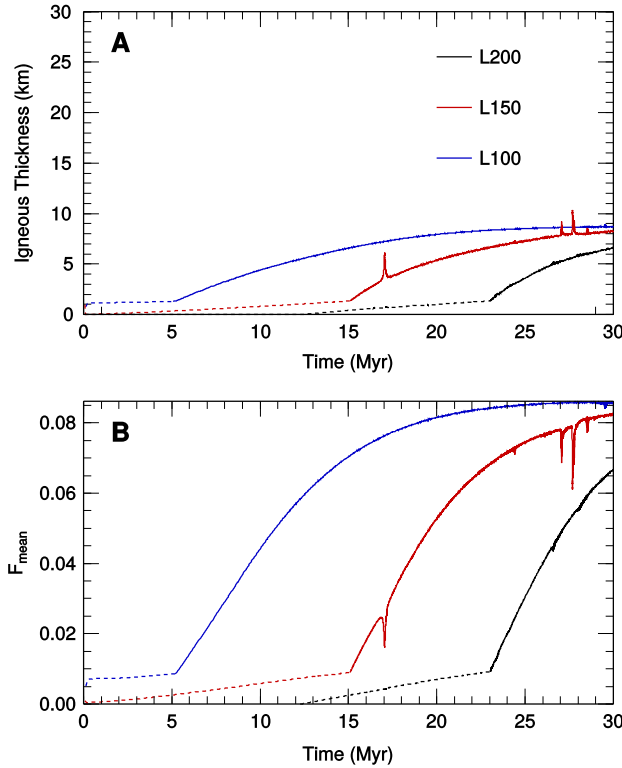


Fig. 2. Thickness of igneous crust generated and mean melt fraction against model run time for mantle potential temperatures 1450°C, and the initial lithosphere thickness is 100, 150 and 200 km (models L100, L150 and L200 in Table 1). (A) Igneous crustal thickness from $h_c = \rho_m/(u_x \rho_l) \int \int \dot{\phi}_{melt} dx dz$, where $\rho_m = 3340 \text{ kg m}^{-3}$ is the mantle density, $u_x = 7 \text{ mm yr}^{-1}$ is the half spreading rate, $\rho_l = 2800 \text{ kg m}^{-3}$ is the melt density and $\dot{\phi}_{melt}$ is the melt production rate. (B) Mean melt fraction given by $F_{mean} = \int F \dot{\phi}_{melt} dx dz / \int F dx dz$, where F is the local melt fraction (Plank et al., 1995). Dashed lines are for hydrodynamic melt production. The spikes in the trends for model L150 are due to convective instabilities nucleated at the edge of the thinned lithosphere. These instabilities increase the melt production rate $\dot{\phi}_{melt}$, hence temporarily increasing crustal thickness. The mean melt fraction reduces at the same time as the zone of high melt production is at depth within regions of low melt fraction therefore biasing the mean melt fraction calculation.

200 km thick lithosphere, respectively. A 50 km increase in lithosphere thickness delays this transition by roughly 10 Myr. The delay time depends on spreading rate; for a half spreading rate of 20 mm yr⁻¹ this delay reduces to 3 Myr and at 80 mm yr⁻¹ it is less than 1 Myr (Armitage et al., 2009). For both mean melt fraction and igneous thickness, the only effect of an increased lithosphere thickness is a systematic delay in the increase in productivity (Fig. 2). Therefore, the evolution of melt composition is similarly shifted in time, but not otherwise affected by the initial lithosphere thickness.

Next we explore how asthenospheric temperature alters the melt productivity. We do this for the more realistic two-phase rifting scenario, to allow for a comparison of melt volumes with the estimated thickness of igneous crust and observed range of durations of rifting. We show results for the models with an initial lithosphere thickness of 100 km, i.e., assuming the present day surrounding lithosphere structure is representative of conditions prior to break-up.

In model 1350N, where the asthenospheric potential temperature is 1350°C, up to 5 km of igneous crust is generated after 35 Myr of evolution (Fig. 3). The mean melt fraction is typically low, ranging from 0.01 at the onset of dry melting to 0.03. The maximum melt fraction reaches 0.08 after 35 Myr of model evolution. For model 1450N, where the potential temperature is 100°C hotter, melt production is significantly increased and ig-

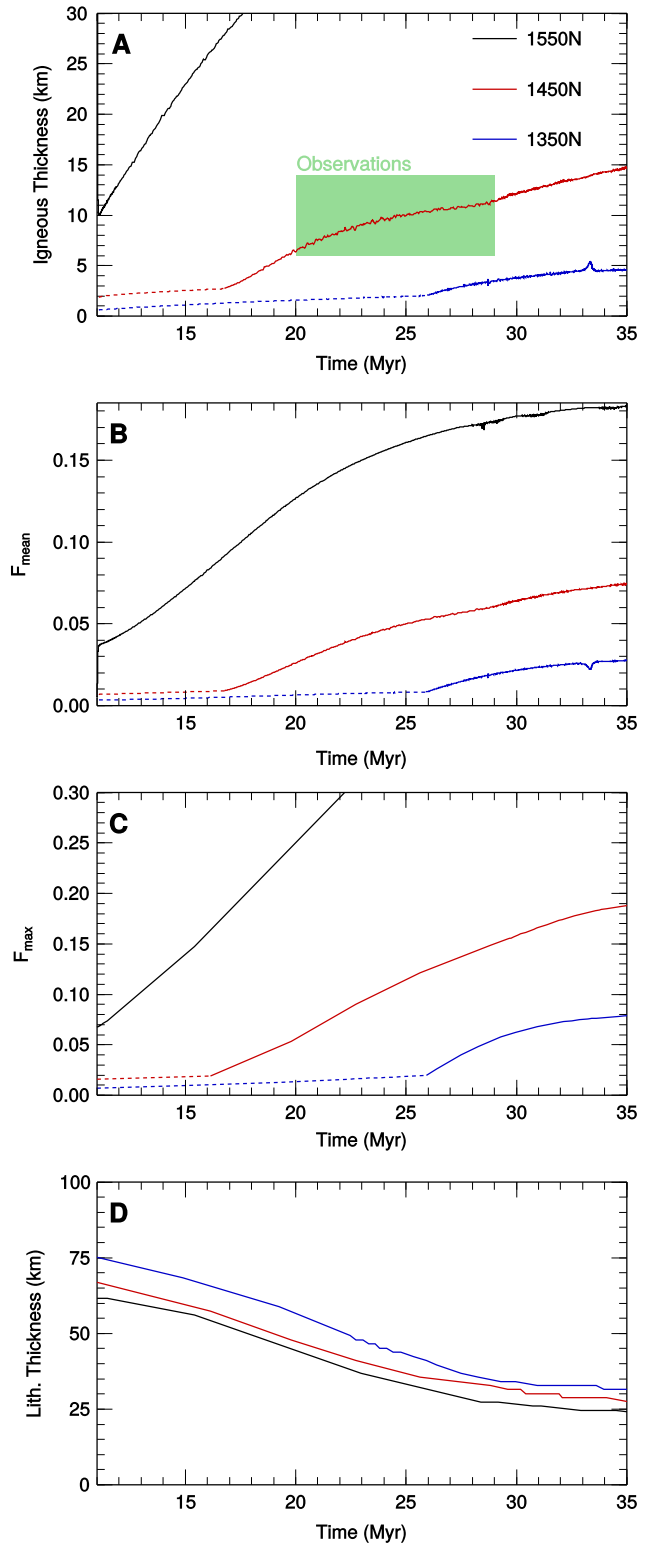


Fig. 3. Melt production and lithosphere thickness as the model rift evolves. Initial lithosphere thickness is 100 km. Dashed lines are for hydrodynamic melt production. (A) Thickness of igneous crust generated against model run time for mantle potential temperatures of 1350, 1450 and 1550°C (models 1350N, 1450N, and 1550N in Table 1). The green-gray region shows the range of igneous thickness calculated from wide angle and receiver function studies (see Supplementary material). (B) Mean melt fraction and (C) maximum melt fraction for the three model cases. (D) Lithosphere thickness taken as the depth to the 1250°C isotherm.

neous crustal thickness reaches 8 km after 21 Myr and 15 km after 35 Myr (Fig. 3). For the 1450N case, the mean melt fraction increases to 0.07 and the maximum melt fraction is 0.19. In model 1550N, where the mantle potential temperature is 1550 °C, melt production rates are very high and the igneous crustal thickness is greater than 15 km after 13 Myr and greater than 30 km after 18 Myr of model evolution (Fig. 3). Furthermore, mean melt fractions are high, up to 0.18, and the maximum melt fraction rapidly increases beyond 0.3. For all models, the depth to the base of the lithosphere, defined as the depth to the 1250 °C isotherm, is similar (Fig. 3D). This is because the thinning of the lithosphere is primarily controlled by the extension, which is at the same rate for all of the models.

3.1.3. Comparison with igneous crustal thickness

In comparison to the observed igneous crustal thickness of between 6 and 14 km, a mantle potential temperature of 1550 °C is too productive and hence too hot to match crustal thickness given the age of the rift zone (Fig. 3). For the case of hydrous melting, a mantle potential temperature of 1350 °C is on the cold side, as it can only approach the lowest estimate for the thickness of intruded melt after the maximum time of extension (Fig. 3). The 1450 °C model predicts 6–12 km of igneous crust after 20 to 29 Ma of rifting, which is within the range of rift durations estimated from observations. For the case of only anhydrous melting a mantle potential temperature of 1350 °C creates less than 6 km, while at 1450 °C the model predicts a thickness >6 km after 18 Myr (see Supplementary Material).

There is a trade off between the temperature of the asthenosphere and the assumed initial lithosphere thickness. For temperatures lower than 1350 °C, an initial lithosphere thickness less than 100 km could produce a reasonable age–igneous thickness trend. Likewise if temperatures are higher than 1450 °C, a lithosphere that is thicker than 100 km would allow matching rift duration and igneous crustal thickness. However, as we will show in the comparison with seismic velocities in Section 3.3, an initial thickness of around 100 km, similar to other Phanerozoic lithosphere (e.g. Artemieva and Mooney, 2001), is most consistent with the range of observations.

3.2. Melt composition

We will now explore how the two preferred models from the previous section, models 1350N and 1450N, create different temporal evolutions in melt chemistry that allows us to better constrain rift duration.

3.2.1. Observations: REE trends

We compare predicted melt compositions to the REE chemistry of late-Pleistocene samples from the Erta Ale (Barrat et al., 1998), Dabbahu (Ferguson et al., 2013) and Asal (Pinzuti et al., 2013; Schilling et al., 1992) magmatic rift zones. These were corrected for crystal fractionation by the incremental addition of olivine, until melts were obtained that are in equilibrium with mantle olivine compositions of Fo₉₀. This was done using an $\text{Fe}^{3+}/\sum \text{Fe}$ ratio of 0.16 (Ferguson et al., 2013) and an Fe–Mg partition coefficient ($K_d = (\text{Fe}^{2+}/\text{Mg})_{\text{olv}}/(\text{Fe}^{2+}/\text{Mg})_{\text{melt}}$) of 0.3. For each zone, the data display a clear decrease in source normalised concentration from middle to heavy REE. The ratio of La to Yb for the rock samples from all three zones have a mean of 5.52 and a standard deviation of 2.26. For Dy/Yb the ratio is 2.02 ± 0.15 (Fig. 4).

3.2.2. Models: Effect of mantle temperature and rift duration

During early extension low degree melts are generated during hydrous melting at high pressures, where garnet is stable in the mantle. During this early period, the most incompatible elements,

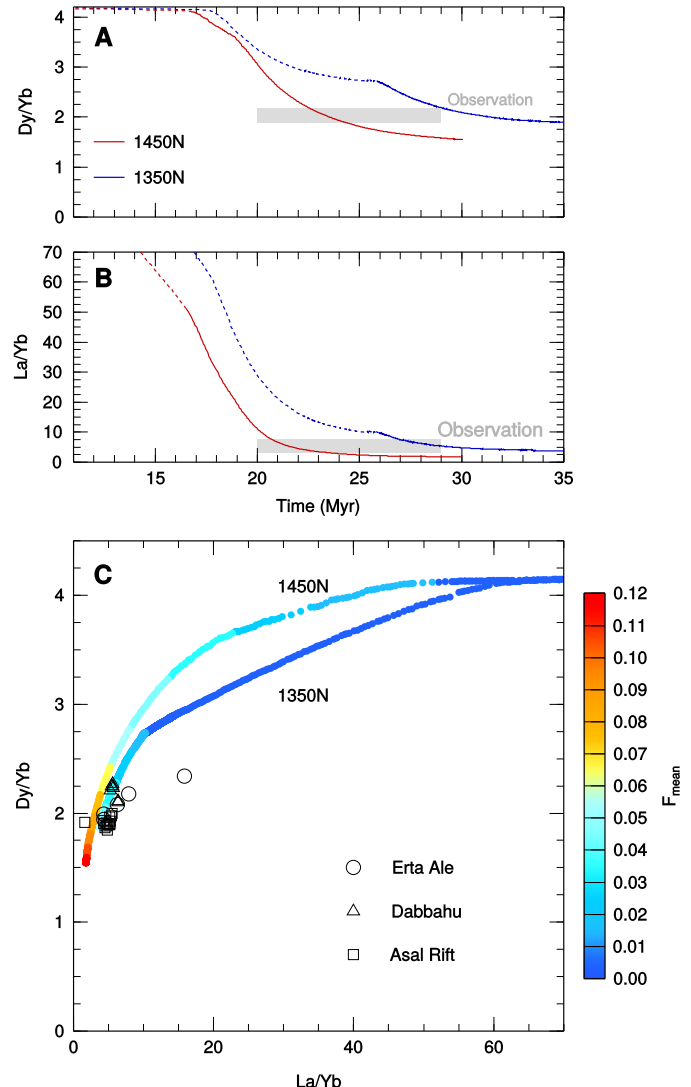


Fig. 4. Model trend in the ratio of La to Yb and Dy to Yb against time as the rift evolves with extension at a half rate of 7 mm yr⁻¹ after an initial period of 11 Myr of extension at a half spreading rate of 3.5 mm yr⁻¹. The model is compared to the observed compositions from the Erta Ale (Barrat et al., 1998), Dabbahu (Ferguson et al., 2013) and Asal magmatic segments (Pinzuti et al., 2013; Schilling et al., 1992). Dashed lines are for hydrous-only melt production. (A) Ratio of Dy to Yb plotted against time. The ratio decreases as more productive dry melting begins, and as the degree of melting increases above the garnet-in transition. (B) Ratio of La to Yb plotted against time. (C) Dy/Yb plotted against La/Yb showing the observed compositions from the three regions. The model trend in composition is plotted with a colour scale that represents the mean melt fraction. Both models trend towards the observed compositions, but along different paths and reaching different mean melt fractions. (For interpretation of the colours in this figure, the reader is referred to the web version of this article.)

such as La and Ce, enter the melt leaving a depleted source. Compatible elements, such as Dy and Yb, predominately remain within the solid mantle matrix during early melt production.

For a fertile mantle with no previous depletion, and a mantle potential temperature of 1350 °C, the wet solidus is crossed at a depth of 120 km and the dry solidus at 55 km; for a mantle potential temperature of 1450 °C, the wet solidus is crossed at 150 km and the dry solidus is at 80 km depth (see Eqs. (4) to (6) in the Supplementary Material). The spinel-out boundary is between 80 and 85 km at 1350 and 1450 °C (McKenzie and O'Nions, 1991). With these parameters the La/Yb ratio decreases earlier than the Dy/Yb ratio, due to the incompatible elements having partition coefficients that are two orders of magnitude smaller in the garnet

stability field (Fig. 4). From the plot of Dy/Yb against time we can see that, if the mantle temperature is 1450 °C, productive dry melting occurs while the melt composition is still dominated by the garnet signature. If however the mantle temperature is 1350 °C there is a second decrease in Dy/Yb at 26 Myr, as more productive dry melting commences (Fig. 4A). If we assume the mantle is dry (models 1350D and 1450D in Table 1) then the REE composition is only matched by the colder model when there is a very small volume of melt (see Supplementary Material).

3.2.3. Comparison with REE trends

In Fig. 4 the evolution of the La/Yb and Dy/Yb ratios approaches the observations after dry melting has initiated and the lithosphere has thinned to less than 50 km (Fig. 3). For a mantle temperature of 1350 °C the model 1350N approaches the observed composition after 29 Myr of model evolution with a mean melt fraction of 0.05 (Fig. 4). For an asthenosphere of 1450 °C the model 1450N approaches the observed composition after 22 Myr of model evolution with a mean melt fraction of 0.08 (Fig. 4).

To further explore which mantle potential temperature best fits the REE signature of the recent Afar lavas, we use a simple measure of maximum likelihood (Wald, 1943), and compare this fit to the χ^2 value for each sample size at the 95 and 70% confidence interval (Fig. 5). For each zone, the data display a clear decrease in source normalised concentration from middle to heavy REE. For our two model scenarios, as the rifting progresses the modelled melt compositions approach those of the observed lavas and then diverge towards more depleted compositions. For all three data sets, the model with a mantle potential temperature of 1450 °C gives the best fit at a time of 22–23 Myr after the initiation of extension, while the cooler model requires a longer duration of extension, 30–35 Myr (Fig. 5).

In detail, for the Erta Ale lavas, the model with a mantle potential temperature of 1450 °C fits well, while the cooler model does not as convincingly re-create REE compositions (Fig. 5A and D). The hotter model can match the Dabbahu magmatic segment data, however, the cooler model fits better (Fig. 5B and E). The southernmost site, the Asal Rift, which is the first on-land section of the Gulf of Aden, has an REE profile that is best matched by the melting of a 1450 °C mantle (Fig. 5C and F). The cold model does also approach a close fit to the composition at older ages, yet there is a systematic over prediction in the concentration of REEs (Fig. 5F). A shorter duration of rifting at Erta Ale is in close agreement with plate reconstructions that suggest extension initiation in the southern Red Sea at 24 ± 4 Ma (Reilinger and McClusky, 2011), though slightly younger than the 26 to 29 Ma estimate of Wolfenden et al. (2005). For the Dabbahu magmatic segment, both the shorter and longer duration of rifting are plausible given the age constraints from kinematic reconstructions (Reilinger and McClusky, 2011; Wolfenden et al., 2005). The elevated temperature at Asal is in agreement with previous estimates of mantle temperatures in this region (Rooney et al., 2012b; Pinzuti et al., 2013).

3.3. Bulk seismic structure

The comparison of the predicted melt production with the observations yielded two preferred model scenarios: model 1450N at ~22 Myr of extension and model 1350N after ~30 Myr. The Afar region is well known for its extreme low-velocity anomalies. A range of surface-wave studies find minimum shear velocities between 3.6 and 4.0 km s^{-1} between about 50 and 100 km depth (Knox et al., 1998; Debayle et al., 2001; Montanger et al., 2007; Fishwick, 2010; Chang and Van der Lee, 2011). Next, the synthetic seismic structures predicted for the two preferred models are compared to these shear wave constraints.

3.3.1. Modelled seismic structure

Fig. 6 displays in the left column model thermal structure, with contours for the amount of retained melt, for models with a 1450 °C and 1350 °C mantle temperature and different amounts of melt retention (models 1350N, 1450N, 1450L and 1450T in Table 1). Asymmetry in the zone of partial melting is created due to the 100 km east to west shift in extension after 11 Myr (see Section 2.5). In the central panels, the melt production and melt fraction is plotted against depth for the centre of extension. In the right hand column of Fig. 6, the corresponding shear velocity structure (dependent on temperature, pressure, composition, melt retention and dehydration) is shown.

The seismic structure is strongly affected by the thickness of the thermal lithosphere. Due to the decreasing $\partial V_S / \partial T$ with increasing pressure (e.g. Goes et al., 2000), adiabatic upwelling of mantle material leads to lower velocities at shallower depths. As a result the cooler model, 1350N (Fig. 6A and B), with the thinner lithosphere (30 km) yields lower minimum velocities than the warmer model 1450N (50 km lithosphere) (Fig. 6C and D). Note that the effect of the thinner lithosphere is even stronger than the effect of the larger amount of melt in model 1450N (up to 0.5% melt retained) than model 1350N (up to 0.3% melt retained).

If melt retention is enhanced, velocities are further decreased. This is illustrated by the model with an order of magnitude lower permeability (1450L), where the maximum melt retention is increased to 0.9%, and the model where melt does not migrate until its porosity exceeds 1% (1450T), where the retained melt fraction is enhanced to 1.1% (Fig. 6E and G). These two models are also plotted at slightly later times than model 1450N (25, 24 and 22 Myr respectively). This contributed to the stronger and wider low velocity zones in the two high melt-retention models.

3.3.2. Comparison with tomographic constraints

We find that all model cases are able to produce low shear velocities in the observed range, due to the combination of strong attenuation at asthenospheric temperatures and the elastic effect on seismic wave speed from presence of melt (Fig. 6). The higher amounts of melt predicted by the models with stronger retention are required to reach the lowest values in the observed range.

Bulk seismic velocities provide a strong indication of a relatively shallow lithosphere–asthenosphere boundary at 50 to 30 km depth. If the lithosphere was thicker than 80 km, as proposed by Ferguson et al. (2013), then seismic velocities would not reach the minimum values observed. A thinning factor of 2 to 3 is therefore required by the seismic constraints and REE patterns. This is within the range of values we estimated to derive igneous thickness estimates in Fig. 3 and of crustal stretching factors inferred for Afar (e.g. Wolfenden et al., 2005). Furthermore, significant fractions of melt only form once the dry solidus is crossed, i.e., melt fractions of around 1%. This requires the lithosphere to have thinned to 50 km from an original thickness outside of the rift of 100 km. Thus, the seismic velocities provide further support for our choice of initial lithospheric thickness, and are consistent with the 1450 °C mantle temperature preferred by the comparison melt volumes and melt chemistry.

3.4. Seismic discontinuities

3.4.1. S-to-P receiver function constraints

A detailed S-to-P receiver function study of the lithosphere and shallow mantle below Afar (Rychert et al., 2012) found two prominent discontinuities below the rift flanks, one at around 30 km with a positive velocity change (i.e. increase of velocity with depth) attributed to the base of the crust, and one at about 80 km depth with a negative polarity associated with the base of the lithosphere (the ‘LAB’, lithosphere–asthenosphere-boundary). Within the rift

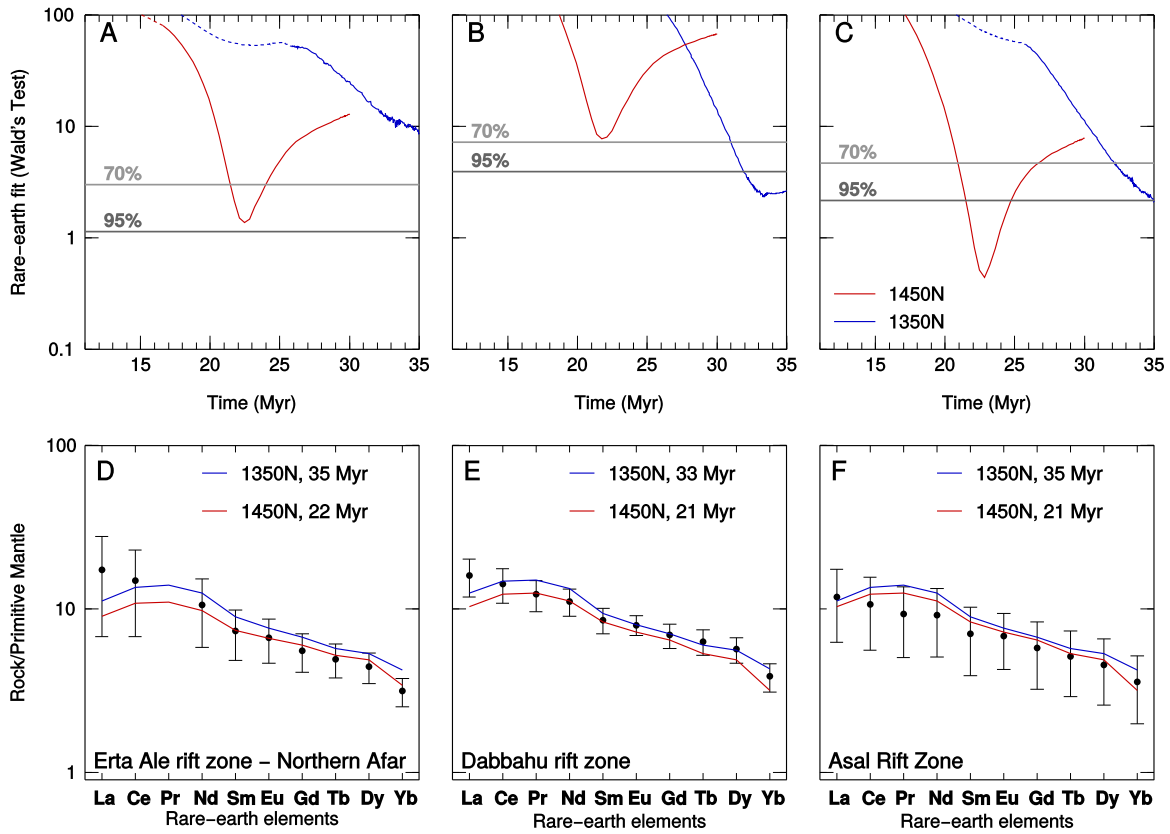


Fig. 5. Comparison of predicted Rare-Earth Element (REE) composition against the observed compositions from the Ertá Ale (Barrat et al., 1998), Dabbahu (Ferguson et al., 2013) and Asal magmatic segments (Pinzuti et al., 2013; Schilling et al., 1992). Parts (A)–(C) show the quality of the fit of the range of REE predicted against the observations, by calculating the misfit using Wald's Test (Wald, 1943). The gray lines display the confidence levels for the quality of fit. Parts (D) to (F) show the pattern of REE compositions at each region and the two model generated best fits. Dashed lines are for hydrous-only melt production.

zone however, the negative polarity signal was absent and instead, under large parts of the rift, a positive polarity signal (with an amplitude 15–20% of that associated with the Moho) was found at around 50–70 km depth in addition to the Moho signal at 30 km depth. Rychert et al. (2012) interpreted the latter discontinuity as the base of the dry melt zone with an 8% change in shear wave velocity which has to occur over a depth interval of at most 10 km.

3.4.2. Models: impedance contrasts and receiver functions

Whether a seismic velocity jump leads to the conversions from S-to-P waves that are imaged with receiver functions, depends on the strength and sharpness of the impedance (product of velocity and density) contrast across the boundary. We show impedance gradients for the two asthenosphere temperatures 1350 °C and 1450 °C and with increased melt retention (models 1350N, 1450N, 1450L, 1450T in Table 1) in Fig. 7 and as 1-D profiles through the centre of extension in Fig. 8D (models 1350N, 1450N, 1450L). By far the strongest impedance contrast is that predicted for the Moho, while a negative impedance contrast characterises the base of the dehydrated lithosphere. A positive impedance contrast develops near the base of the melt zone, but its amplitude is only a very small fraction (<1%) of the Moho contrast even when we impose a threshold of 1% for melt transport (Fig. 7).

Vertical profiles of attenuation, shear velocity structure and shear impedance gradients directly below the centre of the model rift illustrate the velocity jumps (Fig. 8). This figure includes an additional model with low permeability where melt is assumed to have an additional attenuating anelastic effect. The models span a large range of potential melt retention and seismic sensitivity to the presence of melt. In spite of this, in all cases, the transi-

tion from wet to dry melt regions remains too gradual to cause a strong impedance jump.

We calculate a synthetic receiver function for model 1450N and model 1450L (Fig. 9). At the rift axis we predict a profile with two positive peaks, separated by a negative one (Fig. 9B). The first positive and negative peaks of the synthetic receiver function are due to the Moho velocity contrast. The negative Moho side lobe is further enhanced by a negative peak due to the base of the dehydrated lithosphere, which is accompanied by a deeper positive side lobe. The base of the dry melt zone generates a negligible signal in the 1450N model and gives only a very minor contribution to the deepest positive swing in the 1450L model.

3.4.3. Comparison: impedance and receiver functions

Although higher melt retention and increased attenuation of the melt enhance the velocity contrast across the base of the dry melt zone, none of the models produce an impedance contrast that comes close to the sharp 8% increase in V_S inferred from the actual receiver functions. Furthermore, this additional melt effect on attenuation reduces the V_S to very low speeds, significantly below the lowest observation from surface waves (Fig. 8). Not even when all melt is retained, or productivity increased by reducing the solidus-depletion gradient, $\partial T_s / \partial F|_z$ (see Supplementary Material), from 300 to 200 °C, which deteriorates the fit of the REE data, are we able to significantly increase the impedance jump.

The expression of the inferred 8% jump in the receiver function is the absence of the negative lobe due to the Moho. This requires a shallow (between 50 and 70 km depth) positive discontinuity to largely cancel this part of the Moho signal (Rychert et al., 2012). The impedance contrast from our modelled base of the silicate (dry) melt zone occurs deeper in our warmer models, but

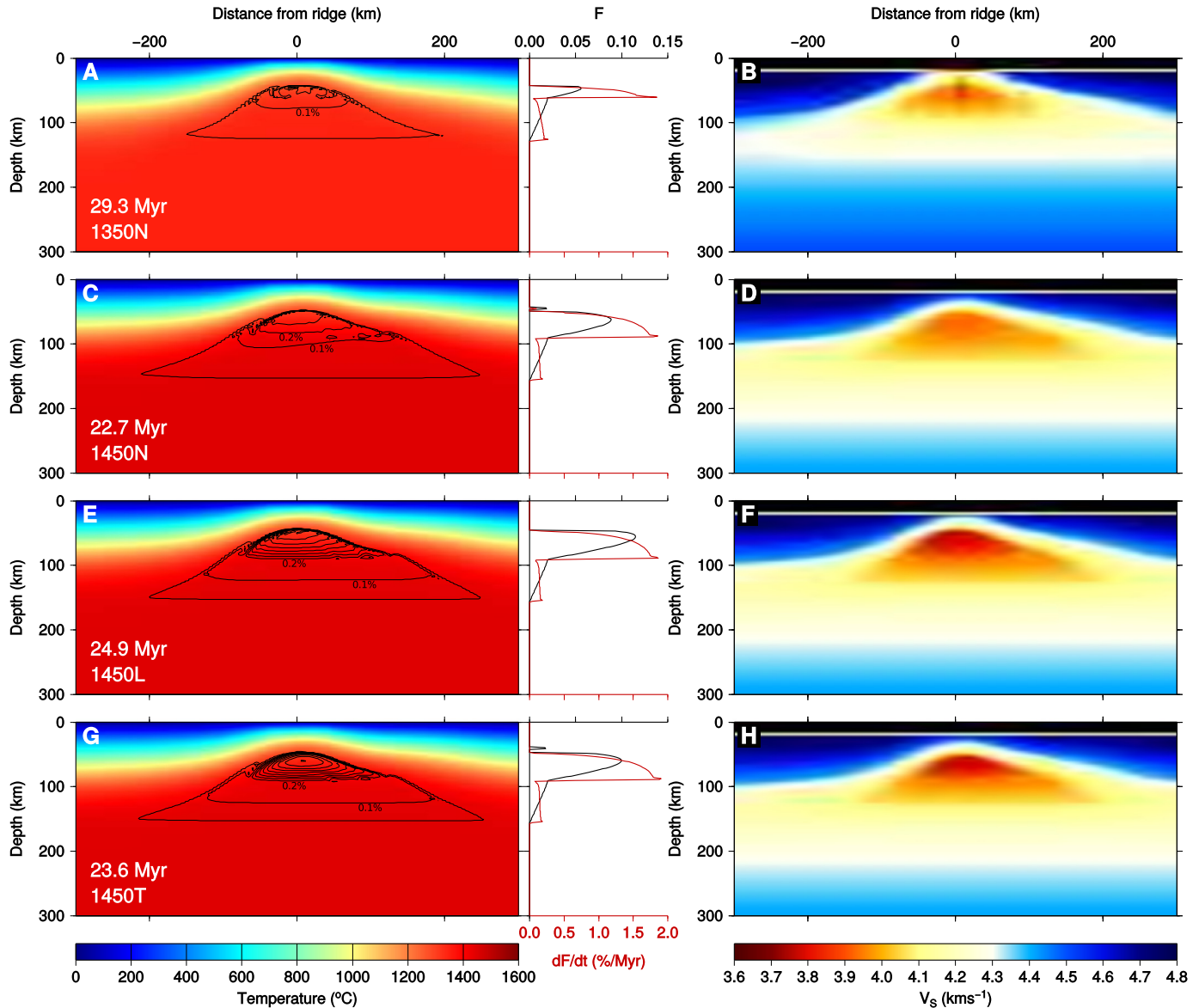


Fig. 6. Modelled temperatures and the volume of melt retained within the partial melt zone for a number of different model cases on the left. The centre plots display the melt fraction (black lines) and the melt production rate against depth at the centre of extension (0 km). Corresponding synthetic shear velocity on the right. Model structures are shown at the best fit time for the REE composition taken from Fig. 5. Contours in the left panels display the extent of the zone of partial melting and then contours at 0.1%. (A, B) Model 1350N with potential temperature of 1350 °C and reference melt permeability (10^{-10} m^2). (C, D) Model 1450N with potential temperature of 1450 °C and reference melt permeability. (E, F) Model 1450L with low permeability (10^{-11} m^2 , compared to 10^{-10} m^2 in parts (A)–(D)). (G, H) Model 1450T with reference permeability, but where melt is immobile if the porosity is below 1%. Maximum melt retention ranges from less than 0.5% (panels A, C) to 1.1% (panel G). All cases give minimum V_s consistent with those imaged below Afar (see text). Seismic velocities are more sensitive to depth of the lithosphere–asthenosphere transition than to potential temperature in the range from 1350 to 1450 °C. The slight asymmetry in the zone of partial melting is due to the 100 km east to west shift after 11 Myr in the centre of extension across the Danakil block. Models 1450N, 1450L and 1450T are plotted at the same numerical time step, which corresponds to slightly different duration's given the differing convective vigour between the models. (For interpretation of the colours in this figure, the reader is referred to the web version of this article.)

even in the 1350N model it is insufficient to mask the negative side lobe from the Moho conversion.

A further difference between our profiles and the structure that the receiver functions found below the rift zone is that the negative polarity jump due to the base of the lithosphere is also present (Fig. 9). It has been proposed by a range of seismic and resistivity studies that the lithosphere below the rift is heavily melt intruded by as much as 3% melt (Stork et al., 2013; Desissa et al., 2013). This melt is thought to occupy a large region at and below the Moho beneath Dabbahu segment (Desissa et al., 2013). If the amount of melt in the lithosphere is at least as large as that in the asthenosphere directly below, the velocity contrast at the lithospheric base could be cancelled. Thus, the

absence of an ‘LAB’ type discontinuity in the receiver functions would further confirm that the lithosphere below the rift is melt-filled. We find that a 1% melt porosity above the zone of partial melting can mask the impedance jump between the dehydrated lithosphere and damp, melt-filled underlying mantle. The synthetic receiver functions also predict a Moho jump that is too strong, unless we assume a low velocity lithosphere. One might argue that such a melt-filled lithosphere should not be called a lithosphere, as it is no longer seismically distinct. However, it may still behave different rheologically than the asthenospheric mantle below, leading to the relatively narrow zone of shallow vertical and along-axis alignment of seismic anisotropy (Hammond et al., 2014; Hammond, 2014).

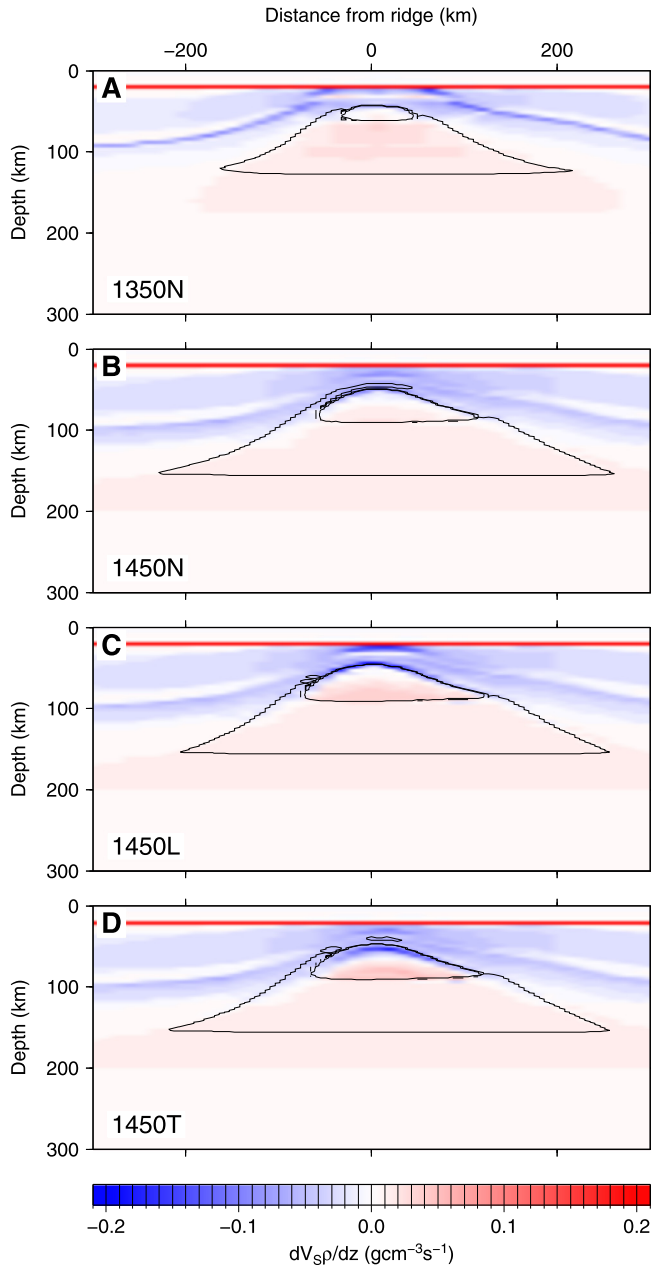


Fig. 7. Vertical shear impedance (V_S times density) gradients for the four models at the best fit time for the REE composition taken from Fig. 5 (corresponding shear velocity structures are shown in Fig. 6B, D). Impedance increases with depth are in red, decreases in blue colours. (A) Model where the mantle temperature is 1350 °C (1350N, Table 1) at 29.3 Myr. (B) Model where the mantle temperature is 1450 °C and the permeability is 10^{-10} m⁻² (1450N, Table 1) at 22.7 Myr. (C) Model where the mantle temperature is 1450 °C and the permeability is 10^{-11} m⁻² (1450L, Table 1) at 24.9 Myr. (D) Model where the mantle temperature is 1450 °C and the permeability is 10^{-10} m⁻² with a 1% threshold on melt transport (1450T, Table 1) at 23.6 Myr. The strongest contrast occurs at the Moho, which reaches an amplitude outside of the range plotted: 4 g cm⁻³ s⁻¹. The base of the dehydrated lithosphere gives rise to a negative impedance contrast, while the base of the dry melt zone corresponds to a weak positive contrast. (For interpretation of the references to colour in this figure legend, the reader is referred to the web version of this article.)

The assumption that there is 1% melt in the lithosphere creates a synthetic receiver function which is closer to the observation (Fig. 9). Yet this assumption is somewhat ad hoc and still cannot replicate the signal previously attributed to the base of the dry melt zone. Therefore, the comparison with receiver functions does not allow us to further narrow down the plausible model scenarios.

4. Discussion

4.1. Melt chemistry

Overall, 1450 °C and a rift age of 22 to 23 Myr gives the best match to the REE data and crustal thickness. Models with a more depleted source composition fit the data but yield the same best-fit age and temperature. The variable quality of the fits to the observed lavas between rift zones may reflect some lateral variations in temperature and rift onset times.

In all of our modelled melts there is a systematic underestimation of the concentration ratios between the most incompatible elements, such as La and Ce, when compared to the observed lavas. The positive slope between La and Pr in Fig. 5 is because of model source depletion. It is possible that our assumption that melt and solid are in equilibrium for a particular model time step, which has a typical duration of 40 kyr, allowing a simple mass balance to be used to estimate the solid composition as melting progresses is not valid. The inverse model used to model REE melt compositions by Ferguson et al. (2013) for example assumes fractional melting throughout. The other possibility is that there is a greater flux of fertile mantle through the melt zone due to a buoyant mantle source, such as a thermal plume beneath Afar that the present model does not capture, which leads to less source depletion.

4.2. The onset of melt retention and seismic discontinuities

Our models indicate that the positive discontinuity amplitude that S -to- P receiver functions image at a depth of 50–70 km below the rift zone cannot be a simple consequence of the isotropic effects of melt on seismic velocities. Different melting models, like that developed by Katz et al. (2003), also predict a gradual onset of melting and hence a gradual reduction in V_S and V_P , especially for melting in the presence of water.

A recent 1-D modelling study (Havlin and Parmentier, 2014) suggests that strong discontinuities associated with melting can be produced in a mantle of higher viscosity and/or lower water content or at high upwelling rates. Our models are not able to match melt constraints using a dry mantle, and it would thus be hard to argue for significantly higher viscosity. Higher upwelling rates provide faster influx of new fertile material and hence enhance melt production and for the same permeability also increase melt retention. According to the models of Havlin and Parmentier (2014), upwelling rates of several tens of cm/yr are required. Using the same numerical model as presented here, Goes et al. (2012) found melt retention increased to 1.3% when the half spreading rate and hence vertical flow was roughly 6 times greater, insufficient for a strong impedance contrast at the onset of dry melting. It is unclear that the conditions under Afar, with much lower spreading rates and potential active upwellings with relatively mild excess temperatures, could produce fast enough upward flow to allow formation of an 8% shear-velocity discontinuity. If so, the receiver function signal could be further support for a hotter mantle with active upwellings, although it may not be a direct effect of the onset of dry melting, which at higher temperatures occurs deeper than 50–70 km depth. Furthermore, increased upwelling at a mantle temperature of 1450 °C, which is consistent with the melt chemistry, would increase crustal thickness beyond that observed.

While it is not easy to explain the velocity increase at 50–70 km depth below Afar by the onset of melting, similar S -to- P observations in a range of hotspots (e.g. Hawaii, Galapagos; Rychert et al., 2013, 2014) do indicate that the discontinuities are a signal of melt in the mantle. Another possible mechanism to sharpen the impedance contrast could be a change in seismic anisotropy with depth, a similar mechanism to that which is suggested below

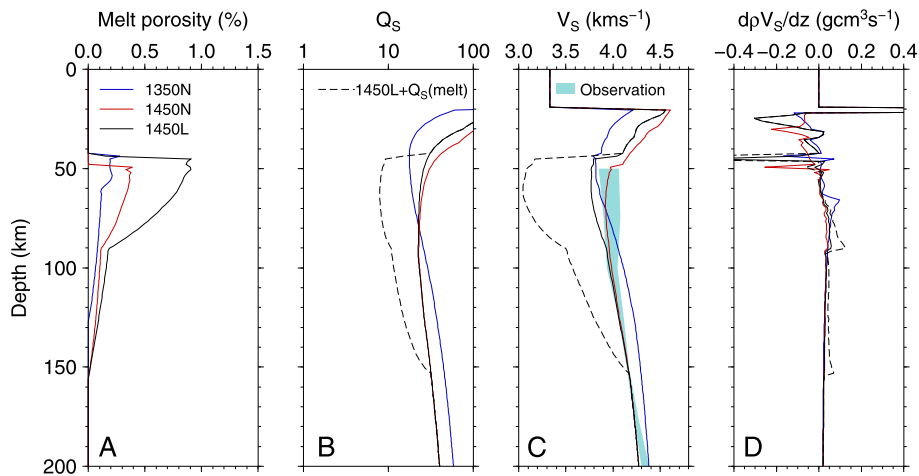


Fig. 8. Shear velocity-depth and shear impedance-depth profiles below the ridge for several different models: (A) Melt porosity for the cool model (1350N; blue line), the hot model (1450N; red line), and the model of low permeability (1450L; 10^{-11} m^2), which is very similar to the model of minimum melt retention (1450T; Fig. 6). (B) Attenuation structure for the three models in panel A, and a fourth model where the low permeability is combined with an increased attenuation due to the partial melt retained in the mantle (dashed line). (C) Shear wave velocity for the four models in panel B with the range of observed shear wave velocities extracted from surface waves below Erta Ale, Dabbahu and Asal (Fishwick, 2010). (D) Shear impedance-depth profiles for the same four models. None of the cases give a velocity and impedance contrast approaching that inferred from Afar receiver functions (about 8% change in V_s over <10 km and about 20% of the Moho impedance contrast, respectively Rychert et al., 2012). (For interpretation of the references to colour in this figure legend, the reader is referred to the web version of this article.)

cratons (e.g. Yuan and Romanowicz, 2010). Melt that retains a preferential orientation is an efficient mechanism to generate seismic anisotropy (Blackman and Kendall, 1997), and so a rapid change in the style of preferred orientation of melt with depth could cause a sharp discontinuity. In rift settings a number of mechanisms exist that could align melt. Where significant topography exists on the lithosphere–asthenosphere boundary, high strain rates can cause melt bands to form (Holtzman and Kendall, 2010). Also, the alignment of melt as it migrates through lithosphere (Faul, 2001) or in the presence of vertical flow in the asthenosphere (Blackman and Kendall, 1997) will likely cause a seismic anisotropy. Shear-wave splitting and P -wave receiver function studies show that vertically aligned melt exists at the rift axis and rift margins in the crust and lithospheric mantle beneath Afar (Hammond et al., 2014; Hammond, 2014), whereas much of the asthenospheric mantle beneath Afar has little shear-wave splitting suggesting horizontally aligned or no preferential alignment of melt (Hammond et al., 2014). A change in alignment of melt between the lithosphere and asthenosphere or due to the onset of melt mobilisation, which enhances preferential orientation as melt fraction approaches 1%, could cause the discontinuity seen in S -wave receiver functions.

5. Conclusions

This study suggests that mantle temperatures are elevated below Afar and the lithosphere has significantly thinned. This agrees with aspects of previous geochemical and seismic interpretations: Rare-earth-element concentrations from mafic magmas point to melt in the garnet stability field, at elevated temperatures 1450 °C. However, rather than requiring a thick lithosphere (Ferguson et al., 2013), our models reproduce the REE data with the addition of hydrous melting. S -to- P receiver functions imaged a seismic discontinuity at ~50–70 km depth which was attributed to the base of the dry melt zone, requiring a thinned lithosphere (Rychert et al., 2012). To also fit constraints on volumes of magma in the crust, our models require that rifting started at ~23 Ma, and the mantle is ~1450 °C, leading to lithospheric thinning by about a factor of 2, to around 50 km, and significant decompressional melting. However, in none of the models are the isotropic effects of retained melt on seismic velocity able to recreate the strong and sharp change in shear speed found in the receiver functions at 50–70 km depth. Alternatively, we propose that the discontinuity

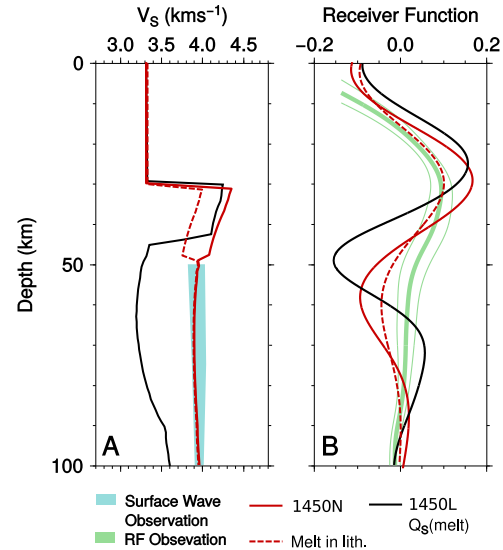


Fig. 9. Synthetic receiver functions for the forward model compared with a characteristic rift receiver function from Rychert et al. (2012). To be able to make a fair comparison with the receiver function derived from observations, we set the Moho depth from 20 to 30 km to be consistent with the published receiver function below Afar (Rychert et al., 2012). (A) Shear wave velocities through the centre of extension for the model 1450N (red dashed line), the same model where we assume 1% melt is in transport within the lithosphere above the zone of partial melting (red solid line) and the model 1450L with additional attenuation due to the presence of melt (black solid line). These vertical profiles are compared against surface wave estimates of V_s from Fishwick (2010) in light blue. (B) Synthetic receiver functions from the model 1450N (red dashed line), model 1450N with melt above the zone of partial melting (red solid line) and the model 1450L with additional attenuation due to melt (black solid line). These synthetic receiver functions are compared to the binned receiver function from Afar in light green, with statistical errors estimated from the 95% confidence interval from a bootstrapping exercise Rychert et al. (2012). (For interpretation of the references to colour in this figure legend, the reader is referred to the web version of this article.)

is a consequence of a change in seismic anisotropy due to melting. In other respects, extension above a mantle with elevated temperatures reconciles the observed magma chemistry, estimates of magmatic crust volumes and minimum mantle shear velocities below the Afar rift.

Acknowledgements

This work was funded by a Royal Astronomical Society Fellowship to John J. Armitage. James O.S. Hammond was funded by NERC fellowship NE/I020342/1. We would like to thank Ian Bastow for initiating this work, Lidia Panico for statistical assistance, Mark Behn and John MacLennan for their constructive reviews.

Appendix A. Supplementary material

Supplementary material related to this article can be found online at <http://dx.doi.org/10.1016/j.epsl.2015.02.039>.

References

- Armitage, J.J., Collier, J.S., Minshull, T.A., 2010. The importance of rift history for volcanic margin formation. *Nature* 465, 913–917. <http://dx.doi.org/10.1038/nature09063>.
- Armitage, J.J., Collier, J.S., Minshull, T.A., Henstock, T.J., 2011. Thin oceanic crust and flood basalts: India–Seychelles breakup. *Geochim. Geophys. Geosyst.* 12, Q0AB07. <http://dx.doi.org/10.1029/2010GC003316>.
- Armitage, J.J., Henstock, T.J., Minshull, T.A., Hopper, J.R., 2009. Lithospheric controls on the rifting of continents at slow rates of extension: application to the North Atlantic. *Geochim. Geophys. Geosyst.* 10, Q06018. <http://dx.doi.org/10.1029/2009GC002404>.
- Artemieva, I.M., Mooney, W.M., 2001. Thermal thickness and evolution of Precambrian lithosphere: a global study. *J. Geophys. Res.* 106, 16387–16414. <http://dx.doi.org/10.1029/2000JB900439>.
- Barrat, J.A., Fourcade, S., Jahn, B.M., Cheminee, J.L., Capdevila, R., 1998. Isotope (Sr, Nd, Pb, O) and trace-element geochemistry of volcanics from the Ert A Ale range (Ethiopia). *J. Volcanol. Geotherm. Res.* 80, 85–100. [http://dx.doi.org/10.1016/S0377-0273\(97\)00016-4](http://dx.doi.org/10.1016/S0377-0273(97)00016-4).
- Bastow, I.D., Keir, D., 2011. The protracted development of the continent–ocean transition in Afar. *Nat. Geosci.* 4, 248–250. <http://dx.doi.org/10.1038/ngeo1095>.
- Blackman, D., Kendall, J.-M., 1997. Sensitivity of teleseismic body waves to mineral texture and melt in the mantle beneath a mid-ocean ridge. *Philos. Trans. R. Soc. A* 355, 217–231.
- Bostock, M.G., 1998. Mantle stratigraphy and evolution of the slave province. *J. Geophys. Res.* 103, 121183–121200. <http://dx.doi.org/10.1029/98JB01069>.
- Cerveny, V., 2005. *Seismic Ray Theory*. Cambridge University Press.
- Chang, S.-J., Van der Lee, S., 2011. Mantle plumes and associated flow beneath Arabia and East Africa. *Earth Planet. Sci. Lett.* 302, 448–454. <http://dx.doi.org/10.1016/j.epsl.2010.12.050>.
- Connolly, J.A.D., 2005. Computation of phase equilibria by linear programming: a tool for geodynamic modeling and its application to subduction zone decarbonation. *Earth Planet. Sci. Lett.* 236, 524–541. <http://dx.doi.org/10.1016/j.epsl.2005.04.033>.
- Dean, S.M., Murton, B.J., Minshull, T.A., Henstock, T.J., White, R.S., 2008. An integrated kinematic and geochemical model to determine lithospheric extension and mantle temperature from syn-rift volcanic compositions. *Earth Planet. Sci. Lett.* 278, 26–39. <http://dx.doi.org/10.1016/j.epsl.2008.11.012>.
- Debayle, E., Lévéque, J.-J., Cara, M., 2001. Seismic evidence for a deeply rooted low-velocity anomaly in the upper mantle beneath northeastern Afro/Arabian continent. *Earth Planet. Sci. Lett.* 193, 423–436.
- Desissa, M., Johnson, N.E., Whaler, K.A., Hautot, S., Fisseha, S., Dawes, G.J.K., 2013. A mantle magma reservoir beneath an incipient mid-ocean ridge in Afar, Ethiopia. *Nat. Geosci.* 6, 861–865. <http://dx.doi.org/10.1038/ngeo1925>.
- Faul, U.H., 2001. Melt retention and segregation beneath mid-ocean ridges. *Nature* 410, 920–923. <http://dx.doi.org/10.1038/35073556>.
- Faul, U.H., Fitz Gerald, J.D., Jackson, I., 2004. Shear wave attenuation and dispersion in melt-bearing olivine polycrystals: 2. Microstructural interpretation and seismological implications. *J. Geophys. Res.* 109, B06202. <http://dx.doi.org/10.1029/2003JB002407>.
- Ferguson, D.J., MacLennan, J., Bastow, I.D., Pyle, D.M., Jones, S.M., Keir, D., Blundy, J.D., Plank, T., Yirgu, G., 2013. Melting during late-stage rifting in Afar is hot and deep. *Nature* 499, 70–73. <http://dx.doi.org/10.1038/nature12292>.
- Fishwick, S., 2010. Surface wave tomography: imaging of the lithosphere–asthenosphere boundary beneath central and southern Africa? *Lithos* 120 (1), 63–73. <http://dx.doi.org/10.1016/j.lithos.2010.05.011>.
- Fishwick, S., Bastow, I.D., 2011. Towards a better understanding of African topography: a review of passive-source seismic studies of the African crust and upper mantle. In: *Geol. Soc. (Lond.) Spec. Publ.*, vol. 357, pp. 343–371. <http://dx.doi.org/10.1144/SP357.19>.
- Gibson, S.A., Geist, D., 2010. Geochemical and geophysical estimates of lithospheric thickness variation beneath Galápagos. *Earth Planet. Sci. Lett.* 300, 275–286. <http://dx.doi.org/10.1016/j.epsl.2010.10.002>.
- Goes, S., Govers, R., Vacher, P., 2000. Shallow mantle temperatures under Europe from P and S wave tomography. *J. Geophys. Res.* 105 (B5), 11153–11169.
- Goes, S., Armitage, J.J., Harmon, N., Smith, H., Huismans, R., 2012. Low seismic velocities below mid-ocean ridges: attenuation versus melt retention. *J. Geophys. Res.* 117, B12403. <http://dx.doi.org/10.1029/2012JB009637>.
- Gribb, T.T., Cooper, R.F., 2000. The effect of an equilibrated melt phase on the shear creep and attenuation behaviour of polycrystalline olivine. *Geophys. Res. Lett.* 27, 2341–2344. <http://dx.doi.org/10.1029/2000GL011443>.
- Hammond, J.O.S., 2014. Constraining melt geometries beneath the Afar Depression, Ethiopia from teleseismic receiver functions: the anisotropic H- κ stacking technique. *Geochem. Geophys. Geosyst.* 15, 1316–1332. <http://dx.doi.org/10.1002/2013GC005186>.
- Hammond, J.O.S., Kendall, J.-M., Wooley, J., Stuart, G.W., Keir, D., Ayele, A., 2014. Differentiating flow, melt, or fossil seismic anisotropy beneath Ethiopia. *Geochem. Geophys. Geosyst.* 15, 1878–1894. <http://dx.doi.org/10.1002/2013GC005185>.
- Hammond, J.O.S., Kendall, J.M., Stuart, G.W., Ebinger, C.J., Bastow, I.D., Keir, D., Ayele, A., Belachew, M., Goitom, B., Ogubazghi, G., Wright, T.J., 2013. Mantle upwelling and initiation of rift segmentation beneath the Afar Depression. *Geology* 41, 635–638. <http://dx.doi.org/10.1130/G33925.1>.
- Hammond, J.O.S., Kendall, J.M., Stuart, G.W., Keir, D., Ebinger, C., Ayele, A., Belachew, M., 2011. The nature of the crust beneath the Afar triple junction: evidence from receiver functions. *Geochem. Geophys. Geosyst.* 12, Q12004. <http://dx.doi.org/10.1029/2011GC003738>.
- Hammond, W.C., Humphreys, E.D., 2000a. Upper mantle seismic wave attenuation: effects of realistic partial melt distribution. *J. Geophys. Res.* 105, 10987–10999. <http://dx.doi.org/10.1029/2000JB900042>.
- Hammond, W.C., Humphreys, E.D., 2000b. Upper mantle seismic wave velocity: effects of realistic partial melt geometries. *J. Geophys. Res.* 105, 10975–10986. <http://dx.doi.org/10.1029/2000JB900041>.
- Havlin, C., Parmentier, E.M., 2014. Implications for melt transport and source heterogeneity in upwelling mantle from the magnitude of Sp converted phases generated at the onset of melting. *Geophys. Res. Lett.* 41, 5444–5450. <http://dx.doi.org/10.1002/2014GL060890>.
- Hayward, N.J., Ebinger, C.J., 1996. Variations in the along-axis segmentation of the Afar Rift system. *Tectonics* 15, 244–257.
- Hirth, G., Kohlstedt, D.L., 1996. Water in the oceanic upper mantle: implications for rheology, melt extraction and the evolution of the lithosphere. *Earth Planet. Sci. Lett.* 144, 93–108.
- Hofmann, C., Courtillot, V., Feraud, G., Rochette, P., Yrigu, G., Ketefo, E., Pik, R., 1997. Timing of the Ethiopian flood basalt event and implications for plume birth and global change. *Nature* 389, 838–841. <http://dx.doi.org/10.1038/39853>.
- Holtzman, B.K., Kendall, J.-M., 2010. Organized melt, seismic anisotropy, and plate boundary lubrication. *Geochem. Geophys. Geosyst.* 11, Q0AB06. <http://dx.doi.org/10.1029/2010GC003296>.
- Katz, R.F., Spiegelman, M., Langmuir, C.H., 2003. A new parameterisation of hydrous mantle melting. *Geochem. Geophys. Geosyst.* 4, 1073. <http://dx.doi.org/10.1029/2002GC000433>.
- Keith, C.M., Crampin, S., 1977. Seismic body waves in anisotropic media – synthetic seismograms. *Geophys. J. R. Astron. Soc.* 49, 225–243. <http://dx.doi.org/10.1111/j.1365-246X.1977.tb03710.x>.
- Knox, R.P., Nyblade, A.A., Langston, C.A., 1998. Upper mantle S velocities beneath Afar and western Saudi Arabia from Rayleigh wave dispersion. *Geophys. Res. Lett.* 25, 4233–4236. <http://dx.doi.org/10.1029/1998GL900130>.
- Lévy, F., Jaupart, C., 2011. Temperature and rheological properties of the mantle beneath the North American craton from an analysis of heat flux and seismic data. *J. Geophys. Res.* 116, b01408. <http://dx.doi.org/10.1029/2010JB007726>.
- Maguire, P.K.H., Keller, G.R., Klemperer, S.L., Mackenzie, G.D., Keranen, K., Harder, S., O'Reilly, B., Thybo, H., Asfaw, L., Khan, M.A., Amha, M., 2006. Crustal structure of the northern Main Ethiopian Rift from the EAGLE controlled-source survey; a snapshot of incipient lithospheric break-up. In: Yirgu, G., Ebinger, C.J., Maguire, P.K.H. (Eds.), *The Afar Volcanic Province within the East African Rift System*. In: *Geol. Soc. (Lond.) Spec. Publ.*, vol. 259, pp. 269–291.
- Markis, J., Ginzburg, A., 1987. The Afar Depression: Transition between continental rifting and sea floor spreading. *Tectonophysics* 141, 199–214. [http://dx.doi.org/10.1016/0040-1951\(87\)90186-7](http://dx.doi.org/10.1016/0040-1951(87)90186-7).
- McCarthy, C., Takei, Y., 2011. Anelasticity and viscosity of partially molten rock analogue: toward seismic detection of small quantities of melt. *Geophys. Res. Lett.* 38, L18306. <http://dx.doi.org/10.1029/2011GL048776>.
- McKenzie, D., O'Nions, R.K., 1991. Partial melt distributions from inversion of rare earth element concentrations. *J. Petrol.* 32, 1021–1091.
- Mechie, J., Prodehl, C., Koepschitsch, G., 1986. Ray path interpretation of the crustal structure beneath Saudi Arabia. *Tectonophysics* 131, 333–352.
- Montanger, J.-P., Marty, B., Stutzmann, E., Sicilia, D., Cara, M., Pik, R., Lévéque, J.-J., Roult, G., Beucler, E., Debayle, E., 2007. Mantle upwellings and convective instabilities revealed by seismic tomography and helium isotope geochemistry beneath eastern Africa. *Geophys. Res. Lett.* 34, L21303. <http://dx.doi.org/10.1029/2007GL031098>.
- Moresi, L., Zhong, S., Gurnis, M., 1996. The accuracy of finite element solutions of Stokes' flow with strongly varying viscosity. *Phys. Earth Planet. Inter.* 97, 83–94.
- McDonough, W.F., Sun, S.S., 1995. The composition of the Earth. *Chem. Geol.* 120, 223–253. [http://dx.doi.org/10.1016/0009-2541\(94\)00140-4](http://dx.doi.org/10.1016/0009-2541(94)00140-4).

- Nielsen, T.K., Hopper, J.R., 2004. From rift to drift: mantle melting during continental breakup. *Geochem. Geophys. Geosyst.* 5, Q07003. <http://dx.doi.org/10.1029/2003GC000662>.
- Nooner, S.L., Bennati, L., Calais, E., Buck, W.R., Hamling, I.J., Wright, T.J., Lewi, E., 2009. Post-rifting relaxation in the Afar region, Ethiopia. *Geophys. Res. Lett.* 36 (21), L21308. <http://dx.doi.org/10.1029/2009GL040502>.
- Nyblade, A.A., 2011. The upper-mantle low-velocity anomaly beneath Ethiopia, Kenya, and Tanzania: constraints on the origin of the African superswell in eastern Africa and plate versus plume models of mantle dynamics. In: Beccalura, L., Blanchini, G., Wilson, M. (Eds.), *Volcanism and Evolution of the African Lithosphere*. In: Spec. Pap., Geol. Soc. Am., vol. 478. Geological Society of America, pp. 37–50.
- Phipps Morgan, J., 2001. Thermodynamics of pressure release melting of a veined plum pudding mantle. *Geochem. Geophys. Geosyst.* 2, 1001. <http://dx.doi.org/10.1029/2000GC000049>.
- Pik, R., Marty, B., Hilton, D.R., 2006. How many mantle plumes in Africa? The geochemical point of view. *Chem. Geol.* 226, 100–114. <http://dx.doi.org/10.1016/j.chemgeo.2005.09.016>.
- Pik, R., Daniel, C., Coulon, C., Yirgu, G., Marty, B., 1999. Isotopic and trace element signatures of Ethiopian flood basalts: evidence for plume-lithosphere interactions. *Geochim. Cosmochim. Acta* 63, 2263–2279. [http://dx.doi.org/10.1016/S0016-7037\(99\)00141-6](http://dx.doi.org/10.1016/S0016-7037(99)00141-6).
- Pinzuti, P., Humler, E., Manighetti, I., Gaudemer, Y., 2013. Petrological constraints on melt generation beneath the Asal Rift (Djibouti) using quaternary basalts. *Geochem. Geophys. Geosyst.* 14, 2932–2953. <http://dx.doi.org/10.1002/ggge.20187>.
- Plank, T., Spiegelman, M., Langmuir, C.H., Forsyth, D.W., 1995. The meaning of “mean F”: clarifying the mean extent of melting at ocean ridges. *J. Geophys. Res.* 100, 15045–15052.
- Reilinger, R., McClusky, S., 2011. Nubia – Arabia – Eurasia plate motions and the dynamics of Mediterranean and Middle East tectonics. *Geophys. J. Int.* 186, 971–979. <http://dx.doi.org/10.1111/j.1365-246X.2011.05133.x>.
- Rooney, T.O., Hanan, B.B., Graham, D.W., Furman, T., Blichert-Toft, J., Schilling, J.G., 2012a. Upper mantle pollution during Afar plume-continental rift interaction. *J. Petrol.* 53, 365–389. <http://dx.doi.org/10.1093/petrology/egr065>.
- Rooney, T.O., Herzberg, C., Bastow, I.D., 2012b. Elevated mantle temperature beneath East Africa. *Geology* 40, 27–30. <http://dx.doi.org/10.1130/G32382.1>.
- Ruegg, J.C., 1975. Main results about the crustal and upper mantle structure of the Djibouti region (T.F.A.I.). In: Pilger, A., Riisler, A. (Eds.), *Afar Depression*, vol. 1. Schweizerbart, Stuttgart, pp. 120–134.
- Rychert, C.A., Harmon, N., Ebinger, C., 2014. Receiver function imaging of lithospheric structure and the onset of melting beneath the Galápagos Archipelago. *Earth Planet. Sci. Lett.* 388, 156–165. <http://dx.doi.org/10.1016/j.epsl.2013.11.027>.
- Rychert, C.A., Laske, G., Harmon, N., Shearer, P.M., 2013. Seismic imaging of melt in a displaced Hawaiian plume. *Nat. Geosci.* 6, 657–660. <http://dx.doi.org/10.1038/ngeo1878>.
- Rychert, C.A., Hammond, J.O.S., Harmon, N., Kendall, J.M., Keir, D., Ebinger, C., Bastow, I.D., Ayele, A., Belachew, M., Stuart, G., 2012. Volcanism in the Afar Rift sustained by decompression melting with minimal plume influence. *Nat. Geosci.* 5, 406–409. <http://dx.doi.org/10.1038/ngeo1455>.
- Rychert, C.A., Rondenay, S., Fischer, K.M., 2007. P-to-S and S-to-P imaging of a sharp lithosphere – asthenosphere boundary beneath eastern North America. *J. Geophys. Res.* 112, B08314. <http://dx.doi.org/10.1029/2006JB004619>.
- Schilling, J.G., Kingsley, R.H., Hanan, B.B., McCully, B.L., 1992. Nd–Sr–Pb isotopic variations along the Gulf of Aden: evidence for Afar mantle plume-continental lithosphere interaction. *J. Geophys. Res.* 97, 10927–10966.
- Schilling, J.G., 1973. Afar mantle plume: rare Earth evidence. *Nature* 242, 2–5.
- Scott, D.R., 1992. Small-scale convection and mantle melting beneath mid-ocean ridges. In: Phipps Morgan, J., Blackman, D.K., Sinton, J.M. (Eds.), *Mantle Flow and Melt Generation at Mid-Ocean Ridges*. In: *Geophys. Monogr.*, vol. 71. American Geophysical Union, pp. 327–352.
- Stork, A.L., Stuart, G.W., Henderson, C.M., Keir, D., Hammond, J.O.S., 2013. Uppermost mantle (p_n) velocity model for the Afar region, Ethiopia: an insight into rifting processes. *Geophys. J. Int.* 193, 321–328. <http://dx.doi.org/10.1093/gji/ggs106>.
- Stracke, A., Bourdon, B., McKenzie, D., 2006. Melt extraction in the Earth's mantle: constraints from U-Th-Pa-Ra studies in oceanic basalts. *Earth Planet. Sci. Lett.* 244, 97–112. <http://dx.doi.org/10.1016/j.epsl.2006.01.057>.
- Wald, A., 1943. Tests of statistical hypotheses concerning several parameters when the number of observations is large. *Trans. Am. Math. Soc.* 54, 426–482.
- White, R.S., McKenzie, D., 1995. Mantle plumes and flood basalts. *J. Geophys. Res.* 100, 17543–17585.
- Wolfenden, E., Ebinger, C., Yirgu, G., Renne, P.R., Kelley, S.P., 2005. Evolution of a volcanic rifted margin: Southern Red Sea, Ethiopia. *Geol. Soc. Am. Bull.* 117, 846–864. <http://dx.doi.org/10.1130/B25516.1>.
- Xu, W., Lithgow-Bertelloni, C., Stixrude, L., Ritsema, J., 2008. The effect of bulk composition and temperature on mantle seismic structure. *Earth Planet. Sci. Lett.* 271, 70–79. <http://dx.doi.org/10.1016/j.epsl.2008.08.012>.
- Yuan, H., Romanowicz, B., 2010. Lithosphere layering in the North American craton. *Nature* 466, 1063–1068. <http://dx.doi.org/10.1038/nature09332>.



Tectonics

RESEARCH ARTICLE

10.1029/2018TC005346

Key Points:

- Surface processes promote plastic strain localization and reduce the width of proximal margins
- Sediment thermal blanketing favors ductile basement deformation during late rifting and widening of distal margins
- During rifting of weak lithosphere the timing of marine incursion modulates the symmetry of conjugate margins

Supporting Information:

- Supporting Information S1
- Movie S1
- Movie S2
- Movie S3
- Movie S4
- Movie S5
- Movie S6
- Movie S7
- Movie S8
- Movie S9
- Movie S10
- Movie S11
- Movie S12
- Movie S13
- Movie S14
- Movie S15
- Movie S16
- Movie S17
- Movie S18
- Movie S19
- Movie S20
- Movie S21
- Movie S22
- Movie S23
- Movie S24

Correspondence to:

M. Andrés-Martínez,
andresma@uni-bremen.de

Citation:

Andrés-Martínez, M., Pérez-Gussinyé, M., Armitage, J. J., & Morgan, J. P. (2019). Thermomechanical implications of sediment transport for the architecture and evolution of continental rifts and margins. *Tectonics*, 38, 641–665. <https://doi.org/10.1029/2018TC005346>

Received 28 SEP 2018

Accepted 2 JAN 2019

Accepted article online 4 FEB 2019

Published online 21 FEB 2019

©2019. American Geophysical Union.
All Rights Reserved.

Thermomechanical Implications of Sediment Transport for the Architecture and Evolution of Continental Rifts and Margins

Miguel Andrés-Martínez¹, Marta Pérez-Gussinyé¹, John Armitage², and Jason P. Morgan³

¹MARUM-Center for Marine Environmental Sciences, University of Bremen, Bremen, Germany, ²Institut de Physique du Globe de Paris, France, ³Royal Holloway, University of London, London, UK

Abstract Erosion and deposition redistribute mass as a continental rift evolves, which modifies crustal loads and influences subsequent deformation. Surface processes therefore impact both the architecture and the evolution of passive margins. Here we use coupled numerical models to explore the interactions between the surface, crust, and lithosphere. This interaction is primarily sensitive to the efficiency of the surface processes in transporting mass from source to sink. If transport is efficient, there are two possible outcomes: (1) Faulting within the zone of extension is longer lived and has larger offsets. This implies a reduction of the number of faults and the width of the proximal domain. (2) Efficient transport of sediment leads to significant deposition and hence thermal blanketing. This will induce a switch from brittle to ductile deformation of the upper crust in the distal domains. The feedbacks between these two outcomes depend on the extension history, the underlying lithospheric rheology, and the influence of submarine deposition on sediment transport. High erosion/sedimentation during early faulting leads to abrupt crustal necking, while intermediate syntectonic sedimentation rates over distal deep submarine hotter crust leads to unstructured wide distal domains. In models where rheological conditions favor the formation of asymmetric conjugate margins, only subaerial transport of sediments into the distal domains can increase conjugate symmetry by plastic localization. These models suggest that passive margin architecture can be strongly shaped by the solid Earth structure, sea level, and climatic conditions during breakup.

1. Introduction

Rifting is a fundamental stage in the Wilson cycle. Although easy to idealize in plate tectonics, rifting is quite complex as multiple processes and their feedbacks appear to play a significant role. These processes range from erosion and sedimentation at the surface to deeper processes such as faulting, flexure due to loading/unloading, lithospheric and crustal thinning, mineral phase changes, convection, mantle exhumation, melting, and melt emplacement. Numerous studies have shown how the broad variety of passive margin architectures around the world can potentially be explained by variations in extension velocity, initial thermal state, rheology, and precursor structures within the lithosphere in which these margins formed (e.g., Brune et al., 2014; Buck, 1991; Huismans & Beaumont, 2003, 2007, 2014; Ros et al., 2017; Sharples et al., 2015; Svartman Dias et al., 2015).

Some recent studies, however, have started to point out the influence of surface processes (SP; i.e., erosion and sedimentation) in shaping rift architecture. For example, in the Gulf of California, more magmatically robust and narrow margins develop in the northern sector (Delfín-Tiburón and Guaymas sector), while less magma rich and wide margins develop in the south central sector (Alarcon sector). Lizarralde et al. (2007) suggested that these differences occur at a length-scale too small to be explained by the above mentioned factors and argued that the variation in architecture along the margin is due to different degrees of mantle fertility/hydration between the north (fertile) and the south (less fertile) aided by higher sediment deposition in the north that leads to an increase in melting due to thermal blanketing.

Surface processes have also been invoked to explain the post-rift evolution of margins, such as the observed persistence of rift shoulder uplift after breakup, through trade-offs between flexural bending, unloading at the shoulder due to erosion, and loading at the marginal basins due to sedimentation (Burov & Cloetingh, 1997; Petit et al., 2007; Redfield & Osmundsen, 2013; Weisell & Karner, 1989). Additionally, Morley and

Westaway (2006) and Clift et al. (2015) showed that during the post-rift period, an increase of sediment influx into marine basins related to a change in climate is capable of inducing ductile lower crustal flow and larger subsidence rates than expected from thermal subsidence. Furthermore, Petit et al. (2007) showed that climate can also influence post-rift escarpment morphology.

Numerical studies have analyzed how surface processes can have an effect on both shallow and deeper Earth dynamics. In passive margins, surface mass transport changes the crustal strength and flexural stresses, and can trigger lower crustal flows that enhance subsidence and rifting (Burov & Cloetingh, 1997; Burov & Poliakov, 2001). During rifting an input of sediments from far-field sources have proven to favor narrow rifting because the loads reduce the buoyancy force difference between the shoulders and the center of the rift, which avoids rift migration (Bialas & Buck, 2009), and also to control the mode transition from asymmetric basins to symmetric due to loading of the hanging wall (Buiter et al., 2008). Olive et al. (2014) showed that active surface processes increase the life span of faults and the amount of horizontal strain that they can accommodate. This occurs because surface processes reduce the topographic and flexural force working against the active fault (Olive et al., 2014). Through analog modeling, Zwaan et al. (2018) showed that sedimentation at grabens and half-grabens aids localization of deformation, enhances fault offsets, reduces hanging wall structure, attenuates lower crustal exhumation, and sustains high angles at faults for a longer period of time, although 3-D rift structure is not significantly affected.

Previous studies focused on particular aspects of SP-tectonic feedbacks such as the effect of SP in the mechanics of a single fault (Olive et al., 2014), the ability of SP to trigger narrow rifting mode through sedimentation (Bialas & Buck, 2009), how SP shape the number of simultaneous active faults and faulting symmetry (Buiter et al., 2008), or how the timing of salt deposition during rifting affects the final salt distribution (Allen & Beaumont, 2016). These works, with the exception of Allen and Beaumont (2016), use relatively simple setups that lack nonlinear and/or temperature-dependent viscosities in the lower crust or lack elasticity and/or a realistic landscape evolution model (e.g., lack of erosion and filling the basin up to a base level). In this work we develop and use a finite element numerical model which fully couples subaerial and submarine landscape evolution to lithospheric extension. We do this by solving sediment transport, mass, momentum, and energy conservation equations. Our focus is to analyze in detail the effects that thermal insulation and stress loading due to sedimentation have on the deformation mode during extension and on the final margin architecture. Finally, we analyze how the occurrence of slower deep submarine SP during the late stages of rifting may modulate the rift geometry. For this purpose we conduct a parametric study in which we vary crustal thickness, lower crustal rheology, the efficiency of subaerial SP, and the presence/absence of sea and hence submarine erosion and sediment transport. This approach allows us to investigate three main unresolved questions regarding the interplays between surface processes and tectonics: (1) how loading/unloading through surface processes interacts with thermal blanketing to shape passive margins; (2) where in space and time loading/unloading versus thermal blanketing effects are dominant, and how these effects are modulated by the initial strength of the crust; and (3) what role the timing of marine incursion plays in the distribution of sediments and final margin architecture. Finally, we use these results to discuss structural differences between natural examples of margins that display different amounts of syn-rift sedimentation.

2. Methodology

In order to address the previously discussed questions, we have developed a new 2-D visco-elasto-plastic geodynamic model based on MILAMIN mechanical and thermal solvers (Dabrowski et al., 2008). The code simulates dynamic topography by using a stress-free surface (Andrés-Martínez et al., 2015; Kaus et al., 2010) and accounts for strain softening, shear heating, and surface processes calculated from a sediment transport model. Below we first describe the tectonic model, then the geomorphologic model, and finally how they are coupled.

2.1. Tectonic Model

We model a 2-D section of the continental lithosphere and upper asthenosphere which is divided in three layers with different thermomechanical properties: (1) upper crust (UC), (2) lower crust (LC), and (3) mantle. Mantle includes an upper section (i.e., lithospheric mantle) consisting of dryer olivine and a deeper asthenospheric section, consisting of wetter olivine, separated by a 5-km transition zone. Mantle rheologies

are calculated based on depletion values and tracked with the material flow along time. The model domain is subjected to half-extension velocities on the sides to simulate far-field stretching.

Our model calculates deformation and pressure by solving (1) the Stokes force-balance equation for incompressible viscous flow (equation (1)) and (2) the equation for mass conservation (equation (2)):

$$\nabla \cdot \tau - \nabla P + \rho g = 0, \quad (1)$$

$$\nabla \cdot v = 0, \quad (2)$$

where τ is the deviatoric stress, P is the total pressure, ρ is the density, g is the gravitational acceleration, and v is the velocity (e.g., Dabrowski et al., 2008; Kaus, 2010; Moresi et al., 2003).

Temperatures are solved using the heat conservation equation:

$$\rho C_p \frac{DT}{Dt} = \nabla \cdot (k \nabla T) + H_r + H_s, \quad (3)$$

where C_p is the heat capacity, T is temperature, t is time, k is thermal conductivity, and H_r and H_s are the radioactive and shear heating volumetric heat productions, respectively.

The constitutive relation between shear stress τ and strain rate $\dot{\epsilon}$ is

$$\tau = \eta_{eff} \left(2\dot{\epsilon}' + \frac{\tau^{old}}{\mu \Delta t} \right), \quad (4)$$

where η_{eff} is the effective or numerical viscosity, $\dot{\epsilon}'$ is the deviatoric strain rate, τ^{old} accounts for previous time step rotated stresses resulting from applying finite-difference time discretization to the Jaumann objective derivative to include elastic behavior (Kaus, 2010; Moresi et al., 2003), μ is the shear modulus, and Δt is the time step.

To calculate the effective viscosity η_{eff} we first need to evaluate whether the material behaves plastically or viscoelastically. For that purpose we adopt the Drucker-Prager yield criterion which implies that yielding is met when the square root of the second invariant of the deviatoric stress (τ_{II}) is larger than the yield stress σ_{yield} , defined as

$$\sigma_{yield} = Psin\phi + Ccos\phi, \quad (5)$$

where ϕ and C are the friction angle and the cohesion of the rocks, respectively (e.g., de Souza Neto et al., 2008). In order to include plasticity into the viscous formulation we use Prandtl-Reuss flow rule, which brings τ_{II} to the yield envelope ($\tau_{II} = \sigma_{yield}$) for yielding materials, defining the effective viscosity η_{eff} as

$$\eta_{eff} = \frac{\sigma_{yield}}{\left(2\dot{\epsilon}' + \frac{\tau^{old}}{\mu \Delta t} \right)_{II}}, \quad (6)$$

where $(\cdot)_{II}$ represents the square root of the second invariant operator (Moresi et al., 2003).

If $\tau_{II} < \sigma_{yield}$ then the material behaves viscoelastically and we define effective viscosity η_{eff} as

$$\eta_{eff} = \left(\frac{1}{\eta_{dis}} + \frac{1}{\eta_{dif}} + \frac{1}{\Delta t \mu} \right)^{-1}, \quad (7)$$

where η_{dis} and η_{dif} are dislocation and diffusion creep viscosities, respectively, such as

$$\eta_{dis/dif} = FB^{-\frac{1}{n}} \dot{\epsilon}_{II}^{\frac{1-n}{n}} \exp \left(\frac{E^* + PV^*}{nRT} \right), \quad (8)$$

where F is a factor to scale parameters obtained from uniaxial/triaxial experiments (defined for principal stresses) to our second-invariant-based formulation of the viscosity, B is the pre-exponential factor of the flow law, n is the power law exponent, $\dot{\epsilon}_{II}$ is the square root of the second invariant of the strain rate, E^* is the activation energy, V^* is the activation volume, R is the gas constant, and T is the absolute temperature. The values of these parameters for both diffusion and dislocation mechanisms and rocks are shown in Table 1. Here we use a wet quartzite flow law to simulate upper crustal deformation (Gleason & Tullis, 1995). Lower crust is expected to be more mafic than the upper crust and feldspar flow laws are expected to represent its

Table 1
Model Parameters

	Wet quartzite (UC and weak LC)	Wet anorthite (intermediate strength LC)	Mafic granulite (strong LC)	Dry olivine (lithospheric mantle)	Wet olivine (asthenospheric mantle)
Thermomechanical parameters					
Dislocation pre-exponential factor $\log(B_{dis})$ [Pa $^{-n}$ s $^{-1}$]	-28.0	-15.40	-21.05	-15.96	-15.81
Dislocation exponent n_{dis}	4.0	3.0	4.2	3.5	3.5
Dislocation activation energy E_{dis}^* [kJ mol $^{-1}$]	223	356	445	530	480
Dislocation activation volume V_{dis}^* [10 $^{-6}$ m 3 mol $^{-1}$]	0	0	0	13	10
Diffusion pre-exponential factor $\log(B_{diff})$ [Pa $^{-1}$ s $^{-1}$]	-	-	-	-8.16	-8.64
Diffusion exponent n_{diff}	-	-	-	1	1
Diffusion activation energy E_{diff}^* [kJ mol $^{-1}$]	-	-	-	375	335
Diffusion activation volume V_{diff}^* [10 $^{-6}$ m 3 mol $^{-1}$]	-	-	-	6	4
Shear modulus μ [GPa]	UC	LC	Lithospheric mantle	Asthenospheric mantle	
Thermal conductivity k [W m $^{-1}$ K $^{-1}$]	36	40	74	74	
Heat capacity C_p [J kg $^{-1}$ K $^{-1}$]	2.1	2.5	3.3	3.3	
Radiogenic heat production H_r [μ W m $^{-3}$]	1,200	1,200	1,200	1,200	
Reference densities ρ_0 [kg m $^{-3}$]	1.3	0.2	0	0	
Thermal expansivity coefficient α_T [10 $^{-5}$ K $^{-1}$]	2,700	2,850	3,300	3,300	
Thermal expansivity coefficient α_T [10 $^{-5}$ K $^{-1}$]	2.4	2.4	3.0	3.0	
Constants		Value	Value	Value	Value
Triaxial scaling parameter		$F = \frac{1}{\frac{n-1}{2} \frac{n+1}{n} \frac{3}{2n}}$	0.041	1	
Depletion factor for density dependence β					
Surface processes parameters		Value	Value	Value	Value
Surface processes time step δt_s [Kyr]		1	0.25	1	1
Subaerial hillslope diffusion K [m 2 year $^{-1}$]					
Subaerial discharge transport coefficient c		Low transport ↓	10 $^{-4}$, 5 × 10 $^{-4}$	10 $^{-4}$, 5 × 10 $^{-4}$	Armitage et al. (2015)
Precipitation rate α [m year $^{-1}$]		High transport	10 $^{-3}$, 5 × 10 $^{-3}$	10 $^{-3}$, 5 × 10 $^{-3}$	Paola et al. (1992)
Submarine diffusion coefficient K_s [m 2 year $^{-1}$]			10 $^{-2}$, 5 × 10 $^{-2}$	10 $^{-2}$, 5 × 10 $^{-2}$	Marr et al. (2000)
Submarine diffusion coefficient decay λ_s [m $^{-1}$]			1	1	Armitage et al. (2014)
			10 2	10 2	Huffman et al. (2009)
			5 × 10 $^{-4}$	5 × 10 $^{-4}$	Kaufman et al. (1991)
					Kaufman et al. (1991)

Note. Rheological parameters from Wilks and Carter (1990); Gleason and Tullis (1995); and Hirth and Kohlstedt (2003). Depletion factor for density dependency from Schutt and Lesser (2006). Remaining parameters from Turcotte and Schubert (2002). Diffusion creep B is calculated using a grain size of 6 mm. Wet olivine water content is 500 ppm H/Si. UC = upper crust; LC = lower crust.

rheology (Christensen & Mooney, 1995; Contrucci et al., 2004; Dean et al., 2000; França & Assumpção, 2004; Hopper et al., 2007). We choose to run different models using two end member flow laws for the lower crust: a strong mafic granulite (GR; chosen to amplify brittle tectonic-surface trade-offs), and a weak wet quartzite (WQ; chosen to amplify ductile ones; Gleason & Tullis, 1995; Wilks & Carter, 1990). In order to reproduce an intermediate lower crustal strength, we run models with a third lower crustal flow law: wet anorthite (AN; Rybacki & Dresen, 2000), as it is weaker than the GR from Wilks and Carter (1990), but still representative of mafic materials (see strength profiles in supporting information Figure S2). Lithospheric mantle is simulated as dry olivine, and asthenosphere as wetter olivine (500 ppm H/Si; Brune et al., 2012; Hirth & Kohlstedt, 2003).

After discretization of the spatial domain we use the finite element method to numerically solve equations (1)–(3). Here, we use a triangular grid with resolutions of 1 km in the UC, 5 km in the LC, and 5 km in the mantle, tracked along with the material (Lagrangian mesh). We use Triangle Mesh Generator package (Shewchuk, 2002) in order to produce the finite element grids. Mesh is subdivided in layers of different properties where layer interfaces coincide with element boundaries so that no drastic property changes occur inside the element but along element boundaries. Furthermore, Triangle increases resolution where layers are thinner than the specified resolution, ensuring that deformation is well resolved at thinned layers (e.g., regions of very attenuated lower crust). When large deformations take place in the Lagrangian mesh (i.e., in shear zones), this can result in extremely elongated triangles, in which case the finite element method may not return an accurate solution for the system. In order to avoid this issue, a remesh with a subsequent resampling of the variables is applied. The resampling of variables is done within elements using shape functions for interpolation. This, together with resampling occurring only when necessary (i.e., not in every time step), limits the amount of numerical diffusion of the variables.

We assume rock density ρ is a function of temperature T and, for mantle rocks, also of the degree of depletion (Armitage et al., 2013; Nielsen & Hopper, 2004; Parmentier & Morgan, 1990; Schutt & Lesher, 2006):

$$\rho = \rho_0 (1 - \alpha(T - T_0) - \beta D), \quad (9)$$

where ρ_0 is the reference density at room temperature T_0 , α is thermal expansivity, and β is a factor multiplying the depletion D (Table 1).

Additionally, the model includes a stress-free surface at the top of the model with a free-surface stabilization algorithm (Andrés-Martínez et al., 2015; Kaus et al., 2010) in order to accurately model dynamic topography and to avoid instabilities typically associated with free surfaces. The model also accounts for strain weakening where previously deformed materials are weaker than nondeformed materials. This allows for the simulation of faults and shear zones, because deformation will localize into weakened bands, which will become increasingly weaker and narrow (Buck & Lavier, 2001; Huismans & Beaumont, 2003). Strain weakening is justified for the plastic behavior of rocks due to a cohesion loss when the yield criteria is met. This loss in cohesion is associated with fault planes since they represent a discontinuity to the rock's integrity (e.g., Buck, 1993). Fluids penetrate faults from the surface, increasing the fluid pressure and also inducing mineral transformations, which together "soften" the effective friction angle (Bos & Spiers, 2002; Handy & Stünitz, 2002). Here, we choose to use only friction angle softening, because at depth cohesion contributes only a small amount to the yield stress in comparison to the friction coefficient that is multiplied by the pressure. Softening is applied as a linear function of the second invariant of finite plastic strain (Huismans & Beaumont, 2007), so that for no plastic deformation the friction angle is 30° and for finite plastic strain ≥ 1 the friction angle is 15°. Furthermore, we include viscous weakening with a linear increase in the pre-exponential factor of the dislocation creep law B (equation (8)). This represents weakening due to grain size reduction and crystallographic preferred orientation (Hansen et al., 2012; Karato & Wu, 1993). The viscous strain weakening rule chosen is such that the pre-exponential factor remains the same for no deformation and linearly increases with viscous deformation up to W_{max} times larger than the original value when the finite viscous strain is ≥ 1 . This maximum weakening factor W_{max} is reduced in an Arrhenius-like fashion with temperature (T) to reduce weakening where crystal growth rates would be fast, with $W_{max} = 30$ when $T \leq 800^\circ\text{C}$ and $W_{max} = 1$ when $T \geq 1200^\circ\text{C}$ (Précigout & Gueydan, 2009; Ros et al., 2017).

Together, free surface and strain weakening allow for the simulation of faults and their associated relief, subsidence, and the elastic response of topography to tectonic and geomorphological loading and unloading. Consequently, the accommodation space for sedimentation and positive topographies for erosion are available, which is critical for this study.

2.1.1. Boundary Conditions and Initial Configuration

Initial model size is 400 km wide and 150 km deep. Half-extension velocities of 5 mm/year (ultraslow) are applied as lateral boundary conditions. For the bottom boundary we use a Winkler boundary condition (Buck & Poliakov, 1998; Burov & Poliakov, 2001), applying a constant upward stress at the bottom nodes. This stress corresponds to the basal lithostatic pressure at the beginning of the model run. This means we treat the base of the model as an unchanging level of isostatic compensation and allow for asthenosphere to flow in or out through the boundary. Thermal boundary conditions are 0 °C at the surface (including sediment surface) and 1300 °C below 120 km where heat transport is assumed to occur adiabatically by convection.

In our model, lithospheric and asthenospheric mantle share the same mesh layer. This means that the material properties in the mantle layer vary from dry olivine in the lithospheric mantle to wetter olivine in the asthenosphere (Table 1). The lithosphere-asthenosphere transition is placed at the initial model between 125 and 130 km depth (Hirth & Kohlstedt, 2003; Morgan, 1997; Morgan et al., 1995). This transition is tracked along time so that its position is known for every time step and the correct rheological parameters can be calculated for the mantle.

In addition, we impose a weak seed at the middle of the domain to nucleate rifting far from the lateral boundaries, avoiding boundary-related artifacts in the deformation. The weak seed is a region with the center located at 30 km depth where temperature is increased at the initial time step by 100 °C following a 2-D Gaussian function with half width 10 × 20 km. This increase in temperature makes viscosity smaller in that region. As the seed is allowed to thermally relax during the model run, it only helps to nucleate rifting and has a diminishing effect in later phases of rift evolution.

2.2. Sediment Transport Model

Topographic changes can be induced by both tectonic deformation and downslope transport of rocks along the surface toward areas of lower relief. For transport to happen, basement rocks need to lose their cohesion by transforming into sediment/regolith through erosion and weathering. Here, we assume that sediment is always available at the surface of the model and, consequently, that sediment transport dominates landscape evolution. We can therefore write that the change in surface elevation rate due to surface processes is equal to the divergence of the sediment flux, assuming there is no density difference between the bedrock and sediment and ignoring the effects of compaction. In 1-D this becomes

$$\frac{\partial h}{\partial t} = -\frac{\partial q_s}{\partial x}, \quad (10)$$

where h is the topography, t is time, q_s represents the sediment flux, and x is the horizontal coordinate (Culling, 1960; Smith & Bretherton, 1972). This implies that the temporal topographic variation for an element depends only on the difference between the input and output sediment fluxes for an element and, consequently, that landscape evolution is a function of spatial variations in sediment transport. This approximation is known as a transport-limited model (Dietrich et al., 2003; Howard, 1994; Kirkby, 1971; Kirkby & Carson, 1972). We chose this approach for our landscape evolution model since it allows for sedimentation to occur.

In the subaerial environment, it is possible to define the sediment transport flux q_s in terms of the water flux q_w as

$$q_s = -(K + cq_w^n) \frac{\partial h}{\partial x}, \quad (11)$$

where K is the slope diffusivity, c is the transport coefficient, and $n \geq 1$ is the power law that defines the type of relationship between the sediment transport and the water flux (Simpson & Schlunegger, 2003; Smith & Bretherton, 1972). This model accounts for hillslope diffusion processes where the topography will tend to a dispersive diffusion (Culling, 1960) and fluvial transport processes that result in concentrative diffusion due to water run off (Graf, 1984). For a simple parameterization we choose a linear relationship between sediment transport and water flux ($n = 1$).

The water flux can be related to the water discharge/effective rainfall α as

$$\frac{\partial}{\partial x}(\mathbf{n}q_w) = -\alpha, \quad (12)$$

where \mathbf{n} is an unit vector directed down the surface gradient (Smith & Bretherton, 1972). By assuming a constant α and integrating equation (12) over the surface in the downstream direction, we obtain

$$q_w = \alpha x_d, \quad (13)$$

where x_d is the downstream distance from the drainage divide. By substituting equations (11) and (13) into (10) we obtain the 1-D sediment mass conservation equation for combined hillslope and discharge-dependent fluvial transport:

$$\frac{\partial h}{\partial t} = \frac{\partial}{\partial x} \left((K + k\alpha x_d) \frac{\partial h}{\partial x} \right), \quad (14)$$

where the downstream distance x_d is calculated at each time step as the distance from the topographic highs to the valley floors. Because q_w is dependent on the length of the drainage, the model mimics 1-D landscapes similar to river profiles in which fluvial processes are dominant.

In the submarine environment, sediment transport occurs in shallow waters due to the motion of waves and the tide. The intensity of these processes decreases with increasing water depth. This behavior can be reproduced by defining the sediment diffusivity as an exponentially decaying function of water depth (Kaufman et al., 1991):

$$\frac{\partial h}{\partial t} = \frac{\partial}{\partial x} \left(K_s e^{(-\lambda_s h_w)} \frac{\partial h}{\partial x} \right) \quad (15)$$

where K_s is the submarine diffusion coefficient, λ_s is the submarine diffusion decay coefficient, and h_w is the water depth (the difference between sea level and the submarine topography). Table 1 shows the sediment transport parameters used in equations (14) and (15).

We calculate the sea level with respect to the top reference surface of models by an isostatic balance, comparing to sea level for a 30-km-thick crust, which is a reasonable crustal thickness for continents with topography near sea level. Note that the initial top of our model is at 0 km, implying that sea level is below the model's 0-km reference topography.

2.3. Coupling of Tectonics and Surface Processes

Coupling between inner Earth dynamics and landscape evolution is done by first solving the tectonic model defined by equations (1)–(3) for a time step Δt , then advecting topography for Δt with the solved velocities and finally solving for sediment transport over the time step (equations (14) and (15)). This explicit approach implies that sediment transport during Δt occurs over a tectonically static topography that was previously calculated for the current time step. Therefore, this approach neglects the intra-time-step feedbacks between the load redistribution caused by the landscape model and the tectonic model. This approach is valid because the wavelength and amplitude of the topographic changes due to sediment transport are sufficiently small that their relaxation time is large compared with the size of the flow solver time step Δt (10 Kyr).

For numerical stability, we choose to run the sediment transport model for a number of smaller time steps Δt_s (1 Kyr) which in total sum to the tectonic time step Δt . Furthermore, the landscape evolution model mesh is adaptive so that high diffusivity contrasts at the interface between subaerial and submarine environments can be adequately resolved. Once the new topography is calculated from the sediment transport model, the y coordinates of the top nodes of the triangular grid are updated.

Variables for nodes and integration points of surface elements are resampled every time step after the topography update. In the case that nodes or integration points are located out of the old mesh due to sedimentation (see Figure S1), then their temperature is set to be the top boundary condition value (0 °C), their finite strain and rotated stress values are set to 0, and viscosity and strain rate (that are used in the next time step as initial guess for the nonlinear mechanical solver) are set to be the average of the closest element in order to ensure model stability. Thermal boundary conditions are set at the top boundary independently of the nature of the exposed rock (basement or sediment), and sediments are given the same thermal conductivity as the upper crust (Table 1).

In summary, the scheme used here for coupling the landscape evolution model to tectonics for a given time step Δt is as follows:

1. Run the flow and thermal solvers (tectonic model; equations (1)–(3)) for Δt , and obtain velocities, pressures, and temperatures.
2. Advect nodes with calculated velocities generating a new “tectonic topography.”
3. Run the landscape evolution model for the new tectonic topography for i of Δt_s time steps, where $\Delta t_s = \Delta t/i$.
4. Update model topography with the final “landscape-model topography.”
5. Resample variables for updated elements to match (and fill) this new top surface.

Ideally, sediments should have different mechanical properties and densities than those of the basement rocks. However, this would imply that the model includes an extra high-resolution discontinuous layer to represent sediments. The numerical resolution of this extra layer would need to be sufficiently high to have Delaunay triangles even when the sediment layer was as thin as a few meters (the case for the initial steps of the model). These extremely high resolutions are shunned because of the high computation time that would be spent in the Stokes flow solution step. Some strategies to reduce the number of small elements could be used, such as to only generate an independent sediment layer when the sediment thickness is on the scale of the resolution set for the crust (1 km). However, for simplicity, we choose to assume that the sediment's mechanical properties and density are crudely that of the upper crust (WQ, Table 1), and we simply include sediments into the upper crustal layer.

In terms of densities, this is analogous to maximum sediment compaction at the time of deposition. The implication of this is that the effects of sediment loading would be slightly diminished (a factor of $\frac{\sim 2,200}{2,700} \text{ kg/m}^3 \approx 0.8$ to the topographic forces). Although this is not a realistic approach, we note that assigning lower densities to the sediments is also inaccurate as topographic diffusion preserves volume, therefore, different sediment densities will imply a decrease in total model mass. In order to preserve mass a more sophisticated landscape evolution model would be needed. However, we consider our simpler approach sufficient for this work as the difference between sediment and basement densities is minimal compared to the air-rock density contrast.

In terms of mechanics, this assumption is valid for shallow to intermediate depth sediments that deform in the elasto-plastic or brittle regime, since the effective viscosity is controlled by the yield criterion and not by the sediment's flow law parameters. However, deeper sediments at temperatures between 200 and 400 °C would be expected to deform by grain boundary diffusion creep driven by pressure solution (McClay, 1977; Rutter & Elliott, 1976). This deformation mechanism would result in larger strain rates for smaller stresses and, therefore, lower effective viscosities (Rutter & Elliott, 1976). Lower effective viscosities of the sediments could change details of deformation inside the sediment layer, potentially allowing for more distributed deformation within the sediment layer and detachment levels when viscosities are low. However, it is not in the scope of this work to accurately model sediment deformation during diagenesis. Instead, we focus on modeling the basement deformation that is affected by sediment loads and thermal blanketing. This is why we favor the simple mechanical characterization of sediment deformation that is chosen here.

3. Results

With the focus of better understanding how sedimentation affects margin architecture for different initial rheological profiles, we have run models in which we vary lower crustal rheologies, initial crustal thicknesses, and different fluvial transport coefficients. The set of models presented here is calculated over a parametric space that includes (1) a range in lower crustal rheologies (see Table 1), from strong to weak: GR, AN, and WQ (Gleason & Tullis, 1995; Hirth & Kohlstedt, 2003; Rybacki & Dresen, 2000; Wilks & Carter, 1990), (2) an initial crustal thickness of 35 or 40 km, (3) different fluvial transport coefficients ($c = 10^{-4}, 5 \times 10^{-4}, 10^{-3}, 5 \times 10^{-3}, 10^{-2}, 5 \times 10^{-2}$, including models with no SP), and (4) models with or without submarine surface transport processes. Combinations of these parameters led to a total of 78 experiments. The extension velocity is kept the same for all the experiments at 5 mm/year half-extension velocity. We will first describe the results of the models without SP in order to frame the interactions between SP and margin deformation (section 3.1). Then we discuss the results of models with SP, both at local and regional scales, with subaerial and submarine sedimentation (here called “Models with sea”), and with only subaerial sedimentation (“Models without sea”), in order to highlight the influence of marine inundation in comparison to models with sea (section 3.2).

3.1. Models Without Surface Processes

Results of models without SP have been extensively discussed in recent literature (i.e., Brune et al., 2014; Buck, 1991; Huismans & Beaumont, 2011; Ros et al., 2017; Svartman Dias et al., 2015). Here, these results are summarized to provide an overview of the different extensional modes observed and to frame the interactions between surface processes and margin deformation, that will be discussed in the following sections. For this purpose, we adopt the framework presented by Buck (1991) to characterize extensional modes. This approach allows us to describe the modeled margin geometry as the result of a succession of deformation phases, distinguishing distinct margin deformation domains. Among our models we can differentiate the three modes of rifting described by Buck (1991): (1) narrow (NR), (2) wide (WR), and (3) core complex (CC), plus (4) lateral rift migration (RM) through a low viscosity channel (Brune et al., 2014). Lateral rift migration generates asymmetric conjugate margins. When the LC is strong enough, lateral rift migration occurs in the upper crust as an array of sequentially active faults, which consistently young and dip oceanward (Pérez-Gussinyé, 2013; Ranero & Pérez-Gussinyé, 2010). Figure 1 exemplifies these rifting modes by showing the rift evolution of two models with 40 km crust, no SP, and different lower crustal rheologies: intermediate strength AN and weak WQ. Results with strong (GR) and intermediate (AN) lower crustal strength are very similar and are mainly discussed in the main paper in basis of the intermediate lower crustal results, for AN. Movies corresponding to the GR, AN, and WQ results are included in the supporting information.

Strong to intermediate lower crustal strength. Stronger LC models (GR and AN) typically begin with narrow extension and deformation localizing into two main faults that nucleate in the weak seed (Figure 1a and supporting information movies S1, S2, S7, and S8). This results in a central hanging wall block (also called the H-block by Lavier & Manatschal, 2006, or the keystone block by Huismans & Beaumont, 2011), which experiences large subsidence and thinning of the lower crust through shear zones. Once the lower crust has been attenuated, deformation moves into the central hanging wall block (Figure 1b). In models with initial 35-km crust, this phase typically ends with crustal breakup (S7 and S8 movies in supporting information). In the 40-km-crust models, the faults in the central block are accompanied by two outward-dipping shear bands which develop at the base of the crust (Figure 1b). These shear bands connect to various upper crustal faults dipping toward the center of the graben. Eventually, rift migration starts when one of the lower crustal shear zones becomes weaker due to strain weakening and accommodates more deformation than the other one. As deformation progresses in the favored shear zone, hot mantle upwelling, shear heating, and strain softening reduce the viscosity even further generating a lower crustal low-viscosity channel (LVC) that brings basal lower crust at the bottom of the LVC upward into the LVC foot-wall (see velocity arrows in Figure 1c) as described by Brune et al. (2014). At this stage several faults dipping both inward and outward detach into the LVC. Subsequently, the sequential faulting mode begins when one of the upper crustal faults starts to dominate deformation and couples with the favored lower crustal outward-dipping shear band or LVC (Figure 1d and section 3.2.3). Note that in the models, sequential faulting does not necessarily occur through a single fault at a time. Instead, up to two faults can be simultaneously active dipping oceanward together with an antithetic fault located in the narrow margin. In models, the sequential faulting phase finishes due to cooling of the upwelled mantle and consequent strengthening of the lower crustal shear band (Brune et al., 2014). The 40-km-crust models finally reach crustal breakup by localization of brittle deformation into the thinnest sector of the asymmetrically thinned crust.

Weak lower crustal strength. In these experiments the initial extensional phase occurs by wide rifting mode. Extension is distributed through a wide region (~200 km) at the center of the model, but faults located above the weak seed accommodate most of the deformation (Figures 1e and S3 and S9 movies in the supporting information). In these models, the shallowest portions of the upper crust deform in the brittle regime while the lower crust is viscous and very weak. These conditions favor lower crustal flow toward the area of upper crustal extension that inhibits crustal thinning and results in a switch in rifting mode, from wide rifting to core complex mode (Figure 1f). As extension progresses and the availability of low viscosity lower crust to feed the CC decreases, the CC die out and deformation moves out of the basin center to concentrate in the outward-dipping shear zones and their linking upper crustal faults (time steps 8 and 11 Myr in S3 and S9 movies in the supporting information). With time, the mantle keeps rising at the center, further weakening this region so that deformation jumps again into the area of the abandoned CC (Figure 1g and time steps 11 and 14 in S3 and S9 movies in the supporting information). In models with initial 35-km crust, breakup occurs in that area after a short phase of deformation, resulting in two symmetric conjugate margins

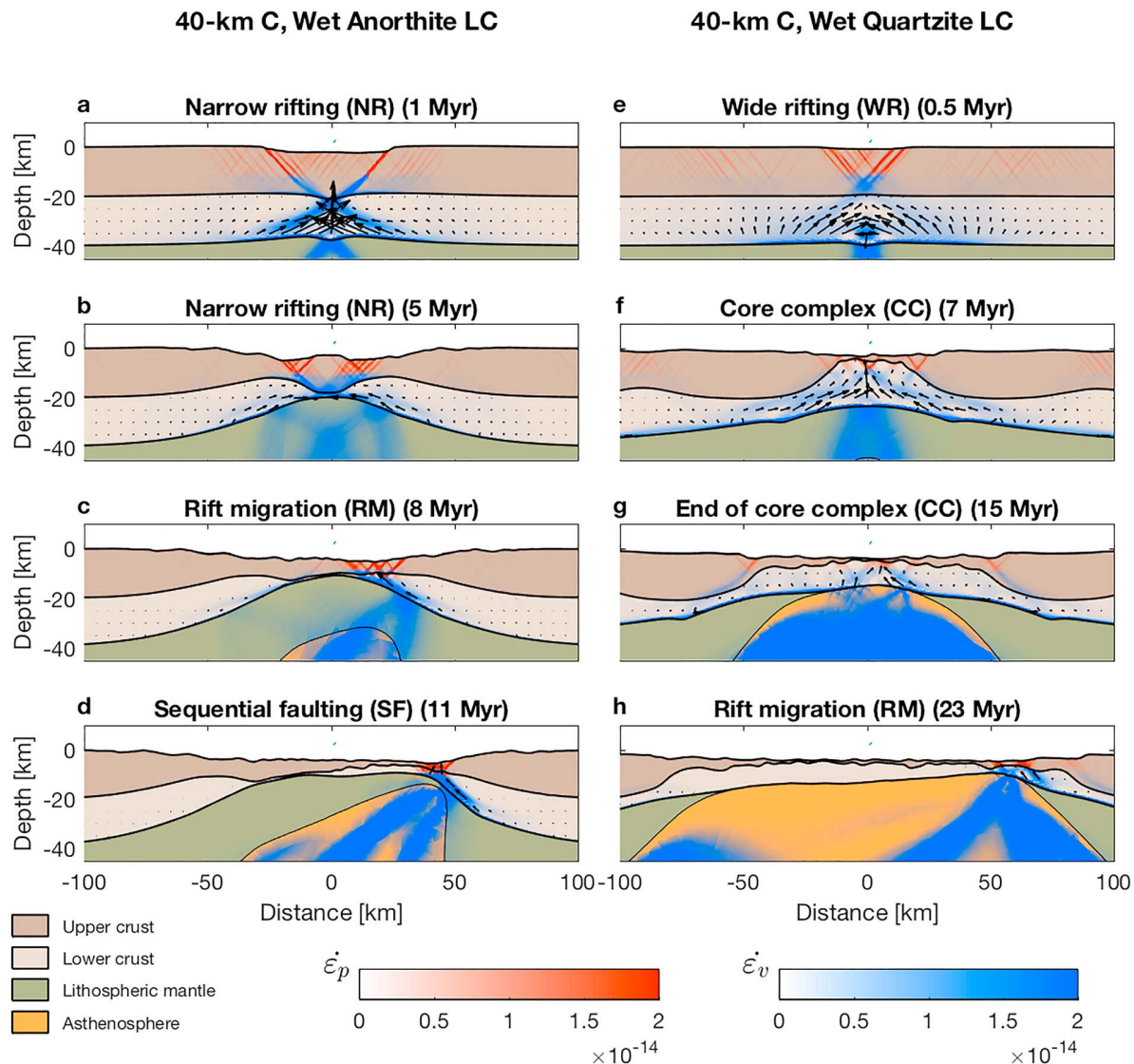


Figure 1. Rifting evolution and extensional modes of models with wet anorthite (a–c) and wet quartzite (d–f) lower crustal rheologies and initial crustal thickness of 40 km. Arrows represent relative-to-surface lower crustal velocities calculated for the given time step. Red and blue colors represent plastic ($\dot{\varepsilon}_p$) and viscous ($\dot{\varepsilon}_v$) second invariants of the strain rates, respectively, [s^{-1}], which are representative of the amount of plastic and viscous deformations occurring at the given time step. LC = lower crust.

(Figure 6a and Figure S7). In models with initial 40-km crust, one of the outward-dipping LC shear zones becomes dominant and produces rift migration toward one side of the system. In this case, the LVC is wider and dips at a lower angle than in the stronger models. Consequently, faults rooting at the migrating LVC are distributed over a wider area, are more numerous, and have smaller offsets than in the stronger models. Although lateral rift migration is active from 18 Myr, sequential faulting in the upper crust only begins much later (from 24 Myr, supporting information S3 movie). As in the stronger models, breakup occurs when cooling leads to the vanishing of the LVC. The final geometry consists of two highly asymmetric conjugate margins, where the widest margin is ~240 km and the narrowest ~40 km wide (Figure 8a). Note that these models create lower amplitude relief than stronger ones due to their more distributed deformation associated with weaker lower crust and faster viscous relaxation times.

3.2. Models With Surface Processes

In this section we first discuss the general implications of erosion and sedimentation under extension at the local scale (sections 3.2.1–3.2.3), and then address effects of SP on regional margin architecture (section 3.2.4).

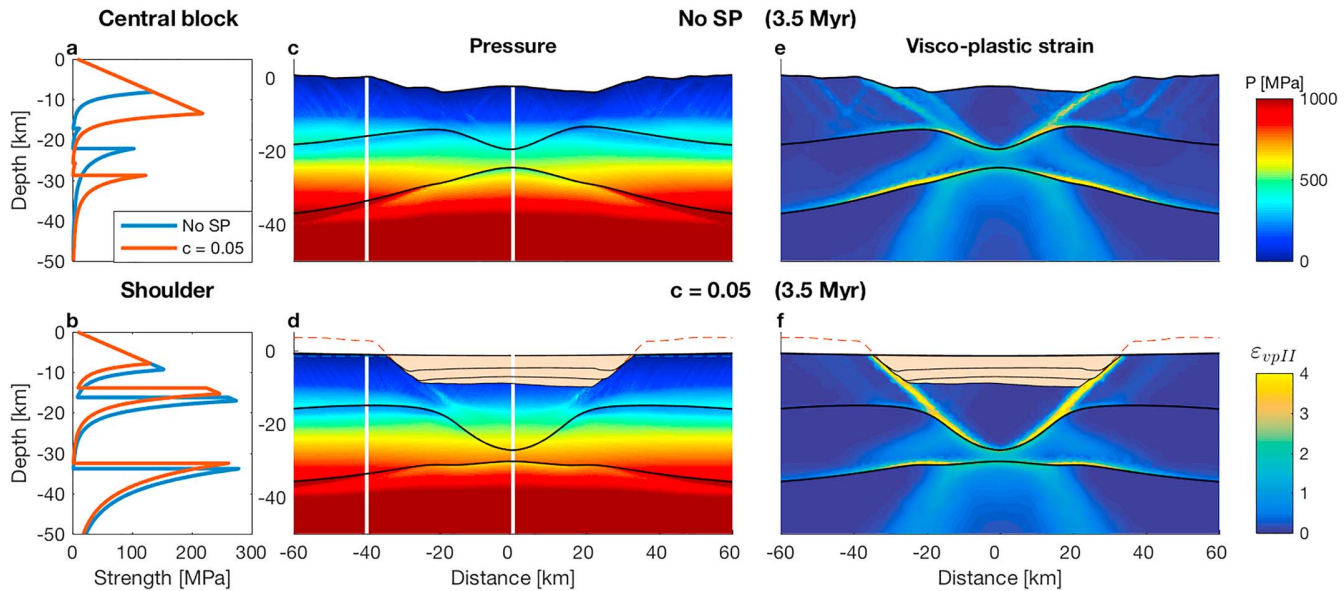


Figure 2. Impacts of surface processes in pressure and strain localization. Strength profiles of a model with no SP and a model with efficient SP ($c = 5 \times 10^{-2}$) are shown in (a) for the central block and in (b) for the rift shoulder. Panels (c) and (d) show pressures (P) for a model with no SP and a model with efficient subaerial SP with fluvial transport coefficient $c = 5 \times 10^{-2}$, respectively. Panels (e) and (f) show second invariant of the visco-plastic strain for both no SP and $c = 5 \times 10^{-2}$ models, respectively. Sediments are colored in light brown, and black lines inside the sediments represent depositional time lines at 1 Myr time intervals. The vertical white lines in (c) and (d) indicate the locations of the strength profiles (a, b). Pressures at the central block are larger in the model with SP (d) than in the model with no SP (c), due to sediment loading. This forcing effect results in larger displacement and fast weakening at the initial faults that leads to strain localization (f vs e). SP = surface processes.

3.2.1. Effects on Pressure, Crustal Strength, and Faulting

In agreement with previous work (e.g., Olive et al., 2014; Zwaan et al., 2018), an increase in the efficiency of surface processes promotes strain localization in the brittle regime. Figure 2 represents the initial faulting phase for a model with no SP (Figures 2a, 2c, and 2e) and efficient SP (Figures 2b, 2d, and 2f). Erosion at the uplifting foot-wall reduces vertical forces at this location, allowing for further uplift (Olive et al., 2014), and prevents fault and foot-wall rotation (Zwaan et al., 2018; Figure 2). Sedimentation occurs in subsiding hanging walls, which increases pressures at the upper crust (Figures 2c and 2d, center of the plot). The increase in the difference between foot- and hanging wall pressures results in larger displacements along faults for a given period of time, with larger accumulated deformations, fault weakening, and deformation localization in the case of efficient SP. This means that in models with efficient SP, deformation can be accommodated on only two main faults (Figure 2d), while several faults act simultaneously in the no SP model (Figure 2c). Furthermore, the addition of sediments on top of the hanging walls leads to an increase of the upper crustal strength (Figure 2a) which prevents faulting of the subsiding crustal block. In the no SP model, faults rooting at the base of the upper crust, into a viscous channel, occur outward from the initial two main faults (Figure 2e). When erosion is active, the consequent thinning of the upper crust leads to a thinning of this viscous channel (Figures 2b and 2f) and, therefore, diminishing the ability of faults to occur outward from the initial faults. The combination of all these factors leads to faults remaining active for a longer period of time, with larger total deformation along them when SP are efficient. When brittle deformation is the dominant extension mechanism, efficient SP lead to an increase in fault offsets, foot-wall uplift, and hanging wall subsidence, a reduction in the number of faults and, consequently, significant changes to the margin structure.

3.2.2. Effects on Temperature and Ductile Deformation

As for brittle deformation, efficient surface processes enhance localization of deformation in the viscous regime due to their effect on reducing the topographic forcing against fault displacement. However, when the sediment thickness is large enough, the thermal blanketing effect of sediments and the greater depth of the basement leads to greater temperatures (Theissen & Rüpke, 2010). This reduces viscosities due to temperature dependence of the flow law (equation (8)) and, therefore, favors ductile over brittle deformation, even in the upper crust (Figure 3). The thermal blanketing effect is greater for weaker rheologies as lower viscosities occur for the same temperatures, preventing rocks to reach their yield stress.

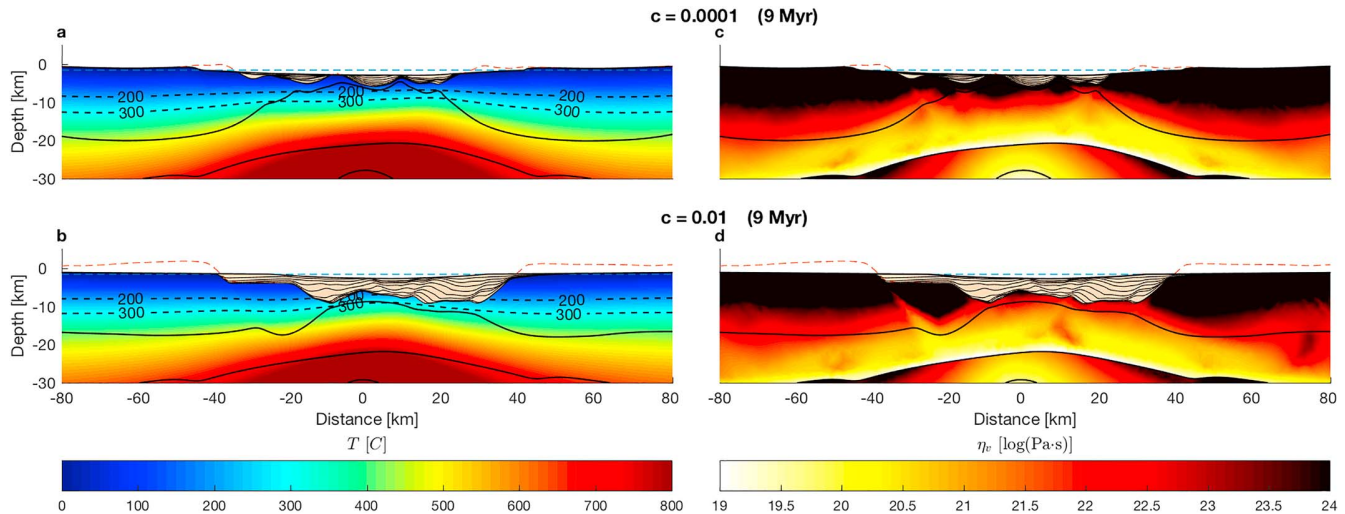


Figure 3. Sediment thermal blanketing and effects on viscosity. Panels (a) and (b) show temperature fields of 40-km crust wet quartzite models with less efficient surface processes ($c = 10^{-4}$) and more efficient surface processes ($c = 10^{-2}$), respectively. Dashed black lines represent isotherms of 200 and 300 °C. Panels (c) and (d) show correspondent viscous fields. Dashed blue lines mark the sea level. Light brown color represent sediments and black lines are depositional time lines for a 1 Myr time interval. Note that, in the central region of (b), upper crustal temperatures are between 200 and 300 °C, while in (a) upper crust temperatures in the central region are below 200 °C. Also, the thermal gradient at the center of (b) is larger than in (a). This difference in crustal temperatures and gradients is the result of thicker sediments in (b) that exert a significant blanketing effect on basal temperatures. This decreases upper crust and lower crust viscosities in (d). Note that sediments are taken into account when calculating the temperature field, but their temperature is not shown in this figure.

3.2.3. Feedbacks Between Loading, Thermal Blanketing, and Rift Migration

Lateral rift migration produces conjugate margin asymmetry in the models. As previously described, the underlying mechanism for RM is the presence of an outward-dipping dominant channel/shear zone of low viscosity (LVC) at the base of the lower crust. The LVC focuses extension to one side of the upwelling mantle dome and connects deformation in the upper crust, lower crust, and mantle. Asymmetric upwelling of the hot mantle toward the LVC weakens the shear zone's hanging wall and forces migration of the deformation toward this area, leading to lateral rift migration. As the LVC migrates, new faults develop in its hanging wall and root into this shear zone. Therefore, this mode is highly dependent on both plastic and viscous deformation, and it is sensitive to the effects of sediment loading and thermal blanketing. Additionally, this mode takes place during later stages of rifting where basins are already deep, and where available sediment is likely to be scarce (i.e., submarine basins).

Figure 4 exemplifies the potential feedbacks between sediment loading and thermal blanketing on lateral rift migration for models with AN lower crust, 40-km initial crustal thickness and different SP efficiencies ($c = 5 \times 10^{-3}, 10^{-2}$ in Figures 4e–4l) and subaerial as well as submarine SP (i.e., models with sea). For comparison, models without surface processes are also shown (no SP in Figures 4a–4d). At 8 Myr, the LVC on the right hand side of the models has just become dominant over the left hand side one (Figures 4a, 4e, 4i, and S2 and S10 movies in the supporting information). However, sequential faulting in the upper crust has not yet started. Instead, a group of faults both dipping oceanward and landward accommodate extension on top of the LVC in all models (Figures 4a, 4e, and 4i). In the model with no SP, sequential faulting starts at 10 Myr (Figure 4b) in contrast with models with SP in which sequential faulting is delayed (Figures 4f and 4j). The delay in the onset of sequential faulting occurs because increasing sediment thickness at the LVC hanging wall leads to larger offsets at LVC antithetic faults (e.g., f0, f1, and f2 in Figures 4e, 4f, 4i, and 4j) and associated crustal subsidence. This reduces the dip of the LVC (compare dip of LVC in Figures 4b and 4j). Additionally, increasing sediment thickness increases crustal temperatures which allows the LVC to continue to deform at low angles and also at the base of the upper crust (see ductile domains at the base of the upper crust in Figures 4e–4g and 4i–4k). Consequently, in models with increasing SP the LVC works as a gently dipping, low viscosity crustal level in which a group of faults detaches, which delays the start of sequential faulting. With increasing extension, deformation also localizes in the $c = 5 \times 10^{-3}$ model, leading to sequential faulting (Figure 4g). At later stages of the model with the largest sediment thickness, crustal

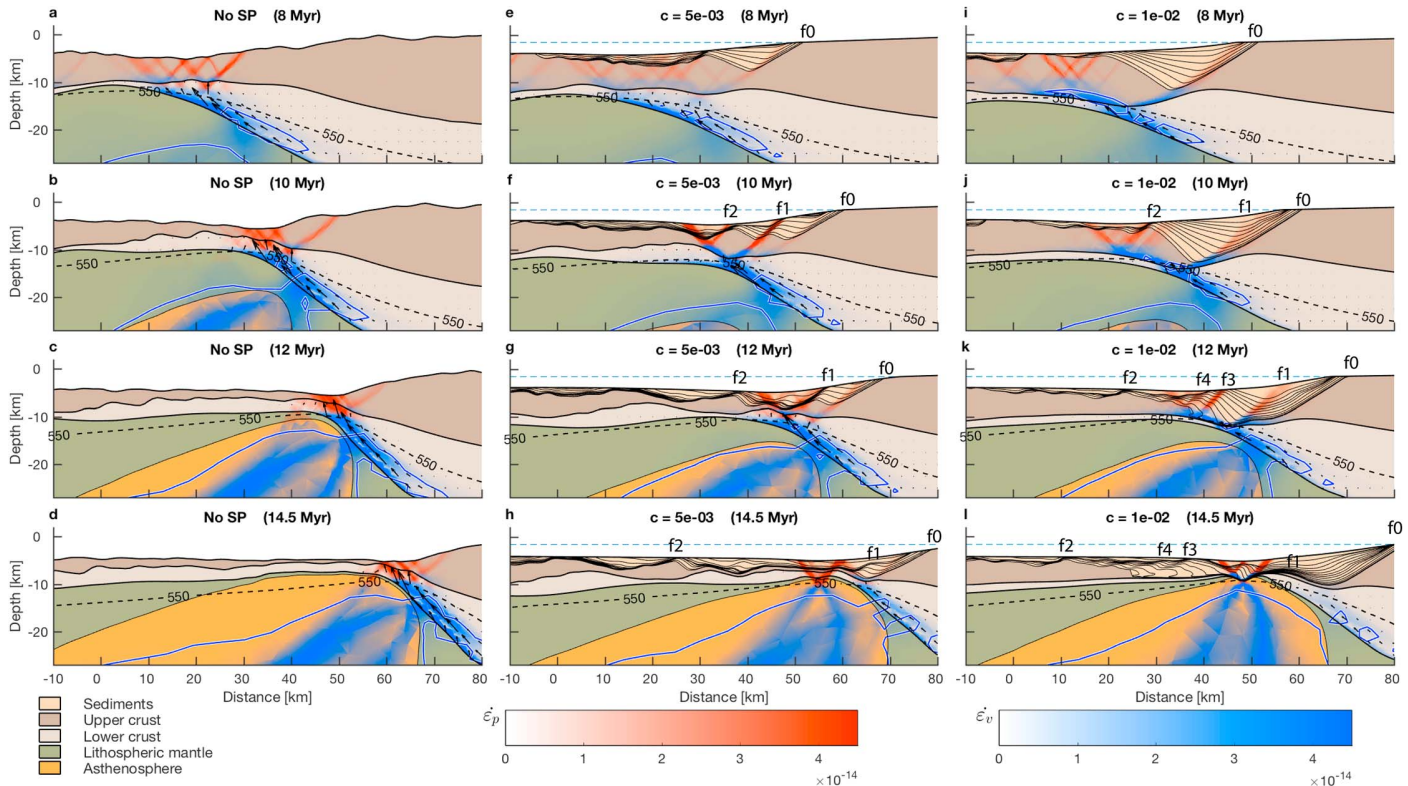


Figure 4. Rift migration for wet anorthite models with 40-km initial crust under different SP efficiencies. Panels (a)–(d) represent the evolution of a model without surface processes, (e)–(h) with SP and $c = 5 \times 10^{-3}$, and (i)–(l) $c = 10^{-2}$ and subaerial as well as marine sedimentation. Black lines inside the sediments represent depositional time lines at 1 Myr time intervals. Black arrows represent velocities of the lower crust relative to the upper crust. Red and blue colors represent plastic ($\dot{\epsilon}_p$) and viscous ($\dot{\epsilon}_v$) strain rates, respectively. The dashed blue line in (e)–(l) marks the sea level. The continuous blue line is the $10^{20.5}$ Pa·s viscosity isoline. f0 to f4 are faults which are antithetic to the low viscosity channel and formed in its hanging wall, in the narrow conjugate side during extension. Note for increasing c , the dip of the low viscosity channel decreases and faults f0–f4 have larger offsets. Also note that some of these faults are later incorporated into the final wide margin (faults f2–f4 in (f)–(h) and (j)–(l)) together with allochthonous sediments, due to rift migration. SP = surface processes.

extension occurs solely by viscous deformation in the crust with several brittle faults in the sediments, which are antithetic to the LVC (f1, f3, and f4 in Figure 4k).

Breakup occurs earlier and is closer to the model center in models with greater SP efficiencies (Figures 4d, 4h, and 4l). This is a consequence of antithetic faults located in the hanging wall of the migrating LVC, which are more active in thinning the hanging wall under increasing sedimentation. Note that these faults are active in the basement and sedimentary sequences and become part of the future wide margin (e.g., faults f2, f3, and f4 in Figures 4f–4h and 4j–4l). Thus, the final wide margin contains both oceanward dipping faults, which formed with the same dip as the LVC shear zone, as suggested in the sequential faulting model (Ranero & Pérez-Gussinyé, 2010), and landward dipping faults induced by sediment loading of the narrow margin. These latter faults bring sediments outsourced from the narrow margin into the wide margin. For the model with the largest subaerial transport coefficient ($c = 10^{-2}$), large sedimentation in the future narrow margin, induces long offset antithetic faults (f0, f1, f3, and f4 in Figures 4j and 4k). These faults, combined with ductile deformation of the upper crust in the last stages of extension, break apart the upper crust and juxtapose lower crust and sediment at the distal part of the wide margin at breakup (Figures 4k, km 35–60, and 4l, km 27–49).

For models with only subaerial SP there is relatively efficient erosion and sediment delivery to the area of active deformation (Figure S27). This results in greater flattening of the dominant shear zone and an increase in the amount of ductile deformation in the upper crust that postpones the onset of sequential faulting. In cases with efficient sediment transport, large piles of sediments in the model center result in longer-lived deformation at this location, ductile deformation within most of the upper crust, and a final symmetric conjugate margin pair.

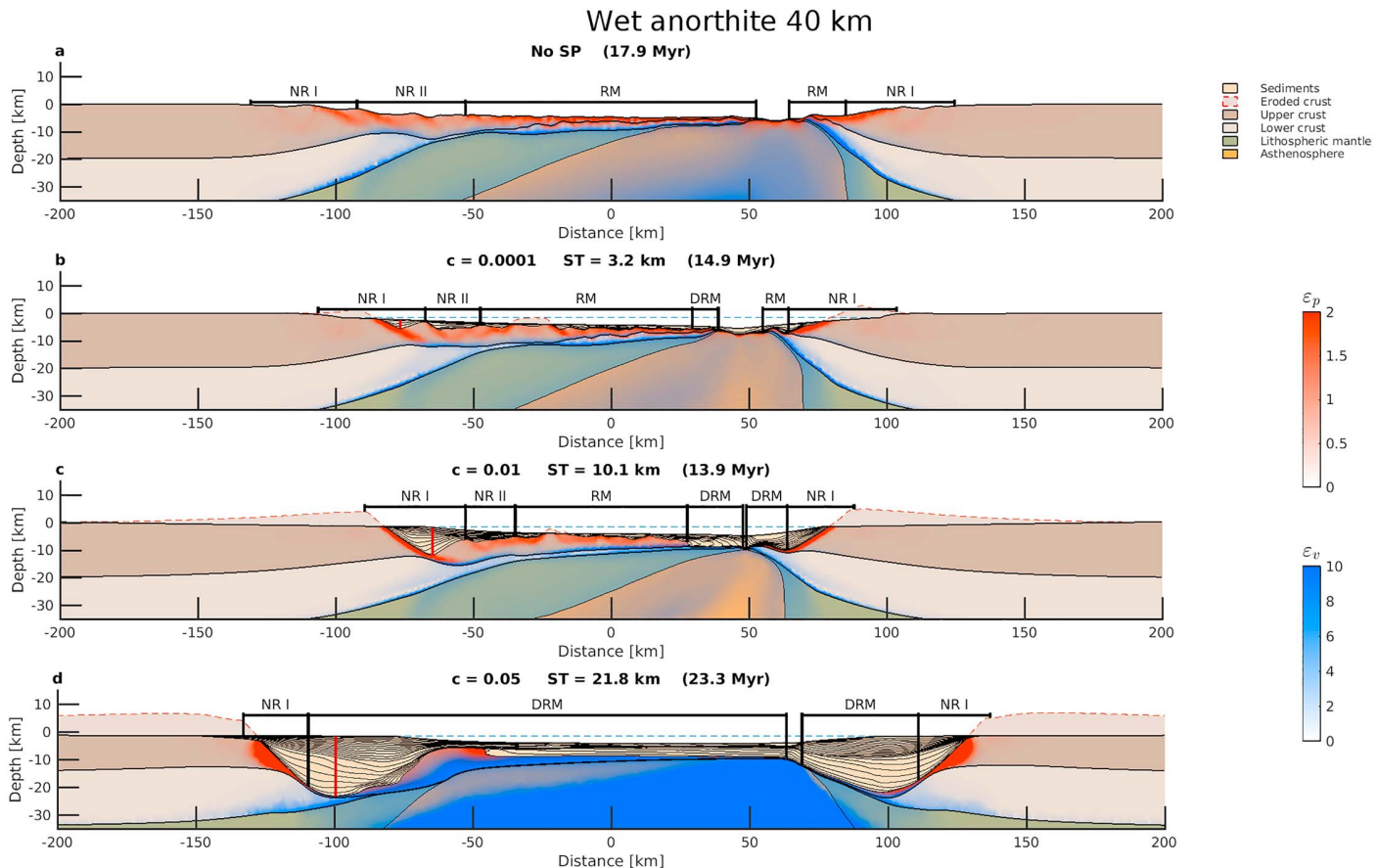


Figure 5. Margin geometry after crustal breakup for a 40-km initial crustal thickness and wet anorthite lower crust. (a) Model without SP and (b–d) models with different subaerial transport coefficient ($c = 10^{-4}, 10^{-2}, 5 \times 10^{-2}$). Red and blue shadows represent plastic (ϵ_p) and viscous (ϵ_v) finite strain (total deformation), respectively. Black lines inside the sediments mark 1-Myr spaced time lines. Margins are divided into deformation domains (section 3.2.4). Vertical red lines represent the maximum ST across the profiles, quantified in each subfigure title. Discontinuous blue line marks the sea level. SP = surface processes; ST = sediment thickness; NR I = initial narrow rifting domain; NR II = narrow rifting domain II; RM = rift migration; DRM = ductile rift migration.

For weak crustal rheologies (WQ), and models with sea, rift migration also takes place through a LVC, but LVC angle is lower and faulting is more distributed than in the cases with stronger rheologies (Figures S28 and S3 movie). As in the previous described cases, an increase in sediment thickness increases the importance of ductile deformation within the lower and upper crust. In cases with very efficient SP, ductile deformation in the basement is so dominant in the narrow margin that brittle deformation in the sediments is very distributed, with clear faults indiscernible at this scale/resolution. If an actual margin would have undergone this type of extension, its seismic section would image pervasive short-offset faulting in the sediments over a nonstructured basement. Syn-rift sequences in the narrow margin would also appear post-rift.

3.2.4. Effects on Regional Margin Architecture

In order to evaluate the contribution of the different rifting modes to the final margin architecture and the effect of surface processes into these extensional modes, we identify different crustal deformation domains for each margin. These deformation domains represent margin sectors in which the last deformation phase in the crust occurs by one of the extensional modes previously defined in section 3.1, plus some additional deformation scenarios observed in the models with sedimentation. We define eight possible domains: (1) initial narrow rifting domain (NR I); (2) narrow rifting domain II (NR II), associated with the extension of the central hanging crustal block or keystone; (3) wide rifting; (WR) (4) core complex domain (CC); and (5) rift migration domain (RM) in which upper crustal deformation is mainly brittle. In addition we can observe (6) a ductile rift migration domain (DRM) in which the last extension phase leads to rift migration accommodated only by ductile deformation in both upper and lower crust; (7) a ductile pure-shear domain (DPS) in

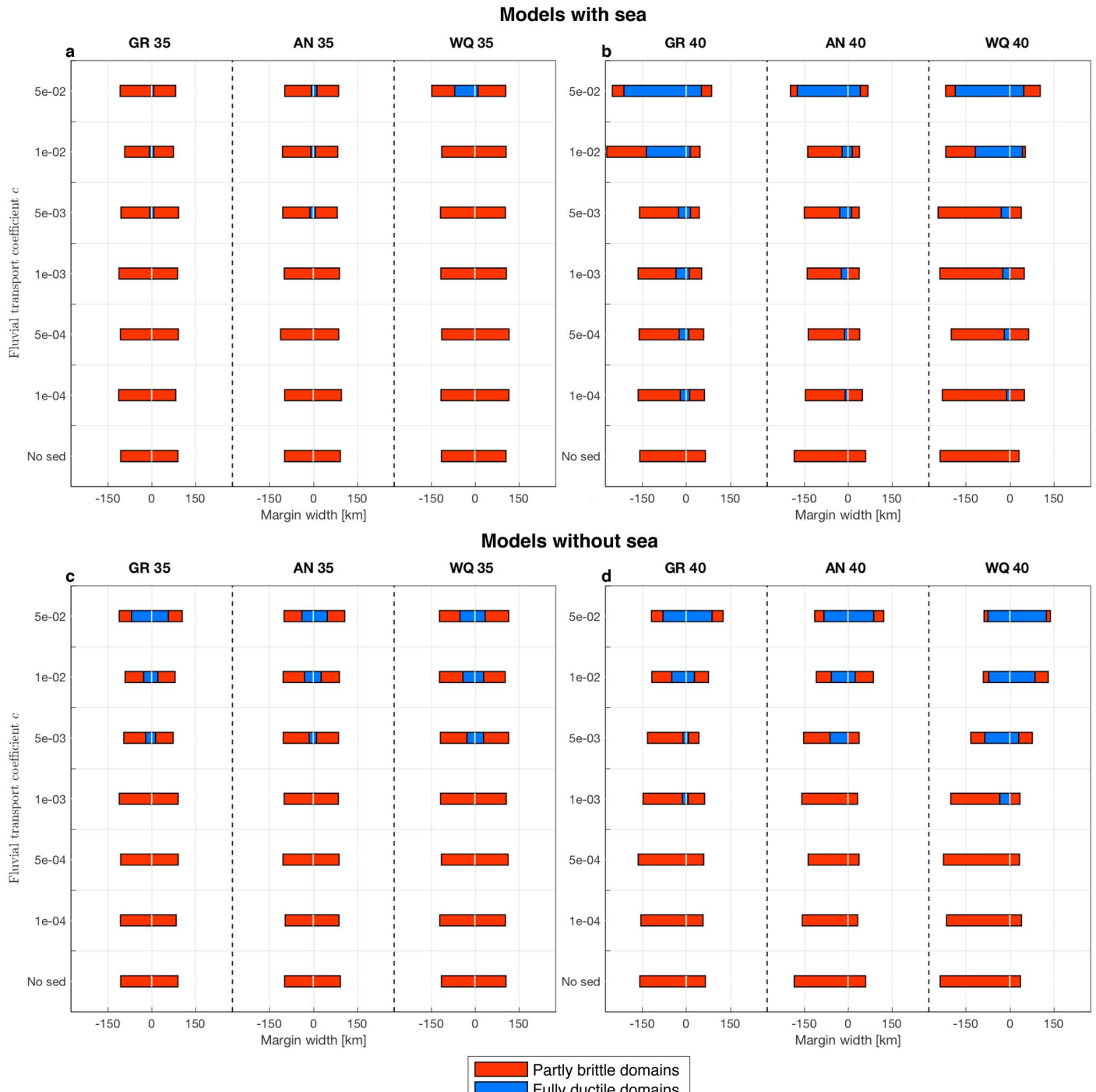


Figure 6. Margin width of models with sea. In (a) margins calculated for initial 35-km crustal thickness, and (b) for 40-km. The white line at 0 represents the crustal breakup, and red and blue stand for partly brittle B and fully ductile D domain widths. Increasing subaerial sediment transport coefficient increases D domain widths. GR = lower crustal rheologies mafic granulite; AN = wet anorthite; WQ = wet quartzite.

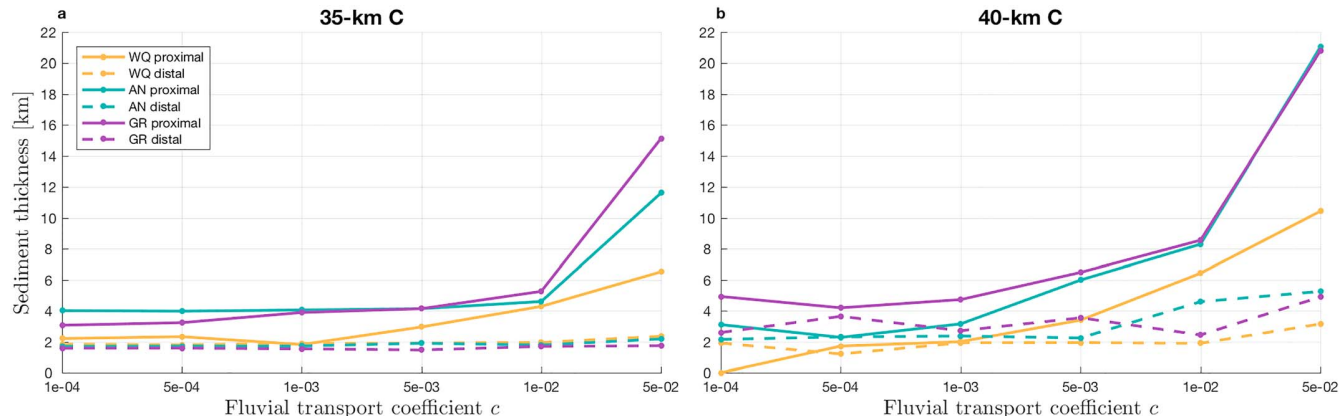


Figure 7. Sediment thickness versus fluvial transport coefficient for different rheologies and initial crustal thickness. Data labeled as proximal represent an average of sediment thickness measured at the basin depocenters closest to the main initial fault at each of the two conjugate margins. Data labeled as distal represent the sediment thickness overlaying the first mantle exhumed after breakup. Note that sediment column is thinner for WQ margins in the proximal sectors of the margins due to smoother topographies related to the extension of a weaker crust. GR = lower crustal rheologies mafic granulite; AN = wet anorthite; WQ = wet quartzite.

which the last extension phase occurs in a pure-shear manner by ductile mechanism in the upper and lower crust; and (8) a shoulder collapse domain (SC) in which a rift shoulder subsides due to lower crustal flow outward from the shoulder into or out of the margin. We examine the different extensional modes during rift evolution in order to identify the crustal deformation domains (see movies in the supporting information). The extension mode at these crustal domains and their width depends on the crustal rheology, the thermal state, the rifting history, and the efficiency of SP. Note that, with the exception of the ductile domains, all domains deform in part brittlely. Consequently, we will refer to all these domains as partly brittle domains (B) and to the ductile domains as fully ductile (D). The total widths of domains that have deformed partly brittlely and those in which the last deformation phase was fully ductile are shown in Figure 6, as a proxy for the effect of SP in plastic/viscous deformation. The different areas that underwent the previously described deformation modes for the models with 40 km initial crustal thickness, and anorthite and wet quartzite LC, are shown in Figures 5 and 8. Corresponding figures for the rest of the models are shown in the supporting information (Figures S3–S26).

Models with sea. At the start of extension, all model topography is above sea level and experiences sediment transport by subaerial processes during the first phase of rifting. Once deformation localizes, effective subsidence of the hanging block results in the ocean filling the graben basin, and a change in depositional environment from subaerial to submarine: shallow sediments near the coast are transported efficiently into the shelf while sediment transport is less efficient in the deep sea. Consequently, the effects of SP on extension mechanisms depend on whether deformation takes place on the shelf or in deeper portions of the new sea, to which less sediment can be transported (equation (15)).

In stronger LC models (GR and AN) and 35-km initial crust, an increase in subaerial transport coefficient c results in larger inflow of sediments into the proximal domains NR I and II, and increasing erosion of the rift shoulder (Figures S3–S6 and S4, S6, S7, and S8 movies). This leads to a slight reduction in the width of domains NR I and II and a reduction of the partly brittle domains, with increasing c (Figure 6a) through sediment loading effects (see section 3.2.1). Small fully ductile domains (DPS) appear for large c as the result of thermal blanketing in combination with hot mantle upwelling. The increase in length of the domains behaving fully ductile compensates for the decrease in length of the domains behaving partly brittlely, so that the total width of margins remains fairly constant with increasing sediment thickness, that is, increasing c (Figure 6a).

With increasing SP efficiency, the stronger models (GR and AN) with 40 km initial crust also suffer a reduction in the width of partly brittle domains, in particular domains NR I and II and the RM domain (see Figures 5 and 6b and Supporting Information Figures S9–S12). While NR I and NR II, become narrower due to sediment loading effects, the length of the RM domain decreases due to an increase in ductility related to thermal insulation by sedimentation and mantle upwelling. This induces a switch to ductile rift migra-

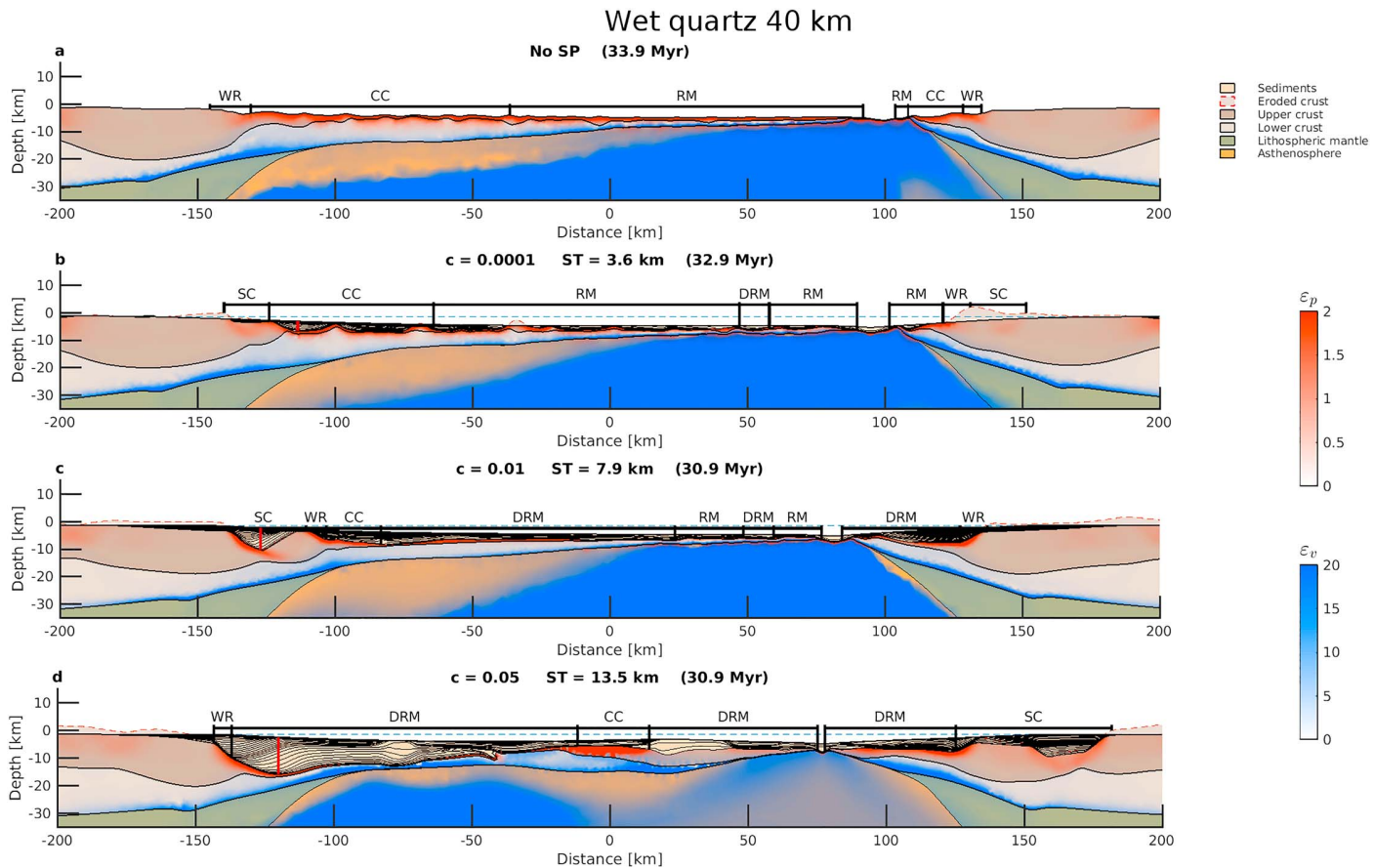


Figure 8. Margin geometry after crustal breakup for a 40-km initial crustal thickness and wet quartzite lower crust. (a) model without SP and (b–d) models with different subaerial transport coefficient ($c = 10^{-4}, 10^{-2}, 5 \times 10^{-2}$). Red and blue shadows represent plastic (ϵ_p) and viscous (ϵ_v) finite strain (total deformation), respectively. Black lines inside the sediments mark 1-Myr spaced time lines. Margins are divided into deformation domains (section 3.2.4). Vertical red lines represent the maximum ST across the profiles, quantified in each subfigure title. Discontinuous blue line marks the sea level. Note that outboard basins associated to the initial WR phase are not included in the deformation domains of this models (see S3 movies in the supporting information) since we focus on the central basin which accommodates most of the extension. SP = surface processes; ST = sediment thickness; WR = wide rifting; CC = core complex; RM = rift migration; DRM = ductile rift migration; SC = shoulder collapse.

tion in the last phases of extension (supporting information movies S1, S2, S10, and S12). The total margin width only changes significantly for $c \leq 10^{-2}$, where widening of ductile domains results in wider margins (Figures 5d and 6b). Note that the degree of symmetry/asymmetry of conjugate margins is not affected by SP when sea is present (Figure 6b).

In weak models (WQ) smoother topographies develop than in stronger models, since deformation is more distributed and LC flow produces rapid relaxation of sharp relief. As erosion depends on slope (equations (14) and (15)), the proximal areas of weak rheology models have lower sediment thickness than strong ones for the same c coefficients (Figure 7). However, distal regions show little variation in sediment thickness for different c , because of the large reduction in sediment transport in marine environments (Figure 7). Consequently, increasing c in 35-km WQ models only affects the widths of proximal domains, which partly deform brittlely when $c \leq 10^{-2}$ (B domains in WQ Figure 6a and WR, CC, and RM in Figure S8). For the same reason, the fully ductile domain D is only present in the 35-km model with $c = 5 \times 10^{-2}$ (Figure 6a).

In weak models with initial 40-km crust, conjugate margin asymmetry occurs through a final phase of rift migration (Figure 8 and movies in the supporting information S3 and S11). Again, slow sedimentation rates in the marine basins result in small effects on width reduction in brittle domains and increase in ductile domain width when $c < 10^{-2}$ (Figures 6b). However, for a given proximal sediment thickness (i.e., ~6.5 km in WQ $c = 10^{-2}$, Figure 7b) D domains in GR and AN models of similar thickness ($c = 5 \times 10^{-3}$ for GR and

AN, Figure 7b) are narrower (~ 50 GR and AN vs ~ 150 km in WQ Figure 6b). We conclude that weaker lower crust is more sensitive to the effects of thermal blanketing. Note that there is also a considerable reduction in margin asymmetry for $c = 5 \times 10^{-2}$ (Figure 8d). In this case, it is due to the suppression of the rift migration phase, with its substitution by several fully ductile rift migration phases in which deformation is less localized and several rift jumps occur (Figure 8d and S11 movie in supporting information).

Models without sea. Extension typically occurs in regions with deep relief. If these deep topographies are not covered by water, only subaerial SP are present during extension. This is important because subaerial SP are more efficient in transporting sediments into the deepest topographies and areas undergoing deformation than are submarine ones. In this section, we present models with only subaerial processes, as an end member for high sediment transport into the distal margin domains.

In this case, 35-km models showcase symmetric conjugate margins for all values of c and all rheologies considered (Figure 6c and Figures S15–S20 and 35-km movies). Reduction of B domain widths (NR I and II) is observed for $c \geq 10^{-3}$ (Figure 6c). D domains are present in models in which $c \geq 10^{-3}$ and their widths increase with increasing c . However, margin length does not change with increasing SP efficiency (Figure 6c) because increasing in D domain widths compensate for the decrease in B width, as also observed in 35-km models with sea.

Models with initial 40-km crustal thickness showcase a larger decrease in B domain widths (NR I, II, and RM) and a larger increase in D domains, with increasing c , in comparison to models with sea (Figure 6d and Figures S21–S26 and 40-km movies). The larger decrease in B width is justified as more sediments deposit on tectonically active sectors across the full rifting history, enhancing strain localization at faults. The increase in ductile domain widths is associated with thermal blanketing effects that reduce, overprint, and/or suppress NR II and RM (Figure 6d and Figures S21–S26). However, in this case, for $c \geq 10^{-2}$ D domains do not occur by rift migration. Instead, conjugate ductile domains deform simultaneously by pure shear extension (DPS in Figures S21–S26 and S14, S15, S17, S18, S21, and S24 movies). This occurs because a high degree of brittle strain localization takes place during initial rifting phases, penalizing rift migration (see section 3.2.3) and leading to a more symmetric setup for later rifting phases (see Figure S27k). High sediment thicknesses in distal basins (i.e., thermal blanketing) favors pure shear viscous deformation in the center of the model during later rifting phases. The ultimate impact on margin geometry of the absence of a sea is therefore a substitution of rift migration domains (RM and DRM) by symmetric ductile pure-shear domains (DPS) with very attenuated crust, leading to symmetric conjugate margins (Figure 6d).

4. Discussion

4.1. New Insights in the Effects of Surface Processes on Rift Development

Our study shows that surface processes have important consequences for the modes of deformation and final architecture of margins. This influence is more obvious with increasing efficiency of surface processes. Because subaerial SP are more efficient than submarine ones, the proximal areas of margins where subaerial SP are more likely to take place are more obviously affected than the submerged distal sectors. In particular, we observe that, during the first phases of rifting, high erosion and sedimentation rates at the foot- and hanging walls, respectively, facilitate displacement on faults. This occurs because topographic and flexural forces opposing slip through an existing fault are reduced by surface processes (Buiter et al., 2008; Burov & Poliakov, 2001; Olive et al., 2014). Owing to this, the increasing efficiency of SP during the initial phases of rifting result in (1) localization of deformation in fewer, larger-offset, and longer-lived faults which can prevent deformation to spread out into the rift shoulders, (2) an increase in fault spacing and fault-block size, (3) a longer-lived narrow rifting phase, and (4) a more symmetric setup of the crustal structure at the end of this initial phase of extension. At the regional scale, a direct consequence of these effects is that domains formed during early stages of rifting (controlled by plastic deformation) under subaerial or shallow marine environments would be narrower and their fault offsets would be larger with increasing subaerial SP efficiency, due to strain localization. This is in agreement with previous analytical, numerical, and analog model results (Allen & Beaumont, 2016; Bialas & Buck, 2009; Buiter et al., 2008; Burov & Poliakov, 2001; Olive et al., 2014; Zwaan et al., 2018). However, those works, with the exception of Allen and Beaumont (2016) which focuses on salt deposition, use simpler setups that lack nonlinear and/or temperature-dependent viscosities in the LC, or lack elasticity and/or a realistic landscape evolution model (e.g., that lack erosion and basin-filling occurs to a fixed base level). This hinders understanding of the effects of marine incursion into the rift area

and of how sedimentation affects the deformation mode and basement structuring throughout the rifting history, including effects on the distal margins.

Our new findings are particularly relevant for the effects of marine incursion and the structuring of distal regions of margins. When submarine as well as subaerial SP take place (models with sea), we see no clear change in conjugate margin symmetry (Figures 6a and 6b). However, we do see a change in the structure of the basement. Here, thermal blanketing leads to a switch from plastic (i.e., deformation by faulting) to viscous deformation, even in the upper crust, at later rifting stages. This is reflected in a distal area where the basement lacks fault-block structure (i.e., an unstructured basement) and its width increases with the efficiency of SP (DRM in Figures 5 and 8). These attenuated unstructured crustal domains are dominated by ductile deformation of the entire crust.

When submarine SP are not present (models without sea), sediment input into the distal margins is larger and may lead to a change in the original symmetry of the conjugate margins. For example, while margins that were originally symmetric stay symmetric (Figure 6c), those that were originally asymmetric without SP may become symmetric given enough sediment input (Figure 6d). This increase in the symmetry of the conjugate margins is due to the fact that large sediment input into the deep basin results in larger localization of deformation on faults at the center of the model, combined with later thermal insulation and predominance of pure shear ductile deformation (Figure 6d). This points out at the importance of changes in sedimentation environments for the conjugate margin symmetry/asymmetry (i.e., a late marine incursion favors symmetry in contrast to an early sea incursion, Figure 6b in contrast with d for $c \geq 10^{-2}$).

We also show that the SP effects on conjugate margin width depend on the underlying rheology at the start of extension: thermal blanketing more strongly affects weaker and thicker crust. This is reflected in wider ductile domains for WQ models when compared with equivalent GR and AN models where sediment thickness is the same (Figure 6b). In the stronger models, there is little variation on margin width (Figures 6 and 7). We can not yet rule out that even models with sea can reproduce larger effects of SP on margin width and conjugate symmetry for rheologies weaker than the ones explored in this study.

4.2. Rifting and Surface Processes in Nature

In nature, margins portray a large variability in their architecture, including width of the conjugate margins, fault population characteristics, abruptness of crustal necking, and so forth. It is widely accepted that this variability is the result of differences in the initial lithospheric thermal structure, rheology of the extending lithosphere, initial crustal thickness, distribution of crustal weaknesses, extension velocities, and magma supply (e.g., Brune et al., 2014; Buck, 1991; Huismans & Beaumont, 2003, 2007, 2014; Hopper et al., 2003; Ros et al., 2017; Svartman Dias et al., 2015; Sharples et al., 2015). In this study we have shown for the first time that variation in erosion and sedimentation rates, as well as in the depositional environment (e.g., subaerial vs submarine environments), are key factors in determining margin morphology and rift evolution. This implies that factors such as climate, weathering, and fluvial network evolution may also play a role in architectural styles and rift development. In order to study a particular rift system and reproducing the final margin structure through modeling one should constrain all these parameters. Reproducing the structure of any particular passive margin observed in nature, or identifying the main factor/s responsible of its morphology, will be addressed in future studies. Here, we restrict our discussion to the most essential analogies between models and nature. These comparisons allow us to explain basement features that have yet to be well understood as the potential consequence of interaction between surface processes and extensional tectonics.

One of these features is the large offset faults observed in models with high surface process efficiencies during the early phases of rifting. Potential analogies to this can be observed in natural examples of continental rifts. For instance, the Lake Baikal rift system accounts in some sections for up to 9 km of syn-rift continental lacustrine sediments with limiting faults that have 8–12 km offset and little offsets at intrabasin faults (Hus et al., 2012; Hutchinson et al., 1992). Likewise, in the western branch of the Eastern African rift system, large-offset (~7 km) planar faults separate uplifted flanks from basins containing large lacustrine sediment piles (e.g., up to 6 km in lake Tanganyika; Ebinger, 1989; Morley, 1988). Our modeling results imply that the large fault offsets in these examples can be explained as a result of strain localization due to efficient erosion/sedimentation loading/unloading during the initial phases of rifting.

Thick syn-rift sediments associated with large offset faults are also observed in the proximal sectors of the Great Australian Bight (GAB) margin. Structurally, the GAB is characterized by localization of the crustal thinning around families of large offset border faults (e.g., the Wallaroo fault system), that separate the shelf basement high from a seaward very attenuated continental crust (Ball et al., 2013; Direen et al., 2012; Stagg et al., 1990; Talwani et al., 1979; Totterdell et al., 2000). These fault systems are active during the initial phases of rifting in the Late Jurassic (Totterdell et al., 2000). Large amount of syntectonic sediments are deposited at the hanging walls of the border faults (~ 4 km), over the crustal necking, and high erosion is observed at the foot-wall (Ball et al., 2013; Direen et al., 2007; Stagg et al., 1990; Totterdell et al., 2000; Totterdell et al., 2003). Furthermore, these sediments were deposited under fluvial and lacustrine environments, at least in the proximal domains of the margin during the early rifting (Totterdell et al., 2000). This could explain why sediments were efficiently transported into the half-grabens developed over the border fault hanging walls, enhancing plastic strain localization and producing efficient crustal thinning as observed in our models with no sea (see Figures S24b, S26b, and S27i–S27j and movies 40AN2nS and 40WQ2nS).

Faulting is scarcely imaged in the basement of the Ceduna basin, seaward from the border faults (i.e., more distal sectors). Here, the large subsidence observed during the Early Cretaceous has been interpreted as the result of a more distal ductile extension phase that could also explain the large beta factors ($\beta > 4$) at the Ceduna basement with no associated basement faulting (Ball et al., 2013; Totterdell et al., 2000). We suggest that this phase of ductile extension is analogous to the development of pure shear ductile domains in the models under the effects of thermal blanketing associated with the thick overlying supersequences of Bronze Whaler and Blue Whale (Figure 6d), deposited under submarine conditions (Totterdell et al., 2000). The conjugate margin of Wilkes Land (WL) also showcases abrupt thinning of the crust along a faulting zone near the shelf edge, and oceanward an attenuated continental crust with evidence of ductile deformation (i.e., anomalously high subsidence), together with thick syn-rift sediments (Colwell et al., 2006). Furthermore, this pair of conjugate margins is symmetric in terms of width. From the results of the models here presented, we infer that the symmetry and structure observed at the GAB-WL margins could be partly controlled by large syn-rift sedimentation over the proximal and intermediate distal margin sectors, possible due to a delayed marine incursion (i.e., AN and WQ for $c \geq 10^{-2}$ in Figure 6 and Figures S24b, S26b, and S27i–S27j and movies 40AN2nS and 40WQ2nS).

Anomalous post-Valanginian regional subsidence is also observed in the Northern Carnarvon basin in the absence of synchronous faulting at the upper crust (Driscoll & Karner, 1998). This margin also showcases thick syn-rift sequences. This anomalous subsidence has been interpreted as the result of lower crustal thinning through a low angle detachment (Driscoll et al., 1995; Karner et al., 2003). This interpretation could be equivalent to the low-angle low viscosity shear zone that forms in our tests with high subaerial SP efficiencies and sea (e.g., narrow margin in Figures 4j–4l).

The Angola margin highlights a distal domain covered by sag basin sediments where evidences of faulting are not present (“Continental Slope Domain” in Aslanian et al., 2009, and “Exhumation and Outer Domains” of Figure 6 in Péron-Pinvidic et al., 2015). Péron-Pinvidic et al. (2015) interpret these regions as areas of possible exhumation of the mantle without ruling out the presence of overlying transitional crust. Another interpretation is that here the basement consists of unstructured lower crust that has deformed ductilely (Aslanian et al., 2009; Karner et al., 2003). One of the arguments against this last interpretation is that, as crust extends and thins, it cools leading to a complete embrittlement of the crust (Pérez-Gussinyé et al., 2001, 2003). However, our models show that this can only occur for low sedimentation rates, such in the West Iberia margin, because otherwise the thermal insulation associated to sedimentation (i.e., hotter basement) would inhibit cooling and keep the LC ductile (e.g., Figures 5b–5d). Our models with AN 40-km (Figures 4h and 4l), show a distal ductile zone with exhumed LC. These distal parts could be analogous to those of the Angola margin which presents a thick sag basin sequence, with planar reflectors off-lapping toward the top-basement (Karner et al., 2003; Péron-Pinvidic et al., 2015; Rowan, 2018), implying that there was enough syntectonic deposition to favor a final phase of ductile crustal extension associated with thermal blanketing. Note that, in our models, sediment thickness required for the formation of ductile domains is smaller for weaker than for stronger LCs (Figure 6), implying that lower crustal strength is also an important factor for the formation of the distal ductile domains.

Margin width changes are observed along axis in the Gulf of California (Lizarralde et al., 2007). These changes have been interpreted as the result of either along-axis changes in sedimentation and/or man-

tle fertility (Bialas & Buck, 2009; Lizarralde et al., 2007). Narrow margins develop in the northern sector (Delfín-Tiburón and Guaymas sector) under thick sediments supplied from the Colorado River, while wide margins develop in the south central sector (Alarcon sector) under thin sediment packages (González-Fernández et al., 2005; Lizarralde et al., 2007; Martín-Barajas et al., 2013). Our results support the hypothesis that SP can potentially explain the axial variation in margin architecture in the Gulf of California, where high sedimentation rates would favor the localization of the deformation and fast crustal thinning in the proximal areas (Figure 6d and Figures S22, S24, and S26). Based on the thick magmatic crust observed in the Guaymas sector, Lizarralde et al. (2007) proposed that thermal blanketing associated with high sedimentation rates combined with fertile mantle result in large volumes of melting that lead to abrupt crustal breakup. On the contrary, Bialas and Buck (2009) suggested that sedimentation would push the isotherms down in the area of deformation and thermal blanketing would occur only for areas of abandoned deformation. In theory, this would lead to colder crustal-sediment column, that together with sediment loading would favor narrow rifting. However, the narrow rifting phase in Bialas and Buck (2009) is active for a prolonged period of time without crustal breakup generating a very attenuated crust (i.e., Figure 10 in Bialas & Buck, 2009), and localization of the deformation seems to occur exclusively within the mantle. To our knowledge, narrow rifting mechanisms are incompatible with the production of large attenuated crustal domains. The modeled margins shown in this work also showcase wide attenuated ductile domains seaward from the point of abrupt crustal necking under large sediment loads (Figure 6d and Figures S22, S24, and S26). However, these domains are the byproduct of a final phase of pure-shear or rift-migration ductile extension, and not of narrow rifting. It is likely that the higher resolution of our models (from 1 km to 100 m in very thin layers vs 4 km), together with our efforts to differentiate viscous from plastic deformation, allow for the observation of these ductile domains and the effects of thermal blanketing. In agreement with Lizarralde et al. (2007), our results show that high sedimentation rates heat the crust and mantle, potentially enhancing melt generation that could intrude thinned ductile crust and accelerate breakup.

Clearly, natural examples show striking analogies to some model outcomes. This is not to say that the structure and symmetry/asymmetry of passive margins is exclusively conditioned by the efficiency of surface processes or contrasting subaerial/submarine deposition. We agree that tectonic inheritance, rift dynamics, thermal state, and lithospheric strength can all play major roles in the geometric configuration of passive margins, as shown by previous works. However, in this work we have shown that realistic distinct surface process efficiencies can potentially lead to variations in margin architecture of similar magnitude to the ones inferred for the other tectonic factors.

5. Conclusions

In this work we have tested the influence of surface processes on rifting structures and the final architecture of rifted margins. For this purpose, we developed a state-of-the-art numerical model that solves for deformation, temperature, and pressure for a layered visco-elasto-plastic lithosphere, and coupled it to a landscape evolution model that accounts for sediment transport under subaerial and submarine environments. With this model we conducted a broad parametric study in which we tested the interactions of different subaerial surface processes efficiencies with different lower crustal rheologies and initial crustal thicknesses.

In agreement with previous works, we find that surface processes promote the localization of the plastic deformation due to the reduction in topographic and flexural forces that oppose fault displacement. Consequently, high erosion and sedimentation rates favor longer-lived faults, larger faulted blocks, and abrupt crustal necking, analogous to observations at the proximal margins from the Great Australian Bight and its conjugate Wilkes Land, the Gulf of California, and strongly sedimented continental rifts such as Baikal and Tanganyika. Conversely, we find that intermediate to high sedimentation rates over hot extending crustal sectors (i.e., late rifting and distal margins) exert an effect of thermal blanketing that favors viscous distributed deformation at the basement and leads to the formation of unstructured attenuated crustal domains, such as the basements of the Ceduna basin in the Great Australian Bight, and the Carnarvon basins in western Australia, and possibly the distal domains of Angola margin. These ductile domains typically develop in more distal margin sectors and during the last rifting phases, most likely under submarine conditions. Here, we note that these unstructured attenuated crustal domains could be easily misinterpreted in seismic sections as part of the continent-ocean transition.

Our experiments show that the timing of the marine incursion may play an important role in the final conjugate geometry for models with weaker lithosphere (i.e., 40-km-thick crust models). These models tend to develop asymmetric conjugate margins by migration of deformation during late rifting stages resulting in wide and narrow conjugated margins. Early marine incursion implies damping of sediment transport into the distal extending areas and, therefore, low syn-rift sedimentation during rift migration. However, due to the asymmetry of deformation, sediments from the narrow margin would be more efficiently supplied to the extending area. If subaerial sediment transport efficiency is rapid enough, sediment supply from the future narrow margin would lead to larger and longer-lived basinward dipping faults located in this area, so that sequential faulting starts later in the margin's evolution. Some of these faults would be transferred to the future wide margin through rift migration, resulting in a final wide margin which contains sequential in time oceanward dipping faults in the basement and landward dipping faults in the overlying sediments that were induced by sediment loading of the narrow margin. Thermal blanketing in the last rifting stages could further result in ductile deformation of the entire crust, generating distal domains of unstructured basement that juxtapose sediments on top of lower crustal rocks. In models with sea, we observe much less change in conjugate margin asymmetry because the reduction in domains that behave partly brittlely is counteracted by an increase in width of domains that behave fully ductilely.

Conversely, equivalent models with no sea highlight increasing symmetry and decreasing margin width with increasing surface process efficiency because more efficient sediment transport into extending areas aids strain localization at the center of the model. This is in agreement with observations from Great Australian Bight, where a continental environment dominated the early and intermediate rifting stages. We suggest that the timing of the marine incursion into a rift may play an important role on the evolution and final architecture of margins. These results also suggest that factors such as climate, the geographic locus of rifting (i.e., in the middle of a super-continent vs a back-arc) and the precursor fluvial network could all play important roles on shaping the structure and symmetry/asymmetry of passive margins.

Acknowledgments

We acknowledge COMPASS industry consortium (Continental Margin Process Analysis, Structures and Stratigraphy) at Royal Holloway, University of London, and MARUM (Center for Marine Environmental Sciences), University of Bremen for funding. J.J.A. acknowledges funding from the Royal Astronomical Society and the Agence National de la Recherche. We acknowledge Albert de Montserrat, Jörg Hasenklever, and Elena Ros for fruitful discussions on numerical modeling implementations. We also thank reviewers Luc Lavier and Jean-Arthur Olive and Editor Laurent Jolivet for valuable reviews that significantly improve the quality of this manuscript. The work presented here is theoretical and no data are used.

References

- Allen, J., & Beaumont, C. (2016). Continental margin syn-rift salt tectonics at intermediate width margins. *Basin Research*, 28(5), 598–633. <https://doi.org/10.1111/bre.12123>
- Andrés-Martínez, M., Morgan, J. P., Pérez-Gussinyé, M., & Rüpkne, L. (2015). A new free-surface stabilization algorithm for geodynamical modelling: Theory and numerical tests. *Physics of the Earth and Planetary Interiors*, 246, 41–51. <https://doi.org/10.1016/j.pepi.2015.07.003>
- Armitage, J. J., Allen, P. A., Burgess, P. M., Hampson, G. J., Whittaker, A. C., Duller, R. A., & Michael, N. A. (2015). Sediment transport model for the Eocene Escanilla sediment-routing system: Implications for the uniqueness of sequence stratigraphic architectures. *Journal of Sedimentary Research*, 85(12), 1510–1524. <https://doi.org/10.2110/jsr.2015.97>
- Armitage, J., Duller, R., & Schmalholz, S. (2014). The influence of long-wavelength tilting and climatic change on sediment accumulation. *Lithosphere*, 6(5), 303–318. <https://doi.org/10.1130/L343.1>
- Armitage, J. J., Jaupart, C., Fourel, L., & Allen, P. A. (2013). The instability of continental passive margins and its effect on continental topography and heat flow. *Journal of Geophysical Research: Solid Earth*, 118, 1817–1836. <https://doi.org/10.1002/jgrb.50097>
- Aslanian, D., Moulin, M., Olivet, J., Unternehr, P., Matias, L., Bache, F., et al. (2009). Brazilian and African passive margins of the central segment of the South Atlantic Ocean: Kinematic constraints. *Tectonophysics*, 468(1), 98–112. <https://doi.org/10.1016/j.tecto.2008.12.016>
- Ball, P., Eagles, G., Ebinger, C., McClay, K., & Totterdell, J. (2013). The spatial and temporal evolution of strain during the separation of Australia and Antarctica. *Geochemistry, Geophysics, Geosystems*, 14, 2771–2799. <https://doi.org/10.1002/ggge.20160>
- Bialas, R. W., & Buck, R. W. (2009). How sediment promotes narrow rifting: Application to the Gulf of California. *Tectonics*, 28, TC4014. <https://doi.org/10.1029/2008TC002394>
- Bos, B., & Spiers, C. J. (2002). Frictional-viscous flow of phyllosilicate-bearing fault rock: Microphysical model and implications for crustal strength profiles. *Journal of Geophysical Research*, 107(B2), 2028. <https://doi.org/10.1029/2001JB000301>
- Brune, S., Heine, C., Pérez-Gussinyé, M., & Sobolev, S. V. (2014). Rift migration explains continental margin asymmetry and crustal hyper-extension. *Nature Communications*, 5, 4014. <https://doi.org/10.1038/ncomms5014>
- Brune, S., Popov, A. A., & Sobolev, S. V. (2012). Modeling suggests that oblique extension facilitates rifting and continental break-up. *Journal of Geophysical Research*, 117, B08402. <https://doi.org/10.1029/2011JB008860>
- Buck, W. R. (1991). Modes of continental lithospheric extension. *Journal of Geophysical Research*, 96(B12), 20,161–20,178. <https://doi.org/10.1029/91JB01485>
- Buck, W. R. (1993). Effect of lithospheric thickness on the formation of high- and low-angle normal faults. *Geology*, 21(10), 933–936. [https://doi.org/10.1130/0091-7613\(1993\)021<0933:EOLTOT>2.3.CO;2](https://doi.org/10.1130/0091-7613(1993)021<0933:EOLTOT>2.3.CO;2)
- Buck, W. R., & Lavier, L. L. (2001). A tale of two kinds of normal fault: The importance of strain weakening in fault development. *Geological Society, London, Special Publications*, 187, 289–303. <https://doi.org/10.1144/GSL.SP.2001.187.01.14>
- Buck, W. R., & Poliakov, A. N. (1998). Abyssal hills formed by stretching oceanic lithosphere. *Nature*, 392, 272–275. <https://doi.org/10.1038/32636>
- Buitjer, S. J. H., Huismans, R. S., & Beaumont, C. (2008). Dissipation analysis as a guide to mode selection during crustal extension and implications for the styles of sedimentary basins. *Journal of Geophysical Research*, 113, B06406. <https://doi.org/10.1029/2007JB005272>
- Burov, E., & Cloetingh, S. (1997). Erosion and rift dynamics: New thermomechanical aspects of post-rift evolution of extensional basins. *Earth Planetary Science Letters*, 150(1–2), 7–26. [https://doi.org/10.1016/S0012-821X\(97\)00069-1](https://doi.org/10.1016/S0012-821X(97)00069-1)

- Burov, E., & Poliakov, A. (2001). Erosion and rheology controls on synrift and postrift evolution: Verifying old and new ideas using a fully coupled numerical model. *Journal of Geophysical Research*, 106(B8), 16,461–16,481. <https://doi.org/10.1029/2001JB000433>
- Christensen, N. I., & Mooney, W. D. (1995). Seismic velocity structure and composition of the continental crust: A global view. *Journal of Geophysical Research*, 100(B6), 9761–9788. <https://doi.org/10.1029/95JB00259>
- Clift, P. D., Brune, S., & Quinteros, J. (2015). Climate changes control offshore crustal structure at South China Sea continental margin. *Earth and Planetary Science Letters*, 420, 66–72. <https://doi.org/10.1016/j.epsl.2015.03.032>
- Colwell, J. B., Stagg, H. M., Direen, N. G., Bernardel, G., & Borissova, I. (2006). The structure of the continental margin off Wilkes Land and Terre Adélie coast, east Antarctica, *Antarctica* (pp. 327–340). Berlin, Heidelberg: Springer.
- Contrucci, I., Matias, L., Moulin, M., Géli, L., Klingelhofer, F., Nouzé, H., et al. (2004). Deep structure of the West African continental margin (Congo, Zaïre, Angola), between 5°S and 8°S, from reflection/refraction seismics and gravity data. *Geophysical Journal International*, 158(2), 529–553. <https://doi.org/10.1111/j.1365-246X.2004.02303.x>
- Culling, W. (1960). Analytical theory of erosion. *The Journal of Geology*, 68(3), 336–344.
- Dabrowski, M., Krotkiewski, M., & Schmid, D. W. (2008). MILAMIN: MATLAB-based finite element method solver for large problems. *Geochemistry, Geophysics, Geosystems*, 9, Q04030. <https://doi.org/10.1029/2007GC001719>
- de Souza Neto, E. A., Perić, D., & Owen, D. R. J. (2008). *Computational methods for plasticity: Theory and applications* (Vol. 6, pp. 137–190). John Wiley. <https://doi.org/10.1002/9780470694626.ch6>
- Dean, S. M., Minshull, T. A., Whitmarsh, R. B., & Louden, K. E. (2000). Deep structure of the ocean-continent transition in the southern Iberia Abyssal Plain from seismic refraction profiles: The IAM-9 transect at 40°20'N. *Journal of Geophysical Research*, 105(B3), 5859–5885.
- Dietrich, W. E., Bellugi, D. G., Sklar, L. S., Stock, J. D., Heimsath, A. M., & Roering, J. J. (2003). Geomorphic transport laws for predicting landscape form and dynamics, *Prediction in geomorphology* (Vol. 135, pp. 103–132). Washington, DC: American Geophysical Union. <https://doi.org/10.1029/135GM09>
- Direen, N. G., Borissova, I., Stagg, H. M. J., Colwell, J. B., & Symonds, P. A. (2007). Nature of the continent-ocean transition zone along the southern Australian continental margin: A comparison of the Naturaliste Plateau, SW Australia, and the central Great Australian Bight sectors. *Geological Society, London, Special Publications*, 282(1), 239–263. <https://doi.org/10.1144/SP282.12>
- Direen, N. G., Stagg, H. M. J., Symonds, P. A., & Norton, I. O. (2012). Variations in rift symmetry: Cautionary examples from the Southern Rift System (Australia-Antarctica). *Geological Society, London, Special Publications*, 369(1), 453–475. <https://doi.org/10.1144/SP369.4>
- Driscoll, N. W., Hogg, J. R., Christie-Blick, N., & Karner, G. D. (1995). Extensional tectonics in the Jeanne d'Arc Basin, offshore Newfoundland: Implications for the timing of break-up between Grand Banks and Iberia. *Geological Society, London, Special Publications*, 90(1), 1–28. <https://doi.org/10.1144/GSL.SP.1995.090.01.01>
- Driscoll, N., & Karner, G. (1998). Lower crustal extension across the northern Carnarvon Basin, Australia: Evidence for an eastward dipping detachment. *Journal of Geophysical Research*, 103(B3), 4975–4991. <https://doi.org/10.1029/97JB03295>
- Ebinger, C. (1989). Tectonic development of the western branch of the East African rift system. *Geological Society of America Bulletin*, 101(7), 885–903.
- França, G. S., & Assumpção, M. (2004). Crustal structure of the Ribeira fold belt, SE Brazil, derived from receiver functions. *Journal of South American Earth Sciences*, 16(8), 743–758. <https://doi.org/10.1016/j.jsames.2003.12.002>
- Gleason, G. C., & Tullis, J. (1995). A flow law for dislocation creep of quartz aggregates determined with the molten salt cell. *Tectonophysics*, 247(1), 1–23. [https://doi.org/10.1016/0040-1951\(95\)00011-B](https://doi.org/10.1016/0040-1951(95)00011-B)
- González-Fernández, A., Dañobeitia, J. J., Delgado-Argote, L. A., Michaud, F., Córdoba, D., & Bartolomé, R. (2005). Mode of extension and rifting history of upper Tiburón and upper Delfín basins, northern Gulf of California. *Journal of Geophysical Research*, 110, B01313. <https://doi.org/10.1029/2003JB002941>
- Graf, W. H. (1984). *Hydraulics of sediment transport*. Littleton, CO: Water Resources Publication.
- Handy, M. R., & Stünitz, H. (2002). Strain localization by fracturing and reaction weakening—A mechanism for initiating exhumation of subcontinental mantle beneath rifted margins. *Geological Society, London, Special Publications*, 200(1), 387–407. <https://doi.org/10.1144/GSL.SP.2001.200.01.22>
- Hansen, L. N., Zimmerman, M. E., & Kohlstedt, D. L. (2012). Laboratory measurements of the viscous anisotropy of olivine aggregates. *Nature*, 492, 415–418. <https://doi.org/10.1038/nature11671>
- Hirth, G., & Kohlstedt, D. (2003). Rheology of the upper mantle and the mantle wedge: A view from the experimentalists. In G. Hirth & D. Kohlstedt (Eds.), *Inside the subduction factory* (pp. 83–105). Washington, DC: American Geophysical Union. <https://doi.org/10.1029/138GM06>
- Hopper, J. R., Dahl-Jensen, T., Holbrook, W. S., Larsen, H. C., Lizarralde, D., Korenaga, J., et al. (2003). Structure of the SE Greenland margin from seismic reflection and refraction data: Implications for nascent spreading center subsidence and asymmetric crustal accretion during North Atlantic opening. *Journal of Geophysical Research*, 108(B5), 2269. <https://doi.org/10.1029/2002JB001996>
- Hopper, J., Funck, T., & Tucholke, B. (2007). Structure of the Flemish Cap margin, Newfoundland: Insights into mantle and crustal processes during continental breakup. *Geological Society, London, Special Publications*, 282(1), 47–61. <https://doi.org/10.1144/SP282.3>
- Howard, A. D. (1994). A detachment-limited model of drainage basin evolution. *Water Resources Research*, 30(7), 2261–2285. <https://doi.org/10.1029/94WR00757>
- Huffman, G., Adler, R., Bolvin, D., & Gu, G. (2009). Improving the global precipitation record: GPCP version 2.1. *Geophysical Research Letters*, 36, L17808. <https://doi.org/10.1029/2009GL040000>
- Huismans, R. S., & Beaumont, C. (2003). Symmetric and asymmetric lithospheric extension: Relative effects of frictional-plastic and viscous strain softening. *Journal of Geophysical Research*, 108(B10), 2496. <https://doi.org/10.1029/2002JB002026>
- Huismans, R. S., & Beaumont, C. (2007). Roles of lithospheric strain softening and heterogeneity in determining the geometry of rifts and continental margins. *Geological Society, London, Special Publications*, 282(1), 111–138. <https://doi.org/10.1144/SP282.6>
- Huismans, R., & Beaumont, C. (2011). Depth-dependent extension, two-stage breakup and cratonic underplating at rifted margins. *Nature*, 473, 74–78. <https://doi.org/10.1038/nature09988>
- Huismans, R. S., & Beaumont, C. (2014). Rifted continental margins: The case for depth-dependent extension. *Earth and Planetary Science Letters*, 407, 148–162. <https://doi.org/10.1016/j.epsl.2014.09.032>
- Hus, R., Poort, J., Charlet, F., Naudts, L., Khlystov, O., Klerkx, J., & De Batist, M. (2012). *Regional geology and tectonics: Phanerozoic rift systems and sedimentary basins*, Lake Baikal (pp. 258–273). B.V: Elsevier. <https://doi.org/10.1016/B978-0-444-56356-9.00010-9>
- Hutchinson, D., Golmshtok, A., Zonenhain, L., Moore, T., Scholz, C., & Klitgord, K. (1992). Depositional and tectonic framework of the rift basins of Lake Baikal from multichannel seismic data. *Geology*, 20(7), 589–592. [https://doi.org/10.1130/0091-7613\(1992\)020<0589:DATFOT>2.3.CO;2](https://doi.org/10.1130/0091-7613(1992)020<0589:DATFOT>2.3.CO;2)
- Karato, S. I., & Wu, P. (1993). Rheology of the upper mantle: A synthesis. *Science*, 260(5109), 771–778.

- Karner, G. D., Driscoll, N. W., & Barker, D. H. N. (2003). Syn-rift regional subsidence across the West African continental margin: The role of lower plate ductile extension. *Petroleum geology of Africa: New themes and developing technologies* (Vol. 207, pp. 105–129). Geological Society of London. <https://doi.org/10.1144/GSL.SP.2003.207.6>
- Kaufman, P., Grotzinger, J. P., & McCormick, D. S. (1991). Depth-dependent diffusion algorithm for simulation of sedimentation in shallow marine depositional systems. *Bulletin - Kansas Geological Survey*, 233, 489–508.
- Kaus, B. J. P. (2010). Factors that control the angle of shear bands in geodynamic numerical models of brittle deformation. *Tectonophysics*, 484(1), 36–47. <https://doi.org/10.1016/j.tecto.2009.08.042>
- Kaus, B. J. P., Mühlhaus, H., & May, D. A. (2010). A stabilization algorithm for geodynamic numerical simulations with a free surface. *Physics of the Earth and Planetary Interiors*, 181(1), 12–20. <https://doi.org/10.1016/j.pepi.2010.04.007>
- Kirkby, M. J. (1971). Hillslope process-response models based on the continuity equation. *Special Publication Institute of British Geographers*, 3(1), 15–30.
- Kirkby, M. J., & Carson, M. A. (1972). *Hillslope form and process*. Cambridge: Cambridge University Press.
- Lavier, L. L., & Manatschal, G. (2006). A mechanism to thin the continental lithosphere at magma-poor margins. *Nature*, 440, 324–328. <https://doi.org/10.1038/nature04608>
- Lizarralde, D., Axen, G., Brown, H., Fletcher, J., González-Fernández, A., Harding, A., et al. (2007). Variation in styles of rifting in the Gulf of California. *Nature*, 448, 466–469. <https://doi.org/10.1038/nature06035>
- Marr, J., Swenson, J., Paola, C., & Voller, V. (2000). A two-diffusion model of fluvial stratigraphy in closed depositional basins. *Basin Research*, 12(3-4), 381–398. <https://doi.org/10.1111/j.1365-2117.2000.00134.x>
- Martin-Barajas, A., González-Escobar, M., Fletcher, J., Pacheco, M., Oskin, M., & Dorsey, R. (2013). Thick deltaic sedimentation and detachment faulting delay the onset of continental rupture in the Northern Gulf of California: Analysis of seismic reflection profiles. *Tectonics*, 32, 1294–1311. <https://doi.org/10.1002/tect.20063>
- McClay, K. R. (1977). Pressure solution and Coble creep in rocks and minerals: A review. *Journal of the Geological Society*, 134(1), 57–70. <https://doi.org/10.1144/gsgs.134.1.0057>
- Moresi, L., Dufour, F., & Mühlhaus, H. B. (2003). A Lagrangian integration point finite element method for large deformation modeling of viscoelastic geomaterials. *Journal of Computational Physics*, 184(2), 476–497. [https://doi.org/10.1016/S0021-9991\(02\)00031-1](https://doi.org/10.1016/S0021-9991(02)00031-1)
- Morgan, J. P. (1997). The generation of a compositional lithosphere by mid-ocean ridge melting and its effect on subsequent off-axis hotspot upwelling and melting. *Earth and Planetary Science Letters*, 146(1), 213–232. [https://doi.org/10.1016/S0012-821X\(96\)00207-5](https://doi.org/10.1016/S0012-821X(96)00207-5)
- Morgan, J. P., Morgan, J. W., & Price, E. (1995). Hotspot melting generates both hotspot volcanism and a hotspot swell? *Journal of Geophysical Research*, 100(B5), 8045–8062. <https://doi.org/10.1029/94JB02887>
- Morley, C. K. (1988). Variable extension in Lake Tanganyika. *Tectonics*, 7(4), 785–801. <https://doi.org/10.1029/TC007i004p00785>
- Morley, C. K., & Westaway, R. (2006). Subsidence in the super-deep Pattani and Malay basins of Southeast Asia: A coupled model incorporating lower-crustal flow in response to post-rift sediment loading. *Basin Research*, 18(1), 51–84. <https://doi.org/10.1111/j.1365-2117.2006.00285.x>
- Nielsen, T. K., & Hopper, J. R. (2004). From rift to drift: Mantle melting during continental breakup. *Geochemistry, Geophysics, Geosystems*, 5, Q07003. <https://doi.org/10.1029/2003GC000662>
- Olive, J., Behn, M., & Malatesta, L. (2014). Modes of extensional faulting controlled by surface processes. *Geophysical Research Letters*, 41, 6725–6733. <https://doi.org/10.1002/2014GL061507>
- Paola, C., Heller, P. L., & Angevine, C. L. (1992). The large-scale dynamics of grain-size variation in alluvial basins, 1: Theory. *Basin Research*, 4(2), 73–90.
- Parmentier, E. M., & Morgan, J. P. (1990). Spreading rate dependence of three-dimensional structure in oceanic spreading centres. *Nature*, 348, 325–328. <https://doi.org/10.1038/348325a0>
- Pérez-Gussinyé, M. (2013). A tectonic model for hyperextension at magma-poor rifted margins: An example from the West Iberia–Newfoundland conjugate margins. *Geological Society, London, Special Publications*, 369(1), 403–427. <https://doi.org/10.1144/SP369.19>
- Pérez-Gussinyé, M., Ranero, C. R., Reston, T. J., & Sawyer, D. (2003). Mechanisms of extension at nonvolcanic margins: Evidence from the Galicia interior basin, west of Iberia. *Journal of Geophysical Research*, 108(B5), 2245. <https://doi.org/10.1029/2001JB000901>
- Pérez-Gussinyé, M., Reston, T. J., & Phipps Morgan, J. (2001). Serpentization and magmatism during extension at non-volcanic margins: The effect of initial lithospheric structure. *Geological Society, London, Special Publications*, 187(1), 551–576. <https://doi.org/10.1144/GSL.SP.2001.187.01.27>
- Péron-Pinvidic, G., Manatschal, G., Masini, E., Sutra, E., Flament, J., Haupert, I., & Unternehr, P. (2015). Unravelling the along-strike variability of the Angola-Gabon rifted margin: A mapping approach. *Geological Society, London, Special Publications*, 438(1), SP438.1. <https://doi.org/10.1144/SP438.1>
- Petit, C., Fournier, M., & Gunnell, Y. (2007). Tectonic and climatic controls on rift escarpments: Erosion and flexural rebound of the Dhofar passive margin (Gulf of Aden, Oman). *Journal of Geophysical Research*, 112, B03406. <https://doi.org/10.1029/2006JB004554>
- Précigout, J., & Gueydan, F. (2009). Mantle weakening and strain localization: Implications for the long-term strength of the continental lithosphere. *Geology*, 37(2), 147–150. <https://doi.org/10.1130/G25239A.1>
- Ranero, C. R., & Pérez-Gussinyé, M. (2010). Sequential faulting explains the asymmetry and extension discrepancy of conjugate margins. *Nature*, 468(7321), 294–299. <https://doi.org/10.1038/nature09520>
- Redfield, T. F., & Osmundsen, P. T. (2013). The long-term topographic response of a continent adjacent to a hyperextended margin: A case study from Scandinavia. *Geological Society of America Bulletin*, 125(1-2), 184–200. <https://doi.org/10.1130/B30691.1>
- Ros, E., Pérez-Gussinyé, M., Araújo, M., Romeiro, M., Andrés-Martínez, M., & Morgan, J. (2017). Lower crustal strength controls on melting and serpentization at magma-poor margins: Potential implications for the South Atlantic. *Geochim Geophys Geosystems*, 18(12), 4538–4557. <https://doi.org/10.1002/2017GC007212>
- Rowan, M. (2018). The South Atlantic and Gulf of Mexico salt basins: Crustal thinning, subsidence and accommodation for salt and presalt strata. *Geological Society, London, Special Publications*, 476, SP476.6. <https://doi.org/10.1144/SP476.6>
- Rutter, E., & Elliott, D. (1976). The kinetics of rock deformation by pressure solution. *Philosophical Transactions of the Royal Society of London A: Mathematical, Physical and Engineering Sciences*, 283(1312), 203–219.
- Rybäck, E., & Dresen, G. (2000). Dislocation and diffusion creep of synthetic anorthite aggregates. *Journal of Geophysical Research*, 105(B11), 26,017–26,036. <https://doi.org/10.1029/2000JB900223>
- Schutt, D., & Lesher, C. (2006). Effects of melt depletion on the density and seismic velocity of garnet and spinel lherzolite. *Journal of Geophysical Research*, 111, B05401. <https://doi.org/10.1029/2003JB002950>
- Sharples, W., Moresi, L.-N., Jadamec, M., & Revote, J. (2015). Styles of rifting and fault spacing in numerical models of crustal extension. *Journal of Geophysical Research: Solid Earth*, 120, 4379–4404. <https://doi.org/10.1002/2014JB011813>

- Shewchuk, J. R. (2002). Delaunay refinement algorithms for triangular mesh generation. *Computational Geometry*, 22(1–3), 21–74. [https://doi.org/10.1016/S0925-7721\(01\)00047-5](https://doi.org/10.1016/S0925-7721(01)00047-5)
- Simpson, G., & Schlunegger, F. (2003). Topographic evolution and morphology of surfaces evolving in response to coupled fluvial and hillslope sediment transport. *Journal of Geophysical Research*, 108(B6), 2300. <https://doi.org/10.1029/2002JB002162>
- Smith, T. R., & Bretherton, F. P. (1972). Stability and the conservation of mass in drainage basin evolution. *Water Resources Research*, 8(6), 1506–1529. <https://doi.org/10.1029/WR008i006p01506>
- Stagg, H., Willcox, J., Needham, D., O'Brien, G., Cockshell, C., Hill, A., et al. (1990). Basins of the Great Australian Bight region—geology and petroleum potential: Continental margins. *Bureau of Mineral Resources, Geology and Geophysics and Department of Mines and Energy, South Australia*. Australian Government Publishing Service.
- Svartman Dias, A., Lavier, L., & Hayman, N. (2015). Conjugate rifted margins width and asymmetry: The interplay between lithospheric strength and thermomechanical processes. *Journal of Geophysical Research: Solid Earth*, 120, 8672–8700. <https://doi.org/10.1002/2015JB012074>
- Talwani, M., Mutter, J., Houtz, R., & Konig, M. (1979). The crustal structure and evolution of the area underlying the magnetic quiet zone on the margin south of Australia: Rifted margins. In *Geological and geophysical investigations of continental margins* (pp. 151–175). AAPG Special Volumes.
- Theissen, S., & Rüpke, L. (2010). Feedbacks of sedimentation on crustal heat flow: New insights from the Voring Basin, Norwegian Sea. *Basin Research*, 22(6), 976–990. <https://doi.org/10.1111/j.1365-2117.2009.00437.x>
- Totterdell, J., Blevin, J., Struckmeyer, H., Bradshaw, B., Colwell, J., & Kennard, J. (2000). A new sequence framework for the Great Australian Bight: Starting with a clean slate. *APPEA Journal-Australian Petroleum Production and Exploration Association*, 40(1), 95–120. <https://doi.org/10.1071/AJ99007>
- Totterdell, J., Bradshaw, B., & Willcox, J. (2003). Structural and tectonic setting of the Great Australian Bight. In G. W. O'Brien, E. Paraschivou, & J. E. Hibbert (Eds.), *Petroleum geology of South Australia* (Vol. 5, pp. 1–57). South Australia: Primary Ind. and Resour.
- Turcotte, D., & Schubert, G. (2002). *Geodynamics*. Cambridge: Cambridge University Press.
- Weissel, J. K., & Karner, G. D. (1989). Flexural uplift of rift flanks due to mechanical unloading of the lithosphere during extension. *Journal of Geophysical Research*, 94(B10), 13,919–13,950. <https://doi.org/10.1029/JB094iB10p13919>
- Wilks, K., & Carter, N. (1990). Rheology of some continental lower crustal rocks. *Tectonophysics*, 182(1–2), 57–77.
- Zwaan, F., Schreurs, G., & Adam, J. (2018). Effects of sedimentation on rift segment evolution and rift interaction in orthogonal and oblique extensional settings: Insights from analogue models analysed with 4D X-ray computed tomography and digital volume correlation techniques. *Global and Planetary Change*, 171, 110–133. <https://doi.org/10.1016/j.gloplacha.2017.11.002>

Geophysical Research Letters

RESEARCH LETTER

10.1029/2019GL081955

Key Points:

- We combine a new history of Icelandic ice cover with a forward model of magma generation
- Peak mantle CO₂ flux is nonlinearly related to magmatic eruption rates
- Icelandic CO₂ degassing likely peaked first at 60 ka and second with three pulses between 20 and 10 ka

Supporting Information:

- Supporting Information S1
- Table S1
- Figure S1
- Figure S2
- Figure S3
- Figure S4
- Data Set S1

Correspondence to:

J. J. Armitage,
armitage@ipgp.fr

Citation:

Armitage, J. J., Ferguson, D., Petersen, K. D., & Creyts, T. T. (2019). The importance of Icelandic ice sheet growth and retreat on mantle CO₂ flux. *Geophysical Research Letters*, 46, 6451–6458. <https://doi.org/10.1029/2019GL081955>

Received 8 JAN 2019

Accepted 20 MAY 2019

Accepted article online 28 MAY 2019

Published online 24 JUN 2019

The Importance of Icelandic Ice Sheet Growth and Retreat on Mantle CO₂ Flux

John J. Armitage¹, David J. Ferguson², Kenni D. Petersen³, and Timothy T. Creyts⁴

¹Dynamique des Fluides Géologiques, Institut de Physique du Globe de Paris, Paris, France, ²School of Earth and Environment, University of Leeds, Leeds, UK, ³Department of Geoscience, University of Aarhus, Aarhus, Denmark,

⁴Lamont-Doherty Earth Observatory, Columbia University, New York, NY, USA

Abstract Climate cycles may significantly affect the eruptive behavior of terrestrial volcanoes due to pressure changes caused by glacial loading, which raises the possibility that climate change may modulate CO₂ degassing via volcanism. In Iceland, magmatism is likely to have been influenced by glacial activity. To explore if deglaciation therefore impacted CO₂ flux, we coupled a model of glacial loading over the last ~120 ka to melt generation and transport. We find that a nuanced relationship exists between magmatism and glacial activity. Enhanced CO₂ degassing happened prior to the main phase of late-Pleistocene deglaciation, and it is sensitive to the duration of the growth of the ice sheet entering into the Last Glacial Maximum (LGM), as well as the rate of ice loss. Ice sheet growth depresses melting in the upper mantle, creating a delayed pulse of CO₂ out-gassing, as the magmatic system recovers from the effects of loading.

1. Introduction

Evidence from several tectonic settings indicates that glaciated volcanic systems respond to changing ice volumes (Glazner et al., 1999; Jellinek et al., 2004; Jull & McKenzie, 1996; MacLennan et al., 2002; Rawson et al., 2016; Sigvaldsson et al., 1992) and suggests there was a widespread volcanic response to late-Pleistocene ice retreat (Huybers & Langmuir, 2009). The most compelling evidence for climate-coupled volcanism comes from Iceland, where changes in early Holocene lava volumes and magma chemistry are consistent with depressurization during glacial unloading (Jull & McKenzie, 1996; MacLennan et al., 2002; Sinton et al., 2005). Magma generation here occurs due to pressure-release melting, as the mantle upwells beneath rift zones. Although the net change in overburden pressures from variations in ice cover have been relatively small, the high rates of change associated with glacial activity can produce significant short-term fluctuations in magmatic output (Jull & McKenzie, 1996; Pagli & Sigmundsson, 2008; Schmidt et al., 2013). Carbon readily partitions into magmas during partial melting (Rosenthal et al., 2015) and is released as a CO₂-rich fluid/vapor as the magma ascends through the crust, making volcanism the primary pathway for transporting carbon from the Earth's mantle to the atmosphere (Dasgupta & Hirschmann, 2010). However, carbon does not enter the melt uniformly during partial melting and is concentrated in early formed magma. Therefore, the extent to which glacially driven changes in primary magma generation alter the flux of CO₂ depends on where in the melting column melt production is enhanced (or suppressed), the rate of melt transport, and the history of ice sheet growth and retreat.

It is thought that CO₂ and the trace element Nb have a relatively similar behavior during decompression melting (Saal et al., 2002), and as such Nb compositions can be used to gauge the quantity of CO₂ erupted. In Iceland there are just over 300 published dated analyses of the Nb composition of Pleistocene lavas (Eason et al., 2015; Gee et al., 1998). This is arguably the most complete geochemical record of Nb compositions within a region that experienced significant Pleistocene deglaciation. In this study we take a new approach and use a high-resolution model of ice sheet history to drive a forward model of melt generation and transport and predict CO₂ degassing. We validate the model predictions against the seismic structure imaged below Iceland, and the observed crustal thickness. We subsequently explore under what conditions climate and magmatism might be related, and the implications for CO₂ degassing.

2. Methods

2.1. Modeling of Melt Generation and Transport

We develop a model of magma generation and transport coupled to a model of the flexure of a viscoelastic beam for the response to change in load due to the ice sheet history (see the supporting information). The

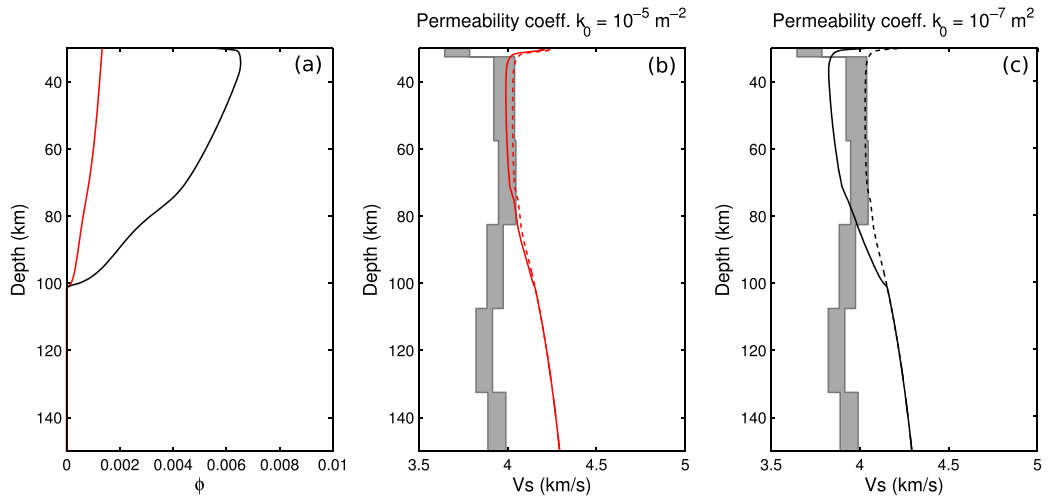


Figure 1. Profiles of porosity and S wave seismic velocity for the two model permeabilities of $k_0 = 10^{-7} \text{ m}^2$ black line and $k_0 = 10^{-5} \text{ m}^2$ red line. (a) Porosity plotted against depth at steady state. (b) S wave velocity from the joint inversion of teleseismic and ambient noise Rayleigh waves (Harmon & Rychert, 2016) and the predicted S wave profile from the high permeability case. The model includes the addition of the adiabatic gradient, the anharmonic effects from the mineralogy, and effects of attenuation (Goes et al., 2012). The dashed line assumes melt has no effect; the solid line includes a 7.9 % reduction in V_S per percent melt (Hammond & Humphreys, 2000). (c) S wave velocity predictions for the low-permeability case.

coupled model consists of a flexural model of the surface displacement due to the changing surface load as the ice sheet changes in thickness. This model of surface displacement is then coupled to either a 1-D vertical column or a 2-D corner flow model where the flow of the mantle is prescribed at either an upwelling rate of 10 or 20 mm/year or lateral spreading rate of 10 mm/year. We use these two upwelling rates to cover the uncertainty in the exact rate of vertical ascent the mantle below Iceland due to mantle buoyancy. The upwelling column is perturbed by the displacement due to loading, where the viscoelastic decay time of the load is set to 1,000 years. The upper surface of the melting model is held at 30 km to be consistent with the Moho depth, which is in the range of 20 to 40 km below Iceland (Jenkins et al., 2018). Carbon partitioning into the melt is assumed to be governed by the coefficients derived by Rosenthal et al. (2015). We use a mantle source composition for Nb of 1.627 ppm, which is intermediate between the end-member sources for Icelandic melts identified by Shorttle and MacLennan (2011). To approximate the melting of the multiple source lithologies, we chose a solidus-depletion gradient of 600 °C, which is intermediate between that of melting experiments on depleted mantle, 900 °C (Wasylenki et al., 2003) and fertile mantle 300 °C (Scott, 1992).

To constrain permeability, we examined the effects of varying the permeability coefficient on the seismic properties of the mantle produced by our 1-D model. The thermal structure and porosity was converted to S wave velocities, assuming that melt reduces the velocity by 7.9% per percent porosity (Hammond & Humphreys, 2000) and including the effects of attenuation (Goes et al., 2012). Recent joint inversion of teleseismic and ambient noise Rayleigh waves in Iceland would suggest that the S wave velocity is between 4 and 3.8 km/s at depths of 50 to 150 km (Harmon & Rychert, 2016; Figure 1). We find that the permeability coefficient, k_0 , needs to be relatively high (10^{-5} m^2) giving a permeability, $k_\phi = k_0 \phi^3$ (where ϕ is porosity), of the order of 10^{-14} m^2 ($\phi \approx 0.001$; Figure 1), because otherwise porosity would be too large and the S wave velocity would decrease below the observed values. This permeability is an order of magnitude higher than the upper range used to explore how sea level change might influence mid-ocean ridge magmatism (Burley & Katz, 2015; Crowley et al., 2015) and suggests rates of magmatic ascent of the order of 10 m/year, in agreement with MacLennan et al. (2002). Previously, it has been suggested that delays in signal propagation from the zone of partial melting at mid-ocean ridges to the surface might be of the order of a Milankovitch-scale period, 40 kyr (Huybers & Langmuir, 2017). However, the high permeability required to match the seismic observations from Iceland implies a magmatic system that much more rapidly responds to change in melting conditions, consistent with the fast transport rates estimated from U-series isotope studies (Elliot & Spiegelman, 2014).

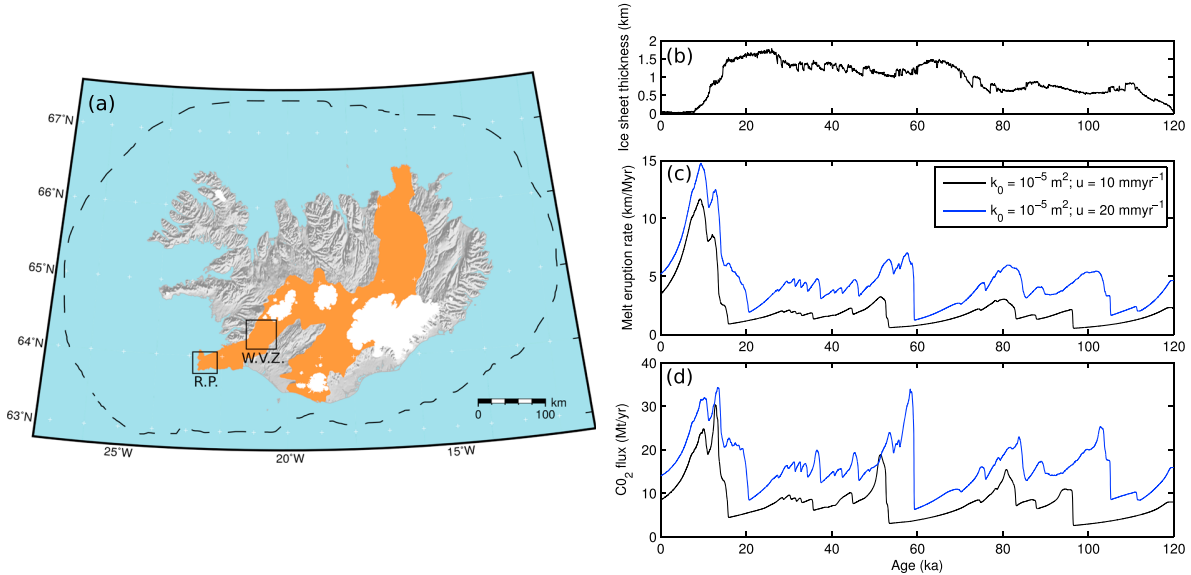


Figure 2. Response of the model to periodic and observed ice sheet thickness changes of the last 120 ka. (a) Map of Iceland showing the locations of the volcanic rift zones in orange and the maximum extent of the ice sheet at the last glacial maximum (dashed line). The boxes show the location of the Reykjanes Peninsular (R. P.) and the Western Volcanic Zone (W. V. Z.). (b) The ice sheet thickness predicted from the ice sheet model M1 over the last 120 ka. (c) Melt eruption rate and (d) carbon flux response to the step change in ice sheet thickness: black line, an upper mantle permeability coefficient of $k_0 = 10^{-5} \text{ m}^2$ and upwelling velocity of 10 mm/year, and blue line, an upwelling velocity of 20 mm/year.

2.2. Glacial Forcing Throughout the Pleistocene

Iceland experienced extensive ice cover during the last glacial period (Patton et al., 2017), with maximum thicknesses in the center of the island of ~ 2 km attained by ~23 ka (Figures 2a and 2b). Deglaciation after the LGM occurred at a varying rate and was discontinuous. For example, a stage of readvance occurred during the colder climate of the Younger Dryas (11.7–12.9 ka; Nordahl & Ingólfsson, 2015). The final phase of deglaciation was particularly rapid, with the main volcanic zones being largely ice free by ~10 ka (Figure 2a). The most uncertain period of the glacial history is the pre-LGM growth of the ice sheet. To create the ice sheet histories shown in Figures 2b and 3a, we calibrated the ice volume since the LGM against the North Greenland Ice Core Project $\delta^{18}\text{O}$ record, and Quaternary sea level curves assuming a linear correlation between these three signals (see Text S1). We focus on two scenarios: M1, based on the ICE-5G sea level curves (Peltier, 2004), and M2, based on the sea level curves of (Pico et al., 2017; Figure S2).

3. Results

3.1. Effect of Glacial Loading and Unloading

We force our melt model with the 120-ka glacial history after a 5-Myr model windup to steady state (model M1; Figure 2b) and using a single value for the ice thickness at each time step, therefore neglecting the effects of the distal parts of the ice sheet on melting beneath the rift margins. The impact of deglaciation events is modulated by the upwelling rate of the solid mantle because the upwelling rate controls the background productivity of the melting model. At slower upwelling rates, that is, 10 mm/year, some periods of deglaciation are not recorded in the flux of magma erupted. An example of this is the warming event at 60 ka (Figure 2), where the 10 mm/year upwelling model produces no response in either the eruption rate or CO_2 flux. If however upwelling is more rapid, 20 mm/year, then there is a clear pulse in melt eruption rate (Figure 2). For a more productive scenario, there is increased shallow melting. The displacement imposed by the flexural response to unloading dissipates with depth. Therefore, if melting is productive and hence shallow it will feel the effects of the unloading to a greater extent when compared to a less productive melting system. Furthermore, when productivity is low, the porosity is low, and the rate of vertical melt flow is slow such that a pulse in melt production will not reach the surface rapidly.

The magnitude of CO_2 flux peaks is not linearly related to the magnitude in eruption rates (Figure 2d). For example, in the 20 mm/year upwelling rate model, the largest CO_2 peak is estimated to occur at ~60 ka and not during the volumetrically larger magmatic pulse at the end of the Pleistocene (Figure 2d). This difference

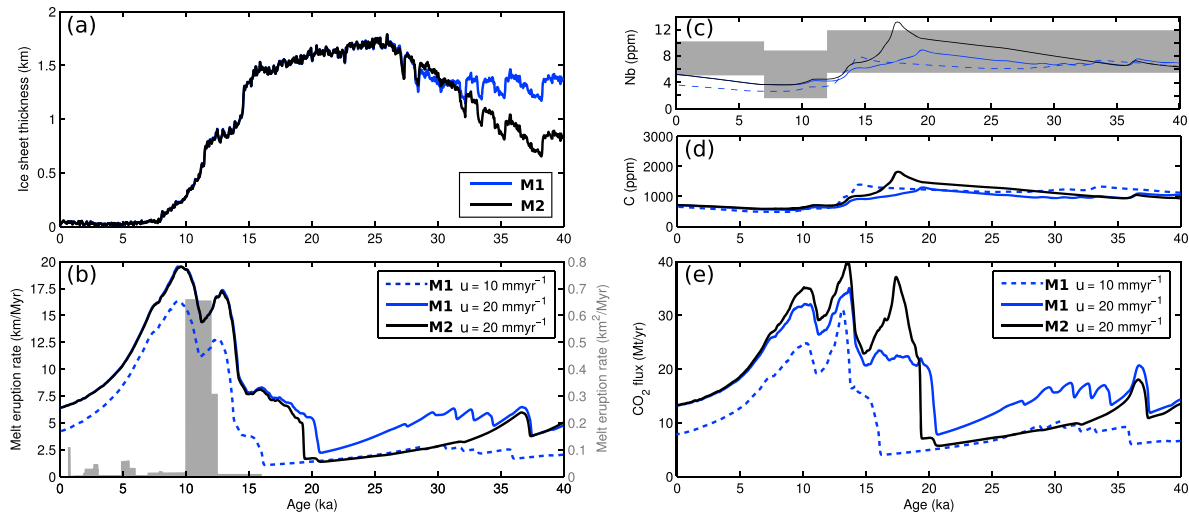


Figure 3. Impact of ice sheet growth and decay on melt eruption and composition over the last 40 ka. (a) Ice sheet models M1 and M2 taken from the sea level models of Peltier (2004) and Pico et al. (2017), respectively. (b) Melt eruption rates (in kilometers of melt per million years): blue solid line, ice sheet history M1 for $k_0 = 10^{-5} \text{ m}^2$ with an upwelling rate of 20 mm/year; blue dashed line, M1 for $k_0 = 10^{-5} \text{ m}^2$ with an upwelling rate of 10 mm/year; black solid line, ice sheet history M2 for $k_0 = 10^{-5} \text{ m}^2$ with an upwelling rate of 20 mm/year. The gray region shows estimated eruption rates from geological observations (MacLennan et al., 2002) (in square kilometer of melt per million years). (c) Observed and predicted Nb concentrations (parts per million), observations are from the Reykjanes Peninsula and the Western Volcanic Zone (Eason et al., 2015; Gee et al., 1998; Sinton et al., 2005), which are binned into three major periods: glacial (>12 ka), early postglacial (between 12 and 7 ka) and recent (<7 ka). (d) Predicted variation of in the concentration of carbon (parts per million) within the erupted melt. (e) Predicted variation in the flux of CO_2 , assuming that the flux of CO_2 that Icelandic volcanism covers an area of 30,000 km^2 , and CO_2 (parts per million) = 3.67 C (parts per million; see equation (23) in the supporting information).

is because when the ~60-ka warming occurred, the melt was enriched in carbon due to the preceding rapid glaciation. Magma supplied from the mantle during the Late-Pleistocene pulse was more depleted in carbon compared to those in the 60-ka event. The implication of this result is that volumetrically small volcanic events might have just as a strong influence on CO_2 degassing as the more significant periods of volcanic eruptions and the magnitude of CO_2 degassing is dependent on the history of glacial forcing.

3.2. Glacial Forcing Through the Latest Pleistocene and Holocene

During the last 40 ka, our model suggests that CO_2 flux is highly dependent on the glacial forcing. There are two distinct late-Pleistocene magmatic pulses, separated by the Younger Dryas cold period (Figures 3a and 3b). However, for the model M2 ice sheet history there are three pulses in CO_2 flux at the end of the Pleistocene, due to the faster ice sheet growth entering the LGM from 35 to 25 ka in this model (Figures 3a and 3e). This peak in CO_2 flux is because the small magnitude but rapid deglaciations after 25-ka tap melts rich in trace elements including Nb and carbon (Figures 3c and 3d).

The observed time series of incompatible trace element concentrations in Icelandic magmas and ice sheet history have been suggested to be strongly associated (Eason et al., 2015; Gee et al., 1998; Jull & McKenzie, 1996; MacLennan et al., 2002; Sinton et al., 2005). Of these studies Gee et al. (1998) and Eason et al. (2015) report on the Nb composition of lavas erupted and give age ranges for the erupted lavas. Dating lava flow in Iceland is complex, given the lack of reliable markers from which ages can be obtained. This means that ages are instead typically taken from the morphology and tephrochronology of erupted flows (MacLennan et al., 2002). Following the work of MacLennan et al. (2002), we bin the reported Nb compositions into three major periods: glacial (>12 ka), early postglacial (between 12 and 7 ka), and recent (<7 ka). The reduction in Nb compositions plotted is in line with the trends observed within the smaller sample size of La and Sm compositions presented in MacLennan et al. (2002) and is therefore likely robust.

We find that the predicted change in Nb from all our models fits within the range of the observations (Figure 3c). The M2 model gives the strongest signature in Nb concentrations of deglaciation during the end of the Pleistocene, while the signature is more subdued in the M1 ice sheet model (Figure 3c). The 1-D forward model used is highly idealized, and yet the agreement between the observations and model is encouraging and suggests the compositional change observed in lavas erupted during the late-Pleistocene to early Holocene is due to rapid deglaciation (Eason et al., 2015; Gee et al., 1998; MacLennan et al., 2002;

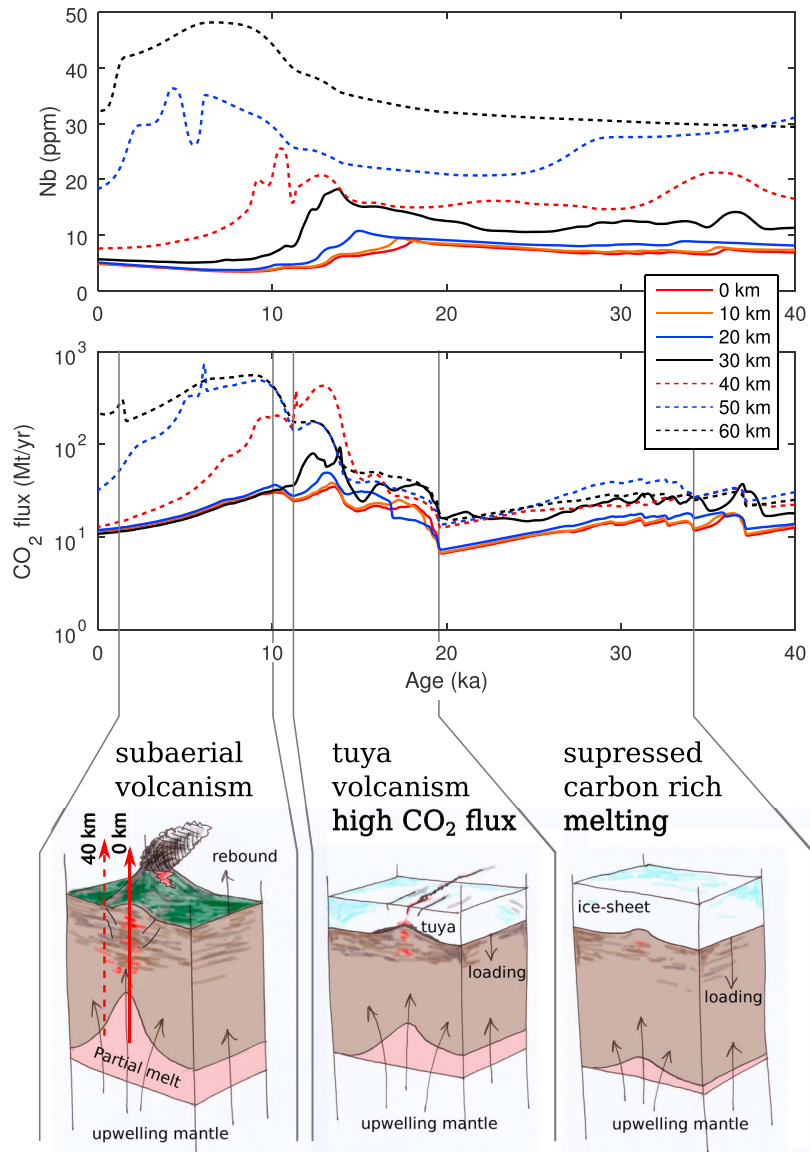


Figure 4. Impact of glacial history on off-axis and on-axis melting. A series of 1-D column melting models forced by the response to deglaciation (ice sheet history model M1) where the mantle flow is of steady state corner flow. (a) Nb concentrations from the center of extension out to 60 km from the center of extension. The mean concentration weighted by the eruption rate is plotted as the thick black line. (b) Predicted CO_2 flux from the series of vertical melting models. The late-Pleistocene eruptions are typified by tuya magmatism. This will have been the case up until at least ~ 14 ka, where either magmatism was suppressed or when eruptions occurred, they will have been beneath at least 1 km of ice cover (Hartley et al., 2016). The suppressed melting regime will have become carbon rich because the shallow low-C melt production is damped due to the ice sheet loading. Upon deglaciation there is increased volcanism, which initially taps the melt rich carbon.

Sinton et al., 2005). This implies that the observed change in melt composition is due to change in ice sheet loading and that the predeglaciation volcanism likely released a significant volume of CO_2 (Figure 3e).

The 1-D column model will underestimate the impact of change in deep melt productivity, as it cannot capture the deep wings of the zone of partial melting. To explore the impact of this, we force a series of 1-D models with the vertical flow taken from steady state corner flow perturbed by the flexural response of the deglaciation of a 200-km-wide ice sheet. The half spreading rate is assumed to be 10 mm/year, and the mantle potential temperature is $1,450^\circ\text{C}$. Melt travels vertically from the zone of partial melting in columns

at 0 to 80 km from the rift axis (Figure 4). The steady state thickness of melt erupted at the surface of the simplified 2-D model is 20 km (Figure S4), and glacial forcing causes this thickness to vary around this value by the order of 10 km except for a large spike at the LGM. The crust of Iceland varies in thickness from 20 to 40 km (e.g., Jenkins et al., 2018), and therefore, a model steady state thickness of 20 km is a reasonable lower end-member prediction given that the crust is made of both extrusions and intrusions.

After glacial perturbation we find that in the central zone, from the ridge center to 40-km distance, the trend in Nb and CO₂ flux is relatively similar, with a reduction in Nb at 15 ka. At distances greater than 40 km, a peak in Nb and CO₂ flux is predicted to occur with an increasing delay compared to the center of extension (Figure 4). This delay is due to the greater distance that the melt has to travel along the vertical path from the top of the melt zone to the surface at increasing distance from the center of extension. In full 2-D models the distal melt will pool as it migrates laterally toward the center of extension (Katz, 2008), yet the difference in ascent velocity due to the increase porosity as the melt pools would likely not be sufficient to overcome the increased distance that the signal will have to travel.

The full solution to the coupled equations of magma dynamics would suggest that melts generated at a distance of up to 60 km from the center of extension are advected to the ridge axis (Katz, 2008). If all of the melt generated up to 60 km from the center of extension is erupted, then the CO₂ flux is significantly increased during the Holocene due to the addition input of melt from the distal parts of the zone of partial melting (Figure 4b). Therefore, these low productivity and deep regions of the zone of partial melting might be a key exporter of mantle carbon into the atmosphere. However, the range of observed Nb concentrations is relatively similar to the axial concentrations, from within <40 km of the rift center (Figure 4). This would suggest that the widest regions of the zone of partial melting are not sampled by the volcanism in the Reykjanes Ridge and Western Volcanic Zone, leading to an estimate of CO₂ fluxes more in line with the simpler 1-D model.

4. Discussion and Conclusions

The models imply that the deglaciation beginning at 18 ka and continuing through the Bölling warming at 14.8 ka released substantial quantities of CO₂ when compared to the last 120 ka (Figures 3c and 4b), and this elevated CO₂ release was because of the preceding growth of the ice sheet. Volcanism during this time would have taken place in a subglacial environment and unsurprisingly does not feature in the postglacial subaerial record. Evidence from subglacial volcanic units (tuyas) erupted during this time period (Hartley et al., 2016) suggests volumetric and compositional trends consistent with those predicted by our model (Figures 3c and 4).

Forcing our model with the long-term 120-ka ice sheet history produces a periodic fluxing of CO₂ from Icelandic volcanoes due to ice loss events over this period, implying a close link between ice dynamics and magmatic out-gassing. The greatest release of CO₂, however, occurred during the period of ice loss just before the Younger Dryas (~14 ka), and therefore before the largest phase of late-Pleistocene deglaciation (Figure 4). The concentration of CO₂ released in this magmatic pulse was enhanced due to the lack of any significant loss of ice volume since ~40 ka. This created a magmatic system capable of fluxing large volumes of carbon during the initial period of post-LGM deglaciation (both models M1 and M2; Figure 3e), possibly contributing to the increased atmospheric CO₂ levels thought to be recorded between 15 and 14 ka in the EPICA Dome C ice core (Köhler et al., 2011). It is therefore possible that this pulse of magmatic CO₂, from Iceland and elsewhere (e.g., Huybers & Langmuir, 2009), bolstered the climate warming, and final phase of deglaciation that proceeded the Younger Dryas.

The CO₂ flux due to deglaciation is strongly influenced by the ice sheet history. Mantle CO₂ flux does not follow a linear relationship with eruption rates: large peaks in CO₂ are also predicted for periods in time when the volume flux is not very high (Figures 2d and 3e). In effect we cannot conclude that all deglaciation events, or other rapid unloading events due to, for example, erosion (e.g., Sternai et al., 2016), lead to a large flux of volatile gasses into the Earth's atmosphere.

Supporting Information

A detailed discussion of the methodology can be found in the supporting information.

Acknowledgments

We would like to thank M. A. Mary Gee (The University of Western Australia) for sharing her Nb composition data from the Reykjanes Peninsula and Tamara Pico (Harvard University) for sharing her sea level curves. John J. Armitage acknowledges funding from an Agence Nationale de la Recherche (France), Accueil de Chercheurs de Haute Niveau, grant InterRift. Numerical computations were partly performed on the S-CAPAD platform, IPGP, France. The 1-D melting model is available from <https://bitbucket.com/johnjarmitage/melt1d-icesheet/>.

References

- Burley, J. M. A., & Katz, R. F. (2015). Variations in mid-ocean ridge CO₂ emissions driven by glacial cycles. *Earth and Planetary Science Letters*, 426, 246–258. <https://doi.org/10.1016/j.epsl.2015.06.031>
- Crowley, J. W., Katz, R. F., Huybers, P., Langmuir, C. H., & Park, S. H. (2015). Glacial cycles drive variations in the production of oceanic crust. *Science*, 347, 1237–1240. <https://doi.org/10.1126/science.1261508>
- Dasgupta, R., & Hirschmann, M. M. (2010). The deep carbon cycle and melting in Earth's interior. *Earth and Planetary Science Letters*, 298, 1–13. <https://doi.org/10.1016/j.epsl.2010.06.039>
- Eason, D. E., Sinton, J. M., Gronvöld, K., & Kurz, M. D. (2015). Effects of deglaciation on the petrology and eruptive history of the Western Volcanic Zone, Iceland. *Bulletin of Volcanology*, 77(47). <https://doi.org/10.1007/s00445-015-0916-0>
- Elliot, T., & Spiegelman, M. (2014). Melt migration in oceanic crustal production: A u-series perspective. In *Treatise on Geochemistry (Second Edition) volume 4* (2nd ed., pp. 543–581). Amsterdam: Elsevier. <https://doi.org/10.1016/B978-0-08-095975-7.00317-X>
- Gee, M. A. M., Taylor, R. N., Thirwall, M., & Murton, B. J. (1998). Glaciostacy controls chemical and isotopic characteristics of tholeiites from the Reykjanes Peninsula, SW Iceland. *Earth and Planetary Science Letters*, 164, 1–5.
- Glazner, A. F., Manley, C. R., Marron, J. S., & Rojstaczer, S. (1999). Fire or ice: Anticorrelation of volcanism and glaciation in California over the past 800,000 years. *Geophysical Research Letters*, 26, 1759–1762. <https://doi.org/10.1029/1999GL900333>
- Goes, S., Armitage, J. J., Harmon, N., Huismans, R., & Smith, H. (2012). Low seis mic velocities below mid-ocean ridges: Attenuation vs. melt retention. *Journal of Geophysical Research*, 117, B12403. <https://doi.org/10.1029/2012JB009637>
- Hammond, W. C., & Humphreys, E. D. (2000). Upper mantle seismic wave velocity: Effects of realistic partial melt geometries. *Journal of Geophysical Research*, 105, 10,975–10,986.
- Harmon, N., & Rychert, C. A. (2016). Joint inversion of teleseismic and ambient noise Rayleigh waves for phase velocity maps, an application to Iceland. *Journal of Geophysical Research: Solid Earth*, 121, 5966–5987. <https://doi.org/10.1002/2016JB012934>
- Hartley, M. E., Thordarson, T., & de Joux, A. (2016). Postglacial eruptive history of the Askja region, North Iceland. *Bulletin of Volcanology*, 78(28). <https://doi.org/10.1007/s00445-016-1022-7>
- Huybers, P., & Langmuir, C. H. (2009). Feedback between deglaciation, volcanism, and atmospheric CO₂. *Earth and Planetary Science Letters*, 286, 479–491. <https://doi.org/10.1016/j.epsl.2009.07.014>
- Huybers, P., & Langmuir, C. H. (2017). Delayed CO₂ emissions from mid-ocean ridge volcanism as a possible cause of late-Pleistocene glacial cycles. *Earth and Planetary Science Letters*, 457, 238–249. <https://doi.org/10.1016/j.epsl.2016.09.021>
- Jellinek, M. A., Mange, M., & Saar, M. O. (2004). Did melting glaciers cause volcanic eruptions in eastern California? probing the mechanisms of dike formation. *Journal of Geophysical Research*, 109, B09206. <https://doi.org/10.1029/2004JB002978>
- Jenkins, J., MacLennan, J., Green, R. G., Cottaar, S., Deuss, A. F., & White, R. S. (2018). Crustal formation on a spreading ridge above a mantle plume: Receiver function imaging of the Icelandic crust. *Journal of Geophysical Research: Solid Earth*, 123, 5190–5208. <https://doi.org/10.1029/2017JB015121>
- Jull, M., & McKenzie, D. (1996). The effect of deglaciation on mantle melting beneath Iceland. *Journal of Geophysical Research*, 101(B10), 21,815–21,828.
- Katz, R. F. (2008). Magma dynamics with the enthalpy method: Benchmark solutions and magmatic focusing at mid-ocean ridges. *Journal of Petrology*, 49, 2099–2121. <https://doi.org/10.1093/petrology/egn058>
- Köhler, P., Knorr, G., Buiron, D., Lourantau, A., & Chappellaz, J. (2011). Abrupt rise in atmospheric CO₂ at the onset of the Bølling/Allerod: In-situ ice core data versus true atmospheric signals. *Climate of the Past*, 7, 473–486. <https://doi.org/10.5194/cp-7-473-2011>
- MacLennan, J., Jull, M., McKenzie, D., Slater, L., & Gronvöld, K. (2002). The link between volcanism and deglaciation in Iceland. *Geochemistry, Geophysics, Geosystems*, 3(11), 1062. <https://doi.org/10.1029/2001GC000282>
- Nordahl, H., & Ingólfsson, O. (2015). Collapse of the Icelandic ice sheet controlled by sea level rise? *Arktos*, 1, 1–13. <https://doi.org/10.1007/s41063-015-0020-x>
- Pagli, C., & Sigmundsson, F. (2008). Will present day glacier retreat increase volcanic activity? Stress induced by recent glacier retreat and its effect on magmatism at the Vatnajökull ice cap, Iceland. *Geophysical Research Letters*, 35, L09304. <https://doi.org/10.1029/2008GL033510>
- Patton, H., Hubbard, A., Bradwell, T., & Schomackere, A. (2017). The configuration, sensitivity and rapid retreat of the Late Weichselian Icelandic ice sheet. *Earth-Science Reviews*, 166, 223–245. <https://doi.org/10.1016/j.earscirev.2017.02.001>
- Peltier, W. R. (2004). Global glacial isostasy and the surface of the ice-age Earth: The ICE-5G (VM2) model and grace. *Annual Reviews of Earth and Planetary Science*, 32, 111–149. (2004).
- Pico, T., Creveling, J. R., & Mitrovica, J. X. (2017). Sea-level records from the U.S. mid-Atlantic constrain Laurentide Ice Sheet extent during Marine Isotope Stage 3. *Nature Communications*, 8(15621). <https://doi.org/10.1038/ncomms15612>
- Rawson, H., Pyle, D. M., Mather, T. A., Smith, V. S., Fontijn, K., Lachowycz, S. M., & Naranjo, J. A. (2016). The magmatic and eruptive response of arc volcanoes to deglaciation: Insights from southern Chile. *Geology*, 44, 251–254. <https://doi.org/10.1130/G37504.1>
- Rosenthal, A., Hauri, E. H., & Hirschmann, M. M. (2015). Experimental determination of C, F, and H partitioning between mantle minerals and carbonated basalt, CO₂/Ba and CO₂/Nb systematics of partial melting, and the CO₂ contents of basaltic source regions. *Earth and Planetary Science Letters*, 415, 77–87. <https://doi.org/10.1016/j.epsl.2014.11.044>
- Saal, A. E., Hauri, E. H., Langmuir, C. H., & Perfit, M. R. (2002). Vapour undersaturation in primitive mid-ocean-ridge basalt and the volatile content of Earth's upper mantle. *Nature*, 419, 451–455. <https://doi.org/10.1038/nature01073>
- Schmidt, P., Lund, B., Hieronymus, C., MacLennan, J., Arnadottir, T., & Pagli, C. (2013). Effects of present-day deglaciation in Iceland on mantle melt production rates. *Journal of Geophysical Research: Solid Earth*, 118, 3366–3379. <https://doi.org/10.1002/jgrb.50273>
- Scott, D. R. (1992). Small-scale convection and mantle melting beneath mid-ocean ridges. In J. Phipps Morgan, D. K. Blackman, & J. M. Sinton (Eds.), *Mantle flow and melt generation at mid-ocean ridges*, *Geophysical Monograph Series* (Vol. 71, pp. 327–352): American Geophysical Union.
- Shorttle, O., & MacLennan, J. (2011). Compositional trends of Icelandic basalts: Implications for short-length scale lithological heterogeneity in mantle plumes. *Geochemistry, Geophysics, Geosystems*, 12, Q11008. <https://doi.org/10.1029/2011GC003748>
- Sigvaldsson, G. E., Annertz, K., & Nilsson, M. (1992). Effect of glacier loading/ deloading on volcanism: postglacial volcanic production rate of the Dyngjufjöll area, central Iceland. *Bulletin of Volcanology*, 54, 385–392. <https://doi.org/10.1007/BF00312320>
- Sinton, J., Grönvöld, K., & Saemundsson, K. (2005). Postglacial eruptive history of the Western Volcanic Zone, Iceland. *Geochemistry, Geophysics, Geosystems*, 6, Q12006. <https://doi.org/10.1029/2005GC001021>

- Sternai, P., Caricchi, L., Castelltort, S., & Champagnac, J. D. (2016). Deglaciation and glacial erosion: A joint control on magma productivity by continental unloading. *Geophysical Research Letters*, 43, 1632–1641. <https://doi.org/10.1002/2015GL067285>
- Wasylenski, L. E., Baker, M. B., Kent, A. J. R., & Stopler, E. M. (2003). Near-solidus melting of the shallow upper mantle: partial melting experiments on depleted peridotite. *Journal of Petrology*, 44, 116–1191.

References From the Supporting Information

- Andersen, K. K., Azuma, N., Barnola, J. M., Bigler, M., Biscaye, P., Caillon, N., et al. (2004). High-resolution record of northern hemisphere climate extending into the last interglacial period. *Nature*, 431, 174–151. <https://doi.org/10.1038/nature02805>
- Andrews, J. T. (2008). The role of the Iceland Ice Sheet in the North Atlantic during the late Quaternary: A review and evidence from Denmark Strait. *Journal of Quaternary Science*, 23, 3–20. <https://doi.org/10.1002/jqs.1142>
- Armitage, J. J., Collier, J. S., Minshull, T. A., & Henstock, T. J. (2011). Thin oceanic crust and flood basalts: India-Seychelles breakup. *Geochemistry, Geophysics, Geosystems*, 12, Q0AB07. <https://doi.org/10.1029/2010GC003316>
- Clark, P. U., Dyle, A. S., Shakun, J. D., Carlson, A. E., Clark, J., Wohlfarth, B., et al. (2009). The last glacial maximum. *Science*, 325, 710–714. <https://doi.org/10.1126/science.1172873>
- Geirsdóttir, A. (2011). Pliocene and pleistocene glaciations of iceland: A brief overview of the glacial history. In J. Ehlers, P. L. Gibbard, & P. Hughes (Eds.), *Quaternary glaciations—Extent and chronology, a closer look* (Vol. 15, pp. 199–210). Amsterdam: Elsevier. <https://doi.org/10.1016/B978-0-444-53447-7.00016-7>
- Gibson, S. A., & Geist, D. (2010). Geochemical and geophysical estimates of lithospheric thickness variation beneath galápagos. *Earth and Planetary Science Letters*, 300, 275–286. <https://doi.org/10.1016/j.epsl.2010.10.002>
- Gurenko, A. A., & Chaussidon, M. (1995). Enriched and depleted primitive melts included in olivine from icelandic tholeiites: Origin by continuous melting of a single mantle column. *Geochimica et Cosmochimica Acta*, 59, 2905–2917.
- Katz, R. F., Spiegelman, M., & Langmuir, C. H. (2003). A new parameterization of hydrous mantle melting. *Geochemistry, Geophysics, Geosystems*, 4(9), 1073. <https://doi.org/10.1029/2002GC000433>
- Lambeck, K., & Chappell, J. (2001). Sea level change through the last glacial cycles. *Science*, 292, 679–686. <https://doi.org/10.1126/science.1059549>
- Lambeck, K., Rouby, H., Purcell, A., Sun, Y., & Sambridge, M. (2014). Sea level and global ice volumes from the Last Glacial Maximum to the Holocene. *Proceedings of the National Academy of Sciences*, 111, 15,296–15,303. <https://doi.org/10.1073/pnas.141176211>
- McKenzie, D., & O’Nions, R. K. (1991). Partial melt distribution from inversion of rare earth element concentrations. *Journal of Petrology*, 32, 1021–1091.
- Miller, K. J., Zhu, W., Montési, L. G. J., & Gaetani, G. A. (2014). Experimental quantification of permeability of partially molten mantle rock. *Earth and Planetary Science Letters*, 388, 273–282. <https://doi.org/10.1016/j.epsl.2013.12.003>
- Ribe, N. M. (1985). The generation and composition of partial melts in the Earth’s mantle. *Earth and Planetary Science Letters*, 73, 361–376.
- Silbeck, J. N. (1975). On the fluid dynamics of ridge crests. In *Notes on the 1975 summer study program in geophysical fluid dynamics at the woods hole oceanographic institution*, 2, 113–122.
- Sleep, N. H., & Snell, N. S. (1976). Thermal contraction and flexure of midcontinent and Atlantic marginal basins. *Geophysical Journal of the Royal Astronomical Society*, 45, 125–154.
- Spiegelman, M. (1996). Geochemical consequences of melt transport in 2-D: The sensitivity of trace elements to mantle dynamics. *Earth and Planetary Science Letters*, 139, 115–132.
- Spratt, R. M., & Lisiecki, L. E. (2016). A late Pleistocene sea level stack. *Climate of the Past*, 12, 1079–1092. <https://doi.org/10.5194/cp-12-1079-2016>

1 Seismic wave-based constraints on geodynamical processes: an 2 application to partial melting beneath the Réunion island

3 **T. Franken¹, J.J. Armitage^{1*}, N. Fuji¹, A. Fournier¹**

4 ¹Université de Paris, Institut de Physique du Globe de Paris, CNRS, F-75005 Paris, France

5 *Now at: IFP Énergies Nouvelles, 1 & 4 avenue de Bois Préau, 92852, Rueil-Malmaison Cedex, France

6 **Key Points:**

- 7 • We combine geodynamic modeling with seismic wave propagation to constrain the
state of the dynamics underneath the Réunion island.
- 8 • We analyze the sensitivity of seismic observables to geodynamical parameters.
- 9 • Our results favor high melt extraction rates underneath the Réunion island.

Abstract

The inversion of seismic observations leads to maps of the interior of the Earth that can be interpreted. Regions of low seismic velocity have historically been interpreted to be due to factors related to high temperature and high melt retention. Subsequently, geodynamic models can be used to test such interpretations. However, the inversions are non-unique, and arguably it would be best to test geodynamic scenarios against observations rather than interpretations. Here we make a first attempt at this. At depths greater than 80 km below Réunion a low shear-wave velocity zone is imaged. Rather than interpret this inverted model, we test a forward model of melt generation and retention against seismic observations. Geodynamic model solutions are converted with a mineral parameter database to P- and S-wave velocity profiles from various initial temperatures T , upwelling velocities \bar{v} and permeabilities k_0 . By embedding these velocity profiles, synthetic seismograms are generated. For a range of k_0 , T and \bar{v} , we generate synthetic traces for 21 teleseismic events registered at a receiver on Réunion island. We measure the traveltime difference between observed and synthetic waveforms, and the inter-phase differential traveltimes for 210 scenarios for several phase arrivals of three components, filtered between 0.01 and 0.2 Hz. The results indicate that upper mantle temperatures beneath Réunion lie within 1400-1450 °C, with permeability coefficients of 10^{-5} - 10^{-6} m². These conditions are associated with porosities of <0.28% and high melt extraction rates of 8.37-18.35 m yr⁻¹. This study demonstrates the potential for fully comparing geodynamic scenarios with seismic observations.

1 Introduction

The geodynamical evolution of planetary interiors at any scale has been constrained by observations made at and/or above the surface of the Earth and planets. Seismological observations, for example, can give some information in the form of a “snapshot” of the

36 structure of Earth's interior. However, it is seldom the seismological parameters that the
 37 geoscience community really wants to know, rather we use them to attempt to understand
 38 thermo-chemical conditions of the planetary interior and their evolution. This is why most
 39 of the studies on the Earth's interior have been based on inversions of such observations.
 40 Here we briefly review the classical inversion procedures. We then present our method-
 41 ology for forward modeling in geodynamics and seismology. Lastly, we introduce melt
 42 migration dynamics beneath Réunion island, to which we applied our methodology.

43 1.1 Inverse vs. forward problems in geoscience

44 A multidisciplinary approach of exploration of the Earth's interior using seismology
 45 could be expressed as in Figure 1. The classic procedure (light blue arrows in Figure 1)
 46 starts from the collection of the seismic raw waveforms \mathbf{d} (see Equation 1). We then filter
 47 the observed waveforms and/or extract secondary information such as traveltimes, surface-
 48 wave phase velocity, receiver function, etc. We then invert these filtered data linearly, or
 49 in a linearized fashion (e.g. seismic tomography, full-wave waveform inversion), in order
 50 to obtain an inverted seismological model in terms of density, (an)isotropic seismic ve-
 51 locity and seismic attenuation. We then interpret the ensemble of seismic parameters as
 52 geodynamically meaningful parameters such as temperature and chemical anomalies in-
 53 side the Earth's mantle, based primarily on petrological knowledge. The geodynamicists
 54 will finally seek the most probable scenario(s) of the Earth's inner evolution, in order to
 55 qualitatively match their "virtual Earth models" to the tomographic "observation". This
 56 workflow (light blue arrows in Figure 1, expressed mathematically as eq. A.1 within Ap-
 57 pendix 1) is unavoidable when we do not have sufficient data or *a priori* information on
 58 the Earth's evolution [French and Romanowicz, 2015; Marjanović *et al.*, 2017].

59 Nevertheless, due to the regularization terms imposed throughout the chain of (lo-
 60 calized and) linearized inversions, it is difficult to quantitatively discuss the probability
 61 of proposed Earth's evolution scenarios[Ritsema *et al.*, 2007; Atkins *et al.*, 2016]. The
 62 only way to self-consistently answer this question is to directly model the full problem
 63 from first principles, and compare the predicted data with the real data: *i.e.* predict a self-
 64 consistent thermo-chemical structure, then predict the seismic properties, and subsequently
 65 make a full comparison with the observation. Here the observation is the seismic signal
 66 received at the Earth's surface. Following this methodology, we must perform every pro-
 67 cedure in a forward manner, and we propose that this approach is more powerful and ob-

68 jective than a series of inversions, in particular when we have geodynamical parameters \mathbf{m}
 69 to investigate (see Equation 1).

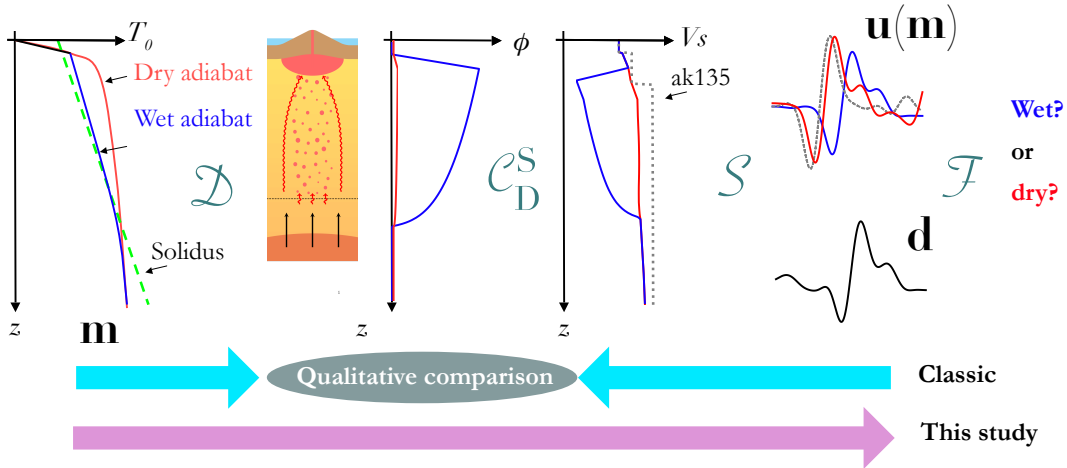
70 When we have a concrete set of geodynamical parameters to explore (e.g. degree
 71 of contribution of chemical heterogeneity to mantle convection or melt retention beneath
 72 a volcanic island, as in this paper), we should be able to directly, and quantitatively, in-
 73 vestigate the appropriateness of each ensemble parameter range, \mathbf{m} , against the observed
 74 seismic waveforms, \mathbf{d} , (Eq. 1). The crucial element to realize this direct comparison is re-
 75 lying on the capacity of forward modeling. Therefore, we propose to find the direct link
 76 between \mathbf{m} and \mathbf{d} by a series of forward modeling,

$$\mathbf{u} = \mathcal{S} \circ C_D^S \circ \mathcal{D}(\mathbf{m}), \quad (1)$$

77 with \mathbf{u} the “seismically (low-)filtered waveform data” instead of “seismically filtered model”
 78 (see the discussion in the appendix section). The operators \mathcal{D} , C_D^S , and \mathcal{S} , denote forward-
 79 modeling operators in geodynamics, petrology, and seismology, respectively (see the de-
 80 tailed discussion in Appendix 1). Due to the series of forward operators, the sensitivity
 81 of \mathbf{u} with respect to \mathbf{m} should be reduced: we therefore insist that this operation is “low-
 82 filtering”. The aim is thus to maximize the sensitivity by choosing a set of attributes from
 83 \mathbf{u} . The operation *per se* could be costly with respect to a series of inversions, but we can
 84 ideally perform a global search instead of local search. As indicated in the red arrow in
 85 Figure 1, we will be able to directly compare these “seismically (low-)filtered waveform
 86 data”, $\mathbf{u}(\mathbf{m})$, as a function of geodynamical model parameters, \mathbf{m} , and the observed data,
 87 \mathbf{d} .

98 1.2 Melt migration dynamics beneath the volcanic regions

99 For our first attempt to perform “waveform (low-) seismic filtering” (eq. 1 and eq. A.8
 100 in Appendix 1), we choose the melt migration dynamics beneath the volcanic regions.
 101 Within the Earth’s interior, melting most likely occurs only at the uppermost and lower-
 102 most mantle, due to the possible crossings of the mantle rock solidus and the geotherm
 103 [Karato, 2014; Herzberg *et al.*, 2013]. Within the asthenosphere below mid-ocean ridges,
 104 such as the East Pacific Rise (EPR), a seismic low velocity zone (LVZ) is found at depths
 105 between approximately 80 and 200 km with several percent of reduction in shear-wave ve-
 106 locity. The origin of such LVZs has been proposed to be due to the presence of partial
 107 melt [Stixrude and Lithgow-Bertelloni, 2005]. Direct comparison with experimental results



88 **Figure 1.** Conceptual schema of our waveform seismic filtering strategy (pink arrow for corresponding
 89 workflow). On the top from the left to right: we first generate (\mathcal{D}) geodynamical scenarios with different ini-
 90 tial conditions \mathbf{m} (T_0 for example: wet and dry in blue and red, respectively) in order to obtain a steady-state
 91 snapshot (vertical variation of porosity ϕ for example). We then translate (\mathcal{C}_D^S) the set of geodynamical pa-
 92 rameters such as ϕ to a set of seismological parameters such as V_S . We then generate (\mathcal{S}) seismic waveforms
 93 \mathbf{u} to investigate the sensitivity of \mathbf{u} with respect to \mathbf{m} . We define a filter \mathcal{F} that can distinguish the different
 94 scenarios \mathbf{m} : we then analyze the observed data \mathbf{d} to select the preferred geodynamical scenario(s). Classical
 95 approaches (light blue arrows) try to fit the intermediate parameter sets such as seismic velocity structure or
 96 porosity structure that has unknown error bars due to a series of inversion procedures. A detailed discussion
 97 can be found in Appendix 1.

on rock assemblies of solid olivine and molten basalt infer small amounts of partial melt at 0.1 to 0.3 wt% levels [Chantel *et al.*, 2016]. Also, high melt transportation velocities (20 m yr^{-1}) at mid-ocean ridges are proposed based on U-series isotope study [Elliott and Spiegelman, 2003; Stracke *et al.*, 2006]. Yet, 2D geodynamical modeling together with a linear estimation on poroelastic effects of partial melt on shear-wave velocity requires a high melt retention (~0.3-2%) to explain the cause of LVZ obtained from surface-wave tomography at East Pacific Rise.

The EPR is one of the most studied and well understood areas of mantle upwelling and magma generation. Seismic observations from the MELT and GLIMPSE experiments at the EPR register a large negative velocity anomaly at the expected depth interval of the primary melting zone [Forsyth, 1998]. Based on S-wave travel time delay and Rayleigh wave phase velocity variations, there is an estimated 1-2% of melt present at this interval [Forsyth, 1998]. The low seismic velocities modeled below the EPR can not be replicated with a classic thermal model, that only considers conductive cooling [Harmon *et al.*, 2009]. This leads to the conclusion that there must be an additional reduction in seismic velocity due to the presence of at least 1% melt, taking the reduction in seismic velocity extrapolated from laboratory experiments [Hammond and Humphreys, 2000].

The question of the quantity of melt retained in the asthenosphere becomes more complicated if attenuation is included [Goes *et al.*, 2012]. The base of the LVZ below the EPR is at close to 100 km depth [Harmon *et al.*, 2009]. For significant melting to occur at this depth, the solidus needs to be lowered due to increased volatile content (e.g. Hirschmann *et al.* [1999]). The removal of volatiles as they partition into the deep melt will create a region of low- V_S and low- Q_S (high attenuation) that coincides with this deep melting [Goes *et al.*, 2012]. Volatile rich melting is however not productive, and no more than 0.1% melt is typically retained within the asthenosphere at depths between 200 and 90 km [Hirschmann *et al.*, 2009]. It is only within the shallow region (<60 km) of silicate melting that larger quantities of melt can be retained [Goes *et al.*, 2012]. This shallow region of low- V_S due to melt retention is un-resolvable at the resolution of the MELT and GLIMPSE experiments, therefore it can be concluded that the LVZ below the EPR is most likely due to the effects of attenuation and not melt retention.

Below volcanic islands such as Hawaii and the Galapagoes, a deep seismic discontinuity has been imaged at depths of 140 to 100 km [Rychert *et al.*, 2013, 2014]. This

140 seismic discontinuity is imaged in the form of S-to-P receiver functions, and has been in-
141 terpreted to represent the onset of deep volatile rich melting [Rychert *et al.*, 2013, 2014].
142 However, this interpretation is incompatible with forward models of melt generation and
143 transport [Havlin and Parmentier, 2014; Armitage *et al.*, 2015]. It was found that the only
144 way to generate a strong seismic discontinuity that could be imaged through S-to-P re-
145 ceiver functions is if the mantle contains no volatiles [Havlin and Parmentier, 2014]. Under
146 such conditions, the rate of melt production is sufficiently high to create a sudden step
147 in porosity, that would significantly reduce seismic velocities.

148 At regions of continental break-up, the same arguments of low- V_S and deep S-to-
149 P receiver functions have been used to argue for a significant quantity of melt retention
150 (e.g. Rychert *et al.* [2012]). However, just as before, forward geodynamic models have
151 been incapable of matching the tomographic models obtained using seismic inversions.
152 By modeling the composition and volume of melt generated in the Afar region of the East
153 African Ridge, it was found that melt retention in the asthenosphere was most likely no
154 more than 0.5 % [Armitage *et al.*, 2015]. In general, along the Afar Rift, forward models
155 have found that the magnitude of the observed seismic velocities can be explained without
156 the need for more than 1% melt retention [Armitage *et al.*, 2018, 2015].

157 Seismic studies consistently infer roughly 1 to 2% melt retention based on for ex-
158 ample the reduction in S-wave velocity below the East Pacific Rise (e.g. Harmon *et al.*
159 [2009]), seismic attenuation at the Juan de Fuca and Gorda ridges [Eilon and Abers, 2017],
160 or to generate the seismic discontinuity observed at the lithosphere - asthenosphere bound-
161 ary (LAB) in the central Atlantic [Mehouachi and Singh, 2018]. There is therefore clearly
162 a disconnect between what forward geodynamic models predict for melt retention (< 1 %)
163 and the quantity seismic interpretation calls for (> 1 %). In order to solve this enigma, we
164 propose a series of forward modeling both in geodynamics and in seismology, analyzing
165 one-station teleseismic data at Réunion island to understand the LVZ (of ~4%) based on
166 the partial melt hypothesis. We attempt to predict the observation, the seismic waveform,
167 from the structure predicted by the forward geodynamic model. We will focus on Réunion
168 given that previous studies indicate that this region likely contains some degree of melt
169 within the asthenosphere [Mazzullo *et al.*, 2017]. We predict the melt porosity and velocity
170 in a 1D upwelling mantle regime, and calculate the corresponding transport velocity of the
171 melt towards the surface. From the 1D model of temperature, pressure and melt fraction
172 we predict V_p and V_S velocities, and use these to generate synthetic waveforms across a

range of plausible mantle conditions. Finally, we integrate seismic observations from the Réunion mantle plume for a comparison with the synthetic seismograms to attain a best fit model in order to constrain mantle permeabilities, melt fractions and melt flow velocities below Réunion island.

1.3 Réunion island

In this study, we work on the 1D melt dynamics beneath the Réunion island. A recent surface wave seismic tomography model shows evidence for a 4% reduction in S-wave velocity at depths of around 80 km [Mazzullo *et al.*, 2017]. This could be indicative of high mantle temperatures and high degrees of melt retention. It is clear that the mantle is melting below La Réunion, but how much is retained within the mantle and contributes to the low velocities found within seismic inversions is unclear.

The first signature of plume activity in the western Indian Ocean dates back to 65–66 Ma in the late Cretaceous during the formation of the Deccan Traps, a large igneous province covering 500,000 km² [Duncan and Hargraves, 1990; Courtillot *et al.*, 2003]. The ascent of a deep mantle plume and its interaction with the base of the lithosphere, inducing surface volcanism and the formation of the Deccan Traps, is postulated as the beginning of the Réunion hotspot track [Richards *et al.*, 1989]. North-eastward plate movement of the African Plate 34 Ma ago created a linear chain of age-progressive islands, forming the Mascarene Plateau, Mauritius, and Réunion. This large oceanic volcanic system is located 800 km east of Madagascar and lies in the southernmost part of the Mascarene Basin. It is therefore assumed that the present day volcanic activity at the Piton de la Fournaise volcano on Réunion island is the surface expression of the upwelling mantle plume, and that there is a large quantity of melt being generated and transported to the surface below this volcanic island.

The petrology and geochemistry of the Piton de la Fournaise lavas can provide information on upper mantle conditions from which they originate, such as the thermal state at formation [Herzberg *et al.*, 2007]. As mantle convection drives mantle rock to the surface, fusible components of the peridotitic mantle rock melt at grain boundaries when solidus temperature and pressure conditions are reached. The residual solid matrix becomes a porous medium for fluid flow, where buoyant forces arise from a density differential between the liquid melt and solid matrix, and drive melt towards the surface. Although the

composition of the melt may be modified during its ascent by fractional crystallization and/or mixing, lava samples can be reconstructed into their primary magma composition from which the MgO content can be used as an indicator of source temperature. Concentrations of MgO are predominantly temperature dependent, meaning magmas with a high MgO content reflect dry and hot source conditions [Hirose and Kushiro, 1993]. Geochemical analysis of primary magmas from Réunion formations show high MgO concentrations of 16-20 wt %, indicating melting conditions of mantle peridotites at temperatures above 1450 °C [Sobolev and Nikogosian, 1994]. Furthermore, a ~ 2 km thick underplated magmatic body deduced from receiver function inversions and seismic refraction profiles [Fontaine et al., 2015; Charvis et al., 1999; Gallart et al., 1999] has been proposed to consist of ultramafic primary melt originating from 60-90 km depths [Richards et al., 2013].

A high temperature upper mantle below Réunion is in line with local seismic tomography studies which confirm a low shear wave velocity zone (LVZ) below the oceanic crust [Fontaine et al., 2015; Mazzullo et al., 2017]. The LVZ phenomenon is not unique to Réunion, but has been observed globally below hotspots, rifts and mid-ocean ridges in areas such as Afar, the East Pacific Rise, Hawaii, the Galapagos and Iceland. There is abundant evidence for partial melting associated to deep mantle upwelling in these areas. However, the quantity of partial melt and its significance to LVZ remain contested by geodynamic, seismic, and petrologic studies: are these LVZ's purely thermal or require an additional mechanism, such as the presence of partial melt (e.g. Goes et al. [2012]; Eilon and Abers [2017]; Cobden et al. [2018])? The dynamics of the system and the mechanisms responsible for the velocity anomaly remaining poorly understood, other explanations involving upper mantle anisotropy, attenuation, volatile content, solid state mineralogy, and grain boundary sliding are still being explored.

2 Methods

How much melt can be retained in LVZ? Or, more in general, what is the cause of LVZ and its role in whole mantle convection? As we discussed in the introduction, we propose a series of forward modeling through geodynamics, petrology and seismology, in order to understand the sensitivity of geodynamical parameters to the seismic observations. Seismic inversion studies of the structure beneath the Réunion island have provided valuable results on the quantification of low shear-wave velocity zones. Here, our forward modeling approach will allow us to control individual model parameters in geodynamics instead of

seismic parameters (see the discussion in the Appendix), in order to test their effects directly on seismic observations: seismic waveforms themselves. We therefore develop a 1D melting model, which is converted to seismic velocities, density and attenuation, and then we propagate a seismic wave through models of a range of mantle conditions (eq. A.8). We explore the sensitivity of geodynamical scenarios to seismic attributes $\mathcal{F}(\mathbf{u})$ and analyze the observed seismic data to conclude. In particular in this study, it consists of the four unknowns:

$$\mathbf{m} = (k_0, T_0, \bar{v}, \phi)^T \quad (2)$$

with k_0 the permeability coefficient, T_0 the initial temperature, \bar{v} the average upwelling velocity and ϕ the porosity.

2.1 1D Geodynamical modeling

The production and transport of melt in the 1D melting system can be described by the following set of modified Stokes equations [McKenzie, 1984; Ribe, 1985]. We consider a 1D system where mantle moves upwards, and as it does so it decompresses and melts (Figure 1). The evolution of this system can be described by a set of continuum equations beginning with temperature. The temperature of the system over time is described by a general advection-diffusion equation that incorporates melting as a source term:

$$mL + \rho c \frac{\partial T}{\partial t} + \rho c \bar{v} \frac{\partial T}{\partial z} - \kappa \frac{\partial^2 T}{\partial z^2} = 0 \quad (3)$$

where m is the melt production rate, L the latent heat of melting, ρ the density, c the specific heat capacity, T the temperature, \bar{v} the average upwelling velocity, z the system depth in kilometers and κ the heat conductivity.

The average upwelling velocity consists of a solid and a liquid upwelling component, with the mantle rock matrix being the solid and the melt as the liquid component:

$$\bar{v} = (1 - \phi)v_s + \phi v_l, \quad (4)$$

where v_s and v_l are (respectively) the velocity of the upwelling matrix and melt and ϕ is the porosity.

Melting of the upwelling mantle rock occurs when its temperature and pressure conditions exceed that of the solidus (Figure 1), which we assume is only a linear function of pressure and is given by:

$$T_s = T_{s0} + \frac{\partial T_s}{\partial p} p \quad (5)$$

where $T_{s0} = 1080^\circ\text{C}$ and $\frac{\partial T_s}{\partial p} = 132 \times 10^{-9} \text{ }^\circ\text{C Pa}^{-1}$ [Scott, 1992]. We assume melt production rate m is governed by the difference in mantle temperature T and solidus temperature T_s , $\Delta T = T - T_s$, the latent heat L from melting, and a depletion term $\partial T_s / \partial \phi$ that accounts for the increased difficulty to melt depleted mantle:

$$m = \Delta T \left(L + \frac{\partial T_s}{\partial \phi} \right)^{-1}. \quad (6)$$

The depletion term is generally controlled by mantle composition, where melting becomes more difficult as pyroxenes and clinopyroxenes are extracted from the solid mantle into the melt and the less fusible olivine remains (e.g. Morgan [2001]). However, since mantle composition is not directly implemented into the 1D model, we approximate depletion using a power law relation:

$$\frac{\partial T_s}{\partial \phi} = C e^{a\phi} \quad (7)$$

where $C = 440 \text{ K}$ is a constant for the initial depletion value [Morgan, 2001] and $a = 5.5$ is a dimensionless depletion coefficient that we use to create a diminishing melt production. Note that C has a dimension of temperature since porosity is dimensionless. This simplified set of melting relations does not capture the full complexities of multi-component melting (e.g. Morgan [2001]; Katz *et al.* [2003]). It does however capture the most important aspects of melt generation to allow for a 1D melt transport model, and give a simple model solution through which to propagate seismic waves.

The melt transport through the system is approximated as the flow of a liquid phase through a porous medium, which is described by Darcy flow. To create a set of closed equations we need to approximate for the relationship between permeability and porosity as follows:

$$k_\phi = k_0 \phi^n, \quad (8)$$

where k_ϕ is the permeability and k_0 is the permeability coefficient, with k_0 and n being constants empirically derived from experiments. At grain-scale melt distributions in partially molten olivine basalts n has been empirically determined to be approximately equal to 2.7 for melt fractions of $\phi > 0.02$ [Miller *et al.*, 2014]. The constant k_0 is much more uncertain, with estimates of mantle permeability k_ϕ ranging from 10^{-15} m^2 to 10^{-10} m^2 (e.g. Burley and Katz [2015]), k_0 is between $\sim 10^{-5} \text{ m}^2$ to 10^{-10} m^2 , assuming $n = 3$. Taking the above closure equation in 8, the flow of the melt, v_l is subsequently given by:

$$\phi(v_l - v_s) = \frac{k_0 \phi^n}{\eta_l} \left(\Delta \rho g + \frac{\partial}{\partial z} p \right) \quad (9)$$

where the term $\Delta\rho g + \partial p/\partial z$ describes the potential gradient which drives the flow, where $\Delta\rho$ is the density difference between fluid and matrix, g the acceleration due to gravity, and $\partial p/\partial z$ the pressure gradient due to compression of the matrix.

A zero compaction length approximation is adopted, which assumes no contribution of matrix compaction to porous flow. The matrix compression term in eq. 9 can be neglected if melt flow is one dimensional and the length scale over which melting occurs is much larger than the reduced compaction length δ_R defined as follows [Ribe, 1985]:

$$\delta_R = \left[\frac{\phi_0 \bar{v} (\zeta_s + \frac{4\eta_s}{3})}{g \Delta\rho} \right] \quad (10)$$

with ζ_s and η_s respectively the bulk and shear viscosity of the solid matrix and ϕ_0 a reference porosity. Assuming ζ_s and $\eta_s = 10^{15} - 10^{18}$ Pa s [e.g. Ribe, 1985], $\Delta\rho = 500$ kg m⁻³ [e.g. Hewitt, 2010] and the reference porosity an estimated range of $\phi_0 = 0.1 - 5$ % we determine an average reduced compaction length for the 1D melting model at 5 – 50 m, with a maximum upper boundary of 5000 m for model extremities. The height of the melting column is approximately 80 km, which is three to four magnitudes larger than our estimated reduced compaction length.

We adopt a Boussinesq approximation for the density ρ , where the density of solid matrix and melt are equivalent except in the buoyancy term [Hewitt, 2010]. The conservation of mass for melt is given by:

$$\rho \frac{\partial \phi}{\partial t} + \rho \frac{\partial}{\partial z} \phi v_l = m. \quad (11)$$

Under the assumption of a zero compaction length and assuming $n = 3$, Darcy's equation (eq. 9) can be written as,

$$\phi (v_l - v_s) = \frac{k_0 \phi^3}{\eta_l} (\Delta\rho g) \quad (12)$$

To get a solvable equation for melt velocity we incorporate eq. 4 in eq. 12, and then substitute this into eq. 11 to get a set of equations for melt production and transport as function of porosity:

$$\rho \frac{\partial \phi}{\partial t} + \rho \bar{v} \frac{\partial \phi}{\partial z} + \frac{k_0 \Delta\rho g}{\eta_l} \frac{\partial}{\partial z} [\phi^3 (1 - \phi)] = m. \quad (13)$$

Here \bar{v} is the imposed upward velocity of the melt and solid matrix, and ϕ is therefore the only unknown and it therefore can be solved numerically.

313 2.2 Numerical method for melt production and transport

314 The 1D partial melting model computes temperature as a function of depth and time
 315 through the general advection-diffusion equation (eq. 3, eq. 13), discretized using Crank-
 316 Nicolson method. At the depth of 410 km we initialize the initial mantle temperature (T_0)
 317 as a fixed temperature boundary condition. At the surface temperature is fixed at 0 °C.
 318 The model has 410 evenly spaced grid points from 410 km depth to the surface of the
 319 Earth. Once the temperature of the system exceeds solidus temperature T_s , the finite dif-
 320 ference scheme determines the production of melt as a function of previous depletion, re-
 321 calculating temperature according to latent heat from melting for each time step according
 322 to eq. 6. The third term in eq. 13 can be expressed as an advection term $q \frac{\partial \phi}{\partial z}$ where:

$$323 q = \frac{k_0 \Delta \rho g}{\eta_l} \left[3\phi^2 \left(1 - \frac{4}{3}\phi \right) \right], \quad (14)$$

324 giving a scheme for calculating ϕ in the next time-step as:

$$325 \phi_j^{l+1} = \phi_j^l - \frac{\bar{v}q(\phi_j^l - \phi_{j-1}^l)}{\Delta z}, \quad (15)$$

326 where superscript l are the points in time and subscripts j the points in space. The free
 327 parameters that we will explore are mantle temperature, upwelling velocity, and the per-
 328 meability coefficient k_0 . Models are run until a steady state is achieved. The melt flow
 329 velocity, temperature, and melt production as a function of depth are calculated for a range
 330 of scenarios variable upwelling velocities of \bar{v} (10 – 70 mm yr⁻¹), initial temperatures of T_0
 331 (1250 – 1500 °C), and permeability coefficients of k_0 (10⁻⁹–10⁻⁵ m²), at increments of re-
 332 spectively 10 mm yr⁻¹, 50 °C and a factor 10, giving 210 different model scenarios. These
 333 parameter ranges describe a series of feasible geodynamic conditions in mantle plume en-
 334 vironments.

335 2.3 Conversion to seismic properties

336 At the Earth's surface we cannot directly "see" the melt retention calculated in the
 337 previous section, but only the geochemical or seismological observations. In this study
 338 we intend to analyze the sensitivity of seismic waveforms with respect to the melt re-
 339 tention. We therefore construct seismological models from geodynamical modeling con-
 ducted beforehand. To realize this idea, temperature, pressure, and porosity are converted
 to isotropic P- and S-wave velocities.

340 To compute seismic velocities for the geodynamical 1D models, we follow the meth-
 341 ods of *Goes et al.* [2012]. Phase diagrams and anharmonic velocities are computed us-
 342 ing Perplex [Connolly, 2005], and the equation of state, solid solution models and 2008-
 343 NaCFMAS mineral parameter data base of Sixtrude and co-workers [*Stixrude and Lithgow-*
 344 *Bertelloni, 2005; Xu et al., 2008*]. Subsequently we assume attenuation is given by [*Cam-*
 345 *marano et al., 2003; Goes et al., 2012*]:

$$Q = A\omega^\alpha \exp\left(\frac{\alpha\gamma T_s}{T}\right). \quad (16)$$

346 This Arrhenius style attenuation relationship is empirical, where the melting tempera-
 347 ture T_s is used as an alternative to estimating the depth dependence on activation volume
 348 [Karato, 1993]. The constants are $A = 0.1$, $\alpha = 0.15$, and $\gamma = 38$, and we set $\omega = 2\pi/20.0$
 349 (with a dominant period of 20 s). Since we use large band-pass filters from 100 s to 5 s
 350 and apply a frequency-independent attenuation during our synthetic seismogram computa-
 351 tion, we used this *ad hoc* value in order that the attenuation remains in the range of $\pm 20\%$
 352 of Arrhenius attenuation described above for all the frequencies. The anharmonic velocity
 353 and anelastic contributions are subsequently combined to give the seismic velocity [*Goes*
 354 *et al., 2012*]:

$$V = V_{\text{anh}} \left[1 - \frac{Q^{-1}}{2 \tan(\pi\alpha/2)} \right]. \quad (17)$$

355 Finally, to include the effect of melt we follow a convention of a 3.6% and 7.9% velocity
 356 reduction per percent melt for respectively the P- and S-wave velocities according to *Ham-*
 357 *mond and Humphreys* [2000], where the velocity derivatives are based on an organized
 358 cuspat pore geometry with relaxed elastic moduli to model a maximum possible effect of
 359 melt on seismic wave velocity. Teleseismic waves excite the relaxed modulus of partially
 360 molten upper mantle rock, and therefore we assume relaxed, pressure equilibrated melt
 361 conditions when relating seismic velocity reduction to the mantle physical state [*Hammond*
 362 *and Humphreys, 2000*].

363 Wave velocities at depths below 410 km are set to *ak135* [Kennett *et al.*, 1995], since
 364 the mineral database only covers the upper mantle up to the Moho. We assume no per-
 365 colation of melt into the crust and set the model porosity to 0% at the Moho to crudely
 366 simulate extraction for simplicity purposes. This is somewhat artificial as there will be a
 367 degree of melt storage within the crust in the form of sills and melt lenses. However, it
 368 is beyond the scope of the 1D model developed here to examine these processes. Given
 369 the wavelength of seismic waves used to probe the structure of the lithosphere and as-

thenosphere to understand melt retention, we believe this region can be assumed to be similar to *ak135*. An artifact from this approximation might be a sharp porosity discontinuity at the top of the LVZ, which is modified into a more gradual porosity transition as seen from observations to avoid overestimation of the impedance contrast during synthetic waveform generation. Perceived from seismic tomography results from the Réunion mantle plume, the LVZ starts at about 27 km depth, and reaches a minimum velocity at 32 km depth [Fontaine *et al.*, 2015]. We apply a moving average filter over this depth range to smooth the top of the porosity curve. The bottom of the model space is truncated at 410 km depth to coincide with the the 410-discontinuity in *ak135* reference model.

379 2.4 Seismological modeling

380 In order to compute full-wave synthetic seismograms for a number of given 1-D
 381 Earth models in this study up to as high frequency as 1 Hz, we use Direct Solution Method
 382 [Geller and Ohminato, 1994; Geller and Takeuchi, 1995; Kawai *et al.*, 2006]. The DSM
 383 obtains the solution of the weak form of the equation of motion by directly solving the
 384 Galerkin weak form of the equation of motion:

$$(384) \quad (\omega^2 \mathbf{T} - \mathbf{H}) \mathbf{c} = -\mathbf{g},$$

385 with ω the angular frequency, \mathbf{T} and \mathbf{H} the mass and stiffness matrices, respectively. \mathbf{g} is
 386 the external force vector and \mathbf{c} is the expansion coefficient of the displacement. We choose
 387 the spherical harmonics along the lateral directions of the Earth and linear spline along
 388 the vertical direction for basis and trial function expansion of all the vectors and matrices
 389 described above. This finite element formulation adheres to natural boundary condition
 390 (free surface boundary) and fluid-solid boundary conditions. Numerical dispersion due
 391 to the discretization can successfully be eliminated through implementation of optimally
 392 accurate operators [Geller and Takeuchi, 1995]. The ellipticity of the Earth is also taken
 393 into account. The reader can refer to the literature cited herein for further theory and the
 394 extension of DSM to 3D Earth models can be found in [Cummins *et al.*, 1997; Fuji *et al.*,
 395 2012; Monteiller *et al.*, 2015].

396 The reference Earth model we use for DSM consists of 1D *ak135* model [Kennett
 397 *et al.*, 1995]. By embedding velocity profiles from our converted models into the reference
 398 model at the 12-410 km depth range, we generate different sets of synthetics for several
 399 source events while varying upper mantle temperatures, upwelling velocities and perme-

abilities. The time window is set to a length of 3276.8 s to include surface waves at high offset source events, in order to avoid numerical artifacts from superimposition of surface wave energy out of the time window. We calculate seismograms up to 0.3125 Hz so that we can filter them up to 0.2 Hz to compare against the observed waveforms. It is worth noting here that DSM naturally prefers a time window of 0.1 s times a power of 2 in order for the inverse Fourier transform to be free from numerical errors. In this study we consider only isotropic homogeneous media since we will analyze teleseismic phases up-going through the melt conduit beneath Réunion island.

408 3 Seismological data

409 We would like to extract the geodynamical information from the direct observation
 410 on the Earth's surface. Unlike current seismic tomography that makes use of a tremen-
 411 dous amount of data, we would like to extract as much information as possible from a
 412 small number of data (21 earthquakes with only one seismic station in Réunion island) to
 413 detect signatures from differences in geodynamical scenarios within each individual seis-
 414 mological datum. In this study we will initially focus on the sensitivities of different com-
 415 binations of permeability, temperature and upwelling velocity on the synthetic waveform.
 416 Furthermore, we compare the synthetic seismograms for each source event with seismic
 417 observations acquired from Réunion. The synthetics are generated using DSM according
 418 to source and receiver configurations of the seismic observations of the Réunion mantle
 419 plume in order to place the models in the context of the Earth.

420 3.1 Receiver

421 Earthquake observation data are obtained from the GEOSCOPE Observatory, a
 422 global network of broadband seismic stations transmitting real-time seismic data to the
 423 Institute de Physique du Globe de Paris (IPGP) data center, from which the data is man-
 424 aged and distributed [Douet *et al.*, 2016]. It comprises of a network of 34 seismological
 425 stations in 18 different countries, and offers a catalog of earthquakes registered between
 426 2006 and 2018 with magnitudes above 5.5-6. All stations are equipped with three broad-
 427 band seismometers type STS1 or a 3-component seismometer type STS2, a digitizer, and a
 428 local storage system for the data [Douet *et al.*, 2016].

436

Table 1. Receiver information RER GEOSCOPE seismic station

Receiver	Latitude (degrees)	Longitude (degrees)	Elevation (m)	Channels	Sampling Rate (Hz)
GEOSCOPE RER	-21.17	155.74	834	BHZ, BHN, BHE	20

429

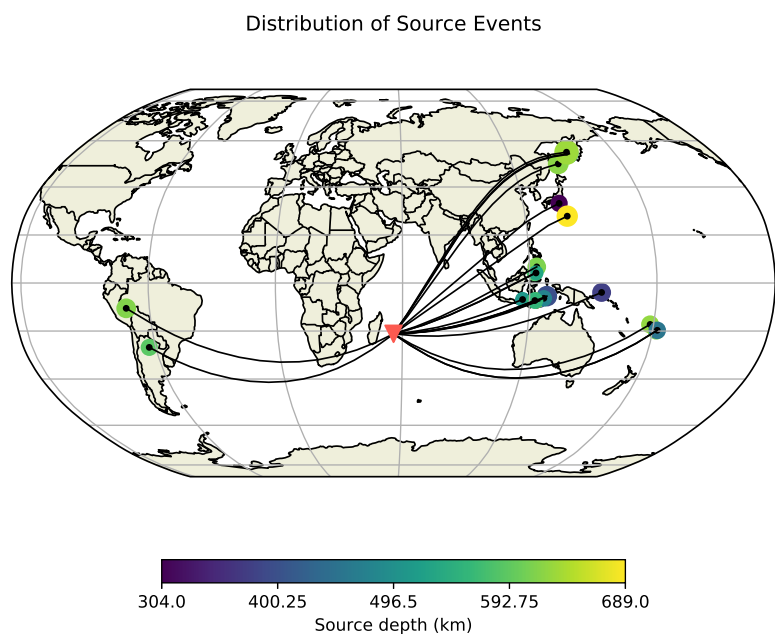
Seismic data is acquired from the GEOSCOPE RER seismic station (table 1), which is part of the GEOSCOPE Observatory network. This seismic station is situated directly above the upwelling plume on top of the Piton de la Fournaise volcano, capturing seismic waves that have traveled through the LVZ that should contain information on the melting zone. Table 1 contains the receiver specifications for the RER receiver. The seismic observations of interest are recorded as time series data on the broadband seismometer channels of the RER station.

437

3.2 Seismic sources

438

From the entire earthquake catalog registered at the RER GEOSCOPE station between January 2006 and December 2015 a selection of events is used for synthetic waveform generation. The selection criteria to decide on adequate source events are based on their source depth, epicentral distance from RER station, signal-to-noise ratio and clarity of the phase arrivals. To avoid seismic interaction with potential upper-mantle and crustal interfaces and/or melting at the source location, we select deep earthquakes with a source depth greater than 300 km so that the upper mantle effects for observed and synthetic seismograms are only on the RER station-side. We ensure teleseismic incidence at the receiver location by selecting source events at epicentral distances at least beyond 30 degrees [Bormann and Wielandt, 2002]. The epicentral distance range of the seismic sources used in this study is from 60 to 120 degrees. In order for an automated waveform correlation to function, we require relatively high signal-to-noise ratio and high amplitude P and S phase arrivals up to a level where the signal is not masked by noise. Source half duration time should not exceed the period at which it has been band-pass filtered since the synthetics are simulated with a Heavyside source time function, that we will convolve with the source time function provided by SCARDEC (see section 4.2). Table 2 displays the seismic events from the RER GEOSCOPE catalog which satisfy all the criteria.



457 **Figure 2.** Geographical distribution of source events (table 2). Depth is displayed by color and earthquake
458 magnitude by size of the circular markers. The location of the RER GEOSCOPE receiver is marked by a red
459 inverted triangle.

455 **Table 2.** List of 21 events used in our analyses. Half Duration times (HD) have been taken from Global
 456 CMT.

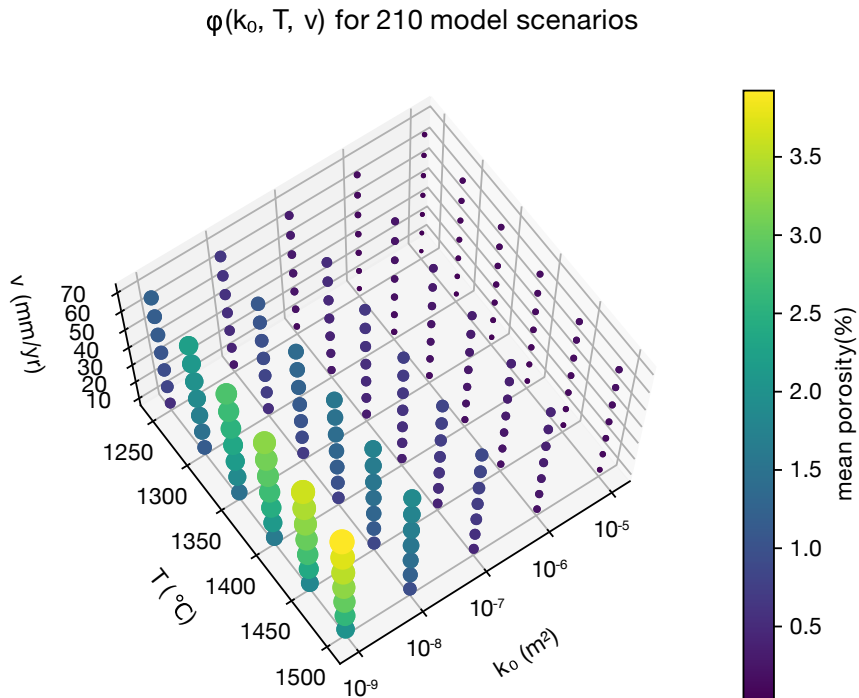
#	Source Event	Date (yyyy/mm/dd)	Time (h:m:s)	Latitude (degrees)	Longitude (degrees)	Epicentral dist. (degrees)	Depth (km)	Magnitude	HD (s)
1	Bali Sea	2011/03/10	17:08:36	-6.87	116.72	60.51	510	6.6	4.8
2	Fiji Islands	2006/01/02	22:13:40	-19.93	-178.18	113.15	609	7.1	9.3
3	Banda Sea	2006/01/27	16:58:53	-5.47	128.13	71.62	397	7.7	16.0
4	Sea of Okhotsk	2008/07/05	02:12:04	53.88	152.89	111.11	636	7.7	17.3
5	Sea of Okhotsk	2008/11/24	09:02:58	54.2	154.32	111.98	518	7.3	10.9
6	Banda Sea	2008/12/06	10:55:26	-7.39	124.75	67.81	404	6.5	3.9
7	Honshu	2009/08/09	10:55:55	33.17	137.94	95.26	304	7.0	8.3
8	Banda Sea	2009/08/28	01:51:20	-7.15	123.43	66.66	633	6.9	6.8
9	Celebes Sea	2009/10/07	21:41:13	4.08	122.37	69.92	587	6.8	5.9
10	Fiji Islands	2009/11/09	10:44:55	-17.24	178.33	111.88	626	7.2	10.5
11	Mindanao	2010/07/23	22:08:11	6.72	123.41	71.96	615	7.3	11.0
12	Santiago Del Estero	2011/01/01	09:56:58	-26.8	-63.14	103.84	590	7.0	8.0
13	Celebes Sea	2011/02/10	14:39:27	4.2	122.97	70.52	533	6.6	4.5
14	Banda Sea	2011/08/30	06:57:41	-6.36	126.75	70.03	476	6.9	6.7
15	Sea of Okhotsk	2012/08/14	02:59:38	49.8	145.06	105.59	622	7.7	17.8
16	Sea of Okhotsk	2013/05/24	05:44:49	54.9	153.28	111.46	632	8.3	35.7
17	New Ireland	2013/07/07	18:35:30	-3.92	153.92	96.18	379	7.4	10.9
18	Fiji Islands	2014/11/01	18:57:22	-19.69	-177.76	113.61	455	7.1	8.7
19	Flores Sea	2015/02/27	13:45:5	-7.297	122.54	65.77	557	7.0	7.5
20	Bonin Islands	2015/05/30	11:23:02	27.84	140.49	95.35	689	7.8	20.7
21	Peru-Brazil Region	2015/11/24	22:45:38	-10.54	-70.94	118.79	617	7.5	16.6

460 **3.3 Data processing**

461 Seismic observations acquired from the RER station are deconvolved with the instru-
 462 ment response of the receiver before being subjected to further processing. Hereafter, the
 463 north and east horizontal components seismograms are rotated respectively along and per-
 464 pendicular to the great circle path into their radial and transverse components in order to
 465 separate the P-SV waves from SH waves.

Both the synthetics and seismic observations are subjected to a band-pass filter, exploring upper corner frequencies of 0.05 Hz to 0.2 Hz (i.e. lowest periods of 20 s to 5 s) with a lower bound kept constant at 0.01 Hz (i.e. 100 s). At frequencies beyond 0.2 Hz the automated cross-correlation algorithm that compares wave arrivals becomes unstable due to increasing discrepancies related to short-wavelength structure. This automated comparison between synthetic and observed data is set up through automated phase picking and time window selection. The cross-correlation time window is chosen based on three factors: i) the maximum band-pass frequency, where the smallest wavelength is determined through Nyquist theorem; ii) windowing range is set to be a quarter of the dominant period; and iii) a trailing window to account for variation throughout all source events. The precursor is essential to capture a length of flat signal foregoing the phase arrival, which significantly improves distinction between the phase arrival and any arbitrary sinusoidal signal. The trailing windows have been empirically set to 10 s for P-waves, 20 s for S-waves, and are predominantly required to account for variation in wavelengths between source events and waveform widening caused by high melt models.

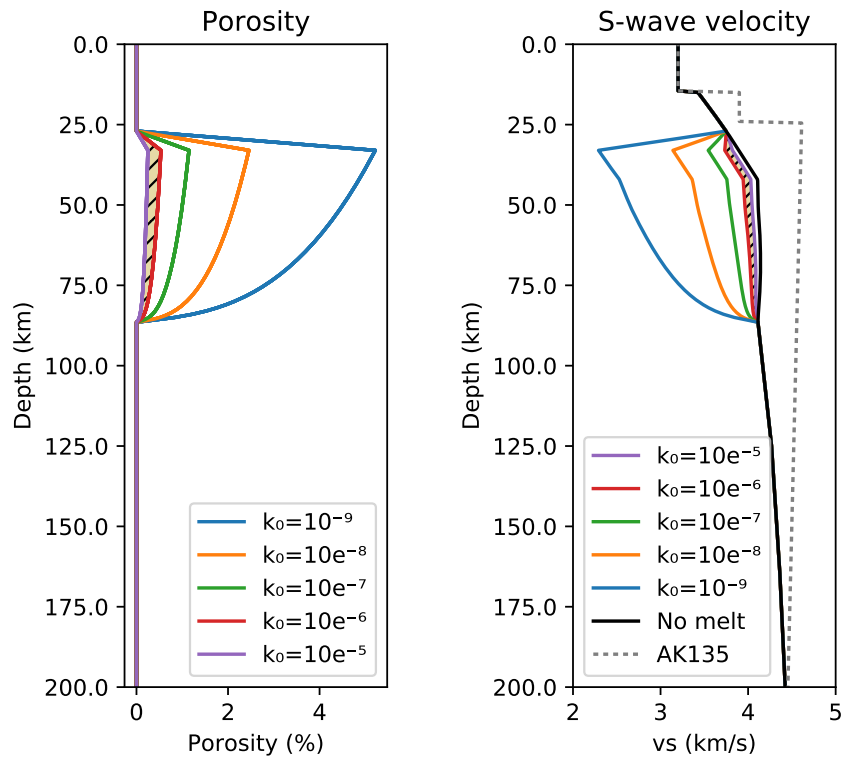
Phase picking is initiated through TauP method [Buland and Chapman, 1983; Crotwell et al., 1999], in order to compute theoretical travel time arrivals for each seismic phase for a given earth model. TauP enables us to center the cross-correlation time window on a given phase of the *ak135* synthetic trace. We proceed to find the time shift between this phase in *ak135* and the presumed phase arrival in the data traces and all synthetic model traces by cross-correlating the two traces. The time-shift is used to shift the cross-correlation window to the phase arrivals for each seismic and synthetic trace, allowing for comparison of phase arrivals between data and models in order to find seismic travel time delay $t_{P,S}^{\text{shift}}$. We compute the differential travel time between the P and S arrival for both the observed seismic trace and synthetic trace, and define the residual between the two as $t_{S-P}^{\text{obs,syn}}$. Since melt affects seismic velocity reduction for P and S waves differently, matching the inter-phase differential travel time of the observed waveforms with the models can help to put a constraint on porosity. Although phase arrivals vary in time with source depth and epicentral distance, we find that relative time travel differences between synthetic and observed traces, such as $t_{P,S}^{\text{shift}}$ and $t_{S-P}^{\text{obs,syn}}$, are insensitive to varying source depth between 300-700 km and are virtually unaffected by changes in epicentral distance at the offsets used in this study (~0.001-0.01 s decrease per degree).

498 **4 Results**499 **4.1 1D melting model**

500 **Figure 3.** The geodynamic model scenarios considered in this study are represented by scatterpoints for
 501 each combination of the free parameters $k_0 = 10^{-9}-10^{-5} \text{ m}^2$, $T_0 = 1250-1500 \text{ }^\circ\text{C}$ and $\bar{v} = 10 - 70 \text{ mm yr}^{-1}$,
 502 giving a total of 210 model scenarios. The mean porosity for each model scenario is illustrated by both scatter
 503 color and size.

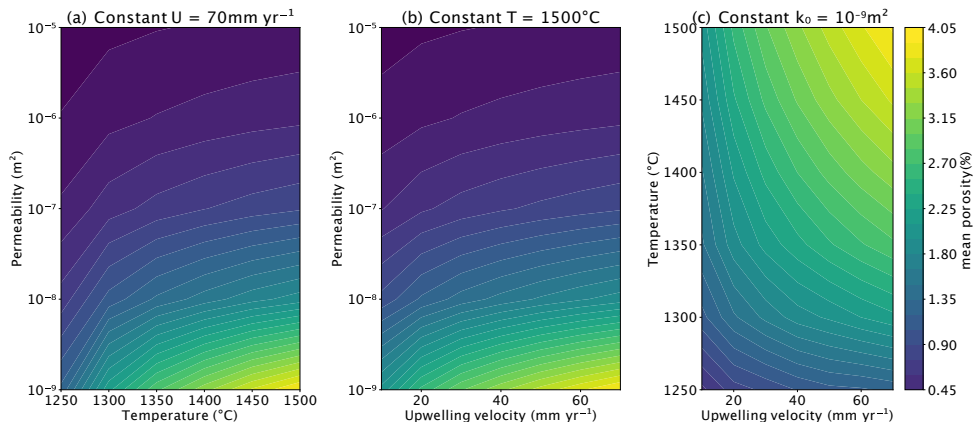
511 The melting model calculates porosity and the depth profile of temperature for all
 512 combinations of the free parameters explored in Figure 3, resulting in 210 geodynamic
 513 model scenarios. For each model scenario the model temperature, pressure and porosity
 514 as a function of depth are converted to seismic wave velocity according to section 2.3.
 515 Seismic wave velocities reduce gradually with reducing depth due to a general decrease
 516 in density and the increasing attenuation of the seismic wave due to temperature effects
 517 [Goes *et al.*, 2012]. At pressure-temperature conditions above the solidus the presence of
 518 melt reduces seismic wave velocity in line with the empirical velocity reduction taken
 519 from *Hammond and Humphreys* [2000]. As a result the models with lower permeabil-

Model scenarios: $T=1450\text{ }^{\circ}\text{C}$, $v=70\text{ mm/yr}$



504 **Figure 4.** Porosity and S-wave velocity as a function of depth for the range of permeability coefficients
 505 explored in figure 3, with temperature and the upwelling rate fixed at respectively $1450\text{ }^{\circ}\text{C}$ and 70 mm yr^{-1} .
 506 The velocity profile for the *ak135* reference model is shown in gray, and velocity profile for a model without
 507 melt is shown in black. The hashed area between the porosity and velocity profiles indicate the most probable
 508 model obtained during our “waveform filtering” inversions for the partial melting beneath Réunion island
 509 according to this study. At 30 km depth melt is assumed to leave the system, as here it is probable that the
 510 porous flow is no longer a valid assumption for the transport of melt.

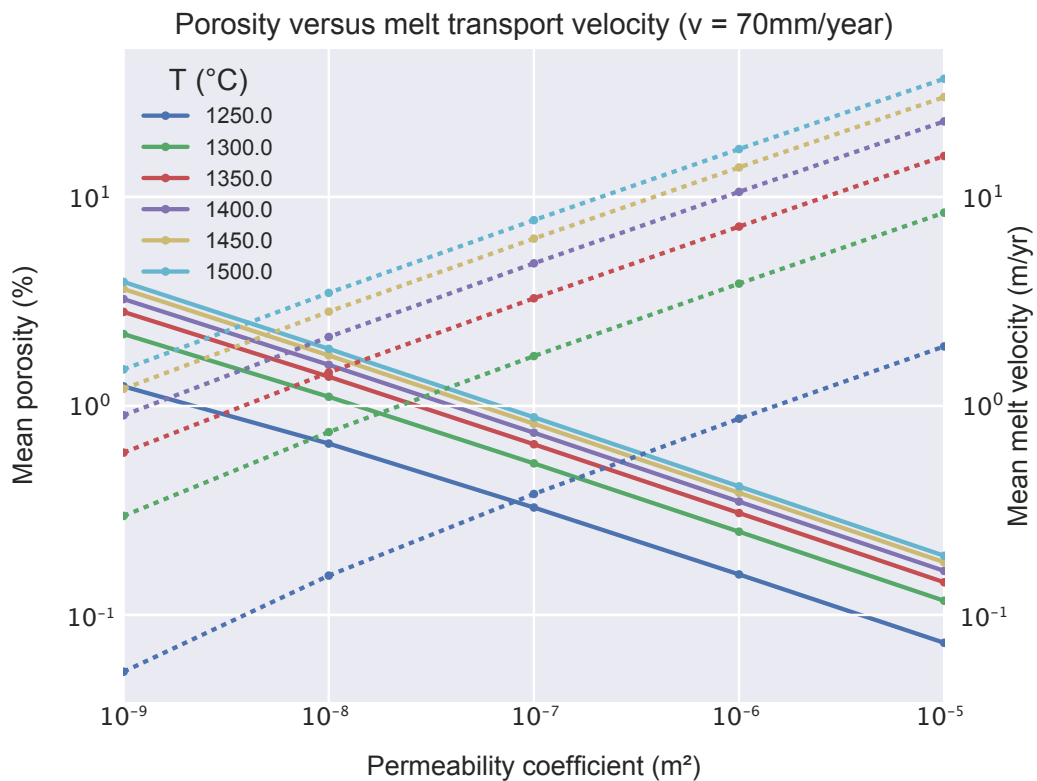
520 ity coefficients that create greater melt retention have a larger reduction in seismic wave
 521 velocity (Figure 4). We take an example case of a basal temperature of 1450 °C and up-
 522 welling rate of 70 mm yr⁻¹ to describe the modeled vertical porosity and the generated
 523 seismic velocity profiles (Figure 4). The depth of the initiation of melting is predomi-
 524 nantly controlled by temperature, and lies at roughly 85 km if the basal temperature is
 525 fixed at 1450 °C. Lower temperatures will yield a shallower onset of melting. Depend-
 526 ing on the assumed permeability, the onset of melting can be marked by a sharp increase
 527 in porosity. In particular, if the permeability is low, say, when $k_0 = 10^{-9}$ m², a porosity
 528 greater than 2% can be rapidly achieved under these conditions (Figure 4). This is equiva-
 529 lent to a permeability of 8×10^{-15} m² in eq. 8. At the other end of spectrum, if we assume
 530 a high permeability $k_0 = 10^{-5}$ m², porosity is between 0.1 and 0.5%, which means that
 531 permeability is between 10^{-14} m² and 10^{-12} m². This range of permeability is within the
 532 range or higher than those experimentally observed in high-temperature high-pressure ex-
 533 periments (e.g. 10^{-16} m² for a porosity of 2% [Miller *et al.*, 2014] or 10^{-14} m² for a poros-
 534 ity of 5% [Connolly *et al.*, 2009]).



535 **Figure 5.** Development of porosity over full range of input parameters k_0 , T and \bar{v} . (a) Temperature
 536 vs. permeability coefficient at a constant upwelling velocity of 70 mm yr⁻¹. (b) Upwelling velocity vs. per-
 537 meability coefficient at a constant temperature of 1500 °C. (c) Upwelling velocity vs. temperature at a con-
 538 stant permeability coefficient of 10^{-9} m².

539 If we compare the mean porosity from the range of input parameters, we find that
 540 in general the assumed permeability coefficient has the most dominant role in controlling
 541 retained melt volumes, over initial temperature and upwelling velocity (Figure 5). The lat-
 542 ter two parameters appear to have an approximately linear effect on melt porosity, with

543 temperature being the more controlling parameter of the two, according to the contour
 544 gradients between Figure 5a and 5b, and the dominating horizontal trend in Figure 5c.
 545 We observe a slight increased melt production gradient with temperature from slight nar-
 546 rowing in vertical contour spacing in Figure 5a. However, change in porosity is largely
 547 driven by permeability coefficient. The smaller the permeability coefficient, the larger the
 548 porosity, which can be found in narrowing of the contours in Figure 5a and 5b.



549 **Figure 6.** Logarithmic plot of the variation in modeled porosity (solid) and melt flow velocity (dashed) with
 550 permeability coefficient and temperature, with upwelling velocity constant at 70 mm yr^{-1} . The relationship
 551 between porosity and mean melt flow velocity is inversely proportional as a function of the permeability
 552 coefficient, and proportional as a function of temperature.

553 Over the tested permeability range the mean porosity ranges from 3.92% at the min-
 554 imum permeability case to 0.03% at the maximum permeability case (Figure 6). The
 555 minimum and maximum mean melt transport velocity values over our input range are
 556 respectively 0.011 m yr^{-1} at minimum permeability and temperature, and 36.77 m yr^{-1}
 557 at maximum permeability and temperature, with a local velocity maximum peaking at

558 90.98 m yr⁻¹ for the maximum. Melt flow velocity is inversely proportional to melt porosity as a function of k_0 (Figure 6; *Weatherley and Katz* [2016]). This is because the increased connectivity enhances the flow of melt, allowing for higher melt flow velocities.
 559
 560
 561 Melt is extracted and transported to the surface more rapidly, resulting in a lower retention of melt at the onset of melting. Hence, more efficient removal of melt avoids melt
 562 accumulation, decreasing maximum porosity with the increase of permeability. U-series
 563 disequilibrium studies constrain melt flow velocities at $\sim 20 - 50$ m yr⁻¹ from short lived
 564 ^{266}Ra excesses [*Elliott and Spiegelman*, 2003; *Stracke et al.*, 2006]. Melt velocities of such
 565 magnitude point towards high permeability coefficients ($k_0 = 10^{-6} - 10^{-5}$ m²), which
 566 would mean low melt porosity below 0.3% and permeability of 10⁻¹⁴ m².
 567

568 4.2 Synthetic Seismograms

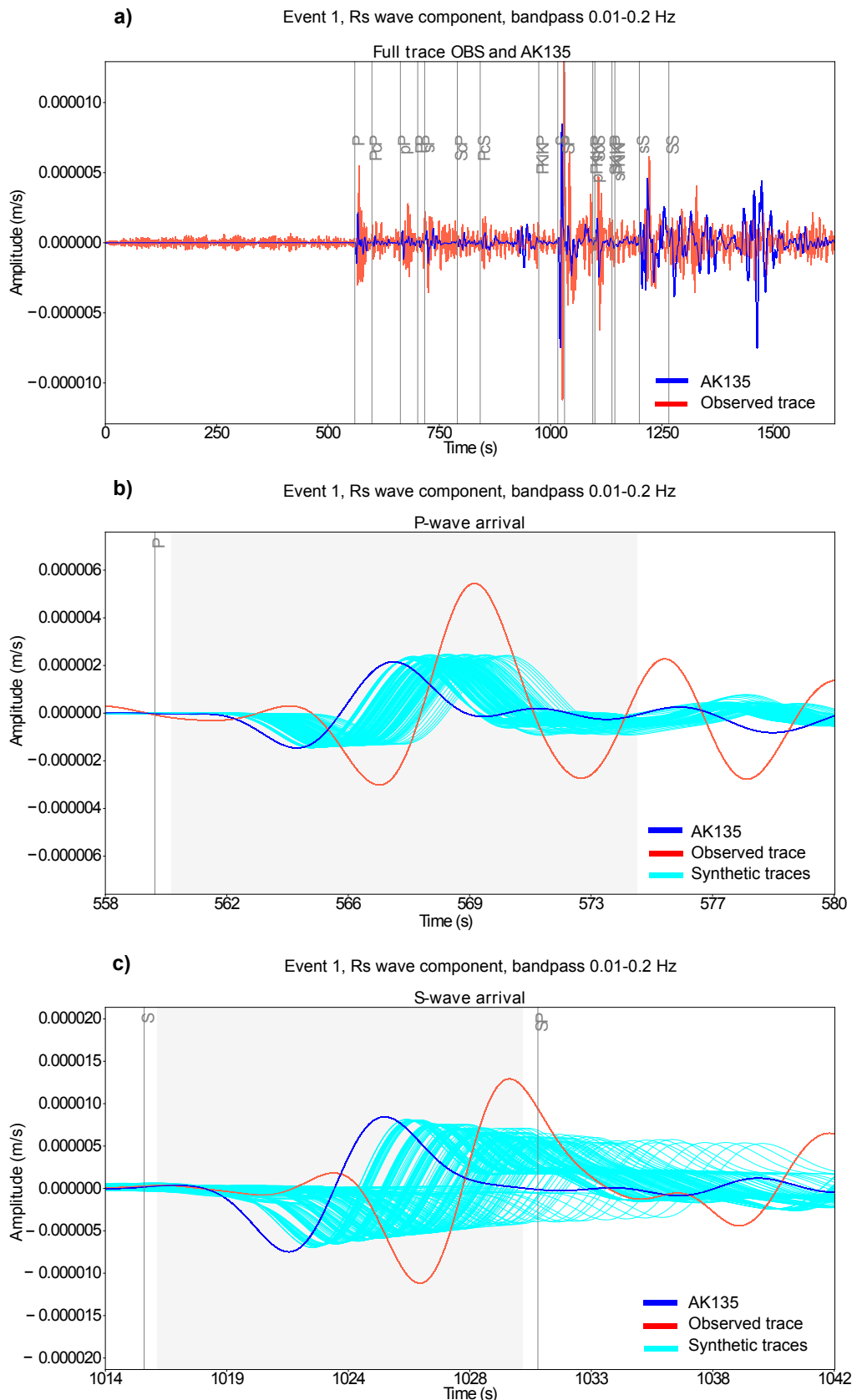
569 For all 21 source events listed in Table 2 we generate synthetic seismograms. The
 570 source adopts the moment tensor of the respective event and is propagated through the
 571 range of 1D models for the different mantle temperatures, upwelling velocities, and per-
 572 meability coefficients, resulting in 210 sets of seismograms per source event (recall Fig-
 573 ure 5). The synthetics are convolved with the source-time function of their respective
 574 source event, since DSM uses a delta function as its moment-rate function. Source-time
 575 functions for each source event were acquired through the SCARDEC source time func-
 576 tions database [*Vallée and Douet*, 2016]. Convolution with the source-time function will
 577 adjust phase arrivals in time. For source events with a half-duration time higher than the
 578 band-pass filtering frequency period, convolution with the source-time function will be
 579 especially important for accurate prediction of the observed waveforms.

580 In the upcoming synthetic waveform analysis we focus on the P-wave and S-wave
 581 arrivals or the Pdiff and SKS phase arrivals, depending on the epicentral distance of the
 582 respective event. The epicentral distances between sources and receiver range from 60 de-
 583 grees to 120 degrees. At epicentral distances beyond 100 degrees P-waves are no longer
 584 direct, but begin to diffract along the core-mantle boundary and are registered as a Pdiff
 585 phase. Similarly, S-waves are also no longer direct beyond a 100 degrees epicentral dis-
 586 tance as well, however we find that in the epicentral distance range of 100-120 degrees
 587 the SKS phase experiences less interference with other phases and has higher amplitude
 588 arrivals than the Sdiff phase for source events at 300-700 km depth.

589 During synthetic waveform analysis we investigate four different frequency bands.
 590 Waveforms are band-pass filtered from 0.01 Hz to upper limits of 0.05 Hz, 0.1 Hz, 0.15 Hz
 591 and 0.2 Hz.

597 For each considered event, phase arrival and wave component, the 210 synthetic
 598 models (Figure 7) are cross-correlated with the seismic observation to find the time shift
 599 between the two traces. Travel time delay $t_{P,S}^{\text{shift}}$ of the model with the observation is plot-
 600 ted against the inter-phase differential travel time $t_{S-P}^{\text{obs,syn}}$ in order to constrain model sce-
 601 narios in time (Figure 8). In most cases, the travel time delay and differential travel time
 602 do not line up at 0 simultaneously, giving a range of likely model scenarios in between
 603 $|t_{S-P}^{\text{obs,syn}}|$ at $t_{P,S}^{\text{shift}} = 0$, and $|t_{P,S}^{\text{shift}}|$ at $t_{S-P}^{\text{obs,syn}} = 0$. We define the best-fit models for a given
 604 phase arrival by simultaneously minimizing $|t_{P,S}^{\text{shift}}|$ and $|t_{S-P}^{\text{obs,syn}}|$ through minimizing the
 605 combined quadratic mean (RMS) of the two variables (Figure 8). The RMS will be min-
 606 imal for instances where $|t_{P,S}^{\text{shift}}|$ and $|t_{S-P}^{\text{obs,syn}}|$ are equal, which is preferable since the two
 607 variables are inherently coupled, where the inability to match one of them is related to the
 608 other.

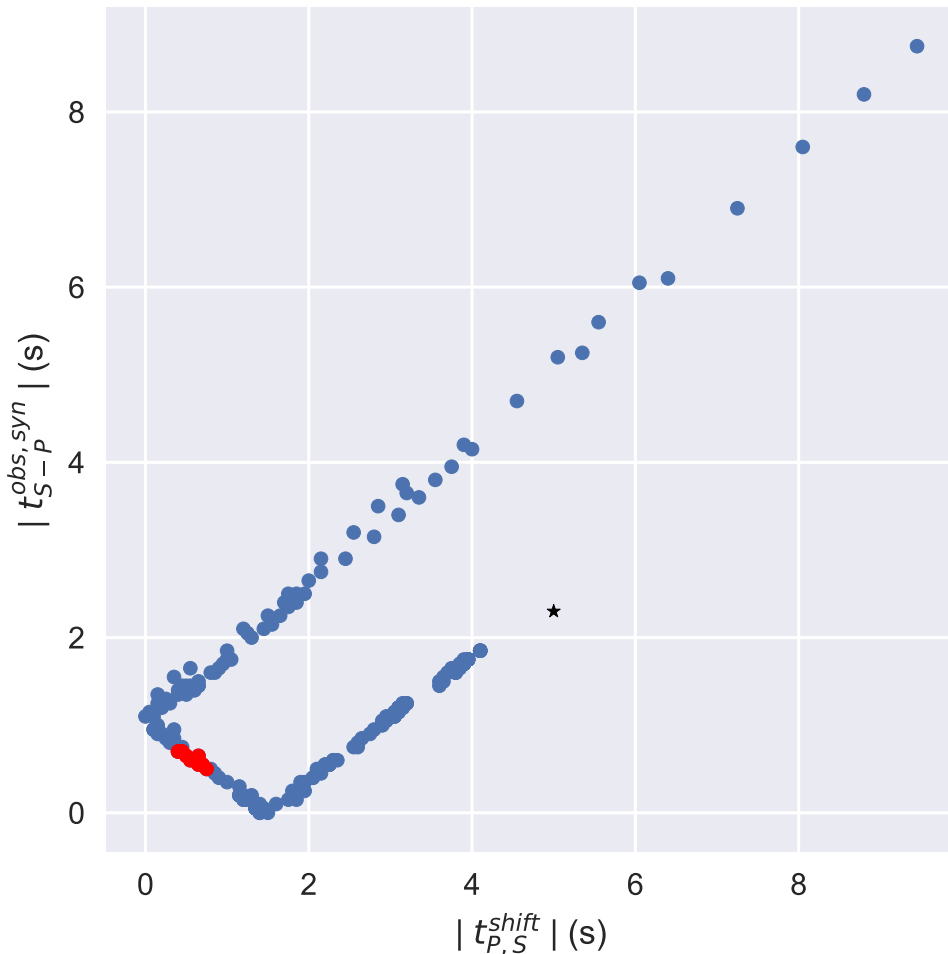
612 Additional quality checking was conducted during the picking of best-fit model sce-
 613 narios among all sets of events, phases, components and band-pass filter bandwidths. Sets
 614 are removed if the models deviate from the expected pattern displayed (red points in Fig-
 615 ure 8), which means that cross correlation between observation and models has failed to
 616 identify the correct arrival. Automated cross correlation of seismic phases is a sensitive
 617 process that is prone to failure if the circumstances are not close to ideal. If the observed
 618 signal does not possess a high signal-to-noise ratio, clear and high amplitude phase ar-
 619 rivals, a distinct source-time function and all together a high similarity with the synthetic
 620 trace, cross-correlation is not guaranteed to work accurately. Cross-correlations at band-
 621 pass filter bandwidths of 0.01 – 0.05Hz performed poorly and were omitted in their en-
 622 tirety, whereas cross-correlations for the other frequency bands tend to improve with in-
 623 creasing frequency. From the initial 21 source events only 12 events passed the quality
 624 check. A majority of the excluded sources are high offset events with epicentral distances
 625 greater than 110°.



592 **Figure 7.** a) Seismogram containing the radial components of the full synthetic waveform generated for
 593 *ak135* base model (blue) and the observed seismic trace (red) for event 1, band-pass filtered from 0.01 to
 594 0.2Hz. b) A close-up of the P-wave arrival of trace presented in a), with the additional 210 synthetic traces
 595 (light blue) generated for our melting models. The gray zone represents the automated cross-correlation
 596 window used to find the time shift with the observed trace. c) The equivalent of b) for the S-wave arrival.
 -27-

Relative travel times between observed and synthetic traces

Event 1: S-wave Rs component

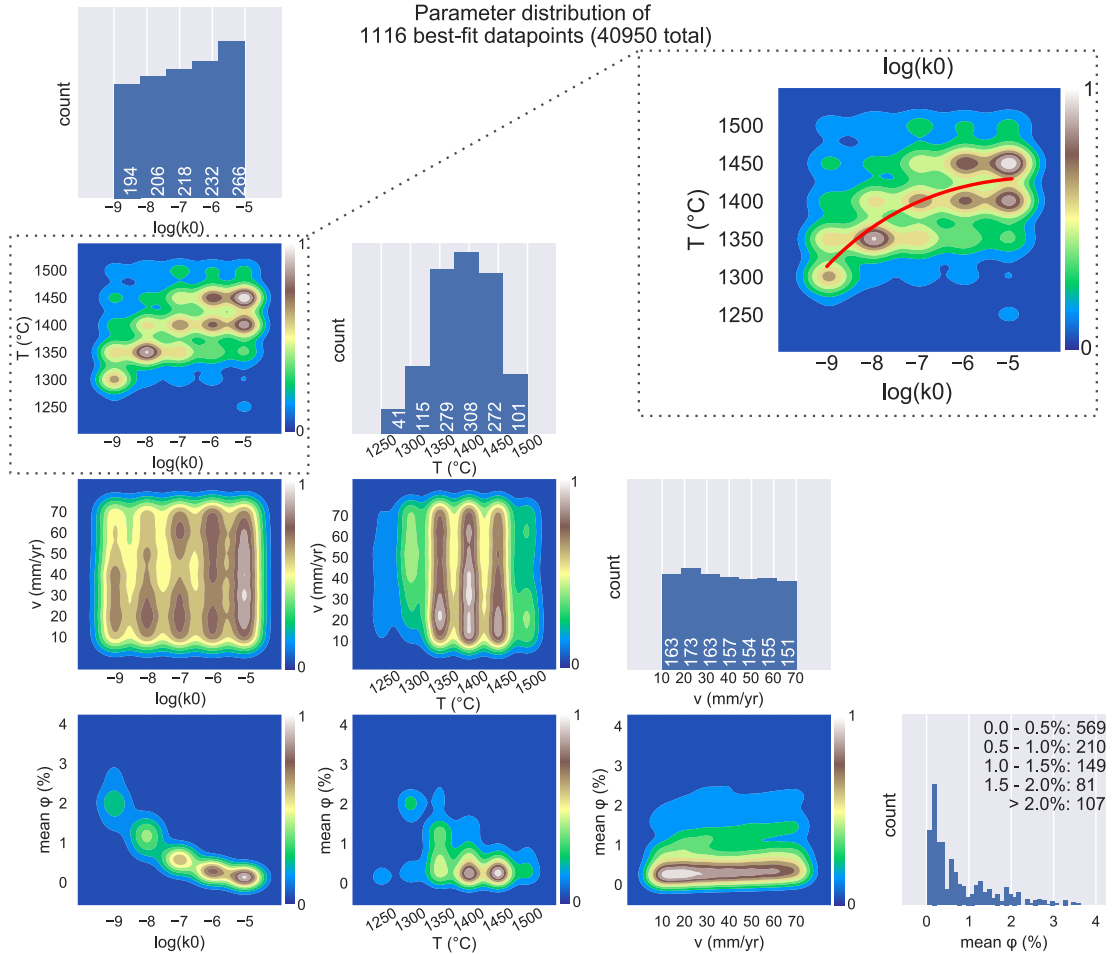


609 **Figure 8.** Plotting the absolute value of the travel time delay $|t_{P,S}^{\text{shift}}|$ versus the absolute value of the differ-
 610 ential travel time $|t_{S-P}^{\text{obs,syn}}|$ for the radial component of the S-wave arrival from the Bali Sea earthquake. Best
 611 fit models by minimized RMS are displayed in red, whereas results for *ak135* are presented by a black star.

626 4.3 Comparison against seismological observations

627 In order to discover which modeled melting scenario describes the upper mantle be-
 628 low Réunion most adequately, we will analyze the distribution of best-fit scenarios among
 629 the free model parameters k_0 , T and \bar{v} for the remaining source events that passed quality
 630 checking. The best fit conditions are, however, non unique solutions, since the porosity we
 631 aim to constrain is a function of all three input parameters. Certain trade-offs between k_0 ,
 632 T and \bar{v} will have the same outcome in porosity.

643 By cross-correlating synthetic traces for 210 model scenarios with the seismic ob-
 644 servation for 12 source events, compiled for 4 phase arrivals (P, S, Pdiff, SKS), 3 wave
 645 components (Rs, Ts, Zs) and all the band-pass filter frequencies (upper corner frequencies
 646 of 0.05, 0.1, 0.15 and 0.2 Hz) we conducted a total 70,896 synthetic to observed phase
 647 comparisons, of which we consider 40,950 cases where cross-correlation between phases
 648 was successful. From these 40,950 cases there were 1116 best matches in time between
 649 observed and synthetic waveforms, which form a distribution around the most probable
 650 model scenario to describe the upper mantle beneath Réunion among the 210 model sce-
 651 narios. The changes in porosity caused by alterations in upwelling velocity are too in-
 652 significant to constrain a specific value of \bar{v} , and all values of \bar{v} are equally represented for
 653 the entire range of temperatures and permeability coefficients (Figure 9). The results indi-
 654 cate that most best-fit scenarios are covered by the temperature range of 1350 – 1450 °C.
 655 There is a gradual preference to higher permeabilities, although all permeability coeffi-
 656 cients are covered. That is because the time delay is a product of melt, which is largely
 657 controlled by the permeability coefficient, and the intrinsic anelasticity that increases with
 658 temperature. For each permeability there is a temperature counterpart which will result in
 659 a similar travel time delay. High temperatures are coupled with high permeability coeffi-
 660 cients, where the travel time delay is dominated by temperature attenuation. On the other
 661 hand there are the melt dominated cases where low temperatures are coupled with low
 662 permeabilities. The $T-k_0$ relationship in Figure 9 suggests that permeability coefficients of
 663 $k_0 = 10^{-9} \text{ m}^2$ are generally coupled with $T = 1300 \text{ }^\circ\text{C}$, $k_0 = 10^{-8} \text{ m}^2$ with $T = 1350 \text{ }^\circ\text{C}$,
 664 $k_0 = 10^{-7} \text{ m}^2$ with $T = 1350 - 1400 \text{ }^\circ\text{C}$, $k_0 = 10^{-6} \text{ m}^2$ with $T = 1400 - 1450 \text{ }^\circ\text{C}$ and
 665 $k_0 = 10^{-5} \text{ m}^2$ also with $T = 1400 - 1450 \text{ }^\circ\text{C}$. At higher permeabilities the tempera-
 666 ture regimes become indistinguishable because the melt percentages are so low that the
 667 travel time delay is dominated by the effect of temperature. These five clusters make up
 668 the possible conditions in the upper mantle below Réunion that can explain our chosen set



633 **Figure 9.** Pair grid plot displaying the distribution of permeability coefficient k_0 , basal temperature T ,
 634 upwelling velocity \bar{v} and mean melt porosity ϕ among the 1116 best-fit traveltimes options out of 40950 data
 635 points (2.7% of the dataset with highest fit). Histograms on the diagonal count the representation of values for
 636 the variables k_0 , T , \bar{v} and ϕ among 1116 data points that have minimized $t_{P,S}^{\text{shift}}$ and $t_{S-P}^{\text{obs,syn}}$ with the observed
 637 traces. The off-diagonals show contour plots setting each of the input variables against each other, highlighting
 638 certain values within variable pairings that give a minimized solution to matching seismic travel times.
 639 The color scale shows relative density between minimum count and maximum count of the values for the
 640 variables in question, indicating which combination of values for any two variables are most likely to give a
 641 best-fit solution. Plotting temperature versus permeability coefficient shows the relationship between T and k_0
 642 in red for which relative travel times are minimized.

of seismic observations. The mean melt porosity for each cluster is with increasing permeability coefficient respectively 1.88%, 1.11%, 0.58%, 0.29% and 0.13%. Depending on the upper mantle temperature each of these melt scenarios is a viable solution. The data suggests the most likely temperature is 1400 – 1450 °C, based on the combined number of matches with $k_0 = 10^{-5} – 10^{-6}\text{m}^2$ with respect to the number of other matches. Secondly, the mean travel time delay and mean differential travel time for each cluster is minimal for $k_0 = 10^{-6} – 10^{-5}\text{m}^2$ at $t_{P,S}^{\text{shift}} = 0.06 \pm 0.51\text{ s}$ and $t_{S-P}^{\text{obs,syn}} = -0.20 \pm 0.46\text{ s}$, supporting a mantle temperature of $T = 1400 – 1450\text{ }^\circ\text{C}$. Under these conditions we can expect porosity of maximum 0.28.

5 Discussion

In this study, we proposed a series of forward modeling from geodynamical modeling to seismic waveform computation (eq. A.8). Instead of collecting a big dataset, we first settled the geodynamical parameters to explore (eq. 2). The consequences are that we were able to generate seismological models $C_D^S \circ \mathcal{D}\mathbf{m}$ that are geodynamically consistent. Hereafter, we discuss our results in detail.

The data suggest that the most likely temperature conditions in the upper mantle beneath Réunion are $T = 1400 – 1450\text{ }^\circ\text{C}$, with permeability coefficients in the range of $k_0 = 10^{-5} – 10^{-6}\text{m}^2$. Equally minimizing $t_{P,S}^{\text{shift}}$ and $t_{S-P}^{\text{obs,syn}}$ through RMS has corrected for not being able to solve for the relative arrivals of the P- and S-waves, and the position in time of the entire wave packet simultaneously. This gives more distinction in the temperature space, while losing some contrast along the permeability coefficients, because the effect of temperature on P and S wave velocities is close to linear and therefore has little effect on inter-phase differential travel times. This makes it a better measure of the position in time of the wave packet as a whole. If, on the other hand, we put 100% weight on $t_{S-P}^{\text{obs,syn}}$ then we lose some constraint on fitting the entire wave packet in time, but tighten the constraints on the relative travel time difference between phase arrivals. This in turn gives better distinction along the k_0 range at the expense of T , because predominantly the permeability coefficient controls inter-phase differential travel times. Both cases emphasize the favored scenarios of $T = 1400 – 1450\text{ }^\circ\text{C}$ and $k_0 = 10^{-5} – 10^{-6}\text{m}^2$. Regardless of the weighting used for $t_{P,S}^{\text{shift}}$ and $t_{S-P}^{\text{obs,syn}}$ during the minimization process of the best-fit scenarios, the outcome remains robust despite slight redistribution of high temperatures and permeabilities.

Our predicted values for temperatures of $T = 1400 - 1450^\circ\text{C}$ approach potential mantle temperatures for the lower end of MgO values suggested for primary magmas from Réunion (16% *wt*) at 1440–1480 °C, according to calculations from the MELTS numerical algorithm [Ghiorso and Sack, 1995; Asimow *et al.*, 2001] and formulations of upper mantle potential temperatures [Herzberg *et al.*, 2007]. Temperature estimates from this study appear slightly too low to explain the full range of MgO values of up to 20% *wt* deduced from the Réunion transitional series, which indicate source temperatures up to 1650 °C [Sobolev and Nikogosian, 1994]. However, this could be the result of the idealized melt microstructures adopted in our models. When performing parameter conversion we assume a uniform network of organized cuspate melt pockets that induce maximum seismic velocity reduction per percent melt, respectively 3.6% and 7.9% for P and S waves in relaxed conditions [Hammond and Humphreys, 2000]. Other melt pocket geometries, such as ellipsoidal or tubular shaped pore spaces, sustain lower velocity reductions per percent melt, namely 2.1% and 4.3% for the former, and 1.2% and 2.7% for the latter for the P and S waves. If we consider a non-uniformly distributed combination of pore geometries instead, we can expect overall a slightly lower effect of melt porosity on seismic velocity reduction. As a consequence the best-fit scenarios will overcompensate either by reducing the permeability coefficient or increasing temperature to attain a minimized travel time delay. This will cause greater polarization across the potential scenarios between the low porosity (high T and k_0) and high porosity (low T and k_0) cases, for which we have better constraints for high temperature.

For the predicted temperature values the onset of melting is at 74.7–86.0 km depth for respectively $T = 1400 - 1450^\circ\text{C}$. This corresponds to a 60–90 km source depth for ultramafic melt that is proposed as origin of the ~2 km thick underplated body observed at the base of the crust (Richards, 2013), and possibly aligns with depth of the LAB [Fontaine *et al.*, 2015].

Values for the permeability coefficient predicted from the results for the upper mantle beneath Réunion are $k_0 = 10^{-6} - 10^{-5}\text{m}^2$, which translate to upper mantle permeabilities of $10^{-14} - 10^{-12}\text{m}^2$ calculated for a porosity range of 0.13 – 0.28%. Coefficients of 10^{-6}m^2 on average result in marginally better matches in time with the seismic observations, and are more in line with experimental results of permeability in high-temperature high-pressure environments, at coefficients of $2 \times 10^{-16}\text{m}^2$ to $5 \times 10^{-13}\text{m}^2$ for porosity between 0.02 – 0.2 [Connolly *et al.*, 2009]. The mean melt transportation velocity values

range in between $8.37 - 18.35 \text{ m yr}^{-1}$ for coefficients of respectively $k_0 = 10^{-6} - 10^{-5} \text{ m}^2$, approaching the lower melt flow rates of 20 m yr^{-1} suggested by Uranium isotope migration rates [Elliott and Spiegelman, 2003; Stracke *et al.*, 2006]. The model melt flow velocity could be higher if opting for a lower exponent n in the permeability-porosity relationship, where values down to 2 are within the accepted range for grain geometries in the upper mantle [Goes *et al.*, 2012; Zhu and Hirth, 2003]. By doing so the predicted permeabilities will decrease to $10^{-13} - 10^{-11} \text{ m}^2$ for $n = 2$, diverging from the earlier constraints put on permeability and only conceivable for coefficients of 10^{-6} m^2 .

Across all source events the mean travel time difference and differential travel time for the best-fit model scenarios with $T = 1400 - 1450^\circ\text{C}$ and $k_0 = 10^{-5} - 10^{-6} \text{ m}^2$ are $t_{P,S}^{\text{shift}} = 0.06 \pm 0.51 \text{ s}$ and $t_{S-P}^{\text{obs,syn}} = -0.20 \pm 0.46 \text{ s}$, since within the majority of source events $t_{P,S}^{\text{shift}}$ and $t_{S-P}^{\text{obs,syn}}$ do not simultaneously converge to 0 s. Overall the synthetic phase arrival is slightly too early (i.e. $t_{P,S}^{\text{shift}}$ is positive) with respect to the observed and therefore the inter-phase differential travel time is slightly wider (i.e. $t_{S-P}^{\text{obs,syn}}$ is negative). Adopting a less idealized melt microstructure network will improve convergence towards 0 s, as it will slightly reduce the P-to-S velocity reduction ratio induced by melt, and therefore reduce relative phase arrivals of compressional versus transverse waves. This relies on the assumption that the *ak135* reference model adequately approximates the geodynamical properties of the earth on a global scale, and that the slight travel time discrepancy is a result of our presumptions on the modeled effect of melt on seismic wave propagation. It is likely that along each raypath for the studied source events there are velocity anomalies with respect to the *ak135* reference model, that are captured in our results through the misalignment in the $t_{P,S}^{\text{shift}} - t_{S-P}^{\text{obs,syn}}$ relationship (Figure 8). The nature of the ratio between $|t_{P,S}^{\text{shift}}|$ at $t_{S-P}^{\text{obs,syn}} = 0$ and $|t_{S-P}^{\text{obs,syn}}|$ at $t_{P,S}^{\text{shift}} = 0 \text{ s}$ for each source event could tell something about the cause and magnitude of the velocity anomalies along the raypath. Furthermore, differences between the radial, transverse and vertical seismic wave components could give insights on anisotropy within the velocity anomalies. When $t_{S-P}^{\text{obs,syn}}$ does not converge to 0 s it suggests that relative velocities between P- and S-waves are altered through any other means than melt presence as defined in this study. Local scale heterogeneities such as lattice-preferred orientation of melt flow, shape preferred orientation of the pore geometry, crystalline anisotropy, or the presence of volatiles in the upper mantle could be relevant if there is notable heterogeneity along the raypaths between different seismic phases at seismic resolutions. When $t_{P,S}^{\text{shift}}$ does not converge to 0 s it indicates

767 that the wave packet as a whole is either early or late with respect to the observations,
 768 and could hint at large scale heterogeneities along the raypaths such as large low-shear-
 769 velocity provinces (LLSVP), ultra-low velocity zone (ULVZ) or mantle plumes. The gen-
 770 eral early phase arrival from the best-fit conditions could indicate a higher expected ve-
 771 locity anomaly from the Réunion mantle plume than modeled, but to identify the source
 772 would require extensive comparisons with tomographic cross-sections along the raypaths
 773 for each source event.

774 6 Conclusion

775 In this study, we proposed a series of forward modeling in geodynamics and seis-
 776 mology in order to understand the direct link between the geodynamical parameters and
 777 seismic observation. We developed a partial melting model for the upper mantle in order
 778 to model melt porosity for 210 different combinations of permeability coefficients, tem-
 779 perature and upwelling velocity. For each model scenario synthetic seismograms were
 780 generated for 21 source events using the Direct Solution method with the *ak135* refer-
 781 ence model as base model for global wave propagation. Analysis of travel time delay and
 782 inter-phase differential travel time of P, Pdiff, S and SKS phase arrivals between synthetic
 783 waveforms and observed traces recorded at the RER GEOSCOPE receiver at Réunion al-
 784 lows us to statistically constrain several local geodynamic conditions in the upper man-
 785 tle. Our results indicate that we are unable to constrain upwelling velocity, but are able
 786 to constrain the most probable combination of temperature and permeability coefficient
 787 at $T = 1400 - 1450^{\circ}\text{C}$ and $k_0 = 10^{-5} - 10^{-6} \text{ m}^2$, which appear consistent with studies
 788 of potential mantle temperature based on MgO content. The proposed high permeabili-
 789 ties promote high rates of melt extraction at $8.37 - 18.35 \text{ m yr}^{-1}$, which is in accordance
 790 with results from Uranium isotope migration studies. Furthermore, from these predicted
 791 conditions follows that the onset of melting in the upper mantle beneath Réunion lies in
 792 between 74.7 – 86.0 km depth and most importantly that melt porosity does not exceed
 793 0.28 %.

794 Low velocity zones in the shallow upper mantle can be explained by a combina-
 795 tion of relatively high mantle temperatures and low percentages of melt retention, which
 796 go hand in hand with rapid melt extraction as a result of high permeability conditions in
 797 the melting zone. The results are able to satisfy prevalent geodynamical and geochemi-
 798 cal predictions of low melt retention and high melt flow rate, while simultaneously ade-

799 quately accounting for seismic data. We found that differences between travel time delay
800 and inter-phase differential travel time of the synthetic traces versus the observed wave-
801 forms can indicate velocity anomalies along the raypath with respect to the base model,
802 and could potentially tell something about their nature.

803 **Acknowledgments**

804 This work was funded by the ANR grant Interrift. Numerical computations were partly
805 performed on the S-CAPAD platform, IPGP, France. We acknowledge IRIS (Incorporated
806 Research Institutions for Seismology) data center for RER station data (<https://doi.org/10.7914/SN/IU>).
807 We also would like to thank Lapo Boschi, Saskia Goes, two anonymous reviewers and the
808 editors for their constructive comments. This is IPGP contribution XXXXX.

809 **A: Appendix: Inverse vs forward problems in geoscience**

810 A conceptual representation of the classical method for exploration of the Earth's
 811 interior inherent to inversion procedures could be written as follows:

$$\mathbf{m}_{\text{inv}} = \mathcal{D}^\dagger \circ C_S^D \circ (\mathcal{F}_{\text{comp}} \circ \mathcal{S})^\dagger \circ \mathcal{F}_{\text{obs}}(\mathbf{d}) \quad (\text{A.1})$$

812 where \mathbf{m}_{inv} is a vector of estimated geodynamical model parameters that we look for, \mathbf{d} a
 813 vector of seismic observed waveforms, with \mathcal{D} the geodynamical modeling operator, C_S^D
 814 parameter conversion operators from petrology to seismology, \mathcal{S} the seismic wave propa-
 815 gation operators and $\mathcal{F}_{\text{comp}}$ and \mathcal{F}_{obs} the seismic data processing operators applied to (or
 816 embedded in) computed data and observed data, respectively. All the operators above are
 817 essentially non-linear in nature (occasionally linear, especially the seismic modeling op-
 818 erator $\mathcal{F}_{\text{comp}} \circ \mathcal{S}$). † denotes “general inverse” of those operators. The reason why we
 819 precise the use of \mathcal{F} inside Eq. A.1 is our incapacity of modeling a whole series of seis-
 820 mic waveform data. When we measure only traveltimes $\mathcal{F}_{\text{obs}}(\mathbf{d})$ for instance, we use a
 821 linear Eikonal operator as $\mathcal{F}_{\text{comp}} \circ \mathcal{S}$. Indeed, due to the high frequency approximation of
 822 wave equations in Eikonal equation, $\mathcal{F}_{\text{comp}}$ can be different from \mathcal{F}_{obs} . Even wave-equation
 823 based expensive operators $\mathcal{F}_{\text{comp}} \circ \mathcal{S}$ [Komatitsch and Vilotte, 1998; Geller and Takeuchi,
 824 1998; Hasegawa *et al.*, 2018] are not an exception: the frequency contents and included
 825 physics will never meet the real Earth. Therefore, we have to (pre-)process the raw data \mathbf{d} .
 826 This discussion should be valid to some extent for other operators such as C and \mathcal{D} but
 827 for the simplicity we do not discuss it in this paper.

828 Eq. A.1 reads as follows:

- 829 (i) We collect the seismic raw waveforms \mathbf{d} from the existing stations.
- 830 (ii) We filter the waveforms, and/or picking traveltimes by cross-correlations or hand-
 831 picking of some phases of interest or surface-wave phase velocity picking, receiver
 832 function calculation, envelope calculation, or simply windowing of waveforms: we
 833 denote all the data processing symbolically as $\mathcal{F}_{\text{obs}}(\mathbf{d})$ to distinguish the raw wave-
 834 form data and the secondary seismic attributes to take into account.
- 835 (iii) Seismic inversion is then applied to the seismic attributes in order to infer the inner
 836 structure of the Earth in terms of density, (an)isotropic seismic velocity and seismic
 837 attenuation. This relies on the general inverse of forward modeling operators $\mathcal{F}_{\text{obs}} \circ$

838 \mathcal{S} regardless of which propagation effects (e.g. full waveform or Eikonal's equation
 839 for ray tracing, 1D or 3D) are considered. In seismology in general, we use some
 840 variations of quasi-Newton methods to linearize the inverse problem [Fuji *et al.*,
 841 2010; Konishi *et al.*, 2014; French and Romanowicz, 2015; Marjanović *et al.*, 2017;
 842 Xiao *et al.*, 2020].

- 843 (iv) Based on an understanding of petrology we can interpret the ensemble of seismic
 844 parameters as geodynamically meaningful parameters such as temperature and
 845 chemical anomaly inside the mantle. Look-up tables of C_S^D or C_D^S are produced
 846 based on either *in situ* experiments or numerical simulation in petrology such as
 847 first-principles *ab initio* calculations [Deschamps *et al.*, 2019; Konishi *et al.*, 2020].
- 848 (v) The geodynamicists can finally then seek the most probable scenario(s) of the Earth's
 849 inner evolution, mostly by trial-and-error forward modeling schemes and few by
 850 time-reversal or adjoint methods in geodynamics. Here, however, we denote this
 851 last step deliberately also as an inverse operator \mathcal{D}^\dagger since the aim is clearly to eval-
 852 uate the misfit of the geodynamical models to seismic tomographic "observation":

$$|\mathcal{D}(\mathbf{m}_{\text{inv}}) - C_S^D \circ \mathcal{S}^\dagger \circ \mathcal{F}_{\text{obs}}(\mathbf{d})|^\alpha \quad (\text{A.2})$$

853 with α a positive constant. We evaluate this misfit often in amplitude spectra or
 854 correlation domain [Steinberger and Torsvik, 2012]. Atkins *et al.* [2016] and Shah-
 855 nas *et al.* [2018] proposed a probabilistic inverse problem, by means of machine
 856 learning, to choose plausible scenarios \mathbf{m}_{inv} once we obtain tomographic "observa-
 857 tion" $C_S^D \circ \mathcal{S}^\dagger \circ \mathcal{F}_{\text{obs}}(\mathbf{d})$.

858 The workflow (eq. A.1) has been invaluable in geosciences since we have little data
 859 other than present-day seismological observation at seismic stations \mathbf{d} to infer the evolu-
 860 tion of the Earth's mantle \mathbf{m} . Statistical confidence of the seismic model $\mathcal{S}^\dagger \circ \mathcal{F}_{\text{obs}}(\mathbf{d})$ has
 861 increased not only due to the increasing number of seismic stations, including ocean bot-
 862 tom seismic arrays, but also due to the theoretical and numerical improvement of $\mathcal{F}_{\text{comp}} \circ \mathcal{S}$
 863 or a better estimation of $(\mathcal{F}_{\text{comp}} \circ \mathcal{S})^\dagger$.

864 The real data \mathbf{d} should be a function of the geodynamic parameters \mathbf{m}_{true} :

$$\mathbf{d} = \mathcal{S} \circ C_D^S \circ \mathcal{D}(\mathbf{m}_{\text{true}}), \quad (\text{A.3})$$

865 The “estimated” geodynamical parameters \mathbf{m}_{inv} are therefore “low resolution filtered” as
 866 follows:

$$\mathbf{m}_{\text{inv}} = \mathcal{D}^\dagger \circ C_S^D \circ \mathcal{S}^\dagger \circ \mathcal{F}_{\text{comp}}^\dagger \circ \mathcal{F}_{\text{obs}} \circ \mathcal{S} \circ C_D^S \circ \mathcal{D}(\mathbf{m}_{\text{true}}). \quad (\text{A.4})$$

867 When we consider only the seismic structure of the Earth’s interior, the resolution opera-
 868 tor,

$$\mathcal{R} = \mathcal{S}^\dagger \circ \mathcal{F}_{\text{comp}}^\dagger \circ \mathcal{F}_{\text{obs}} \circ \mathcal{S} \quad (\text{A.5})$$

869 is the same as the “seismic tomographic filter operator” proposed by [Ritsema *et al.*, 2007;
 870 Schuberth *et al.*, 2012; Koelemeijer *et al.*, 2018]. Evaluation of the “seismically filtered
 871 model”:

$$\mathbf{p} = \mathcal{R} \circ C_D^S \circ \mathcal{D}(\mathbf{m}) \quad (\text{A.6})$$

872 is interesting since it represents the sensitivity of our seismic tomographic model with
 873 respect to geodynamical model parameters.

874 Nevertheless, due to the non-linearity of each forward operator and the approxima-
 875 tions of its linearized inverse operator, it is difficult to quantitatively discuss the proba-
 876 bility of proposed Earth’s evolution scenarios. The only way to self-consistently answer
 877 this question is to directly model the full problem from first principles and compare the
 878 predicted data with the real data (eq. A.3), *i.e.* predict a self-consistent thermo-chemical
 879 structure, then predict the seismic properties and subsequently make a full comparison
 880 with the observation: the seismic signal received at the Earth’s surface. We must perform
 881 every procedure in a forward manner. This approach could be more powerful and objec-
 882 tive than a series of inversions (eq. A.1), in particular when we have concrete geodynami-
 883 cal parameters \mathbf{m} to look for.

884 Here in this paper, we propose to find the direct link between \mathbf{m} and \mathbf{d} by a series
 885 of forward modeling:

$$\mathbf{u} = \mathcal{S} \circ C_D^S \circ \mathcal{D}(\mathbf{m}) \quad (\text{A.7})$$

886 with \mathbf{u} the “seismically filtered waveform data” instead of “seismically filtered model”.
 887 Sensitivity analysis of \mathbf{u} as a function of \mathbf{m} is more straightforward than the evaluation of
 888 \mathbf{p} in eq. A.6. We then apply the \mathbf{u} with a new processing operator \mathcal{F} applied to synthetic
 889 and observed waveforms in order to compute the misfit function:

$$|\mathcal{F}(\mathbf{u}) - \mathcal{F}(\mathbf{d})|^\alpha = |\mathcal{F} \circ \mathcal{S} \circ C_D^S \circ \mathcal{D}(\mathbf{m}) - \mathcal{F}(\mathbf{d})|^\alpha. \quad (\text{A.8})$$

890 The workflow presented in A.8 is represented in Figure 1. As the direct comparison be-
891 tween \mathbf{d} and \mathbf{u} is hard to realize, as is also the case in eq. A.2, the choice of \mathcal{F} (the sim-
892 plification of the problem) is the key. In the methodology section, we will explain how to
893 connect realize the workflow (eq. A.8).

894 References

- 895 Armitage, J. J., D. J. Ferguson, S. Goes, J. Hammond, E. Calais, C. A. Rychert, and N. Harmon (2015),
 896 Upper mantle temperature and the onset of extension and break-up in afar, africa, *Earth Planet Sc
 897 Lett*, 418(Nature 465 2010), 78–90, doi:10.1016/j.epsl.2015.02.039.
- 898 Armitage, J. J., K. D. Petersen, and P. Marta (2018), The role of crustal strength in controlling magma-
 899 tism and melt chemistry during rifting and breakup, *Geochem Geophys Geosystems*, 19(2), 534–550,
 900 doi:10.1002/2017GC007326.
- 901 Asimow, P., M. Hirschmann, and E. Stolper (2001), Calculation of peridotite partial melting
 902 from thermodynamic models of minerals and melts, IV. adiabatic decompression and the
 903 composition and mean properties of mid-ocean ridge basalts, *J Petrol*, 42(5), 963–998, doi:
 904 10.1093/petrology/42.5.963.
- 905 Atkins, S., A. Valentine, P. Tackley, and J. Trampert (2016), Using pattern recognition to in-
 906 fer parameters governing mantle convection, *Phys. Earth Planet. Inter.*, 257, 171–186, doi:
 907 10.1016/j.pepi.2016.05.016.
- 908 Bormann, P., and E. Wielandt (2002), *Chapter 4 Seismic signals and noise*, pp. 1–62, 2 ed.
- 909 Buland, R., and C. Chapman (1983), The computation of seismic travel times, *Bull. Seismol. Soc. Am.*,
 910 73(5), 1271–1302.
- 911 Burley, J., and R. F. Katz (2015), Variations in mid-ocean ridge CO₂ emissions driven by glacial cy-
 912 cles, *Earth Planet Sc Lett*, 426(Nature 421 6925 2003), 246–258, doi:10.1016/j.epsl.2015.06.031.
- 913 Cammarano, F., S. Goes, P. Vacher, and D. Giardini (2003), Inferring upper-mantle temperatures from
 914 seismic velocities, *Phys Earth Planet In*, 138(3-4), 197–222, doi:10.1016/S0031-9201(03)00156-0.
- 915 Chantel, J., G. Manthilake, D. Andrault, D. Novella, T. Yu, and Y. Wang (2016), Experimental
 916 evidence supports mantle partial melting in the asthenosphere, *Sci Adv*, 2(5), e1600,246, doi:
 917 10.1126/sciadv.1600246.
- 918 Charvis, P., A. Laesapura, and J. Gallart (1999), Spatial distribution of hotspot material added to the
 919 lithosphere under la réunion, from wide-angle seismic data, *J. Geophys. Res. Solid Earth*, 104(B2),
 920 2875–2893, doi:10.1029/98JB02841.
- 921 Cobden, L., J. Trampert, and A. Fichtner (2018), Insights on upper mantle melting, rheology, and
 922 anelastic behavior from seismic shear wave tomography, *Geochemistry, Geophysics, Geosystems*,
 923 19(10), 3892–3916.
- 924 Connolly, J. (2005), Computation of phase equilibria by linear programming: A tool for geodynamic
 925 modeling and its application to subduction zone decarbonation, *Earth Planet Sc Lett*, 236(1-2), 524–

- 926 541, doi:10.1016/j.epsl.2005.04.033.
- 927 Connolly, J., M. Schmidt, G. Solferino, and N. Bagdassarov (2009), Permeability of astheno-
928 spheric mantle and melt extraction rates at mid-ocean ridges, *Nature*, 462(7270), 209–212, doi:
929 10.1038/nature08517.
- 930 Courtillot, V., A. Davaille, J. Besse, and J. Stock (2003), Three distinct types of hotspots in the earth's
931 mantle, *Earth Planet Sc Lett*, 205(3-4), 295–308, doi:10.1016/S0012-821X(02)01048-8.
- 932 Crotwell, H., T. Owens, and J. Ritsema (1999), The TauP toolkit: Flexible seismic travel-time and ray-
933 path utilities, *Seismol Res Lett*, 70(2), 154–160, doi:10.1785/gssrl.70.2.154.
- 934 Cummins, P., N. Takeuchi, and R. Geller (1997), Computation of complete synthetic seismograms for
935 laterally heterogeneous models using the direct solution method, *Geophys J Int*, 130(1), 1–16, doi:
936 10.1111/j.1365-246X.1997.tb00983.x.
- 937 Deschamps, F., K. Konishi, N. Fuji, and L. Cobden (2019), Radial thermo-chemical structure
938 beneath western and northern pacific from seismic waveform inversion, 520, 153–163, doi:
939 10.1016/j.epsl.2019.05.040.
- 940 Douet, V., M. Vallée, D. Zigone, S. Bonaimé, E. Stutzmann, A. Maggi, C. Pardo, A. Bernard, N. Leroy,
941 F. Pesqueira, et al. (2016), The geoscope broadband seismic observatory, in *EGU General Assembly
942 Conference Abstracts*, vol. 18.
- 943 Duncan, R., and R. Hargraves (1990), 40Ar/39Ar geochronology of basement rocks from the mas-
944 carene plateau, the chagos bank, and the maldives ridge, *Proc Ocean Drill Prog Sci Results*, 115,
945 43–51.
- 946 Eilon, Z. C., and G. A. Abers (2017), High seismic attenuation at a mid-ocean ridge reveals the distri-
947 bution of deep melt, *Sci Adv*, 3(5), e1602,829, doi:10.1126/sciadv.1602829.
- 948 Elliott, T., and M. Spiegelman (2003), Melt migration in oceanic crustal production: a u-series perspec-
949 tive, *Treatise on geochemistry*.
- 950 Fontaine, F. R., G. Barruol, H. Tkalčić, I. Wölbern, G. Rümpker, T. Bodin, and M. Haugmar (2015),
951 Crustal and uppermost mantle structure variation beneath la réunion hotspot track, *Geophys J Int*,
952 203(1), 107–126, doi:10.1093/gji/ggv279.
- 953 Forsyth, D. (1998), Imaging the deep seismic structure beneath a Mid-Ocean ridge: The MELT experi-
954 ment, *Science*, 280(5367), 1215–1218, doi:10.1126/science.280.5367.1215.
- 955 French, S., and B. Romanowicz (2015), Broad plumes rooted at the base of the earth's mantle beneath
956 major hotspots, *Nature*, 525, 95–99.
- 957 Fuji, N., K. Kawai, and R. Geller (2010), A methodology for inversion of broadband seismic wave-
958 forms for elastic and anelastic structure and its application to the mantle transition zone beneath the

- 959 northwestern pacific, *Phys. Earth Planet. Inter.*, 180, 118–137.
- 960 Fuji, N., S. Chevrot, L. Zhao, R. J. Geller, and K. Kawai (2012), Finite-frequency structural sensitivi-
961 ties of short-period compressional body waves, *Geophys J Int*, 190(1), 522–540, doi:10.1111/j.1365-
962 246X.2012.05495.x.
- 963 Gallart, J., L. Driad, P. Charvis, and M. Sapin (1999), Perturbation to the lithosphere along the hotspot
964 track of la réunion from an offshore-onshore seismic transect, *J. Geophys. Res.*, 104(B2), 2895–
965 2908, doi:10.1029/98JB02840.
- 966 Geller, R., and T. Ohminato (1994), Computation of synthetic seismograms and their partial derivatives
967 for heterogeneous media with arbitrary natural boundary conditions using the direct solution . . . ,
968 *Geophys. J. Int.*, 116, 421–446.
- 969 Geller, R., and N. Takeuchi (1995), A new method for computing highly accurate DSM synthetic seis-
970 mograms, *Geophysical Journal International*, doi:10.1111/j.1365-246X.1995.tb06865.x.
- 971 Geller, R., and N. Takeuchi (1998), Optimally accurate second-order time-domain finite difference
972 scheme for the elastic equation of motion: one-dimensional cases, *Geophysical Journal Interna-*
973 *tional*.
- 974 Ghiorso, M. S., and R. O. Sack (1995), Chemical mass transfer in magmatic processes IV. a revised and
975 internally consistent thermodynamic model for the interpolation and extrapolation of liquid-solid
976 equilibria in magmatic systems at elevated temperatures and pressures, *Contrib Mineral Petr*, 119(2-
977 3), 197–212, doi:10.1007/BF00307281.
- 978 Goes, S., J. Armitage, N. Harmon, H. Smith, and R. Huismans (2012), Low seismic velocities be-
979 low mid-ocean ridges: Attenuation versus melt retention, *J Geophys Res Solid Earth* 1978 2012,
980 117(B12), n/a–n/a, doi:10.1029/2012JB009637.
- 981 Hammond, W., and E. Humphreys (2000), Upper mantle seismic wave velocity: Effects of realistic
982 partial melt geometries, *J. Geophys. Res.*, 105(B5), 10,975–10,986, doi:10.1029/2000JB900041.
- 983 Harmon, N., D. W. Forsyth, and D. S. Weeraratne (2009), Thickening of young pacific lithosphere from
984 high-resolution rayleigh wave tomography: A test of the conductive cooling model, *Earth Planet Sc*
985 *Lett*, 278(1-2), 96–106, doi:10.1016/j.epsl.2008.11.025.
- 986 Hasegawa, K., N. Fuji, and K. Konishi (2018), Improvement of accuracy of the spectral element
987 method for elastic wave computation using modified numerical integration operators, *Comp. Meth-*
988 *ods Appl. Mech. Eng.*, 342, 200–223.
- 989 Havlin, C., and E. Parmentier (2014), Implications for melt transport and source heterogeneity in up-
990 welling mantle from the magnitude of sp converted phases generated at the onset of melting, *Geo-*
991 *phys Res Lett*, 41(15), 5444–5450, doi:10.1002/2014GL060890.

- 992 Herzberg, C., P. Asimow, N. Arndt, Y. Niu, C. Lesher, J. Fitton, M. Cheadle, and A. Saunders (2007),
993 Temperatures in ambient mantle and plumes: Constraints from basalts, picrites, and komatiites,
994 *Geochem Geophys Geosystems*, 8(2), n/a–n/a, doi:10.1029/2006GC001390.
- 995 Herzberg, C., P. D. Asimow, D. A. Ionov, C. Vidito, M. G. Jackson, and D. Geist (2013), Nickel and
996 helium evidence for melt above the core–mantle boundary, *Nature*, 493(7432), 393–397.
- 997 Hewitt, I. J. (2010), Modelling melting rates in upwelling mantle, *Earth Planet Sc Lett*, 300(3-4), 264–
998 274, doi:10.1016/j.epsl.2010.10.010.
- 999 Hirose, K., and I. Kushiro (1993), Partial melting of dry peridotites at high pressures: Determination of
1000 compositions of melts segregated from peridotite using aggregates of diamond, *Earth Planet Sc Lett*,
1001 114(4), 477–489, doi:10.1016/0012-821X(93)90077-M.
- 1002 Hirschmann, M., M. Ghiorso, and M. Stolper (1999), Calculation of peridotite partial melting from
1003 thermodynamic models of minerals and melts. II. isobaric variations in melts near the solidus and
1004 owing to variable source composition, *J Petrol*, 40(2), 297–313, doi:10.1093/petroj/40.2.297.
- 1005 Hirschmann, M., T. Tenner, C. Aubaud, and A. Withers (2009), Dehydration melting of nominally
1006 anhydrous mantle: The primacy of partitioning, *Phys Earth Planet In*, 176(1-2), 54–68, doi:
1007 10.1016/j.pepi.2009.04.001.
- 1008 Karato, S. (1993), Importance of anelasticity in the interpretation of seismic tomography, *Geophysical*
1009 *Research Letters*, doi:10.1029/93GL01767@10.1002/(ISSN)1944-8007.GRL40.
- 1010 Karato, S.-i. (2014), Does partial melting explain geophysical anomalies?, *Phys Earth Planet In*, 228,
1011 300–306, doi:10.1016/j.pepi.2013.08.006.
- 1012 Katz, R. F., M. Spiegelman, and C. H. Langmuir (2003), A new parameterization of hydrous mantle
1013 melting, *Geochem Geophys Geosystems*, 4(9), n/a–n/a, doi:10.1029/2002GC000433.
- 1014 Kawai, K., N. Takeuchi, and R. J. Geller (2006), Complete synthetic seismograms up to 2 hz for trans-
1015 versely isotropic spherically symmetric media, *Geophys J Int*, 164(2), 411–424, doi:10.1111/j.1365-
1016 246X.2005.02829.x.
- 1017 Kennett, B., E. Engdahl, and R. Buland (1995), Constraints on seismic velocities in the earth from trav-
1018 eltimes, *Geophys J Int*, 122(1), 108–124, doi:10.1111/j.1365-246X.1995.tb03540.x.
- 1019 Koelemeijer, P., B. Schuberth, D. Davies, A. Deuss, and J. Ritsema (2018), Constraints on the presence
1020 of post-perovskite in earth’s lowermost mantle from tomographic-geodynamic model comparisons,
1021 *Earth Planet. Sci. Lett.*, 494, 226–238.
- 1022 Komatitsch, D., and J. Vilotte (1998), The spectral element method: an efficient tool to simulate the
1023 seismic response of 2d and 3d geological structures, *Bull. Seis. Soc. Am.*, 88, 368–392.

- 1024 Konishi, K., K. Kawai, R. Geller, and N. Fuji (2014), Waveform inversion for localized three-
1025 dimensional seismic velocity structure in the lowermost mantle beneath the western pacific, *Geo-*
1026 *phys. J. Int.*, 199, 1245–1267.
- 1027 Konishi, K., N. Fuji, and F. Deschamps (2020), Three-dimensional elastic and anelastic structure
1028 of the lowermost mantle beneath the western pacific from finite-frequency tomography, doi:
1029 10.1029/2019JB018089.
- 1030 Marjanović, M., N. Fuji, S. Singh, T. Belahi, and J. Escartín (2017), Seismic signatures of hydrother-
1031 mal pathways along the east pacific rise between 9° 16' e and 9° 56' n, *J. Geophys. Res.*, 122,
1032 10,241–10,262.
- 1033 Mazzullo, A., E. Stutzmann, J. Montagner, S. Kiselev, S. Maurya, G. Barruol, and K. Sigloch (2017),
1034 Anisotropic tomography around la réunion island from rayleigh waves, *J Geophys Res Solid Earth*,
1035 122(11), 9132–9148, doi:10.1002/2017JB014354.
- 1036 McKenzie, D. (1984), The generation and compaction of partially molten rock, *J Petrol*, 25(3), 713–
1037 765, doi:10.1093/petrology/25.3.713.
- 1038 Mehouachi, F., and S. C. Singh (2018), Water-rich sublithospheric melt channel in the equatorial at-
1039 lantic ocean, *Nat Geosci*, 11(1), 65–69, doi:10.1038/s41561-017-0034-z.
- 1040 Miller, K. J., W.-I. Zhu, L. Montési, and G. A. Gaetani (2014), Experimental quantification of
1041 permeability of partially molten mantle rock, 388(*J. Geophys. Res.* 100 1995), 273–282, doi:
1042 10.1016/j.epsl.2013.12.003.
- 1043 Monteiller, V., S. Chevrot, D. Komatitsch, and Y. Wang (2015), Three-dimensional full waveform in-
1044 version of short-period teleseismic wavefields based upon the sem-dsm hybrid method, *Geophysical*
1045 *Journal International*, 202(2), 811–827.
- 1046 Morgan, J. (2001), Thermodynamics of pressure release melting of a veined plum pudding mantle,
1047 *Geochem Geophys Geosystems*, 2(4), n/a–n/a, doi:10.1029/2000GC000049.
- 1048 Ribe, N. (1985), The deformation and compaction of partial molten zones, *Geophysical Journal Inter-*
1049 *national*, doi:10.1111/j.1365-246X.1985.tb06499.x.
- 1050 Richards, M., R. Duncan, and V. Science (1989), Flood basalts and hot-spot tracks: plume heads and
1051 tails, *Science*, doi:10.1126/science.246.4926.103.
- 1052 Richards, M., C. Eduardo, L. Carolina, M. Ghiorso, and L. Stixrude (2013), Petrological interpretation
1053 of deep crustal intrusive bodies beneath oceanic hotspot provinces, *Geochem Geophys Geosystems*,
1054 14(3), 604–619, doi:10.1029/2012GC004448.
- 1055 Ritsema, J., A. McNamara, and A. Bull (2007), Tomographic filtering of geodynamic models: impli-
1056 cations for model interpretation and large-scale mantle structure, *J. Geophys. Res.*, 112, B01,303,

- 1057 doi:10.1029/2006JB004566.
- 1058 Rychert, C. A., J. O. Hammond, N. Harmon, M. J. Kendall, D. Keir, C. Ebinger, I. D. Bastow, A. Ayele,
1059 M. Belachew, and G. Stuart (2012), Volcanism in the afar rift sustained by decompression melting
1060 with minimal plume influence, *Nat Geosci*, 5(6), 406–409, doi:10.1038/ngeo1455.
- 1061 Rychert, C. A., G. Laske, N. Harmon, and P. M. Shearer (2013), Seismic imaging of melt in a displaced
1062 hawaiian plume, *Nat Geosci*, 6(8), 657–660, doi:10.1038/ngeo1878.
- 1063 Rychert, C. A., N. Harmon, and C. Ebinger (2014), Receiver function imaging of lithospheric structure
1064 and the onset of melting beneath the galápagos archipelago, *Earth Planet Sc Lett*, 388, 156–165,
1065 doi:10.1016/j.epsl.2013.11.027.
- 1066 Schuberth, B. S., C. Zaroli, and G. Nolet (2012), Synthetic seismograms for a synthetic earth: long-
1067 period p- and s-wave traveltimes can be explained by temperature alone, *Geophys J Int*,
1068 188(3), 1393–1412, doi:10.1111/j.1365-246X.2011.05333.x.
- 1069 Scott, D. (1992), Small-scale convection and mantle melting beneath mid-ocean ridges, *Washington
1070 DC American Geophysical Union*
- 1071 Shahnas, M., D. Yuen, and R. Pysklywec (2018), Inverse problems in geodynamics using machine
1072 learning algorithms, *J. Geophys. Res. Solid Earth*, 123, 296–310, doi:10.1002/2017JB014846.
- 1073 Sobolev, A., and I. Nikogosian (1994), Petrology of long-lived mantle plume magmatism: Hawaii,
1074 pacific and reunion island, indian ocean, *Petrology*.
- 1075 Steinberger, B., and T. Torsvik (2012), A geodynamic model of plumes from the margins of large low
1076 shear velocity provinces, *Geoch. Geophys. Geosys.*, 13, Q01W09, doi:10.1029/2011GC003808.
- 1077 Stixrude, L., and C. Lithgow-Bertelloni (2005), Thermodynamics of mantle minerals – i. physical prop-
1078 erties, *Geophys J Int*, 162(2), 610–632, doi:10.1111/j.1365-246X.2005.02642.x.
- 1079 Stracke, A., B. Bourdon, and M. Dan (2006), Melt extraction in the earth's mantle: Constraints
1080 from U–Th–Pa–Ra studies in oceanic basalts, *Earth Planet Sc Lett*, 244(1-2), 97–112, doi:
1081 10.1016/j.epsl.2006.01.057.
- 1082 Vallée, M., and V. Douet (2016), A new database of source time functions (STFs) extracted from the
1083 SCARDEC method, *Phys Earth Planet In*, 257, 149–157, doi:10.1016/j.pepi.2016.05.012.
- 1084 Weatherley, S. M., and R. F. Katz (2016), Melt transport rates in heterogeneous mantle beneath mid-
1085 ocean ridges, *Geochim Cosmochim Ac*, 172, 39–54, doi:10.1016/j.gca.2015.09.029.
- 1086 Xiao, Z., N. Fuji, T. Iidaka, Y. Gao, X. Sun, and Q. Liu (2020), Seismic structure beneath the tibetan
1087 plateau from iterative finite-frequency tomography based on chinarray: New insights into the indo-
1088 asian collision, doi:10.1029/2019JB018344.

- 1089 Xu, W., C. Lithgow-Bertelloni, L. Sixtrude, and J. Ritsema (2008), The effect of bulk composition
1090 and temperature on mantle seismic structure, *Earth and Planetary Science Letters*, 275, 70–79, doi:
1091 10.1016/j.epsl.2008.08.012.
- 1092 Zhu, W., and G. Hirth (2003), A network model for permeability in partially molten rocks, *Earth*
1093 *Planet Sc Lett*, 212(3-4), 407–416, doi:10.1016/S0012-821X(03)00264-4.

Chapitre A. Example Publications Part 1 : Mantle

Annexe B

Example Publications Part 2 : Surface

In this final annex I have selected five example publications that explore how surface processes are recorded within the geological record. They also demonstrate the various numerical models I have developed and the collaborations I have formed in order to try and broaden my understanding of the many parts to sedimentology and geomorphology.

1 Transformation of tectonic and climatic signals from source to sedimentary archive – Nature Geoscience

This is where my interest in sedimentology all began. While at Imperial College I got distracted by the work my friends were doing on grain size deposition in alluvial fans. Encouraged by them I developed a novel model that could predict grain sizes deposited as a function of past tectonics and climate (precipitation). This model was used to then demonstrate that change in climate and tectonics leave diagnostically different signatures in the landscape.

2 Physical stratigraphic model for the Eocene Escanilla sediment routing system : Implications for the uniqueness of sequence stratigraphic architectures – Journal of Sedimentary Research

Perhaps my longest title. With funding from the Royal Astronomical Society, I tried to see if I could use the model published in Nature Geosciences in 2011 to invert the sedimentary record for past climate change. This publication was the result of that work, where the position of key sedimentological markers, such as the gravel front, were used to invert for change in run-off and hence precipitation.

3 Deciphering the origin of cyclical gravel front and shoreline progradation and retrogradation in the stratigraphic record – Basin Research

Once I had found that my methodology worked for terrestrial deposits I decided to push beyond the shoreline, and explore how the gravel front and shoreline are impacted by climate change and sea-level change. In this study I demonstrate that both a change in run-off and sea level can give similar stratigraphic responses. The difference between the two is recorded in the most proximal regions, suggesting that to fully understand stratigraphy we need complete sections from terrestrial coarse gravel deposits down to marine mud and sand.

4 Numerical modelling landscape and sediment flux response to precipitation rate change – Earth Surface Dynamics

Landscape evolution models (LEMs) for geological processes tend to treat erosion as either a kinematic wave equation or a diffusive process. In this study I explored the implications of these two end-member models on the response to change in surface run-off. I found that both models gave similar response, suggesting that it will be difficult to decipher which assumptions are relevant for modelling past landscape change. However, the models both suggest landscape responds more rapidly to a

wetting event than a drying event, suggesting that short lived gravel deposition is a signature of increased surface run-off.

5 Short communication : flow as distributed lines within the landscape – Earth Surface Dynamics

While developing the above mentioned study, I noticed that some LEMs were highly resolution dependent. That is to say that the numerical result was a function of the grid resolution. In this final paper I explored the causes of this resolution dependence, and found that how surface water is routed down slope plays a key role in numerical model stability. By routing flow down all slopes I developed a LEM that is not resolution dependent. It remains to be seen if the community will notice.

Transformation of tectonic and climatic signals from source to sedimentary archive

John J. Armitage*, Robert A. Duller, Alex C. Whittaker and Philip A. Allen

The Earth's sedimentary successions are an archive of past tectonic and climate events^{1,2}. The physical characteristics of the sediment record are controlled by three main factors: the sediment supply from the eroding source region, the grain size distribution of that sediment supply, and the area available for sediment accumulation in the downstream regions^{3,4}. The interplay of these factors can make the interpretation of a climatic or tectonic signal complex, particularly as these processes are nonlinear. Here we assess the evolution of a tectonically active landscape undergoing erosional and depositional processes, using a numerical model that incorporates variations in grain size and the volumetric sediment budget. Our simulations indicate that changes in precipitation and tectonic uplift both generate characteristic patterns of grain size and stratigraphic geometry. An increase in catchment precipitation results in the deposition of a laterally extensive sheet of coarse gravel. The responses to a changing tectonic regime are more diverse: a large increase in uplift rate results first in the deposition of sediments of larger grain size at proximal sites, followed by a reduction in grain size at distal locations. We conclude that the stratigraphic record is strongly controlled by the grain size of sediments released from catchments undergoing tectonic or climatic change.

The sedimentary response to erosion of an upland source region and down-system aggradation occurs at a range of temporal and spatial scales⁵. Over geological timescales, the architecture and granulometry of fluvial successions are dependent on the prevailing tectonic and climatic conditions; however, inverting the sedimentary record for these key parameters is non-trivial^{6,7}. A large number of theoretical and field studies^{8–10} have demonstrated that tectonics, climate, erosion and deposition are dynamically linked by a sediment routing system, which relays source signals to permanent sinks. However, these processes operate at a range of timescales^{5,6,11} and field investigations have generally yielded valuable but qualitative interpretations of the stratigraphic impact of past tectonic and climatic changes (for example ref. 12).

Two strands of forward models have been developed to explore the landscape response to climatic and tectonic change. The first builds on theoretical, empirical and heuristic relationships to develop a quasi-realistic evolving landscape (for example, ref. 7). These studies embed field-derived hillslope, fluvial and sediment transport laws, but are typically focused on relatively short-term geomorphological observables, rather than on the erosion and deposition of sediment over geological timescales. Moreover, the hydraulic and geomorphic laws on which such models are built are often poorly constrained or unknowable for ancient source-to-sink systems. The second approach, which we adopt here, is to parameterize the erosional system using a nonlinear diffusional model that can describe the gross characteristics of topographic evolution and sediment release^{13–15} (Fig. 1, see

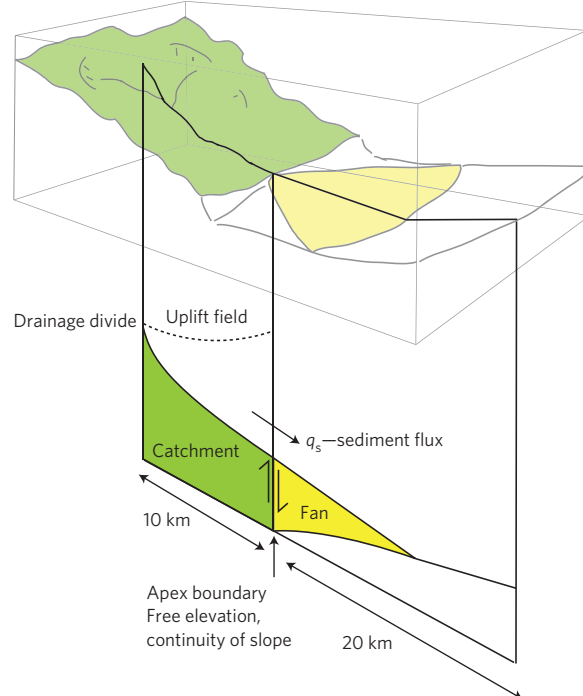


Figure 1 | Diagram of model domain. The uplifting catchment (green) is bounded by a vertical normal fault. The fault marks the transition from catchment to fan (yellow). In this idealized model domain, we maintain a continuity of slope and elevation across the apex^{15,29}.

Methods). Deposition can then be calculated using a volume balance approach¹⁵. This methodology allows for a simple set of equations to be solved through well-constrained observations. Previous workers have focused on stratigraphic architecture and sediment volumes¹⁵. We include grain size fining down-system using a field-verified, similarity-based approach^{2,16}.

Before a change in precipitation or fault slip rate within the catchment-fan system (Fig. 1), the model evolves for 5 Myr at a slip rate of 1 mm yr^{-1} and a precipitation rate of 1 m yr^{-1} , to achieve a steady-state sediment flux¹⁵ (Fig. 2a). A subsequent doubling of the precipitation rate generates a sharp increase in sediment flux that returns to the steady-state condition with a response time of about 0.5 Myr (Fig. 2a). The increased sediment flux as the catchment responds to the increase in precipitation promotes a lengthening of the depositional fan by a factor of two, marked by the 20 mm grain size contour (Fig. 2b). In a vertical sediment column situated 5 km from the fan apex, there is an abrupt increase in mean grain size (Fig. 2b). A halving of the precipitation rate generates a sharp reduction in sediment flux that returns to the

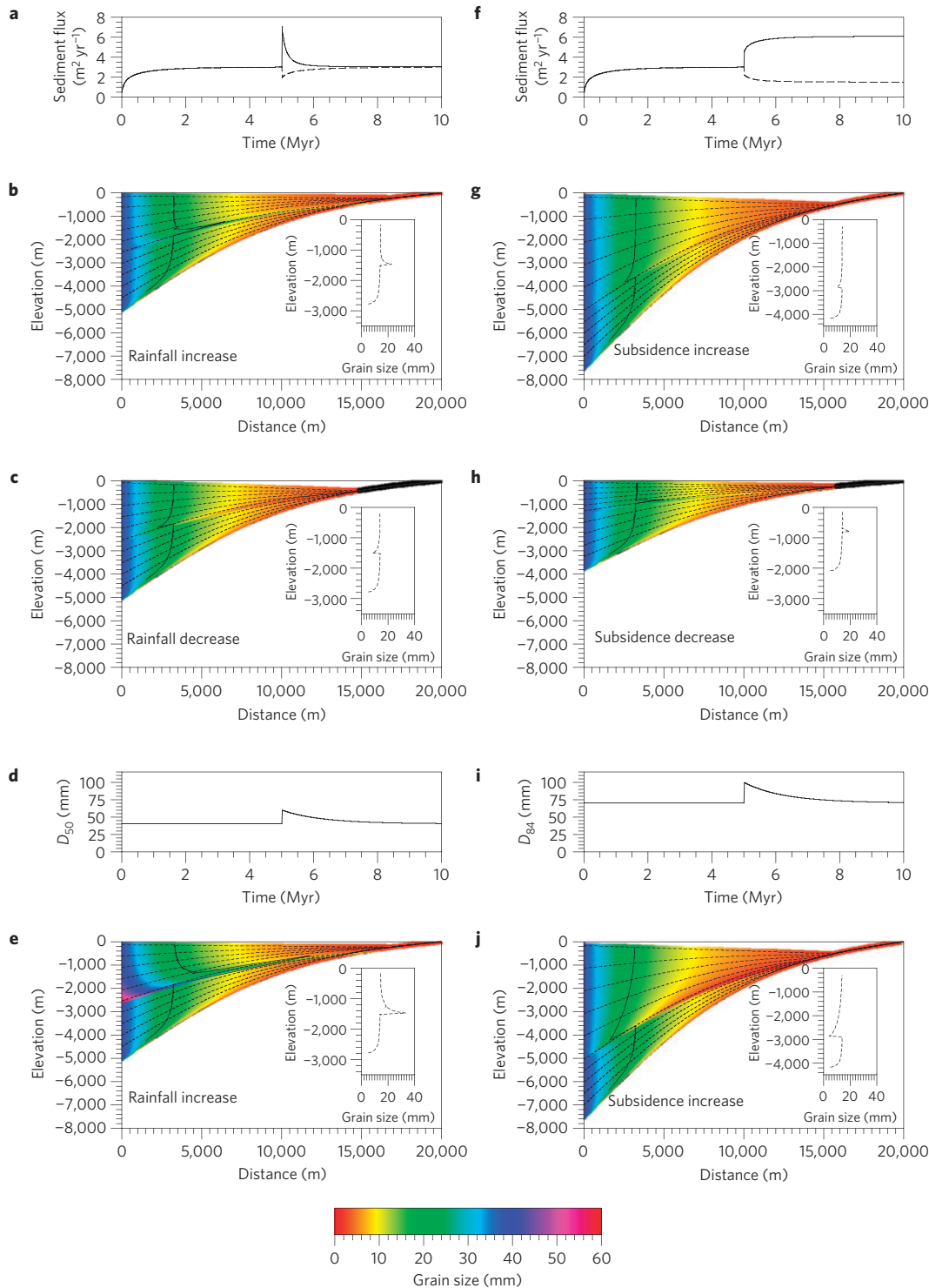


Figure 2 | Response of the sedimentary system to climate and tectonic perturbations. **a**, Sediment flux from catchment for a twofold increase (solid line) and decrease (dashed line) in precipitation. **b,c**, Grain size distribution (GSD) within fan for models in **a**. Solid line shows 20 mm grain size; dashes indicate 1 Myr intervals; insets show vertical grain size profiles 5 km from apex. **d**, D_{50} released from catchment if a twofold precipitation increase is coupled to exported sediment grain size. **e**, Fan GSD for model **d**. **f**, Sediment flux from catchment for a twofold increase (solid line) and decrease (dashed line) in uplift. **g,h**, Fan GSD for models in **f**. **i**, D_{84} released from catchment if uplift increase drives coarse sediment export. **j**, Fan GSD for model **i**. Initial conditions: precipitation, $1 \text{ m}^2 \text{ yr}^{-1}$; uplift rate, 1 mm yr^{-1} ; D_{50} , 40 mm; D_{84} , 70 mm.

steady-state condition with a longer response time of about 1 Myr (Fig. 2a). The decreased sediment flux in response to the change in precipitation promotes a backstepping of the fan toe, reducing the length of the fan. This reduction in system length is accompanied by an increase in the rate of down-system fining^{2,16}, whereby the

coarser fraction of the supplied material is deposited a kilometre closer to the apex (Fig. 2c).

An increase in precipitation will increase the sediment grain size exported from the catchment because channel bed grain size scales with basal shear stress¹⁷. To relate median grain size,

D_{50} , to the change in rainfall, α , we use existing derivations that combine Manning's equation with boundary shear stress to link grain size to catchment water discharge¹⁸. Assuming that water flux is directly proportional to rainfall within the catchment, $D_{50} \propto \alpha^{3/5}$. Increased erosion in the catchment acts to reduce channel slope until topographic steady state is attained. Input granulometry responds on a similar timescale to sediment flux¹⁹, so the grain size distribution returns to the initial condition at a decay half-time of 1 Myr (Fig. 2d). The response recorded within the basin to a coupled increase in precipitation and sediment calibre is a marked progradation (of order 10 km) of coarse material down-system (Fig. 2e).

Following a perturbation in fault slip rate, the response time for the catchment to reach a new steady state is of the order of 1 Myr (Fig. 2f). An increase in fault slip rate from 1 to 2 mm yr⁻¹ generates an increase in sediment flux as erosion within the catchment works to remove the additional mass of rock. A change in subsidence rate within the basin is instantaneous, whereas catchment erosion takes time to respond. Consequently, the amount of material eroded is initially less than the new steady state (Fig. 2f). Fan length is initially short and down-system rate of grain size fining high during this period of transient response^{2,5,15}. Down-system grain size trends then return to the same values observed before the perturbation (Fig. 2g). The transient response to an increase in fault slip rate is recorded within the stratigraphy as a small (about 1 km) backstepping of the fan toe and a grain size reduction (Fig. 2g). In contrast, a reduction in fault slip rate causes a progradation of a thin wedge of coarse material into the basin, transporting larger grains (>20 mm) up to a kilometre further down-system (Fig. 2h). The response to a fault slip rate reduction is similar to that of an increase in precipitation, but the grain size signal does not travel down the full length of the system (Fig. 2e,h).

Field data from the central Apennines of Italy have shown that larger clasts are typically exported from fault-bounded catchments following an increase in fault slip rate¹⁹. For a doubling of slip rate, median grain size of the supply remains relatively unchanged, whereas the coarse end increases from a D_{84} of 70 to 100 mm (ref. 19; Fig. 2i). The increase in D_{84} is transient as increased erosion lowers topographic slopes, before returning to the initial steady-state values over a decay half-time of 1 Myr (ref. 19). The response of the depositional system to an increase in the ratio D_{84}/D_{50} in the sediment released is to accentuate the abrupt backstepping of the fan toe and to promote a more rapid rate of grain size fining (Fig. 2j). The increase in D_{84}/D_{50} increases the rate of selective deposition, as larger grains are preferentially extracted up-system².

The deposition of conglomeratic sheets down-system has been previously linked to increases in precipitation in the upstream catchment²⁰. For example, a 10-m-thick coarse gravel unit in the 0.6–3-Myr-old St David Formation in the San Pedro Valley of southern Arizona was deposited during a period of tectonic quiescence²¹. Similarly, the Palaeocene–Eocene boundary in the Tremp basin of the Spanish Pyrenees coincides with the presence of a conglomerate sheet that is about 10 m thick, bounded above and below by different palaeosols that indicate an increase in precipitation rate²². Sheet conglomerates can be formed from a sharp reduction in subsidence (Fig. 2h). However, the grain size increase is not as pronounced and the progradation is less extensive than that produced by a precipitation increase (Fig. 2b,e). Increased precipitation²³ and unforced internal dynamics²⁴ may lead to fan-head entrenchment, which may transiently lead to down-system extension of the fan, but this cannot be captured by our time-integrated model. These arguments indicate that thin, laterally extensive gravel sheets within sedimentary basins are best explained by a long-term change in precipitation in upstream catchments.

The Fucino basin, central Italy, is a recently drained lake containing fluvial-deltaic deposits that prograded into the basin from the northwest-southeast boundary faults from the late

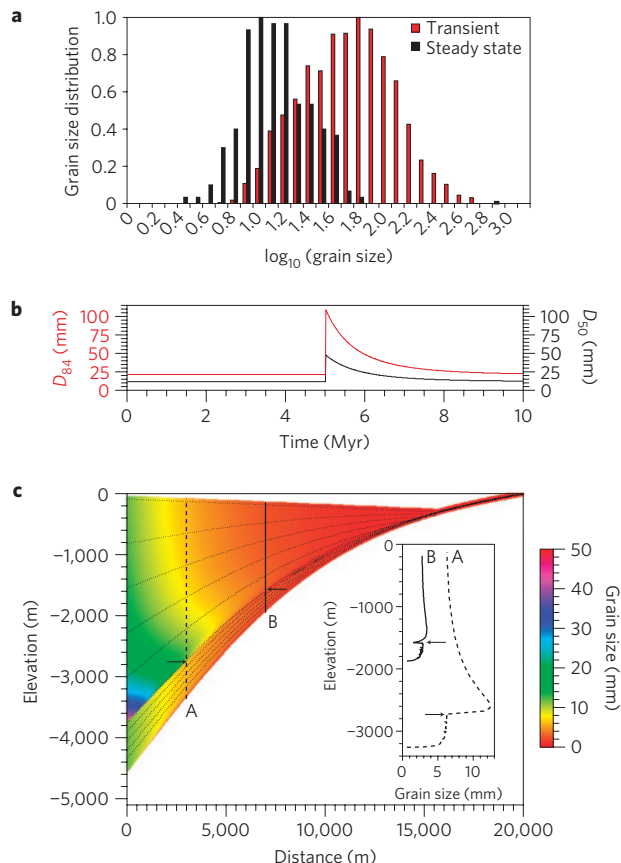


Figure 3 | Predicted response to a fivefold increase in uplift within the Gole di Celano and the Fucino basin system. **a**, Normalized Wolman point count grain size measurements from the Gole di Celano for regions that are responding (transient) to a slip rate increase from 0.3 to 1.5 mm yr⁻¹ and those that have yet to respond (steady state)¹⁹. The grain size has been converted to a log₁₀ scale so that the two distributions are Gaussian. **b**, Response of input grain size (D_{50} and D_{84}) due to the change in slip rate. **c**, Grain size distribution for a $\times 5$ increase in slip rate. Inset: Vertical grain size profiles. Small arrows mark the slip rate perturbation recorded within the granulometry.

Pliocene onwards²⁵. The Fucino fault experienced an increase in slip rate from 0.3 to 1.5 mm yr⁻¹ due to fault linkage at 800 kyr BP (refs 9,26). This was accompanied by an increase in both the median ($D_{50} = 11\text{--}50$ mm) and coarse ($D_{84} = 20\text{--}110$ mm) grain size percentiles exported from the Gole di Celano that cross-cuts the fault (Fig. 3a,b).

The response to a fivefold increase in fault slip rate is complex. From our modelling of the response to slip rate perturbations, a backstepping of coarse material would be predicted. However, the coupling between catchment and fan is not straightforward in this field-calibrated scenario. The increase in D_{50} and D_{84} has different effects on the downstream fining. The increase in median grain size leaving the catchment increases the size of gravel entering the fan. Therefore, the increase in slip rate, resulting in a larger input median grain size, produces a wedge of coarse material that extends into the basin (Fig. 3c). Concomitantly, the larger D_{84}/D_{50} ratio promotes an increase in the rate of down-system grain size fining. At ≤ 5 km from the fan apex, the sediment grain size increases with time owing to the slip rate perturbation, whereas at distances ≥ 5 km a reduction is recorded (Fig. 3c). The progradation of coarse gravel predicted close to the fault and observed within the fan deposits from the Celano and neighbouring areas entering the Fucino basin^{19,25} does not correspond to an increase in fan length, or a sudden increase in

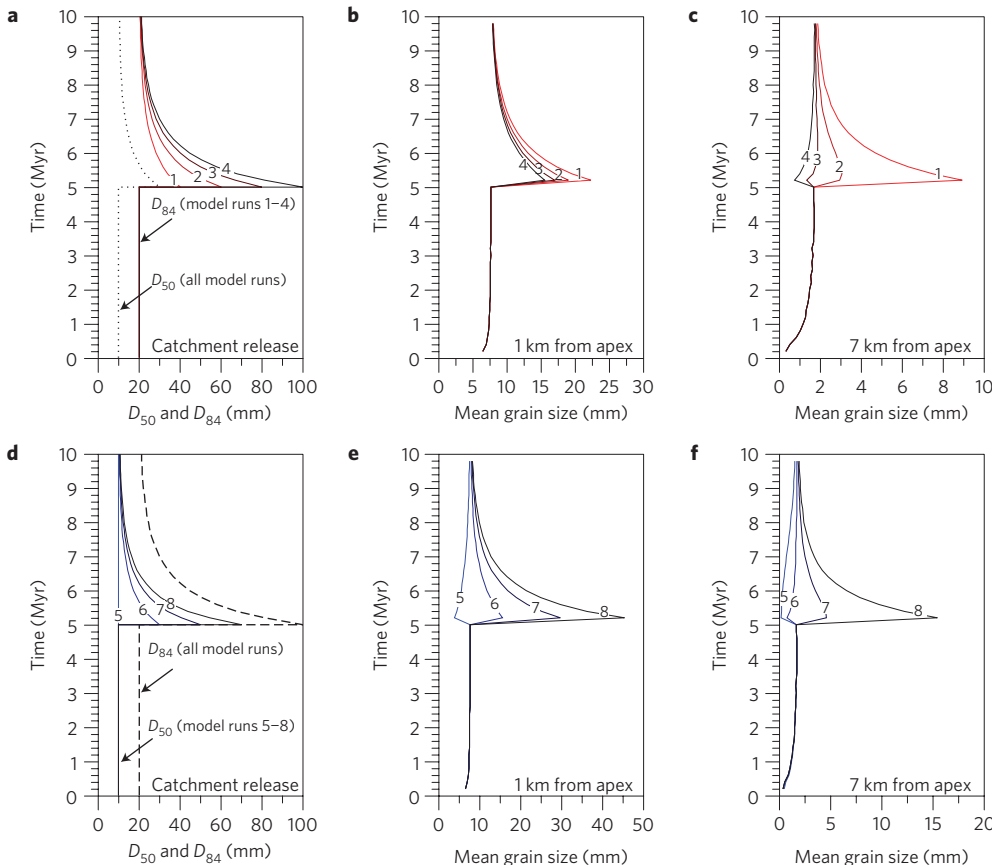


Figure 4 | Down-system grain size signals following a doubling of subsidence and uplift from 1 mm yr^{-1} to 2 mm yr^{-1} . **a**, Input sediment distributions: dotted line— D_{50} , red to black lines— D_{84} of peak of 40–100 mm. **b,c**, Mean grain size deposited in vertical sediment columns 1 and 7 km from the fan apex. Red to black lines are as in **a** and represent the variation in input D_{84} . **d**, Input sediment distributions: dashed line— D_{84} , blue to black lines D_{50} of a peak of 20–70 mm. **e,f**, Mean grain size deposited in vertical sediment columns 1 and 7 km from the fan apex. Blue to black lines are as in **d** and represent the variation in input D_{50} .

sediment flux; instead they are a stratigraphic record of the transient response of the eroding landscape.

Sequence stratigraphy is built on an expectation that the lap-out relationships of stratal packages are diagnostic of forcing mechanisms and that along time-lines, trends of shallowing (progradation) or deepening (backstepping) are spatially consistent. Our model of a catchment–fan system indicates that stratigraphic grain size and geometries respond in a more complex way to changes in forcing mechanisms. A temporal increase in grain size and onlap of gravel may be recorded close to the fan apex, whereas a reduction in grain size and backstepping of gravel are recorded far from the fan apex (Fig. 4). This downstream change in signal across a stratal package can be described as a transformation in phase, from a positive increase to negative decrease in grain size. There is evidently a trade-off between increased fining due to increased D_{84} of the sediment supply and backstepping of fan architecture, and progradation of large grains due to increased D_{50} . As D_{84}/D_{50} gets larger ($>4:1$), this phase shift gets larger (Fig. 4).

The terrestrial sedimentary archive is intimately linked to the eroding landscape, but these connections are not linear^{6,11}. By combining field observations with a clear physical model of landscape erosion and deposition, we have demonstrated how the response of landscapes to long-term changes in climate and tectonics is recorded and transformed in sedimentary strata. Grain size characteristics released from a catchment impose a strong, but not necessarily linear, control on the stratigraphic record of downstream grain size fining. In illustrating how climatic and tectonic signals are transformed from source region to stratigraphic end-product, and

how they may be discriminated from each other, this contribution provides improved concepts for the inversion of the sedimentary record for past changes in external forcing mechanisms.

Methods

Below we provide a brief summary of the methods; further information is provided in the Supplementary Information. We target a relatively simple sediment routing system comprising a small 10-km-long frontal catchment and <20-km-long alluvial fan, separated by a vertical normal fault (Fig. 1). Erosion and deposition are considered along the centre of the catchment and fan^{6,15} (Fig. 1). Simplifying the sedimentary system to a two-dimensional plane can be justified as long as there is no long-term flux of sediment in and out of the plane. This can be safely assumed if the mountain front has a series of transverse catchment–fans that are not interconnected, and where over time, any along-strike inequalities in sediment deposition are evened out by channel and fan segment switching in response to differential topographic gradients. The uplifted catchment is eroded, supplying a sediment discharge that is deposited within the basin. Erosion is of the form of a diffusive-concentrative equation¹⁵,

$$\frac{\partial h}{\partial t} = -\frac{\partial q_s}{\partial x} + U(x, t) = \frac{\partial}{\partial x} (\kappa + c(\alpha x)^n) \frac{\partial h}{\partial x} + U(x, t) \quad (1)$$

The sediment flux, q_s , is split into hillslope diffusion, $\kappa(\partial h/\partial x)$, and fluvial diffusion, $c(\alpha x)^n(\partial h/\partial x)$, assuming that fluvial processes are proportional to precipitation. In equation (1), h is elevation, x is down-system distance, $\kappa = 0.01 \text{ m}^2 \text{ yr}^{-1}$ is the linear diffusivity, $c = 1 \times 10^{-6} (\text{m}^2 \text{ yr}^{-1})^{1-n}$ is the nonlinear sediment transport coefficient, α is the precipitation rate and $n = 2$ is the exponent that describes the dependency of sediment discharge on fluid transport^{14,15}. $U(x, t)$ is the uplift within the catchment, which can be varied as the system evolves. Equation (1) is made dimensionless by the length of the catchment, $l_x = 10 \text{ km}$, and the timescale l_x^2/κ , giving

$$h = l_x \tilde{h} \quad x = l_x \tilde{x} \quad t = \frac{l_x^2}{\kappa} \tilde{t}$$

Equation (1) therefore becomes,

$$\frac{\partial \tilde{h}}{\partial \tilde{t}} = \frac{\partial}{\partial \tilde{x}} (1 + D_e \tilde{x}^n) \frac{\partial \tilde{h}}{\partial \tilde{x}} + \tilde{U} \quad (2)$$

where \tilde{U} is the dimensionless uplift and D_e expresses the relative importance of concentrative processes versus diffusive processes,

$$D_e = \frac{c (\alpha l_x)^n}{\kappa}$$

The uplift field is that of fault-bounded blocks²⁷. Equation (2) is solved using a standard finite-element approach with linear weighting functions and linear time-steps²⁸. Sediment flux, q_s , is sensitive to the boundary condition at the catchment outlet, which we refer to as the apex boundary condition (Fig. 1).

Depositional architecture is calculated by a volume balance approach, assuming that no erosion occurs within the depositional fan¹⁴. In our model the absolute elevation of the apex boundary condition is free to move, but we impose continuity of gradient at the apex boundary condition, as observed in natural catchment-fan systems²⁹. We then iterate to determine the gradient of the fan surface that equals the gradient of the catchment outlet surface that balances the volume of sediment released¹⁵. The slope of the fan is assumed to be constant. Therefore, at each time increment, the new depositional wedge is determined, and selective deposition theory is used to estimate down-system grain size fining in the stratigraphy. By treating fan deposition as a simple balance of sediment budget with accommodation space provided, we time integrate the individual processes such as changes in fan width within single channel flows. Therefore, whereas at the timescale of single flood events the depositional geometry and downstream fining may be representative of the sediment hydrodynamics of the active layer, at the long timescales considered here the depositional geometry and downstream fining in stratigraphy can be approximated by our volume balance approach.

The initial grain size signal is transformed down-system by selective deposition using an adapted version of self-similar solutions for down-system grain size trends^{2,16}. The self-similar solutions assume a normal distribution of sediment grain size. We therefore convert the grain size distribution to a logarithmic scale and sort by the diagnostic standard deviation, ϕ_0 , and mean, \bar{D}_0 (see Supplementary Information). Down-system fining is then governed by the following set of equations¹⁶,

$$\bar{D}(x^*) = \bar{D}_0 + \phi_0 \frac{1}{C_v} (e^{-C_v y^*} - 1)$$

where $x^* = x/l_f$ and $l_f = 20$ km is the length of the basin, $C_v = 0.7$ (ref. 2), $C_v = 0.25$ (see Supplementary Information) and y^* is a spatial transformation of x^* . This is given by³⁰,

$$\frac{dy^*}{dx^*} = R^*$$

R^* is the distribution of deposition given by

$$R^* = (1 - \lambda_p) \frac{S(x^*)}{q_s(x^*)}$$

where $\lambda_p = 0.3$ is the sediment porosity, $S(x^*)$ is the dimensionless area of accommodation space generated at a given time step and $q_s(x^*)$ is the equivalent down-system distribution of sediment flux.

Received 26 October 2010; accepted 21 January 2011; published online 27 February 2011

References

- Zhang, P. Z., Molnar, P. & Downs, W. R. Increased sedimentation rates and grain sizes 2–4 Myr ago due to the influence of climate change on erosion rates. *Nature* **410**, 891–897 (2001).
- Duller, R. A. *et al.* From grain size to tectonics. *J. Geophys. Res.* **115**, F03022 (2010).
- Flemings, P. B. & Jordan, T. E. A synthetic stratigraphic model of foreland basin development. *J. Geophys. Res.* **94**, 3851–3866 (1989).
- Paola, C., Heller, P. & Angevine, C. The large-scale dynamics of grain-size variation in alluvial basins: 1. Theory. *Basin Res.* **4**, 73–90 (1992).
- Braun, J. in *Anologue and Numerical Modelling of Crustal-Scale Processes* Vol. 253 (eds Buiter, S. J. H. & Schreurs, G.) 307–325 (Geological Society, Special Publications, 2006).
- Humphrey, N. F. & Heller, P. L. Natural oscillations in coupled geomorphic systems—an alternative origin for cyclic sedimentation. *Geology* **23**, 499–502 (1995).
- Clevis, Q., d'Boer, P. & Wachter, M. Numerical modelling of drainage basin evolution and three-dimensional alluvial fan stratigraphy. *Sedim. Geol.* **163**, 85–110 (2003).
- Montgomery, D. R. & Stolar, D. B. Reconsidering Himalayan river anticlines. *Geomorphology* **82**, 4–15 (2006).
- Whittaker, A. C. *et al.* Contrasting transient and steady-state rivers crossing active normal faults: New field observations from the Central Apennines, Italy. *Basin Res.* **19**, 529–556 (2007).
- Cowie, P. A. *et al.* New constraints on sediment-flux-dependent river incision: Implications for extracting tectonic signals from river profiles. *Geology* **36**, 535–538 (2008).
- Allen, P. A. in *Landscape Evolution: Denudation, Climate and Tectonics Over Different Time and Space Scales* Vol. 269 (eds Gallacher, K., Jones, K. S. J. & Wainwright, J.) 7–28 (Geological Society, Special Publications, 2008).
- Horton, B. K., Constenius, K. N. & DeCelles, P. G. Tectonic control on coarse grained foreland-basin sequences: An example from the Cordilleran foreland basin, Utah. *Geology* **32**, 637–640 (2004).
- Smith, T. R. & Bretherton, F. Stability and conservation of mass in drainage basin evolution. *Wat. Resour. Res.* **8**, 1506–1529 (1972).
- Simpson, G. & Schlunegger, F. Topographic evolution and morphology of surfaces evolving in response to coupled fluvial and hillslope sediment transport. *J. Geophys. Res.* **108**, B62300 (2003).
- Densmore, A. L., Allen, P. A. & Simpson, G. Development and response of a coupled catchment fan system under changing tectonic and climatic forcing. *J. Geophys. Res.* **112**, F01002 (2007).
- Fedele, J. J. & Paola, C. Similarity solutions for fluvial sediment fining by selective deposition. *J. Geophys. Res.* **112**, F02038 (2007).
- Wiberg, P. L. & Smith, J. D. Calculations of the critical shear-stress for motion of uniform and heterogeneous sediments. *Wat. Resour. Res.* **23**, 1471–1480 (1987).
- Attal, M. *et al.* Modelling fluvial incision and transient landscape evolution: Influence of dynamic channel adjustment. *J. Geophys. Res.* **113**, F03013 (2008).
- Whittaker, A. C., Attal, M. & Allen, P. A. Characterising the origin, nature and fate of sediment exported from catchments perturbed by active tectonics. *Basin Res.* **22**, 809–828 (2010).
- Heller, P. L. & Paola, C. The large-scale dynamics of grain size variation in alluvial basins, 2: Application to syntectonic conglomerate. *Basin Res.* **4**, 91–102 (1992).
- Lindsay, E. H. *et al.* Sediments, geomorphology, magnetostratigraphy and vertebrate paleontology in the San Pedro Valley, Arizona. *J. Geol.* **98**, 605–619 (1990).
- Schmitz, B. & Pujalte, V. Abrupt increase in seasonal extreme precipitation at the Paleocene–Eocene boundary. *Geology* **35**, 215–218 (2007).
- Dünnforth, M. *et al.* Controls on sediment evacuation from glacially modified and unmodified catchments in the eastern Sierra Nevada, California. *Earth Surf. Proc. Land.* **33**, 1602–1613 (2008).
- Pepin, E., Carretier, S. & Herail, G. Erosion dynamics modelling in a coupled catchment-fan system with constant external forcing. *Geomorphology* **122**, 78–90 (2010).
- Cavinato, G. P. *et al.* Sedimentary and tectonic evolution of Plio-Pleistocene alluvial and lacustrine deposits of Fucino Basin (central Italy). *Sedim. Geol.* **148**, 29–59 (2002).
- Roberts, G. P. *et al.* Fault scaling relationships, deformation rates and seismic hazards: An example from the Lazio-Abruzzo Apennines, central Italy. *J. Struct. Geol.* **26**, 377–398 (2004).
- Anders, M. H. *et al.* The growth of fault-bounded tilt blocks. *Tectonics* **12**, 1451–1459 (1993).
- Zienkiewicz, O. C. & Taylor, R. L. *The Finite Element Method* Vol. 1. (Butterworth-Heinemann, 2000).
- Bull, W. B. *Geomorphology of Segmented Alluvial Fans in Western Fresno County, California* (Prof. Paper, US Geological Survey, 1964).
- Paola, C. & Seal, R. Grain size patchiness as a cause of selective deposition and downstream fining. *Wat. Resour. Res.* **31**, 1395–1407 (1995).

Acknowledgements

The numerical model was developed through collaborations with G. Simpson (Université de Genève) and A. Densmore (University of Durham), and with the help of H.M. Nick (Utrecht University). We would also like to thank H. M. Bjornseth and I. Lunt (Statoil) for their constructive input on this work. This work was funded by Statoil through a generic research programme on sediment routing systems.

Author contributions

J.J.A. designed and carried out the numerical experiments. All authors contributed equally to the analysis of the results and writing of the manuscript.

Additional information

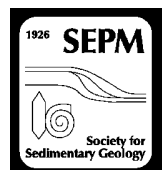
The authors declare no competing financial interests. Supplementary information accompanies this paper on www.nature.com/naturegeoscience. Reprints and permissions information is available online at http://npg.nature.com/reprintsandpermissions. Correspondence and requests for materials should be addressed to J.J.A.

Journal of Sedimentary Research

Journal of Sedimentary Research, 2015, v. 85, 1510–1524

Research Article

DOI: <http://dx.doi.org/10.2110/jsr.2015.97>



SEDIMENT TRANSPORT MODEL FOR THE EOCENE ESCANILLA SEDIMENT-ROUTING SYSTEM: IMPLICATIONS FOR THE UNIQUENESS OF SEQUENCE STRATIGRAPHIC ARCHITECTURES

JOHN J. ARMITAGE,^{*1} PHILIP A. ALLEN,² PETER M. BURGESS,¹ GARY J. HAMPSON,² ALEXANDER C. WHITTAKER,²
ROBERT A. DULLER,³ AND NIKOLAS A. MICHAEL⁴

¹Department of Earth Science, Royal Holloway, University of London, Egham, U.K.

²Department of Earth Science and Engineering, Imperial College London, London, U.K.

³Department of Earth, Ocean and Ecological Sciences, School of Environmental Sciences, University of Liverpool, Liverpool, U.K.

⁴GTT Division, EXPEC ARC, Saudi Aramco, Dhahran, 31311, Saudi Arabia

ABSTRACT: Stratigraphic architectures are fundamentally controlled by the interplay at different temporal and spatial scales of accommodation and sediment supply, modulated by autogenic responses of the sediment routing system and its constituent segments. The flux and caliber of sediment supply is a function of climate, catchment area, and tectonics in the source regions, and unraveling these forcing mechanisms from the observed stratigraphic architecture remains a key research challenge. The mid-to-late Eocene Escanilla sediment routing system had its source regions in the south-central Pyrenean orogen, northern Spain, and transported sediment from wedge-top basins along tectonic strike to marine depocenters. By constructing a volumetric budget of the sedimentary system, it has been demonstrated that there were marked changes in the grain-size distribution released from the sediment sources and also in the position of the gravel front, across three ~ 2.6 Myr time intervals from 41.6 to 33.9 Ma. Classical sequence stratigraphic interpretations would relate the movement of depositional boundaries such as the gravel front to changes of base level, either in isolation or in combination with sediment supply. Herein, we explore the possibility that the position of the gravel front was primarily driven by variability of grain-size distributions released from the source regions as a result of changes in catchment uplift rate and/or surface run-off.

Using a simple model of sediment transport that captures first-order processes, we simulate the lateral movement of gravel deposition in the proximal part of the Escanilla sediment-routing system. Movement of the gravel front is a function of both accommodation generation and the transport capacity of the sediment routing system. We assume that the transport capacity is a linear function of the local slope and the water flux. By assuming that the observed thickness of deposits is equivalent to the accommodation available during deposition, we then use the stratigraphic architecture to constrain the change in catchment size and water flux over the three time intervals of the Escanilla paleo-sediment-routing system. Multiple scenarios are investigated in order to find the most plausible tectonic and climatic history. Model results indicate that during the mid-Eocene there was an increase in catchment length and sediment flux, most likely driven by tectonic uplift in the Pyrenean orogen. Subsequent marked progradation of the gravel front during the late Eocene was the consequence of reduced transport capacity due to a reduction in surface run-off. The latter model result is in agreement with records of pollen taxa that indicate increased climatic aridity in the late Eocene. The combination of a sediment transport model with a full sediment budget makes it possible to test the non-uniqueness of these results.

INTRODUCTION

The sediment-routing-system concept and sequence stratigraphy provide different, but potentially complementary, approaches to characterize and interpret stratigraphic architectures. Sediment routing systems comprise a sediment cascade from single or multiple source regions to long-term depositional sinks via a series of geomorphic environments characterized by intermittent storage (Burt and Allison 2010). The sequence stratigraphy paradigm is built on the

recognition from subsurface seismic data and surface outcrops of characteristic geometrical relationships, and of their associated expression in vertical successions of strata (e.g., in well logs, cores), in the depositional records of sedimentary basins (e.g., Vail et al. 1977; Galloway 1989; Van Wagoner et al. 1990). There are essentially two unknowns in the sequence stratigraphic model: accommodation and sediment supply (Galloway 1989; Van Wagoner et al. 1990; Heller et al. 1993; Schlager 1993; Carvajal and Steel 2006; Carvajal et al. 2008). Accommodation combines sea level and its equivalent base level in deep-water and nonmarine settings, tectonic subsidence and uplift, syndepositional compaction, and initial topography, and can generally be approximated only from sediment thickness. Sediment supply varies both temporally and spatially, and sets the boundary condition for sediment dispersal in the basin.

* Present Address: Dynamique des Fluides Géologiques, Université Paris Diderot, Sorbonne Paris Cité, Institut de Physique du Globe de Paris, UMR 7154 CNRS, F-75013 Paris, France

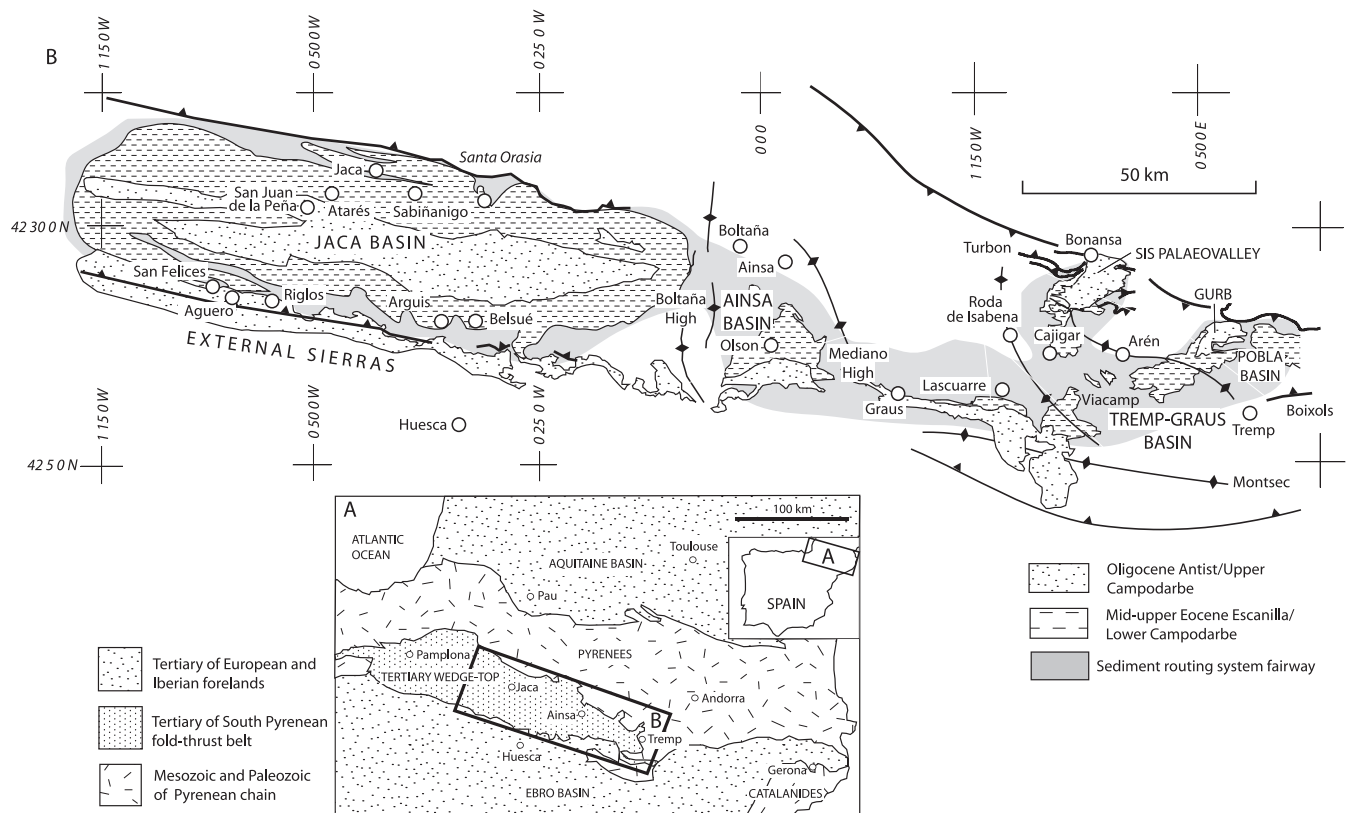


FIG. 1.—A) Location of the Escanilla paleo-sediment-routing system in the Tertiary wedge top of the south-central Pyrenees, northern Spain. B) Detail of the Escanilla paleo-sediment-routing system fairway, after Michael et al. (2014a).

Since accommodation can be estimated from spatial variations in sediment thickness, the ratio of accommodation to sediment supply (A/S ratio) can be qualitatively interpreted from observed stratigraphic architectures (e.g., Muto and Steel 1997; Martinsen et al. 1999). The sediment-routing-system concept is useful in constraining such interpretations of stratigraphic architectures because of its emphasis on sediment flux, which cannot be quantitatively estimated independently of accommodation using classical methods of sequence stratigraphic interpretation. In return, sequence stratigraphic frameworks can provide the stratigraphic context within which coeval segments of sediment routing systems are identified and connected together for further analysis (e.g., Carvajal and Steel 2012).

The grain-size distribution of the sediment supply not only affects rates of downstream fining (Fedele and Paola 2007; Duller et al. 2010), but temporal changes in the grain-size distribution may also generate distinctive stratigraphic architectural patterns (Allen et al. 2015). Consequently, the trajectory of the shoreline or shelf-slope break (Helland-Hansen and Martinsen 1996; Steel and Olsen 2002; Helland-Hansen and Hampson 2009), or of other moving boundaries in the sediment routing system, such as the gravel front (Paola et al. 1992), may be a complex response at different temporal and spatial scales to (i) the volume and grain-size distribution of the sediment supply; and (ii) the rate of generation and spatial distribution of accommodation. A range of numerical modeling and physical experiments has been directed at examining in detail some of the controls on and feedbacks between processes that influence accommodation and sediment supply, and are thus involved in the generation of sequence architectures (Harbaugh et al. 1999; Swenson 2005; Paola et al. 2009; Martin et al. 2009; Armitage et al. 2011). Such studies commonly point to the problem of non-uniqueness in inverting the stratigraphic record for forcing mechanisms (Burgess and Prince 2015). To an extent, the issue of non-uniqueness can be sidestepped by using the A/S ratio as an interpretation tool,

because the various processes that influence accommodation and sediment supply are considered in combination (Muto and Steel 1997; Catuneanu et al. 2009). Although this approach provides a framework for the interpretation of observed stratigraphic architectures (e.g., Martinsen et al. 1999), it does not permit analysis of interactions and feedbacks between processes. Accommodation may also be problematic to define in nonmarine strata, where it is partly dependent on sedimentation (Muto and Steel 2000). Sequence stratigraphic interpretation of such strata, which dominate the proximal portions of stratigraphic sequences and preserved sediment routing systems, relies on concepts that are awkward to test with observational data (e.g., Wright and Marriott 1993; Shanley and McCabe 1994; Holbrook et al. 2006). In practice, temporal variations in the proportion and stacking density of fluvial conglomerate and sandstone bodies are commonly used as a proxy for changes in A/S ratio, with strata characterized by densely stacked conglomerate and sandstone bodies interpreted to have been deposited under low A/S ratios (e.g., Wright and Marriott 1993; Shanley and McCabe 1994). The simplistic, model-driven nature of such interpretations has been highlighted by case studies in which high-resolution dates or paleogeographic variations in sediment thickness allow temporal and spatial variations in accommodation development to be constrained independently of sandstone proportions (e.g., Willis 1993; Giuseppe and Heller 1998). Difficulty in defining accommodation in nonmarine strata further complicates interpretation of sediment supply and the upstream processes that control it in the proximal portions of stratigraphic sequences.

In order to examine the relevance of the sediment-routing-system model for sequence stratigraphic interpretation, we make use of a recently documented case study from the geological record where the sediment budget has been constrained over a period of approximately 8 Myr (Michael 2013; Michael et al. 2013, 2014a, 2014b). The Escanilla sediment-routing system, which spans the Lutetian to Priabonian (41.6–33.9 Ma; Michael et al. 2013), had its source

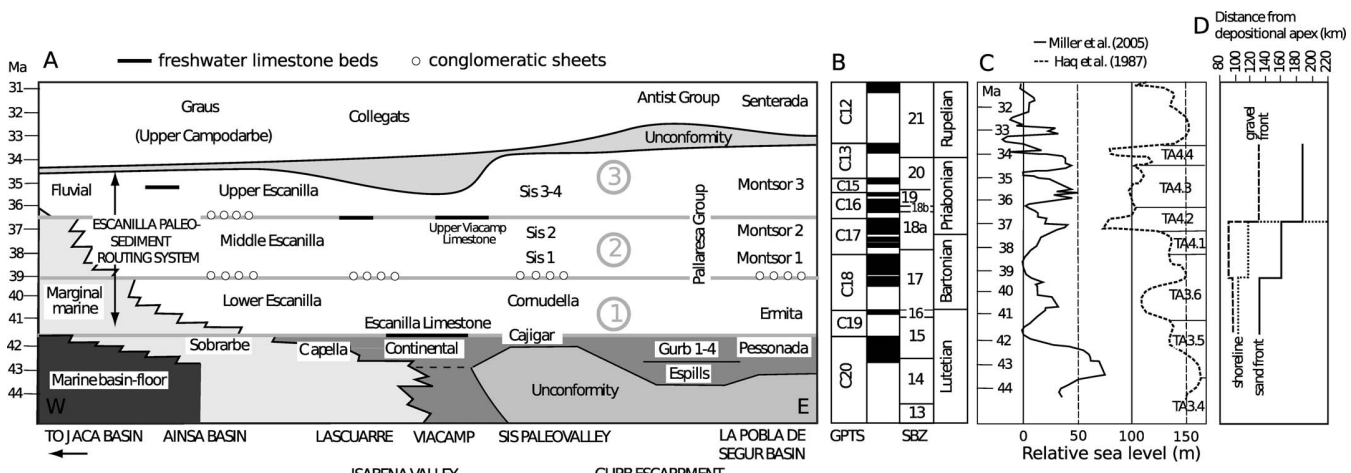


FIG. 2.—A) Summary of the chronostratigraphy of the Escanilla paleo–sediment-routing system in a proximal (right) to distal (left) profile, adapted from Michael et al. (2014a), showing three time intervals. The white circles are conglomeratic sheets, the black horizontal bars are freshwater limestone beds. Both are used to aid correlation. B) Age of the deposits from GPTS, Global Paleomagnetic Time Scale; and SBZ, larger foraminifera shallow benthic zone. C) Global (eustatic) sea-level curves following Haq et al. (1987) and Miller et al. (2005). D) Distance from depositional apex of moving boundaries from Michael et al. (2013) and Michael et al. (2014a).

regions in the south-central Pyrenean orogen, and transported sediment from wedge-top basins along tectonic strike to marine depocenters in the west. The results of the Escanilla study are used to initialize a numerical model for subaerial sediment transport and deposition. We then explore the impact that change in sediment delivery to the basin and change in the capacity of the sedimentary system to transport that sediment has on stratigraphic architecture. The model results test the hypothesis that progradation and retrogradation of moving boundaries, such as the gravel front, can be explained in terms of change in delivery of sediment from source regions. Our work thus examines whether flux of sediment from source regions may be a primary control on observed sequence architectures, particularly in proximal and alluvial regions.

METHODS

Sediment Transport

The Escanilla paleo–sediment-routing system can be simplified into two major catchments in the south-central Pyrenees that fed an along-strike series of wedge-top basins (Fig. 1; Michael et al. 2013; Michael et al. 2014a). A third source of sediment, the Santa Orasia system, supplied sediment to the Jaca Basin in the latest Eocene. However, the Santa Orasia source is volumetrically very small, adding less than 25% of the total volume of material supplied to the Jaca Basin and enters the sediment routing system downstream of the main region of gravel fining (Michael et al. 2013; Michael et al. 2014a). The sediment fairway can then be simplified to a single depositional cross section that extends from the Gurb–Pobla and Sis depocenters through the Tremp–Graus, Ainsa, and Jaca basins (Figs. 1, 2; Michael et al. 2013). The relative simplicity of this system allows us to collapse it into a 1-D, upsystem-to-downsystem profile and to model it as a 1-D system (Figs. 1–3). Our focus is on the proximal part of the sediment routing system, and in particular on movement of the gravel front, since this moving boundary was easy to identify from field-based measurements of particle sizes and grain-size fractions.

1-D Sediment Transport Model

To numerically model the 1-D sediment routing system we assume that there is a plentiful supply of transportable sediment. Following Smith and Bretherton (1972) and Simpson and Schlunegger (2003), we then derive a model for

sediment transport that allows the change in surface run-off with depositional length, x (m), to be accounted for:

$$\partial_t z = U + \partial_x [(\kappa + cq_w^n) \partial_x z] \quad (1)$$

and

$$q_w = \alpha x \quad (2)$$

where z (m) is elevation, U (m yr^{-1}) is the spatial distribution of subsidence, q_w ($\text{m}^2 \text{yr}^{-1}$) is the water flux, and α (m yr^{-1}) is the precipitation rate. The constants κ , c , and n are explained below. These equations for sediment transport are solved implicitly using a finite-element method with linear weighting functions (see Armitage et al. 2011; Armitage et al. 2014). The model time step is of 10,000 yr, and the model has a spatial resolution of 1-km-long elements. The values of the three constants in the concentrative and dispersive diffusive equation (Equation 1) are controlled by three parameters: κ is a linear diffusion coefficient that is intended to capture all the processes that lead to the rounded curvature of hillslopes, c is the fluvial incision coefficient and is related to the ability of surface flowing water to transport sediment, and the exponent n , which has a value greater than 1 (Smith and Bretherton 1972).

The three parameters are difficult to constrain from basic physical principles. The fluvial transport coefficient c and exponent n can be upscaled from empirical bed-load transport laws. Assuming Meyer-Peter–Müller bed-load transport laws, $n \sim 1$, and following Paola et al. (1992) and Marr et al. (2000) we can estimate that $0.01 < c \leq 1$. If, however, we assume $n = 2$, which is consistent with the Einstein–Brown formulation of bed-load transport (Simpson and Schlunegger 2003; Densmore et al. 2007; Armitage et al. 2011), then from tuning the model to geological timescales, $10^{-7} < c \leq 10^{-5} \text{ m}^{-2} \text{ yr}$ (see Armitage et al. 2013).

Hillslope processes such as landslides and soil creep can be approximated by a slope-dependent process with diffusion coefficients analogous to κ of order $10^{-1} \text{ m}^2 \text{ yr}^{-1}$ for landslides and $10^{-4} \text{ m}^2 \text{ yr}^{-1}$ for soil creep (Martin and Church 1997). These estimates are derived from short-term observations of less than one hundred years. Classic models of foreland-basin stratigraphic development find that a linear diffusion coefficient of 100 to 5,000 $\text{m}^2 \text{ yr}^{-1}$ is more suitable for matching sediment accumulation at geological time scales (Flemings and Jordan 1989; Sinclair et al. 1991). The early diffusive models of Flemings and Jordan (1989) and those that followed lumped both fluvial and hillslope

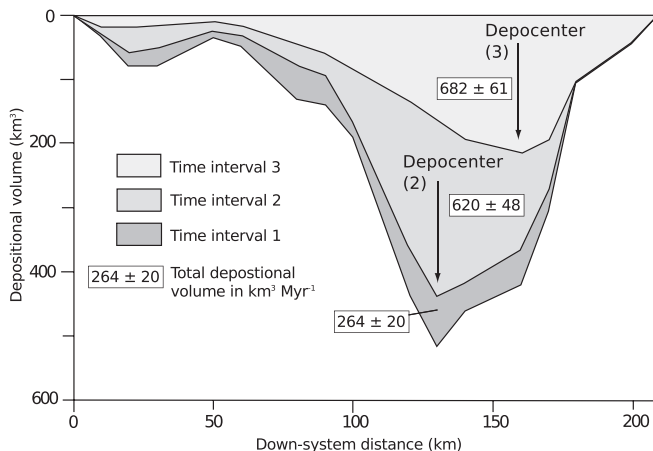


FIG. 3.—Distribution of deposition for the three different time intervals mapped from the Escanilla paleo–sediment-routing system (Michael et al. 2014b).

processes into a single diffusion coefficient, hence the value is much larger than those observed over short timescales. As system length increases, within the framework of Equation 1, the value of κ becomes insignificant compared to the fluvial terms. The effective diffusion coefficient at the outlet of a catchment of length L is defined by

$$\kappa_{\text{eff}} = \kappa + c(\alpha L)^n \quad (3)$$

The effect of diffusive hillslope processes in the idealized 1-D model becomes important only at the uppermost reaches of the catchment. This is because the hillslope term in Equation 1 becomes important when $\kappa \sim c/(zx)^n$, which can be only the case when x is small, hence applicable only in the headwaters of the catchment.

In order to predict both the area of sediment deposited in the 1-D model and the movement of internal boundaries such as the gravel front, the down-system trends in the grain-size of deposited sediment are calculated. The sediment grain-size distribution is modified down-system by selective deposition following the theoretical model and observations of Fedele and Paola (2007), Duller et al. (2010), and Whittaker et al. (2011). We assume perfect sorting, where only gravel is deposited until it is exhausted, followed by only sand and finally by fine-grained material (silt and clay grade; Paola et al. 1992). This assumption results in a gravel front displaced towards the source region compared to its real-world position where proximal deposits are an admixture of gravel and sand. We examine this effect below by invoking a gravel fractionation coefficient.

Gravel undergoes fining according to an exponential function of Sternberg type (Fedele and Paola 2007; Duller et al. 2010);

$$D(\tilde{x}) = D_{g0} + \varphi_0 \frac{1}{C_v} (e^{-C_g \tilde{y}} - 1). \quad (4)$$

The fining of the sand and smaller grain sizes is given by Sternberg (1875)

$$D(\tilde{x}) = D_{si} e^{-C_s \tilde{y}} \quad (5)$$

In equations 4 and 5 \tilde{x} is the dimensionless down-system length, $D_{g0} = \log_{10}(D_{50})$ is the median of the gravel input taken from the 50th percentile from Wolman pebble-count data, $\varphi_0 = \log_{10}(D_{84}/D_{50}) = 0.24$ is the input variance of the gravel assuming that the distribution is log-normal, $D_{si} = \log_{10}(2 \text{ mm})$ is the initial grain-size for sand and finer material in the sediment input,

TABLE 1.—Data used to initialize the numerical stratigraphic model based on field observations of the Escanilla paleo–sediment-routing system.

Time Interval	Age (Ma)	Duration (Myr)	Gravel Fraction (%)	Sand Fraction (%)	Fines Fraction (%)	Total Volume (km³ Myr⁻¹)
T1	41.6–39.1	2.5	8	23	69	246 ± 20
T2	39.1–36.5	2.6	5	22	73	620 ± 48
T3	36.5–33.9	2.6	13	27	60	713 ± 1
Total	41.6–33.9	7.7	8.8	24.5	66.7	-

and \tilde{y} is the spatial transformation of the down-system distance given by Paola and Seal (1995);

$$\frac{d\tilde{y}}{d\tilde{x}} = \frac{r(\tilde{x})}{q_s(\tilde{x})}, \quad (6)$$

where $r(\tilde{x})$ is the down-system distribution of deposition and $q_s(\tilde{x})$ is the down-system distribution of sediment discharge. In Equations 4 and 5 the coefficients are $C_v = 0.25$, $C_g = 0.7$ (Fedele and Paola 2007; Duller et al. 2010; Armitage et al. 2011), and $C_s = 0.3$. Note that we do not use the self-similar model of Fedele and Paola (2007) for the sand and finer grain sizes, as this would cause there to be no grain sizes larger than the mean for the down-system fining; instead we use the classic “Sternberg model” where the input is the initial grain-size.

Derivation of Data for Model Initialization

The Escanilla Formation and time-equivalent strata were divided into three time units based on biostratigraphic and paleomagnetic constraints backed up by sedimentologic logging, paleocurrent analysis, provenance data, and the mapping of distinctive marker horizons such as lacustrine limestones and conglomeratic sheets, as described in Michael et al. (2013), Michael et al. (2014a), and Michael et al. (2014b) (Fig. 2A; Table 1). Absolute ages were obtained using the paleomagnetic standard (Gradstein et al. 2004). The calculation of a sediment budget for the Escanilla sediment-routing system requires the spatial and temporal connection of proximal alluvial fanglomerates with alluvial-plain, coastal, and distal marine deposits. The sediment-routing fairway was mapped and cross-sectional volumes calculated at 23 locations in the down-system direction as described by Michael et al. (2014a). At each location the quantities of gravel conglomerates, sand-grade, and fine-grade fractions were obtained from sedimentological logging. In this way, the down-system pattern of deposited volume, together with the grain-size fraction, was obtained for each of the three time intervals. The position of the gravel cline (where gravel percentages rapidly decline), the gravel front (where gravel is exhausted), and the sand front (where sand is exhausted), are shown in Figure 4 (see Michael et al. 2013).

The location and size of the catchments feeding the Escanilla paleo–sediment-routing system were estimated using a range of provenance indicators (clast lithologies, heavy minerals, U-Pb geochronology of detrital zircons) combined with structural reconstruction of the south-central Pyrenees (Muñoz et al. 2013). The bulk of the sediment of the Escanilla sediment-routing system was derived from two ca. 60-km-long catchments etched into the Axial Zone, which together provided nearly 4000 km³ of particulate sediment over a time period of 7.7 Myr, equivalent to a mean erosion rate of 0.5 to 0.8 mm yr⁻¹ in the source region (Michael et al. 2014b).

The positions of moving boundaries are given in terms of the horizontal distance and in mass-balance coordinates in Table 2 (see Fig. 4; Michael et al. 2013). This mass-balance coordinate system is a spatial transformation of the down-system distance into one that describes the loss of mass (or volume) from that in transport to deposition (Strong et al. 2005; Paola and Martin 2012). To transform the spatial coordinates into a mass-balance coordinate χ for any downstream distance, we divide the cumulative depositional

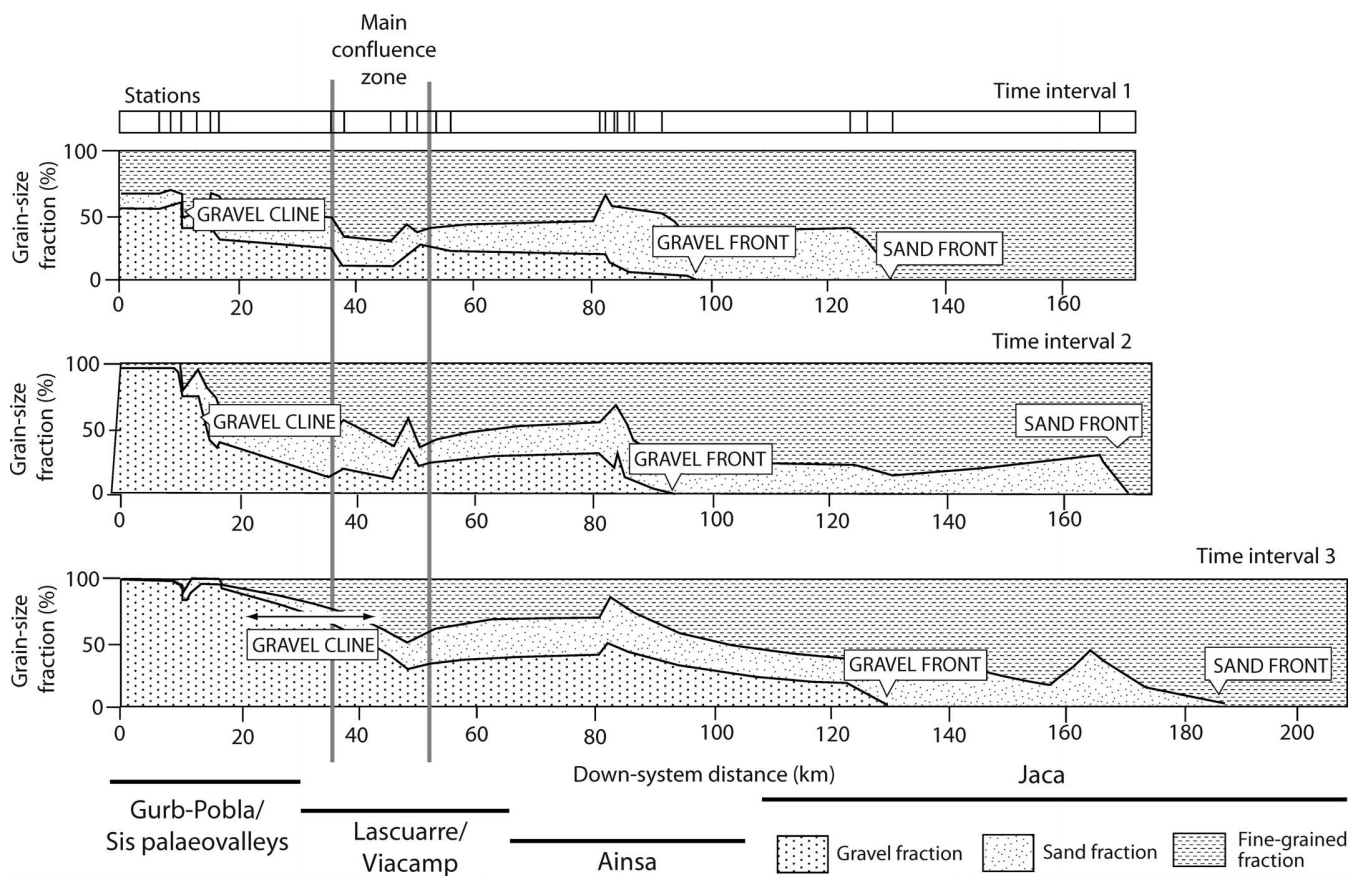


FIG. 4.—Distribution of gravel, sandstones, and fines (siltstones and mudstones) for the three time intervals T1, T2, and T3 (see Table 1; Michael et al. 2013), based on calculation of grain-size fractions at a number of stations distributed in the down-system direction.

volume of sediment at that point by the total depositional volume of the system Q_{tot} :

$$\chi = \frac{1}{Q_{tot}} \int Q_{dep} dx \quad (7)$$

where Q_{dep} is the depositional flux at any point x (see Michael et al. 2013). Inspection of Figure 4 and Table 2 shows that the gravel front does indeed retreat slightly during time interval 2 at the same time as the percentage gravel fraction in the supply also decreases (Table 3).

The numerical model fines the sediment assuming a single mean grain-size in the sediment supply. It first fines gravel clasts and once there is no gravel left the model fines the remaining volume of material assuming that it is made of sand and finer grain-sizes only. This perfect sorting (cf. Paola et al. 1992), however, is idealized. To compare the model to observations, a gravel fractionation coefficient can be defined that represents the total cumulative volume of sediment deposited at the gravel front compared to the volume of gravel in the supply (alternatively, the distance to the observed gravel front compared to the theoretical distance assuming perfect sorting). We can then use this coefficient as a first-order method to adjust the observed gravel front to where it would be assuming perfect sorting (see Section 3.1). The fractionation coefficient varies between 2.3 and 3.8 (Table 3), indicating rather poor efficiency of fractionation of different grain sizes.

External Forcing, Boundary, and Initial Conditions

The numerical model is subject to external forcing in the form of a distribution of subsidence that varies in space and time, a flux of sediment from the

catchment on the left boundary and a precipitation rate within the model domain and catchment. The model domain is 1000 km long. The initial condition is a linear topographic profile with an elevation of 500 m on the left boundary and 0 m on the right boundary. The right boundary is of fixed elevation at 0 km. The left boundary has an influx of sediment (either 12 or 20 m² yr⁻¹, see Table 4). Before applying the model to the history of the Escanilla paleo-sediment-routing system we allow for a 5 Myr model wind-up time, as this is sufficient time to allow the model topography to evolve towards the equilibrium profile (Armitage et al. 2011).

After the 5 Myr model wind-up time, we impose a subsidence rate that changes through the three time intervals with model time spans of T1, 5–7.5 Myr; T2, 7.5–10.1 Myr; T3, 10.1–12.7 Myr. The profile of subsidence is estimated by interpolating, using a spline function, between the measured thickness of the deposits at specific locations down-system (Michael et al. 2014b; Fig. 3). To understand how change in the various model parameters impacts the movement of the gravel front and the depositional architecture, we first systematically vary κ , c , and n in Equation 1 (Table 4). In the following section we vary the precipitation rate, catchment length, and distribution of grain-size in the gravel input (Table 4). We make the simple assumption that the input sediment flux for each time interval is equal to the total volume per million years deposited within the basin (Table 1). For the simple 1-D model, the volume flux needs to be converted into an area flux. To do so we assume that the width of the outlet at the left boundary of the model is 20 km, representing the combination of two catchments providing sediment to the basin. This allows a sediment influx of 12, 31, and 34 m² yr⁻¹ during time intervals T1, T2, and T3 to be approximated (Table 4). The numerical model also incorporates a headward expansion of the catchments over time from 40 km in T1 to 60 km in T2 and

TABLE 2.—Position of moving boundaries from a field study of the Escanilla paleo-sediment-routing system in terms of horizontal distance from the apex of the depositional system and in mass-balance coordinates. Data are from Michael (2013) and Michael et al. (2013).

Time Interval	Gravel Cline (km)	Gravel Front (km)	Sand Front (km)	Depositional Length (km)
T1	10	95	130	165
T2	17	90	165	175
T3	30	130	185	210
Total mass balance co-ordinate χ				
T1	0.010	0.38	0.7	1
T2	0.015	0.14	1	1
T3	0.030	0.38	1	1

T3 (Table 4) as suggested from provenance data summarized in Michael et al. (2014b) and consistent with previously inferred tectonic movements in the Pyrenean Orogen (Marzo and Steel 2000).

Finally, we then run through the parameter space to find the combination of parameters that best fits the observed location of the gravel front. The model assumes perfect sorting, that is, the grain-size deposited at a model point refers to mean gravel, mean sand, and mean fines. Consequently, when assessing the representativeness of model simulations, the predicted location of the gravel front is different from that which is observed. The comparison of model prediction and field observation of the position of the gravel front is facilitated by transforming the spatial coordinates into mass-balance coordinates and then adjusting the observed location of the gravel front assuming that only gravel is deposited first. The model parameters can then be selected that match this adjusted position. The implications of the best-fit model are then discussed with reference to stratigraphic observations and interpretations.

RESULTS

Effect of Model Parameters on Depositional Architecture

The effect of changing the three model parameters (κ , the linear diffusion coefficient, c , the transport coefficient and n , the exponent on the water flux) on the deposition of sediment in terms of grain-size is displayed in Figure 5. It is immediately apparent that change in the linear diffusion coefficient over four orders of magnitude has no impact on the depositional volumes and the

TABLE 3.—Volumes of grain-size fractions in the Escanilla paleo-sediment-routing system. The gravel fractionation coefficient is the measured position of the gravel front compared to the theoretical position for perfect sorting, measured in the mass-balance coordinate. Data are from Michael (2013) and Michael et al. (2013).

Time Interval	Volume Gravel ($\text{km}^3 \text{Myr}^{-1}$)	Volume Sands ($\text{km}^3 \text{Myr}^{-1}$)	Volume Fines ($\text{km}^3 \text{Myr}^{-1}$)	Gravel Fractionation Coefficient
T1	19	57	170	2.5
T2	29	134	456	2.3
T3	87	188	407	3.8

distribution of gravel and finer-grained deposits (Fig. 5A–C). This is because at large distances, throughout the depositional area, the water flux-dependent part of the model equations dominate. The linear diffusion term becomes dominant only in the very proximal part of the erosional profile. Therefore, in all runs beyond this first trio (Fig. 5A–C) we simply set $\kappa = 1 \text{ m}^2 \text{ yr}^{-1}$.

In contrast, change in the transport coefficient c has a large impact on the distribution of gravel and finer grain deposits within the depositional realm (Fig. 5D–I). An increase in the transport capacity causes the gravel front and sand front (contoured as 1.75 mm grain-size) in all three time intervals to migrate farther down-system. Changing the value of n likewise shifts the location of the gravel front, yet there is a trade-off with the value of c such that the appropriate combination of values of n and c can achieve similar results in the down-system grain-size distribution. However, changes in c have a stronger effect than variations in n .

The gravel front of the Escanilla paleo-sediment-routing system is located at between 90 and 130 km distance down-system from the depositional apex during the three time intervals (Figs. 2, 4, Table 2). Using the mass-balance framework we then calculated the fractionation coefficient by comparing the position of the gravel front for perfect sorting to the observed position (Table 3). By calculating the cumulative integral of deposition in the model, the transformation of the perfect-sorting gravel front in mass-balance space (χ ; Table 3) to spatial coordinates can then be calculated (Table 5). Using this as a guide, a transport model with $n = 1$ and $c = 0.1$ gives a reasonable location of the gravel front at between 25 and 100 km. A transport model with $n = 2$ and $c = 10^{-5} \text{ m}^2 \text{ yr}^{-1}$ likewise gives a reasonable location of the gravel front at between 40 and 100 km.

TABLE 4.—Model names and parameters; n , exponent on water flux; c , fluvial transport coefficient; κ , linear diffusion coefficient; $q_{s(in)}$, influx of sediment at the left boundary; α , precipitation rate; l_c , catchment length; D_{go} , mean grain-size of gravel input.

Parameter Units	n	C ($\text{m}^2 \text{ yr}^{-1}$) $^{1-n}$	K $\text{m}^2 \text{ yr}^{-1}$	Time Interval T1			Time Interval T2			Time Interval T3		
				$q_{s(in)}$ $\text{m}^2 \text{ yr}^{-1}$	α m yr^{-1}	l_c km	D_0 mm	$q_{s(in)}$ $\text{m}^2 \text{ yr}^{-1}$	α m yr^{-1}	l_c km	D_0 mm	$q_{s(in)}$ $\text{m}^2 \text{ yr}^{-1}$
Figure 4												
	1	0.1	0.01	20	0.2	40	40	20	0.2	40	40	20
	1	0.1	1	20	0.2	40	40	20	0.2	40	40	20
	1	0.1	1	20	0.2	40	40	20	0.2	40	40	20
	1	0.01	1	20	0.2	40	40	20	0.2	40	40	20
	1	1.0	1	20	0.2	40	40	20	0.2	40	40	20
	2	10^{-5}	1	20	0.2	40	40	20	0.2	40	40	20
	2	10^{-6}	1	20	0.2	40	40	20	0.2	40	40	20
	2	10^{-7}	1	20	0.2	40	40	20	0.2	40	40	20
Figure 5												
M1A	1	0.1	1	12	0.2	40	31	0.2	40	46	34	0.2
M1B	1	0.1	1	12	0.2	40	24	31	0.2	46	34'	0.2
M1C	1	0.1	1	12	0.2	40	24	31	0.4	60	34	0.4
M2A	2	10^{-5}	1	12	0.2	40	40	31	0.2	40	34	0.2
M2B	2	10^{-5}	1	12	0.2	40	24	31	0.2	46	34	0.2
M2C	2	10^{-5}	1	12	0.2	40	24	31	0.4	60	34	0.4

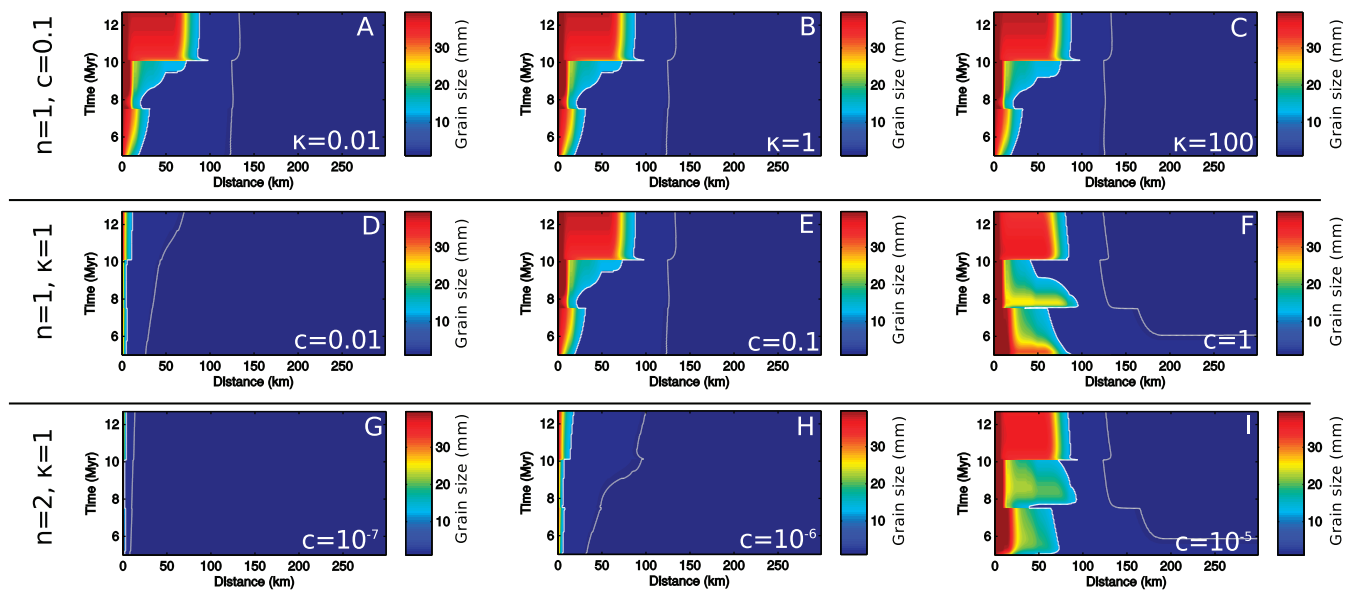


FIG. 5.—Wheeler diagrams of the grain-size (in mm) deposited in the idealized Escanilla sediment-routing system to compare model output for the parameters in Table 4. In parts A to C the linear diffusion coefficient κ is varied from 0.01 to $100 \text{ m}^2 \text{ yr}^{-1}$, while $n = 1$ and $c = 0.1$. In Parts D to F the transport coefficient c is varied from 0.01 to 1, while $n = 1$ and $\kappa = 1 \text{ m}^2 \text{ yr}^{-1}$. In Parts G to I the transport coefficient c is varied from 10^{-7} to $10^{-5} \text{ m}^2 \text{ yr}$ while $n = 2$ and $\kappa = 1 \text{ m}^2 \text{ yr}^{-1}$. The location of the idealized gravel front due to perfect sorting is given by the white contour. The gray contour plots 1.75 mm grain-size.

Effect of Change in the Characteristics of the Sediment Supply

The predicted depositional architecture is a function of both the model parameters (Fig. 5) and the boundary conditions (Fig. 6). From the volumetric budget of sediment deposited in the Escanilla system we first explore how the model responds to a change in flux of the sediment supply as it undertakes the transitions from time interval T1 to T2, and from T2 to T3 (Fig. 6A, D, G, J; models M1A and M2A in Table 4). The result of increasing the sediment flux from 12 to $31 \text{ m}^2 \text{ yr}^{-1}$ from T1 to T2 is to transiently reduce the distance to which gravel and finer grain sizes are deposited, as the increased flux requires increasing slope at the left boundary, thereby increasing the thickness of deposits at short distances down-system. The position of the gravel front and sand front (1.75 mm grain-size contour) at the beginning of time interval T2 is reduced to only a few kilometers from the apex (Fig. 6A, G). For the two models M1A and M2A, in mass-balance coordinates the locations of the gravel and sand fronts do not move significantly from time interval T1 to T2, because the ratio of input flux to accommodation space is similar (Fig. 6D, J). From time interval T2 to T3 there is then progradation of the gravel front as supply increases relative to accommodation and the system recovers towards the topographic steady-state that balances the input sediment flux and the distribution of subsidence (Fig. 6A, G).

The addition of a change in the gravel grain-size distribution of the sediment supply (models M1B and M2B) does not change the location of the gravel front because the total fraction of gravel entering the basin has not changed (Fig. 6B, E, H, K). It does, however, alter the interpretation of the gravel cline, because during time interval T1 there is a smaller quantity of coarse material

entering the basin relative to T2 and T3. The subsequent addition of an increase in precipitation rate from 0.2 to 0.4 m yr^{-1} and an expansion of the catchment length from 40 to 60 km from time interval T1 to T2 have a dramatic effect on the position of the gravel front and the sand front (Fig. 6C, F, I, L; models M1C ad M2C). Farther models show that this shift in deposition is primarily due to change in precipitation rate, because this affects the water flux in both the catchment acting as a source region and in the depositional segment, whereas an increase in catchment length only increases the water flux leaving the source region.

Increasing the precipitation rate from 0.2 to 0.4 m yr^{-1} increases the sediment transport capacity as the model undergoes the transition from time interval T1 to T2. This increased transport capacity lowers slope at the input (left) boundary and therefore reduces the change in elevation at this boundary due to the increased input of sediment from T1 to T2. The response is a progradation of coarse material during time interval T2 as the larger input of material is deposited as a thinner wedge down-system (Fig. 6C, I). The effect is strongest when $n = 2$, as in this case the transport is a function of precipitation rate multiplied by down-system length squared. For model M1C where $n = 1$, the gravel front is located between 25 and 90 km, with a progradation during time interval T3 to 90 km (Fig. 6C). For model M2C where $n = 2$, the gravel front varies between 50 and 100 km with a marked progradation during the early part of time interval T2 (Fig. 6I).

The combined effects of changes in the flux of the sediment supply and the transport capacity cause marked shifts in the deposition of gravel and sand. While providing information on the temporal evolution of the gravel front and gravel cline, the Wheeler diagrams in Figures 5 and 6 do not show the thickness of deposits. Models M1C and M2C are likely the most realistic because they take into account the widest set of observational constraints. The stratigraphic architecture predicted by these two models shows a thickening of deposits down-system of 100 km (Fig. 7), which is consistent with field observations and is driven by the down-system increase of subsidence that creates more accommodation in this region. If we assume $n = 1$ in the transport equations (model M1C), then there is some erosion of the proximal 50 km of deposits within time interval T1 (Fig. 7C). An area corresponding to $4 \times 10^4 \text{ m}^2$ is eroded off the most proximal deposits of time interval T1. Other than this erosion, the stratigraphic architecture is similar to that observed. If,

TABLE 5.—Observed gravel front and the location of the gravel front adjusted for perfect sorting.

Time Interval	Observed Gravel Front (km)	Fraction Coefficient	Perfect Sorting Gravel Front (km)
T1	95	2.5	58
T2	90	2.3	40
T3	130	3.8	78

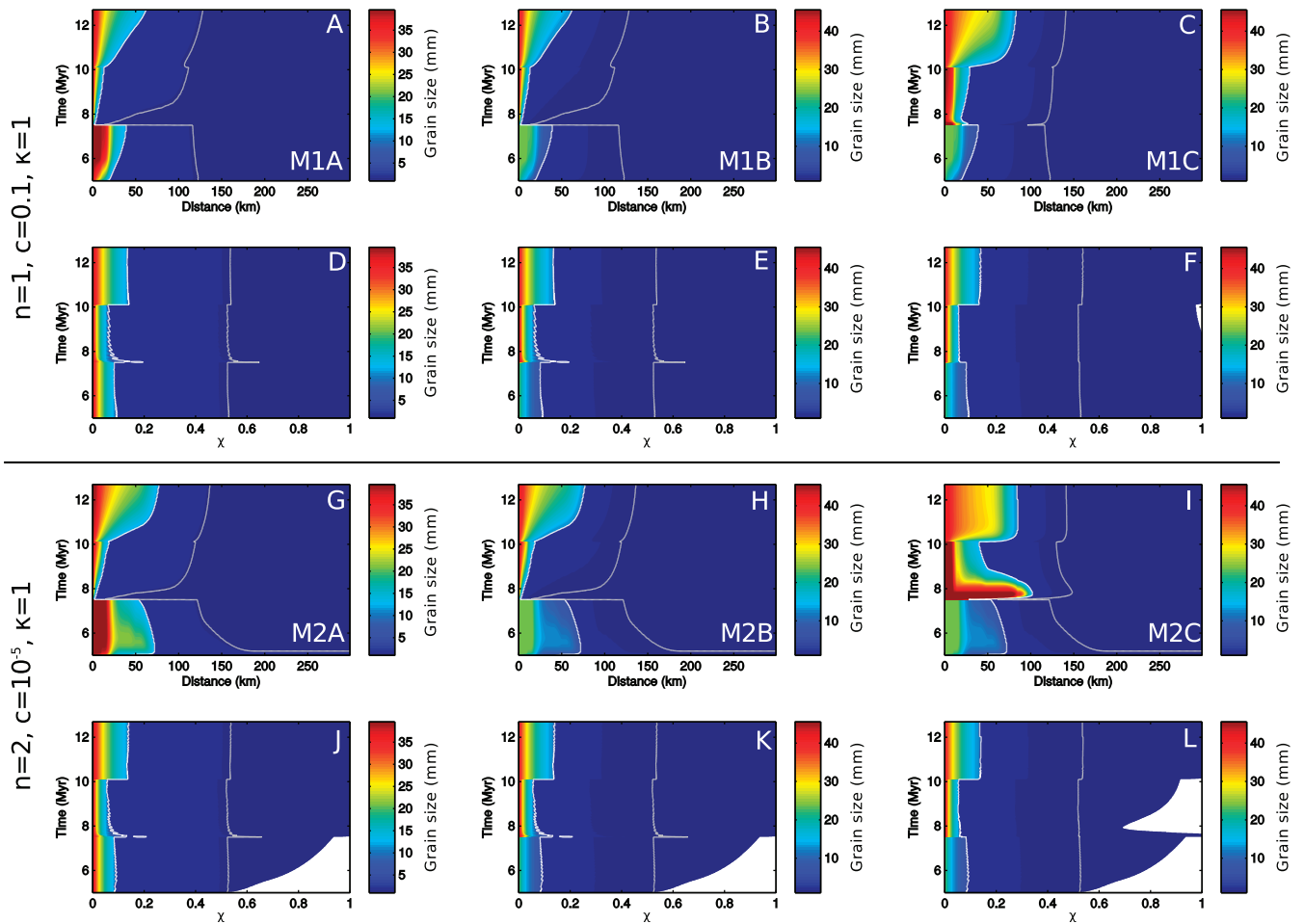


FIG. 6.—Wheeler diagrams of the grain-size (in mm) deposited in the idealized Escanilla paleo-sediment-routing system and the same information transformed into mass-balance coordinates χ . The models displayed correspond to the parameter combinations given in the lower part of Table 4. Parts A to F show the results for models in which $n = 1$, $c = 0.1$ and $\kappa = 1 \text{ m}^2 \text{ yr}^{-1}$. Parts G to L show the results for models in which $n = 2$, $c = 10^{-5} \text{ m}^{-2} \text{ yr}^{-1}$ and $\kappa = 1 \text{ m}^2 \text{ yr}^{-1}$. From left to right: Models M1A and M2A, which include a change in input sediment flux during time intervals T1, T2, and T3. Models M1B and M2B also include a change in the mean grain-size entering the basin. Models M1C and M2C also include a change in catchment length and precipitation rate. The location of the idealized gravel front due to perfect sorting is given by the white contour. The gray contour plots the 1.75 mm grain-size. The white space in Parts J to L display the regions where χ does not reach 1 in the down-system direction because of basin bypass, i.e., the basin is not closed and so mass is lost.

however, $n = 2$ (model M2C) then there is significant erosion of the uppermost deposits from time interval T1, so that $5 \times 10^6 \text{ m}^2$ of deposits are eroded between down-system distances of 0 and 50 km (Fig. 7D). Such erosion is not documented in the Escanilla sediment routing system, which suggests that the transport efficiency of the model with $n = 2$ is too high to offer a realistic set of solutions. Furthermore, in models with $n = 2$ there is an unreasonable amount of basin sediment bypass beyond the basin margin represented by the lower model boundary, as shown by the periods where the flux out of the basin is greater than zero, and recorded by the mass-balance coordinate χ not reaching 1 (Figs. 5J–L, 6B).

Finding a Best-Fit Model

To find the parameters and boundary conditions that best match the observed stratigraphic record of the Escanilla paleo-sediment-routing system, it is necessary to find a model run that simulates the correct location of the gravel front in each time period (Table 5). It is also necessary to find a model run that has minimal sediment bypass beyond the basin limit, as the implicit assumption is that the sediment budget of the Escanilla paleo-sediment-routing system is closed (Michael et al. 2013, 2014b). It has already been shown that a change

in the linear diffusivity, κ , has very little effect on the stratigraphic architecture (Fig. 5A–C). This parameter is therefore fixed at $1 \text{ m}^2 \text{ yr}^{-1}$. Furthermore, the case where $n = 1$ is preferred, because when $n = 2$ the high transport efficiency leads to both proximal erosion and a significant amount of sediment bypass beyond the basin limit (Figs. 5J–L, 6B, D).

The procedure used to find the best-fit model is illustrated in Figure 8. Two parameters are varied that have the largest influence on the position of the gravel front: precipitation rate, α , and the transport coefficient, c . Starting with time interval T1, one hundred simulations were run, varying both precipitation rate and the transport coefficient (Fig. 8A, B). We then compare the predicted maximum location of the gravel front and the location of the observed gravel front adjusted for perfect sorting (Table 5). In Figure 8 the ratio of the amount of sediment that leaves the model domain compared to the input sediment flux is plotted, to check that the model with the matching gravel front does not produce significant bypass of sediment.

We find that the best fit for time interval T1 occurs when the precipitation rate $\alpha = 0.19 \text{ m yr}^{-1}$ and the transport coefficient $c = 0.17$. The best-fit values of precipitation rate and transport coefficient are then used to model both the wind-up period of 5 Myr and time interval T1. These two parameters were then changed for time interval T2 (Fig. 8B, C). The best-fit model for the

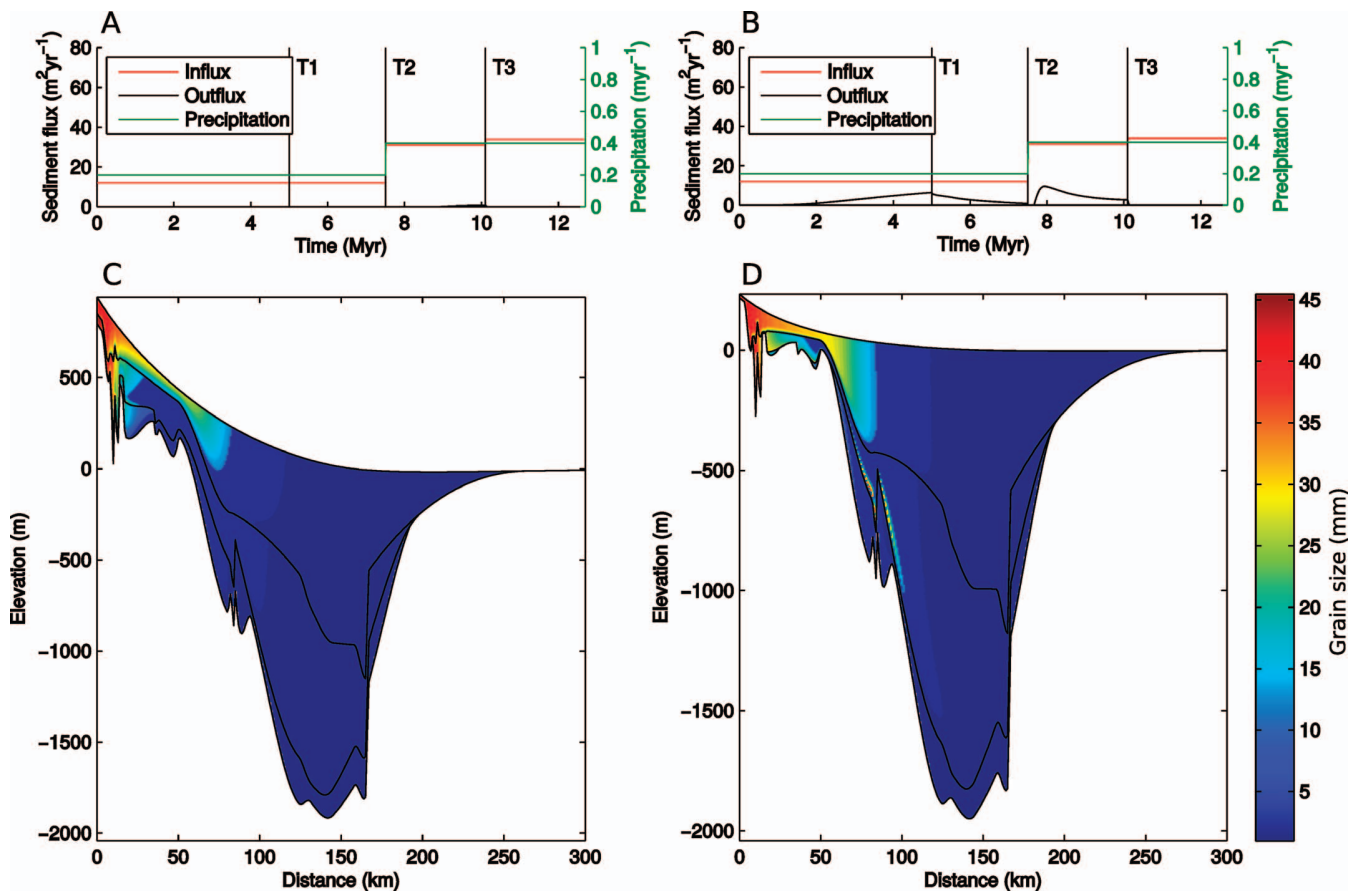


FIG. 7.—Stratigraphy for models M1C and M2C in Table 4. **A)** Input sediment flux, sediment flux out at the lower model boundary (at 1000 km), and precipitation rate plotted against time for model M1C. The 5 Myr wind up time is shown followed by three time intervals, T1, T2, and T3. **B)** As in Part A but for model M2C. **C)** Grain-size of sediment deposited plotted at the end of the model M1C run showing the modeled stratigraphy for the three time intervals. The stratigraphy for the wind-up period is not shown. **D)** As in Part C but for model M2C.

location of the adjusted gravel front is found to be when the transport coefficient $c = 0.17$. However, precipitation rates are required to increase to $\alpha = 0.41 \text{ m yr}^{-1}$ (Fig. 8A, B). There is a small amount of sediment bypass beyond the basin under these conditions. Next, the model is restarted using the best-fit parameters for both time intervals T1 and T2 and the range of precipitation and transport coefficient for time interval T3 is tested. Once again, the transport coefficient that best matches the location of the gravel front is $c = 0.17$, accompanied by a reduction in precipitation rate to $\alpha = 0.23 \text{ m yr}^{-1}$ (Fig. 8A, B).

The location of the gravel front is controlled by the distribution of accommodation and the transport of material down-slope. When the location of the gravel front is plotted against the product of precipitation rate and transport coefficient (Fig. 8C) the trend has a complex functional form that is dependent on the distribution of accommodation. However, a clear trend is observed, suggesting that there is a unique transport capacity that gives rise to the location of the gravel front when combined with the distribution of accommodation. The transport coefficient c can be estimated from first principles under the assumption $n = 1$ (Paola et al. 1992). Depending on the grain size in transport, $0.1 < c < 1$ (Marr et al. 2000; Paola et al. 1992). In a previous numerical model it was found that for the transport of sediment over very long distances $c \sim 0.01$ (Armitage et al. 2014). For the Escanilla sediment routing system we find that $c = 0.17$, which is within the range of estimates of c derived from first principles (Marr et al. 2000; Paola et al. 1992).

DISCUSSION

The Escanilla Paleo-Sediment-Routing System and Predicted Stratigraphy

The duration of the Escanilla paleo-sediment-routing system spans the Lutetian to Priabonian stages of the Eocene (41.6–33.9 Ma; Michael et al. 2013, 2014a). Over this time period, there was an overall progradation of facies belts to the west, along the strike of the central Pyrenean orogen. Fluvial environments persisted in the eastern sector of the sediment-routing system in the mid-to-late Eocene (Muñoz 1992; Puigdefàbregas et al. 1992; Benthon and Burbank 1996), sourced from the internal zones of the south-central Pyrenees. Fluvial systems in the east supplied deltaic coasts, shallow marine environments, and pro-delta slopes in the Ainsa Basin and deep marine basin floor environments in the Jaca Basin to the east (Nijman 1998; Dreyer et al. 1999) (Fig. 2). The sediments of the alluvial segment are therefore linked with coeval marine deposits to the east, the shoreline migrating a distance of approximately 100 km between time interval T1 and time interval T3. The gravel and sand fronts also migrate westwards over time, but the gravel front retreats slightly during time interval T2, independent of the overall progradation of the system. In the Escanilla paleo-sediment-routing system the eustatic sea-level curves do not correspond to observed stratigraphic boundaries and architectures in the Escanilla routing system (Fig. 2), due, at least in part, to locally variable tectonic subsidence in the Pyrenean foreland basins (e.g., Marzo and Steel 2000).

Regional and proxy data, which are independent of outcrop observations, can be used to constrain climate, hinterland tectonics, and relative sea level

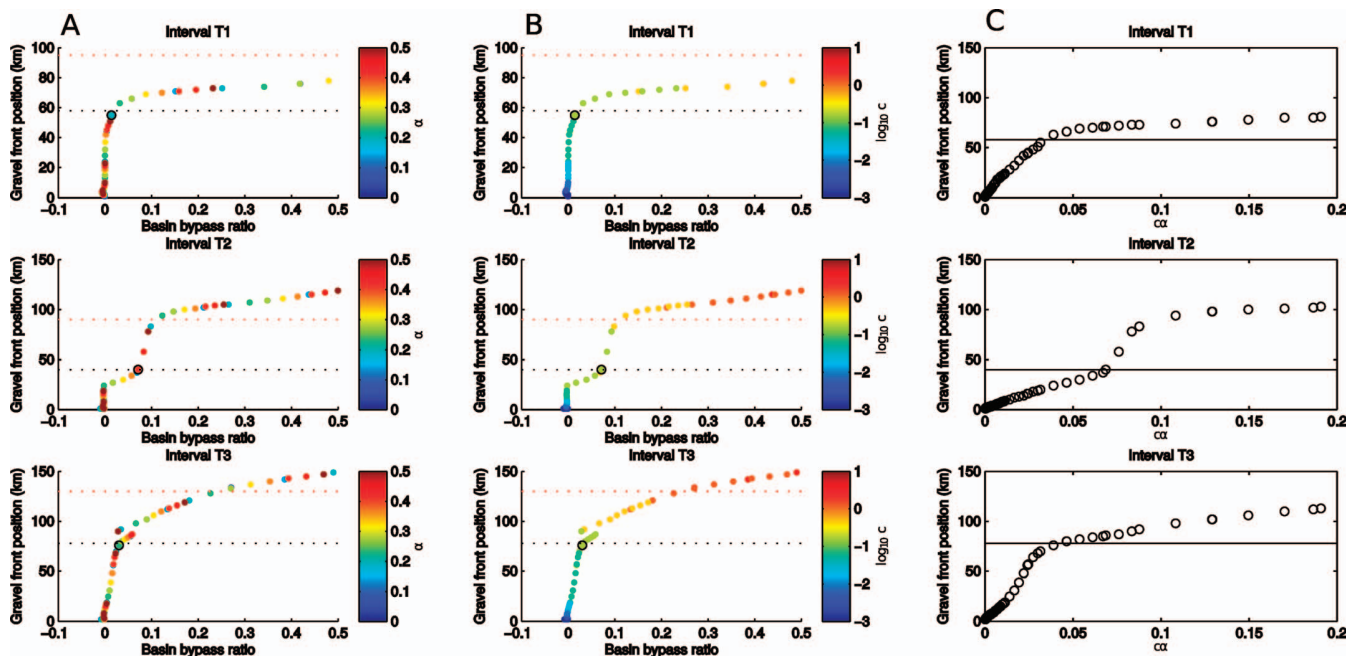


FIG. 8.—Scatter plots of the basin bypass ratio, defined as the ratio of sediment flux out of the basin to sediment influx, against the maximum distance that the gravel front reaches for different precipitation rates and transport coefficients during the time intervals T1, T2, and T3. **A)** Scatter plot of gravel front vs. bypass for the three model time intervals. The colors are for different values of precipitation rate. The red dotted line is the location of the gravel front, and the black dotted line is the location of the gravel front adjusted for perfect sorting. The black circle shows the best-fit model for the particular time interval. **B)** As in Part A, but the color scale shows the transport coefficient. **C)** Scatter plot of the product of the transport coefficient c and precipitation rate α . The black line is the location of the adjusted gravel front. It can be seen that there is an ideal combination of precipitation and transport coefficient that gives a match to the adjusted location of the gravel front.

during the mid-Eocene to the basal Oligocene, in order to test the viability of the best-fit model (Fig. 9). During time intervals T1 and T2 the location of the gravel front contracts slightly from 58 to 40 km when adjusted for perfect sorting (Table 5). Subsidence rates inferred from depositional thicknesses, however, increase by up to a factor of four from time interval T1 to interval T2 (Fig. 3). The sediment flux entering the basin is likewise increased by a factor of three to match the volume of sediment deposited. In the absence of a change in precipitation, the position of the gravel front would decrease to < 25 km (Fig. 6A, B, G, H). An increase in the precipitation rate and hence transport capacity reduces the slope and hence the elevation at the catchment outlet at the left boundary of the model, and sets the gravel front at 40 km down-system. The increase in precipitation is therefore required to prevent significant retreat of the gravel front.

The migration of the shoreline during the Bartonian to Priabonian is shown in Figure 2D. The transition from deltaic to fluvial deposits in the Jaca and Ainsa basins records progradation of the Escanilla paleo-sediment-routing system during this time interval, and has been attributed to a fall in base level by some authors (Bentham et al. 1992). Evidence from thermochronology suggests that erosion of the hinterland regions was relatively steady at between 0.25 to 0.3 mm yr⁻¹ in the mid-to-late Eocene, increasing to > 1 mm yr⁻¹ in the latest Eocene–early Oligocene (after time interval T3), as uplift continued in the Axial Zone (e.g., Beamud et al. 2010; Whitchurch et al. 2011; Michael et al. 2014b). Palynological data from the Ebro Basin indicate that in the middle Bartonian the climate was very warm and humid, suggesting high precipitation rates at the transition from T1 to T2 (Cavagnetto and Anadón 1996). Therefore, it is possible that increased sediment flux due to increased runoff led to the change in the position of the gravel front without requiring base-level change.

The gravel front migrated from 40 to 78 km down-system in time interval T3 when adjusted for perfect sorting (Table 5). Progradation of the gravel front occurred in part due to the change in the distribution of accommodation, as

displayed by the models where input sediment flux and precipitation do not vary significantly between T2 and T3 (Fig. 6). In these models the gravel front is located at approximately 100 km or more down-system (Figs. 5, 6). To account for the adjusted observed location of the gravel front while maintaining the flux required to match the observed deposited volume, a reduction in transport capacity is required. This is best achieved through a reduction in precipitation rates from roughly 0.4 to 0.2 m yr⁻¹ (Fig. 9). The record from pollen taxa indicates that there was a transition to more open vegetation in the Priabonian (Cavagnetto and Anadón 1996). The implications of our sediment transport model are therefore consistent with palynological evidence that the climate became drier during time interval T3.

The model simulates propagation of the gravel front during time intervals T1 and T2 followed by a cycle of retrogradation and subsequent progradation during time interval T3 (Fig. 9). Synthetic sedimentary logs can be extracted from different distances along the model length to show how these responses to changing sediment supply and precipitation rate may be recorded in stratigraphy (Fig. 10). The synthetic logs show that close to the catchment outlets (10–20 km from the depositional apex) the stratigraphy is simulated to be dominated by gravel, as observed within the Pobla Basin and Sis Paleovalley (Figs. 1, 9A; Michael et al. 2014b). Farther down-system in the Tremp (Lascuarre locality at 40–60 km) and Ainsa (70–90 km) basins (Fig. 1), the synthetic logs allow the model predictions to be compared to observations recorded in measured logs (Michael et al. 2014b). To make this comparison, the observed sedimentary logs are filtered using a Gaussian filter with a window of 50 m in order to highlight the large-scale trend. The filtered logs from the Lascuarre area and Ainsa Basin show deposition of mainly sandstones and fine-grade sediments during intervals T1 and T2 (Fig. 10). It is only towards the end of time interval T3 that there was significant gravel deposition with clast sizes of 20 mm in the Lascuarre log (Vincent 2001; Fig. 10B). The Ainsa log likewise shows that there was significant gravel conglomerate deposition only during the later part of time interval T3 (Fig. 10C).

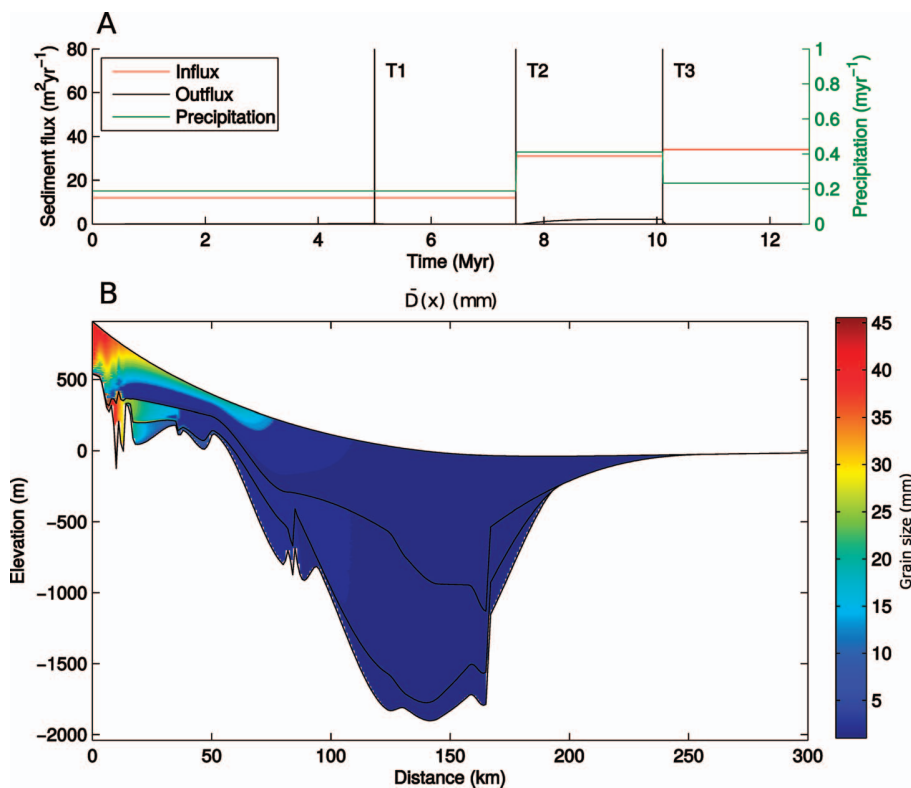


FIG. 9.—Stratigraphic architecture predicted by the forward model run that most closely matches the observed location of the gravel front adjusted for perfect sorting. A) Sediment flux in and out of the basin and precipitation rate against time. B) Distribution of grain-size deposited in the idealized Escanilla paleo-sediment-routing system.

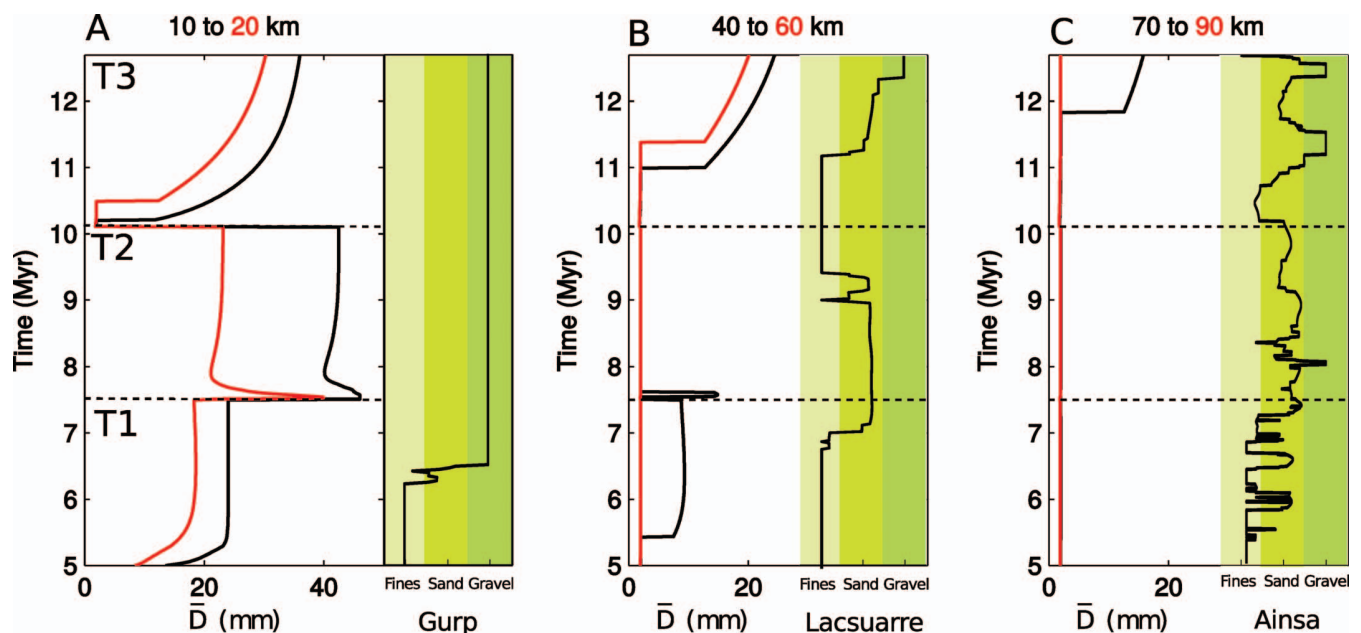


FIG. 10.—Synthetic sedimentary logs taken at six distances down the system (see Fig. 9). A) Logs at 10 (black) and 20 km (red) distance down-system. Also displayed is a filtered sedimentary log taken from the Gurb escarpment in the Pobla Basin (Fig. 1; Michael et al. 2014b). B) Logs at 40 (black) and 60 km (red) distance down-system. Also displayed is a filtered sedimentary log taken from Lacsuarre in the Tremp Basin (Fig. 1; Michael et al. 2014b). C) Logs at 70 (black) and 90 km (red) distance down-system. Also displayed is a filtered sedimentary log from the Ainsa Basin (Fig. 1; Michael et al. 2014b). The three sedimentary logs have been filtered using a Gaussian filter with a window of 50 m, in order to highlight the main trends in the spatial distribution of fines, sand, and gravel grain sizes.

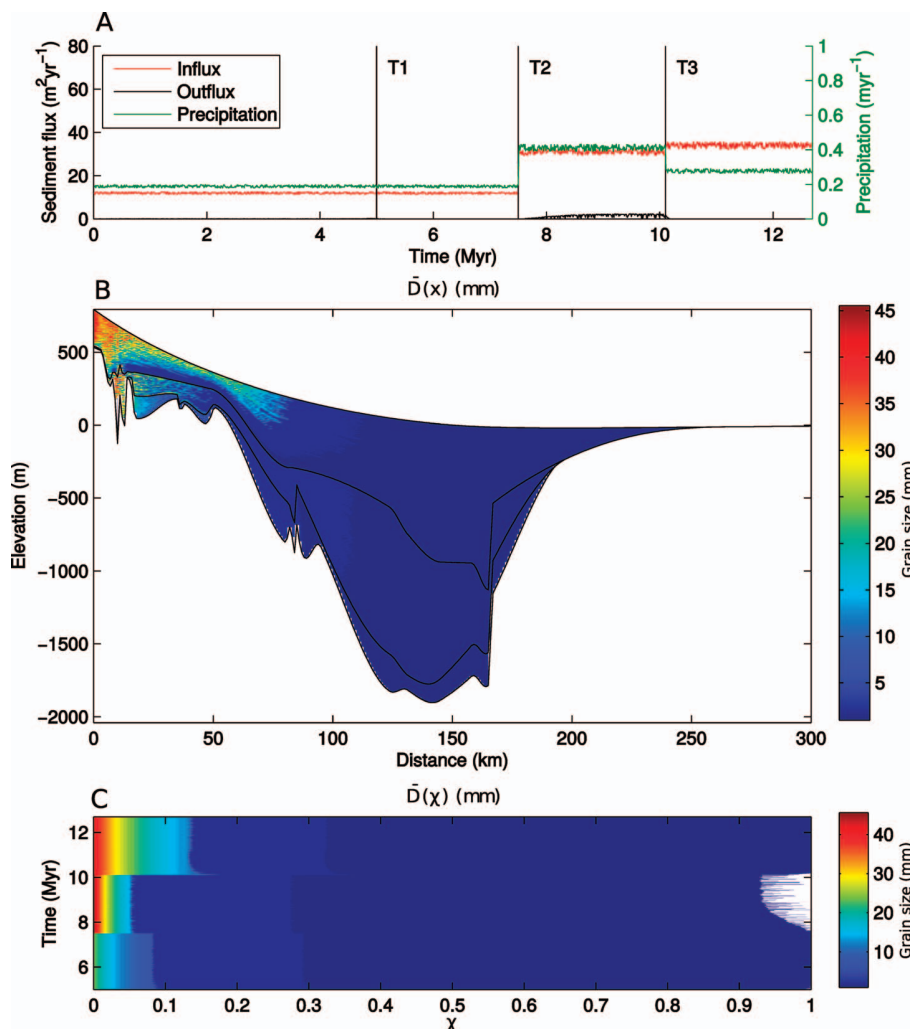


FIG. 11.—Stratigraphic architecture predicted by the forward model run that most closely matches the observed location of the gravel front adjusted for perfect sorting (Fig. 9) but with the addition of a small, 1% variation in the precipitation rate and sediment flux. A) Sediment flux in and out of the basin and precipitation rate against time. B) Distribution of mean grain size deposited in the idealized Escanilla paleo-sediment-routing system. C) Distribution of mean grain-size in mass-balance space. Note how the spatial variation in the gravel-front location in individual time intervals is masked. Furthermore there is a small amount of basin bypass in T2 marked by the white region at high values of χ .

The model can predict the gross trend of gravel deposition increasing towards the end of T3 but cannot match the more detailed changes in deposition from fines to sands during time intervals T1 and T2 (Fig. 10). The progradation during T3 is a function of a steady sediment flux accompanied by a reduction in transport capacity. This causes a transient increase in slope at the catchment outlet, the left boundary. To accommodate this increased transport slope there is an increase in elevation and hence deposition at this boundary. The system then progrades again towards steady-state conditions that are representative of the distribution of accommodation (cf. Armitage et al. 2011). The stratigraphic architecture therefore reflects the relationship between flux of the sediment supply and transport capacity.

Small Variations in System Forcing

Given that the flux of the sediment supply and precipitation rate can act together to cause progradation and retrogradation, we have added noise of a magnitude 1% of the magnitude of the input signal to both precipitation rate and input sediment flux in order to visualize any high-frequency stratigraphic variations (Figs. 11, 12). The signal-to-noise ratio is small (Fig. 11A), but the resulting stratigraphic architecture shows a noticeable variation in grain-size (Figs. 11B, 12). This is because the change in the flux of the sediment supply and precipitation rate may either enhance progradation or reduce it, depending on whether peaks in these input signals coincide or

not. When transformed into mass-balance coordinates, the spatial variation is removed as the mass-balance space accounts for changes in the flux of the sediment supply and depositional thickness (Fig. 11C).

A qualitative comparison with the sedimentary logs suggests that the model with a small variation in the precipitation rate and the flux of the sediment input shows an improved correlation with the observations (Fig. 12B, C). The gross trend of prograding gravel deposits during T3 remains, but there is now also an increase in coarser deposits during T2, which corresponds with the increased abundance of sandstones observed during T2 at Lascuarre and Ainsa (Fig. 12B, C).

IMPLICATIONS FOR SEQUENCE STRATIGRAPHY

The physical sediment transport model used in this study, and the chronostratigraphic resolution of the Escanilla paleo-sediment-routing system, limits our results to stratigraphic architectures developed over several million years (cf. third-order sequences of Van Wagoner et al. 1990). Model runs generate synthetic patterns of grain-size distributions that resemble retrogradation and progradation of facies belts at this temporal scale. For example, a change from retrogradation to progradation of grain-size belts is found at the transition from T2 to T3, as revealed by synthetic logs (Figs. 10, 12) and cross-sectional basin profiles (Figs. 9, 11). These stratigraphic patterns were generated by the physical model through the interplay between the transport capacity of the

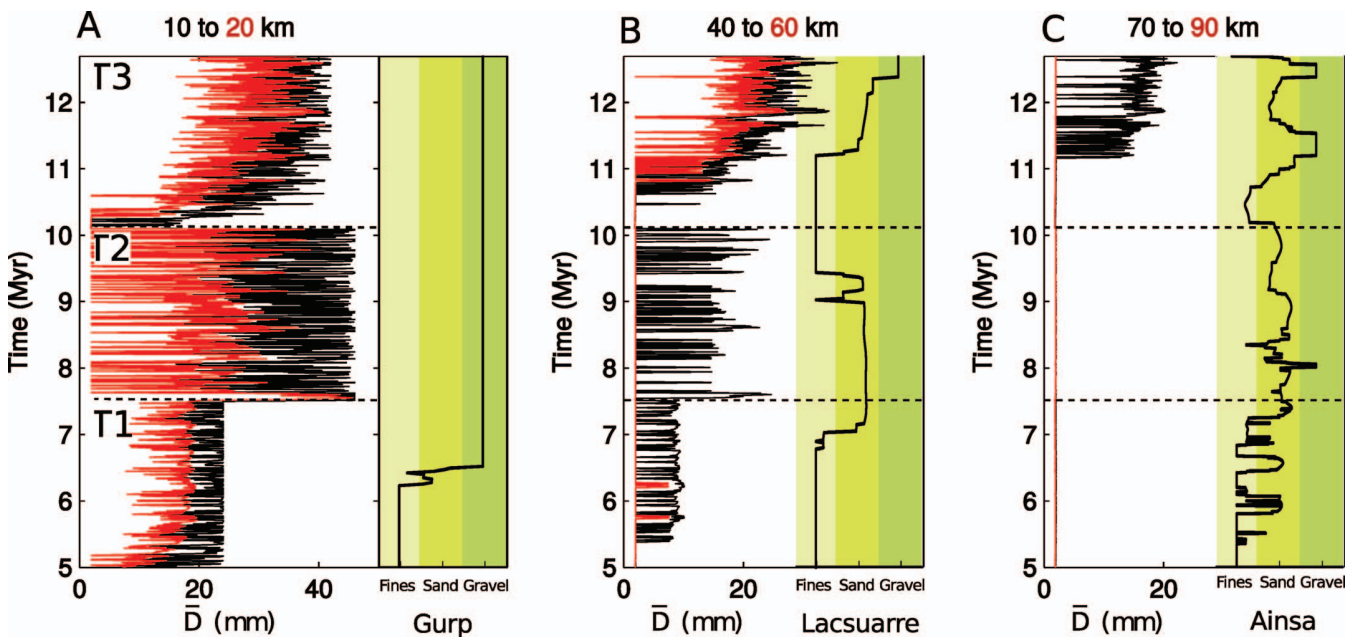


FIG. 12.—Synthetic sedimentary logs taken at six distances down-system where there is a small 1% variation in the input sediment flux and precipitation rate magnitude (see Fig. 11). A) Logs at 10 (black) and 20 km (red) distance down-system. Also displayed is a filtered sedimentary log taken from the Gurb escarpment in the Pobla Basin (Fig. 1; Michael et al. 2014b). B) Logs at 40 (black) and 60 km (red) distance down-system. Also displayed is a filtered sedimentary log taken from Lacsuarre in the Tremp Basin (Fig. 1; Michael et al. 2014b). C) Logs at 70 (black) and 90 km (red) distance down-system. Also displayed is a filtered sedimentary log from the Ainsa Basin (Fig. 1; Michael et al. 2014b). The three sedimentary logs have been filtered using a Gaussian filter with a window of 50 m, in order to highlight the main trends in the spatial distribution of fines, sand, and gravel grain sizes.

sediment-routing system, the supply of sediment from upland catchments, and the creation of accommodation space. In this context, movement of the gravel front proves to be a sensitive index of sediment-routing-system dynamics that allows the roles of sediment supply and accommodation generation as forcing mechanisms to be tested in the Escanilla sediment routing system (Figs. 5, 6). In order to reproduce the position of the gravel front in time intervals T1, T2, and T3, the sediment flux and transport capacity of the system must have changed at the transition between the time intervals (Fig. 9). Changes in accommodation and base level are insufficient to generate the observed stratigraphic patterns of gravel-front position.

The role of sediment supply in generating sequence stratigraphic architectures has long been recognized (e.g., Galloway 1989; Van Wagoner et al. 1990; Heller et al. 1993; Schlager 1993; Carvajal and Steel 2006; Carvajal et al. 2008). However, the use of a physical sediment transport model initialized and tested by observations from a well-documented case study enables the processes controlling sediment supply to be investigated quantitatively, and provides powerful support for the value of considering multiple controls on sequence architectures (e.g., “complexity paradigm” of Miall and Miall 2001). Unless the full sediment budget is known and placed within a sediment-routing-system context, interpretation and inversion of forcing mechanisms from stratigraphic observations is likely to suffer strongly from non-uniqueness. These results emphasize that the uncritical interpretation of a dominant accommodation control on sequence architecture (e.g., due to relative sea-level or base-level changes) may be misleading, particularly in the absence of a source-to-sink context and/or data that independently constrain sediment supply.

CONCLUSIONS

Stratigraphic architectures are controlled by the interplay at different spatial and temporal scales of accommodation generation and the magnitude and

grain-size mix of the sediment supply to a depositional basin. We have developed a simple 1-D sediment transport model that is initialized and constrained by data from the Eocene Escanilla sediment-routing system of the southern Pyrenees of northern Spain, where a sediment budget for the source-to-sink system has been evaluated previously. In the physical sediment transport model, transport capacity is a linear function of the local slope and the water flux, and the sediment flux of the input is estimated as that required to generate the observed stratigraphic thicknesses. Grain-size in the basin is calculated using a Sternberg-type exponential rule driven by selective deposition.

The Escanilla paleo-sediment-routing system is divided into three time intervals, T1 to T3, each of approximately 2.6 Myr duration, characterized by different magnitudes of the sediment supply. Field observations show that there was a temporal increase in the sediment flux from T1 to T3. A best-fit model was found by running 300 model simulations with different values of precipitation and transport coefficient, and testing model outcomes with the observed position of the gravel front. The increase in sediment input from time interval T1 to time interval T2 was accompanied by shortening of the distance from the catchment outlet to the gravel front, most likely caused by an increase in precipitation causing higher water fluxes, which is consistent with paleoclimate information from the mid-to-late Eocene. The gravel-front extended down-system during T3. To explain this new gravel front position while maintaining the sediment flux at the level to explain stratigraphic thicknesses, the transport capacity is required to decrease. This is best explained by a reduction in precipitation in time interval T3, which again matches with paleoclimate proxies in the late Eocene.

Shifting of the position of moving boundaries such as the gravel front is accompanied by patterns of retrogradation and progradation of grain-size trends. Such patterns, which are analogous to shoreline and shelf-break trajectories, are used as a standard tool in characterizing sequence stratigraphic patterns and assessing their forcing mechanisms. We find that patterns of retrogradation and progradation that match field observations can be generated by changes in sediment flux and transport capacity without recourse to any

change in accommodation (e.g., due to changes in base level). Such an interpretation of a sediment-supply control is impossible without the context of a sediment-routing system and associated sediment budget. The absence of these sediment-supply constraints magnifies the non-uniqueness of solutions for forcing mechanisms derived by the interpretation or inversion of stratigraphic architectures.

ACKNOWLEDGMENTS

This work was funded by a Royal Astronomical Society Research Fellowship awarded to JJA. Work on the Escanilla system began through funding for a generic sediment-routing-system program generously provided by Statoil to PAA and through a doctoral project by NAM funded in part by Saudi Aramco. We thank Jeremiah Moody (Chevron Energy Technology Company) and Ron Steel (University of Texas) for very thorough and helpful reviews.

REFERENCES

- ALLEN, P.A., ARMITAGE, J.J., WHITTAKER, A.C., MICHAEL, N.A., RODA-BOLUDA, D., AND D'ARCY, M., 2015, Fragmentation model of the grain-size mix of sediment supplied to basins: *Journal of Geology*, v. 123, p. 405–427.
- ARMITAGE, J.J., DULLER, R.A., WHITTAKER, A.C., AND ALLEN, P.A., 2011, Transformation of tectonic and climatic signals from source to sedimentary archive: *Nature Geoscience*, v. 4, p. 231–235.
- ARMITAGE, J.J., DUNKLEY JONES, T., DULLER, R.A., WHITTAKER, A.C., AND ALLEN, P.A., 2013, Temporal buffering of climate-driven sediment flux cycles by transient catchment response: *Earth and Planetary Science Letters*, v. 369–370, p. 200–210.
- ARMITAGE, J.J., DULLER, R.A., AND SCHMALHOLZ, S.M., 2014, The influence of long-wavelength tilting and climatic change on sediment accumulation: *Lithosphere*, v. 6, p. 303–318.
- BEAMUD, E., MUÑOZ, J.A., FITZGERALD, P.G., BALDWIN, S.L., GARCÉS, M., CABRERA, L., AND METCALF, J.R., 2010, Magnetostratigraphy and detrital apatite fission track thermochronology in syntectonic conglomerates: constraints on the exhumation of the south-central Pyrenees: *Basin Research*, v. 13, p. 309–331.
- BENTHAM, P.A., AND BURBANK, D.W., 1996, Chronology of Eocene foreland basin evolution along the western margin of the south-central Pyrenees, in Friend, P.F., and Dabrio, C.J., eds., *Tertiary Basins of Spain: the Stratigraphic Record of Crustal Kinematics*: Cambridge, U.K., Cambridge University Press, p. 144–152.
- BENTHAM, P.A., BURBANK, D.W., AND PUIGDEFÀREGRAS, C., 1992, Temporal and spatial controls on the alluvial architecture of an axial drainage system: late Eocene Escanilla Formation, southern Pyrenean foreland basin, Spain: *Basin Research*, v. 4, p. 335–352.
- BURGESS, P.M., AND PRINCE, G.D., 2015, Non-unique stratigraphic geometries: implications for sequence stratigraphic interpretations: *Basin Research*, v. 27, p. 351–365.
- BURT, T.J., AND ALLISON, R.J., 2010, Sediment cascades, in Burt, T.J., and Allison, R.J., eds., *Sediment Cascades in the Environment: an Integrated Approach*: Chichester, U.K., John Wiley and Sons, p. 1–15.
- CARVAL, C.R., AND STEEL, R.J., 2006, Thick turbidite successions from supply-dominated shelves during sea-level highstand: *Geology*, v. 34, p. 665–668.
- CARVAL, C., AND STEEL, R.J., 2012, Source-to-sink sediment volumes within a tectonostatigraphic model for a Laramide shelf-to-deep-water basin: methods and results, in Busby, C., and Azor, A., eds., *Tectonics of Sedimentary Basins: Recent Advances*: Oxford, U.K., Blackwell Publishing, p. 131–151.
- CARVAL, C., STEEL, R.J., AND PETTER, A.L., 2008, Sediment supply: the main driver of shelf-margin growth: *Earth-Science Reviews*, v. 96, p. 221–248.
- CATUNEANU, O., ABREU, V., BHATTACHARYA, J.P., BLUM, M.D., DALRYMPLE, R.W., ERIKSSON, P.G., FIELDING, C.R., FISHER, W.L., GALLOWAY, W.E., GIBLING, M.R., GILES, K.A., HOLBROOK, J.M., JORDAN, R., KENDALL, C.G., MACURDA, B., MARTINSEN, O.J., MIAU, A.D., NEAL, J.E., NUMMEDAL, D., POMAR, L., POSAMENTIER, H.W., PRATT, B.R., SARG, J.F., SHANLEY, K.W., STEEL, R.J., STRASSER, A., TUCKER, M.E., AND WINKER, C., 2009, Towards the standardization of sequence stratigraphy: *Earth-Science Reviews*, v. 92, p. 1–33.
- CAVAGNETTO, C., AND ANADÓN, P., 1996, Preliminary palynological data on floristic and climatic changes during the middle Eocene–early Oligocene of the eastern Ebro basin, northeast Spain: Review of Palaeobotany and Palynology, v. 92, p. 281–305.
- DENSMORE, A.L., ALLEN, P.A., AND SIMPSON, G., 2007, Development and response of a coupled catchment fan system under changing tectonic and climatic forcing: *Journal of Geophysical Research*, v. 112 (F01002), doi: 10.1029/2006JF000474.
- DULLER, R.A., WHITTAKER, A.C., FEDELE, J.J., WHITCHURCH, A.L., SPRINGETT, J., SMITHILLS, R., FORDYCE, S., AND ALLEN, P.A., 2010, From grain size to tectonics: *Journal of Geophysical Research*, v. 115 (F03022), doi: 10.1029/2009JF001495.
- DREYER, T., CORREGIDOR, J., ARBUES, P., AND PUIGDEFÀREGRAS, C., 1999, Architecture of the tectonically influenced Sobrarbe deltaic complex in the Ainsa Basin, northern Spain: *Sedimentary Geology*, v. 127, p. 127–169.
- FEDELE, J.J., AND PAOLA, C., 2007, Similarity solutions for alluvial sediment fining by selective deposition: *Journal of Geophysical Research*, v. 112 (F02038), doi: 10.1029/2005JF000409.
- FLEMINGS, P.B., AND JORDAN, T.E., 1989, A synthetic stratigraphic model of foreland basin development: *Journal of Geophysical Research*, v. 94, p. 3851–3866, doi: 10.1029/JB094iB04p03851.
- GALLOWAY, W.E., 1989, Genetic stratigraphic sequences in basin analysis I: architecture and genesis of flooding-surface bounded depositional units: *American Association of Petroleum Geologists, Bulletin*, v. 73, p. 125–142.
- GRADSTEIN, F.M., OGG, J.G., AND SMITH, A.G., eds., 2004, *A Geologic Time Scale 2004*: Cambridge, U.K., Cambridge University Press, 589 p.
- GUISEPPE, A.C., AND HELLER, P.L., 1998, Long-term river response to regional doming in the Price River formation, central Utah: *Geology*, v. 26, p. 239–242.
- HARBAUGH, J.W., WATNEY, W.L., RANKEY, E.C., SLINGERLAND, R., GOLDSTEIN, R.H., AND FRANSEEN, E.K., 1999, Numerical Experiments in Stratigraphy: Recent Advances in Stratigraphic and Sedimentologic Computer Simulation: SEPM, Special Publication 62, 362 p.
- HAQ, B.U., HARDENBOL, J., AND VAIL, P.R., 1987, Chronology of fluctuating sea levels since the Triassic: *Science*, v. 235, p. 1156–1167.
- HELLAND-HANSEN, W., AND HAMPSON, G.J., 2009, Trajectory analysis: concepts and applications: *Basin Research*, v. 21, p. 454–483.
- HELLAND-HANSEN, W., AND MARTINSEN, O.J., 1996, Shoreline trajectories and sequences: description of variable depositional-dip scenarios: *Journal of Sedimentary Research*, v. 66, p. 670–688.
- HELLER, P.L., BURNS, B.A., AND MARZO, M., 1993, Stratigraphic solution sets for determining the roles of sediment supply, subsidence, and sea level on transgressions and regressions: *Geology*, v. 21, p. 747–750.
- HOLBROOK, J., SCOTT, R.W., AND OBOH-IKUEBONE, F.E., 2006, Base-level buffers and buttresses: a model for upstream versus downstream control on fluvial geometry and architecture within sequences: *Journal of Sedimentary Research*, v. 76, p. 162–174.
- MARR, J.G., SWENSON, J.G., PAOLA, C., AND VOLLER, V.R., 2000, A two-diffusion model of fluvial stratigraphy in closed depositional basins: *Basin Research*, v. 12, p. 381–398.
- MARTIN, J., PAOLA, C., ABREU, V., NEAL, J., AND SHEETS, B., 2009, Sequence stratigraphy of experimental strata under known conditions of differential subsidence and variable base level: *American Association of Petroleum Geologists, Bulletin*, v. 93, p. 503–533.
- MARTIN, Y., AND CHURCH, M., 1997, Diffusion in landscape development models: on the nature of basic transport relations: *Earth Surface Processes and Landforms*, v. 22, p. 273–279.
- MARTINSEN, O.J., RYSETH, A., HELLAND-HANSEN, W., FLESCHÉ, H., TORKILDSEN, G., AND IDIL, S., 1999, Stratigraphic base level and fluvial architecture: Ericson Sandstone (Campanian), Rock Springs Uplift, SW Wyoming, USA: *Sedimentology*, v. 46, p. 235–259.
- MARZO, M., AND STEEL, R.J., 2000, Unusual features of sediment-supply-dominated, transgressive-regressive sequences: Paleogene clastic wedges, SE Pyrenean foreland basin, Spain: *Sedimentary Geology*, v. 138, p. 3–15.
- MÍAII, A.D., AND MÍAII, C.E., 2001, Sequence stratigraphy as a scientific enterprise: the evolution and persistence of conflicting paradigms: *Earth-Science Reviews*, v. 54, p. 321–348.
- MICHAEL, N.A., 2013, Functioning of an ancient sediment routing system, the Escanilla Formation, south-central Pyrenees [Ph.D. thesis]: Imperial College London, 318 p.
- MICHAEL, N.A., WHITTAKER, A.C., AND ALLEN, P.A., 2013, The functioning of sediment routing systems using a mass balance approach: example from the Eocene of the Southern Pyrenees: *Journal of Geology*, v. 121, p. 581–606.
- MICHAEL, N.A., CARTER, A., WHITTAKER, A.C., AND ALLEN, P.A., 2014a, Erosion rates in the source region of an ancient sediment routing system: comparison of depositional volumes with thermochronometric estimates: *Geological Society of London, Journal*, v. 171, p. 401–412.
- MICHAEL, N.A., WHITTAKER, A.C., CARTER, A., AND ALLEN, P.A., 2014b, Volumetric budget and grain-size fractionation of a geological sediment routing system: Eocene Escanilla Formation, south-central Pyrenees: *Geological Society of America, Bulletin*, v. 126, p. 585–599.
- MILLER, K.G., KOMINZ, M.A., BROWNING, J.V., WRIGHT, J.D., MOUNTAIN, G.S., KATZ, M.E., SUGARMAN, P.J., CRAMER, B.S., CHRISTIE-BLICK, N., AND PEKAR, S.F., 2005, The Phanerozoic record of global sea-level change: *Science*, v. 310, p. 1293–1298.
- MUÑOZ, J.A., 1992, Evolution of a continental collision belt: ECORS, Pyrenees crustal balanced section, in McClay, K.R., ed., *Thrust Tectonics*: London, Chapman and Hall, p. 235–246.
- MUÑOZ, J.A., BEAMUD, E., FERNÁNDEZ, O., ARBUÉS, P., DINARÉS-TURELL, J., AND POLET, J., 2013, The Ainsa Fold and Thrust Oblique Zone: kinematics of a curved contractional system from paleomagnetic and structural data: *Tectonics*, v. 32, p. 1142–1175.
- MUTO, T., AND STEEL, R.J., 1997, Principles of regression and transgression: the nature of the interplay between accommodation and sediment supply: *Journal of Sedimentary Research*, v. 67, p. 994–1000.
- MUTO, T., AND STEEL, R.J., 2000, The accommodation concept in sequence stratigraphy: some dimensional problems and possible redefinition: *Sedimentary Geology*, v. 130, p. 1–10.
- NUMAN, W., 1998, Cyclicity and basin axis shift in a piggyback basin: towards modelling of the Eocene Tremp–Ager Basin, South Pyrenees, Spain, in Masle, A., Puigdefàregas, C., Luterbacher, H.P., and Fernández, M., eds., *Cenozoic Foreland Basins of Western Europe*: Geological Society of London, Special Publication 134, p. 135–162.
- PAOLA, C., AND MARTIN, J.M., 2012, Mass-balance effects in depositional systems: *Journal of Sedimentary Research*, v. 82, p. 435–450.
- PAOLA, C., AND SEAL, R., 1995, Grain-size patchiness as a cause of selective deposition and downstream fining: *Water Resources Research*, v. 31, p. 1395–1407.
- PAOLA, C., HELLER, P.L., AND ANGEVINE, C.L., 1992, The large-scale dynamics of grain-size variation in alluvial basins, 1: Theory: *Basin Research*, v. 4, p. 73–90.
- PAOLA, C., STRAUB, K., MOHRIG, D., AND REINHARDT, L., 2009, The “unreasonable effectiveness” of stratigraphic and geomorphic experiments: *Earth-Science Reviews*, v. 97, p. 1–43.
- PUIGDEFÀREGRAS, C., MUÑOZ, J.A., AND VÈRGES, J., 1992, Thrusting and foreland basin evolution in the southern Pyrenees, in McClay, K.R., ed., *Thrust Tectonics*: London, Chapman and Hall, p. 247–254.
- SCHLAGER, W., 1993, Accommodation and supply: a dual control on stratigraphic sequences: *Sedimentary Geology*, v. 86, p. 111–136.
- SHANLEY, K.W., AND McCABE, P.J., 1994, Perspectives on the sequence stratigraphy of continental strata: *American Association of Petroleum Geologists, Bulletin*, v. 78, p. 544–568.

- SIMPSON, G., AND SCHLUNEGGER, F., 2003, Topographic evolution and morphology of surfaces evolving in response to coupled fluvial and hillslope sediment transport: *Journal of Geophysical Research*, v. 108 (B62300), doi: 10.1029/2002JB002162.
- SINCLAIR, H.D., COAKLEY, B.J., ALLEN, P.A., AND WATTS, A.B., 1991, Simulation of foreland basin stratigraphy using a diffusion-model of mountain belt uplift and erosion: an example from the central Alps, Switzerland: *Tectonics*, v. 10, p. 599–620.
- SMITH, T.R., AND BRETHERTON, F.P., 1972, Stability and conservation of mass in drainage basin evolution: *Water Resources Research*, v. 8, p. 1506–1529.
- STEEL, R., AND OLSEN, T., 2002, Clinoforms, clinoform trajectories, and deepwater sands, *in* Armentrout, J.M., and Rosen, N.C., eds., *Sequence Stratigraphic Models for Exploration and Production: Evolving Methodology, Emerging Models and Applications Histories: SEPM, Gulf Coast Section, 22nd Annual Research Conference*, p. 367–380.
- STERNBERG, H., 1875, Untersuchungen über Längen und Querprofil geschiebeführende Flüsse: *Zeitschrift für das Bauwesen*, v. 25, p. 483–506.
- STRONG, N., SHEETS, B., HICKSON, T., AND PAOLA, C., 2005, A mass-balance framework for quantifying downstream changes in fluvial architecture, *in* Blum, M.D., Marriott, S.B., and Leclair, S.F., eds., *Fluvial Sedimentology VII*: Oxford, UK, Blackwell Publishing, v. 35, p. 243–253.
- SWENSON, J.B., 2005, Relative importance of fluvial input and wave energy in controlling the timescale for distributary-channel avulsion: *Geophysical Research Letters*, v. 32 (L23404), doi: 10.1029/2005GL024758.
- VAIL, P.R., MITCHUM, R.M., JR., TODD, R.G., WIDMIER, J.M., THOMPSON, S., III, SANTEE, J.B., BUBB, J.N., AND HATLELID, W.G., 1977, Seismic stratigraphy and global changes of sea level, *in* Payton, C.E., ed., *Seismic Stratigraphy Applications to Hydrocarbon Exploration: American Association of Petroleum Geologists, Memoir*, v. 26, p. 49–212.
- VAN WAGONER, J.C., MITCHUM, R.M., CAMPION, K.M., AND RAHMANIAN, V.D., 1990, Siliciclastic Sequence Stratigraphy in Well Logs, Cores, and Outcrops: *Association of Petroleum Geologists, Methods in Exploration* 7, 55 p.
- VINCENT, S.J., 2001, The Sis palaeovalley: a record of proximal fluvial sedimentation and drainage basin development in response to Pyrenean mountain building: *Sedimentology*, v. 48, p. 1235–1276.
- WHITCHURCH, A.L., CARTER, A., SINCLAIR, H.D., DULLER, R.A., WHITTAKER, A.C., AND ALLEN, P.A., 2011, Sediment routing system evolution within a diachronously uplifting orogen: insights from detrital zircon thermochronological analyses from the south-central Pyrenees: *American Journal of Science*, v. 311, p. 442–482.
- WHITTAKER, A.C., DULLER, R.A., SPRINGETT, J., SMITHILLS, R.A., WHITCHURCH, A.L., AND ALLEN, P.A., 2011, Decoding downstream trends in stratigraphic grain-size as a function of tectonic subsidence and sediment supply: *Geological Society of America, Bulletin*, v. 123, p. 1363–1382.
- WILLIS, B.J., 1993, Ancient river systems in the Himalayan foredeep, Chinji Village area, northern Pakistan: *Sedimentary Geology*, v. 88, p. 1–76.
- WRIGHT, V.P., AND MARRIOTT, S.B., 1993, The sequence stratigraphy of fluvial depositional systems: the role of floodplain sediment storage: *Sedimentary Geology*, v. 86, p. 203–210.

Received 6 February 2015; accepted 7 October 2015.

Deciphering the origin of cyclical gravel front and shoreline progradation and retrogradation in the stratigraphic record

John J. Armitage,^{*,1} Peter M. Burgess,^{*,2} Gary J. Hampson[†] and Philip A. Allen[†]

^{*}Department of Earth Science, Royal Holloway, University of London, Egham, UK

[†]Department of Earth Science and Engineering, Imperial College London, London, UK

ABSTRACT

Nearly all successions of the near-shore strata exhibit cyclical movements of the shoreline, which have commonly been attributed to cyclical oscillations in relative sea level (combining eustasy and subsidence) or, more rarely, to cyclical variations in sediment supply. It has become accepted that cyclical change in sediment delivery from source catchments may lead to cyclical movement of boundaries such as the gravel front, particularly in the proximal segments of sediment-routing systems. In order to quantitatively assess how variations in sediment transport as a consequence of change in relative sea-level and surface run-off control stratigraphic architecture, we develop a simple numerical model of sediment transport and explore the sensitivity of moving boundaries within the sediment-routing system to change in upstream (sediment flux, precipitation rate) and downstream (sea level) controls. We find that downstream controls impact the shoreline and sand front, while the upstream controls can impact the whole system depending on the amplitude of change in sediment flux and precipitation rate. The model implies that under certain conditions, the relative movement of the gravel front and shoreline is a diagnostic marker of whether the sediment-routing system experienced oscillations in sea level or climatic conditions. The model is then used to assess the controls on stratigraphic architecture in a well-documented palaeo-sediment-routing system in the Late Cretaceous Western Interior Seaway of North America. Model results suggest that significant movement of the gravel front is forced by pronounced ($\pm 50\%$) oscillations in precipitation rate. The absence of such movement in gravel front position in the studied strata implies that time-equivalent movement of the shoreline was driven by relative sea-level change. We suggest that tracking the relative trajectories of internal boundaries such as the gravel front and shoreline is a powerful tool in constraining the interpretation of stratigraphic sequences.

INTRODUCTION

Change in sediment supply, sea level and subsidence are ubiquitously cited as the main controls on stratigraphic architecture (e.g. Vail *et al.*, 1977; Van Wagoner *et al.*, 1990; Catuneanu *et al.*, 2009), but the extent to which any of these controls leave a unique signature within the stratigraphic record is not yet clear (e.g. Burgess *et al.*, 2006; Burgess & Prince, 2015). Periodic changes in relative sea level may be accompanied by climatic change of the same periodicity if both sea level and climate are forced by Milankovitch orbital cycles. Such regional and

global climatic cycles can have the effect of increasing or reducing surface run-off and sediment supply at the same time as changing sea-level (Blum & Hattier-Womack, 2009).

Sea-level change has clear implications for deposition within the coastal plain as the shoreline transits across this region. The response of the sediment-routing system to shoreline migration likely decays upstream of the shoreline (e.g. Fisk, 1944; Blum & Törnqvist, 2000; Swenson, 2005). Downstream of the shoreline, the associated change in sediment flux into the submarine domain, along with change in water depth will determine stratal geometry, shoreline migration and generation of sequence stratigraphic boundaries (e.g. Heller *et al.*, 1993; Burgess & Prince, 2015).

Climate change has less clear implications for sediment deposition. Periodic change in precipitation and surface water flow within the fluvial segment could amplify, damp and/or delay the sediment flux signal due the processes of sediment transport (Jerolmack & Paola, 2010; Simpson & Castelltort, 2012; Armitage *et al.*, 2013; Godard *et al.*,

Correspondence: John J. Armitage, Department of Earth Science, Royal Holloway, University of London, Egham TW20 0EX, UK. E-mail: armitage@ipgp.fr

¹Present Address: Institut de Physique du Globe de Paris, 1 rue Jussieu, Paris 75005, France.

²Present Address: Earth, Ocean and Ecological Sciences, School of Environmental Sciences, University of Liverpool, Liverpool, UK.

2013; Braun *et al.*, 2015). Furthermore, the timescale of sediment flux perturbation that may be recorded within the fluvial and deltaic segments is a function of the length of the sediment routing system (e.g. Dade & Friend, 1998; Métivier, 1999; Castelltort & Van Den Dreissche, 2003). It is therefore uncertain from a theoretical stand point whether sediment flux signals from the catchment can be transferred to the shoreline without modification. There is however some observational evidence from sediment-routing systems that records of change in coastal to marine sediment accumulation are due to change in sediment flux from the catchment (Covault & Graham, 2010; Covault *et al.*, 2011; Carvajal & Steel, 2012). If an upstream signal of increased sediment flux is transferred across the fluvial segment of the sediment routing system, then we could reasonably assume that it will supply more sediment to the shoreline and thus alter the shoreline trajectory.

The lack of a unique solution to the interpretation of stratigraphic architecture is a long-standing problem within the methodology of sequence stratigraphy, and in the desire to understand how sediment accumulation is a record of past climate, tectonics and internal system dynamics. Previous studies have tried to gain an insight into how strata form using forward models of sediment transport (e.g. Burgess *et al.*, 2006; Paola & Martin, 2012). From measuring the transfer of mass from sediment in transport to deposition from laboratory scale experiments, it has been observed that the application of idealised grain size sorting models may provide a way to analyse the movement of internal grain size boundaries within the sediment-routing systems (Paola & Martin, 2012). Therefore, in order to quantitatively assess how variations in sediment transport due to change in relative sea level and surface run-off influence stratigraphic architectures, we will explore the sensitivity of such moving boundaries within a numerical sediment-routing system to change in upstream (sediment flux, precipitation rate) and downstream (sea level) controls. The internal boundaries that we focus on are (1) the downstream limit of alluvial conglomerates, the gravel front (Paola *et al.*, 1992) (2) the shoreline, and (3) the down system limit of shallow marine sandstones, the sand front (Michael *et al.*, 2013). These moving boundaries can be mapped within strata (e.g. Hampson *et al.*, 2014; Michael *et al.*, 2014), and therefore have the potential to be used to diagnose past forcing of sediment-routing systems if it is known how they respond to change.

In this context, we will explore three central questions:

- (1) How sensitive are the positions of the gravel front, shoreline and sand front to sediment transport mechanisms. In other words, how closely linked via sediment transport are coastal plain, shelf and shoreline morphology and grain size distributions, and how does this linkage relate to control by sediment transport.
- (2) What is the impact of upstream (sediment flux, precipitation rate) and downstream (sea level) controls on

the positions of the gravel front, shoreline and sand front? The aim is to explore the uniqueness of relative sea-level control on shoreline position, implicit in many sequence stratigraphic interpretations. Experimental modelling will help to determine if there are signals upstream of the shoreline that can be used to differentiate driving mechanisms.

- (3) Do the different parameters that influence shoreline position impart diagnostic characteristics to coastal plain and shelf stratigraphic architectures?

In the first part of the paper, we investigate these three questions using a generic model of a large sediment-routing system that contains both subaerial and subaqueous depositional domains. Sensitivity tests for the generic model establish a parameter space that is used to investigate a case study from the geological record. In the second part of the paper, we focus on a sediment-routing system within the Western Interior Basin, USA, in which stratal geometries, shoreline migration and sediment budget have been constrained for a period of approximately 6 Myr during the Late Cretaceous (Hampson, 2010; Hampson *et al.*, 2014). The sediment-routing system represented by the Star Point Sandstone, Blackhawk Formation, lower part of the Castlegate Sandstone and coeval Mancos Shale is exposed in the Book Cliffs of east-central Utah and west-central Colorado, USA. These strata represent the birthplace of outcrop-scale sequence stratigraphy, and are widely visited by the academic and industry groups to teach sequence stratigraphic methods and models; the Book Cliffs outcrops therefore provide an ideal case study with which to illustrate the importance of the three questions posed above.

METHODS

We couple a 1-D model of sediment transport down depositional dip based on the flow of surface water to a 1-D model of deposition in the submarine domain (Fig. 1). Subaerial sediment transport is modelled following Smith & Bretherton (1972) and Armitage *et al.* (2015), where we assume that sediment flux is a function of both local slope and surface water flux:

$$q_s = -(\kappa + cq_w^n) \frac{\partial z}{\partial x}, \quad (1)$$

where z is elevation, x is the down system distance, κ is the linear diffusion coefficient, c is the fluvial transport coefficient, $n \geq 1$, and the water flux is given by,

$$q_w = \alpha x, \quad (2)$$

where α is the precipitation rate (see Table 1).

At the input boundary, we introduce a sediment flux and a water flux, $q_w(\text{in}) = \alpha l_c$ to define the sediment transport at the left boundary (Fig. 1). The catchment length, l_c , is assumed to be 150 km. We assume that the subaerial transport model extends from the proximal

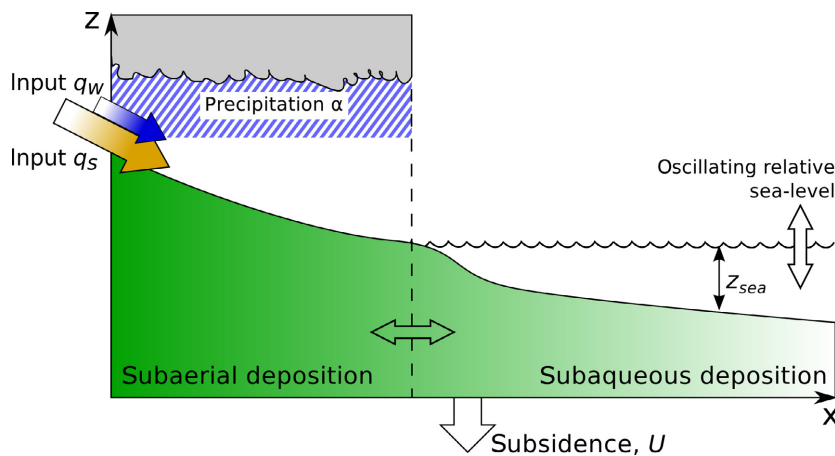


Fig. 1. Diagram of model domain. On the left are the input sediment flux, q_s , and input water flux, q_w , which is a function of the precipitation rate multiplied by the catchment length (assumed to be 150 km). At the base, accommodation space is generated through a spatial distribution of subsidence, U . In the subaerial domain, sediment transport is a function of slope and precipitation rate, α , see Eqns (1) and (2). In the subaqueous domain, sediment transport is a function of water depth, z_{sea} , see Eqn (3). The boundary between these domains is a function of elevation and relative sea-level, and is free to move depending on the transport of sediment.

Table 1. List of model parameters

Parameter	Description	Value
κ	Linear hill slope diffusion coefficient	1 m ² year ⁻¹
c	Fluvial transport coefficient	10 ⁻¹
n	Transport exponent	1
κ_{sea}	Subaqueous diffusion coefficient	10 ⁴ to 10 ⁵ m ² year ⁻¹
κ_{decay}	Subaqueous diffusion decay coefficient	5 × 10 ³ to 5 × 10 ⁵ m ⁻¹

model boundary, which is the catchment outlet, to the shoreline. At this point, we assume that the primary mechanism of sediment transport changes, and instead a combination of tidal and wave energy carries sediment farther down slope as a heuristic function of water depth (e.g. Kaufman *et al.*, 1991),

$$q_s = -\kappa_{sea} e^{(-\kappa_{decay} \text{abs}(z_{sea} - z))} \frac{\partial z}{\partial x}, \quad (3)$$

where κ_{sea} is the linear diffusion coefficient for subaqueous sediment transport. κ_{decay} is the coefficient that parameterises the effect of water depth, z_{sea} , on subaqueous sediment transport (see Table 1; Kaufman *et al.*, 1991). The change in elevation, z , is then given from the Exner equation of conservation of mass,

$$\frac{\partial z}{\partial t} = U - \frac{\partial q_s}{\partial x}, \quad (4)$$

where U is uplift (positive) or subsidence (negative).

The sediment transport in the sediment-routing system is therefore described by a nonlinear diffusion equation in which the diffusion coefficient is a function of system length landward of the shoreline. Seaward of the

shoreline the diffusion coefficient is a function of elevation. The system equation is solved iteratively using a simple finite element numerical model. From the initial condition, or previous time step, the diffusion coefficient is calculated given the relationship between elevation and sea level. To avoid sharp changes in diffusion coefficient that can cause numerical errors at the shoreline, the diffusion coefficient is spatially smoothed using a moving average filter. Furthermore, to keep a stable solution where there is a strong contrast in diffusion coefficient, the model resolution is increased in the vicinity of the shoreline. This results in the model being unable to generate a sharp break in slope at the shoreline.

Grain size is sorted down-system assuming first gravels, and then sand and finer grains are deposited (Armitage *et al.*, 2015). The solution to the diffusion equation gives the topographic height for each point along the 1-D profile and hence the thickness of the deposits at a model time step. We then fill this slice of deposited mass with the gravel fraction, until there is none left. Subsequently, the rest of the depositional thickness is filled with the sand and fines. The position at which gravel is exhausted in the model is therefore based on the assumption of perfect sorting as defined in Paola *et al.* (1992). Within the region of gravel deposition, the grain size is sorted down system using the model of Fedele & Paola (2007). Below this point, the sand and fines are sorted following a Sternberg-type exponential sorting model (Sternberg, 1875; Robinson & Slingerland, 1998b).

The model domain is 5000 km long in the x -direction with an inflow boundary on the left hand side and fixed elevation on the right hand side (Fig. 1). Subsidence is defined as either a spatially uniform rate, or a spatial distribution that matches the rate of accumulation inferred from observed thickness variations along a dip-oriented cross-section from studied strata in the Western Interior Basin. The model parameters are listed in Table 1.

RESULTS OF GENERIC MODELS

Effect of transport on position of shoreline and gravel front

In the first set of numerical experiments with the generic model domain, we explore how the sediment transport coefficients in the submarine domain control the position of the shoreline as surface run-off is increased within the subaerial domain. We assume that the gravel fraction of the source sediment supply is 10%. For the subaerial domain, we use the set of parameters that were found to approximate sediment transport within the Middle Miocene Escanilla sediment-routing system, which is a roughly 300 km long terrestrial to marine depositional sedimentary system in the Spanish Pyrenees (Table 1; Armitage *et al.*, 2015). These values are chosen as they matched the patterns of sediment accumulation in the subaerial depositional domain of a sediment-routing system with a depositional length of *ca.* 200 km. The linear diffusion coefficient κ in Eqn (1) only impacts sediment transport within the upper reaches of the catchment where it is larger in magnitude than the fluvial term, cq_p^n . The values of c and n were tuned to match the position of the gravel front in the Escanilla palaeosedimentary-routing system (Armitage *et al.*, 2015). Given that the catchments of palaeo-sediment-routing systems have been removed by erosion, such that they cannot be directly observed, we will use these values for the hypothetical catchment. Subsidence is spatially uniform at a rate of $-0.5 \text{ mm year}^{-1}$ (where positive values denote uplift), and $50 \text{ m}^2 \text{ year}^{-1}$ of sediment is fluxed into the proximal edge of the model domain at the left hand side.

From modelling a range of values for precipitation rate, α , and submarine transport coefficient κ_{sea} ; $0.1 \leq \alpha \leq 2 \text{ m year}^{-1}$, and $10^4 \leq \kappa_{\text{sea}} \leq 10^5 \text{ m}^2 \text{ year}^{-1}$ in Eqns (1) and (3), we find that the final position of the gravel front and shoreline is a function of the transport rate in both subaerial and subaqueous depositional domains (Fig. 2). The distance from the catchment outlet to the gravel front increases with increasing precipitation rate, as the input sediment flux is transported farther down slope. This increase in transport distance also causes progradation. The effect is modified, however, by the strength of the submarine transport coefficient, κ_{sea} , which defines the slope at the shoreline. The position of the gravel front is also clearly a function of the source gravel fraction (e.g. Marr *et al.*, 2000; Allen *et al.*, 2015; Armitage *et al.*, 2015). We have assumed that the gravel fraction is constant in time. For this simple set-up of uniform subsidence, if the gravel fraction were 50% larger at 15% gravel, then the gravel front is 10% farther down system and if likewise for a 50% reduction the gravel front extends out to a 10% shorter distance.

In addition to sediment flux, shoreline progradation or retrogradation is a function of the transport capacity of the submarine environment (Fig. 3). There is an initial period of shoreline retreat as the initial surface becomes submerged due to the spatially uniform subsidence. If the magnitude of κ_{sea} is low, then there is subsequently a steady progradation of the shoreline as the locus of deposition moves down system (Fig. 3a; Table 2). If however κ_{sea} is high there is a steady retrogradation of the shoreline at a slower rate than the initial model evolution (Fig. 3b; Table 2). This behaviour of the shoreline for high values of κ_{sea} is in the opposite sense to that of the contour of the

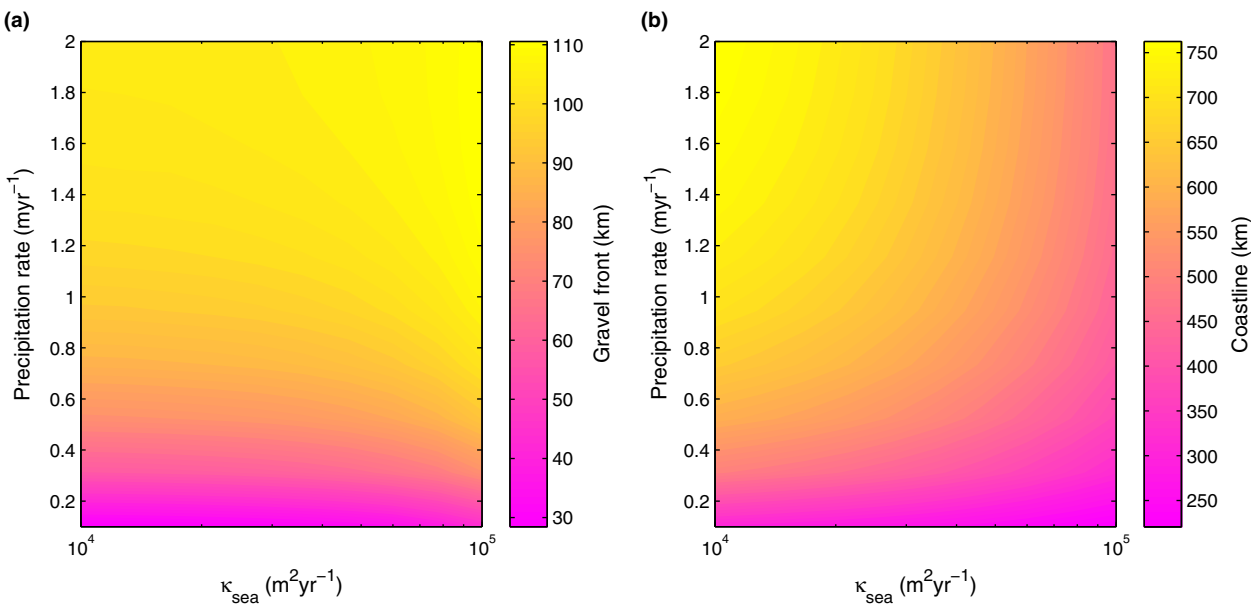


Fig. 2. Plots of the down system positions of (a) the gravel front and (b) the shoreline after 10 Myr of model evolution, as a function of model precipitation rate, α (Eqn 2) and the magnitude of κ_{sea} within the submarine diffusive transport equations (Eqn 3).

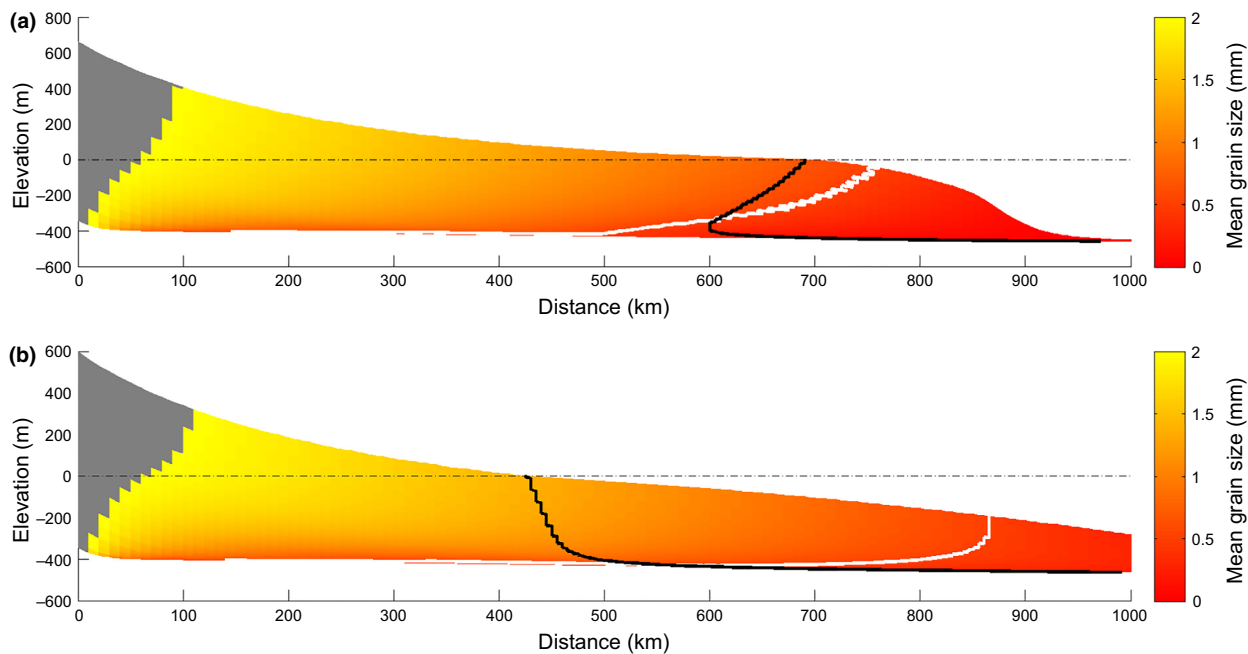


Fig. 3. Model stratigraphic cross-sections for two values of κ_{sea} (Eqn 3). κ_{decay} (Eqn 3) is held constant at $5 \times 10^4 \text{ m}^{-1}$. (a) Grain size deposited for a model where $\kappa_{\text{sea}} = 10^4 \text{ m}^2 \text{ year}^{-1}$, with spatially uniform subsidence at 0.5 mm year^{-1} . Precipitation rate is 1 m year^{-1} and the input sediment flux is $50 \text{ m}^2 \text{ year}^{-1}$ on the left model boundary. Regions of gravel grains are blocked out in gray. The mean grain size of grains finer than 2 mm in diameter is plotted, with the grain size of 0.5 mm displayed as a white contour that approximates the sand front. The shoreline position through time is marked as a solid black line, and the dashed black line marks sea level. (b) Grain size deposited where $\kappa_{\text{sea}} = 10^5 \text{ m}^2 \text{ year}^{-1}$.

0.5 mm grain size (Fig. 3b, white contours). This latter contour is a proxy for the sand front, and progrades for both values of κ_{sea} (Fig. 3, white contours).

The positions of the gravel front and shoreline are also a function of the vertical profile of the submarine diffusion (Fig. 4). This is because a decrease in κ_{decay} leads to an increase in the effective submarine sediment transport. Progradation or retrogradation of the shoreline position is a function of the transport capacity in the marine environment (Fig. 5). In the case where κ_{decay} is $5 \times 10^3 \text{ m}^{-1}$ (Fig. 5a), the shoreline retreats throughout deposition of the modelled strata (Table 2), while the 0.5 mm grain size contour progrades seaward. Conversely for the case κ_{decay} is $5 \times 10^5 \text{ m}^{-1}$ (Fig. 5b, Table 2), the shoreline and sand front (0.5 mm grain size contour) both prograde as the model evolves. The positions of the shoreline and sand front in this latter case are also quite similar (Fig. 5b).

Finally, change in the transport rate within the submarine domain can effect deposition within the subaerial domain of the sediment-routing system. For $\kappa_{\text{sea}} = 5 \times 10^4 \text{ m}^2 \text{ year}^{-1}$ and $\kappa_{\text{decay}} = 5 \times 10^3 \text{ m}^{-1}$ (Fig. 5a) the gravel front progrades at a rate of 8 km Myr^{-1} , which is twice as fast as the other four scenarios in Table 2. This model has the largest effective transport rate within the submarine domain, which results in the least change in slope at the shoreline (Fig. 5a). By implication, patterns of subaerial deposition are expected to be more closely linked to those of subaqueous deposition in sediment-routing systems that are characterised by

uniform gradients (i.e. ramps) than in those with pronounced breaks in slope (i.e. with shelf-slope clinoforms).

Oscillating sea level and precipitation rate

Under conditions of steady external forcing, the gravel front progrades as the sediment-routing system evolves and the shoreline either progrades or retrogrades depending on the rate of submarine diffusive transport. It is highly unlikely that precipitation rates and sea level remained steady over the multi-million year timescales represented by comparable stratal units in the geological record. Following in the footsteps of previous studies such as Paola *et al.*, (1992) and Burgess *et al.*, (2008), we therefore look at how the model responds to oscillating precipitation rates and relative sea level. We assume a constant gravel fraction of 10%.

Periodic change in precipitation rate causes a periodic response in the positions of the gravel front and shoreline (Fig. 6). However, the time of maximum regression of the gravel front is slightly delayed with respect to the time of maximum precipitation rate. The shoreline migrates by a few kilometres as a function of a 10% change in precipitation rate (Fig. 6b). If, however, precipitation rate changes by 50% then the delay in maximum gravel front regression relative to peak precipitation rate is increased (Fig. 7a). The shoreline trajectory records cyclical progradation and retrogradation over a dip extent of 50 km , superimposed on overall progradation of the shoreline (Table 2). If precipitation rates oscillate by 50%

Table 2. Gravel front and shoreline trajectory analysis

Figures	κ_{sea} (m ² year ⁻¹)	κ_{decay} (m ⁻¹)	Forcing	Gravel front trajectory	Shoreline trajectory
3a	10^5	5×10^4	Steady sea level, precipitation rate and input sediment flux	Steady progradation at <i>ca.</i> 4 km Myr ⁻¹	Steady retrogradation at <i>ca.</i> 4 km Myr ⁻¹
3b	10^4	5×10^4	Steady sea level, precipitation rate and input sediment flux	Steady progradation at <i>ca.</i> 4 km Myr ⁻¹	Steady progradation at <i>ca.</i> 12 km Myr ⁻¹
5a	5×10^4	5×10^3	Steady sea level, precipitation rate and input sediment flux	Steady progradation at <i>ca.</i> 8 km Myr ⁻¹	Steady progradation at <i>ca.</i> 13 km Myr ⁻¹
5b	5×10^4	5×10^5	Steady sea level, precipitation rate and input sediment flux	Steady progradation at <i>ca.</i> 4 km Myr ⁻¹	Steady progradation at <i>ca.</i> 14 km Myr ⁻¹
8a	10^5	5×10^4	Oscillating precipitation rate ($\pm 50\%$), steady sea level and input sediment flux	Cycles of progradation and retrogradation over a distance of <i>ca.</i> 270 km	Cycles of progradation and retrogradation over 50 km. Long term retrogradation of order 5 km Myr ⁻¹
9a	10^4	5×10^4	Oscillating precipitation rate ($\pm 50\%$), steady sea level and input sediment	Cycles of progradation and retrogradation over a distance of <i>ca.</i> 270 km	Cycles of progradation and retrogradation over 20 km. Long term retrogradation of order 10 km Myr ⁻¹
8b	10^5	5×10^4	Oscillating sea level (± 10 m), steady precipitation rate and input sediment flux	Steady progradation	Cycles of progradation and retrogradation over 40 km. Long term retrogradation of order 5 km Myr ⁻¹
9b	10^4	5×10^4	Oscillating sea level (± 10 m), steady precipitation rate and input sediment flux	Steady progradation	Cycles of progradation and retrogradation over 50 km. Long term retrogradation of order 10 km Myr ⁻¹
11a	10^5	5×10^4	Oscillating precipitation rate ($\pm 10\%$), and input sediment flux ($\pm 10\%$), steady sea level	Steady progradation	Cycles of progradation and retrogradation over 20 km. Long term retrogradation of order 5 km Myr ⁻¹
11b	10^5	5×10^4	Oscillating precipitation rate ($\pm 50\%$), and input sediment flux ($\pm 10\%$), steady sea level	Cycles of progradation and retrogradation over a distance of <i>ca.</i> 270 km	Cycles of progradation and retrogradation over 50 km. Long term retrogradation of order 5 km Myr ⁻¹

around their mean, then the periodicity and amplitude of shoreline migration is similar to those predicted in the model for a ± 10 m change in relative sea-level (Figs 6d and 7b; Table 2).

The numerical model suggests that the delay between the movement of the gravel front in response to precipitation signal is a function of the amplitude of the oscillation in precipitation rates, yet the delay in the periodic movement of the shoreline remains relatively unaffected by the amplitude of precipitation-rate oscillations (Fig. 7c). This difference arises because the position of the gravel front is a function of the subaerial transport equations and its response time, τ , is an inverse function of precipitation rate (Armitage *et al.*, 2013):

$$\tau \sim \frac{L^{2-n}}{c\alpha^n} \quad (5)$$

where L is the system length. Thus, the response time of the gravel front is shorter for an increased precipitation rate. The shoreline position is however a function of transport in both subaerial and subaqueous regimes, and is therefore less dependent on the precipitation rate.

In contrast to the model results for oscillating precipitation rates, oscillations in relative sea level of a magnitude of ± 10 m have no effect on the position of the gravel front, which lies far up system of the shoreline (Fig. 6c, Table 2). The shoreline trajectory records cycles of progradation and retrogradation of a magnitude of 40–50 km, superimposed on an overall progradation of the shoreline similar to that observed in models without cyclical changes in relative sea level (Figs 6d, 8 and 9, Table 2). The amplitude of shoreline migration due to relative sea level change are relatively insensitive to subaerial sediment transport rate, and the shoreline migrates by similar amounts for a κ_{sea} of both 10^4 and 10^5 m² year⁻¹ (Figs 8 and 9).

The modelled scenarios of change in relative sea level and precipitation rate are both characterised by change in the spatial distribution of grain size, which oscillates in phase with the movement of the shoreline, (Figs 8 and 9). Depending on the subaerial transport rate, the 0.5 mm grain size contour, which approximates the sand front is predicted to lie either seaward of the shoreline ($\kappa_{\text{sea}} = 10^5$, Fig. 8) or at a similar location to the

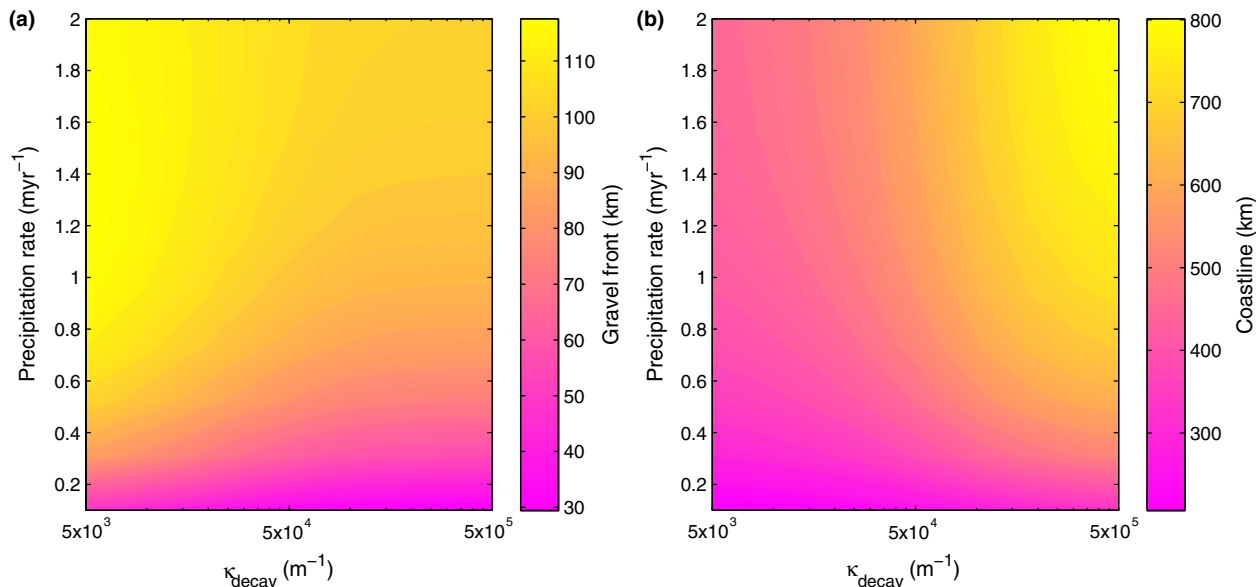


Fig. 4. Plots of the down system position of (a) the gravel front and (b) the shoreline after 10 Myr of model evolution, as a function of model precipitation rate, α (Eqn 2) and the magnitude of κ_{decay} within the submarine diffusive transport equations (Eqn 3).

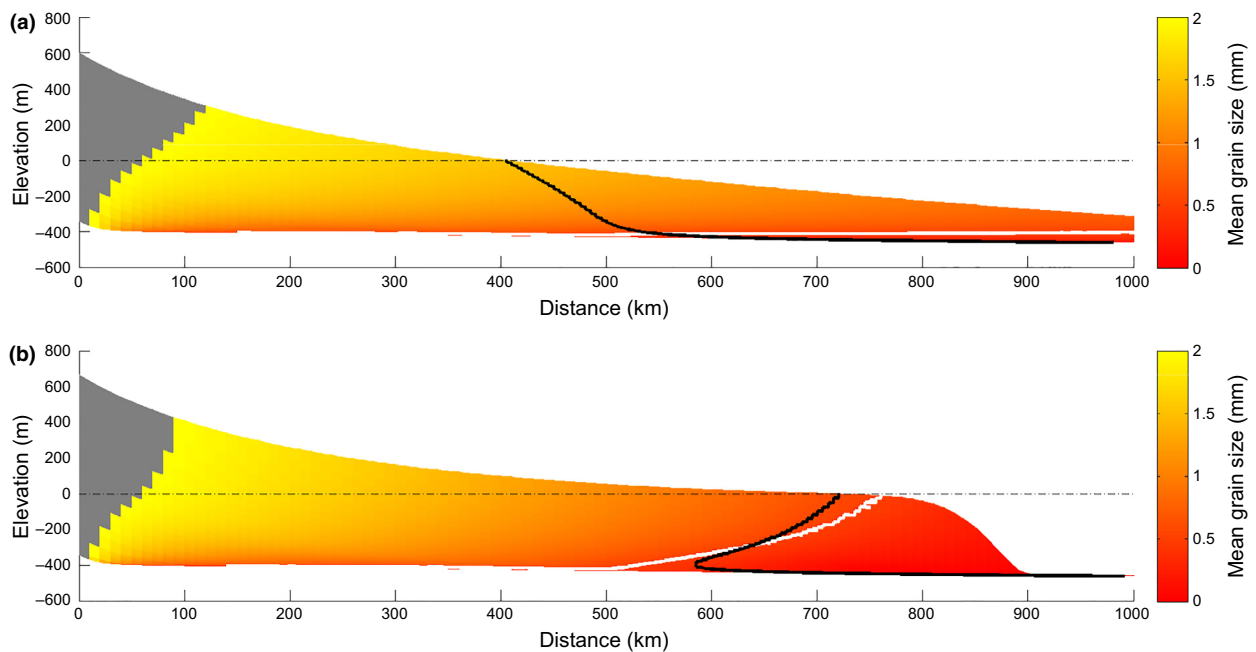


Fig. 5. Model stratigraphic sections for two values of κ_{decay} (Eqn 3). κ_{sea} (Eqn 3) is held constant at $5 \times 10^4 \text{ m}^2 \text{ year}^{-1}$. (a) Grain size deposited for a model where $\kappa_{\text{decay}} = 5 \times 10^3 \text{ m}^{-1}$, with spatially uniform subsidence at 0.5 mm year^{-1} . Precipitation rate is 1 m year^{-1} and the input sediment flux is $50 \text{ m}^2 \text{ year}^{-1}$ on the left model boundary. Regions of gravel grains are blocked out in gray. The mean grain size of grains finer than 2 mm in diameter is plotted, with the grain size of 0.5 mm displayed as a white contour that approximates the sand front. The shoreline position through time is marked as a solid black line, and the dashed black line marks sea level. (b) Grain size deposited where $\kappa_{\text{decay}} = 5 \times 10^5 \text{ m}^{-1}$.

shoreline ($\kappa_{\text{sea}} = 10^4$, Fig. 9). The effects of changes in relative sea level and precipitation rate are distinguished by the movement of the gravel front: change in relative sea level has no impact on the gravel front position (Figs 8b and 9b), whereas change in precipitation rates has a clear impact on movement of the gravel front (Figs 8a and 9a).

Oscillating precipitation and input sediment flux

In addition to precipitation and relative sea level, input sediment flux may also vary through time. The exact form of the response of sediment flux into the depositional system as a function of cyclical change in precipitation is

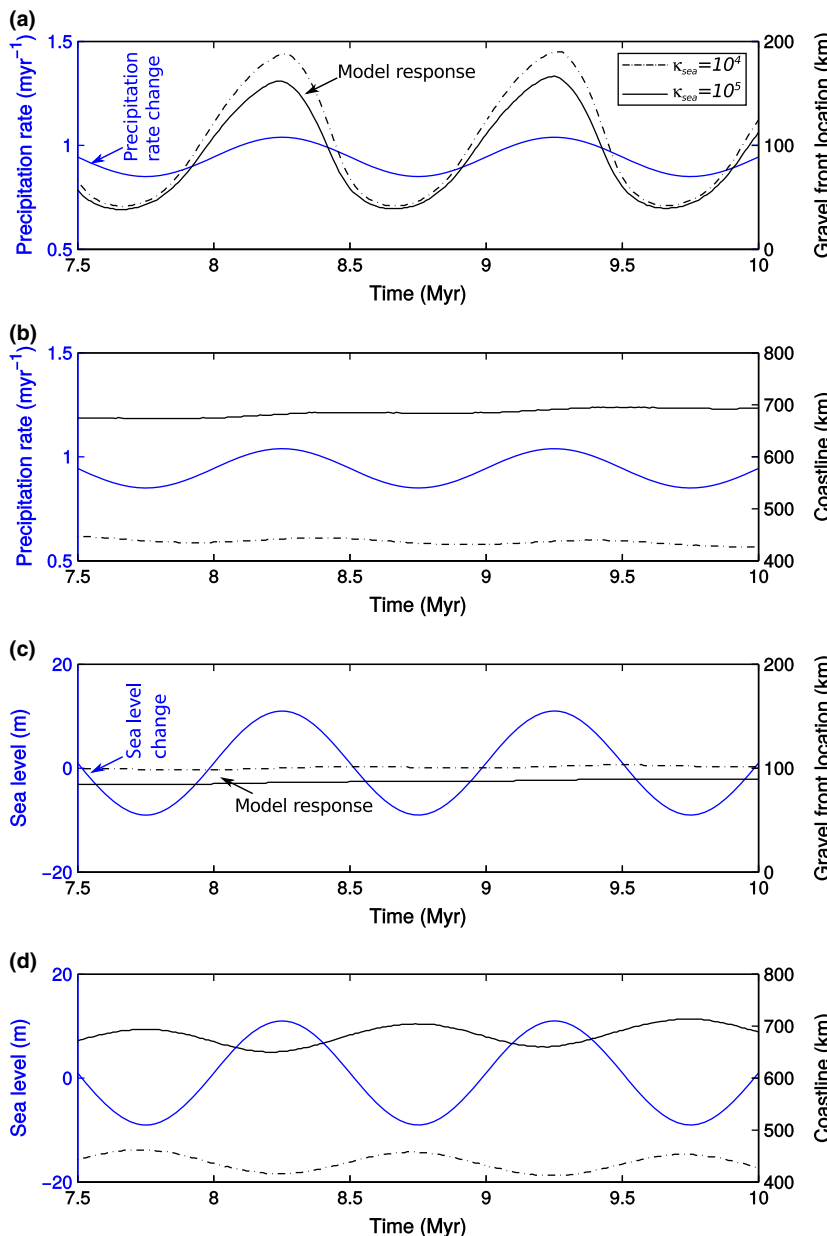


Fig. 6. Response of the sediment transport model where $\kappa_{\text{sea}} = 10^4 \text{ m}^2 \text{ year}^{-1}$ (dashed black lines) and $\kappa_{\text{sea}} = 10^5 \text{ m}^2 \text{ year}^{-1}$ (solid black lines) to oscillating precipitation rates at ±10% of the mean or sea level with a period of 1 Myr and an amplitude of ±10 m (blue lines). (a) Movement of the position of the gravel front as a consequence of change in precipitation rates. (b) Movement of the shoreline as a consequence of change in precipitation rates. (c) Movement of the position of the gravel front as a consequence of change in sea level. (d) Movement of the shoreline as a consequence of change in sea level.

uncertain (see Romans *et al.*, 2015). To explore how the model behaves when both precipitation rates and sediment flux change, we model two scenarios: (1) There is no change in precipitation rate and the input sediment flux oscillates (Fig. 10 red line). (2) Precipitation rate and sediment flux oscillate in phase, by which we mean an increase in precipitation rate is coincident with an increase in input sediment flux (Fig. 10 blue and black lines). As before, in these models, we assume that the gravel fraction in the source remains constant at 10%.

The effect of oscillations in input sediment flux by ±10% of the mean value without a variation in precipitation rate is to cause an in-phase migration of the gravel front (Fig. 10b,c, red lines). When the input sediment flux is increased the distance to the gravel front decreases and when the input sediment flux is decreased the distance to the gravel front increases (Fig. 10c, red line).

This can be explained by the increased input sediment flux requiring an increase in the slope at the proximal model boundary to transport the sediment. This therefore increases the area of deposits in the proximal domain causing a greater quantity of gravel to be extracted. Oscillations in the input sediment flux of ±10% however have no effect on the shoreline (Fig. 10d red line), as they are accommodated solely within the subaerial domain.

For a contemporaneous oscillation in precipitation rate of ±10% magnitude and input sediment flux of ±10% magnitude (Fig. 10, blue lines) we find that conversely the location of the gravel front does not move through time (Fig. 10c). This is because the response of the sediment-routing system to precipitation rate changes are exactly the opposite to the response to changes in input sediment flux. An increase in precipitation rate increases the transport capacity and reduces the model slope,

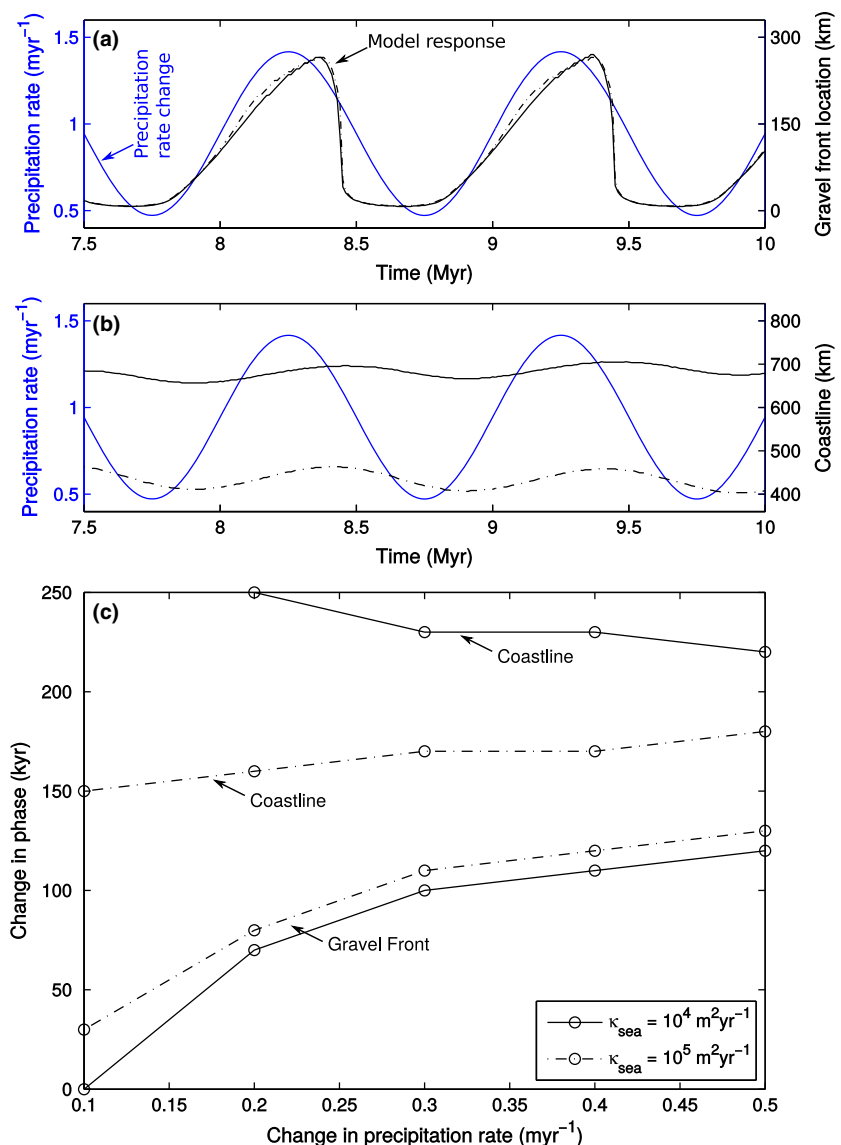


Fig. 7. Response of the sediment transport model where $\kappa_{\text{sea}} = 10^4 \text{ m}^2 \text{ year}^{-1}$ (dashed black lines) and $\kappa_{\text{sea}} = 10^5 \text{ m}^2 \text{ year}^{-1}$ (solid black lines) to increasing magnitude of change in precipitation rates (blue lines). (a) Movement of the position of the gravel front as a consequence of a $\pm 50\%$ change in precipitation rates. (b) Movement of the shoreline as a consequence of a $\pm 50\%$ change in precipitation rates. (c) Delay in the peak response (i.e. timing of maximum regression) of the gravel front position and shoreline with respect to the peak in precipitation rates. The gravel front is always up system of the shoreline. The shoreline for a $\pm 0.1 \text{ m year}^{-1}$ (10%) change in precipitation rates with $\kappa_{\text{sea}} = 10^4 \text{ m}^2 \text{ year}^{-1}$ is omitted as there was no periodicity in predicted shoreline trajectory.

countering the increase in model slope due to the increase in input sediment flux. The shoreline trajectory is however sensitive to the precipitation rate change despite the oscillation in input sediment flux. This is because the shoreline is sufficiently far from the proximal region of the model to be unaffected by the change in input sediment flux. The shoreline trajectory records cyclic progradation and retrogradation over a dip extent of 20 km (Figs 10d and 11).

The system response to a change in both input sediment flux and precipitation rate is therefore similar to that generated when only relative sea-level is altered (Figs 6, 8 and 9; Table 2), assuming that flux and precipitation rate cause relatively minor changes in the grain size distribution. A comparison of the predicted change in down system deposition for the same transport properties (Figs 8 and 11) shows that if input sediment flux increases with increasing precipitation, then there is a strong signal of oscillation in the position of the sand front and the shoreline, yet no movement in the gravel front other than

overall progradation during the modelled time span (Fig. 11a). This is remarkably similar to the model response to oscillating relative sea-level (Fig. 8b). In contrast, if the amplitude of precipitation oscillations is greater than $\pm 10\%$ (Fig. 10 black solid and dashed line), then the system response is similar to that when there is no change in input sediment flux (Figs 8a and 11b). Therefore, as the magnitude of precipitation-rate change is increased relative to the input sediment flux, the precipitation signal becomes dominant (Fig. 10, black solid and dashed lines).

High-frequency oscillations in precipitation rate

That there is a delay in maximum movement of the gravel front compared to maximum precipitation rate (Fig. 7c) raises the possibility that high-frequency ($< 1 \text{ Myr}$ periodicity) oscillations in precipitation rate would be buffered. To explore this possibility, we have run the model

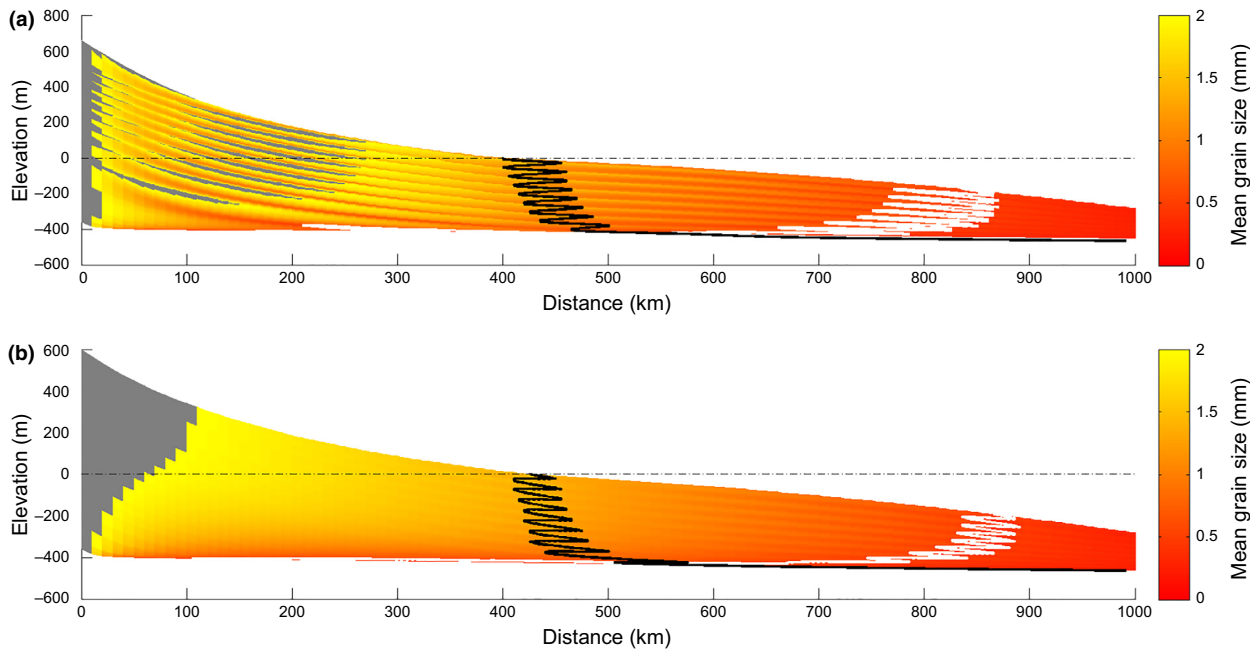


Fig. 8. Model stratigraphic sections for oscillating precipitation rates and oscillating sea level. κ_{decay} (Eqn 3) is held constant at $5 \times 10^4 \text{ m}^{-1}$. (a) Grain size deposited for a model case where $\kappa_{\text{sea}} = 10^5 \text{ m}^2 \text{ year}^{-1}$ and there is a $\pm 50\%$ change in precipitation rate about a mean of 1 m year^{-1} with a period of 1 Myr. Regions of gravel grains are blocked out in gray. The mean grain size of grains finer than 2 mm in diameter is plotted, with the grain size of 0.5 mm displayed as a white contour that approximates the sand front. The shoreline position through time is marked as a solid black line, and the dashed black line marks sea level. (b) As part a, but where precipitation rates are held constant and sea level oscillates periodically by $\pm 10 \text{ m}$.

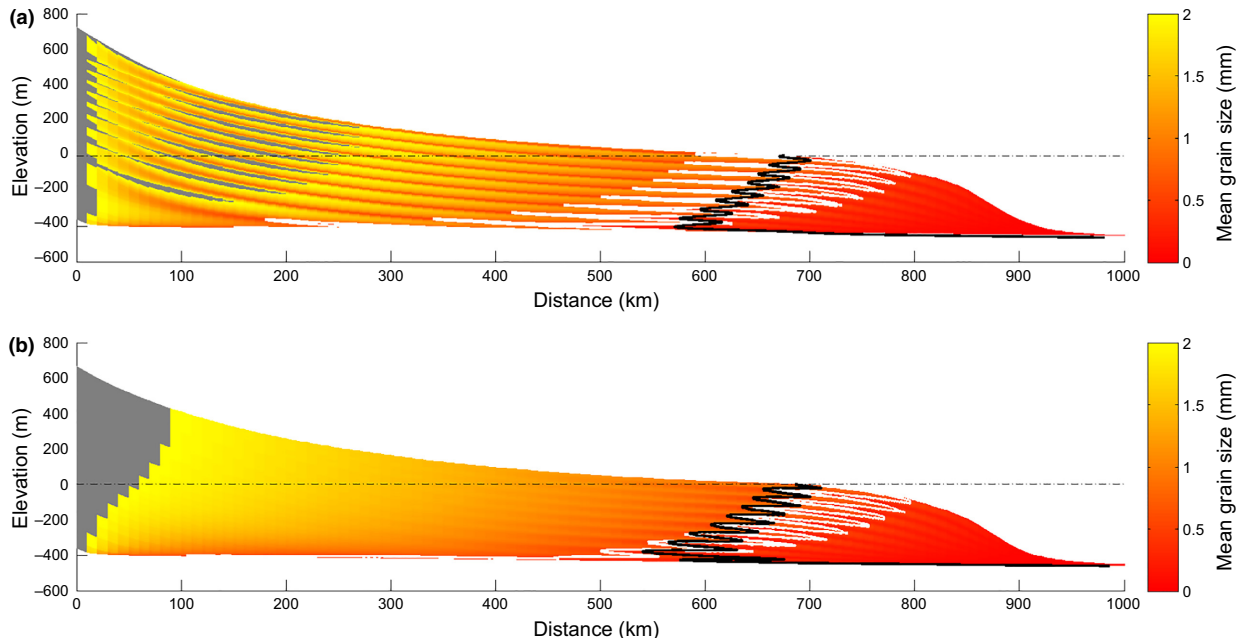


Fig. 9. Model stratigraphic sections for oscillating precipitation rates and oscillating sea level. κ_{decay} (Eqn 3) is held constant at $5 \times 10^4 \text{ m}^{-1}$. (a) Grain size deposited for a model case where $\kappa_{\text{sea}} = 10^4 \text{ m}^2 \text{ year}^{-1}$ and there is a $\pm 50\%$ change in precipitation rate about a mean of 1 m year^{-1} with a period of 1 Myr. Regions of gravel grains are blocked out in gray. The mean grain size of grains finer than 2 mm in diameter is plotted, with the grain size of 0.5 mm displayed as a white contour that approximates the sand front. The shoreline position through time is marked as a solid black, and the dashed black line marks sea level. (b) As part a, but where precipitation rates are held constant and sea level oscillated periodically $\pm 10 \text{ m}$.

with periodic change in precipitation rate that defines 100, 200, 500 and 1000 kyr cycles (Fig. 12). The delay in gravel front response is found to be a function of the

forcing frequency (Fig. 12c). However, the movement of the gravel front has a periodicity that is the same as the high-frequency precipitation signal (Fig. 12a,b).

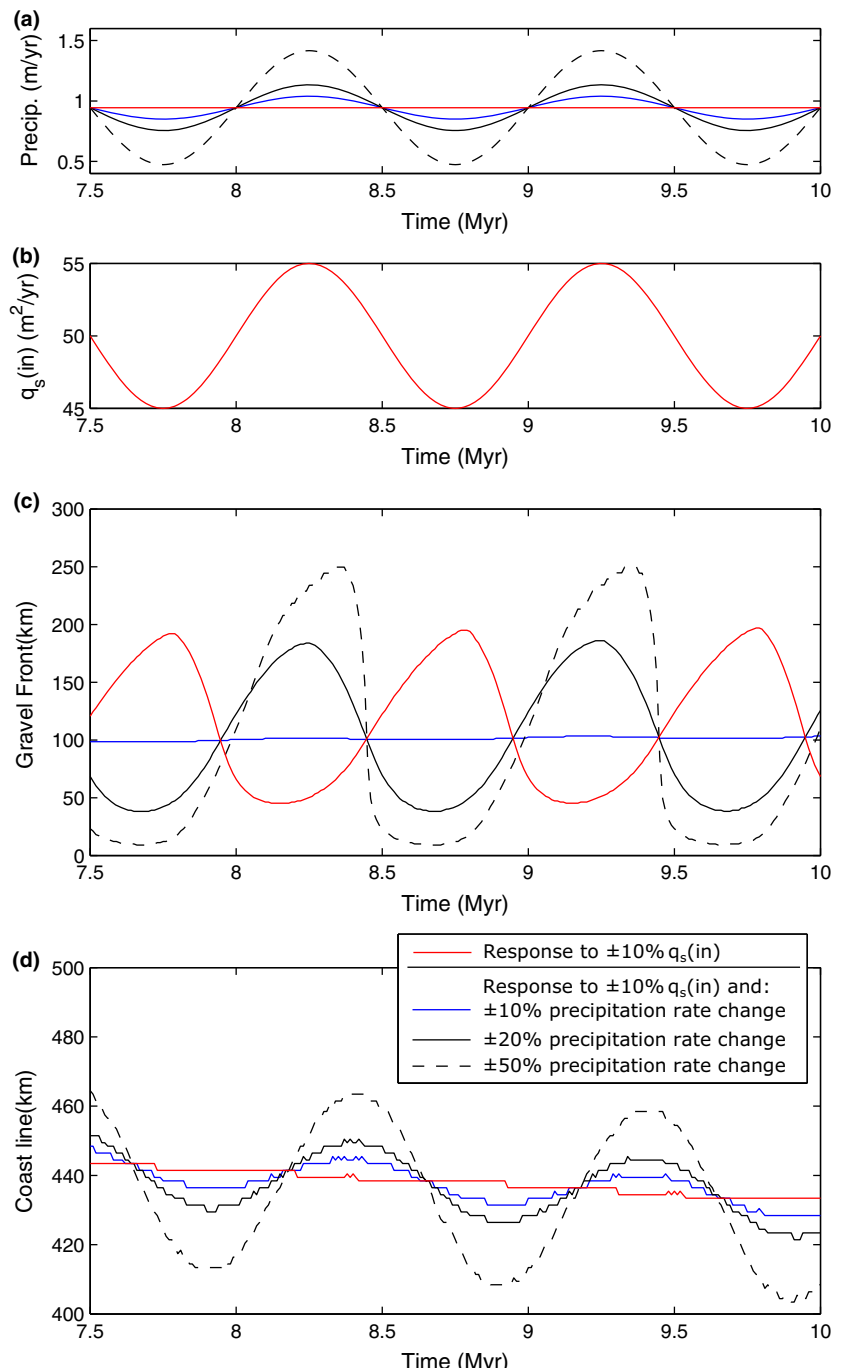


Fig. 10. Response of the sediment transport model to change in input sediment flux, $q_s(\text{in})$, and change in precipitation rates, α . (a) Modelled periodic oscillations in precipitation rate in parts c and d. (b) Modelled periodic oscillations in input sediment flux in parts c and d. (c) Movement of the position of the gravel front due to periodic oscillations in input sediment flux only (red line) and combinations of change in input sediment flux and precipitation (blue and black lines). (d) Movement of the shoreline due to periodic oscillations in input sediment flux only (red line) and combinations of periodic oscillations in input sediment flux and precipitation rate (blue and black lines).

This shows that under these model assumptions, the response recorded through the movement of the gravel front to a change in precipitation rate is out of phase but not buffered.

The phase shift relative to the period of the forcing is longer for shorter periodic change in precipitation rate (Fig. 12c). As would be expected within this diffusive model, there is no destruction of the response by the transport system (see Jerolmack & Paola, 2010), however, there is a delay in peak movement of the gravel front with respect to peak amplitude in precipitation rate. This may further complicate the interpretation of forcing mechanisms from the sedimentary record, when the modelled

system responses are coupled with processes that operate over short timescales and are not captured by this model (e.g. Jerolmack & Paola, 2010; Simpson & Castelltort, 2012).

APPLICATION TO CRETACEOUS SEDIMENT-ROUTING SYSTEM, WESTERN INTERIOR SEAWAY, USA

To test whether the model predictions have any value in interpreting real stratigraphic archives, we forward model aspects of Cretaceous alluvial, coastal plain and shallow

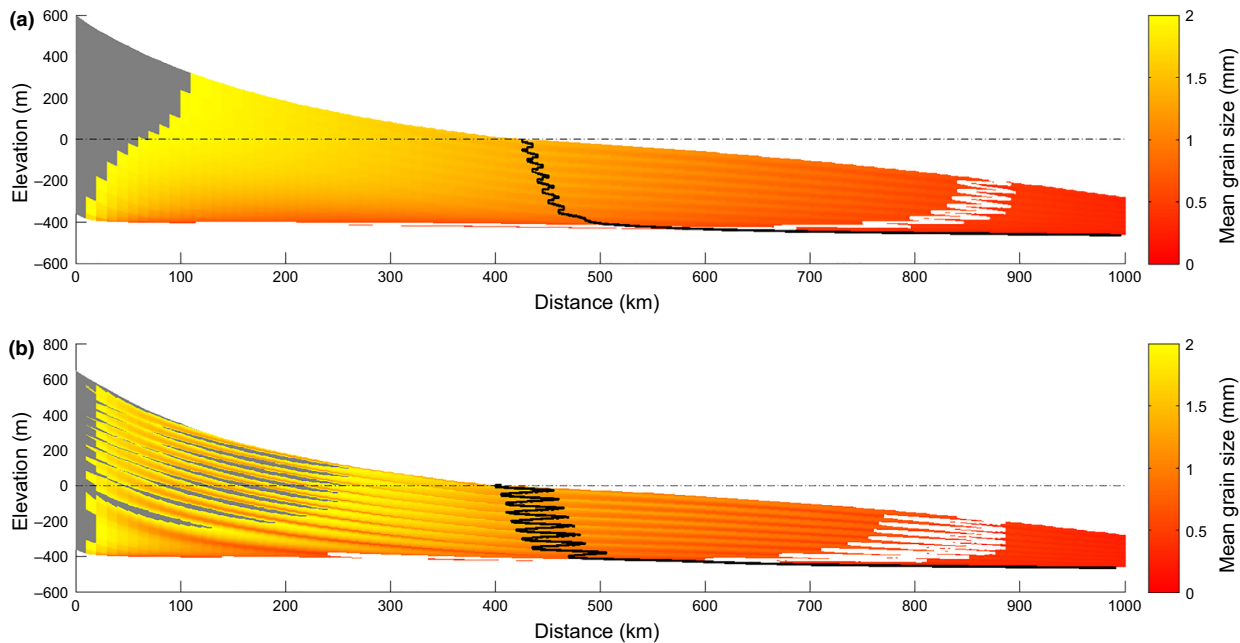


Fig. 11. Model stratigraphic sections for oscillating precipitation rate combined with oscillating input sediment flux. κ_{decay} (Eqn 3) is held constant at $5 \times 10^4 \text{ m}^{-1}$. (a) Grain size deposited for a model case where $\kappa_{\text{sea}} = 10^5 \text{ m}^2 \text{ year}^{-1}$ and there is a $\pm 10\%$ change in precipitation rates about a mean of 1 m year^{-1} with a period of 1 Myr coupled with a $\pm 10\%$ change in input sediment flux around a mean of $50 \text{ m}^2 \text{ year}^{-1}$. Regions of gravel grains are blocked out in gray. The mean grain size of grains finer than 2 mm in diameter is plotted, with the grain size of 0.5 mm displayed as a white contour that approximates the sand front. The shoreline position through time is marked as a solid black line, and the dashed black line marks sea level. (b) As part a, but for a $\pm 50\%$ oscillations in precipitation rates about a mean of 1 m year^{-1} with a period of 1 Myr, coupled with a $\pm 10\%$ oscillation in input sediment flux around a mean of $50 \text{ m}^2 \text{ year}^{-1}$.

marine strata exposed in the Book Cliffs of eastern Utah and western Colorado, USA. Here, the proportions of gravel and sand have been estimated for the depositional system (Table 3; Hampson *et al.*, 2014). These strata are also arguably the most documented and widely visited outcrop example of coastal plain and shallow marine strata that contain multiple, nested cycles of shoreline progradation and retrogradation, yet the exact nature of the controls on shoreline migration is the subject of ongoing debate.

The investigated strata are the preserved record of a large palaeo-sediment-routing system that advanced into the foreland-to-intracratonic Upper Cretaceous Western Interior Basin of North America, in Utah and Colorado, USA (Fig. 13). Predominantly, siliciclastic sediment was eroded from the Sevier fold and thrust belt along the western margin of the basin, and transported eastwards into the Western Interior Seaway (Kauffman & Caldwell, 1993; Decelles and Coogan, 2006). The sediment-routing system accumulated an eastward-thinning wedge of coastal plain to shallow marine strata that passes basinward into offshore shales, and which comprise the Star Point Sandstone, Blackhawk Formation, lower part of the Castlegate Sandstone and part of the Mancos Shale (Figs 13 and 14). This sediment-routing system is of late Santonian to Middle Campanian age (84–78 Ma), and occupied a subtropical palaeolatitude of *ca.* 42°N with a warm, humid climate throughout its deposition

(Kauffman & Caldwell, 1993). Mean annual rainfall has been estimated to be of the order of 1.4 m year^{-1} (p. 52–56 in Wolfe & Upchurch, 1987).

On a gross scale, this system displays gradual progradation over its 5–6 Myr duration (Fig. 14; see Balsley, 1980; Hampson *et al.* 2012). This overall progradation is generally interpreted to record a progressive decrease in tectonic subsidence and accommodation (e.g. Taylor & Lovell, 1995; Adams & Battacharya, 2005; Hampson *et al.*, 2012). At a smaller scale, shallow marine deposits are organised into eight stratigraphic intervals bounded by major flooding surfaces, with each interval representing a potential cycle of progradation and retrogradation (Fig. 14; Hampson, 2010; Hampson *et al.*, 2014). Each interval corresponds approximately to a shallow marine member of the Blackhawk Formation, and has an estimated duration of 0.3–1.0 Myr (Hampson *et al.*, 2014). Several regressive-transgressive shallow-marine tongues (cf. parasequences) of *ca.* 60–330 kyr duration are progradationally to aggradationally stacked in each interval (cf. parasequence set). Multiple forcing mechanisms have been proposed for individual regressive-transgressive tongues and for intervals bounded by major flooding surfaces that contain stacked tongues: relative sea-level fluctuations that combine eustasy with tectonic subsidence (e.g. Van Wagoner *et al.*, 1990; Kamola & Huntoon, 1995; Kamola & Van Wagoner, 1995; Houston *et al.*, 2000), autogenic responses to lengthening of the

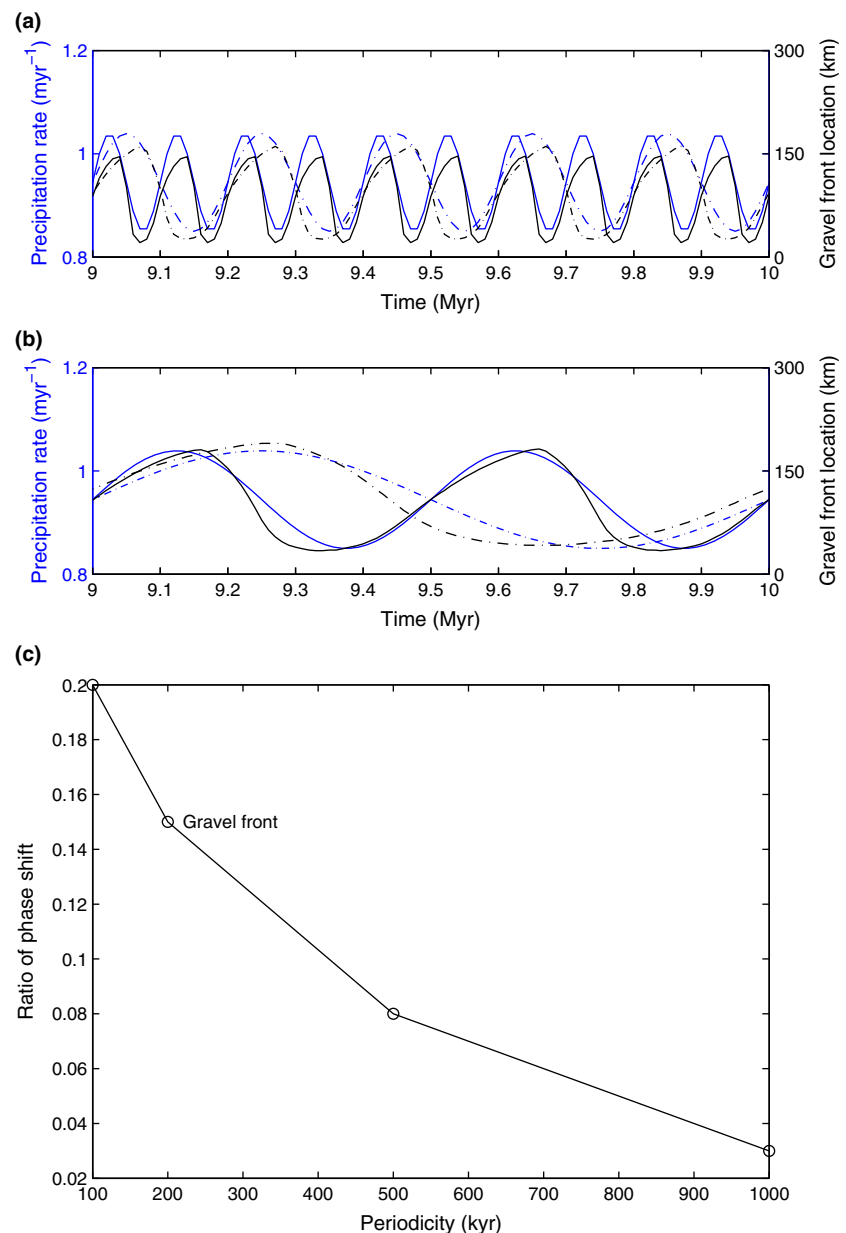


Fig. 12. Response of the sediment transport model where $\kappa_{\text{sea}} = 10^5 \text{ m}^2 \text{ year}^{-1}$ to different frequencies of oscillations in precipitation rate (100, 200, 500 and 1000 kyr). (a) Precipitation rates (blue lines) and gravel front position (black lines) for 100 and 200 kyr oscillations (solid and dashed lines respectively). (b) Precipitation rates (blue lines) and gravel front position (black lines) for 500 and 1000 kyr oscillations (solid and dashed lines respectively). (c) Phase shift in response of the position of the gravel front relative to the period of precipitation rate change plotted against the frequency of precipitation-rate oscillations.

coastal plain (Hampson, 2010), and variable sediment supply (Hampson *et al.*, 2014). Herein, we will use the eight stratigraphic intervals bounded by major flooding surfaces (Fig. 14; Hampson *et al.*, 2014) as a framework in which to explore how both sediment supply and relative sea-level may have influenced deposition within this ancient sediment-routing system.

Isopach maps and palaeogeographic reconstructions indicate that the Star Point – Blackhawk – lower Castlegate wedge is relatively uniform in thickness, facies composition and gross stratigraphic architecture for *ca.* 200 km along depositional strike (NNE–SSW) at the scale of interest (e.g. Fig. 13b; Hampson, 2010; Hampson *et al.*, 2014). The sediment-routing system can therefore be simplified to a representative 2-D cross-section oriented WNW–ESE, as a first approximation. Sediment supply can then be considered in terms of fluvial influx from the left of the modelled cross-section, along the axis

of the sediment-routing system, and net influx or net out flux of sediment from the shallow marine domain of the modelled cross-section, perpendicular to the axis of the sediment-routing system (Hampson, *et al.* 2014). The estimates of Hampson, *et al.* (2014) indicate that only fine-grained sediment (silt, mud) was added or removed from the distal segments of the sediment-routing system by along-strike shallow marine sediment transport, and the effects of this sediment transport can thus be mimicked for the perfect sorting assumption used here by varying the volume of fine-grained sediment in the fluvial sediment supply.

Our intention is not to reproduce the observed progradation of the Star Point – Blackhawk – lower Castlegate wedge, but to evaluate the controls on the gross architecture and stacking of the eight stratigraphic intervals (Fig. 14). We adopt a similar approach to that used to model the Escanilla palaeo-sediment-routing system (Armitage

Table 3. Model input conditions for application to the Star Point – Blackhawk – lower Castlegate – Manacos sediment routing system

Time Period	T0	T1	T2	T3	T4	T5	T6	T7	T8
Duration (Myr)	5	1	0.6	0.5	0.3	0.4	0.8	0.5	1
Input Sediment Flux ($\text{m}^2 \text{ year}^{-1}$)	7	7	14.1	23.2	119.7	47	32.7	19.1	19
Gravel Fraction (%)	0.7	0.7	0.8	0.5	0.1	0.3	0.5	0	18.8
Sand Fraction (%)	41.4	41.4	37.6	37.2	20.4	15.4	20.7	22.3	40.1
Fines Fraction (%)	57.8	57.8	61.6	62.4	79.5	84.3	78.9	77.7	41.1
Distance (km)	Subsidence rate (mm year^{-1})								
0	0.15	0	0	0	0	0	0	0	0
9000	0.15	0	0	0	0	0	0	0	0.05
28 000	0.15	0	0	0	0	0	0	0	0.13
35 000	0.15	0	0	0	0	0	0	0	0.1
57 000	0.15	0.1	0.12	0.16	0.23	0.15	0.19	0	0.1
61 000	0.15	0.1	0.12	0.16	0.23	0.15	0.19	0	0.09
74 000	0.15	0.1	0.12	0.16	0.23	0.15	0.19	0	0.08
84 000	0.15	0.1	0.12	0.16	0.23	0.15	0.14	0	0.07
106 000	0.15	0.1	0.08	0.16	0.23	0.15	0.09	0	0.06
120 000	0.15	0.1	0.07	0.16	0.23	0.15	0.08	0	0.05
163 000	0.15	0.09	0.02	0.1	0.23	0.13	0.08	0.12	0.04
180 000	0.15	0.07	0	0.06	0.17	0.13	0.08	0.12	0.03
191 000	0.15	0.11	0.07	0.08	0.1	0.1	0.08	0.06	0.03
198 000	0.15	0.11	0.07	0.08	0.1	0.1	0.08	0.06	0.02
204 000	0.15	0.11	0.07	0.08	0.1	0.1	0.08	0.06	0.01
212 000	0.1	0.11	0.07	0.08	0.1	0.1	0.08	0.06	0.01
222 000	0.1	0.11	0.07	0.08	0.1	0.1	0.08	0.06	0.03
230 000	0.1	0.12	0.07	0.08	0.1	0.1	0.08	0.06	0.03
239 000	0.1	0.11	0.07	0.08	0.1	0.1	0.08	0.06	0.03
250 000	0.1	0.11	0.07	0.08	0.1	0.1	0.08	0.06	0.03
260 000	0.1	0.11	0.07	0.08	0.1	0.1	0.08	0.06	0.03
270 000	0.1	0.11	0.07	0.08	0.1	0.1	0.08	0.06	0.03
287 000	0.1	0.08	0.07	0.08	0.1	0.1	0.08	0.06	0.03
310 000	0.1	0.07	0.07	0.08	0.1	0.1	0.08	0.06	0.03
338 000	0.1	0.06	0.07	0.08	0.1	0.1	0.08	0.06	0.03
368 000	0.1	0.04	0.07	0.08	0.1	0.1	0.08	0.06	0.03
388 000	0.1	0.04	0.07	0.08	0.1	0.1	0.08	0.06	0.03
425 000	0.1	0.04	0.07	0.08	0.1	0.1	0.08	0.06	0.03

et al., 2015), and take the observed stratal thickness plus an estimate of palaeo-water depth in the submarine depositional domain as a proxy for subsidence down the axis of the sediment-routing system (Table 3). Since information about the catchment is lacking we leave κ , c and n unchanged (see Table 1). We initiate the model with a subsidence profile as listed in Table 3, which serves to build a topographic slope that does not interfere with the subsequent model behaviour. κ_{sea} in Eqn (3) is $10^4 \text{ m}^2 \text{ year}^{-1}$ and $\kappa_{\text{decay}} = 5 \times 10^4 \text{ m}^{-1}$. The sediment flux and its gravel fraction during the eight time intervals (Table 3) is calculated from the observed depositional thickness and deposited sediment volumes (see Hampson *et al.* 2014, for details). The estimated errors in specific sediment volumes and their gravel, sand and shale fractions along the representative 2-D cross-section (Fig. 14) are $\pm 26\text{--}37\%$ for each stratigraphic interval (after table 1 in Hampson *et al.*, 2014). These errors arise from uncertainty in the definition and thickness of stratigraphic intervals, and in the partitioning and textural

characteristics of facies within the intervals. Uncertainty due to poor exposure of proximal strata that abut against the Charleston-Nebo Salient (Fig. 14, after Horton *et al.*, 2004) contributes only approximately one-third of the error in estimated sediment volumes and grain size fractions (Hampson *et al.*, 2014). The gravel fraction in the youngest stratigraphic interval, which contains the Castlegate Sandstone, is significantly larger than in the underlying seven intervals (Table 3). Errors in sediment flux estimates are significantly larger because age data are sparse. Nonetheless, the values summarised in Table 3 are first-order estimates that provide a plausible and internally consistent scenario (see Hampson *et al.*, 2014 for discussion). Precipitation rate is initially 1.4 m year^{-1} and is either held fixed through time, or changes by $\pm 50\%$ over a period of 2 Myr or 100 kyr. Sea level is likewise either held constant at an elevation of 0 m, or is oscillated by $\pm 10\text{m}$ at a period of 2 Myr or 100 kyr.

In the absence of any oscillation in precipitation rate or relative sea level, the modelled sediment-routing system

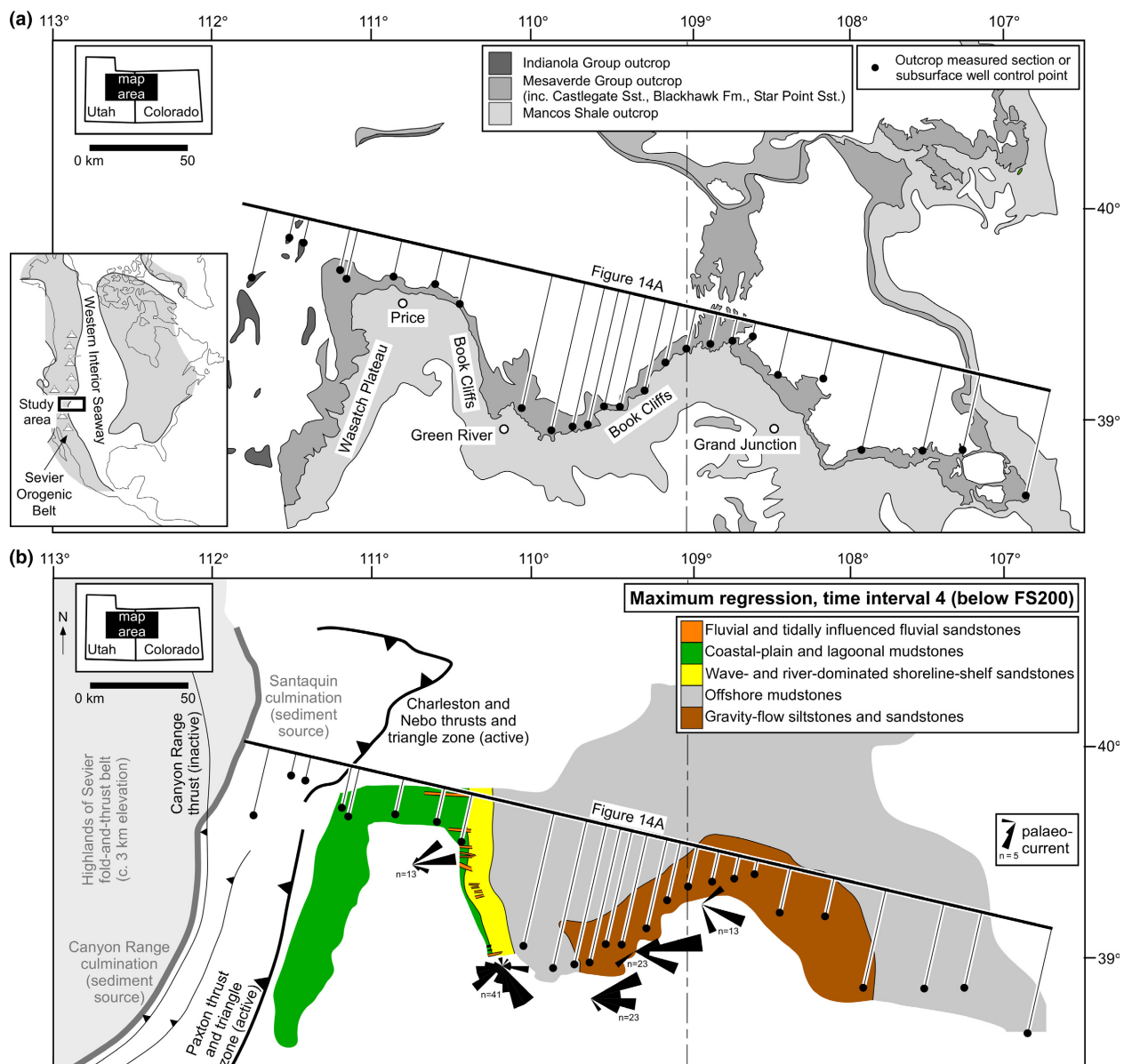


Fig. 13. Maps showing (a) the extent and distribution of the outcrop belt that contains the Star Point – Blackhawk – Castlegate sediment-routing system deposits, and (b) facies-belt extent at maximum regression within time interval 4, between major flooding surfaces FS200 and FS100 (Fig. 14), and the positions of tectonic features that influenced geomorphology, drainage, and sediment supply from the Sevier Orogen are shown (after Johnson, 2003; Horton *et al.*, 2004; DeCelles & Coogan, 2006; Hampson *et al.*, 2014). The inset map in part a shows the location of the study area on the western margin of the late Cretaceous Western Interior Seaway (after Kauffman & Caldwell, 1993).

generates overall progradation of the shoreline (Fig. 15a). Progradation of both the shoreline and sand front (0.5 mm grain size contour) occurs through all time intervals, with the exception of time interval 4, in which the high input sediment flux reduces the selective downstream fining such that the 0.5 mm grain size is not reached within the modelled domain (Fig. 15a). The addition of a 2 Myr periodic change in relative sea level of magnitude of $\pm 10\text{ m}$ (Fig. 15b) or a 2 Myr periodic change in precipitation rate of magnitude $\pm 50\%$ (Fig. 15c) does not significantly alter the modelled stratigraphic architecture, although the amplitude of shoreline migration is

enhanced by a few tens of kilometres at some major flooding surface (e.g. at FS400, between time intervals T6 and T7) compared to the model with no change in precipitation rate or relative sea level (Fig. 15).

Higher frequency change in relative sea level and precipitation rate has a much clearer effect on the predicted stratigraphic architecture (Fig. 16). Oscillations in relative sea level of $\pm 10\text{ m}$ at a period of 100 kyr cause migration of the shoreline and sand front over a dip extent of approximately 20 km (Fig. 16a). As expected, the gravel front remains relatively unchanged by these oscillations in relative sea level. Conversely, a 100 kyr periodic

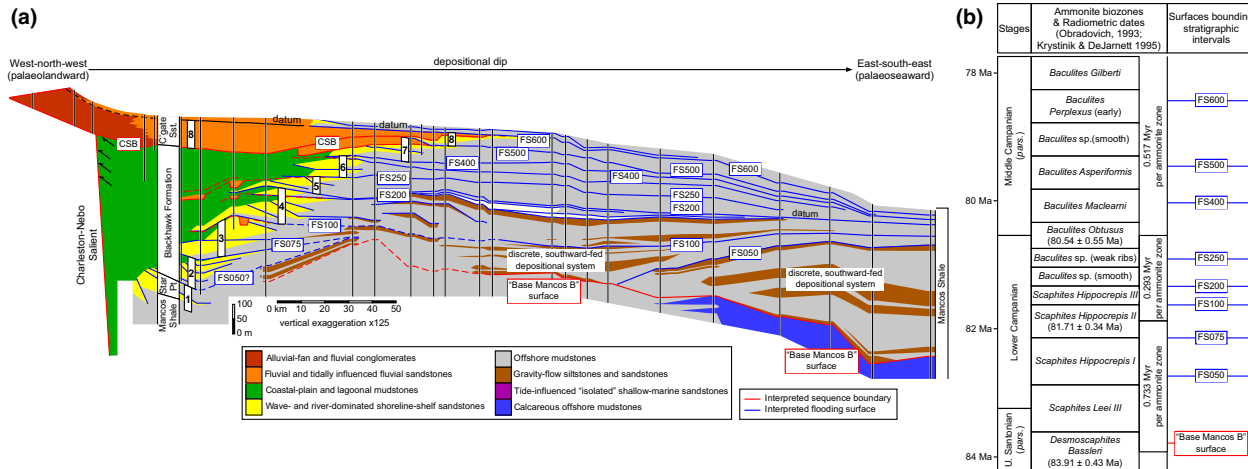


Fig. 14. (a) Correlation panel illustrating stratigraphic architecture through the Book Cliffs outcrops and adjacent areas (after Horton *et al.*, 2004; Hampson, 2010; Hampson *et al.*, 2014 and references therein). Interpreted major flooding surfaces and erosional unconformities (sequence boundaries) are labelled. Deposits corresponding to time intervals 1–8 are indicated. Up system correlation of the lower part of the Castlegate Sandstone (time interval 8) is after Robinson & Slingerland (1998a) and McLaurin & Steel (2000). A variety of stratigraphic surfaces are used as datum surfaces for different parts of the panel, and each surface is assigned the depositional dip of an eastward-dipping coastal plain or shelf profile where used as a datum. The panel is located in Fig. 13. (b) Ammonite biostratigraphy, radiometric dates (Obradovich, 1993), and estimated ammonite biozone durations (Krystnik & DeJarnett, 1995) for the studied strata, showing the interpreted ages of major flooding.

oscillation in precipitation rate of a magnitude of $\pm 50\%$ causes significant movement in the position of the gravel front, which exhibits cyclical progradations and retrogradation over a dip extent of approximately 70 km (Fig. 16b). The movement of the sand front farther downstream is similar to that forced by changes in relative sea-level, yet there is less associated movement of the shoreline (Fig. 16b). Movement of the sand front in the modelled strata cannot therefore be used as an observation that can distinguish between change in surface runoff or relative sea-level change.

Observed shifts in the position of the shoreline are of 20–40 km within the coastal to shallow marine deposits (Fig. 14). Such shifts can therefore be matched by the modelled high-frequency oscillations in either precipitation rate or relative sea level (Fig. 16). The distinguishing factor is the pattern of coeval gravel front migration in upstream locations. The lower Castlegate Sandstone contains the gravel tongue that caps the Star Point – Blackhawk – lower Castlegate wedge (Fig. 14). Cyclical change in run off would be expressed within the lower Castlegate Sandstone by high-amplitude shifts in gravel front position (c.f. Fig. 16). Although the lower Castlegate Sandstone contains some evidence of high-frequency alloogenetic forcing, in the form of systematic vertical stacking of channel-belt sandstone bodies (McLaurin & Steel, 2007), it does not by any means provide definitive support for cyclical movement of the gravel front predicted by the idealised model. By implication, the observed movement of the shoreline within the Star Point – Blackhawk – lower Castlegate wedge was more likely a consequence of high-frequency change in relative sea-level, as inferred from other stratigraphic intervals and palaeographic locations in the Western Interior Seaway (e.g. Plint & Kreitner, 2007).

DISCUSSION

Our numerical model implies that patterns in the relative movement of internal boundaries, the gravel front, shoreline and sand front, can be used to diagnose forcing mechanism(s) from observed stratigraphic architectures. The gravel front is strongly controlled by terrestrial sediment transport, and therefore, if there is significant cyclical change in the surface flow of water, then the gravel front responds via cyclical progradation and retrogradation (Fig. 6). The timing of maximum regression of the gravel front will lag behind the peak increase in precipitation rate (e.g. by several tens to one hundred thousand years; Figs 7a and 12), yet this delay is most likely not observable given the age constraints available in most ancient stratigraphic records.

The shoreline and the sand front are sensitive to both terrestrial and submarine sediment transport (Figs 6–9). The magnitude of the cycles of shoreline and sand front progradation and retrogradation are a function of the precipitation rate change and the magnitude of relative sea-level change. A cyclical change in precipitation rates from 1.5 to 0.5 m year^{-1} forces the shoreline and sand front to move by a similar magnitude as for a $\pm 10 \text{ m}$ change in sea level (Table 2). This finding implies that movement of the shoreline and sand front cannot on their own be used as an indicator of change in relative sea level, and neither are they an indicator of change in sediment flux (Figs 8 and 9). The gravel front responds to a change in precipitation rate but is found to be insensitive to relative sea-level change. Movement of the gravel front is therefore potentially a powerful tool to diagnose forcing mechanisms of stratigraphic architecture, and to decipher past climatic change from sedimentary archives.

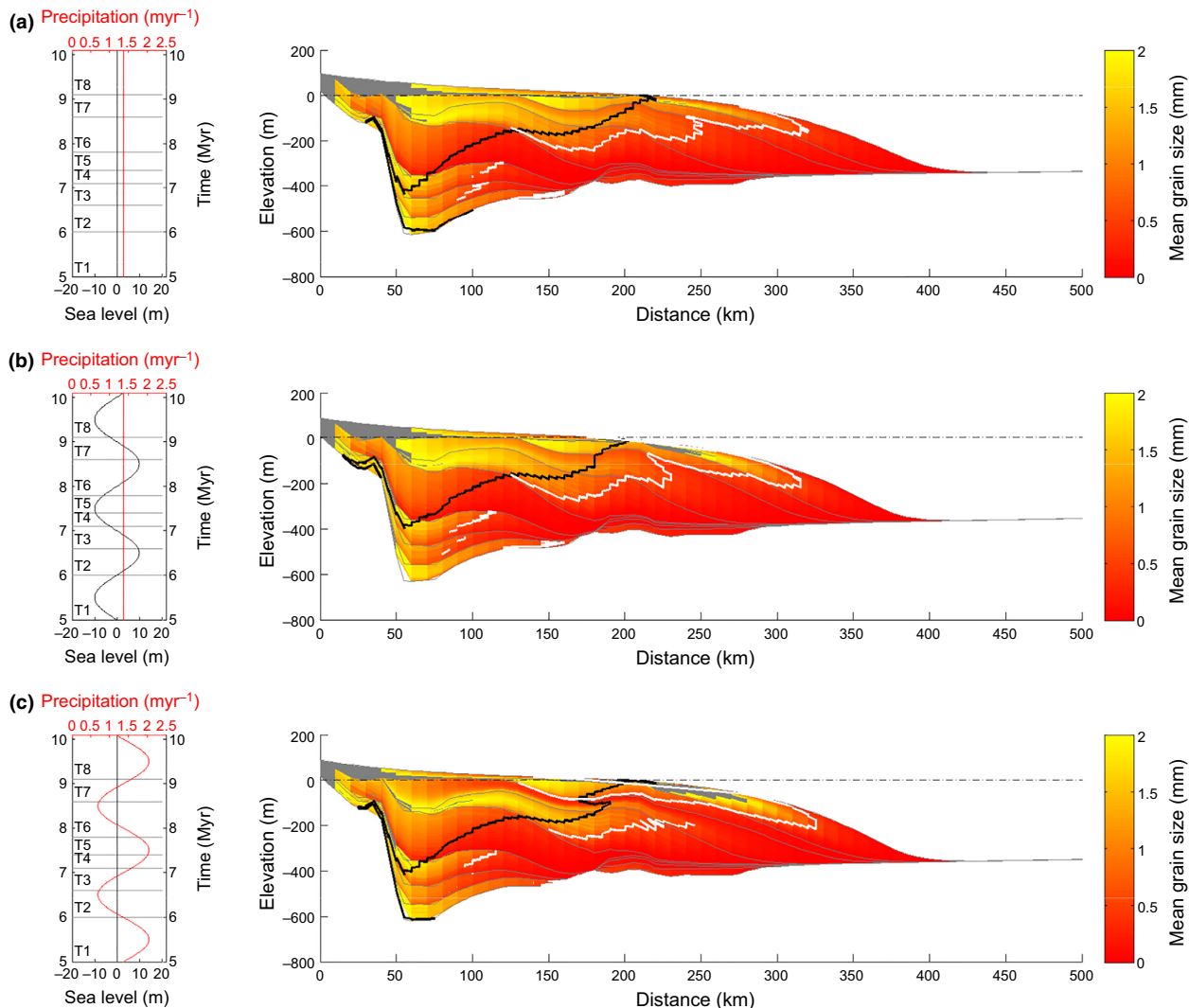


Fig. 15. Synthetic strata for three models of the stratigraphic architecture in the Star Point – Blackhawk – lower Castlegate wedge, based on the Book Cliffs outcrops. (a) Predicted stratigraphic architecture assuming no change in sea level or precipitation rate (1.4 m year^{-1}) throughout the model duration. (b) Predicted stratigraphic architecture assuming a 2 Myr periodic change in relative sea level of amplitude $\pm 10 \text{ m}$. (c) Predicted stratigraphic architecture assuming a 2 Myr periodic change in precipitation rates of amplitude $\pm 50\%$. Regions of gravel grains are blocked out in gray. The mean grain size of grains finer than 2 mm in diameter is plotted, with the grain size of 0.5 mm displayed as a white contour that approximates the sand front. The shoreline position through time is marked as a solid black line, and the dashed black line marks sea level.

If however the input sediment flux from the catchment feeding the sediment-routing system changes along with the precipitation rate, then the gravel front is no longer a faithful recorder of change in surface run-off (Fig. 11). Depending on the magnitude of change in input sediment flux and precipitation rate, the gravel front may not respond in a cyclical manner to the external forcing. This is because, within the construct of the model, the increase in area of sediment delivered from the catchment to the sediment-routing system is balanced by the increase in transport rate to move that material. Although it is possible that this balance in input sediment flux and transport only exists within simple idealised numerical models, the wider point is that multiple cyclical forcing mechanisms may counter each other. Given the complexity of sediment-routing systems, and the clear potential for

autogenic behaviours to create cyclical patterns within stratal units (e.g. Hajek *et al.*, 2010), the presence of cyclical movement of the gravel front and shoreline does not necessarily mean there was unsteady forcing by precipitation rate, input sediment flux or relative sea-level. That said, our model would suggest that change in the movement of the shoreline without movement in the gravel front is either a function of relative sea-level change, or of change in precipitation rate coupled with change in sediment delivery to the depositional sink. The simplest explanation would be the former, but it is important to stress that this is not a unique interpretation of the observed stratigraphic architecture.

In our generic model simulations, we have assumed a constant gravel fraction in the sediment supply while oscillating input sediment flux and precipitation rate. It is

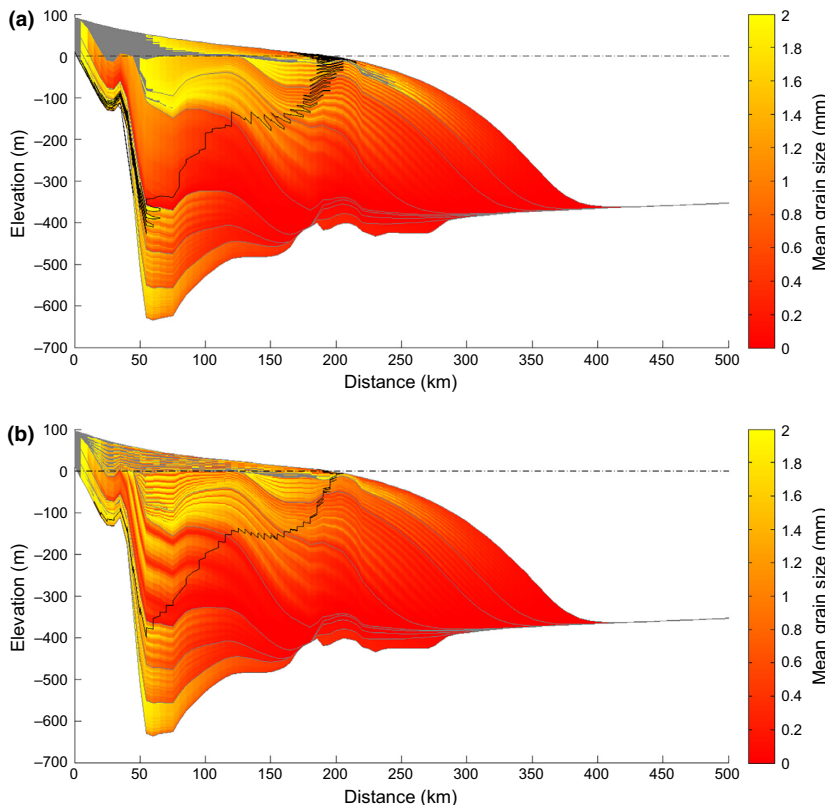


Fig. 16. Synthetic strata for two models of the stratigraphic architecture in the Star Point – Blackhawk – lower Castlegate wedge, based on the Book Cliffs outcrops. (a) Predicted stratigraphic architecture assuming a 100 kyr periodic oscillation in relative sea-level of amplitude ± 10 m. (b) Predicted stratigraphic architecture assuming a 100 kyr periodic oscillation in precipitation rate of amplitude $\pm 50\%$. Regions of gravel grains are blocked out in gray. The mean grain size of grains finer than 2 mm in diameter is plotted. The shoreline position through time is marked as a solid black line, and the dashed black line marks sea level.

plausible that, for example, increased precipitation can increase the fraction of gravel eroded within the source catchment (Allen *et al.*, 2015). From previous numerical models, it has been shown that such an increase in the coarse grain-size fraction coupled with increased precipitation rate increases the signal of progradation within the depositional system (Armitage *et al.*, 2011). When exploring the sensitivity of the gravel front to gravel fraction, we found that a $\pm 50\%$ difference in gravel fraction moves the location of the gravel front by $\pm 10\%$. In applying our model to a geological location, we however make the assumption that the fraction of gravel and sand within the deposits of the sediment-routing system is representative of the source. We suggest that this assumption limits the potential for misinterpretation of the model relative to the observed stratigraphic record.

When this model is applied to the Star Point – Blackhawk – lower Castlegate – Mancos sediment-routing system, based on the interpretation outlined in Table 3, we find that the overall progradational stratigraphic architecture can be readily matched. High-frequency changes in sea level and/or precipitation rate, of a period of 100 kyr, have a clear effect on migration of the shoreline and sand front (Fig. 16). If we assume that the observed depositional thickness of sediment is representative of the sediment flux into the basin, then the migration history of the gravel front would be a quantifiable measure to distinguish whether cyclical patterns of progradation and retrogradation were the result of cyclical change in precipitation rates or sea level (Fig. 16). Data describing the architecture of proximal deposits in the Star Point –

Blackhawk – lower Castlegate – Mancos sediment-routing system are rare, however, on balance the evidence suggests limited movement of the gravel front. Therefore, a high-frequency cyclical change in relative sea level is the most probable of modelled mechanisms to account for the observed stratigraphic architecture.

We estimated the potential error in the observed gravel, sand and shale fractions to be of the order of $\pm 30\%$. Therefore, we could be either overestimating or underestimating the position of the gravel front by no more than $\pm 10\%$ of the depositional length of the sediment-routing system (i.e. by up to ± 40 km). When comparing the model to the observed stratigraphic section, it is worth explaining that we are interested in matching the trend, or relative change in the position of the moving boundary as well as the magnitude. Therefore, error in our interpretation would be introduced only if we make a nonsystematic error in accounting for the deposited sediment.

The predicted location of the shoreline is a function of the water flux, the sediment transport coefficient (c in Eqn 1) and the sea level. We assume that the transport coefficient is independent of grain size. While such a transport coefficient is potentially grain size dependent (e.g. Marr *et al.* 2000), at large distances down the sub-aerial system, the overall diffusion coefficient for the Exner balance is dominated by the water flux. This is because for large x , $q_m^n \gg c$ in Eqn (1). Therefore, it is reasonable to suggest that the predicted topography at large values of x and hence shoreline is not strongly altered by the fraction of gravel, sand and finer grains within the sediment source. Therefore, while the model

presented is a simplification of the complex processes of sediment transport and deposition, we propose that the results are most likely valid and remain useful for interpreting the stratigraphic record.

CONCLUSIONS

We have developed a simple nonlinear diffusive model of sediment transport to explore how cyclical changes in sediment delivery, surface run-off (precipitation rate) and relative sea-level effect stratigraphic architecture. In particular, we have focused on how change in these external drivers influence the movement of internal depositional boundaries: the gravel front, the shoreline and the sand front. The subaerial and subaqueous domains have a greater linkage in terms of delivery of sediment from source to sink for a higher transport rate in the marine system. The increased transport rate leads to ramp-like stratigraphic architecture, rather than cliniforms. Furthermore, in the generic application of the model where subsidence is constant in time and uniform in space, we find that change in sediment transport in the subaqueous domain does not significantly impact the terrestrial domain, i.e. the gravel front. However, change in sediment transport in the subaerial domain impacts the whole system including the shoreline and sand front, which typically rests basinwards of the shoreline.

The results of the numerical model imply that change in precipitation rate and change in relative sea level generate diagnostically different responses in movement of the gravel front. Both mechanisms force the shoreline and sand front to move by similar distances, yet it is only when precipitation rate changes that the gravel front responds. This simple diagnostic response is then modified when the sediment flux delivered to the sediment-routing system is also cyclically changed with the change in precipitation rates. If both input sediment flux and precipitation rates change in phase, then movement of the gravel front can be greatly reduced to give similar patterns of deposition as those that result from relative sea level change.

The lack of a unique diagnostic measure for the forcing mechanisms of ancient sediment-routing systems can be overcome if the input sediment flux from the catchment can be measured independently. This can be achieved if the majority of the depositional system is preserved, allowing for a sediment budget to be calculated. By applying the model to the deposits of such a sediment-routing system, the Cretaceous Star Point – Blackhawk – lower Castlegate – Mancos system exposed in the Book Cliffs of Utah and Colorado, we find that cyclical progradation and retrogradation of the shoreline and sand front can be a consequence of either oscillating precipitation rate or relative sea level. Movement of the gravel front becomes the diagnostic indicator of forcing of the sediment-routing system by an upstream (sediment flux, precipitation rate) or downstream (relative sea level) control.

ACKNOWLEDGEMENTS

This work was funded by a Royal Astronomical Society Research Fellowship awarded to John Armitage. We thank Cynthia Ebinger, Teresa Jordan and an anonymous reviewer for their time and comments that improved this manuscript.

CONFLICT OF INTEREST

No conflict of interest declared.

REFERENCES

- ADAMS, M.M. & BATTACHARYA, J.P. (2005) No change in fluvial style across a sequence boundary, Cretaceous Blackhawk and Castlegate Formations of central Utah, USA. *J. Sediment. Res.*, **75**, 1038–1051.
- ALLEN, P.A., ARMITAGE, J.J., WHITTAKER, A.C., MICHAEL, N.A., RODA-BOLUDA, D. & D'ARCY, M. (2015) Fragmentation model of the grain size mix of sediment supplied to basins. *J. Geol.*, **123**, 405–427.
- ARMITAGE, J.J., ALLEN, P.A., BURGESS, P.M., HAMPSON, G.J., WHITTAKER, A.C., DULLER, R.A. & MICHAEL, N.A. (2015) Physical stratigraphic model for the Eocene Escanilla sediment routing system: Implications for the uniqueness of sequence stratigraphic architectures. *J. Sediment. Res.*, **85**, 1510–1524.
- ARMITAGE, J.J., DULLER, R.A., WHITTAKER, A.C. & ALLEN, P.A. (2011) Transformation of tectonic 17 and climatic signals from source to sedimentary archive. *Nat. Geosci.*, **4**, 231–235.
- ARMITAGE, J.J., DUNKLEY JONES, T., DULLER, R.A., WHITTAKER, A.C. & ALLEN, P.A. (2013) Temporal buffering of climate-driven sediment flux cycles by transient catchment response. *Earth Planet. Sci. Lett.*, **369–370**, 200–210.
- BALSLEY, J.K. (1980) *Cretaceous wave-dominated delta systems, Book Cliffs, east-central Utah. Continuing Education Course Field Guide*. American Association of Petroleum Geologists.
- BLUM, M.D. & HATTIER-WOMACK, J. (2009) Climate change, sea-level change, and fluvial sediment supply to deepwater depositional systems. In: *External Controls on Deep-Water Depositional Systems* (Ed. by Kneller B.C., Martinsen O.J. & McCaffrey B.) *SEPM Spec. Publ.*, **92**. SEPM, Tulsa, Oklahoma, 15–39.
- BLUM, M.D. & TÖRNQVIST, T.E. (2000) Fluvial responses to climate and sea-level change: a review and look forward. *Sedimentology*, **47**(Suppl. 1), 2–48.
- BRAUN, J., VOISIN, C., GOURLAN, A.T. & CHAUVEL, C. (2015) Erosional response of an actively uplifting mountain belt to cyclic rainfall variations. *Earth Surf. Dynam.*, **3**, 1–14.
- BURGESS, P.M., LAMMERS, H., VAN OOSTERHOUT, C. & GRANJEON, D. (2006) Multivariate sequence stratigraphy: tackling complexity and uncertainty with stratigraphic forward modelling, multiple scenarios, and conditional frequency maps. *Am. Associat. Petrol. Geol. Bullet.*, **90**, 1883–1901.
- BURGESS, P.M. & PRINCE, G.D. (2015) Non-unique stratal geometries: implications for sequence stratigraphic interpretations. *Basin Res.*, **27**, 351–365.

- BURGESS, P.M., STEEL, R. & GRANJEON, D. (2008) Stratigraphic forward modeling of basin-margin clinoform systems: Implications for controls on topset and shelf width and timing of formation of shelf-edge deltas. In: *Recent Advances in Models of Siliciclastic Shallow-Marine Stratigraphy*. (Ed. by Hampson G.J., Steel R.J., Burgess P.M. & Dalrymple R.W.) *SEPM Spec. Publ.*, Society for Sedimentary Geology, **90**, 35–45.
- CARVAJAL, C. & STEEL, R. (2012) Source-to-sink sediment volumes within a tectono-stratigraphic model for a Laramide shelf-to-deep-water basin: Methods and results. In: *Tectonics of Sedimentary Basins: Recent Advances* (Ed. by C. Busby & A. Azor Perez), pp. 131–151. Wiley-Blackwell, Oxford, UK.
- CASTELLORT, S. & VAN DEN DREISSCHE, J. (2003) How plausible are high-frequency sediment supply driven cycles in the stratigraphic record? *Sediment. Geol.*, **157**, 3–13.
- CATUNEANU, O., ABREU, V., BHATTACHARYA, J.P., BLUM, M.D., DALRYMPLE, R.W., ERIKSSON, P.G., FIELDING, C.R., FISHER, W.L., GALLOWAY, W.E., GIBLING, M.R., GILESK, K.A., HOLBROOK, J.M., JORDAN, R., KENDALL, C.G., MACURDA, B., MARTINSEN, O.J., MIAILL, A.D., NEAL, J.E., NUMMEDA, D., POMAR, L., POSAMENTIER, H.W., PRATT, B.R., SARG, J.F., SHANLEY, K.W., STEEL, R.J., STRASSER, A., TUCKER, M.E. & WINKER, C. (2009) Towards the standardization of sequence stratigraphy. *Earth-Sci. Rev.*, **92**, 1–33.
- COVVAULT, J.A. & GRAHAM, S.A. (2010) Submarine fans at all sea-level stands: tectono-morphologic and climatic controls on terrigenous sediment delivery to the deep sea. *Geology*, **38**, 939–942.
- COVVAULT, J.A., ROMANS, B.W., GRAHAM, S.A., FILDANI, A. & HILLEY, G.E. (2011) Terrestrial source to deep-sea sink sediment budgets at high and low sea levels: Insights from tectonically active southern California. *Geology*, **39**, 619–622.
- DADE, W.B. & FRIEND, P.F. (1998) Grain-size, sediment-transport regime, and channel slope in alluvial rivers. *J. Geol.*, **106**, 661–675.
- DECCELLES, P.G. & COOGAN, J.C. (2006) Regional structure and kinematic history of the Sevier fold-and-thrust belt, central Utah. *Geol. Soc. Am. Bullet.*, **118**, 841–864.
- FEDELE, J.J. & PAOLA, C. (2007) Similarity solutions for alluvial sediment fining by selective deposition. *J. Geophys. Res.*, **112** (F02038). doi: 10.1029/2005JF000409.
- FISK, H.N. (1944) *Geological Investigation of the Alluvial Valley of the Lower Mississippi River*. War Department, Corps of Engineers, p. 78.
- GODARD, V., TUCKER, G.E., BURCH FISHER, G., BURKBANK, D.W. & BOOKHAGEN, B. (2013) Frequency dependent landscape response to climatic forcing. *Geophys. Res. Lett.*, **40**, 859–863.
- HAJEK, E.A., HELLER, P.L. & SHEETS, B.A. (2010) Significance of channel-belt clustering in alluvial basins. *Geology*, **38**, 535–538.
- HAMPSON, G.J. (2010) Sediment dispersal and quantitative stratigraphic architecture across an ancient shelf. *Sedimentology*, **57**, 96–141.
- HAMPSON, G.J., DULLER, R.A., PETTER, A.L., ROBINSON, R.A.J. & ALLEN, P.A. (2014) Mass-balance constraints on stratigraphic interpretation of linked alluvial-coastal-shelf deposits from source to sink: example from Cretaceous Western Interior Basin, Utah and Colorado, USA. *J. Sediment. Res.*, **84**, 935–960.
- HAMPSON, G.J., ROYHAN GANI, M., SAHOO, H., RITTERSBACHER, A., IRFAN, N., RANSON, A., JEWELL, T.O., GANI, N.D.S., HOWELL, J. A., BUCKLEY, S.J. & BRACKEN, B. (2012) Alluvial-to-coastal plain stratigraphic architecture and large-scale patterns of fluvial sandbody distribution in a progradational clastic wedge: Upper Cretaceous Blackhawk Formation, Wasatch Plateau, central Utah, USA. *Sedimentology*, **59**, 2226–2258.
- HELLER, P.L., BURNS, B.A. & MARZO, M. (1993) Stratigraphic solution sets for determining the roles of sediment supply, subsidence and sea level on transgressions and regressions. *Geology*, **21**, 747–750.
- HORTON, B.K., CONSTENSIUS, K.N. & DECELLES, P.G. (2004) Tectonic control on coarse-grained foreland-basin sequences: an example from the Cordilleran foreland basin, Utah. *Geology*, **32**, 637–640.
- HOUSTON, W.S., HUNTOON, J.E. & KAMOLA, D.L. (2000) Modeling of cretaceous foreland-basin parasequences, utah, with implications for timing of sevier thrusting. *Geology*, **28**, 267–270.
- JEROLMACK, D.J. & PAOLA, C. (2010) Shredding of environmental signals by sediment transport. *Geophys. Res. Lett.*, **37** (L19401). doi: 10.1029/2010GL044638.
- JOHNSON, R.C. (2003) Depositional framework of the Upper Cretaceous Mancos Shale and the lower part of the Upper Cretaceous Mesaverde Group, Western Colorado and Eastern Utah. In: *Petroleum Systems and Geologic Assessment of Oil and Gas in the Uinta/Piceance Province, Utah and Colorado*. No. DDS-69-B in *Digital Data Series*. U.S. Geological Survey, Ch. 10.
- KAMOLA, D.L. & HUNTOON, J.E. (1995) Repetitive stratal patterns in a foreland basin sandstone and their possible tectonic significance. *Geology*, **23**, 177–180.
- KAMOLA, D.L. & VAN WAGONER, J.C. (1995) Stratigraphy and facies architecture of parasequences with examples from Spring Canyon Member, Blackhawk Formation, Utah. In: *Sequence Stratigraphy of Foreland Basin Deposits*. No. 64 in *Memoir* (Ed. Van Wagoner J.C. & Bertram G.T.), American Association of Petroleum Geologists, 27–54.
- KAUFFMAN, E.G. & CALDWELL, W.G.E. (1993) The western interior basin in space and time. In: *Evolution of the Western Interior Basin. Special Paper*, 39 (Ed. by Caldwell W.G.E. & Kauffman E.G.) Geological Association of Canada, 1–30.
- KAUFMAN, P., GROTZINGER, J.P. & MCCORMICK, D.S. (1991) Depth-dependent diffusion algorithm for simulation of sedimentation in shallow marine depositional systems. *Bulletin – Kansas Geol. Surv.*, **233**, 489–508.
- KRYSTNIK, L.F. & DEJARNETT, B.B. (1995) Lateral variability of sequence stratigraphic framework in the Campanian and Lower Maastrichtian of the Western Interior Seaway. In: *Sequence Stratigraphy of Foreland Basin Deposits*. No. 64 in *Memoir* (Ed. by Van Wagoner J.C. & Bertram G.T.) American Association of Petroleum Geologists, 11–26.
- MARR, J.G., SWENSON, J.G., PAOLA, C. & VOLLMER, V.R. (2000) A two-diffusion model of fluvial stratigraphy in closed depositional basins. *Basin Res.*, **12**, 381–398.
- MCLAURIN, B.T. & STEEL, R.J. (2000) Fourth-order nonmarine to marine sequences, Middle Castle gate Formation, Book Cliffs, Utah. *Geology*, **28**, 359–362.
- MCLAURIN, B.T. & STEEL, R.J. (2007) Architecture and origin of an amalgamated fluvial sheet sand, lower Castlegate Formation, Book Cliffs, Utah. *Sediment. Geol.*, **197**, 291–311.
- MÉTIVIER, F. (1999) Diffusivelike buffering and saturation of large rivers. *Phys. Rev. E*, **60**, 5827–5832.
- MICHAEL, N.A., WHITTAKER, A.C. & ALLEN, P.A. (2013) The functioning of sediment routing systems using a mass balance

- approach: example from the Eocene of the Southern Pyrenees. *J. Geol.*, **121**(581–606), doi: 10.1086/673176.
- MICHAEL, N.A., WHITTAKER, A.C., CARTER, A. & ALLEN, P.A. (2014) Volumetric budget and grain-size fractionation of a geological sediment routing system: Eocene Escanilla Formation, south-central Pyrenees. *Geol. Soc. Am. Bullet.*, **126**, 585–599.
- OBRADOVICH, J.D. (1993) A Cretaceous time scale. In: *Evolution of the Western Interior Basin* (Ed. by Caldwell W.G.E. & Kauffman E.G.), Special Paper, 39. Geological Association of Canada, 379–378.
- PAOLA, C., HELLER, P.L. & ANGEVINE, C.L. (1992) The large-scale dynamics of grain-size variation in alluvial basins, 1: Theory. *Basin Res.*, **4**, 73–90.
- PAOLA, C. & MARTIN, J.M. (2012) Mass-balance effects in depositional systems. *J. Sediment. Res.*, **82**, 435–450.
- PLINT, A.G. & KREITNER, M.A. (2007) Extensive thin sequences spanning cretaceous foredeep suggest high-frequency eustatic control: Late Cenomanian, Western Canada foreland basin. *Geology*, **35**, 735–738.
- ROBINSON, R.A.J. & SLINGERLAND, R.L. (1998a) Grain-size trends, basin subsidence and sediment supply in the Campanian Castlegate Sandstone and equivalent conglomerates of central Utah. *Basin Res.*, **10**, 109–127.
- ROBINSON, R.A.J. & SLINGERLAND, R.L. (1998b) Origin of fluvial grain-size trends in a foreland basin the: Pocono Formation on the Central Appalachian Basin. *J. Sediment. Res.*, **68**, 473–486.
- ROMANS, B.W., CASTELLORT, S., COVAULT, J.A., FILDANI, A. & WALSH, J.P. (2015) Environmental signal propagation in sedimentary systems across timescales. *Earth Sci. Rev.* doi: 10.1016/j.earscirev.2015.07.012.
- SIMPSON, G. & CASTELLORT, S. (2012) Model shows that rivers transmit high-frequency climate cycles to the sedimentary record. *Geology*, **40**, 1131–1134.
- SMITH, T.R. & BRETHERTON, F.P. (1972) Stability and conservation of mass in drainage basin evolution. *Water Res. Res.*, **8**, 1506–1529.
- STERNBERG, H. (1875) Untersuchungen über Längen und Querprofil geschiebeführnde Flüsse. *Zeitschrift für das Bauwesen*, **25**, 483–506.
- SWENSON, J.B. (2005) Relative importance of fluvial input and wave energy in controlling the timescale for distributary-channel avulsion. *Geophys. Res. Lett.*, **32**, L23404.
- TAYLOR, D.R. & LOVELL, R.W.W. (1995) High-frequency sequence stratigraphy and paleogeography of the Kenilworth member, Blackhawk Formation, Book Cliffs, Utah, U.S.A. In: *Sequence Stratigraphy of Foreland Basin Deposits. No. 64 in Memoir* (Ed. by Van Wagoner J.C. & Bertram G.T.) American Association of Petroleum Geologists, 257–275.
- VAIL, P.R., MITCHUM, R.M. Jr., TODD, R.G., WIDMIER, J.M., THOMPSON III, S., SANTEE, J.B., BUBB, J.N. & HATLELID, W.G. (1977) Seismic stratigraphy and global changes of sea-level. In: *Seismic Stratigraphy Applications to Hydrocarbon Exploration* (Ed. Payton C.E.) Vol. 26 of American Association of Petroleum Geologists Memoir, AAPG, 49–212.
- VAN WAGONER, J.C., MITCHUM, R.M., CAMPION, K.M. & RAHMANIAN, V.D. (1990) Siliciclastic sequence stratigraphy in well logs, cores, and outcrops. Vol. 7 of *Methods in Exploration*. Association of Petroleum Geologists, 55 p.
- WOLFE, J.A. & UPCHURCH, G.R. (1987) North american non-marine climates and vegetation during the late cretaceous. *Palaeogeo. Palaeoclimatol. Palaeoecol.*, **61**, 33–77.

Manuscript received 14 October 2015; In revised form 29 January 2016; Manuscript accepted 3 May 2016.



Numerical modelling of landscape and sediment flux response to precipitation rate change

John J. Armitage¹, Alexander C. Whittaker², Mustapha Zakari¹, and Benjamin Campforts³

¹Institut de Physique du Globe de Paris, Université Sorbonne Paris Cité, Paris, France

²Department of Earth Science and Engineering, Imperial College London, London, UK

³Division Geography, Department of Earth and Environmental Sciences, KU Leuven, Heverlee, Belgium

Correspondence: John J. Armitage (armitage@ipgp.fr)

Received: 11 May 2017 – Discussion started: 19 May 2017

Revised: 9 January 2018 – Accepted: 11 January 2018 – Published: 15 February 2018

Abstract. Laboratory-scale experiments of erosion have demonstrated that landscapes have a natural (or intrinsic) response time to a change in precipitation rate. In the last few decades there has been growth in the development of numerical models that attempt to capture landscape evolution over long timescales. However, there is still an uncertainty regarding the validity of the basic assumptions of mass transport that are made in deriving these models. In this contribution we therefore return to a principal assumption of sediment transport within the mass balance for surface processes; we explore the sensitivity of the classic end-member landscape evolution models and the sediment fluxes they produce to a change in precipitation rates. One end-member model takes the mathematical form of a kinetic wave equation and is known as the stream power model, in which sediment is assumed to be transported immediately out of the model domain. The second end-member model is the transport model and it takes the form of a diffusion equation, assuming that the sediment flux is a function of the water flux and slope. We find that both of these end-member models have a response time that has a proportionality to the precipitation rate that follows a negative power law. However, for the stream power model the exponent on the water flux term must be less than one, and for the transport model the exponent must be greater than one, in order to match the observed concavity of natural systems. This difference in exponent means that the transport model generally responds more rapidly to an increase in precipitation rates, on the order of 10^5 years for post-perturbation sediment fluxes to return to within 50 % of their initial values, for theoretical landscapes with a scale of 100×100 km. Additionally from the same starting conditions, the amplitude of the sediment flux perturbation in the transport model is greater, with much larger sensitivity to catchment size. An important finding is that both models respond more quickly to a wetting event than a drying event, and we argue that this asymmetry in response time has significant implications for depositional stratigraphies. Finally, we evaluate the extent to which these constraints on response times and sediment fluxes from simple models help us understand the geological record of landscape response to rapid environmental changes in the past, such as the Paleocene–Eocene thermal maximum (PETM). In the Spanish Pyrenees, for instance, a relatively rapid (10 to 50 kyr) duration of the deposition of gravel is observed for a climatic shift that is thought to be towards increased precipitation rates. We suggest that the rapid response observed is more easily explained through a diffusive transport model because (1) the model has a faster response time, which is consistent with the documented stratigraphic data, (2) there is a high-amplitude spike in sediment flux, and (3) the assumption of instantaneous transport is difficult to justify for the transport of large grain sizes as an alluvial bedload. Consequently, while these end-member models do not reproduce all the complexity of processes seen in real landscapes, we argue that variations in long-term erosional dynamics within source catchments can fundamentally control when, how, and where sedimentary archives can record past environmental change.

1 Introduction

How river networks form and how landscapes erode remains a basic research question despite more than a century of experimentation and study. At a fundamental level, the root of the problem is a lack of an equation of motion for erosion derived from first principles (e.g. Dodds and Rothman, 2000). A range of heuristic erosion equations have, however, been proposed from stochastic models (e.g. Banavar et al., 1997; Pastor-Satorras and Rothman, 1998) to deterministic models based on the St. Venant shallow water equations (e.g. Smith and Bretherton, 1972; Izumi and Parker, 1995; Smith, 2010), diffusive *transport-limited* conditions (e.g. Whipple and Tucker, 2002), or the stream power law (e.g. Howard and Kerby, 1983; Whipple and Tucker, 2002; Willett et al., 2014, among many others). These models, in various forms, have been explored to try to understand how landscape evolves and responds to tectono-environmental change. In general terms, numerical studies have found that landscapes typically recover from a shift in tectonic uplift after 10^5 to 10^6 years (reviewed in Romans et al., 2016). These apparently long response timescales to tectonic perturbations have been supported by field observations of landscapes upstream of active faults (e.g. Whittaker et al., 2007; Cowie et al., 2008; Whittaker and Boulton, 2012), although the precise appropriateness of any time-integrated erosion law to specific field sites is not always easy to establish. Sediment flux response times for the advective stream power law have been previously characterized by Whipple (2001) and Baldwin et al. (2003), and for the transport model they have been studied by Armitage et al. (2011) and Armitage et al. (2013), but not systematically or using 2-D models. Furthermore, to our knowledge no comparison between the transport models has been previously made.

The response of landscapes and sediment routing systems to a change in the magnitude or timescale of precipitation rates is expected to depend on the long-term erosion law implemented (Castelltort and Van Den Dreissche, 2003; Armitage et al., 2011, 2013). Some numerical modelling studies based on treating erosion as a length-dependent diffusive problem suggest that landscape responses to a change in rainfall are also on the order of 10^5 to 10^6 years, similar to tectonic perturbations, although they produce diagnostically different stratigraphic signatures from the latter (e.g. Armitage et al., 2011). However, other modelling contributions with different assumptions suggest that response times to a precipitation change may be more rapid (Simpson and Castelltort, 2012), although field data sets remain equivocal (see Demoulin et al., 2017, for a recent review). In laboratory studies, a series of experiments in which granular piles of a length scale of the order of centimetres are eroded due to surface water have demonstrated that a change in precipitation rate leads a period of adjustment of the landscape topography

until a new steady state is achieved (e.g. Bonnet and Crave, 2003; Rohais et al., 2011). These experiments use a mixture of granular silica of a mean diameter between 10 and 20 μm that is eroded by water released from a fine sprinkler system above. Given the complexity of these experiments, unfortunately there have been insufficient different precipitation rates studied to fully understand how the recovery timescale varies as a function of precipitation or other parameters.

It has been increasingly recognized over the last 2 decades that many basic geomorphic measures of catchments, such as the scaling between channel slopes and catchment drainage areas, are typically unable to distinguish the erosional processes behind their formation (e.g. Tinkler and Whol, 1998; Dodds and Rothman, 2000; Tucker and Whipple, 2002; Whipple, 2004). Erosion and transport can be described by equations that encompass both advective and diffusive processes (e.g. Smith and Bretherton, 1972) and at topographic steady state, it is very well established that fluvial erosion models based on either of these two end-members can produce very similar river longitudinal profiles (e.g. Tucker and Whipple, 2002; van der Beek and Bishop, 2003).

Non-uniqueness or equifinality is a common problem when comparing the morphology generated from landscape evolution models (e.g. Hancock et al., 2016). Consequently, we aim to explore whether the sediment flux responses of fluvial systems to a precipitation perturbation may be diagnostically different for the two end-member deterministic models across a range of parameter space. This issue is pertinent because within sedimentary basins, a change in the erosional dynamics upstream could be recorded by changes in the total sediment volumes stored in sedimentary basins (e.g. Allen et al., 2013; Michael et al., 2014), in sediment delivery or sediment accumulation rates linked to landscape response times (Foreman et al., 2012; Armitage et al., 2015), and/or in the grain sizes deposited as a function of sediment flux output (Paola et al., 1992; Armitage et al., 2011; Whittaker et al., 2011; D'Arcy et al., 2016).

In this article we make a comparative study between the transport and stream power model to further explore the potential differences between these two end-member hypothetical landscape evolution models. We will focus on the transient period of adjustment to a perturbation in precipitation rates, and using end-member numerical models we attempt to evaluate how the response time varies as a function of the model forcing. To this end we aim to find the model parameters that generate similar landscape morphologies such that we can subsequently explore how the same end-member models respond to a change in precipitation rate. We believe that the results of this study have implications for understanding the responses of landscapes to past changes in climate and could potentially be compared with and tested against further laboratory experiments.

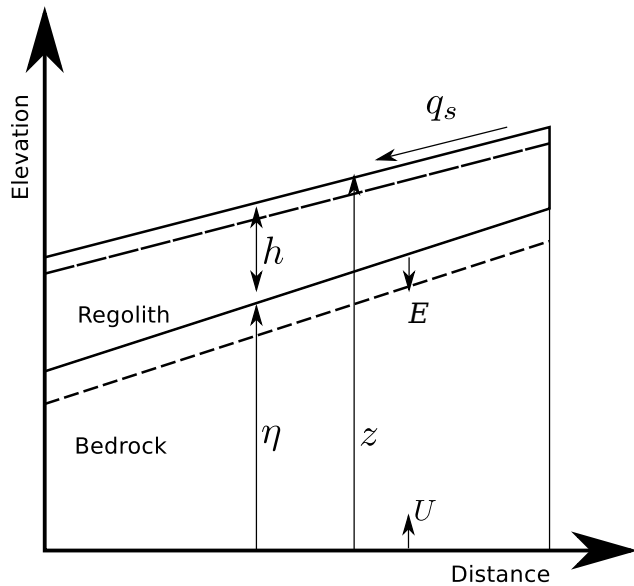


Figure 1. Diagram showing the conservation of mass within a 2-D domain where mass enters the system through uplift, U (units of m s^{-1}), and exists as sediment transported, q_s ($\text{m}^2 \text{s}^{-1}$), out of the domain. E (m s^{-1}) is the rate of production of regolith, h (m) is the thickness of regolith, η (m) is the bedrock elevation, and z (m) is the total elevation.

2 Methods

2.1 Erosion within a single dimension system

We aim to understand the effects of the most basic assumptions of mass transport in landscape evolution on the sediment flux record. In other words, how do the response times vary for the advective stream power law and the diffusive transport model? To this end we derive the two models from first principles to demonstrate clearly how, from the same starting point, the fundamental assumptions made about mass transport initially give rise to very different model equations. We use this framework as a context for our investigation of an eroding system responding to precipitation change. We first define a one-dimensional system from which the basic equations can be assembled. Following Dietrich et al. (2003) we define a landscape of elevation z composed of bedrock, thickness η (units of metres), and a surface layer of sediment with thickness h (units of metres; see Fig. 1). This landscape is forced externally through uplift rate U (units of m yr^{-1}). The bedrock is transferred into sediment through erosion at a rate E (units of m yr^{-1}) and the sediment is transported across the system with a flux q_s (units of $\text{m}^2 \text{yr}^{-1}$). Assuming that the densities of sediment and bedrock are equal, then the change in bedrock thickness is

$$\partial_t \eta = U - E, \quad (1)$$

and the rate of change in sediment thickness is

$$\partial_t h = E - \partial_x q_s. \quad (2)$$

It then follows that the rate of change in landscape elevation is

$$\partial_t z = \partial_t \eta + \partial_t h. \quad (3)$$

It is important to realize that to solve Eq. (3), we are required to make some assumptions that fundamentally affect the erosional dynamics of the modelled system, and we illustrate this below.

One basic assumption to make is that there is always a supply of transportable sediment; we can then follow through with the summation in Eq. (3), giving

$$\partial_t z = U - \partial_x q_s. \quad (4)$$

This may be appropriate when modelling the transport of sediment along the riverbed and when considering the formation of alluvial fans (e.g. Paola et al., 1992; Whipple and Tucker, 2002; Guerit et al., 2014). In the absence of surface water we can assume that sediment flux is simply a function of local slope $q_s = -\kappa \partial_x z$, where κ is the hill slope diffusion coefficient. In the presence of flowing water, the sediment flux is a function of the flowing water and local slope $q_s = -cq_w^\delta (\partial_x z)^\gamma$, where c is the transport coefficient (units $(\text{m}^2 \text{yr}^{-1})^{1-n}$), q_w is the water flux per unit width (units $\text{m}^2 \text{yr}^{-1}$), and the exponents $\delta > 1$ and $\gamma \geq 1$ are dependent on how sediment grains are transported along the bed (Smith and Bretherton, 1972; Paola et al., 1992). Furthermore, $\delta > 1$ is required to create concentrated flow (Smith and Bretherton, 1972). The change in landscape elevation is then given by

$$\partial_t z = U + \partial_x (\kappa \partial_x z + cq_w^\delta (\partial_x z)^\gamma), \quad (5)$$

which can be written as

$$\partial_t z = U + \partial_x \left([\kappa + cq_w^\delta (\partial_x z)^{\gamma-1}] \partial_x z \right). \quad (6)$$

Equation (6) is non-linear in the case that $\gamma \neq 1$. In deriving this equation of elevation change due to sediment transport we have simply summed the two terms for sediment flux, the linear and potentially non-linear slope-dependent terms. This summation has been done as it is the simplest way to generate landscape profiles that have the desired convex and concave elements observed in natural landscapes (Smith and Bretherton, 1972).

To solve this equation in one dimension we assume that the water flux is a function of the precipitation transported down the river network. The water collected is taken from the upstream drainage area, a , which is related to the main stream length, l , by $l \propto a^h$, where h is the exponent taken from the empirical Hack's law (Hack, 1957). The main stream length is related to the longitudinal length of the catchment

by $l \propto x^d$, where $1 \leq d \leq 1.1$ (Tarboton et al., 1990; Maritan et al., 1996). Therefore, we can write $x \propto a^{h/d}$, and the water flux is the precipitation rate, α (m yr^{-1}), multiplied by the length of the drainage system,

$$q_w = k_w \alpha x^p, \quad (7)$$

where k_w is a constant of proportionality with units m^{1-p} and $p = d/h$. Furthermore it is observed that river catchments are typically longer than they are wide, and so $p < 2$ (Dodds and Rothman, 2000). Therefore given that $0.5 < h < 0.7$ (e.g. Rigon et al., 1996), then $1.4 < p < 2$, and the transport model (Eq. 6) becomes

$$\partial_t z = U + \partial_x \left(\left[\kappa + c k_w \alpha^\delta x^{p\delta} (\partial_x z)^{\gamma-1} \right] \partial_x z \right). \quad (8)$$

For simplicity, we will also assume $k_w = 1$ and vary c when exploring the model behaviour.

However, returning to Eq. (3), it is clear that the transport model is not the only solution. If we assume that the rate of change in sediment thickness is zero over geological timescales, which is to say all sediment created is transported out of the model domain, then Eq. (3) becomes

$$\partial_t z = U - E. \quad (9)$$

This assumption has been made previously when studying small mountain catchments where the river may erode directly into the bedrock. However, recent numerical studies, such as Rudge et al. (2015), have expanded this model to cover continent-scale landscapes.

It is clearly plausible to suppose that erosion is primarily due to flowing water, so the assumption of geologically instantaneous transport may well be valid for mass that is transported as suspended load within the water column. Such an assumption is less clear for bedload transport. We can assume that the speed at which suspended loads travel down-system is a function of the height achieved within each hop, which is a function of the water depth, settling velocity, and flow velocity. For small grains $< 1 \text{ mm}$, the settling velocity is given by the force balance between the weight of the grain and the viscous drag given by the Stokes law (Dietrich, 1982). For a particle of diameter $1 \times 10^{-4} \text{ m}$ and density 2800 kg m^{-3} the settling velocity is $\sim 0.01 \text{ m s}^{-1}$. Therefore the distance travelled assuming a flow velocity of 1 km h^{-1} and an elevation of suspension of 1 m is roughly 3 km . Using a similar argument the travel distance of a sediment grain typical of the Bengal Fan is estimated to be $\sim 10^4 \text{ m}$ (Ganti et al., 2014). This suggests that rapid transport of sediment across a continent is possible.

The percentage of mass transported in suspension may also be quite significant. For a small Alpine braided river it was found that the majority of mass was transported as suspended load (Meunier et al., 2006), and for the river systems draining the Tian Shan, China, 70 % of mass is transported as suspended and dissolved load (Liu et al., 2011). Therefore

significant mass may be transported rapidly, geologically instantaneously, down-system, suggesting that the assumption that $\partial_t h \sim 0$ may be valid in some circumstances.

Assuming surface flow is the primary driver of landscape erosion and that positive x is in the downstream direction, then erosion, E , as a function of the power of the flow to detach particles of rock per unit width can be written as

$$E = -k_b \rho_w g q_w^m (\partial_x z)^n, \quad (10)$$

where k_b is a dimensional constant that parameterizes bedrock erodibility (Howard and Kerby, 1983; units $(\text{m}^2 \text{ yr}^{-1})^{1-m} \text{ yr kg}^{-1}$), ρ_w is water density, g is gravity, and m and n are constants. The exponent $m \sim 0.5$, as it is a function of how the stream flow width is proportional to the water flux (e.g. Lacey, 1930; Leopold and Maddock, 1953; Whittaker et al., 2007). The exponent $n > 0$ acts upon the slope.

In two dimensions the change in elevation is then given by

$$\partial_t z = U + k q_w^m (\partial_x z)^n, \quad (11)$$

where the constant k lumps together the other constants (units $\text{m}^{-1} (\text{m}^2 \text{ yr}^{-1})^{1-m}$), and if $n \neq 1$ Eq. (11) becomes non-linear. Using a version of Eq. (11) to invert river profiles for uplift histories, it is argued by some authors that n is close to unity (Rudge et al., 2015). However, certain river profiles may arguably be indicative of $n > 1$ (Lague, 2014). Furthermore if $n > 1$, Eq. (11) becomes non-linear and the model response to precipitation rate change will become a function of both uplift and precipitation rates (Whipple, 2001).

To solve Eq. (11) in 1-D, as before we will assume that $q_w = k_w \alpha x^p$ where $1.4 < p < 2$. The stream power law for landscape erosion in 1-D is then

$$\partial_t z = U + k_p \alpha^m x^{mp} (\partial_x z)^n, \quad (12)$$

where $k_p = k k_w \rho_w g$ (units $\text{m}^{-p} (\text{m}^2 \text{ yr}^{-1})^{1-m}$).

We have demonstrated two different fundamental equations for change in elevation in 2-D (Eqs. 6 and 11) and the equivalent 1-D forms (Eqs. 8 and 12). These two models of elevation change differ in that Eq. (11) is an advection equation and Eq. (6) is a diffusion equation. This means that the time evolution of Eq. (11) would be a migrating wave of erosion travelling either up or down the catchment (Braun et al., 2015). This wave could also potentially take the form of a shock wave, in which due to the change in gradient the lower reaches of the migrating wave could travel faster than the upper reaches, creating a breaking wave (Smith et al., 2000; Pritchard et al., 2009). The time evolution of Eq. (6) is very different because here the evolution is dominated by diffusive processes. The diffusion coefficient is a function of the down-system collection of water, which can lead to the concentration of flow and the creation of realistic morphologies (Smith and Bretherton, 1972). It is not, however, completely established how the transport model responds differently to changes in precipitation forcing in comparison to the stream power model.

2.2 Linear and non-linear solutions

If $n = 1$ (Eqs. 11 and 12) and $\gamma = 1$ (Eqs. 6 and 8) then the models are linear, and we can solve the equations both analytically and in 1-D and 2-D numerical schemes. For the stream power model we use an implicit finite-difference scheme (Braun and Willett, 2013) and for the transport model we use an explicit finite-element scheme with linear elements (Simpson and Schlunegger, 2003). If $n \neq 1$ and if $\gamma \neq 1$ the equations become non-linear. In this case the numerical solutions can become unstable for simple explicit schemes and may suffer from too much numerical diffusion for implicit schemes, unless the size of the time step is limited by the appropriate Courant–Friedrichs–Lowy (CFL) condition (Campforts and Covers, 2015). Given the short time steps required to obtain an accurate solution, we explore the non-linear solutions for erosion down a river-long profile in 1-D. We solve for the stream power model (Eq. 12) using an explicit total variation diminishing scheme with the appropriate CFL condition (Campforts and Covers, 2015). For the transport model (Eq. 8) we use an explicit finite-element model with quadratic elements and the appropriate CFL condition to find a stable solution.

2.3 Generalizing to a two-dimensional system

To solve Eqs. (6) and (11) over a 2-D domain requires an algorithm to route surface flow down the landscape. In our case, to explore how a model landscape responds to a change in precipitation rate we will make the simplest assumption available: that water flows down the steepest slope. We then solve for Eq. (11) using the numerical model Fastscape (Braun and Willett, 2013), with a resolution of 1000 by 1000 nodes for a 100 by 100 km domain, giving a spatial resolution of 100 m. Erosion by sediment transport in 2-D is solved following the MATLAB model of Simpson and Schlunegger (2003), which is available from Simpson (2017). We solve Eq. (6) on a triangular grid with a resolution of 316 by 316 nodes for a 100 by 100 km domain, giving a spatial resolution of the order of 300 m. We also explored how the models evolve for a domain that is 500 by 500 km in size. The time step used for both models is 10 kyr.

We will explore how an idealized landscape evolves under uniform uplift at a rate of 0.1 mm yr^{-1} . The initial condition is of a flat surface with a small amount of noise added to create a roughness. The boundary conditions are fixed elevation at the left and right sides and no flow at the sides. To explore the response of the two models to a change in precipitation rate we start the model with an initial precipitation rate of $\alpha_0 = 1 \text{ m yr}^{-1}$. For the linear models we then increase or decrease the precipitation rate to a new value, α_1 , after 10 Myr of model run time. This is to be sure that the steady state has been reached before applying the perturbation. For the non-linear models (Sects. 3.3 and 3.4), the precipitation rate is changed after 5 Myr as in this case steady state was

reached earlier. As the coefficients c and k have units that are related to the exponents δ and m in Eqs. (6) and (11), respectively (e.g. Whipple and Meade, 2006; Armitage et al., 2013), when modelling increasing values of δ and m the coefficients are likewise increased.

The response time for the transport model scales by the effective diffusivity and can be given by

$$\tau_t = \frac{L^2}{\kappa + cq_w^\delta}, \quad (13)$$

where L is the model length scale (in this case the length of the domain). For the stream power model the response time is a function of the velocity at which the kinematic wave travels up the catchment (e.g. Whipple and Tucker, 1999; Whipple, 2001). The response time is therefore given by the time it takes for this wave of incision to travel up the catchment length, l_c ,

$$\tau_{sp} = \frac{l_c}{kq_w^m}. \quad (14)$$

Therefore we expect the response time to be a function of the choice of both the constants c and k and the exponents δ and m within both models. The effect of varying the coefficients m and δ independently has been previously explored (e.g. Whipple and Meade, 2006; Armitage et al., 2013), and we therefore will not do so in detail again here. Instead we aim to compare the two models and therefore search for the values of c , k , m , and δ that generate similar topography at steady state. This steady state is then perturbed by a change in precipitation rate.

2.4 Generating similar landscapes

It has been previously demonstrated that both end-member models can generate convex-up long profiles (e.g. Kirkby, 1971; Smith and Bretherton, 1972; Smith et al., 2000; Whipple and Tucker, 2002; Crosby et al., 2007). From solving both Eqs. (8) and (12), where $\gamma = 1$ and $n = 1$, we find that in the range $1 < \delta \leq 1.5$ and $0.3 \leq m \leq 0.7$ the two end-member models are comparable (see Appendix A). Given the possible additional degree of freedom introduced if we also vary γ and n , it is clear that river-long profiles are not a unique identifier of erosional processes. However, in order to compare how the end-member models respond to a change in precipitation rate, it is preferable to perturb catchments of a similar morphology. We will subsequently explore how the models in their linear and non-linear forms respond to a change in precipitation rates within the Results section.

2.4.1 Erosion by sediment transport

Six models have been run without a change in precipitation to find the steady-state topography. The models explored are first a set of three with varying δ and constant c , i.e.

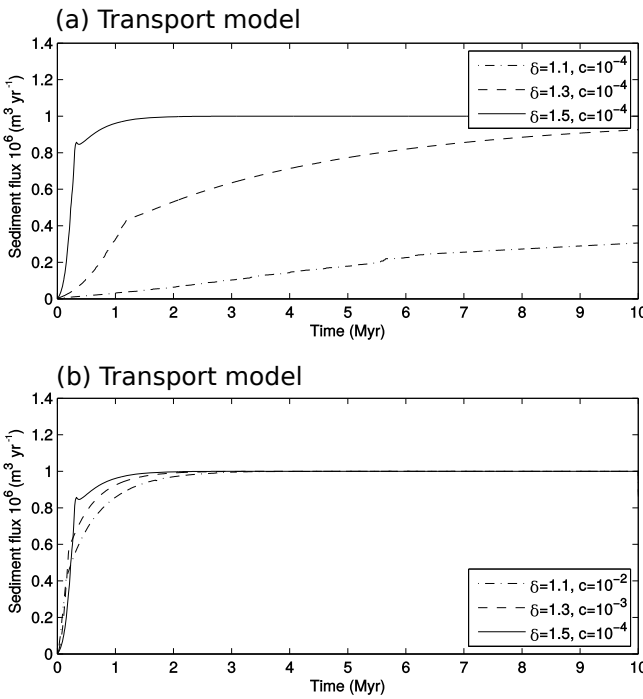


Figure 2. Sediment flux out of the model domain for the transport models in which **(a)** $\delta = 1.1, 1.3, $\kappa = 10^{-2}$ and $c = 10^{-4} (\text{m}^2 \text{yr}^{-1})^{1-\delta}$; **(b)** $\delta = 1.1, 1.3$, and 1.5 , $\kappa = 10^{-2}$ and $c = 10^{-2}, 10^{-3}$, and $10^{-4} (\text{m}^2 \text{yr}^{-1})^{1-\delta}$.$

$\delta = 1.1, 1.3$, and 1.5 with $c = 10^{-4} (\text{m}^2 \text{yr}^{-1})^{1-\delta}$ (Fig. 2a), and a set of three in which δ and c co-vary, i.e. $\delta = 1.1$ with $c = 10^{-2} (\text{m}^2 \text{yr}^{-1})^{1-\delta}$, $\delta = 1.3$ with $c = 10^{-3} (\text{m}^2 \text{yr}^{-1})^{1-\delta}$, and $\delta = 1.5$ with $c = 10^{-4} (\text{m}^2 \text{yr}^{-1})^{1-\delta}$ (Fig. 2b). These values are chosen because they generate response times within the range of observations from normal fault-bounded sedimentary systems that have responded to changes in slip rate (Densmore et al., 2007; Armitage et al., 2011).

When the transport coefficient c is the same for the three values of the exponent δ , the model wind-up time increases with decreasing δ and takes several million years when $\delta < 1.5$ (Fig. 2a). Steady-state sediment flux is greater for increasing δ when c is kept constant. The dimensions (units) of c depend on δ , which means that the value of the coefficient c must be adjusted when δ is changed to yield the same unit erosion rate per water flux regardless of δ (see Armitage et al., 2013). Consequently, when c is suitably adjusted the model can reach a steady state in a similar time for all three values of δ (Fig. 2b).

We subsequently analyse the topography for the relationship between trunk river slope and drainage area, as shown in Fig. 3, using TopoToolbox2 (Schwanghart and Scherler, 2014). For the case in which $\delta = 1.5$ the scaling between channel slopes and catchment drainage areas, the slope-area exponent θ , is equal to -0.42 , and for $\delta = 1.3$, θ is equal to -0.23 (Fig. 3b). The same value is calculated using the spa-

Table 1. Slope–area relationship for trunk streams derived using χ analysis (Perron and Royden, 2012)

Sediment transport	k_s	θ
$\delta = 1.3$	0.86	-0.23
$\delta = 1.5$	1.76	-0.42
Stream power		
$m = 0.3$	0.95	-0.29
$m = 0.5$	6.52	-0.46
$m = 0.7$	71.42	-0.68

tial transformation described in Perron and Royden (2012), commonly referred to as χ analysis (Table 1). Given the reduction in θ from $\delta = 1.5$ to 1.3 , we did not analyse the case for $\delta = 1.1$ as the slope–area relationship will clearly lie below the observed range ($-0.7 < \theta < -0.35$; e.g. Snyder et al., 2000; Wobus et al., 2006). Therefore, for river networks defined by routing water down the steepest slope of descent, the transport model can create catchment morphologies that have a concavity similar to that observed in nature if $\delta \sim 1.5$.

2.4.2 Comparison to erosion by stream power

In order to provide a comparison for the morphology of the transport model we explore how the stream power model evolves to a steady state. The landscape derived from the stream power model, as shown in Eq. (11), evolves towards a steady state with a slightly different behaviour in comparison to the transport model (Fig. 4). As before we ran six models for which in this case the first set of three are $m = 0.3, 0.5$, and 0.7 with $k = 10^{-5} \text{ m}^{-1} (\text{m}^2 \text{yr}^{-1})^{1-m}$ (Fig. 4a). The second set of three are of $m = 0.3$ with $k = 10^{-4} \text{ m}^{-1} (\text{m}^2 \text{yr}^{-1})^{1-m}$, $m = 0.5$ with $k = 10^{-5} \text{ m}^{-1} (\text{m}^2 \text{yr}^{-1})^{1-m}$, and $m = 0.7$ with $k = 10^{-6} \text{ m}^{-1} (\text{m}^2 \text{yr}^{-1})^{1-m}$ (Fig. 4b). This range of m is chosen as it spans the range of observed concavities within catchments. As with the transport model the coefficient k can be adjusted along with m as they are related, and increasing k reduces the model wind-up time (Fig. 4b). Decreasing the exponent m increases the timescale taken to reach a steady state (Fig. 4a); however, by varying k by a factor of 100, the steady-state sediment flux is reached within 3 Myr for the three values of m (Fig. 4b).

Following the previous examples, we analyse the topography for the relationship between trunk river slope and drainage area (Fig. 5). Both the transport model and the stream power model can create landscapes with similar slope–area relationships calculated using the χ -analysis approach (Table 1). For both models, the values of the intercept, k_s , and the gradient, θ , are of similar magnitudes for

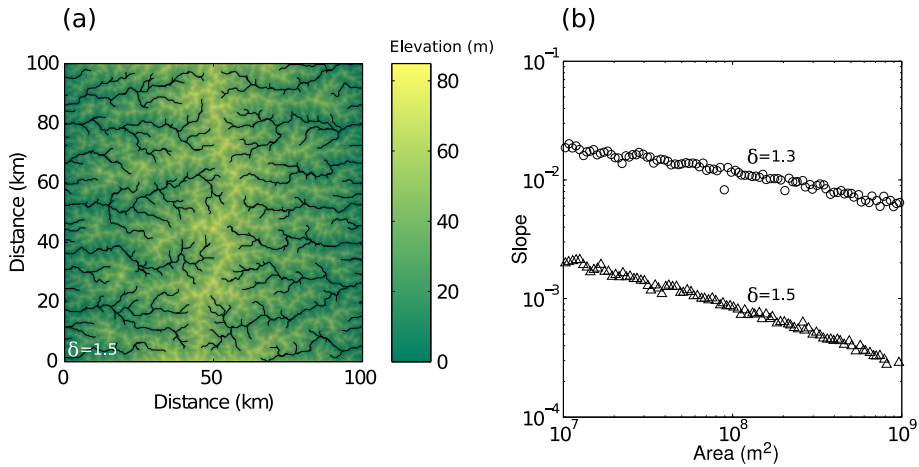


Figure 3. (a) Steady-state topography after 10 Myr for the transport model in which $\delta = 1.5$ and $c = 10^{-4} (\text{m}^2 \text{yr}^{-1})^{1-\delta}$. (b) Slope–area relationship for the transport model for $\delta = 1.3$ and $\delta = 1.5$.

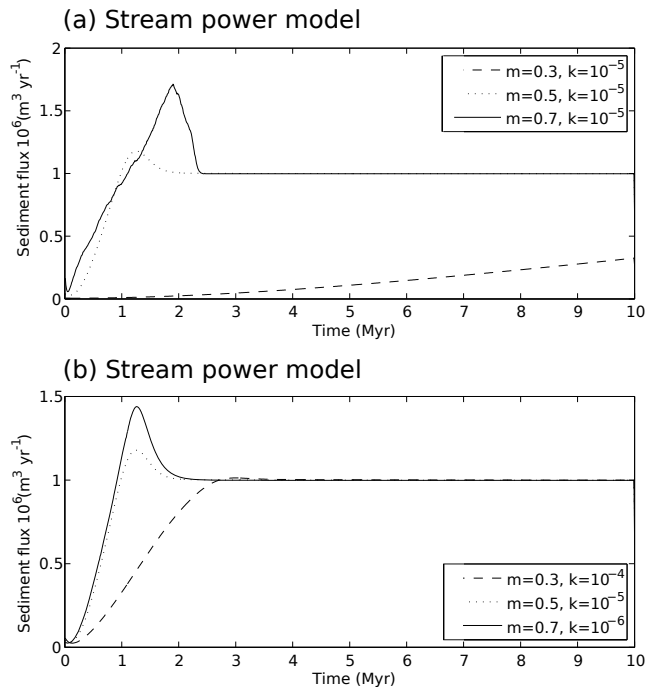


Figure 4. Sediment flux out of the model domain for the stream power models in which (a) $m = 0.3, 0.5$, and 0.7 and $k = 10^{-5} (\text{m}^2 \text{yr}^{-1})^{1-m}$; (b) $m = 0.3, 0.5$, and 0.7 and $k = 10^{-4}, 10^{-5}$, and $10^{-6} \text{ m}^{-1} (\text{m}^2 \text{yr}^{-1})^{1-m}$.

$\delta = 1.5$ and $m = 0.5$. Absolute elevation for the model shown in Fig. 5a is higher than the transport model example due to the larger value of k relative to c . However, importantly, both models can create similar landscape morphologies at steady state.

3 Results

The stream power and transport models can both fit the observed slope–area relationships of the present day landscape morphology, for example θ ranging from -0.35 to -0.7 (Snyder et al., 2000; Wobus et al., 2006), when the water flux exponent is $m \sim 0.5$ or $\delta \sim 1.5$ for the stream power and transport model, respectively. Therefore, both models may be a reasonable representation of how, on a gross scale, a landscape erodes. We therefore keep the exponents in the range $0.3 \leq m \leq 0.7$ and $1.3 \leq \delta \leq 1.5$ and explore how the models in their linear and non-linear forms respond to a change in precipitation rates.

3.1 Response to precipitation rate reduction

When the model is perturbed by a change in precipitation rate the sediment flux output will first change as the erosive power changes (e.g. Fig. 6). The model will subsequently return to the steady-state output, as the slope of the fluvial system will adjust to the new precipitation rate, and the landscape will re-achieve the same steady state. In Fig. 6a we display the response of erosion for the transport model in terms of sediment flux out of the model domain for a reduction in precipitation rate from 1 to 0.5 m yr^{-1} at 10 Myr of model evolution. We explore how the transport model responds for $\delta = 1.5$, $c = 10^{-4}$ and $\delta = 1.3$, $c = 10^{-3}$ as these two values of δ generate reasonable slope–area relationships (Fig. 3b, Table 1). The response to a reduction in precipitation is similar for the two model parameter sets, with the flux initially reducing by half and then recovering to within 10 % of steady-state values within ~ 2 Myr (Fig. 6a; see Table 2). Changing the transport coefficient, c , does not affect the predicted gradient of catchment slope versus catchment area (see Appendix A, Fig. A2). However, changing c changes the model elevation (Fig. A2). Furthermore, the larger the value of c the faster the response

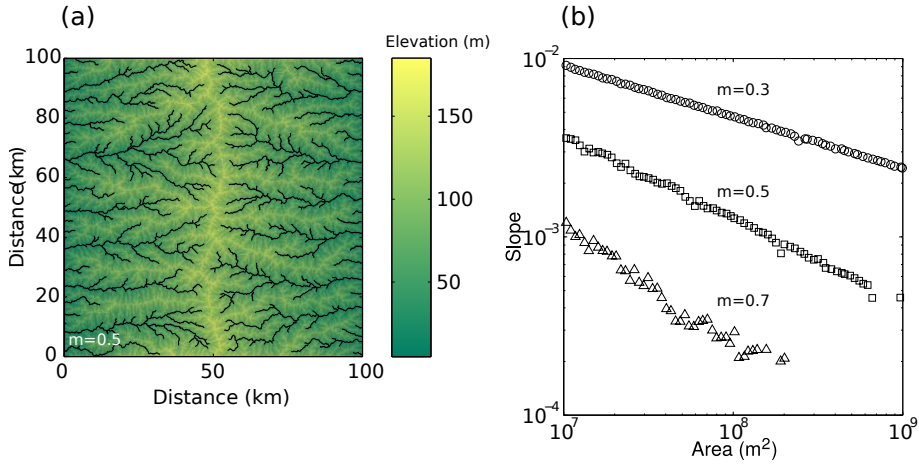


Figure 5. (a) Steady-state topography after 10 Myr for the transport model in which $m = 0.5$ and $k = 10^{-5} \text{ m}^{-1} (\text{m}^2 \text{ yr}^{-1})^{1-m}$. (b) Slope-area relationship for the transport model for $m = 0.3, 0.5$, and 0.7 .

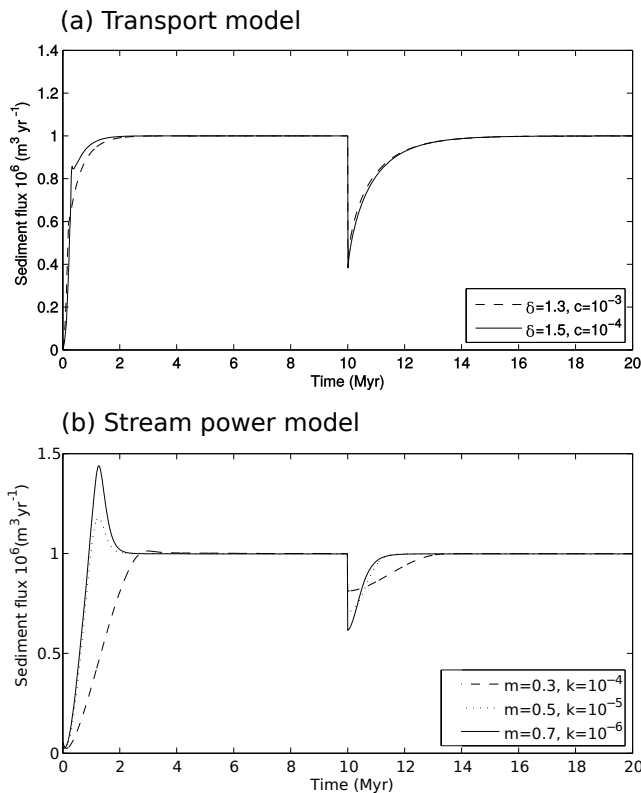


Figure 6. Response of the transport and stream power model to a reduction in precipitation rate. (a) Sediment flux for the transport model for a step reduction in precipitation from 1 to 0.5 m yr^{-1} after 10 Myr. Two models are plotted in which $\delta = 1.3$ and 1.5 , $\kappa = 10^{-2}$, and $c = 10^{-3}$ and $10^{-4} (\text{m}^2 \text{ yr}^{-1})^{1-\delta}$. (b) Sediment flux for the stream power model for a step reduction in precipitation from $\alpha_0 = 1$ to $\alpha_1 = 0.5 \text{ m yr}^{-1}$ after 10 Myr. Three models are plotted in which $m = 0.3, 0.5$, and 0.7 and $k = 10^{-4}, 10^{-5}$, and $10^{-6} \text{ m}^{-1} (\text{m}^2 \text{ yr}^{-1})^{1-m}$.

Table 2. Response to a change in precipitation rate; α_1 represents the value that the precipitation rate changes to from $\alpha_0 = 1 \text{ mm yr}^{-1}$. Response time is given for two model sizes, 100 and 500 km, and as the time for the model to recover to within 50 % (1/2) and 10 % (1/10) of the steady-state sediment flux.

$L = 100 \text{ km}$	Transport			Detachment	
	α_1 yr^{-1}	$\tau_{1/2}$ Myr	$\tau_{1/10}$ Myr	$\tau_{1/2}$ Myr	$\tau_{1/10}$ Myr
0.25	1.42	6.07	0.98	1.66	
0.50	0.53	2.19	0.70	1.18	
0.75	0.30	1.21	0.57	0.98	
2.00	0.09	0.31	0.34	0.60	

$L = 500 \text{ km}$	Transport			Detachment	
	α_1 yr^{-1}	$\tau_{1/2}$ Myr	$\tau_{1/10}$ Myr	$\tau_{1/2}$ Myr	$\tau_{1/10}$ Myr
2.00	0.17	0.64	0.34	0.60	

(Eq. 13; see Armitage et al., 2013). A small increase in the exponent δ will strongly reduce response times, as it will increase the water flux term (Eq. 13). Therefore an order-of-magnitude decrease in c counters the change in δ for the two model sets (Fig. 6a). For the values chosen both models respond at a similar rate to the change in precipitation (Fig. 6a; see Table 2).

The response of the stream power model to an identical reduction in precipitation at a model time of 10 Myr takes a similar form, with an initial decrease in sediment flux out followed by a gradual recovery (Fig. 6b). In a similar manner as the transport model, response is a function of the exponent m and the coefficient k (Eq. 14). We have modelled three parameter sets: $m = 0.3$ and $k = 10^{-4}$, $m = 0.5$ and $k = 10^{-5}$, and $m = 0.7$ and $k = 10^{-6}$ (Fig. 6b). The response time to

achieve a return to 10 % of the steady-state sediment flux varies from 3 Myr in the case of $m = 0.3$ to less than 1 Myr when $m = 0.7$. In addition to response time being longer for smaller values of m , the peak magnitude of the flux response is reduced for smaller values of m (Fig. 6b).

The magnitude of the response for all the runs is greater for the transport model when compared to the stream power model (Fig. 6). Consequently, response time, while being a function of the transport coefficients c and k , may still systematically differ between the two models: the transport model with $\delta = 1.5$ and $c = 10^{-4}$ generates a maximum model elevation of ~ 240 m, and the stream power model with $m = 0.5$ and $k = 10^{-5}$ generates a maximum elevation of ~ 180 m. These two models have a similar slope-area relationship at steady state (Table 1) and are therefore comparable, suggesting a faster response to a reduction in precipitation rates for the stream power model (Fig. 6).

To explore how the difference in response time and magnitude is expressed in the landscape, we extract the river profiles of the main trunk systems for models in which $\delta = 1.5$ and $m = 0.5$ during the response to the reduction in precipitation rate, while the uplift rate is constant (Figs. 7 and 8). For the transport model in which $\delta = 1.5$ and $c = 10^{-4}$, the catchment elevation increases to a new steady state that has an elevation that is roughly 2.6 times higher than the steady-state elevation after 10 Myr (Fig. 7). Just under half of this new topographic elevation is achieved within the first 500 kyr. In contrast, for the stream power model in which $m = 0.5$ and $k = 10^{-5}$, the steady-state topography is achieved within a fraction of the time when compared to the transport model. This is in line with the more rapid response of this model to a relative drying of the climate using these parameters (compare Fig. 6a and b). Furthermore the increase in elevation due to the reduced surface water flux is only a factor of ~ 1.2 , which is less than half of the increase for the transport model. Our results confirm that two different end-member erosion models encompassing advective and diffusive phenomena can produce landscapes with similar morphologies if particular parameter sets are selected accordingly.

3.2 Response to different magnitudes of precipitation rate change

The response time of the transport model is known to be a function of the transport coefficient and the magnitude of the precipitation rate (see Armitage et al., 2013). This behaviour is displayed in Fig. 9a, in which the response of the transport model with $\delta = 1.5$ and $c = 10^{-4}$ for a change in precipitation from 1 to 0.25, 0.5, 0.75, and 2 m yr^{-1} is plotted. The response time, measured as the time for the sediment flux to recover by half and by 90 % to the steady-state value, is shown additionally in Fig. 10 as black solid and dashed lines, respectively, and in Table 2. For a reduction to 0.25 m yr^{-1} the prediction is for a long response time of 6.07 Myr, while

for an increase to 2 m yr^{-1} the prediction is for a rapid response time of 310 kyr for 90 % recovery towards previous sediment flux values. The equivalent half-life, recovery by 50 % towards previous sediment flux values, is 1.42 Myr and 90 kyr.

The stream power model likewise has a response time that is a function of precipitation rate (Fig. 9b). For a reduction to 0.25 m yr^{-1} the prediction is for a response time of 1.66 Myr, while for an increase to 2 m yr^{-1} the prediction is for a recovery time of 600 kyr for 90 % recovery (Table 2). The equivalent half-life is 0.98 Myr and 340 kyr (Table 2). The stream power model is therefore faster to recover for a reduction in precipitation rate yet slower to respond to an increase in precipitation rate. This is because the response time of the stream power model is more weakly a function of precipitation rate. Importantly, these results therefore suggest that there is a fundamental asymmetry in the response timescale to a climate perturbation. The models suggest that it takes longer for surface processes to recover from a drying event compared to a wetting event.

Both models display a response time that is a function of the precipitation rate (Figs. 9 and 10). The relationship between precipitation rate and the transport model response can be expressed as

$$\tau_t \propto \alpha^{-\delta}, \quad (15)$$

where in this case $\delta = 1.5$. This proportionality is in agreement with our numerical model results, in which the slope of trend for the transport model in the log–log plot is -1.5 (Fig. 10).

In contrast, the response time of the stream power model is not as strongly inversely dependent on the precipitation rate (Fig. 10). For this model, the response time is a function of the velocity at which the wave of incision travels upstream. This velocity is directly related to the inverse of the water flux, q_w^m , which is in turn a function of the drainage length and precipitation rate, α . Therefore for the stream power model we can write that response time is

$$\tau_{sp} \propto \alpha^{-m}. \quad (16)$$

This proportionality, which is in agreement with the approximate analytical solutions of Whipple (2001), is likewise in agreement with our numerical model results, in which the slope of trend for the stream power model in the log–log plot is -0.5 (Fig. 10). Consequently, for these two models, which were derived from the same starting point (Fig. 1) and applied to catchments of similar topography and morphology, we find that above a certain magnitude of precipitation rate change, the transport model responds more rapidly than the stream power model and vice versa.

The position of the critical point at which the stream power model responds more rapidly than the transport model is a function of the water flux and the collection of coefficients. In the model comparison developed here, we have compared

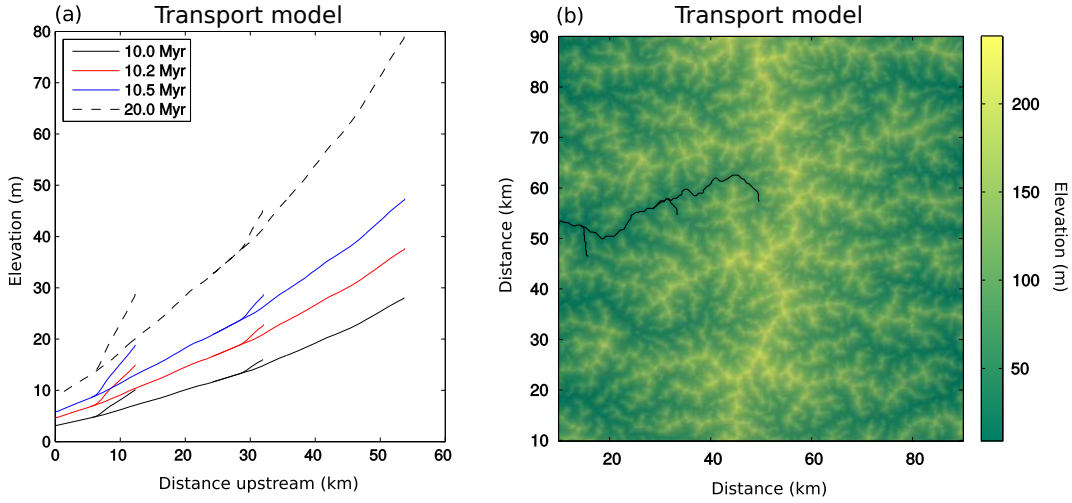


Figure 7. Transport model evolution due to a reduction in precipitation. **(a)** Selected river-long profile response to a change in precipitation. The black line is the profile just before a factor of 2 reduction in precipitation. The red and blue lines are 200 and 500 kyr after the reduction in precipitation. The dashed black line is the steady-state profile. **(b)** Trunk stream used for the analysis with the steady-state elevation.

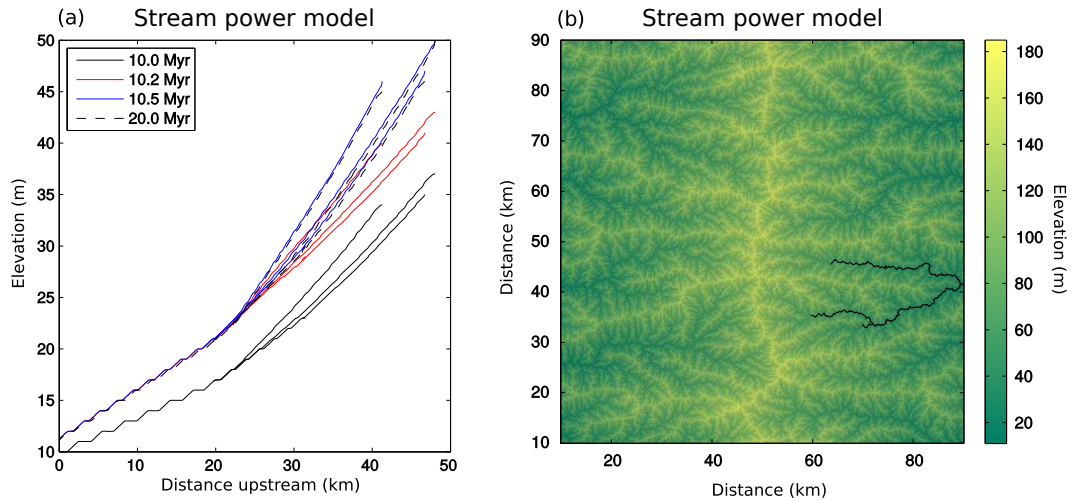


Figure 8. Stream power model evolution due to a reduction in precipitation. **(a)** Selected river-long profile response to a change in precipitation. The black line is the profile just before a factor of 2 reduction in precipitation. The red and blue lines are 200 and 500 kyr after the reduction in precipitation. The dashed black line is the steady-state profile. **(b)** Trunk stream used for the analysis with the steady-state elevation.

two model catchments that have a similar slope-area exponent, θ between -0.4 and -0.5 ($\delta = 1.5$ and $m = 0.5$) and model domain length of $L = 100$ km, giving catchments of roughly 50 km length. In this case the 90 % recovery of the sediment flux signal is predicted to be more rapid for the transport model when compared to the stream power model for an increase in precipitation rate (Fig. 10). If, however, the model domain is increased to $L = 500$ km then it takes twice as long for the transport model to recover from an increase in precipitation rate from 1 to 2 m yr^{-1} : 0.63 Myr compared to 0.31 Myr for $L = 100$ km (Fig. 11a and Table 2).

The stream power model is insensitive to the size of the model domain because of the particular choice of $m = 0.5$ and the shape of drainage network that forms under the assumptions of routing water down the steepest slope of descent (Fig. 11b). Taking the drainage length to be directly proportional to the catchment area, $l_d \propto a$, and given that catchment length is proportional to drainage area raised to the Hack exponent, h , we can re-write Eq. (14) as

$$\tau_{\text{sp}} \propto \frac{a^h}{(\alpha a)^m}. \quad (17)$$

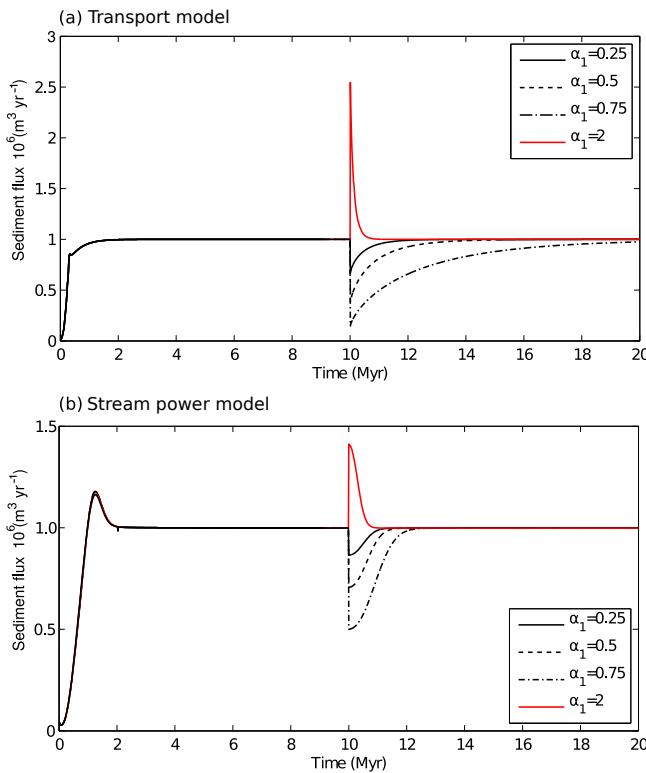


Figure 9. (a) Response of the transport model to a change in precipitation rate. Equation (6) is solved for $\delta = 1.5$ and $c = 1 \times 10^{-4} (\text{m}^2 \text{ yr}^{-1})^{1-\delta}$. The precipitation rate is initially $\alpha_0 = 1 \text{ m yr}^{-1}$ and changes to $\alpha_1 = 0.25, 0.5, 0.75, \text{ or } 2 \text{ m yr}^{-1}$ after 10 Myr. (b) Response of the stream power model to a change in precipitation rate. Equation (6) is solved for $m = 0.5$ and $k = 1 \times 10^{-5} \text{ m}^{-1} (\text{m}^2 \text{ yr}^{-1})^{1-m}$. The precipitation rate is initially $\alpha_0 = 1 \text{ m yr}^{-1}$ and changes to $\alpha_1 = 0.25, 0.5, 0.75, \text{ or } 2 \text{ m yr}^{-1}$ after 10 Myr.

Therefore, in the case that $h = 0.5$ and $m = 0.5$, as in the numerical model here, the response time becomes independent of system length (see Whittaker and Boulton, 2012). If $h < m$ then response times would decrease with increasing drainage basin size, and if $h > m$ then response times would increase with drainage basin size. There is good empirical evidence for $0.5 < h < 0.7$ (e.g. Rigon et al., 1996), which fundamentally controls the plan view shape of catchments, yet there is not a complete consensus on the value of m (see Lague, 2014; Temme et al., 2017).

A final key difference between the transient sediment flux responses of the two models is that the peak magnitude of system response to a change in precipitation rate is systematically larger for the transport model (Fig. 9). For an increase in precipitation rates from 1 to 2 m yr^{-1} , the sediment flux increases from $1 \times 10^6 \text{ m}^3$ to $2.5 \times 10^6 \text{ m}^3$ for erosion by sediment transport. This is 3 times greater than the equivalent increase for the stream power model. The reduction in sediment flux is likewise larger for the transport model (Fig. 9).

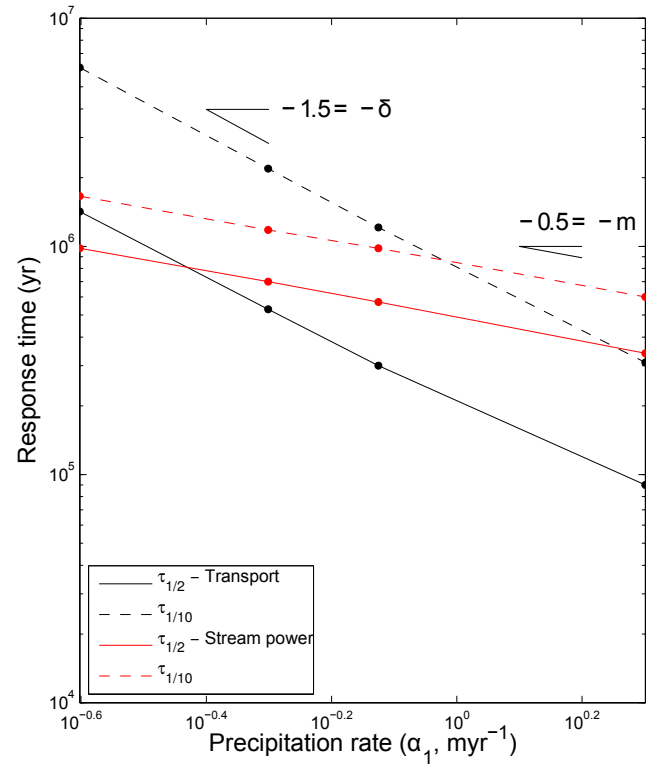


Figure 10. Log–log plot of response time to a change in precipitation rate of α_1 from an initial value of $\alpha_0 = 1 \text{ m yr}^{-1}$ when the model domain is 100 by 100 km (see Table 2); $\tau_{1/2}$ is the time for the sediment flux to recover by half of the magnitude change in sediment flux and $\tau_{1/10}$ is the time for the sediment flux to recover by 90 %.

Therefore, although response time is a function of precipitation rate, the magnitude of change is consistently larger for the transport model.

3.3 Non-linear response timescales

Up to this point we have compared how the models respond to a precipitation rate change when the solutions are linear. However, there is reasonable debate as to the value of the slope exponent n in the stream power model (e.g. Lague, 2014; Croissant and Braun, 2014; Rudge et al., 2015) and likewise within the transport model it is plausible that the slope exponent $\gamma > 1$. The response time for the stream power model for various values of n has been explored within Baldwin et al. (2003). Here we expand on this by exploring the equivalent response times for the transport model. To explore the implications of the non-linearity introduced by relaxing the constraint that $n = 1$ and $\gamma = 1$ for both models, we solve Eqs. (8) and (12) for $p = 1.1$, $\delta = 1.5$, and $c = 5 \times 10^{-5}$ and $m = 0.5$ and $k = 10^{-4}$, respectively, with different uplift rates. We have modelled the response due to an uplift rate between 0.1 and 1.0 mm yr^{-1} for the case in which $\gamma = 1.2$ and $n = 1.2$ in Eqs. (8) and (12) (Fig. 12).

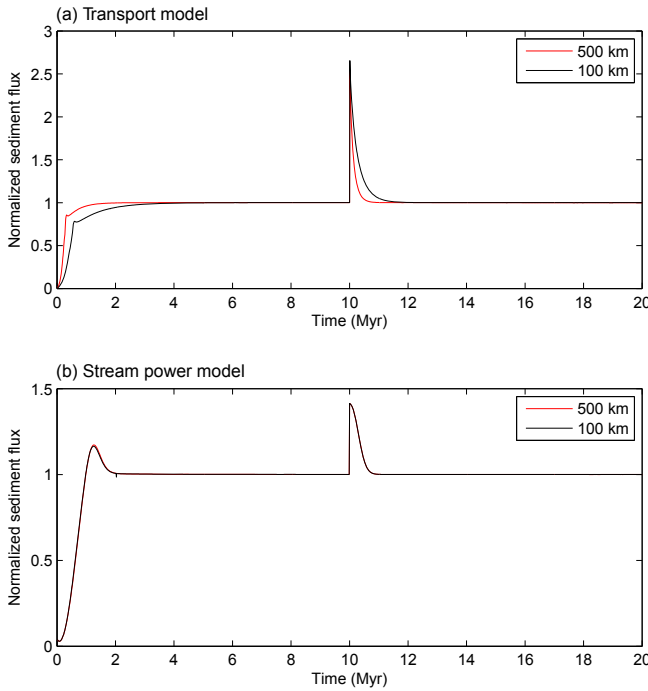


Figure 11. (a) Response of the transport model to a change in precipitation rate for two different model dimensions, 100 by 100 km and 500 by 500 km. Equation (6) is solved for $\delta = 1.5$ and $c = 1 \times 10^{-4} (\text{m}^2 \text{yr}^{-1})^{1-\delta}$. The precipitation rate is initially $\alpha_0 = 1 \text{ m yr}^{-1}$ and changes to $\alpha_1 = 2 \text{ m yr}^{-1}$ after 10 Myr. (b) Response of the stream power model to a change in precipitation rate for two different model dimensions, 100 by 100 km and 500 by 500 km. Equation (6) is solved for $m = 0.5$ and $k = 1 \times 10^{-5} \text{ m}^{-1} (\text{m}^2 \text{yr}^{-1})^{1-m}$. The precipitation rate is initially $\alpha_0 = 1 \text{ m yr}^{-1}$ and changes to $\alpha_1 = 2 \text{ m yr}^{-1}$ after 10 Myr.

We find that for both the transport and stream power model, when the slope exponent is greater than one, the model response time is a function of uplift rate. The faster the rate of uplift, the faster the system responds to a change in precipitation rate. If the response time for a system recovery to steady state by 50 or 10 % is plotted on a log–log plot against uplift rate we find that the response time is proportional to the uplift rate raised to a negative power (Fig. 13). In the case of $n = 1.2$ or $\gamma = 1.2$ the slope of trend is -0.1667 , and for $n = 2$ or $\gamma = 2$ the slope of trend is -0.5 (Fig. 13). These slopes are in agreement with the approximate analytical solutions of Whipple (2001) and numerical models of Baldwin et al. (2003); i.e. the stream power response time τ_{sp} has a proportionality,

$$\tau_{\text{sp}} \propto U^{\frac{1}{n}-1}, \quad (18)$$

and equivalently we infer from our numerical model (Fig. 13) the transport model response time as

$$\tau_t \propto U^{\frac{1}{\gamma}-1}. \quad (19)$$

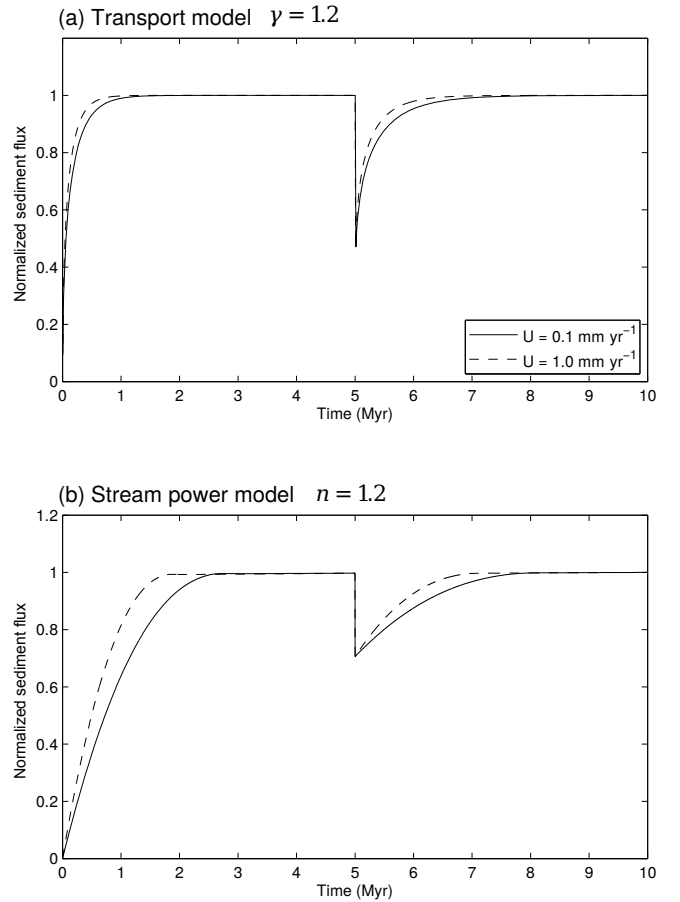


Figure 12. (a) Response of the transport model to a change in precipitation rate for two values of uplift, 0.1 and 1.0 mm yr^{-1} . Equation (8) is solved for $\gamma = 1.2$, $\delta = 1.5$, $p = 1.1$, and $c = 5 \times 10^{-5} (\text{m}^2 \text{yr}^{-1})^{1-\delta}$. The precipitation rate is initially $\alpha_0 = 1 \text{ m yr}^{-1}$ and changes to $\alpha_1 = 0.5$. (b) Response of the stream power model to a change in precipitation rate for two values of uplift, 0.1 and 1.0 mm yr^{-1} . Equation (12) is solved for $n = 1.2$, $m = 0.5$, $p = 1.1$, and $k = 1 \times 10^{-4} \text{ m}^{-1} (\text{m}^2 \text{yr}^{-1})^{1-m}$. The precipitation rate is initially $\alpha_0 = 1 \text{ m yr}^{-1}$ and changes to $\alpha_1 = 0.5$ after 5 Myr.

This implies that both models have the same form of response dependency on uplift rates. Therefore, regardless of the rate of uplift we should expect the transport model to respond more rapidly to a large increase in precipitation rate and the stream power model to respond more rapidly to a reduction in precipitation rate (Fig. 10). Our results are also consistent with the field-based findings of Whittaker and Boulton (2012), who showed that landscape response times for rivers close to the detachment-limited end-member were shorter for terrain uplifted by faster-slipping active faults.

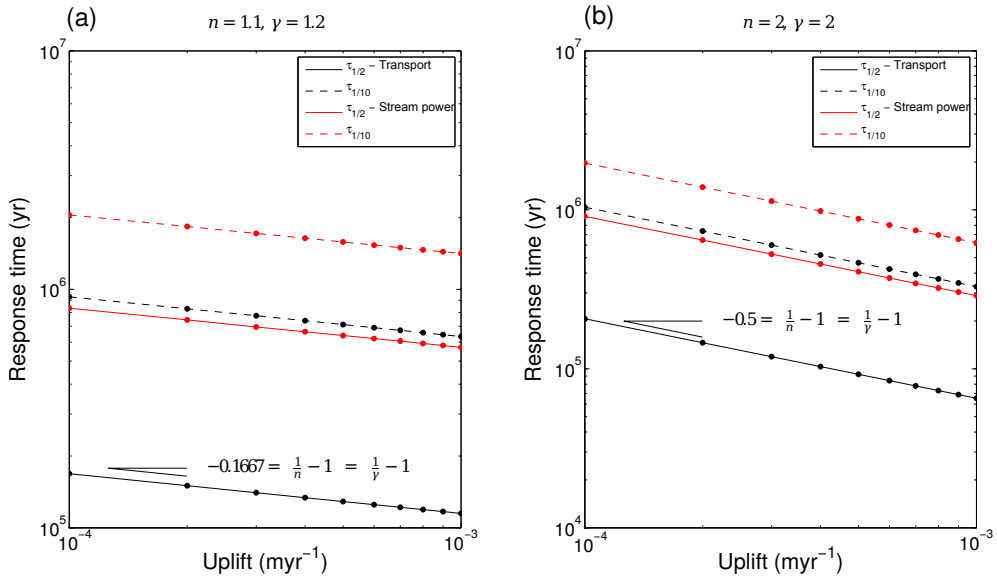


Figure 13. Log–log plot of response time for different slope exponents and uplift rates to a change to a precipitation rate from an initial value of $\alpha_0 = 1$ to $\alpha_1 = 0.5 \text{ m yr}^{-1}$; $\tau_{1/2}$ is the time for the sediment flux to recover by half of the magnitude change in sediment flux and $\tau_{1/10}$ is the time for the sediment flux to recover by 90 %. **(a)** Response time for the transport model (Eq. 8) and stream power model (Eq. 12) when the slope exponent $\gamma = 1.2$ and $n = 1.2$, respectively. A linear trend is found with a gradient of $-0.1667 = \frac{1}{n} - 1 = \frac{1}{\gamma} - 1$. **(b)** Response time for the transport model and stream power model when the slope exponent $\gamma = 2$ and $n = 2$, respectively. A linear trend is found with a gradient of $-0.5 = \frac{1}{n} - 1 = \frac{1}{\gamma} - 1$.

3.4 Response time as a function of the initial precipitation rate

Up until this point we have only explored how the numerical models respond to an increase or decrease in precipitation rate by keeping the initial precipitation rate fixed at $\alpha_0 = 1 \text{ m yr}^{-1}$ and varying the final precipitation rate α_1 . In this final section we will instead keep the final precipitation rate fixed at $\alpha_1 = 1 \text{ m yr}^{-1}$ and vary the initial precipitation rate α_0 from values of 0.5 to 1.5 m yr^{-1} . We will focus again on the 1-D models and look at the linear and non-linear cases with $n = 1.2$ and $\gamma = 1.2$.

For the linear and non-linear transport model we find that if the initial precipitation is less than the final precipitation ($\alpha_0 < \alpha_1$) then the response time is not very sensitive to the initial precipitation rate (Fig. 14a). If $\alpha_0 > \alpha_1$ then the response time is a function of the initial precipitation rate, but the relationship cannot be explained by a simple power law (Fig. 14a). The change in response time as a function of the initial precipitation rate is, however, small compared to the change in response time as a function of the final precipitation rate.

In the case of the linear and non-linear stream power model, the response time has no dependence on the initial precipitation rate and is only a function of the final precipitation rate (Fig. 14b). With all other parameters being held constant, the initial precipitation rate will set up the topography and hence the slope of the pre-perturbation landscape. Elevations will be lower for higher precipitation rates, and the topographic gradient will be smaller. For the case of the

stream power model, the change in erosion rates migrates up the catchment and so the old topography does not impact the response time. For the transport model, however, the remnant topography does have a small effect on the response time, but only if the previous precipitation rate was higher than the new post-perturbation precipitation rate.

4 Discussion

In deriving the two end-member models to describe landscape evolution, we showed that if the rate of transport of sediment were assumed to be instantaneous (i.e. all sediment is transported out of the model domain) then the stream power model would be appropriate to describe catchment erosion. However, if it is instead assumed that the rate of sediment transport is not instantaneous, then we arrive at a model in which erosion scales with the rate of change of sediment flux, which itself is dependent on both linear and potentially non-linear slope-dependent terms. These two end-members can produce similar steady-state landscapes, as noted by a number of previous studies (e.g. Whipple and Tucker, 2002; Tucker and Whipple, 2002). However, as we demonstrate above, when perturbed by a change in conditions such as rainfall rate, they can produce very different landscape responses, which vary in terms of their style, magnitude, and tempo. We explore the nature and implications of these responses below.

It is also important to stress that the catchment responses and the predicted sediment fluxes out of these two model

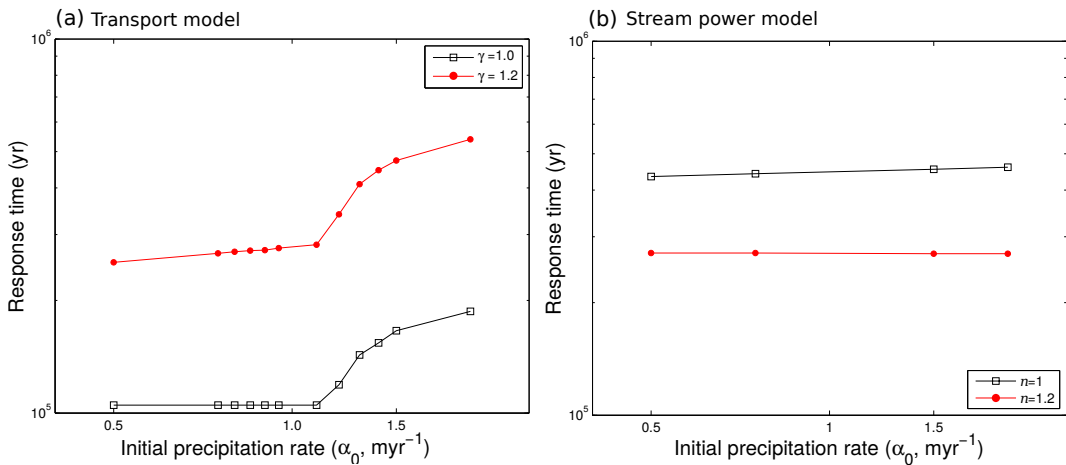


Figure 14. Log–log plots for the transport model and the stream power model in 1-D for a step change in precipitation rate; the initial precipitation rate, α_0 , varies from 0.5 to 1.5 m yr^{-1} , and the final precipitation rate is fixed at $\alpha_1 = 1 \text{ m yr}^{-1}$. **(a)** Results for the transport model. **(b)** Results for the stream power model.

domains might be variously relevant to different erosional and depositional domains (see Lague, 2014; Temme et al., 2017). A model of instantaneous sediment transport might be more relevant for suspended sedimentary loads, for which transport times can be very small, while the transport model might be more appropriate for bedload-dominated systems, even in cases in which bedrock is clearly incised (e.g. Paola et al., 1992; Valla et al., 2010). Furthermore, given that these two models have different response times, it is possible that fine-grained deposits might record signals of climate change differently from, for example, the gravel deposits within alluvial valleys. Below, we will therefore first discuss how the two model responses compare in terms of their response time and place our results in the wider context of sediment routing system response to environmental change. Second, we will compare the model results with three records of change in sediment deposition during the Paleocene–Eocene thermal maximum (PETM), a known and well-constrained period of rapid climate change. Finally, we will summarize the key implications from our results.

4.1 Response times as a function of model choice

Under certain parameter sets it is relatively straightforward to generate two landscapes eroded by the transport or stream power model that have similar elevation, slope, and area metrics (Figs. 3 and 5). To find a path to break the apparent non-uniqueness of these solutions we have explored the transient sediment flux response out of the model domain for two end-member solutions to erosion. The first observation is that both models respond at a first order in a broadly similar way to a precipitation rate (climate) driver (Figs. 9 and 10). Both models have a response that is an inverse function of the magnitude of precipitation rate change. Both models have a response that is related to uplift in an identical man-

ner (Fig. 13). However, the responses for catchments that are comparable in slope–area relationship and maximum elevation, but which are governed by different erosional dynamics defined by c , k , m , and δ , actually display different response times by almost 1 order of magnitude (Figs. 2 and 4).

We have demonstrated that models limited by their ability to transport sediment tend to have shorter response times to an increase in rainfall rate and thus re-achieve pre-perturbation sediment flux values more rapidly compared to stream-power-dominated systems, particularly when catchment length scales are small (e.g. $< 100 \text{ km}$, Fig. 10). These model observations suggest that the sediment fluxes from small alluvial catchments, even when captured in downstream depocentres, may be difficult to tie to changing climate parameters unless depositional chronologies are exceptionally well constrained (e.g. D’Arcy et al., 2017). Conversely, catchments whose erosional dynamics lie close to the stream power end-member model may be well placed to record longer-term climate shifts, but may be buffered to very high-frequency variations in the climate driver (see Simpson and Castelltort, 2012; Armitage et al., 2013). It is important to stress that the trend in response is asymmetric, by which we mean that both models show a faster response for a precipitation increase relative to a precipitation decrease (Fig. 10). This is an important outcome, which has to date not been widely recognized or investigate in field scenarios. In particular, it raises the prospect that for glacial–interglacial cycles characterized by wetter, cooler stadial periods and dryer, warmer interstadials, the rapid climate recovery from peak glacial conditions typically seen in $\delta^{18}\text{O}$ records might be mediated by a longer landscape response time to this change. Conversely, physically slower boundary condition changes towards wetter conditions may give rise to faster landscape response times. We suggest that an ex-

ploration of these differences may be a promising avenue of future research.

Given that the response time is a function of the water flux exponent (m or δ) and that the water flux exponent for the transport model is greater than that for the stream power model, there will be a cross-over point at which the stream power model responds faster than the transport model. This cross-over point is a function of the erodibility coefficient k and the transport coefficient c . In the scenario in which we have tried to initiate the perturbation in precipitation rates from similar catchments, we find that this cross-over point is towards large reductions in precipitation rates (Fig. 10). This implies that the transport model generally responds faster than the stream power model (10^5 to 10^6 yr) for examples in which the parameter combinations used here produce similar steady-state landscapes.

For such conditions, the stream power model predicts a landscape response time to a change in precipitation of the order of 10^6 yr, and this time is related to the precipitation rate to the inverse power of m (Fig. 10). The transport model predicts a wider range of response times of the order of 10^6 to 10^5 yr that is related to the precipitation rate to the inverse power of δ ; in this case the response time is also length dependent (Fig. 10 and Table 2). It has been suggested that a transition from a landscape controlled by detachment-limited erosion (stream power model) to sediment transport at longer system lengths may explain the longevity of mountain ranges (Baldwin et al., 2003). This hypothesis is somewhat backed up by the analysis of response times for the transport model, as the response time increases with system length (Table 2) unlike the stream power model, which has a response that is only slightly modified by system length (Whipple, 2001; Baldwin et al., 2003). To date, physical constraints on landscape and sediment flux response times to climate changes in the geologic past are relatively scarce (Ganti et al., 2014; Romans et al., 2016; Temme et al., 2017) because real systems are complex. They include internal dynamics, such as vegetation and autogenic behaviour, which are often omitted from model studies, and because of the need for stratigraphic archives to be complete with well-established chronologies (Allen et al., 2013; Forman and Straub, 2017). In principle, however, the dominant long-term incision process governing catchment behaviour fundamentally determines the sediment flux response and may itself help identify catchment erosional dynamics; we explore this question in Sect. 4.2.

Finally, it is worth noting that the model response time has implications for the inverse modelling of river profiles. When river-long profiles are inverted for uplift, erosion is typically assumed to be captured by the stream power model (e.g. Pritchard et al., 2009). Studies of continent-scale inversion have found that the best fit value of k for the stream power model increases by 2 orders of magnitude to fit river profiles in Africa relative to Australia (Rudge et al., 2015). Such a large change in k would result in a highly significant difference in response time from continent to continent, which in

itself would imply that tectonic and climatic signals are preserved in landscapes and sediment archives over vastly different time periods (see Demoulin et al., 2017). Such an outcome may reflect fundamental differences in bedrock erodibility (Roy et al., 2015), but alternatively could be satisfactorily explained by differing long-term erosional dynamics and sediment transport. These differences are enhanced in the case in which $n > 1$ in the stream power erosion model.

4.2 Relevance of model responses to sediment records of climate change

To what extent do these model results, which start from similar steady-state topographies, help us to understand whether stratigraphic records of sediment accumulation through time do or do not reflect the effects of climatic change on sediment routing systems governed by differing long-term erosional dynamics? One motivation for this study has come from the increasing number of field and stratigraphic investigations of terrestrial sedimentary deposits, apparently contemporaneous with (and taken to record) known past climate perturbations, such as the Palaeocene–Eocene thermal maximum (PETM), a hyperthermal event that occurred around 56 Ma. Stratigraphers often correlate changing stratigraphic characteristics with changing environmental boundary conditions in a qualitative way (see Romans et al., 2016; Allen, 2017). However, to evaluate quantitatively how sediment routing systems respond to climate with reference to real examples, it is imperative to consider systems in which the timescales of erosion (or as a proxy, deposition) are known, stratigraphic sections are complete, and the driving mechanisms well documented (see Allen et al., 2013; D’Arcy et al., 2017).

To compare our model predictions with observations it is clear that we have to use the depositional record. Therefore, there is an implicit assumption that stratigraphy is a faithful recorder of erosion. It is, however, possible that climatic change will also alter processes that control sediment deposition, for example by altering how sediment partitions from transport into stratigraphy. By using estimates of the total volume of sediment deposited within the Escanilla Eocene sedimentary system in the Spanish Pyrenees, it has been demonstrated that climatic change can recreate observed changes in grain size deposition (Armitage et al., 2015). This example of a close model-to-stratigraphic-observation prediction might be evidence that the stratigraphic record is a faithful record of a change in sediment flux delivery to the depositional environment.

The PETM is arguably the most rapid global warming event of the Cenozoic, with a rise in global surface temperatures by 5 to 9 °C (Dunkley Jones et al., 2010), forming a clear step change in climate for which depositional records are well constrained in a number of basins worldwide (Forman et al., 2012). It is therefore a good example for high-level comparison with our model outputs. While the large-magnitude glacial–interglacial cycles of the past 1 Myr are

also plausible candidates to investigate these links in principle (see Armitage et al., 2013), we note that many terrestrial records of sedimentation over ca. 100 kyr, such as fluvial terraces and alluvial fans, have depositional chronologies that are often incomplete or reworked (D'Arcy et al., 2017; Demoulin et al., 2017).

The initial warming associated with the PETM event occurred at ca. 55.5 Ma and may have been as abrupt as 20 kyr, with a duration of 100 to 200 kyr based on the synthesis of $\delta^{13}\text{C}$ and $\delta^{18}\text{O}$ records (e.g. Schmitz and Pujalte, 2007; Foreman et al., 2012). The event has been associated with clear changes to global weather patterns; for instance, hydrogen isotope records suggest increased moisture delivery towards the poles at the onset of the PETM, consistent with predictions of storm track migrations during global warming (Sluijs et al., 2006). This event has also been argued by an increasing number of authors to have produced a significant geomorphic and erosional impact based on sedimentary evidence and its apparent effect on the global hydrological cycle and catchment run-off (e.g. Foreman et al., 2012; Foreman, 2014).

A clear response to the PETM is recorded within both the Spanish Pyrenees and the western US; however, the responses are arguably not the same. At the onset of the PETM there is strong evidence for the contemporaneous increase in precipitation rates and the deposition of coarse gravels known as the Claret Conglomerate (Schmitz and Pujalte, 2007) in the Tremp Basin of the Spanish Pyrenees. In the western US the PETM is marked by the deposition of well-documented channel sandstone bodies in the Piceance Creek and Bighorn basins (Foreman et al., 2012; Foreman, 2014, e.g.). In the US cases, the deposits include coarse channelized sands, marked by upper flow regime bed forms, some of which are consistent with a synchronous increase in both water and sediment discharge. At Claret, where the style of sedimentation abruptly changes from a semi-arid alluvial plain to an extensive braid plain or megafan deposit, the conglomerate has a thickness of ~ 10 m, while the total carbon isotope excursion (CIE) in the same section measures ~ 35 m (Manners et al., 2013).

4.2.1 Claret Conglomerate, Spanish Pyrenees

The Claret Conglomerate was likely deposited rapidly, representing a fast response to climate change. If we assume a constant rate of deposition, then the Claret Conglomerate accounts for roughly 30 % of the total duration of deposition for the CIE (170 kyr; Röhl et al., 2007), suggesting that deposition occurred over a duration of up to 50 kyr. Indeed, Schmitz and Pujalte (2007) argue that the deposition of this unit may have been markedly quicker than the conservative estimate above, perhaps taking less than 10 kyr, based on their detailed comparison of $\delta^{13}\text{C}$ and $\delta^{18}\text{O}$ records at the field site compared to marine records of the excursion. Therefore unless there is a major unconformity within the CIE, the implication is that the erosional system responded rapidly at

this particular field site, in 10 to 50 kyr, to a significant shift in climatic conditions. These values suggest sedimentation rates of up to 1 mm yr^{-1} . If such a sedimentation rate had been sustained for the duration of the deposition of the Tremp Group (Maastrichtian to the end of the Palaeocene), the sediment thickness would be > 15 km. This is an order of magnitude more than actually observed (Cuevas, 1992) and would therefore suggest that sediment fluxes increased dramatically at the PETM.

Erosional source catchment areas were likely < 100 km in length given the palaeo-geography of the Pyrenees at the time (Manners et al., 2013). The very short duration of the erosional response, which is required for the sediments to be transported and deposited on a timescale of ca. 10^4 years, is therefore difficult to model within a stream power (advection) end-member model for catchments of this scale (Table 2), although a version of such a model has been recently used to explore the controls on the evolution of later Miocene megafans in the northern Pyrenees (e.g. Mouchené et al., 2017). To use the stream power model would require a significant increase in the bedrock erodibility parameter, k , within the model (by greater than 1 order of magnitude), implying slopes and topography in the palaeo-Pyrenees that were highly subdued. In contrast, the sediment transport model more easily reproduces the documented response timescales given an increase in precipitation; it is also consistent with the volumetrically significant export of bedload-transported gravel clasts and therefore honours the independent field data more effectively. We also note that the transport model displays a response time that has a stronger dependence on precipitation rate change and has a greater amplitude of perturbation (e.g. Fig. 9). We therefore suggest that the erosional pulse that led to the deposition of the Claret Conglomerate is most appropriately modelled as a diffusive system response to a sharp increase in precipitation over the source catchments of the developing Pyrenean mountain chain at that time.

4.2.2 Sandstone bodies in the Piceance Creek and Bighorn basins, western US

The time-equivalent sections in the Bighorn and Piceance Creek basins of the western US also provide clear evidence of anomalous sedimentation at the PETM; however, in this case the duration of deposition is somewhat longer, > 100 kyr (Foreman et al., 2012; Foreman, 2014). Here the deposits are of smaller grain sizes, with the boundary sandstone sequence in the Bighorn Basin being made up of fine to coarse sand with little gravel (Foreman, 2014). In the Piceance Creek basin, the PETM section documents the rapid progradation of coarse-grained sands, which is consistent with greater discharges, over silty underlying strata and in that sense these observations also match sediment transport model predictions for rapid increases in sediment flux driven by enhanced precipitation (Foreman et al., 2012). However,

it is notable that the documented changes in fluvial style persisted beyond the PETM and we therefore suggest that the fast response of the system to the increase in precipitation, but the persistence of coarser-grain sedimentation as the climate presumably dried and cooled, may indeed reflect the marked asymmetry in sediment flux responses to wetting and drying noted in Fig. 9.

In contrast, the Bighorn Basin boundary sandstone sediments are contained within the PETM time period and indicate uniform flow depths and widths during this time, while also being coarser than the underlying horizons. Moreover, proxy data suggest a net decrease rather than an increase in precipitation (Foreman et al., 2012; Foreman, 2014). While the progradation of such coarse-grained facies could be represented as a diffusive process driven by increasing rainfall-driven discharge (Paola et al., 1992; Armitage et al., 2011), this is apparently inconsistent with the sedimentological characteristics of the deposit. Although sediment fluxes are not explicitly reconstructed in this work, this response apparently requires greater volumes and grain sizes of sediment delivered despite lowered rainfall conditions and is thus difficult to capture in either of the end-member models used here. Foreman et al. (2012) and Foreman (2014) argue for the preferential removal of fine-grained floodplain deposits speculatively linked to changing vegetation and the reduced cohesion of overbank sediments. Consequently, while two of the PETM sections considered here are broadly consistent with landscape responses governed by a sediment transport model, some depositional stratigraphies are not immediately consistent with either end-member model and may reflect important complexity, such as the effects of vegetation, lacking from simple model solutions.

4.3 Summary and model limitations

In this section we consider the implications of our model outputs, both generally for interpreting sediment routing system response to boundary condition change and specifically in the context of the well-studied PETM event. While the sediment flux response of the models to a change in precipitation are at a first-order level broadly similar, there are four key differences to highlight. First, starting from the same initial conditions, the sediment transport model appears to be more sensitive to precipitation change than the equivalent stream power model. It is therefore a good candidate for which rapid catchment-wide responses are recorded to, for example, a climate change event, as we argued for the PETM Claret Conglomerate in the Spanish Pyrenees. Second, we note that in both model cases there is a quicker response to a wetting than a drying event, something which has not been well established or demonstrated from field observations. Nevertheless we argue that field data sets, including PETM studies, may already have recorded this asymmetry, although it may not have been recognized as such. Third, the sediment transport model has a greater magnitude of peak sediment flux

and is particularly sensitive to catchment size. Finally, we note that response time in both models is a function of uplift rate for $n > 1$, which means that in such cases, perhaps counter-intuitively, the more perturbed the system the faster it responds (see Whittaker and Boulton, 2012).

However, it is important to recognize that in deriving these two classic end-member models we have simplified landscape evolution considerably. We acknowledge that change in the model parameters, c , k , m , and δ , will alter the response times depicted here (see Armitage et al., 2013). However, in order to compare the two models we have specifically used values of c , k , m , and δ that generate comparable model landscapes, and we then changed the precipitation rate to understand the form of the model response. No model incorporates all the complexities that characterize sediment routing systems from source to sink (see Allen, 2017) and the act of simplification inherent in considering erosional end-member models necessitates that in arguing for the applicability of one over the other, we simply consider the broad styles of behaviour suggested by model outputs. We do not, for example, consider autogenic behaviours (e.g. Forman and Straub, 2017), nor do we consider coupled issues of vegetation turnover in response to climate change, which may play an important role in examples such as the Bighorn Basin considered here (see Foreman, 2014). Nonetheless, a significant finding of this work has been the clear asymmetry in response time of these end-member models in terms of a wetting event (faster) compared to a drying event (slower). This implies that aridification events are harder to preserve in the sedimentary record, not only because they are typically associated with reduced sediment fluxes, but also because the timescale of landscape response may be $> 10^6$ years.

5 Conclusions

Deterministic numerical models of landscape evolution rest on fundamental assumptions on how sediment is transported down-system. The stream power law is based on the assumption that all sediment generated is transported instantaneously out of the landscape. Transport models assume that there is an endless supply of sediment to be transported. The existence of knickpoints within river-long profiles, assumed to be produced by a system perturbation such as a base level, has been used to provide evidence in support of the stream power law in upland areas (e.g. Whipple and Tucker, 1999; Snyder et al., 2000; Whittaker et al., 2008). Knickpoints, however, can likewise be a result of changes in lithology (Grimaud et al., 2014; Roy et al., 2015) and are certainly not a unique indicator of erosion dynamics (e.g. Tucker and Whipple, 2002; Valla et al., 2010; Grimaud et al., 2016). In this contribution we therefore attempted to understand how the sediment flux signal out of the eroding catchment may generate a distinguishable difference between the end-member models in terms of a response to a change in run-off.

This idea is motivated from field observations of past landscape responses to climate excursions, such as the PETM, which are manifested in the rapid deposition of coarse sedimentary packages in terrestrial depocentres (Armitage et al., 2011; Foreman et al., 2012).

Both models suggest that the response time of landscape to a change in precipitation rate has a proportionality of the form of a negative power law (Eqs. 15 and 16). The key difference is in the value of the exponent. For the stream power model, the exponent must be less than one in order to match the observed concavity of river profiles. In contrast, for the transport model the exponent on the precipitation rate must be greater than one in order to generate a river network (Smith and Bretherton, 1972) and to generate the observed concavity of river profiles. This results in the transport model responding more rapidly to an increase in precipitation rate in comparison to the stream power law model (Fig. 10). In contrast, the stream power model is faster to respond to a reduction in rainfall rate. This is fundamentally because the response time of this model is more weakly a function of precipitation than the sediment transport model. Significantly, therefore, our results show that there is a fundamental asymmetry in the response of both models to a climatic perturbation, with the response time to a drying event longer than that to an increase in rainfall. In general terms, the magnitude of the response to a change in precipitation rate appears greater across the range of model space investigated here for the sediment transport (diffusive) model solutions, while for the stream power (advective) model, the magnitude of the sediment flux perturbation is smaller, but is more localized within the catchment with respect to knickpoint retreat.

While this study does not address whether or not these sediment flux signals will be preserved in the stratigraphic record, a problem that fundamentally rests on the availability of accommodation to capture the eroded sediment (see Allen et al., 2013; Whittaker et al., 2011), it does suggest that landscapes governed by these simple erosional end-members should be sensitive to climate change. Moreover, there are some important diagnostic differences between their sediment flux responses to an identical perturbation, including the amplitude, timescale, and locus of the erosional response. Using published stratigraphic examples, we suggest that the timescales and magnitude of coarse sediment deposition in the Spanish Pyrenees at the time of the PETM are best described using the diffusive transport model end-member. Moreover, we argue that these model end-members allow us to constrain the range of likely sediment flux scenarios that precipitation changes may generate and that numerical models, in conjunction with a range of field and independently constrained proxy data sets, are best placed to tease apart when and in what circumstances climate signals are likely to have been generated in erosional catchment systems, which fundamentally determines whether they can be subsequently *captured* in sedimentary depocentres downstream.

Code availability. The 1-D solution to the transport model is available from John Armitage (armitage@ipgp.fr). The 1-D solution to the stream power model is available from Benjamin Campforts (benjamin.comforts@kuleuven.be). Fastscape is available from Jean Braun (GFZ Potsdam) by request. The 2-D solution to the transport model was developed by Guy Simpson (University of Geneva) and is available as part of Simpson (2017).

Appendix A: Steady-state 1-D profiles

The solution to the one-dimensional stream power law (Eq. 12) assuming that at the end of the catchment at $x = L$ elevation $z = 0$ and $mp \neq 1$ is

$$z_{\text{sss}} = \frac{U}{mk\alpha^m(mp-1)} \left(x^{(1-mp)} - Lx^{(1-mp)} \right), \quad (\text{A1})$$

and for the case in which $mp = 1$ this simplifies to

$$z_{\text{sss}} = \frac{U}{k\alpha^m} \log_e(L/x). \quad (\text{A2})$$

For the transport model (Eq. 8) there is an exact solution for the case that $\delta p = 2$, which assumes that at $x = 0$, $\partial_x z = 0$ and at $x = L$, $z = 0$:

$$z_{\text{sst}} = -\frac{UL}{2\kappa D_e} \left(\log(D_e x^2 + 1) + \log(D_e + 1) \right), \quad (\text{A3})$$

where

$$D_e = \frac{ck_w\alpha^{2/p}L^2}{\kappa}. \quad (\text{A4})$$

For other values of δp the steady-state solution is solved numerically; Eq. (8) is solved using the finite-element method with linear weight functions. We use a non-uniform 1-D nodal spacing, for which the spatial resolution is increased with increasing gradient. The numerical model is benchmarked against the analytical solution for the case in which $np = 2$.

The steady-state solutions are plotted in the case that $\delta = p = \sqrt{2}$ and for reference the stream power model solution with $m = 0.5$ and $p = \sqrt{2}$ (Fig. A1). Such a value of p assumes that $h \sim 0.7$, which is towards the higher end for observed Hack exponents, and that the river catchment is very elongated. When plotting the logarithm of the model slope against drainage area (Fig. A1b), for which area is given by $a = x^p/k_w$ and assuming $k_w = 1$, for the simple stream power law derived here the slope-area exponent $\theta = -m$. The value of the dimensional constant k has no impact on the slope-area exponent as expected. The transport model likewise creates river-long profiles that have on average a negative curvature. For small values of x there is, however, a region of positive curvature in which $\kappa > ck_w\alpha^\delta L^{\delta p}$. For the slope-area analysis this leads to a positive gradient in the trend for small catchment areas. This relationship subsequently has a negative slope for larger catchments. The point of inflection is dependent on the value of D_e ; for smaller values of κ the region of positive gradient is reduced. There is therefore a critical catchment area that is dependent on the diffusive term κ . After this critical point the slope-area relationship becomes negative. At distances down-system, where the upstream area is greater than this critical area, the gradient $\theta = -0.88$; θ is insensitive to the coefficient c as would be expected.

Table A1. Gradient, θ , of the slope vs. area trend at steady state for 1-D sediment transport (Eq. 8, Fig. A2).

δ	$p = 1.40$		$p = 1.67$		$p = 2.00$	
	c	θ	c	θ	c	θ
1	10^{-6}	-0.50	10^{-5}	-0.40	10^{-4}	-0.30
1.5	10^{-8}	-1.01	10^{-7}	-0.91	10^{-6}	-0.81
2	10^{-10}	-1.51	10^{-9}	-1.41	10^{-8}	-1.31

The range of gradients found for river catchments for this type of slope-area analysis, usually referred to as concavity, generally lies within the range $\theta = -0.35$ to -0.70 (Snyder et al., 2000; Wobus et al., 2006). It is trivial to find the values of m for the steady-state solution to the stream power law that fit such values of θ . To further explore how θ depends on δ and p within the transport model we solve Eq. (8) numerically for $\delta = 1$, 1.5, and 2 while keeping $h = 0.7$ or 0.6 (Fig. A2). The result is that θ varies from -0.3 for the case of $\delta = 1$ to -1.31 for $\delta = 2$. The values of the gradient for the slope-area analysis for $1.4 < p < 2$, in which we assume $d = 1$ and hence $p = 1/h$, are displayed in Table A1. For the transport model the slope is dependent on both δ and p .

Clearly there is a combination of δp values that is equally capable of fitting the observed river-long profile. Furthermore, for the transport model the slope is a function of the Hack exponent h (and therefore p) and the choice of δ . This because of the diffusivity term that leads to positive curvature and rounded 1-D profiles (Figs. A1b and A2). The magnitude of the water flux term within the transport equation (Eq. 8) is dependent on how much water the river network captures, which is in turn a function of how elongated the catchment is.

The positive slope-area relationship for the transport model for small catchment areas (see Figs. A1b and A2b) has been previously explored in Willgoose et al. (1991). The gradient of the relationship between slope and catchment area is dominantly a function of the exponent δ within Eq. (6). The value of this exponent is likely within the range of $1 < \delta < 2$ depending on the bedload transport law assumed (Armitage et al., 2013). If the observations of trunk river slope against catchment area are representative of a landscape at steady state, then for the smaller range of $1 < \delta \leq 1.5$, a realistic catchment topography can be generated.

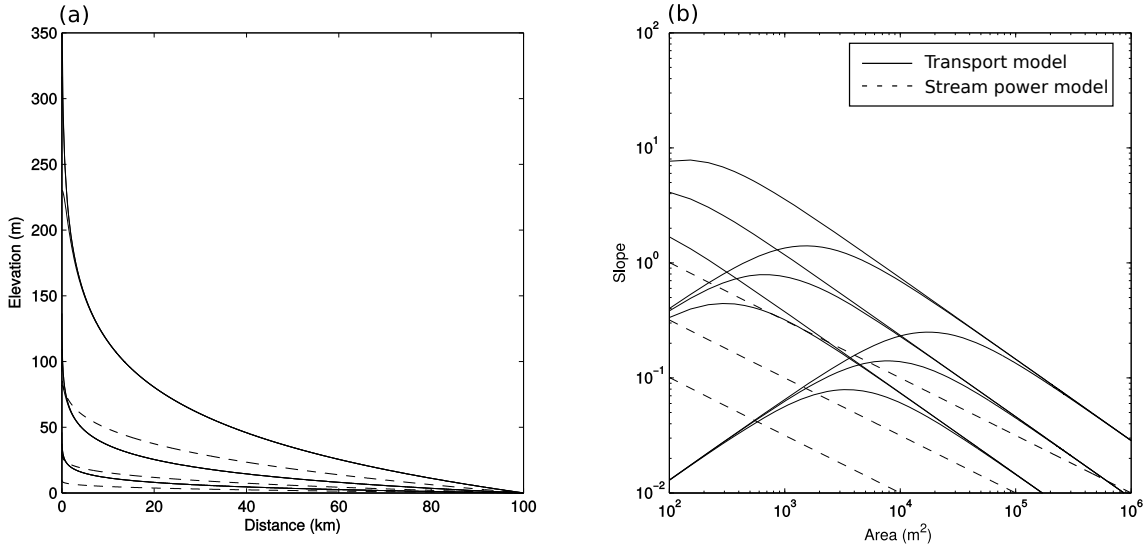


Figure A1. (a) Steady-state profiles of elevation against down-system length and (b) the slope of the profile plotted against the drainage area assuming that area $a = x^p$, where $p = 1/h = \sqrt{2}$ and h is the Hack exponent. Dashed lines are for the stream power law (Eq. 12) with $m = 0.5$ and $k = 10^{-4}, 10^{-3.5}$, and 10^{-3} . The solid lines are for the transport model (Eq. 8 with $n = \sqrt{2}, \kappa = 10^{-3}, 1$, and $10^3 \text{ m}^2 \text{ yr}^{-1}$ and $c = 10^{-6}, 10^{-5.5}$, and 10^{-5}).

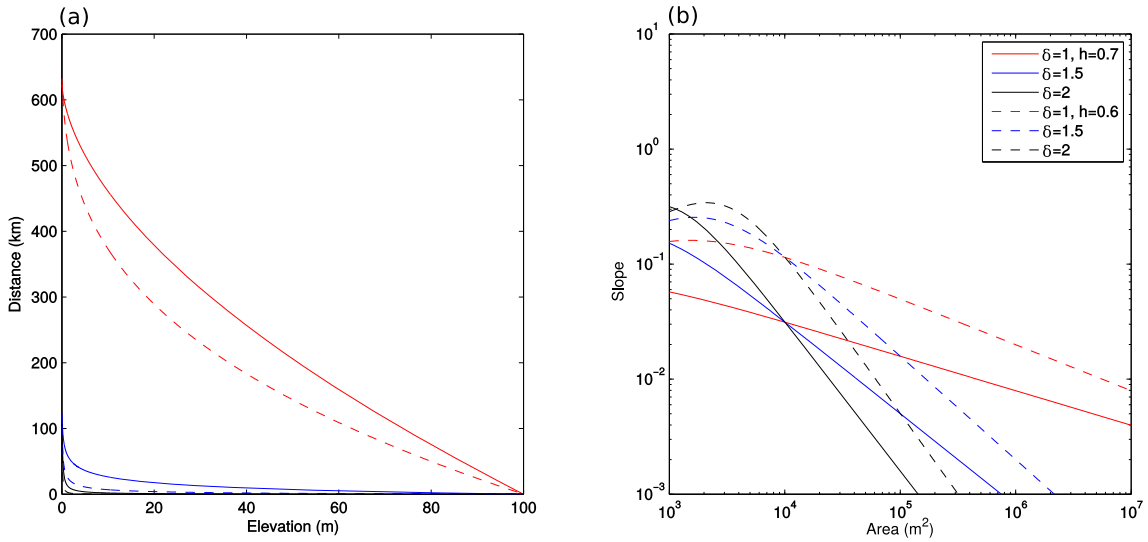


Figure A2. (a) Steady-state elevation and (b) slope-area relationship for the numerical solution to 1-D sediment transport (Eq. 8) for which the area, a , is taken to be related to distance x by $a = x^p$, where $p = 1/h$ and h is the Hack exponent. Red lines are for the case in which $n = 1$, blue lines for $n = 1.5$, and black lines for $n = 2$. Solid lines are for $h = 0.7$. Dashed lines are for $h = 0.6$.

Competing interests. The authors declare that they have no conflict of interest.

Acknowledgements. We would like to thank Guy Simpson (University of Geneva) for sharing his numerical model that solves the Smith and Bretherton (1972) equations in two dimensions. We thank Tom Dunkley Jones (University of Birmingham) for discussions on the duration of conglomeratic deposition during the PETM, Gareth Roberts (Imperial College London) for discussions on slope exponents, and Jean Braun (GFZ Potsdam) for sharing his numerical model Fastscape. This work was initiated under funding by the Royal Astronomical Society through a research fellowship awarded to John Armitage while he was at Royal Holloway University of London.

Edited by: Jean Braun

Reviewed by: Laure Guerit and one anonymous referee

References

- Allen, P. A.: Sediment Routing Systems: The Fate of Sediment from Source to Sink, Cambridge University Press, 2017.
- Allen, P. A., Armitage, J. J., Carter, A., Duller, R. A., Michael, N. A., Sinclair, H. D., Whitchurch, A. L., and Whittaker, A. C.: The Q_s problem: Sediment volumetric balance of proximal foreland basin systems, *Sedimentology*, 60, 102–130, <https://doi.org/10.1111/sed.12015>, 2013.
- Armitage, J. J., Duller, R. A., Whittaker, A. C., and Allen, P. A.: Transformation of tectonic and climatic signals from source to sedimentary archive, *Nat. Geosci.*, 4, 231–235, <https://doi.org/10.1038/ngeo1087>, 2011.
- Armitage, J. J., Dunkley Jones, T., Duller, R. A., Whittaker, A. C., and Allen, P. A.: Temporal buffering of climate-driven sediment flux cycles by transient catchment response, *Earth Planet. Sci. Lett.*, 369–370, 200–210, <https://doi.org/10.1016/j.epsl.2013.03.020>, 2013.
- Armitage, J. J., Allen, P. A., Burgess, P. M., Hampson, G. J., Whittaker, A. C., Duller, R. A., and Michael, N. A.: Physical stratigraphic model for the Eocene Escanilla sediment routing system: Implications for the uniqueness of sequence stratigraphic architectures, *J. Sediment. Res.*, 85, 1510–1524, <https://doi.org/10.2110/jsr.2015.97>, 2015.
- Baldwin, J. A., Whipple, K. X., and Tucker, G. E.: Implications of the shear stress river incision model for the timescale of post-torogenic decay of topography, *J. Geophys. Res.*, 108, 2158, <https://doi.org/10.1029/2001JB000550>, 2003.
- Banavar, J. R., Colaiori, F., Flammini, A., Giacometti, A., Maritan, A., and Rinaldo, A.: Sculpting of a fractal river basin, *Phys. Rev. Lett.*, 23, 4522–4525, 1997.
- Bonnet, S. and Crave, A.: Landscape response to climate change: Insights from experimental modeling and implications for tectonic versus climatic uplift of topography, *Geology*, 31, 123–126, 2003.
- Braun, J. and Willett, S. D.: A very efficient $O(n)$, implicit and parallel method to solve the stream power equation governing fluvial incision and landscape evolution, *Geomorphology*, 180/181, 170–179, <https://doi.org/10.1016/j.geomorph.2012.10.008>, 2013.
- Braun, J., Voisin, C., Gourlan, A. T., and Chauvel, C.: Erosional response of an actively uplifting mountain belt to cyclic rainfall variations, *Earth Surf. Dynam.*, 3, 1–14, <https://doi.org/10.5194/esurf-3-1-2015>, 2015.
- Campforts, B. and Covers, G.: Keeping the edge: A numerical method that avoids knickpoint smearing when solving the stream power law, *J. Geophys. Res.*, 120, 1189–1205, <https://doi.org/10.1002/2014JF003376>, 2015.
- Castelltort, S. and Van Den Dreische, J.: How plausible are high-frequency sediment supply-driven cycles in the stratigraphic record?, *Sediment. Geol.*, 157, 3–13, [https://doi.org/10.1016/S0037-0738\(03\)00066-6](https://doi.org/10.1016/S0037-0738(03)00066-6), 2003.
- Cowie, P. A., Whittaker, A. C., Attal, M., Roberts, G., Tucker, G. E., and Ganas, A.: New constraints on sediment-flux-dependent river incision: Implications for extracting tectonic signals from river profiles, *Geology*, 36, 535–538, <https://doi.org/10.1130/G24681A.1>, 2008.
- Croissant, T. and Braun, J.: Constraining the stream power law: a novel approach combining a landscape evolution model and an inversion method, *Earth Surf. Dynam.*, 2, 155–166, <https://doi.org/10.5194/esurf-2-155-2014>, 2014.
- Crosby, B. T., Whipple, K. X., Gasparini, N. M., and Wobus, C. W.: Formation of fluvial hanging valleys: Theory and simulation, *J. Geophys. Res.*, 112, F03510, <https://doi.org/10.1029/2006JF000566>, 2007.
- Cuevas, J. L.: Estratigrafia del “Garumniense” de la Conca de Tremp, Prepirineo de Lerida, Acata Geological Hispanica, 27, 95–108, 1992.
- D’Arcy, M., Whittaker, A. C., and Roda-Boluda, D. C.: Measuring alluvial fan sensitivity to past climate changes using a self-similarity approach to grain-size fining, Death Valley, California, *Sedimentology*, 64, 388–424, <https://doi.org/10.1111/sed.12308>, 2016.
- D’Arcy, M., Whittaker, A. C., and Roda-Boluda, D. C.: Measuring alluvial fan sensitivity to past climate changes using a self-similarity approach to grain-size fining, Death Valley, California, *Sedimentology*, 64, 388–424, <https://doi.org/10.1111/sed.12308>, 2017.
- Demoulin, A., Mather, A., and Whittaker, A.: Fluvial archives, a valuable record of vertical crustal deformation, *Quaternary Sci. Rev.*, 166, 10–37, <https://doi.org/10.1016/j.quascirev.2016.11.011>, 2017.
- Densmore, A. L., Allen, P. A., and Simpson, G.: Development and response of a coupled catchment fan system under changing tectonic and climatic forcing, *J. Geophys. Res.*, 112, F01002, <https://doi.org/10.1029/2006JF000474>, 2007.
- Dietrich, W. E., Bellugi, D. G., Sklar, L. S., Srock, J. D., Heimsath, A. M., and Roering, J. J.: Geomorphic transport laws for predicting landscape form and dynamics, in: Prediction in Geomorphology, edited by: Wilcock, P. R. and Iverson, R. M., Geoph. Monog. Series, 135, 1–30, <https://doi.org/10.1029/135GM09>, 2003.
- Dietrich, W. M.: Settling velocity of natural particles, *Water Resour. Res.*, 18, 1615–1626, 1982.
- Dodds, P. S. and Rothman, D. H.: Geometry of river networks. I. Scaling, fluctuations and deviations, *Phys. Rev. E*, 63, 016115, <https://doi.org/10.1103/PhysRevE.63.016115>, 2000.

- Dunkley Jones, T., Ridgwell, A., Lunt, D. J., Maslin, M. A., Schmidt, D. N., and Valdes, P. J.: A Palaeogene perspective on climate sensitivity and methane hydrate instability, *P. T. Roy. Soc. Pt. A.*, 368, 2395–2415, <https://doi.org/10.1098/rsta.2010.0053>, 2010.
- Foreman, B. Z.: Climate-driven generation of a fluvial sheet sand body at the Paleocene-Eocene boundary in north-west Wyoming (USA), *Basin Res.*, 26, 225–241, <https://doi.org/10.1111/bre.12027>, 2014.
- Foreman, B. Z., Heller, P. L., and Clementz, M. T.: Fluvial response to abrupt global warming at the Palaeocene/Eocene boundary, *Nature*, 491, 92–95, <https://doi.org/10.1038/nature11513>, 2012.
- Forman, B. Z. and Straub, K. M.: Autogenic geomorphic processes determine the resolution and fidelity of terrestrial paleoclimate records, *Sci. Adv.*, 3, e1700683, <https://doi.org/10.1126/sciadv.1700683>, 2017.
- Ganti, V., Lamb, M. P., and McElroy, B.: Quantitative bounds on morphodynamics and implications for reading the sedimentary record, *Nat. Comun.*, 5, 3298, <https://doi.org/10.1038/ncomms4298>, 2014.
- Grimaud, J. L., Chardon, D., and Beauvais, A.: Very long-term incision of big rivers, *Earth Planet. Sci. Lett.*, 405, 74–84, <https://doi.org/10.1016/j.epsl.2014.08.021>, 2014.
- Grimaud, J. L., Paola, C., and Voller, V.: Experimental migration of knickpoints: influence of style of base-level fall and bed lithology, *Earth Surf. Dynam.*, 4, 11–23, <https://doi.org/10.5194/esurf-4-11-2016>, 2016.
- Guerit, L., Métivier, F., Devauchelle, O., Lajeunesse, E., and Barrier, L.: Laboratory alluvial fans in one dimension, *Phys. Rev. E*, 90, 022203, <https://doi.org/10.1103/PhysRevE.90.022203>, 2014.
- Hack, J. T.: Studies of longitudinal profiles in Virginia and Maryland, US Geological Survey Professional Paper, 294-B, 1957.
- Hancock, G. R., Coulthard, T. J., and Lowry, J. B. C.: Predicting uncertainty in sediment transport and landscape evolution - the influence of initial surface conditions, *Comput. Geosci.*, 90, 117–130, <https://doi.org/10.1016/j.cageo.2015.08.014>, 2016.
- Howard, A. D. and Kerby, G.: Channel changes in badlands, *Geol. Soc. Am. Bull.*, 94, 739–752, 1983.
- Izumi, N. and Parker, G.: Inception of channelization and drainage basin formation: upstream-driven theory, *J. Fluid Mech.*, 283, 341–363, 1995.
- Kirkby, M. J.: Hillslope process-response models based on the continuity equation, Special Publication Institute of British Geographers, 3, 15–30, 1971.
- Lacey, G.: Stable channels in alluvium, in: Minutes of the Proceedings, edited by: Grierson, W. W., Institution of Civil Engineers Publishing, vol. 229, 259–292, 1930.
- Lague, D.: The stream power river incision model: evidence, theory and beyond, *Earth Surf. Proc. Land.*, 39, 38–61, <https://doi.org/10.1002/esp.3462>, 2014.
- Leopold, L. B. and Maddock, T.: The hydraulic geometry of stream channels and some physiographic implications, Tech. Rep. 252, US Geological Survey Professional Papers, 57 pp., 1953.
- Liu, Y., Métivier, F., Gaillerdet, J., Ye, B., Meunier, P., Narteau, C., Lajeunesse, E., Han, T., and Malverti, L.: Erosion rates deduced from seasonal mass balance along the upper Urumqi River in Tianshan, *Solid Earth*, 2, 283–301, <https://doi.org/10.5194/se-2-283-2011>, 2011.
- Manners, H. R., Grimes, S. T., Sutton, P. A., Domingo, L., Leng, M. J., Twitchett, R. J., Hart, M. B., Dunkley Jones, T., Pancost, R. D., Duller, R., and Lopez-Martinez, N.: Magnitude and profile of organic carbon isotope records from the Paleocene – Eocene Thermal Maximum: Evidence from northern Spain, *Earth Planet. Sci. Lett.*, 376, 220–230, <https://doi.org/10.1016/j.epsl.2013.06.016>, 2013.
- Maritan, A., Rinaldo, A., Rigon, R., Giacometti, A., and Rodriguez-Iturbe, I.: Scaling laws for river networks, *Phys. Rev. E*, 53, 1510–1515, 1996.
- Meunier, P., Métivier, F., Lajeunesse, E., Mériaux, A. S., and Faure, J.: Flow pattern and sediment transport in a braided river: The “torrent de St Pierre” (French Alps), *J. Hydrol.*, 330, 496–505, <https://doi.org/10.1016/j.jhydrol.2006.04.009>, 2006.
- Michael, N. A., Whittaker, A. C., Carter, A., and Allen, P. A.: Volumetric budget and grain-size fractionation of a geological sediment routing system: Eocene Escanilla Formation, south-central Pyrenees, *Geol. Soc. Am. Bull.*, 126, 585–599, <https://doi.org/10.1130/B30954.1>, 2014.
- Mouchené, M., van der Beek, P., Carretier, S., and Moutheau, F.: Autogenic versus allogenic controls on the evolution of a coupled fluvial megafan-mountainous catchment system: numerical modelling and comparison with the Lannemezan megafan system (northern Pyrenees, France), *Earth Surf. Dynam.*, 5, 125–143, <https://doi.org/10.5194/esurf-5-125-2017>, 2017.
- Paola, C., Heller, P. L., and Angevine, C. L.: The large-scale dynamics of grain-size variation in alluvial basins, 1: Theory, *Basin Res.*, 4, 73–90, <https://doi.org/10.1111/j.1365-2117.1992.tb00145.x>, 1992.
- Pastor-Satorras, R. and Rothman, D. H.: Stochastic Equation for the Erosion of Inclined Topography, *Phys. Rev. Lett.*, 80, 4349–4352, <https://doi.org/10.1103/PhysRevLett.80.4349>, 1998.
- Perron, J. T. and Royden, L.: An integral approach to bedrock river profile analysis, *Earth Surf. Proc. Land.*, 38, 570–576, <https://doi.org/10.1002/esp.3302>, 2012.
- Pritchard, D., Roberts, G. G., White, N. J., and Richardson, C. N.: Uplift histories from river profiles, *Geophys. Res. Lett.*, 36, L24301, <https://doi.org/10.1029/2009GL040928>, 2009.
- Rigon, R., Rodriguez-Iturbe, I., Maritan, A., Giacometti, A., Tarboton, D. G., and Rinaldo, A.: On Hack’s law, *Water Resour. Res.*, 32, 3367–3374, 1996.
- Rohais, S., Bonnet, S., and Eschard, R.: Sedimentary record of tectonic and climatic erosional perturbations in an experimental coupled catchment-fan system, *Basin Res.*, 23, 1–15, <https://doi.org/10.1111/j.1365-2117.2011.00520.x>, 2011.
- Röhl, U., Westerhold, T., Bralower, T. J., and Zachos, J. C.: On the duration of the Paleocene-Eocene thermal maximum (PETM), *Geochem. Geophys. Geosy.*, 8, Q12002, <https://doi.org/10.1029/2007GC001784>, 2007.
- Romans, B. W., Castelltort, S., Covault, J. A., Fildani, A., and Walsh, J. P.: Environmental signal propagation in sedimentary systems across timescales, *Earth-Sci. Rev.*, 153, 7–29, <https://doi.org/10.1016/j.earscirev.2015.07.012>, 2016.
- Roy, S. G., Koons, P. O., Upton, P., and Tucker, G. E.: The influence of crustal strength fields on the patterns and rates of fluvial incision, *J. Geophys. Res.*, 120, 275–299, <https://doi.org/10.1002/2014JF003281>, 2015.
- Rudge, J. F., Roberts, G. G., White, N. J., and Richardson, C. N.: Uplift histories of Africa and Australia from linear inverse mod-

- eling of drainage inventories, *J. Geophys. Res.*, 120, 894–914, <https://doi.org/10.1002/2014JF003297>, 2015.
- Schmitz, B. and Pujalte, V.: Abrupt increase in seasonal extreme precipitation at the Paleocene-Eocene boundary, *Geology*, 35, 215–218, <https://doi.org/10.1130/G23261A.1>, 2007.
- Schwanghart, W. and Scherler, D.: Short Communication: Topo-Toolbox 2 – MATLAB-based software for topographic analysis and modeling in Earth surface sciences, *Earth Surf. Dynam.*, 2, 1–7, <https://doi.org/10.5194/esurf-2-1-2014>, 2014.
- Simpson, G.: Practical Finite Element Modeling in Earth Science using Matlab, Wiley-Blackwell, 2017.
- Simpson, G. and Castelltort, S.: Model shows that rivers transmit high-frequency climate cycles to the sedimentary record, *Geology*, 40, 1131–1134, <https://doi.org/10.1130/G33451.1>, 2012.
- Simpson, G. and Schlunegger, F.: Topographic evolution and morphology of surfaces evolving in response to coupled fluvial and hillslope sediment transport, *J. Geophys. Res.*, 108, 2300, <https://doi.org/10.1029/2002JB002162>, 2003.
- Sluijs, A., Schouten, S., Pagani, M., Woltering, M., Brinkhuis, H., Sanninghe Damsté, J. S., Dickens, G. R., Huber, M., Reichart, G. J., Stein, R., Mattheissen, J., Lourens, L. J., Pendleton, N., Backman, J., Moran, K., and the Expedition 302 scientists: Subtropical Arctic Ocean temperatures during the Palaeocene/Eocene thermal maximum, *Nature*, 411, 610–613, <https://doi.org/10.1038/nature04668>, 2006.
- Smith, T. R.: A theory for the emergence of channelized drainage, *J. Geophys. Res.*, 115, F02023, <https://doi.org/10.1029/2008JF001114>, 2010.
- Smith, T. R. and Bretherton, F. P.: Stability and conservation of mass in drainage basin evolution, *Water Resour. Res.*, 8, 1506–1529, <https://doi.org/10.1029/WR008i006p01506>, 1972.
- Smith, T. R., Merchant, G. E., and Birnir, B.: Transient attractors: towards a theory of the graded stream for alluvial and bedrock channels, *Comput. Geosci.*, 26, 541–580, [https://doi.org/10.1016/S0098-3004\(99\)00128-4](https://doi.org/10.1016/S0098-3004(99)00128-4), 2000.
- Snyder, N. P., Whipple, K. X., Tucker, E., and Merritts, D. J.: Landscape response to tectonic forcing: Digital elevation model analysis of stream profiles in the Mendocino triple junction region, northern California, *Geol. Soc. Am. Bull.*, 112, 1250–1263, [https://doi.org/10.1130/0016-7606\(2000\)112<1250:LRTTFD>2.0.CO;2](https://doi.org/10.1130/0016-7606(2000)112<1250:LRTTFD>2.0.CO;2), 2000.
- Tarboton, D. G., Bras, R. L., and Rodriguez-Iturbe, I.: Comment on “On the fractal dimension of stream network” by Paolo La Barbera and Renzo Rosso, *Water Resour. Res.*, 26, 2243–2244, <https://doi.org/10.1029/WR026i009p02243>, 1990.
- Temme, A. J. A. M., Armitage, J. J., Attal, M., van Gorp, W., Coulthard, T. J., and Schoorl, J. M.: Choosing and using landscape evolution models to inform field stratigraphy and landscape reconstruction studies, *Earth Surf. Proc. Land.*, 42, 2167–2183, <https://doi.org/10.1002/esp.4162>, 2017.
- Tinkler, K. J. and Whol, E. E.: Rivers over Rock: fluvial processes in bedrock channels, American Geophysical Union, Washington, USA, *Geophys. Monog. Series*, 107, <https://doi.org/10.1029/GM107>, 1998.
- Tucker, G. E. and Whipple, K. X.: Topographic outcomes predicted by stream erosion models: Sensitivity analysis and intermodel comparison, *J. Geophys. Res.*, 107, 2179, <https://doi.org/10.1029/2001JB000162>, 2002.
- Valla, P. G., van der Beek, P. A., and Lague, D.: Fluvial incision into bedrock: Insights from morphometric analysis and numerical modeling of gorges incising glacial hanging valleys (Western Alps, France), *J. Geophys. Res.*, 116, F02010, <https://doi.org/10.1029/2008JF001079>, 2010.
- van der Beek, P. and Bishop, P.: Cenozoic river profile development in the Upper Lachlan catchment (SE Australia) as a test of quantitative fluvial incision models, *J. Geophys. Res.*, 108, 2309, <https://doi.org/10.1029/2002JB002125>, 2003.
- Whipple, K. X.: Fluvial landscape response time: how plausible is steady-state denudation, *Am. J. Sci.*, 301, 313–325, 2001.
- Whipple, K. X.: Bedrock rivers and the geomorphology of active orogens, *Ann. Rev. Earth Planet. Sci.*, 32, 151–185, <https://doi.org/10.1146/annurev.earth.32.101802.120356>, 2004.
- Whipple, K. X. and Meade, B. J.: Orogen response to changes in climatic and tectonic forcing, *Earth Planet. Sci. Lett.*, 243, 218–228, <https://doi.org/10.1016/j.epsl.2005.12.022>, 2006.
- Whipple, K. X. and Tucker, G. E.: Dynamics of the stream-power river incision model: Implications for height limits of mountain ranges, landscape response times, and research needs, *J. Geophys. Res.*, 104, 17661–17674, 1999.
- Whipple, K. X. and Tucker, G. E.: Implications of sediment-flux-dependent river incision models for landscape evolution, *J. Geophys. Res.*, 107, <https://doi.org/10.1029/2000JB000044>, 2002.
- Whittaker, A. C. and Boulton, S. J.: Tectonic and climatic controls on knickpoint retreat rates and landscape response times, *J. Geophys. Res.*, 117, F02024, <https://doi.org/10.1029/2011JF002157>, 2012.
- Whittaker, A. C., Cowie, P. A., Attal, M., Tucker, G. E., and Roberts, G. P.: Bedrock channel adjustment to tectonic forcing: Implications for predicting river incision rates, *Geology*, 35, 103–106, <https://doi.org/10.1130/G23106A.1>, 2007.
- Whittaker, A. C., Attal, M., Cowie, P. A., Tucker, G. E., and Roberts, G.: Decoding temporal and spatial patterns of fault uplift using transient river long-profiles, *Geomorphology*, 100, 506–526, <https://doi.org/10.1016/j.geomorph.2008.01.018>, 2008.
- Whittaker, A. C., Duller, R. A., Springett, J., Smithells, R. A., Whitchurch, A. L., and Allen, P. A.: Decoding downstream trends in stratigraphic grain size as a function of tectonic subsidence and sediment supply, *Geol. Soc. Am. Bull.*, 123, 1363–1382, 2011.
- Willett, S. D., McCoy, S. W., Perron, J. T., Goren, L., and Chen, C.: Dynamic Reorganization of River Basins, *Science*, 343, 6175, <https://doi.org/10.1126/science.1248765>, 2014.
- Willgoose, G., Bras, R. L., and Rodriguez-Iturbe, I.: A physical explanation of an observed link area-slope relationship, *Water Resour. Res.*, 27, 1697–1702, 1991.
- Wobus, C., Whipple, K. X., Kirby, E., Snyder, N., Johnson, J., Spyropoulos, K., Crosby, B., and Sheehan, D.: Tectonics from topography: Procedures, promise, and pitfalls, *Geol. Soc. Am. Sp.*, 398, 55–74, 2006.



Short communication: flow as distributed lines within the landscape

John J. Armitage

Dynamique des Fluides Géologiques, Institut de Physique du Globe de Paris, Paris, France

Correspondence: John J. Armitage (armitage@ipgp.fr)

Received: 13 June 2018 – Discussion started: 27 June 2018

Revised: 20 December 2018 – Accepted: 21 December 2018 – Published: 17 January 2019

Abstract. Landscape evolution models (LEMs) aim to capture an aggregation of the processes of erosion and deposition within the earth's surface and predict the evolving topography. Over long timescales, i.e. greater than 1 million years, the computational cost is such that numerical resolution is coarse and all small-scale properties of the transport of material cannot be captured. A key aspect, therefore, of such a long timescale LEM is the algorithm chosen to route water down the surface. I explore the consequences of two end-member assumptions of how water flows over the surface of an LEM – either down a single flow direction (SFD) or down multiple flow directions (MFDs) – on model sediment flux and valley spacing. I find that by distributing flow along the edges of the mesh cells, node to node, the resolution dependence of the evolution of an LEM is significantly reduced. Furthermore, the flow paths of water predicted by this node-to-node MFD algorithm are significantly closer to those observed in nature. This reflects the observation that river channels are not necessarily fixed in space, and a distributive flow captures the sub-grid-scale processes that create non-steady flow paths. Likewise, drainage divides are not fixed in time. By comparing results between the distributive transport-limited LEM and the stream power model “Divide And Capture”, which was developed to capture the sub-grid migration of drainage divides, I find that in both cases the approximation for sub-grid-scale processes leads to resolution-independent valley spacing. I would, therefore, suggest that LEMs need to capture processes at a sub-grid-scale to accurately model the earth's surface over long timescales.

1 Introduction

It is known that resolution impacts landscape evolution models (LEMs) (Schoorl et al., 2000). The resolution dependence of LEMs is caused by how run-off is routed down the model surface. It has been demonstrated that either distributing flow down all slopes (multiple flow direction, MFD) or simply allowing flow to descend down the steepest slope (single flow direction, SFD), gives different outcomes for landscape evolution models (Schoorl et al., 2000; Pelletier, 2004). It has been noted that landscape potentially has a characteristic wavelength for the spacing of valleys (Perron et al., 2008). Therefore, a landscape evolution model should be able to reproduce such regular topographic features independently of the model resolution. For a model of channelized flow, it was, however, found that the routing of run-off led to a resolution dependence in the valley spacing, which could be overcome

by the addition of a parameterized flow width that was less than the numerical grid spacing (Perron et al., 2008).

There is a potential problem with parameterizing the flow width to be fixed at a sub grid level. The response time of LEMs to a change in external forcing is strongly dependent on the surface run-off (Armitage et al., 2018). This means that the model response time becomes likewise dependent on the chosen flow width. Ideally, the LEM would be independent of grid resolution without introducing a predefined length scale that impacts the model response.

Water is the primary agent of landscape erosion. There are multiple pathways within the hydrological cycle from evaporation, transpiration, and groundwater flow; however, for many landscapes the river network is the primary route through which water flows downslope. Mean river width varies from 5 km to a few metres (Allen and Pavelsky, 2018).

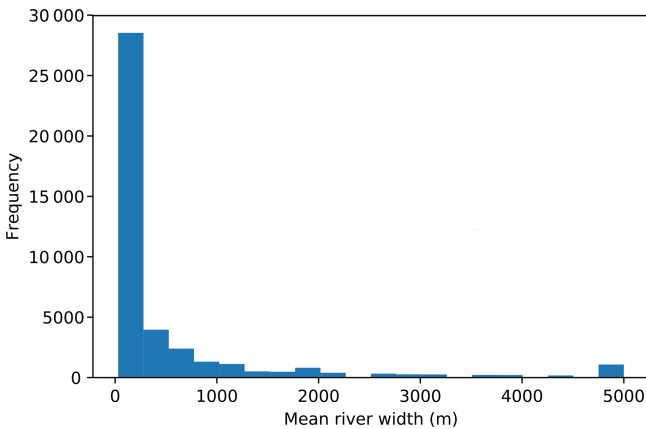


Figure 1. Distribution of mean river width taken from the Global River Widths from Landsat (GRWL) Database (Allen and Pavelsky, 2018).

The very wide rivers, greater than 1 km, are, however, outliers within this global data set, with the median of the distribution of mean river width being 124 m, with the upper quartile at 432 m (Fig. 1). In LEMs developed for understanding long-term landscape evolution, the large timescales necessitate large spatial scales, where a single grid cell can be 1 km wide or more (Temme et al., 2017). A spatial resolution of cells larger than a few metres becomes necessary when modelling at the scale of a continent (e.g. Salles et al., 2017). This means that flow has a width at a subgrid level.

If the width of the flow path for run-off is narrower than can be reasonably modelled, then can the flow paths be treated as lines, from model node to node (Fig. 2), where water collects along these lines? To explore this idea and understand LEM sensitivity to resolution, I wish to explore how a simple LEM evolves under four scenarios (Fig. 2): (1) simple SFD from cell area to cell area, (2) an MFD version of this cell-to-cell algorithm, (3) a node-to-node SFD, and (4) a node-to-node MFD.

2 A landscape evolution model

In this study I will assume landscape evolution can be effectively simulated with the classic set of diffusive equations described in Smith and Bretherton (1972):

$$\frac{\partial z}{\partial t} = \nabla \cdot [(\kappa + cq_w^n) \nabla z] + U, \quad (1)$$

where κ is a linear diffusion coefficient, c is the fluvial diffusion coefficient, q_w is the water flux, n is the water flux exponent, and U is uplift. This heuristic concentrative–diffusive equation is capable of generating realistic landscape morphology, with the slope–area relationships commonly observed (Simpson and Schlunegger, 2003; Armitage et al., 2018). Strictly, it assumes that there is always a layer of material to be transported by surface run-off, and as such it

can be classed as a transport-limited model. It accounts for both erosion and deposition and is, therefore, appropriate for modelling landscape evolution beyond mountain ranges and into the depositional setting (see models such as DIONISOS; Granjeon and Joseph, 1999). It differs from mixed erosion and deposition models such as Kooi and Beaumont (1994) and Davy and Lague (2009) because those models split the divergence of the sediment flux into two terms: a rate of erosion and a rate of deposition. Here, instead I assume that the sediment flux is a function of water flux and slope.

Equation (1) is solved with a finite-element scheme written using Python and the FEniCS libraries (I will call the code “fLEM”; see the “Code availability” section). The equations are solved on a Delaunay mesh, where the mesh is made up of predominantly equilateral triangles with an opening angle of 60°. Model boundary conditions are initially of fixed elevation on the sides normal to the x axis and a zero gradient on the sides normal to the y axis. The model aspect ratio is 4 to 1. Uplift is fixed at $U = 10^{-4} \text{ m yr}^{-1}$, the linear diffusion coefficient is $\kappa = 1 \text{ m}^2 \text{ yr}^{-1}$, the fluvial diffusion coefficient is $c = 10^{-4} (\text{m}^2 \text{ yr}^{-1})^{n-1}$, and the water flux exponent is $n = 1.5$.

Water can be routed from cell to cell, where precipitation is collected over the area of each cell, sent downwards, and accumulates. In this cell-to-cell configuration the water flux has units of length squared per unit time and is given by

$$q_w[\text{cell}] = \frac{\alpha a}{l_s}, \quad (2)$$

where α is precipitation rate, a is the cell area, and l_s is the length from cell centre to cell centre down the steepest slope (Fig. 2a and b). This gives a water discharge per unit length, which has the advantage of not having to explicitly state the sub-grid width of the flow (Simpson and Schlunegger, 2003). However, implicitly this implies that the flow is over the width of a cell. An alternative is to route water from node to node along cell edges and for it to accumulate. I assume that along the length of each cell edge water can be added to the flow line, assuming that the input is linearly related to the length of the flow line,

$$q_w[\text{node}] = \alpha l, \quad (3)$$

where l is the length of the edge that joins the upslope node to the downslope node (Fig. 2c and d). This means that the cell area is ignored and instead water enters the flow path uniformly along its length and accumulates downslope.

Equation (3) makes the assumption that water accumulates as a function of length. Water flux is observed to be related to catchment area: $Q_w \propto A^{0.8}$ (Syvitski and Milliman, 2007). The catchment length, l , is then related to area by $l \propto A^{1/p}$, where $1.4 < p < 2.0$ (Armitage et al., 2018). At the lower end of the range, this gives $Q_w \propto l^{1.12}$, suggesting that accumulating water as a linear function of flow length is a reasonable simplification. A knock-on effect of this assumption is

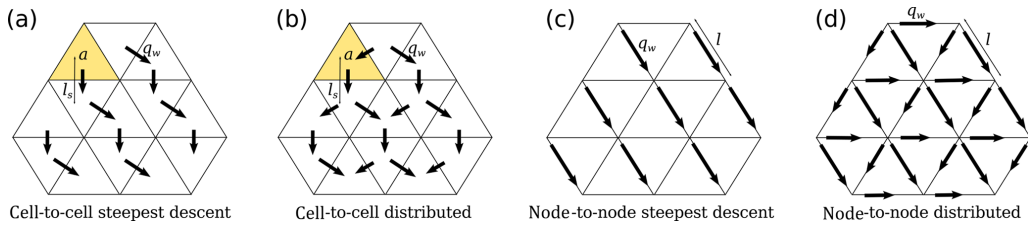


Figure 2. Diagram of flow routing from cell to cell and node to node for either a single flow direction (SFD) or a multiple flow direction (MFD) algorithm weighted by the relative gradient.

that the magnitude of the water flux predicted for the node-to-node routing is less than that of the cell-to-cell, as in the latter water is accumulated over cell areas which is naturally larger than the cells' edges.

Both Eqs. (2) and (3) do not attempt to capture the interaction between water flux and river width; rather, these are two methods to approximate run-off within a coarse numerical grid. For both the cell-to-cell and node-to-node methods the flow can then be routed down a SFD or routed down MFDs weighted by the relative gradient, as in, for example, Schoorl et al. (2000). I run the numerical model with a uniform precipitation rate of $\alpha = 1 \text{ m yr}^{-1}$.

Equation (1) is made dimensionless following Simpson and Schlunegger (2003) using the linear diffusion timescale and the model length in the x direction, L . This means that Eq. (1) can be rewritten as

$$\frac{\partial \tilde{z}}{\partial \tilde{t}} = \nabla \left[(1 + D\tilde{q}_w^n) \tilde{\nabla} \tilde{z} \right] + U \quad (4)$$

and

$$\tilde{\nabla} \cdot \left(\frac{\tilde{\nabla} \tilde{z}}{|\tilde{\nabla} \tilde{z}|} \right) \tilde{q}_w = -1, \quad (5)$$

where $x = \tilde{x}L$, $y = \tilde{y}L$, $z = \tilde{z}L$, $t = \tilde{t}L^2/\kappa$, $q = \tilde{q}\alpha L$, and

$$D = \frac{c\alpha^n L^n}{\kappa}. \quad (6)$$

3 The effect of model resolution

At a low model resolution, 512×128 cells, all four methods of flow routing give a similar landscape morphology after 5 Myr of model evolution (Figs. 3 and 4). However, elevations are significantly lower for the cell-to-cell flow routing model as the water flux term is lower for the node-to-node routing algorithm (Figs. 3 and 4). As the resolution is increased to 2048×512 cells, the landscape morphology starts to diverge. For the cell-to-cell SFD algorithm, the landscape shows more small-scale branching, as previously discussed by Braun and Sambridge (1997) (Fig. 3b and c). For the SFD algorithm it can be seen that the high-resolution model has multiple peaks along the ridges (Fig. 3b). This roughness to

the topography is removed if the flow is distributed downslope from cell to cell (MFD; Fig. 3d).

For the node-to-node SFD algorithm, the increase in resolution has led to significant branching of the valleys, which is clearly visible when the water flux is plotted (Fig. 4a and b). For the node-to-node MFD algorithm, the morphology and distribution of water flux are similar for both the low and high resolution (Fig. 4c and d); yet as with the cell-to-cell algorithm, increased resolution leads to increased branching of the network. The two MFD models give a smoother topography, as by distributing flow, local carving of the landscape is reduced.

To understand better how increasing resolution impacts the model evolution the total sediment flux eroded from the model domain is plotted against time, and the final valley spacing is calculated (Figs. 5 and 6). To calculate the valley spacing I take horizontal swaths of the spatial distribution of water flux. For each swath profile a peak finding algorithm (Negri and Vestrí, 2017) is used to find the distance from peak to peak in water flux. This distance is then averaged over the 100 swath profiles and over 10 model runs to give the minimum, lower quartile, median, upper quartile, and maximum valley wavelength (Figs. 5 and 6).

For the cell-to-cell SFD it can be seen that the evolution of the model is resolution dependent, as the wind-up time reduces as resolution is increased from 64 to 512 cells along the y axis (Fig. 5a). Furthermore, the mean valley spacing reduces with increasing resolution (Fig. 5b). This behaviour is not ideal, as it means that model behaviour to perturbations in forcing might become resolution dependent. For the MFD wind-up times remain resolution dependent, while the mean valley spacing is similar for the four different resolutions (Fig. 5c and d).

The node-to-node SFD algorithm is no better than the cell-to-cell SFD. In this case wind-up time is resolution dependent, and the valley spacing increases with increasing resolution (Fig. 6a and b). For the node-to-node SFD, at a resolution of 256 cells or less along the y axis, there is an instability in the sediment flux output. This is due to the flow tipping between adjacent nodes due to small differences in relative elevation after each time iteration. This unstable behaviour disappears for the higher resolution of 512 cells along the y axis (Fig. 6a).

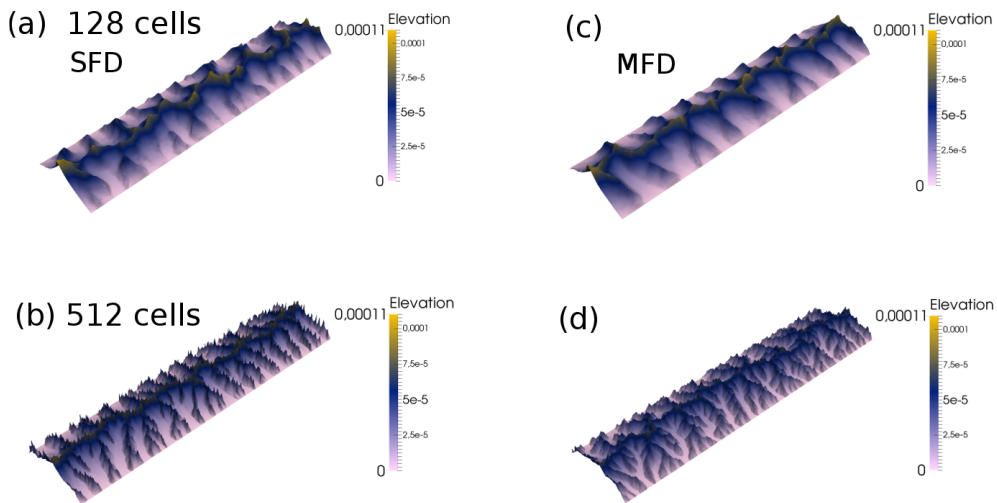


Figure 3. Dimensionless elevation from the cell-to-cell flow routing landscape evolution model with different flow routing algorithms at different numerical resolutions after a dimensionless runtime of 1.563×10^{-6} (5 Myr), with an aspect ratio of 4×1 . **(a)** Cell-to-cell single flow direction (SFD) algorithm with a resolution of 512×128 cells. **(b)** The same model but with a resolution of 2048×512 cells. Panels **(c)** and **(d)**: cell-to-cell multiple flow direction (MFD) algorithm.

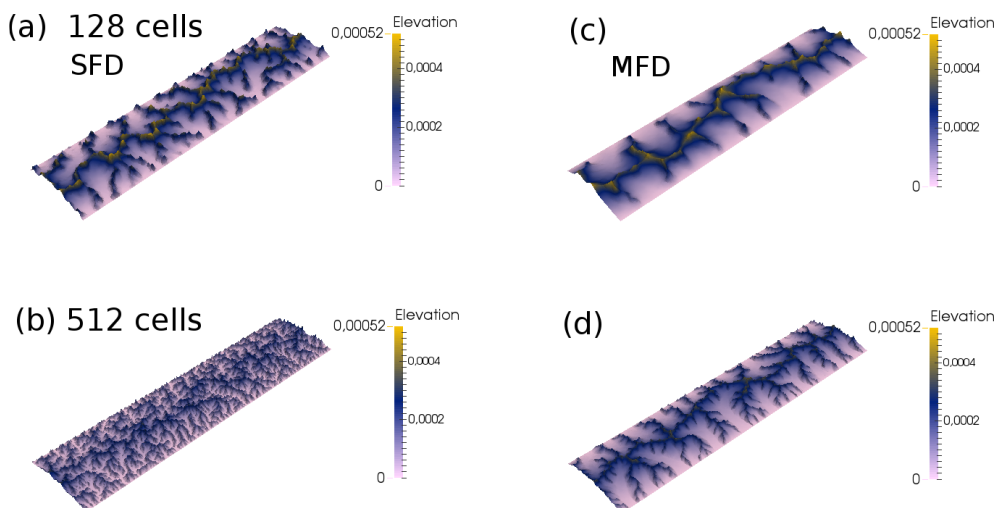


Figure 4. Dimensionless elevation from the node-to-node flow routing landscape evolution model with different flow routing algorithms at different numerical resolutions after a dimensionless runtime of 1.563×10^{-6} (5 Myr), with an aspect ratio of 4×1 . **(a)** Node-to-node single flow direction (SFD) algorithm with a resolution of 512×128 cells. **(b)** The same model but with a resolution of 2048×512 cells. Panels **(c)** and **(d)**: node-to-node multiple flow direction (MFD) algorithm.

It is only when node-to-node MFD is used that the LEM becomes significantly less resolution dependent (Fig. 6c and d). For the node-to-node MFD the time evolution of sediment flux is similar for all resolutions, and the valley spacing is similar as resolution is increased. The steady-state sediment flux is, however, not completely stable (Fig. 6c). This is due to the migration of the flow across the valley floors created within the model topography (Fig. 7). Even once a balance has been achieved between erosion and uplift, small lateral changes in elevation can be seen to create a negative to positive change in elevation of a few metres between time

iterations, where the time step is 100 years (Fig. 7b). This is associated with an equivalent change in water flux (Fig. 7c).

Changing the flow routing algorithm changes the model wind-up time. This is because the rate at which the network grows and the magnitude of the water flux are affected by the choice of flow routing. The response time of the model is proportional to the water flux raised to the power n (Armitage et al., 2018). Therefore, if the drainage network forms rapidly, as is the case for cell-to-cell routing, then the model wind-up is more rapid. For the node-to-node routing, it takes longer for the network to grow (Fig. 5). Furthermore, the

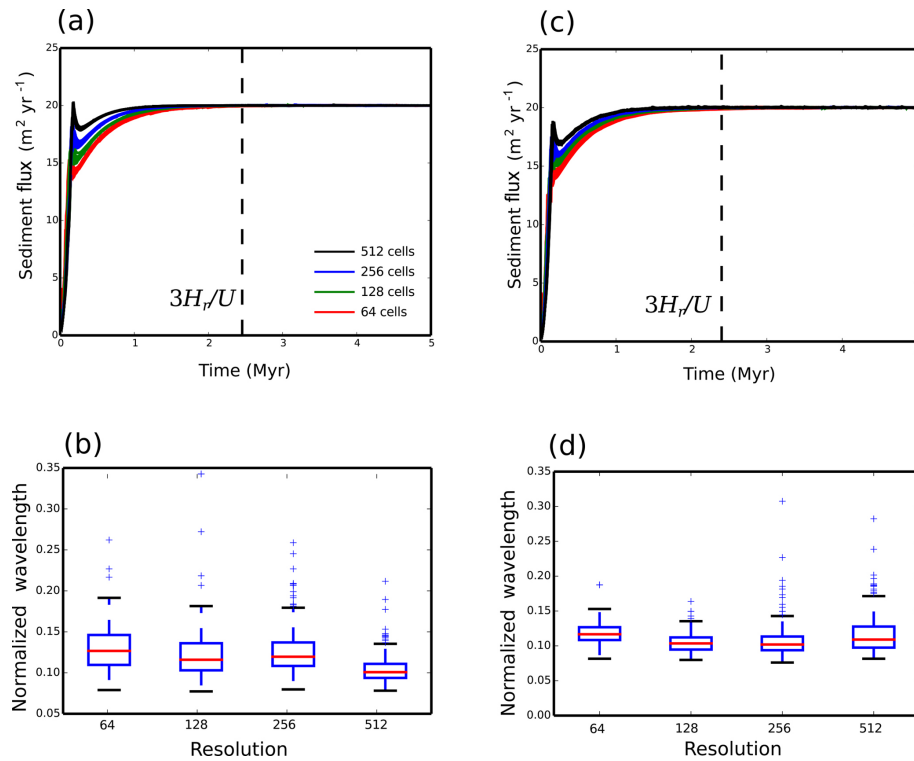


Figure 5. Dimensional sediment flux that exits the model domain and box-whisker plots of the dimensionless valley-to-valley wavelength for each model for different resolutions, where the number of cells along the y axis is shown. **(a)** Sediment flux and **(b)** valley-to-valley wavelength for the cell-to-cell SFD algorithm. **(c)** Sediment flux and **(d)** valley-to-valley wavelength for the cell-to-cell MFD algorithm. The dashed line in panels **(a)**, **(c)**, and **(e)** marks the time at which erosion balances uplift, given by $t \geq 3H_r/U$, where H_r is the relief height and U is the uplift rate (Howard, 1994).

MFD model is the slowest to evolve to a steady state, where the total sediment flux is balanced by the uplift (Fig. 6). I have chosen to focus on $n = 1.5$ as this value previously gave more realistic slope-area relationships at steady state (Armitage et al., 2018). However, it is interesting to note that growth of the network is a function of both the routing algorithm and the value of n .

4 Sub-grid-scale processes

The model that has the least resolution dependence is the node-to-node MFD (Figs. 4c and d and 6c and d). The difference between this model and the other three is that this version has the maximum possible flow directions available within my set-up. By treating flow paths as lines within the numerical grid, from any node there are six paths, which is twice as many as in the cell-to-cell MFD. This means that there is greater distribution of the flow and a reduced localizing of flow paths within the node-to-node distributed model. For SFD, increasing resolution, however, leads to multiple branches (Figs. 3b and 4b).

The grid cells in the models presented are large. At the highest resolution (2048 by 512 cells), the width of each triangle is of the order of 200 m if I was modelling a landscape

100 km wide. The model is, therefore, some approximation of local processes that give rise to the large-scale landscape. By distributing flow in multiple directions the model is in a sense approximating the hydrological processes that operate on a sub-grid-scale that give rise to the river network. The assumption of SFD is, however, too strong, and the sub-grid-scale processes are ignored.

The transport-limited model that I explore has certain limitations. In particular the valleys floors are wide and not representative of V-shaped valleys that would be expected from fluvial incision into bedrock (Fig. 4). In order to generate such valleys, a detachment-limited model, such as the stream power law, would be more appropriate. However, many stream power law models also suffer resolution dependence, as they typically use an SFD to route water (e.g. Braun and Sambridge, 1997; Braun and Willett, 2013). Pelletier (2010) looked at using MFD routing for the stream power law and found that there remained some spatial resolution dependence. The model of Pelletier (2010) used a rectangular grid and removed resolution issues by using a predictor–corrector algorithm to adjust for resolution effects. However, for the transport-limited model used here, I find that with a triangular grid the MFD routing is resolution independent without additional corrections. This is likely related to the fact that

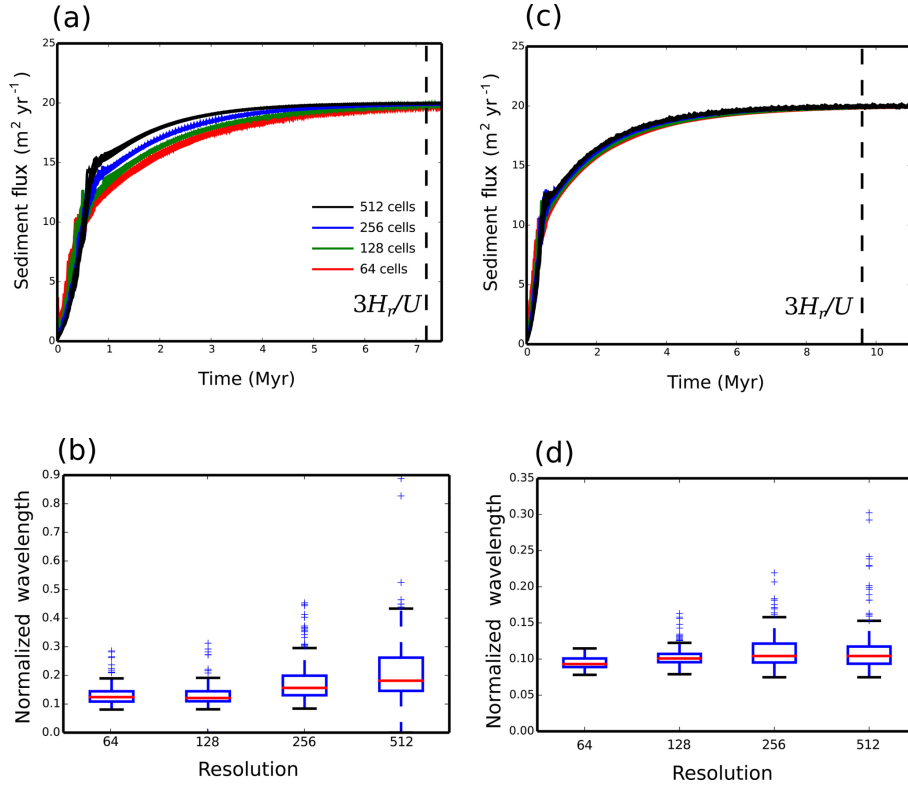


Figure 6. Dimensional sediment flux that exits the model domain and box–whisker plots of the dimensionless valley-to-valley wavelength for each model for different resolutions, where the number of cells along the y axis is shown. (a) Sediment flux and (b) the node-to-node SFD algorithm. (c) Sediment flux and (d) valley-to-valley wavelength for the node-to-node MFD algorithm. The dashed line in panels (a) and (c) marks the time at which erosion balances uplift, given by $t \geq 3H_r/U$, where H_r is the relief height and U is the uplift rate (Howard, 1994).

the length of each cell face is equal, while for rectangular cells the diagonal flow direction is longer than the cell faces. The implication is that for LEMs, a mesh that has cells with node-to-node spacing of equal length is preferable to a rectangular grid; however, this hypothesis will require further exploration.

MFD routing might approximate local processes that distribute flow. Another key sub-grid-scale process is the migration of drainage divides. A drainage divide is the opposite of the flow path, as it separates the valleys. The numerical model Divide And Capture (DAC) was developed to explore whether by using an analytical solution to the stream power law, the sub-grid-scale migration of drainage divides could be captured (Goren et al., 2014). DAC, therefore, uses a variant of a stream power law model; yet like the transport-limited model I present, DAC uses a triangular grid. However, DAC routes flow down the steepest route of descent (SFD). By exploring how model resolution impacts the main drainage divide, it was demonstrated that the inclusion of a sub-grid level calculation for water divides is crucial to remove otherwise spurious results (Goren et al., 2014).

By using the same set-up of a domain of 4 to 1 aspect ratio, uplift at 0.1 mm yr^{-1} , and a precipitation rate of 1 m yr^{-1} ,

I have explored how valley spacing varies as a function of resolution in the DAC model. DAC uses an adaptive mesh; therefore, the settings on how the re-meshing occurs needed to be altered to achieve an increase in the number of cells. By comparing two models at a different resolution (23 172 cells compared to 93 734), it can be seen that the median wavelength is very similar (Fig. 8).

The implication of the results I present here, and from the development of DAC, is that processes at a sub-grid level are of a crucial importance to model stability, and hence great care must be taken in generating reduced-complexity LEMs. At a small spatial and temporal scale, the landscape evolution model CAESAR-LISFLOOD (Coulthard et al., 2013), which has a rectangular grid, has been tested for different resolutions and is found to converge to the same solution at sufficiently high resolution. CAESAR-LISFLOOD uses a version of the shallow-water equations to solve for river flow, where water flows in four directions (Manhattan neighbours) and, therefore, uses an MFD rather than an SFD algorithm. Furthermore CAESAR-LISFLOOD operates on a resolution that is smaller than the width of an individual channel. This suggests that at a small spatial scales, where water depth is captured, a rectangular grid combined with an MFD al-

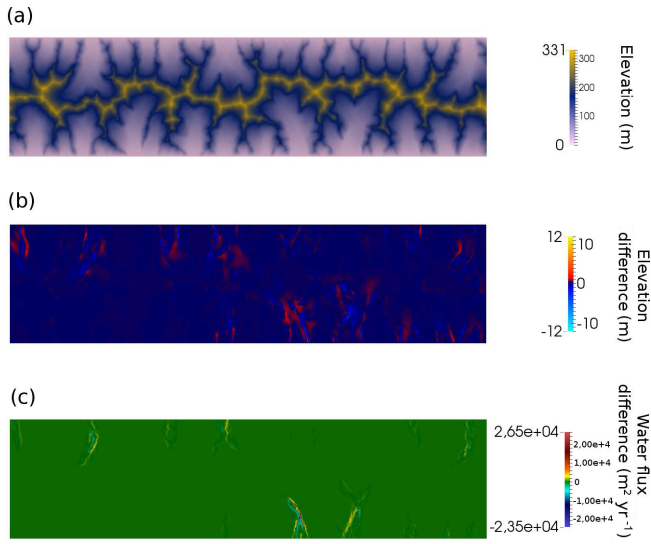


Figure 7. Final steady state of an example model run for the node-to-node MFD algorithm. **(a)** Final model elevation where the domain is 800 km long by 100 km wide and uplift is fixed at $U = 10^{-4} \text{ m yr}^{-1}$, the linear diffusion coefficient is $\kappa = 1 \text{ m}^2 \text{ yr}^{-1}$, the fluvial diffusion coefficient is $c = 10^{-4} (\text{m}^2 \text{ yr}^{-1})^{n-1}$, and the water flux exponent is $n = 1.5$. **(b)** Difference in elevation between the last two model time steps, where the time step duration is 100 years. **(c)** Difference in water flux between the last two model time steps.

gorithm is appropriate. Such a high-resolution model, however, cannot be run over periods greater than several millennia (e.g. Coulthard and van der Weil, 2013). Therefore, to explore how landscape evolves over millions of years, I suggest we must distribute flow across the model domain and use meshes of equal node-to-node spacing to avoid resolution dependence.

5 Steady state but not steady topography

In experiments of sediment transport it has been noted that when the catchment outlet is fixed in time, the landscape does not achieve a steady fixed topography (Hasbergen and Paola, 2000). It has been previously suggested that this behaviour can be replicated within an LEM by introducing a distributed routing algorithm (Pelletier, 2004). This modelling result has, however, been challenged by, for example, Perron et al. (2008), where it has been suggested that distributive flow routing algorithms in fact create a fixed topography at steady state. My model, however, is in agreement with the initial findings of Pelletier (2004). It has been previously noted that an MFD algorithm will give more diffuse valley bottoms compared to an SFD algorithm (Freeman, 1991). If landscapes are indeed never steady, then perhaps this unsteady nature is due to the diffuse sediment transport across wide flood plains, which feeds up into the drainage

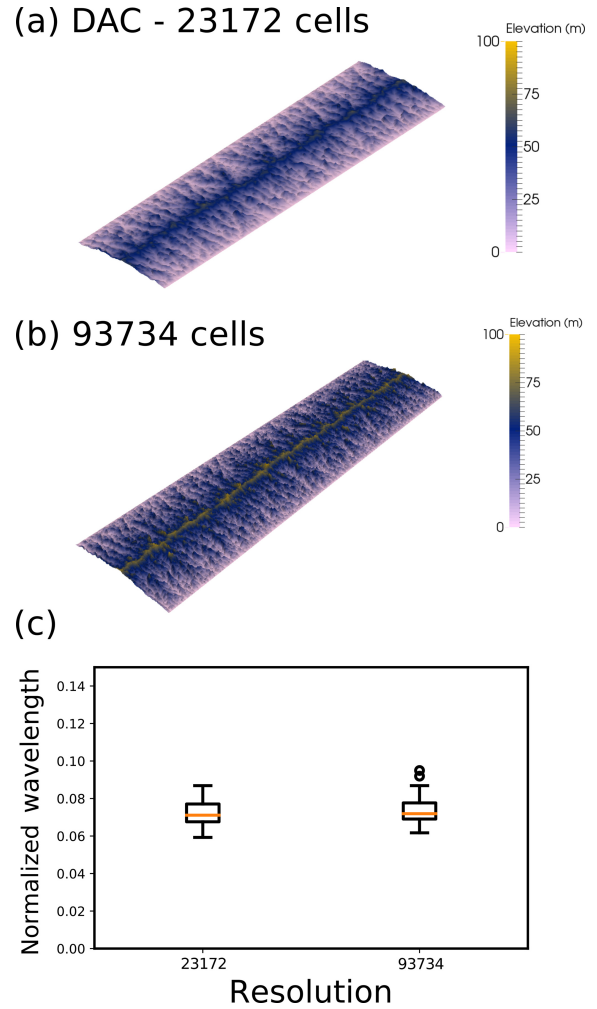


Figure 8. Comparison of two model results using Divide And Capture (DAC; Goren et al., 2014) at different resolutions. **(a)** Model steady state for an initial resolution of 51 by 204 cells, which after adaptive re-meshing increases to 23 172 cells. **(b)** Model steady state for an initial resolution of 101 by 404 cells, which after adaptive re-meshing increases to 93 734 cells. **(c)** Comparison of the wavelength of valleys for the two models, taken from 20 swaths 1.25 km wide from the left-hand boundary (see code availability for python scripts and DAC input files).

basins. It is, after all, within the valley floor that the distributed flow routing is the most unsteady (Fig. 7c).

In nature we observe that river networks are not fixed in space and time; rather, various processes lead to changing flow directions. To further explore how realistic the cell-to-cell SFD and node-to-node MFD algorithms are, I compare how the flow of water is predicted to evolve after a 20 kyr interval. The initial condition is a palaeo-DEM generated from ASTER data from the Ebro Basin, Spain (Fig. 9a). The river valleys have been filled and the landscape has been smoothed in an attempt to approximate this landscape in the late Pleistocene. This landscape is then allowed to evolve, assuming

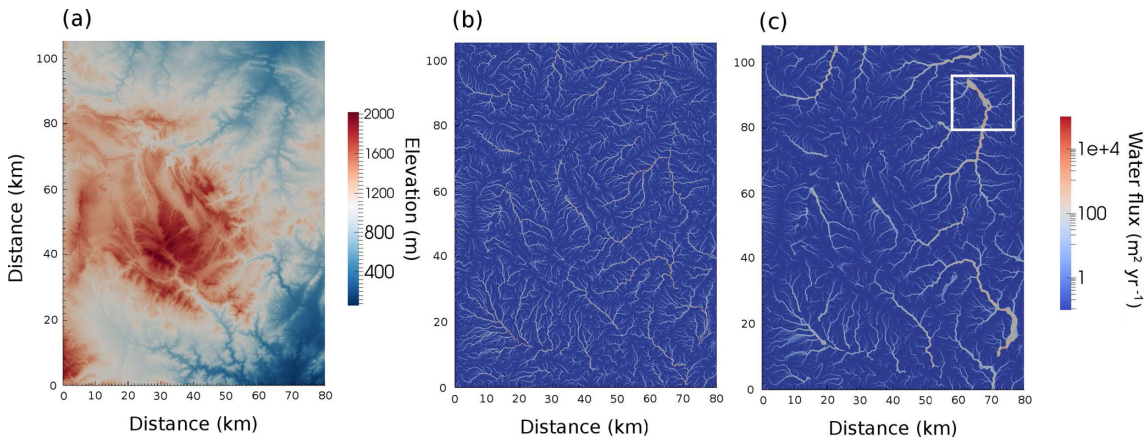


Figure 9. Application of the cell-to-cell SFD and node-node MFD algorithms to a palaeo-DEM (digital elevation model). **(a)** Palaeo-DEM created from ASTER data of the Ebro region of Spain. **(b)** Water flux after 20 kyr of model evolution assuming an SFD with a model resolution of 1024×1024 cells. Uplift is assumed to be very small at $10^{-5} \text{ m yr}^{-1}$, with a precipitation rate held constant at 0.1 m yr^{-1} . **(c)** Water flux for after 20 kyr for a model assuming the node-to-node MFD routing. The white box in the top right highlights a region of the Riu Bergantes catchment where the river is known to have shifted course during the Holocene.

a uniform uplift of $10^{-5} \text{ m yr}^{-1}$ and a precipitation rate held constant at 0.1 m yr^{-1} . I assume that $c = 10^{-5} (\text{m}^2 \text{ yr}^{-1})^{n-1}$, $\kappa = 10^{-1} \text{ m}^2 \text{ yr}^{-1}$, and $n = 1.5$. Under these conditions the landscape is left to evolve for 20 kyr (Fig. 9) with zero gradient boundaries on the east, west, and southern sides and fixed elevation on the northern boundary.

The initial condition is derived from a real landscape, and as the model allows for deposition in regions of low slope, both model routing algorithms do not create drainage patterns that fully connect to the boundaries (Fig. 9b and c). This problem of too much deposition within regions of low slope, such that the water flux does not reach the model boundaries, can be overcome with the application of a “carving” algorithm. As for example applied within the TopoToolbox Landscape Evolution Model (TTLEM), a minima imposition can be used to make sure rivers keep on flowing down through regions of low slope (Campforts et al., 2017). Such an additional algorithm will, however, affect how the network grows within the model, so for this example, I have left the routing algorithm to drain internally.

Despite this imperfection, the internal drainage patterns still prove to be insightful. The cell-to-cell SFD algorithm creates single paths for the flow of water (Fig. 9b). After the 20 kyr duration, it is observed that high water flux is concentrated within the deep valleys. The node-to-node MFD algorithm creates multiple flow paths that exit the mountain valleys and migrate onto the flood plains (Fig. 9c). Field studies of the Riu Bergantes have found that this catchment has experienced periods of significant sediment reworking, potentially related to climatic change (Whitfield et al., 2013). The region outlined with the white box in Fig. 9c shows evidence of terrace formation related to lateral movement of the Riu Bergantes during the Holocene (Whitfield et al., 2013). In particular, where the flow paths create a small island (see

Fig. 9c, centre of the white box), there is evidence from terrace deposits that the course of the Riu Bergantes has flipped from the eastern to the western side of this island. The cell-to-cell SFD cannot create this observed behaviour. Therefore, as well as creating landscape evolution that is not resolution dependent, the MFD algorithm creates landscape evolution that is, relative to the SFD, closer to that observed in nature.

6 Conclusions

In the study of the evolution of the earth’s surface we are increasingly turning to models that attempt to capture the complexities of surface processes. It is, however, clear that many LEMs are resolution dependent (Schoorl et al., 2000). The source of this resolution dependence is the numerical methods that we employ to route surface water. Unless we model landscape evolution at a spatial scale that is smaller than an individual river, we must somehow approximate this flow. By treating flow from node to node within the model mesh and by distributing flow down these lines, the LEM developed here is no longer resolution dependent. Furthermore the model evolution is closer to what we observe. Therefore, I would strongly suggest that for LEMs that operate at a scale larger than the resolution of a river, we must use MFDs.

Code availability. The code fLEM is available from the following repository: <https://bitbucket.org/johnjarmitage/flem/> (Armitage, 2019a). The valley wavelength Python script and DAC input files are available from the following repository: <https://bitbucket.org/johnjarmitage/dac-scripts/> (Armitage, 2019b). DAC was developed by Liran Goren; see https://gitlab.ethz.ch/esd_public/DAC_release/wikis/home (last access: 16 January 2019).

Competing interests. The author declares that there is no conflict of interest.

Acknowledgements. This work was inspired by a series of meetings organized by the Facsimile working group and by a visit to the Riu Bergantes catchment in Spain in October 2017. John Armitage is funded through the French Agence National de la Recherche, Accueil de Chercheurs de Haut Niveau call, grant “InterRift”. I would like to thank Kosuke Ueda and Liran Goren for help in running DAC. I would also like to thank Liran Goren and Andrew Wickert for their reviews.

Edited by: Jean Braun

Reviewed by: Liran Goren, Andrew Wickert, and one anonymous referee

References

- Allen, G. H. and Pavelsky, T. M.: Global extent of rivers and streams, *Science*, 361, 585–588, <https://doi.org/10.1126/science.aat0636>, 2018.
- Armitage, J.: fLEM, available at: <https://bitbucket.org/johnjarmitage/flem/>, last access: 16 January 2019a.
- Armitage, J.: dac-scripts, available at: <https://bitbucket.org/johnjarmitage/dac-scripts/>, last access: 16 January 2019b.
- Armitage, J. J., Whittaker, A. C., Zakari, M., and Campforts, B.: Numerical modelling of landscape and sediment flux response to precipitation rate change, *Earth Surf. Dynam.*, 6, 77–99, <https://doi.org/10.5194/esurf-6-77-2018>, 2018.
- Braun, J. and Sambridge, M.: Modelling landscape evolution on geological time scales: a new method based on irregular spatial discretization, *Basin Res.*, 9, 27–52, 1997.
- Braun, J. and Willett, S. D.: A very efficient $O(n)$, implicit and parallel method to solve the stream power equation governing fluvial incision and landscape evolution, *Geomorphology*, 180–181, 170–179, <https://doi.org/10.1016/j.geomorph.2012.10.008>, 2013.
- Campforts, B., Schwanghart, W., and Govers, G.: Accurate simulation of transient landscape evolution by eliminating numerical diffusion: the TTLEM 1.0 model, *Earth Surf. Dynam.*, 5, 47–66, <https://doi.org/10.5194/esurf-5-47-2017>, 2017.
- Coulthard, T. J. and Van de Wiel, M. J.: Climate, tectonics or morphology: what signals can we see in drainage basin sediment yields?, *Earth Surf. Dynam.*, 1, 13–27, <https://doi.org/10.5194/esurf-1-13-2013>, 2013.
- Coulthard, T. J., Neal, J. C., Ramirez, P. D. B., de Almedia, G. A. M., and Hancock, G. R.: Integrating the LISFLOOD-FP 2D hydrodynamic model with the CAESAR model: implications for modelling landscape evolution, *Earth Surf. Proc. Land.*, 38, 1897–1906, <https://doi.org/10.1002/esp.3478>, 2013.
- Davy, P. and Lague, D.: Fluvial erosion/transport equation of landscape evolution models revisited, *J. Geophys. Res.-Earth*, 114, F03007, <https://doi.org/10.1029/2008JF001146>, 2009.
- Freeman, T. G.: Calculating catchment area with divergent flow based on a regular grid, *Comput. Geosci.*, 17, 413–422, 1991.
- Goren, L., Willett, S. D., Herman, F., and Braun, J.: Coupled numerical-analytical approach to landscape evolution modelling, *Earth Surf. Proc. Land.*, 39, 522–545, <https://doi.org/10.1002/esp.3514>, 2014.
- Granjeon, D. and Joseph, P.: Concepts and applications of a 3-D multiple lithology, diffusive model in stratigraphic modelling, in: Numerical Experiments in Stratigraphy, edited by: Harbaugh, J. W., Watney, W. L., Rankey, E. C., Slingerland, R., and Goldstein, R. H., Society for Sedimentary Geology, 62, Special Publications, 197–210, 1999.
- Hasbergen, L. E. and Paola, C.: Landscape instability in an experimental drainage basin, *Geology*, 28, 1067–1070, 2000.
- Howard, A.: A detachment-limited model of drainage basin evolution, *Water Resour. Res.*, 30, 2261–2285, 1994.
- Kooi, H. and Beaumont, C.: Escarpment evolution on high-elevated rifted margins; insights derived from a surface-processes model that combines diffusion, advection and reaction, *J. Geophys. Res.*, 99, 12191–12209, 1994.
- Negri, L. H. and Vestrí, C.: peakutils: v1.1.0, <https://doi.org/10.5281/zenodo.887917>, 2017.
- Pelletier, J. D.: Persistent drainage migration in a numerical landscape evolution model, *Geophys. Res. Lett.*, 31, L20501, <https://doi.org/10.1029/2004GL020802>, 2004.
- Pelletier, J. D.: Minimizing the grid-resolution dependence of flow-routing algorithms for geomorphic applications, *Geomorphology*, 122, 91–98, <https://doi.org/10.1016/j.geomorph.2010.06.001>, 2010.
- Perron, J. T., Dietrich, W. E., and Kirchner, J. W.: Controls on the spacing of first-order valleys, *J. Geophys. Res.*, 113, F04061, <https://doi.org/10.1029/2007JF000977>, 2008.
- Salles, T., Flament, N., and Muller, D.: Influence of mantle flow on the drainage of eastern Australia since the Jurasic Period, *Geochem. Geophy. Geosy.*, 18, 280–305, <https://doi.org/10.1002/2016GC006617>, 2017.
- Schoorl, J. M., Sonneveld, M. P. W., and Veldkamp, A.: Three-dimensional landscape process modelling: the effect of DEM resolution, *Earth Surf. Proc. Land.*, 25, 1025–1034, 2000.
- Simpson, G. and Schlunegger, F.: Topographic evolution and morphology of surfaces evolving in response to coupled fluvial and hillslope sediment transport, *J. Geophys. Res.*, 108, 2300, <https://doi.org/10.1029/2002JB002162>, 2003.
- Smith, T. R. and Bretherton, F. P.: Stability and conservation of mass in drainage basin evolution, *Water Resour. Res.*, 8, 1506–1529, <https://doi.org/10.1029/WR008i006p01506>, 1972.
- Syvitski, J. P. and Milliman, J. D.: Geology, geography, and humans battle for dominance over the delivery of fluvial sediment to the coastal ocean, *J. Geol.*, 115, 1–19, <https://doi.org/10.1086/509246>, 2007.
- Temme, A. J. A. M., Armitage, J. J., Attal, M., van Gorp, W., Coulthard, T. J., and Schoorl, J. M.: Choosing and using landscape evolution models to inform field stratigraphy and landscape reconstruction studies, *Earth Surf. Proc. Land.*, 42, 2167–2183, <https://doi.org/10.1002/esp.4162>, 2017.
- Whitfield, R. G., Macklin, M. G., Brewer, P. A., Lang, A., Mauz, B., and Whitfield, E.: The nature, timing and controls of the Quaternary development of the Rio Bergantes, Ebro basin, northeast Spain, *Geomorphology*, 196, 106–121, <https://doi.org/10.1016/j.geomorph.2012.04.014>, 2013.

Chapitre B. Example Publications Part 2 : Surface

Bibliographie

- Allen, P. A. and Armitage, J. J. (2012). Cratonic basins. In Busby, C. and Azor, A., editors, *Syntectonic Basin Development, Active to Ancient : Recent Advances*, chapter 30, pages 602–620. Wiley-Blackwell, Oxford. [5](#)
- Andrés-Martinez, M., Pérez-Gussinyé, M., Armitage, J. J., and Phipps Morgan, J. (2019). Thermomechanical implications of sediment transport for the architecture and evolution of continental rifts and margins. *Tectonics*, 38 :641–665. doi : 10.1029/2018TC00534. [5](#)
- Armitage, J. J. (2019). Short communication : flow as distributed lines within the landscape. *Earth Surface Dynamics*, 7 :67–75. doi : 10.5194/esurf-7-67-2019. [19](#), [26](#), [27](#)
- Armitage, J. J. and Allen, P. A. (2010). Cratonic basins and the long-term subsidence history of continental interiors. *Journal of the Geological Society, London*, 167 :61–70. doi :10.1144/0016-76492009-108. [5](#), [24](#)
- Armitage, J. J., Allen, P. A., Burgess, P. M., Hampson, G. J., Whittaker, A. C., Duller, R. A., and Michael, N. A. (2015a). Physical stratigraphic model for the Eocene Escanilla sediment routing system : Implications for the uniqueness of sequence stratigraphic architectures. *Journal of Sedimentary Research*, 85 :1510–1524. doi : 10.2110/jsr.2015.97. [10](#), [14](#), [20](#), [24](#)
- Armitage, J. J., Burgess, P. M., Hampson, G. J., and Allen, P. A. (2018a). Deciphering the origin of cyclical gravel front and shoreline progradation and retrogradation in the stratigraphic record. *Basin Research*, 30(15-35). doi : 10.1111/bre.12203. [20](#), [24](#)
- Armitage, J. J. and Collier, J. S. (2018). The thermal structure of volcanic passive margins. *Petroleum Geoscience*, 24 :393–40. doi : 10.1144/petgeo2016-101. [6](#), [10](#)
- Armitage, J. J., Collier, J. S., and Minshull, T. A. (2010). The importance of rift history for volcanic margin formation. *Nature*, 465 :913–917. doi :10.1038/nature09063. [9](#), [23](#)
- Armitage, J. J., Collier, J. S., Minshull, T. A., and Henstock, T. J. (2011a). Thin oceanic crust and flood basalts : India-Seychelles breakup. *Geochemistry Geophysics Geosystems*, 12(Q0AB07). doi :10.1029/2010GC003316. [9](#), [10](#), [23](#)
- Armitage, J. J., Duller, R. A., and Schmalholz, S. M. (2014). The influence of long-wavelength tilting and climatic change on sediment accumulation. *Lithosphere*, 6 :303–318. doi : 10.1130/L343.1. [5](#)
- Armitage, J. J., Duller, R. A., Whittaker, A. C., and Allen, P. A. (2011b). Transformation of tectonic and climatic signals from source to sedimentary archive. *Nature Geoscience*, 4 :231–235. doi : 10.1038/ngeo1087. [20](#), [23](#), [24](#)
- Armitage, J. J., Ferguson, D. J., Goes, S., Hammond, J. O. S., Calais, E., Rychert, C. A., and Harmon, N. (2015b). Upper mantle temperature and the onset of extension and break-up in Afar, Africa. *Earth and Planetary Science Letters*, 418 :78–90. doi : 0.1016/j.epsl.2015.02.039. [5](#), [9](#), [24](#)

BIBLIOGRAPHIE

- Armitage, J. J., Ferguson, D. J., Petersen, K. D., and Creyts, T. T. (2019). The importance of Icelandic ice sheet growth and retreat on mantle CO₂ flux. *Geophysical Research Letters*, 46 :6451–6458. doi : 10.1029/2019GL081955. 7, 9, 15
- Armitage, J. J., Henstock, T. J., Minshull, T. A., and Hopper, J. R. (2008). Modelling the composition of melts formed during continental break-up of the North Atlantic. *Earth Planetary Science Letters*, 269 :248–258. doi : 10.1016/j.epsl.2008.02.024. 7, 9
- Armitage, J. J., Henstock, T. J., Minshull, T. A., and Hopper, J. R. (2009). Lithospheric controls on the rifting of continents at slow rates of extension : Application to the north atlantic. *Geochemistry Geophysics Geosystems*, 10(Q06018). doi : 10.1029/2009GC002404. 9, 10
- Armitage, J. J., Jaupart, C., Fourel, L., and Allen, P. A. (2013). The instability of continental passive margins and its effect on continental topography and heat flow. *Journal of Geophysical Research*, 118(4) :1817–1836. doi :10.1002/jgrb.50097. 5, 6, 24
- Armitage, J. J., Petersen, K. D., and Pérez-Gussinyé, M. (2018b). The role of crustal strength in controlling magmatism and melt chemistry during rifting break-up. *Geochemistry Geophysics Geosystems*, 19 :534–550. doi : 10.1002/2017GC007326. 7, 9, 11, 13
- Armitage, J. J., Warner, N. H., Goddard, K., and Gupta, S. (2011c). Timescales of alluvial fan development by precipitation on Mars. *Geophysical Research Letters*, 38(L17203). doi : 10.1029/2011GL048907. 24
- Armitage, J. J., Whittaker, A. C., Zakari, M., and Campforts, B. (2018c). Numerical modelling landscape and sediment flux response to precipitation rate change. *Earth Surface Dynamics*, 6 :77–99. doi : 10.5194/esurf-6-77-2018. 19
- Bastow, I. D., Stuart, G. W., Kendall, J. M., and Ebinger, C. J. (2005). Upper-mantle seismic structure in a region of incipient continental breakup : northern Ethiopian rift. *Geophysical Journal International*, 162 :479–493. doi : 10.1111/j.1365-246X.2005.02666.x. 5
- Bates, P. D., Horritt, M. S., and Fewtrell, T. (2010). A simple inertial formulation of the shallow water equations for efficient two-dimensional flood inundation modelling. *Journal of Hydrology*, 236 :54–77. doi : 10.1016/S0022-1694(00)00278-X. 26
- Beven, K. J. and Kirkby, M. J. (1979). A physically based, variable contributing area model of basin hydrology. *Hydrological Sciences Bulletin*, 24 :43–69. doi : 10.1080/02626667909491834. 26
- Brooke, S. A. S., Whittaker, A. C., Armitage, J. J., D'Arcy, M., and Watkins, S. E. (2018). Quantifying sediment transport dynamics on alluvial fans from spatial and temporal changes in grain size, Death Valley, California. *Journal of Geophysical Research – Earth Surface*, 123 :2039–2067. doi : 10.1029/2018JF004622. 23
- Brun, J. P. (1999). Narrow rifts versus wide rifts : inferences for the mechanics of rifting from laboratory experiments. *Philisophical Transactions of the Royal Society London A*, 357(1753) :695–712. 9
- Brune, S., Corti, G., and Ranalli, G. (2017). Controls of inherited lithospheric heterogeneity on rift linkage : Numerical and analogue models of interaction between the Kenyan and Ethiopian rifts across the turkana depression. *Tectonics*. doi : 10.1002/2017TC004739. 9
- Buck, W. R. (1991). Modes of continental lithosphere extension. *Journal of Geophysical Research*, 96 :20161–20178. 9

BIBLIOGRAPHIE

- Chang, S. and Van der Lee, S. (2011). Mantle plumes and associated flow beneath Arabia and East Africa. *Earth and Planetary Science Letters*, 302 :448–454. doi : 10.1016/j.epsl.2010.12.050. 13
- Civiero, C., Armitage, J. J., Goes, S., and Hammond, J. O. S. (2019). The seismic signature of upper-mantle plumes : Application to the northern East African Rift. *Geochemistry, Geophysics, Geosystems*, 20 :6106–6122. doi : 10.1029/2019GC008636. 7, 13
- Clements, T. and Denolle, M. A. (2018). Tracking groundwater levels using the ambient seismic field. *Geophysical Research Letters*, 45 :6459–6465. doi : 10.1029/2018GL077706. 28
- Collier, J. S., Minshull, T. A., Hammond, J. O. S., Whitmarsh, R. B., Kendal, J. M., Sansom, V., Lane, C. I., and Rumpker, G. (2009). Factors controlling the degree of magmatism during continental break-up : new insights from a wide-angle seismic experiment across the conjugate Seychelles-Indian margins. *Journal of Geophysical Research*, 114(B03101). doi : 10.1029/2008JB005898. 10
- Condon, L. E., Markovich, K. H., Kelleher, C. A., McDonnell, J. J., Ferguson, G., and McIntosh, J. C. (2020). Where is the bottom of a watershed. *Water Resources Research*, 56. doi : 10.1029/2019WR026010. 25, 27
- Coulthard, T. J., Neal, J. C., and Ramirez, P. D. B., de Almedia, G. A. M., and Hancock, G. R. (2013). Integrating the LISFLOOD-FP 2D hydrodynamic model with the CAESAR model : implications for modelling landscape evolution. *Earth Surface Processes and Landforms*, 38 :1897–1906. doi : 10.1002/esp.3478. 26, 27
- Devauchelle, O., Petroff, A. P., Seybold, H. F., and Rothman, D. H. (2012). Ramification of stream networks. *Proceedings of the National Academy of Science*, 109 :20832–20836. doi : 10.1073/pnas.1215218109. 25, 27
- Dietrich, W. E., Bellugi, D. G., Sklar, L. S., Srock, J. D., Heimsath, A. M., and Roering, J. J. (2003). Geomorphic transport laws for predicting landscape form and dynamics. In Wilcock, P. R. and Iverson, R. M., editors, *Prediction in Geomorphology*, volume 135 of *Geophysical Monograph*, pages 1–30. American Geophysical Union. doi : 10.1029/135GM09. 17
- Dodds, P. S. and Rothman, D. H. (2000). Geometry of river networks. I. Scaling, fluctuations and deviations. *Physical Review E*, 63(016115). doi : 10.1103/PhysRevE.63.016115. 18, 27
- Duller, R. A., Armitage, J. J., Manner, H. R., Grimes, S., and Dunkley Jones, T. (2019). Delayed sedimentary response to abrupt climate change at the Paleocene-Eocene boundary, northern Spain. *Geology*, 47 :159–162. doi : 10.1130/G45631.1. 20
- Duller, R. A., Whittaker, A. C., Fedele, J. J., Whitchurch, A. L., Springett, J., Smithells, R., Fordyce, S., and Allen, P. A. (2010). From grain size to tectonics. *Journal of Geophysical Research*, 115(F03022). doi : 10.1029/2009JF001495. 19, 20
- Eksinchol, I., Rudge, J. F., and MacLennan, J. (2019). Rate of melt ascent beneath Iceland from the magmatic response to deglaciation. *Geochemistry, Geophysics, Geosystems*, 20 :2585–2605. doi : 0.029/2019GC008222. 14
- Elliot, T. and Spiegelman, M. (2014). Melt migration in oceanic crustal production : A u-series perspective. In *Treatise on Geochemistry*, pages 543–581. Elsevier, 2nd edition. doi : 10.1016/B978-0-08-095975-7.00317-X. 6
- Emry, E. L., Shen, Y., Nyblade, A. A., Flinders, A., and Bao, X. (2009). Upper mantle earth structure in Africa from full-wave ambient noise tomography. *Geochemistry, Geophysics, Geosystems*, 20 :120–147. doi : 10.1029/2018GC007804. 13

BIBLIOGRAPHIE

- Fan, Y., Clarck, M., Lawrence, D. M., Swenson, S., Band, L. E., Brantly, S. L., and et al (2019). Hillslope hydrology in global change research and earth system modeling. *Water Resources Research*, 55 :1737–1772. doi : 10.1029/2018WR023903. **27**
- Fedele, J. J. and Paola, C. (2007). Similarity solutions for alluvial sediment fining by selective deposition. *Journal of Geophysical Research*, 112(F02038). doi : 10.1029/2005JF000409. **19**
- Feynman, R. P., Leighton, R. B., and Sands, M. (1964). *The Feynman Lectures on Physics*. Addison Wesley, Menlo Park, California. **27**
- Fitton, J. G., Saunders, A. D., Larsen, L. M., Hardarson, B. S., and Norry, M. J. (1998). Volcanic rocks from the southeast Greenland margin at 63°N : composition, petrogenesis, and mantle sources. *Proceedings of the Ocean Drilling Program, Scientific Results*, 152 :331–350. **6**
- Forsyth, D. W., Webb, S. C., Dorman, L. M., and Shen, Y. (1998). Phase velocities of Rayleigh waves in the MELT experiment on the East Pacific Rise. *Science*, 280 :1235–1238. **14**
- Franken, T., Armitage, J. J., Fuji, N., and Fournier, A. (2020). Seismic wave-based constraints on geodynamical processes : an application to partial melting beneath the Réunion island. *Geochemistry, Geophysics, Geosystems*. doi : TBA. **7, 14, 16, 24**
- Garcia-Castellanos, D. (2002). Interplay between lithospheric flexure and river transport in foreland basins. *Basin Research*, 14 :89–04. doi : doi.org/10.1046/j.1365-2117.2002.00174.x. **27**
- Goes, S., Armitage, J. J., Harmon, N., Huismans, R., and Smith, H. (2012). Low seismic velocities below mid-ocean ridges : Attenuation vs. melt retention. *Journal of Geophysical Research*, 117 :B12403. doi : 10.1029/2012JB009637. **5, 7, 9, 14, 24**
- Guérin, A., Devauchelle, O., Robert, V., Kitou, T., Dessert, C., Quiquerez, A., Allemand, P., and Lajeunesse, E. (2019). Stream-discharge surges generated by groundwater flow. *Geophysical Research Letters*, 46 :7447–7455. doi : 10.1029/2019GL08229. **28**
- Guerit, L., Métivier, F., Devauchelle, O., Lajeunesse, E., and Barrier, L. (2014). Laboratory alluvial fans in one dimension. *Physical Review E*, 90(022203). doi : 10.1103/PhysRevE.90.022203. **17**
- Hack, J. T. (1957). Studies of longitudinal profiles in Virginia and Maryland. *U.S. Geological Survey Professional Paper*, 294-B(1). **18**
- Hammond, J. O. S., Kendall, J. M., Stuart, G. W., Keir, D., Ebinger, C., Ayele, A., and Belachew, M. (2011). The nature of the crust beneath the afar triple junction : evidence from receiver functions. *Geochemistry Geophysics Geosystems*, 12 :Q12004. doi : 10.1029/2011GC003738. **12**
- Hammond, J. O. S., nd G W Stuart, J. M. K., Ebinger, C. J., Bastow, I. D., Keir, D., Ayele, A., Belachew, M., Goitom, B., Ogubazghi, G., and Write, T. J. (2013). Mantle upwelling and initiation of rift segmentation beneath the afar depression. *Geology*, 41 :635–638. doi : 10.1130/G33925.1. **13**
- Hampson, G. J. (2010). Sediment dispersal and quantitative stratigraphic architecture across an ancient shelf. *Sedimentology*, 57 :96–141. doi : 10.1111/j.1365-3091.2009.01093.x. **22**
- Hampson, G. J., Duller, R. A., Petter, A. L., Robinson, R. A. J., and Allen, P. A. (2014). Mass-balance constraints on stratigraphic interpretation of linked alluvial–coastal–shelfal deposits from source to sink : Example from Cretaceous Western Interior Basin, Utah and Colorado, USA. *Journal of Sedimentary Research*, 84 :935–960. doi : 10.2110/jsr.2014.78. **22**

BIBLIOGRAPHIE

- Harmon, N., Forsyth, D. W., and Weeranatne, D. S. (2009). Thickening of young pacific lithosphere from high-resolution rayleigh wave tomography : A test of the conductive cooling mode. *Earth and Planetary Science Letters*, 278 :96–106. doi : 10.1016/j.epsl.2008.11.025. 14
- Herzberg, C., Asimow, P. D., Arndt, N., Niu, Y., Lesher, C. M., Fitton, J. G., Cheedle, M. J., and Saunders, A. D. (2007). Temperatures in ambient mantle and plumes : Constraints from basalts, picrites, and komatiites. *Geochemistry Geophysics Geosystems*, 8. doi :10.1029/2006GC001390. 5
- Hewitt, I. J. (2010). Modelling melting rates in upwelling mantle. *Earth and Planetary Science Letters*, 300 :264–274. doi : 10.1016/j.epsl.2010.10.010. 7
- Hopper, J. R., Dahl-Jensen, T., Holbrook, W. S., Larsen, H. C., Lizarradle, D., Korenaga, J., Kent, G. M., and Kelemen, P. B. (2003). Structure of the SE Greenland margin from seismic reflection and refraction data : Implications for nascent spreading centre subsidence and asymmetric crustal accretion during North Atlantic opening. *Journal of Geophysical Research*, 108 :doi : 10.1029/2002JB001996. 10
- Horton, B. K., Constensius, K. N., and DeCelles, P. G. (2004). Tectonic control on coarse-grained foreland-basin sequences : an example from the Cordilleran foreland basin, Utah. *Geology*, 32 :637–640. doi : 10.1130/G20407.1. 22
- Howard, A. (1994). A detachment-limited model of drainage basin evolution. *Water Resources Research*, 30 :2261–2285. 25
- Howard, A. D. and Kerby, G. (1983). Channel changes in badlands. *Geological Society of America Bulletin*, 94 :739–752. 25
- Huybers, P. and Langmuir, C. H. (2009). Feedback between deglacation, volcanism, and atmospheric CO₂. *Earth and Planetary Science Letters*, 286 :479–49. doi : 10.1016/j.epsl.2009.07.014. 15
- IPCC (2014). Summary for policymakers. In Field, C. B., Barros, V. R., Dokken, D. J., Mach, K. J., Mastrandrea, M. D., Bilir, T. E., Chatterjee, M., Ebi, K. L., Estrada, Y. O., Genova, R. C., Girma, B., Kissel, E. S., Levy, A. N., MacCracken, S., Mastrandrea, P. R., and White, L. L., editors, *Climate Change 2014 : Impacts, Adaption and Vulnerability. Part A : Global and Sectoral Aspects. Contribution of Working Group II to the Fifth Assessment Report of the Intergovernmental Panel on Climate Change*, pages 1–32. Cambridge University Press, Cambridge, United Kingdom. 25
- Jull, M. and McKenzie, D. (1996). The effect of deglaciation on mantle melting beneath Iceland. *Journal of Geophysical Research*, 101(B10) :21815–21828. 14
- Katz, R. F., Spiegelman, M., and Langmuir, C. H. (2003). A new parameterization of hydrous mantle melting. *Geochemistry Geophysics Geosystems*, 4 :1073. doi : 10.1029/2002GC000433. 8
- Kaufman, P., Grotzinger, J. P., and McCormick, D. S. (1991). Depth-dependent diffusion algorithm for simulation of sedimentation in shallow marine depositional systems. *Bulletin - Kansas Geological Survey*, 233 :489–508. 22
- Keranen, K. M., Klemperer, S. L., Julia, J., Lawrence, J. F., and Nyblade, A. A. (2009). Low lower crustal velocity across Ethiopia : Is the Main Ethiopian Rift a narrow rift in a hot craton ? *Geochemistry Geophysics Geosystems*, 10(5). doi : 10.1029/2008GC002293. 9, 13

BIBLIOGRAPHIE

- Krystinik, L. F. and DeJarnett, B. B. (1995). Lateral variability of sequence stratigraphic framework in the Campanian and Lower Maastrichtian of the Western Interior Seaway. In Van Wagoner, J. C. and Bertram, G. T., editors, *Sequence Stratigraphy of Foreland Basin Deposits*, pages 11–26. American Association of Petroleum Geologists. 22
- Lacey, G. (1930). Stable channels in alluvium. In Grierson, W. W., editor, *Minutes of the Proceedings*, volume 229, pages 259–292. Institution of Civil Engineers Publishing. 26
- Leopold, L. B. and Maddock, T. (1953). The hydraulic geometry of stream channels and some physiographic implications. Technical Report 252, U.S. Geological Survey Professional Papers. 57 p. 26
- Lucazeau, F., Armitage, J., and Kadima Kabongo, E. (2015). Thermal regime and evolution of the Congo Basin as an intracratonic basin. In de Wit, M., Guillocheau, F., and de Wit, M., editors, *Geology and Resource Potential of the Congo Basin, Regional Geology Reviews*, pages 229–244. Springer, Berlin, Heidelberg. doi : 10.1007/978-3-642-29482-2_12. 5
- MacLennan, J., Jull, M., McKenzie, D., Slater, L., and Grönvold, K. (2002). The link between volcanism and deglaciation in Iceland. *Geochemistry Geophysics Geosystems*, 3(11, 1062). doi : 10.1029/2001GC000282. 14
- Maritan, A., Rinaldo, A., Rigon, R., Giacometti, A., and Rodriguez-Iturbe, I. (1996). Scaling laws for river networks. *Physical Review E*, 53 :1510–1515. 18
- Mazzullo, A., Stutzmann, E., Montagner, J., Kiselev, S., Maurya, S., Barruol, G., and Sigloch, K. (2017). Anisotropic tomography around la réunion island from rayleigh waves. *Journal of Geophysical Research – Solid Earth*, 122 :932–9148. doi : 10.1002/2017JB014354. 5, 15
- McKenzie, D. and O’Nions, R. K. (1991). Partial melt distribution from inversion of rare earth element concentrations. *Journal of Petrology*, 32 :1021–1091. 9
- McLaurin, B. T. and Steel, R. J. (2000). Fourth-order nonmarine to marine sequences, Middle Castle gate Formation, Book Cliffs, Utah. *Geology*, 28 :359–362. 22
- Michael, N. A., Whittaker, A. C., and Allen, P. A. (2013). The functioning of sediment routing systems using a mass balance approach : Example from the Eocene of the Southern Pyrenees. *Journal of Geology*, 121(581-606). doi : 10.1086/673176. 20
- Michael, N. A., Whittaker, A. C., Carter, A., and Allen, P. A. (2014). Volumetric budget and grain-size fractionation of a geological sediment routing system : Eocene Escanilla Formation, south-central Pyrenees. *Geological Society of America Bulletin*, 126 :585–599. doi : 10.1130/B30954.1. 21
- Miller, K. J., Zhu, W., Montési, L. G. J., and Gaetani, G. A. (2014). Experimental quantification of permeability of partially molten mantle rock. *Earth and Planetary Science Letters*, 388 :273–282. doi : 10.1016/j.epsl.2013.12.003. 7
- Minshull, T. A., Lane, C. I., Collier, J. S., and Whitmarsh, R. B. (2008). The relationship between rifting and magmatism in the northeastern Arabian Sea. *Nature Geoscience*, 1 :463–467. 10
- Nooner, S. L., Bennati, L., Calais, E., Buck, W. R., Hamling, I. J., Wright, T. J., and Lewis, E. (2009). Post-rifting relaxation in the Afar region, Ethiopia. *Geophysical Research Letters*, 36(21) :L21308. doi : 10.1029/2009GL040502. 12
- Obrodrovich, J. D. (1993). A Cretaceous time scale. In Caldwell, W. G. E. and Kauffman, E. G., editors, *Evolution of the Western Interior Basin*, Special Paper, 39, pages 379–378. Geological Association of Canada. 22

BIBLIOGRAPHIE

- Paola, C., Heller, P. L., and Angevine, C. L. (1992). The large-scale dynamics of grain-size variation in alluvial basins, 1 : Theory. *Basin Research*, 4 :73–90. doi : 10.1111/j.1365-2117.1992.tb00145.x. [17](#), [18](#), [19](#)
- Paola, C. and Seal, R. (1995). Grain-size patchiness as a cause of selective deposition and downstream fining. *Water Resources Research*, 31 :1395–1407. doi : 10.1029/94WR02975. [20](#)
- Petersen, K. D., Armitage, J. J., Nielsen, S. B., and Thybo, H. (2015). Mantle temperature as a control on the time scale of thermal evolution of extensional basins. *Earth and Planetary Science Letters*, 409 :61–70. doi : 10.1016/j.epsl.2014.10.043. [9](#), [24](#)
- Reilinger, R. and McClusky, S. (2011). Nubia – Arabia – Eurasia plate motions and the dynamics of Mediterranean and Middle East tectonics. *Geophysical Journal International*, 186 :971–979. doi : 10.1111/j.1365-246X.2011.05133.x. [12](#)
- Ribe, N. M. (1985). The generation and composition of partial melts in the earth's mantle. *Earth and Planetary Science Letters*, 73 :361–376. [7](#)
- Rigon, R., Rodriguez-Iturbe, I., Maritan, A., Giacometti, A., Tarboton, D. G., and Rinaldo, A. (1996). On Hack's law. *Water Resources Research*, 32 :3367–3374. [18](#)
- Robinson, R. A. J. and Slingerland, R. L. (1998). Origin of fluvial grain-size trends in a foreland basin : the Pocono Formation on teh Central Appalachian Basin. *Journal of Sedimentary Research*, 68 :473–486. [22](#)
- Rooney, T. O., Herzberg, C., and Bastow, I. D. (2012). Elevated mantle temperature beneath East Africa. *Geology*, 40 :27–30. doi :10.1130/G32382.1. [5](#)
- Ros, E., Pérez-Gussinyé, M., Araujo, M., Thoaldo Romeiro, M., Andres-Martinez, M., and Morgan, J. (2017). Lower crustal strength controls on melting and serpentinization at magma-poor margins : Potential implications for the south atlantic. *Geochemistry Geophysics Geosystems*. 10.1002/2017GC007212. [9](#)
- Rychert, C. A., Hammond, J. O. S., Harmon, N., Kendall, J. M., Keir, D., Ebinger, C., Bastow, I. D., Ayele, A., Belachew, M., and Stuart, G. (2012). Volcanism in the Afar Rift sustained by decompression melting with minimal plume influence. *Nature Geoscience*, 5 :406–409. doi : 10.1038/ngeo1455. [14](#)
- Rychert, C. A., Harmon, N., and Armitage, J. J. (2018). Seismic imaging of thickened lithosphere resulting from plume pulsing beneath Iceland. *Geochemistry, Geophysics, Geosystems*, 19 :1789–1799. doi : 10.1029/2018GC007501. [14](#)
- Rychert, C. A., Harmon, N., and Ebinger, C. (2014). Receiver function imaging of lithospheric structure and the onset of melting beneath the Galápagos Archipelago. *Earth and Planetary Science Letters*, 388 :156–165. doi : 10.1016/j.epsl.2013.11.027. [14](#)
- Schoorl, J. M., Sonneveld, M. P. W., and Veldkamp, A. (2000). Three-dimensional landscape process modelling : the effect of dem resolution. *Earth Surface Processes and Landforms*, 25 :1025–1034. [19](#), [26](#), [27](#)
- Schorghofer, N. and Rothman, D. H. (2002). Acausal relations between topographic slope and drainage area. *Geophysical Research Letters*, 29(13) :1633. doi : 10.1029/2002GL015144. [27](#)
- Scott, D. R. (1992). Small-scale convection and mantle melting beneath mid-ocean ridges. In Phipps Morgan, J., Blackman, D. K., and Sinton, J. M., editors, *Mantle flow and melt generation at mid-ocean ridges*, volume Geophysical Monograph 71, pages 327–352. American Geophysical Union. [7](#)

BIBLIOGRAPHIE

- Scott, D. R. and Stevenson, D. J. (1989). A self-consistent model of melting, magma migration and buoyancy-driven circulation beneath mid-ocean ridges. *Journal of Geophysical Research*, 94(B3) :2973–2988. [7](#)
- Simpson, G. and Schlunegger, F. (2003). Topographic evolution and morphology of surfaces evolving in response to coupled fluvial and hillslope sediment transport. *Journal of Geophysical Research*, 108(B62300). doi : 10.1029/2002JB002162. [19](#)
- Sinton, J., Grönvold, K., and Saemundsson, K. (2005). Postglacial eruptive history of the Western Volcanic Zone, Iceland. *Geochemistry, Geophysics, Geosystems*, 6(Q12006). doi : 10.1029/2005GC001021. [14](#)
- Skinner, C. J., Coulthard, T. J., Schwanghart, W., Vande Weil, M. J., and Hancock, G. (2018). Global sensitivity analysis of parameter uncertainty in landscape evolution models. *Geoscientific Model Development*, 11 :4873–4888. doi : 10.5194/gmd-11-4873-2018. [26](#)
- Smith, T. R. and Bretherton, F. P. (1972). Stability and conservation of mass in drainage basin evolution. *Water Resources Research*, 8 :1506–1529. doi : 10.1029/WR008i006p01506. [18](#)
- Spiegelman, M. (1996). Geochemical consequences of melt transport in 2-D : The sensitivity of trace elements to mantle dynamics. *Earth and Planetary Science Letters*, 139 :115–132. [9](#)
- Sternberg, H. (1875). Untersuchungen über Längen und Querprofil geschiebeführnde Flüsse. *Zeitschrift fur das Bauwesen*, 25 :483–506. [20](#)
- Syvitski, J. P. and Milliman, J. D. (2007). Geology, geography, and humans battle for dominance over the delivery of fluvial sediment to the coastal ocean. *Journla of Geology*, 115 :1–19. doi : 10.1086/509246. [19](#)
- Taposeea, C. A., Armitage, J. J., and Collier, J. S. (2017). Asthenosphere and lithosphere structure controls on early onset oceanic crust production in the southern south atlantic. *Tectonophysics*, 716 :4–20. doi : 10.1016/j.tecto.2016.06.026. [10](#)
- Tarboton, D. G., Bras, R. L., and Rodriguez-Iturbe, I. (1990). Comment on “on the fractal dimension of stream network” by paolo la barbera and renzo rosso. *Water Resources Research*, 26 :2243–2244. doi : 10.1029/WR026i009p02243. [18](#)
- Temme, A. J. A. M., Armitage, J. J., Attal, M., van Gorp, W., Coulthard, T. J., and Schoorl, J. M. (2017). Choosing and using landscape evolution models to inform field stratigraphy and landscape reconstruction studies. *Earth Surface Processes and Landforms*, 42 :2167–2183. doi : 10.1002/esp.4162. [26](#)
- Van de Weil, M. J., Coulthard, T., Macklin, M., and Lewin, J. (2007). Embedding reach-scale fluvial dynamics within the CAESAR cellular automaton landscape evolution model. *Geomorphology*, 90 :283–301. doi : 10.1016/j.geomorph.2006.10.024. [26](#)
- Weatherley, S. M. and Katz, R. F. (2016). Melt transport rates in heterogeneous mantle beneath mid-ocean ridges. *Geochimica et Cosmochimica Acta*, 172 :39–54. doi : 10.1016/j.gca.2015.09.029. [14](#)
- Whipple, K. X. and Tucker, G. E. (2002). Implications of sediment-flux-dependent river incision models for landscape evolution. *Journal of Geophysical Research*, 107(B2, 2039). doi : 10.1029/2000JB000044. [17](#)
- White, R. S., Smith, L. K., Roberts, A. W., Christie, P. A. F., Kusznir, N. J., and the rest of the iSIMM Team (2008). Lower-crustal intrusion on the North Atlantic continental margin. *Nature*, 452 :460–465. doi : 10.1038/nature06687. [10](#)

BIBLIOGRAPHIE

Whittaker, A. C., Cowie, P. A., Attal, M., Tucker, G. E., and Roberts, G. P. (2007). Bedrock channel adjustment to tectonic forcing : Implications for predicting river incision rates. *Geology*, 35 :103–106. doi : 10.1130/G23106A.1. **26**